

Digital Holographic Microscopy Based on Graphic Process Unit

Han-Yen Tu¹, Yi-Ta Lee², and Chau-Jern Cheng²

¹Department of Electrical Engineering, Chinese Culture University, Taipei 11114, Taiwan

²Institute of Electro-Optical Science and Technology, National Taiwan Normal University
Taipei 11677, Taiwan

Abstract— This paper presents a fast computation and processing for off-axis digital holographic microscopy (DHM) based on a graphic processing unit (GPU). DHM is a highly effective imaging technique capable of reconstructing the three-dimensional (3-D) structure by retrieving the amplitude and phase information of the specimen. To obtain the 3-D profile of the specimen, numerous calculations for image reconstruction are required. For achieving enormous calculations of image reconstruction and improving the computational speed for their practical applications, we have performed the preceding computation and processing of DHM through the GPU. This method leads to effectively accelerate the computation performance with the parallel computing architecture and algorithm. Further, we perform accurate 3-D profile of the specimen by the use of filtering algorithm adjusting the contrast of reconstructed images. The proposed GPU-based DHM provides the potential for significantly speed-up of numerical calculation compared to the counterpart of the central processing unit (CPU). The high-speed cost-effective computational capability derives 3-D profile measurement in real time and on-line processing.

1. INTRODUCTION

Digital holographic microscopy (DHM) [1] is a highly effective imaging technique recording the complex (amplitude and phase) wavefront [2] simultaneously of a specimen in digital form. 3-D object wavefront can be recorded using a charge-coupled device (CCD) or a complementary metal oxide semiconductor (CMOS). Their 3-D structure can be reconstructed by digital processing from the recorded interference holograms. To obtain the 3-D profile of the specimen, numerous calculations for image reconstruction and phase unwrapping procedures are required. However, these intensive computations made real-time reconstruction difficult even if we use a modern central processing unit to calculate. These enormous calculations need to be accelerated for the development of fast numerical calculation especially for real-time imaging applications. In order to accelerate the computational speed for 3-D image process, many effective methods are developed. For example, field programmable gate array (FPGA) technology is an effective means using hardware to obtain fast computational speed [3, 4]. However, this approach is restricted by high design cost and long development time. Another perspective candidate for intensive computation with highly parallel processing architecture, graphic processing units, which can operate 32-bit floating-point addition, multiplication, and multiply-add instructions in the attractively low cost hardware and short development time. In our previous study [5], we found the wrapped phase maps derived from their digital holograms are required to be unwrapped to continuous phase maps without loss of quality. The intensive computation of phase unwrapping for 3-D profile measurement was accelerated by a graphic processing unit. The GPU-based DHM system can obtain unwrapped phase images from digital holograms, and yield the accurate continuous phase and geometrical profile of the microlens array in less computation time than the CPU-based implementation. The GPU's algorithm performs tens of times faster than those of CPU. In this paper, we also describe and experimentally demonstrate a real-time GPU-based DHM system using the GPU with parallel computing architecture and algorithm for remarkably superior 3-D image numerical calculation.

2. GPU-BASED DIGITAL HOLOGRAPHIC MICROSCOPY SYSTEM

To obtain the 3-D profile of the specimen, numerous calculations for the Fresnel diffraction and phase unwrapping procedures are required. The Fresnel diffraction and angular spectrum can be accelerated by the fast fourier transform (FFT) algorithm. In this section, we describe our real-time DHM system using the GPU chip and evaluate the performance subsequently. Fig. 1 is a schematic diagram of our real-time DHM using GPU. It primarily comprises an off-axis digital holographic microscope optical system and a GPU-based real-time calculation system. The DHM system has a modified Mach-Zehnder interferometric architecture and a diode-pump solid state (DPSS) laser with a wavelength of 532 nm coherent light source. The CMOS camera offers a maximum resolution

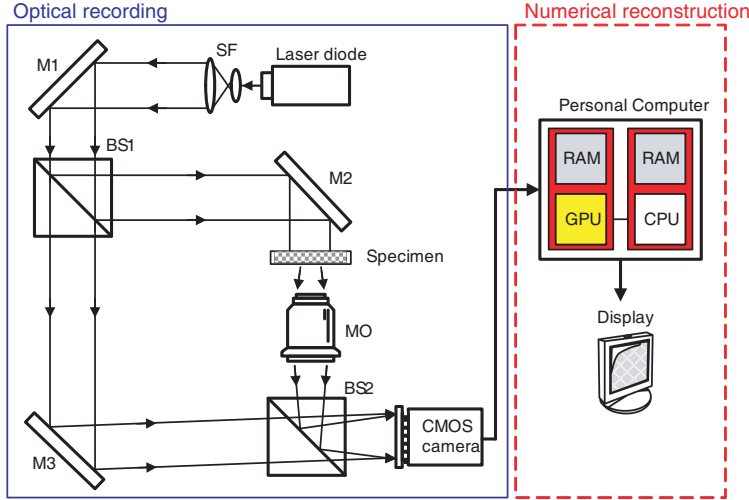


Figure 1: GPU-based digital holographic microscope system (SF: spatial filter; BS1, BS2: beam splitters; M1, M2, M3: mirrors; MO: objective).

for 1280×1024 pixel size and a pixel pitch of $5.2 \times 5.2 \mu\text{m}^2$. As the laser collimated and expanded to the beam splitter (BS1), the output split into two beams, the object and reference then recombined with each other using another beam splitter (BS2). Interference fringe patterns were recorded on the CMOS camera. The personal computer has an Intel Core2Quad Q8400 CPU, with a clock rate of 2.66 GHz and a random access memory of 3.25 Gbytes controls the GPU and the CMOS camera. The GPU card with Geforce GTX275 made by Nvidia (240 stream processors). The clock rate and the memory of GPU are 1.4 GHz and 896 Mbytes, respectively. The memory bandwidth of the GPU are 127 GB/s. The calculation capacity is estimated to be around 1008 GFLOPs (floating-point number operations per second). The compute unified device architecture (CUDA) provides the programming environment.

One can numerically reconstruct the 3-D object by the Fresnel diffraction of the object wave from the CCD plane to the image plane at a reconstruction distance z expressed as

$$U(\xi', \eta', z) = \frac{e^{j k z}}{j \lambda z} \iint_{-\infty}^{+\infty} U_O(x', y') e^{j \frac{\pi}{\lambda z} [(\xi' - x')^2 + (\eta' - y')^2]} dx' dy' \quad (1)$$

The equation can be rewritten in the form as

$$U_o(u, v, z) = \frac{e^{j k z}}{j \lambda z} e^{j \pi \lambda z (u^2 + v^2)} \Im \left\{ U_O(x', y') e^{j \frac{\pi}{\lambda z} (x'^2 + y'^2)} \right\} \quad (2)$$

If the CMOS camera offers $M \times N$ pixel size and a pixel pitch of $\Delta x \times \Delta y$, then the discrete form of (2) in frequency space can be expressed as

$$U_o(m, n) = \frac{e^{j k z}}{j \lambda z} e^{j \pi \lambda z \left(\frac{m^2}{M^2 \Delta x^2} + \frac{n^2}{N^2 \Delta y^2} \right)} \Im \left\{ U_i(k, l) e^{j \frac{\pi}{\lambda z} (k^2 \Delta x^2 + l^2 \Delta y^2)} \right\} \quad (3)$$

We can reconstruct the 3-D object image by modeling the light propagation parallel to the hologram plane. The mathematically described of the Fresnel transform can be implemented easily using the FFT. Notably, we can use the effectively operate of CUFFT library [6] on the GPU. The recorded interference fringe patterns on the CMOS camera can be reconstructed by multiple-threading technique. Multiple processors use the same kernel to execute the same code on the parallel computing architecture. Thus intensive computation can be processed with parallel algorithms. The kernel modules will be sent to a set of threads to excuse heavy computation for numerical processing speed-up. 3-D image will be reconstructed from the recorded holograms in real-time by the following executed procedures. Input the interference fringe patterns and filter masks from a host computer to the device memory of the GPU first. Then the host computer invokes the corresponding “Kernels” to the device and their results will be stored in the device

memory.

Kernel 1 Calculate the FFT of $U_O(k, l)$ and assume $U_O(K, L) = FFT\{U_O(k, l)\}$.

Kernel 2 Execute the filter processing for $U_O(K, L)$ then assume $U'_O(K, L) = Filter\{FFT\{U_O(k, l)\}\}$.

Kernel 3 Calculate the inverse FFT of the filter matrix $U'_O(K, L)$, let $U_O(k, l) = FFT^{-1}\{U'_O(K, L)\}$.

Kernel 4 Calculate $U_1(k, l)$ by multiplying $e^{j\frac{\pi}{\lambda z}(k^2\Delta x^2+l^2\Delta y^2)}$ and assume $U_1(k, l) = U_O(k, l) \cdot e^{j\frac{\pi}{\lambda z}(k^2\Delta x^2+l^2\Delta y^2)}$.

Kernel 5 Apply a discrete FFT to the product $U_1(m, n) = FFT\{U_1(k, l)\}$.

Kernel 6 Do multiplication with phase factor of $U_2(m, n) = \frac{e^{jkz}}{j\lambda z} e^{j\pi\lambda z(\frac{m^2}{M^2\Delta x^2}+\frac{n^2}{N^2\Delta y^2})}$.

Kernel 7 Calculate the multiplication of U_1 and U_2 , then get $U_O(m, n) = U_1(m, n) \cdot U_2(m, n)$.

We can download the reconstruction of three-dimensional image information from the GPU to display the 3-D image on the host computer. For 3-D display technology, we render the device memory directly to avoid superabundant copy of data transfer over the system bus. This is attractive for rapid processing for vast calculations and on-line processing. CUDA programming provides a suitable environment for GPU-based application. Fresnel transform calculations can be expected to perform in real-time in an inexpensive way.

3. EXPERIMENT RESULTS

For achieving enormous calculations of image reconstruction, we have performed the preceding computation and processing of DHM through parallel computing architectures and algorithms. We tested our implementation on the above development environment with Microsoft Windows XP Professional SP2 as the operating system and Visual Studio 2008 Professional as the C compiler. For simplicity, the hologram captured by the CMOS camera was cropped to 512×512 pixels to fit the field of view of the objective of the DHM system. For measuring different specimens, the GPU-based DHM system can be equipped with different objectives to measure the profile of the specimen at a lateral resolution of about $1.3 \mu\text{m}$. This method leads to effectively accelerate the computation performance. Fig. 2 shows the execution time for a single 2D FFT calculation for different resolutions and settings for 100 iterations. The time required to perform the 2D FFT for 512×512 pixels image is 0.28 ms in average. In contrast, the time required using a CPU only is around 26 ms. Our GPU implementation of 2D FFTs calculation of an image provides a relative speedup around 100 times faster compared to the CPU implementation. The results performed from the sizes up to 1024×1024 and 2048×2048 image are also demonstrated significant ability to speed up. Thus, this approach is useful even for large digital holograms, requiring more memory than currently available on graphics hardware. Also, we applied the same GPU-based DHM system to perform the Fresnel diffraction calculation. Fig. 3 shows the performance of 100 iterations on a host computer and GPU for Fresnel diffraction calculation. The GPU-based implementation outperforms a single CPU-based, and a speedup of over tens of times for Fresnel diffraction calculation.

Further, we accomplish accurate 3-D profile measurement of the specimen by the use of filtering adjustment technique and derive the contrast of reconstructed images. In the experiment, USAF

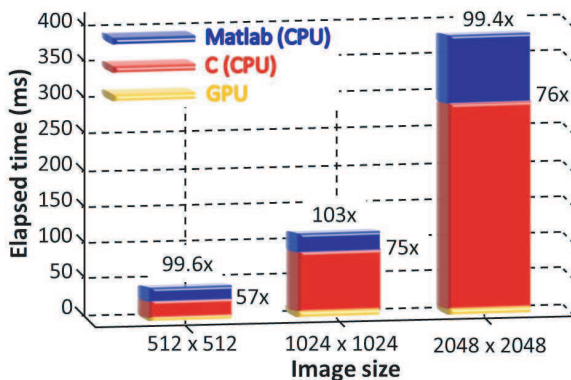


Figure 2: Performance of 100 iterations on a host computer and GPU of 2D FFTs calculation.

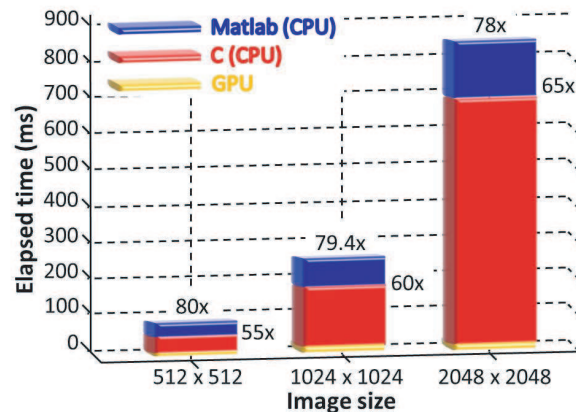


Figure 3: Performance of 100 iterations on a host computer and GPU of Fresnel diffraction calculation.

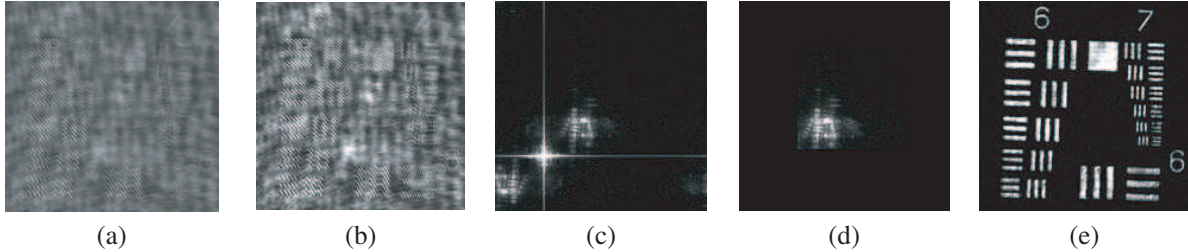


Figure 4: Reconstructed phase images of resolution target (a) off-axis digital hologram, (b) unfiltered reconstructed image, (c) spectrum of unfiltered processing, (d) spectrum of filtered processing and (e) filtered reconstructed image.

1951 resolution target was tested using the DHM system, yielding the experimental results shown in Fig. 4. Fig. 4 shows the proposed GPU-based DHM with filtering adjustment algorithm and performs the image with superior quality from the hologram. In our previous study [5], phase unwrapping procedure can be accelerated using the same GPU-based DHM system. These results verify the GPU-based DHM system is a highly effective imaging technique, as well as the high quality 3D display, capable of 3-D real-time reconstruction.

4. CONCLUSION

In summary, this study proposed and experimentally demonstrated that it is possible to perform real-time reconstruction of digital holograms using GPU-implementation on graphics hardware for off-axis DHM. The GPU-based DHM system can effectively accelerate the intensive computation of phase unwrapping and 3-D image reconstruction from digital holograms with the parallel computing architectures and algorithms. The proposed study is evaluated and compared to a CPU-based implementation can provide over tens of times speedup for image size of 2048×2048 . In our future work, we are planning to develop another filtering algorithm and phase-unwrapping method to implement superior image quality and computational speed for their practical applications.

ACKNOWLEDGMENT

The authors would like to thank the National Science Council of the Republic of China, Taiwan, for financially supporting this research under Contract No. NSC 99-2221-E-129-001.

REFERENCES

1. Cuche, E., P. Marquet, and C. Depeursinge, “Simultaneous amplitude-contrast and quantitative phase — Contrast microscopy by numerical reconstruction of Fresnel off-axis holograms,” *Appl. Opt.*, Vol. 38, 6994–7001, 1999.
2. Cheng, C. J., Y. C. Lin, M. L. Hsieh, and H. Y. Tu, “Complex modulation characterization of liquid crystal spatial light modulators using digital holographic microscopy,” *Jpn. J. Appl. Phys.*, Vol. 47, 3527–3529, 2008.
3. Masuda, N., T. Ito, K. Kayama, H. Kono, S. Satake, T. Kunugi, and K. Sato, “Special purpose computer for digital holographic particle tracking velocimetry,” *Opt. Express*, Vol. 14, 603–608, 2006.
4. Abe, Y., N. Masuda, H. Wakabayashi, Y. Kazo, T. Ito, S. Satake, T. Kunugi, and K. Sato, “Special purpose computer system for flow visualization using holography technology,” *Opt. Express*, Vol. 16, 7686–7692, 2008.
5. Tu, H. Y., Y. T. Lee, C. J. Cheng, and W. J. Hwang, “Real-time phase unwrapping of digital holographic microscopy using graphic processing unit,” *International Conference on Optics and Photonics in Taiwan*, 2010.
6. Nvidia, “CUDA FFT Library Version 1.1 Reference Documentation,” Nvidia, 2007.

A Study of Optical Design of Blu-ray Pickup Head System with Liquid Crystal Element

Chih-Ta Yen¹, Hui-Chen Yeh², Yi-Chin Fang³, and Jui-Hsin Hsu³

¹Department of Electrical Engineering, National Formosa University, Yunlin, Taiwan

²Advanced Optical Design Center

National Kaohsiung First University of Science and Technology, Taiwan

³Department of the Mechanical and Automation Engineering

National Kaohsiung First University of Science and Technology, Taiwan

Abstract— This research proposes a newly developed module: a newly developed optical design and a concept of active compensation method of Blu-ray pick up head system [1] with liquid crystal element. A hole-pattern electrode liquid crystal optics with input of external voltage are employed, that generates a symmetric non-uniform electrical field in the liquid crystal layer; this will direct liquid crystal molecules into the appropriate gradient refractive indices distribution, then resulting in convergence or divergence of specific light beam. From point view of optical design, liquid crystal optics delivers fast and the most important, active compensation through optical design when errors occur. Simulation and tolerance analysis work will be done by Code V [2] software inclusive of different tolerance analysis such as de-focus, tilt, de-center and their related compensation. The results conclude that optical design with liquid crystal optics as an active compensation device reach success with elimination of aberrations up to 46% compared to traditional ones.

1. INTRODUCTION

Optical head and its compensation design play the role at optical storage system because DVD systems are always sensitive to vibrations. The traditional method of compensating method is an objective lens works with suspension actuator then has system compensated mechanically [3]. However, modern BR-DVD storage system with high numerical aperture (NA) indicate that advanced compensation of focus and tracking error play the significant role at such kind of system [1]. Therefore, in this research, a newly developed optical design and a concept of active compensation method of Blu-ray pick up head system with liquid crystal element is proposed in this research.

A hole-pattern electrode liquid crystal optics with input of external voltage are employed, that generates a symmetric non-uniform electrical field in the liquid crystal layer; this will direct liquid crystal molecules into the appropriate gradient refractive indices distribution, then resulting in convergence or divergence of specific light beam. In other words, with electrical field, LC lens might be driven the normal molecules into different directions so as to be modulated as the Gradient-Index (GRIN) pattern [4].

There are many different types of LC lens such as electrode arrays, a hole-patterned electrode, a resistive electrode, a glass lens sandwiched between two LC layers, concentric ring electrodes, and spherical electrode, etc [5]. Several researches have announced the LC lens deliver positive and negative optical power as well as the effective focus length within infinity to 10 cm.

In this study, liquid crystal optics delivers fast and the most important, active compensation through optical design when errors occur. Section 2 will introduce optics and its fundamental rules. Section 3 will demonstrate optical design and its specification. Section 4 will be simulation work and analysis then following are Section 5, conclusion.

2. OPTICS AND ITS FUNDAMENTAL RULES

Aberrations play the role at performance of optical system. Aberrations can be defined as on axis and off-axis. On axis aberrations are like spherical aberration, coma, which is commonly seen at optical storage system due to high N.A. Off-axis aberration such as astigmatism, distortion and field curvature are rarely found at optical storage system due to limitation of image height. In most cases, Astigmatism is found at optical storage system only if decenter or tilt occurs.

2.1. The Zoom Principle of LC Lens

LC lens might vary its optical power thanks to external electric field shift of liquid crystal molecules. With inherent properties of birefringence liquid crystal, the refractive index can be varied as gradient distribution in order to make light convergent or divergent, that was similar to the refractive index gradient index (GRIN) lens. The refractive index changes in the formula as following [2]:

$$n(r) = n_o[1 - A * r^2/2] \quad (1)$$

r : The lens from the center to both sides of the radial distance; A : The gradient constant of refractive index; n_o : The refractive index at axis; $n(r)$: The refractive index from the optical axis r .

2.2. Discussion of Pupil Shift Aberrations

The imaging optical system as shown in reference [6], we can obtain the relationship between old and new aberration function's coefficient as following:

$$\text{Spherical aberration coefficient: } A_{s2} = A_{s1} \quad (2)$$

$$\text{Coma coefficient: } A_{c2} = A_{c1} - 4bA_{s1} \quad (3)$$

$$\text{Astigmatism coefficient: } A_{a2} = A_{a1} - 2bA_{c1} + 4b^2A_{s1} \quad (4)$$

$$\text{Field curvature coefficient: } A_{d2} = A_{d1} - bA_{c1} + 2b^2A_{s1} \quad (5)$$

$$\begin{aligned} \text{Distortion coefficient: } A_{t2} &= A_{t1} - 2b(A_{a1} + A_{d1}) + 3b^2A_{s1} - 4b^3A_{s1} \\ \text{where } b &= (L_1 - L_2)h'/r_1L_2 \text{ and } r_1 \text{ is radius of the exit pupil.} \end{aligned} \quad (6)$$

3. OPTICAL DESIGN AND SPECIFICATION

There are two different designs of Blu-ray pick up head system in this research. We set the aperture stops on objective lens like traditional ones and another is on LC lens as a newly developed lens. The ratio of optical power of objective lens is 85% and liquid crystal lens is 15%. The parameters of Blu-ray pick up head system [1].

3.1. Optical Design of Objective

At on-axis condition, the relationship of radius of objective lens D_o , numerical aperture NA_o and effective focal length f_o as following equation:

$$\frac{D_o}{2} = NA_o \times f_o \quad (7)$$

According to patent [7] No. US7123424, the associated coefficients can be calculated as Table 1.

3.2. Optical Design of LC Lens

Hole-patterned liquid crystal lens are able to vary its optical power. With LC optics, lens could be zoomed as defined. Normally, compensation of optical storage system needn't vary too much with regard to optical power so that we choose to use single-crystal, three-electrode, dual voltage-controlled hole-patterned liquid crystal lens [5, 8, 9]. The focus length of LC lens can be controlled by two external voltages. Liquid crystal material is a single axis, nematic liquid crystal with horizontal alignment. Modulated voltage vary the direction of liquid crystal molecules to generate positive and negative optical power. We choose the material of LC lens is Merck 6080 and $\Delta n = 0.1975$. The parameters of LC lens as shown in Table 2.

Table 1: Objective lens parameters.

f_o	NA_o	D_o
1.72 mm	0.85	2.924 mm

Table 2: Liquid crystal material parameters.

n_e	n_o	$\Delta n = n_e - n_o$
1.7062	1.5087	0.1975

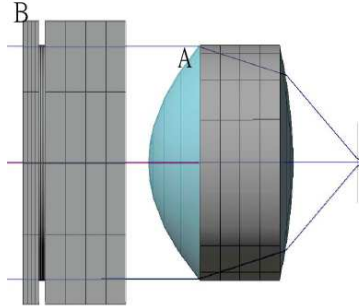


Figure 1: Transmission LC lens Blu-ray pick up head system.

Table 3: The percentage comparison of between on LC lens and traditional objective lens.

Defocus	(LC Lens-objective) /Object lens		
	Spherical aberration	Coma	Astigmatism
-50 μm	-0.48%	35.97%	-29.36%
0 μm	-89.23%	-0.26%	-16.55%
+50 μm	-0.39%	-143.43%	-2.10%

As shown in Fig. 1, compared objective lens and hole-patterned LC lens with different setting of the aperture stops: traditional ones on objective lens (at place A) and newly developed ones on hole-patterned LC lens (at place B), respectively. In this research, design of two optimal Blu-ray pick up head system by Code V software.

4. SIMULATION RESULTS AND DISCUSSIONS

4.1. Methodology

With regard to compensation of tolerance from objective lens center shift and tilt, the traditional compensation depends on whole objective lens working as the actuator with aperture stop on it. In this study, the LC lens with varied focal length works as an aperture stop not only take the advantage of being the actuator with more variations for active optimization compared to traditional ones but also improve the optical performance of BR DVD system due to potentials to correct aberrations.

4.2. Simulation

The conditions of objective offset and disc defocus are set as following:

1. There are seven conditions of objective offset: a. Y-decenter: 0, Alpha-Tilt: 0; b. Y-decenter: 5 μm, Alpha-Tilt: 0; c. Y-decenter: 10 μm, Alpha-Tilt: 0; d. Y-decenter: 0, Alpha-Tilt: 0.04°; e. Y-decenter: 0, Alpha-Tilt: 0.08°; f. Y-decenter: 5 μm, Alpha-Tilt: 0.04°; g. Y-decenter: 10 μm, Alpha-Tilt: 0.08°;
2. The conditions of disc defocus: -50 μm, 0 μm, +50 μm.
3. The Compensation claim: After defocus compensation, defocus is less than 10 nm i.e., $(1/40)\lambda$.

4.3. Simulation Results

The simulation results of optical aberration corrections can be obtained by two different objective lens designs: Traditional one and new design optics with LC lens; as following:

1. Spherical aberration:

When defocus 0 μm and objective lens shift, new design with LC lens can eliminate spherical aberration up to 90% better than traditional objective as shown in Table 3.

2. Coma aberration:

- a. Defocus on $-50 \mu\text{m} < \text{Defocus} < 0 \mu\text{m}$:

Spherical aberration of traditional lens is 40% better than new design with LC lens.

- b. Defocus on $0 \mu\text{m} < \text{Defocus} < 50 \mu\text{m}$:

The coma has been minimized at defocus $45 \mu\text{m}$ of new design with LC lens. Conclusively, new design with LC lens can eliminate coma up to 140% better than traditional objective as shown in Table 3.

3. Astigmatism:

The LC lens can reduce astigmatism up to 30% compared to traditional objective on defocus length $-50 \mu\text{m}$ as shown in Table 3.

According to the simulation results, it might conclude that new design with LC lens is averagely superior to traditional lens according to different conditions of Y-decenter and Alpha-Tilt on different defocus durations as listed in Table 3.

5. CONCLUSIONS

The simulation results of proposed designs methods conclude that:

- (1) From point view of optical design, aperture stop on the transparent liquid crystal lens has better performance than conventional method which might set the aperture stop on the objective lens within defocus range of the disc from $-50 \mu\text{m}$ to $+50 \mu\text{m}$.
- (2) From point view of tolerance analysis of new optical design proposed in this study, the aperture stop on the objective lens will reduce 90% spherical aberration, 140% coma and 30% astigmatism compared to traditional ones.
- (3) The advantage of employment of transparent liquid crystal lens are following:
 - a. No more mechanism work. No delay.
 - b. More flexible and freedom for optical design.
 - c. Much better performance.
 - d. Active compensation with LC optics greatly improves system performance.

REFERENCES

1. Blu-ray Disc White Paper: Blu-ray Disc Format, 2010.
2. Optical Research Associates, *Code V Reference Manual*, Vol. 2, Ch. 8.
3. Cheng, H. Y., and Y. T. Wu, "Dynamic mechanical and electrical system modeling of a four-wire type actuator on a DVD," *Journal of Da-Yeh University*, Vol. 11, No. 1, 65–69, 2002.
4. Tseng, L. Y., "Pick-up head assembly for optical disc employing electrically tunable liquid crystal lens," *WIPO*, No: WO 2009/146059 A2, 2009.
5. Ye, M., B. Wang, S. Yanase, and S. Sato, "Liquid crystal lens in imaging system," *IDW'07*, IPD2-3, 2393–2396, Sapporo, Japan, 2007.
6. Mahajan, V. N., "Aberration theory made simple," *SPIE*, 1991.
7. Sekine, M., "Objective lens for optical information recording medium," Patent No: US 7,123,424, 2006.
8. Wang, B., M. Ye, and S. Sato, "Liquid crystal lens with focal length variable from negative to positive values," *IEEE Photonics Technol. Lett.*, Vol. 18, No. 1, 79–81, 2006.
9. Ye, M., B. Wang, and S. Sato, "Effects of dielectric constant of glass substrates on properties of liquid crystal lens," *IEEE Photon. Technol. Lett.*, Vol. 19, No. 17, 1295–1297, 2007.

A Study of Optical Design of Miniature Zoom Optics with Liquid Lenses

Cheng-Mu Tsai¹, Yi-Chin Fang², Cheng-Lun Chung², Wei-Ting Li², and Je-Yi Huang²

¹Department of Computer and Communication, Kun Shan University
No. 949, Dawan Rd., Yongkang District, Tainan City 710, Taiwan, R.O.C.

²Institute of Electro-Optical Engineering
National Kaohsiung First University of Science and Technology
No. 2, Jhuoyue Rd., Nanzih District, Kaohsiung City 811, Taiwan, R.O.C.

Abstract— A new optical design of 2X miniature zoom optics with liquid lens elements are proposed in this research. Liquid lenses are optical components especially designed to vary optical power focusing in small form factor imaging systems. They can either be used as an add-on on a stand alone fixed focus lens module to convert it into an auto-focus module; or be integrated within the auto-focus lens module at design stage. Besides, liquid lens could be as a vari-focal component, which takes advantage of reduce the size of the optical zoom lens. In this research, two liquid lenses are employed in this research in order to minimize the overall length of miniature zoom optics. Compared with complexity of conventional zoom method with complicated mechanical cam system, new proposed zoom optics with two liquid optics will be a great improvement because of remove of complicated opto-mechanical system required. In other words, focus, zoom and zoom compensation will be handled by electronics of liquid optics with signal from electronic chips, which might significantly minimize volumetric size of zoom optics. However, there are difficulties in optimization of zoom optics with liquid lens when employing traditional LDS method. In this paper, we propose a new method, a discrete lens group shift (DLGS), to solve this problem. This research presents some optical design with decent performance, which represents success of miniature zoom optics with liquid optics.

1. INTRODUCTION

Miniaturize zoom optics for miniature optical system such as mobile phone or others is fast growing in the worldwide market; however, conventional zoom method with complicated mechanical cam system has its difficulties and limitation with regard to not only the overall length of optics but also cost issue [1]. Liquid lenses are optical components especially designed to vary optical power for non-image and imaging systems, which have potentials to significantly reduce overall length for optical zoom lens [1, 2]. On the contrary, most traditional zoom lens designs are based on smoothly moving lens groups by using analog mechanical cam control, which makes system complicated and large than expected.

However, there are difficulties in optimization of zoom optics with liquid lens when employing traditional LDS method. In this paper, we propose a new method, a discrete lens group shift (DLGS), to solve this problem. The DLGS can be easily realized by applying matured electronic technology implement. The technology of motor control has developed for several years [3] so that image processing program could be inserted into this device to increase the quality of image effectively [4]. Therefore, genetic algorithm (GA) program [5–8] is employed in this research not only for elimination of chromatic aberrations and field curves during optimization but also find the best solution for discrete zoom set for minimization of aberration. Finally, the GLGS is used for promoting the performance in discrete compensative way and optimizes the camera. A new concept which using the GLGS associated with GA program to optimize the camera in irregular compensative way is disclosed in this research.

2. INITIAL LAYOUT OF THE OPTICAL ZOOM DESIGN

This optical design employs four lens groups to layout the 2X zoom with 2cm overall length. However, the lens with short overall length has difficulties in layout by single using traditional mechanical cam shifting the lens group. Instead, we propose two liquid lenses applied to miniaturize the overall length. The liquid lenses named ARCTIC 416 of simulation are produced by the Varioptic SA [2], which is applied in this research. Table 1 gives the specifications of lens design. Figure 1 shows the two dimension (2D) plots.

Table 1: Specifications of lens design.

Zoom Position	EFL (mm)	F/#	OAL (mm)	Image Distance (mm)	Image Height (mm)
1	8	4.4	13.18	1.47	2.4
2	9	4.8	13.18	2.64	2.4
3	10	5.2	14.57	3.35	2.4
4	11	5.6	16.00	3.49	2.4
5	12	6.0	16.75	4.09	2.4
6	13	6.4	17.09	4.99	2.4
7	14	6.8	19.00	5.48	2.4
8	15	7.2	19.00	6.59	2.4
9	16	8.0	19.00	7.70	2.4

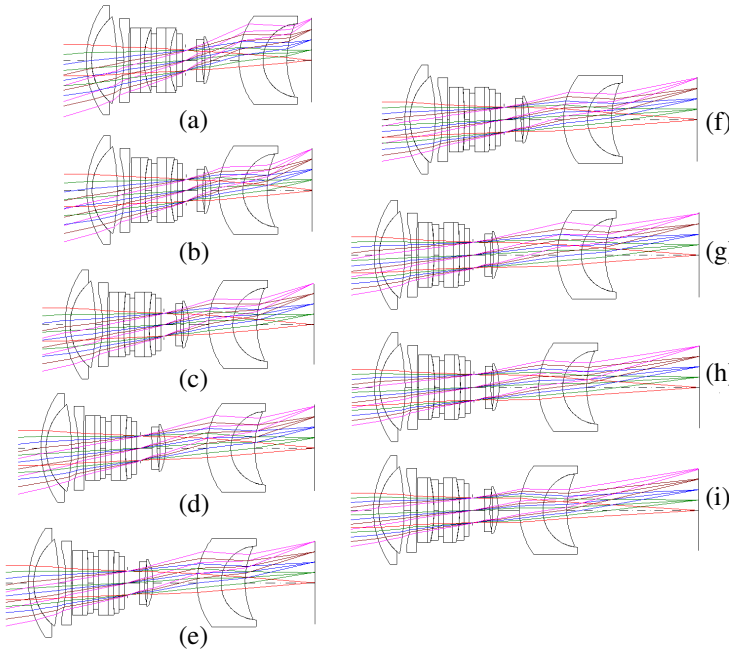


Figure 1: 2D plot optimized by Code V software. (a) Zoom 1. (b) Zoom 2. (c) Zoom 3. (d) Zoom 4. (e) Zoom 5. (f) Zoom 6. (g) Zoom 7. (h) Zoom 8. (i) Zoom 9.

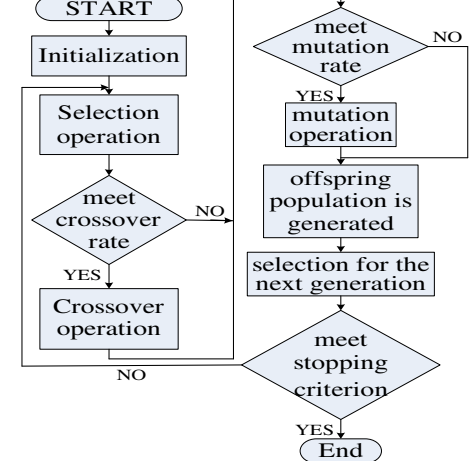


Figure 2: Flow diagram of the genetic algorithm.

3. GENETIC ALGORITHM OPTIMIZATION ON ZOOM LENS

GA process starts with randomly creating an initial population and then allowing reproduction, crossover and mutation to proceed, according to the Fitness Function [5–8], as displayed in Figure 2. The first work in the GA proposal is to determine the parameter of GA such as population size p_p , population size of offspring p_o , crossover rate p_c , and mutation probability p_m . p_p individuals would be randomly created in initial setting. Then, the selection is base on the fitness value for roulette wheel method. Fitness value $Fit(n)$ in the proposal is defined as below:

$$\begin{aligned}
 Fit(n) = & \sum_{z=1}^9 \sum_{k=1}^5 w_k |SPO_z^k| + w_6 \sum_{z=1}^9 |AX_z| + w_7 \sum_{z=1}^9 |LAT_z| \\
 & + w_8 \sum_{z=1}^9 |EFL_z^N - EFL_z^O| + w_9 \sum_{z=1}^9 |FIE_z|
 \end{aligned} \tag{1}$$

where $w_1 \sim w_9$ are weights to tune the fitness value for various situation. SPO_z^k is defined as the spot size at each field k of each zoom z . EFL_z^N and EFL_z^O are the simulation effective focal length and required one of each zoom z . AX_z and LAT_z are the value of primary axial and lateral chromatic aberration of each zoom z . FIE_z is the value of field curves of each zoom z . The distribution area $P(n)$ of wheel is calculated as below:

$$P(n) = (\max - Fit(n)) / sum \quad n = 1, 2, \dots, p_p \quad (2)$$

where the \max is a fitness value of the worst individual and the sum is the sum of the fitness value in each generation. For the crossover, two chromosomes $\mathbf{x} = (x_1, x_2, \dots, x_n)$ and $\mathbf{y} = (y_1, y_2, \dots, y_n)$ from the population are selected randomly according the roulette wheel method, then crossover operation might be determined based on the crossover rate p_c in the next step. By this case, multi-point crossover method is used for crossover strategy. The α is a random number from 0 to 1. If $\alpha \geq 0.5$, then the chromosomes x_i and y_i interchange, otherwise they do not. After crossover operation, multi-point mutation method is used for mutation strategy. The α is a random number from 0 to 1. If $\alpha \leq p_m$, then execute:

$$x'_i = x_i + \beta(u_i - l_i) \quad (3)$$

where β is a random number from 0 to 1, and u_i and l_i are the up and low boundary of x_i . GA program is employed in this research not only for elimination of chromatic aberrations and field curves during optimization but also find the best solution for discrete zoom set for minimization of aberration. Table 2 gives the weight setting of $Fit(n)$, and Table 3 gives the parameter setting. Multi-point mutation method is used for each curvature and thickness gene, and the glass gene is chosen randomly from glass database in the mutation operation.

4. SIMULATION AND ANALYSIS

In this research, we study the optical design and optimization of miniature zoom optics with liquid optics. From the point view of elimination of chromatic aberration, a solutions is given [6–8] that some special combinations of refractive index and Abbe number of optical glass with the liquid lens must be find during extended optimization. The effect between the aspheric coefficient and

Table 2: Weight setting.

$w_1 \sim w_5$ (Spot Size)	150 (the weight $w_1 \sim w_5$ is 60, 30, 15, 15, and 30 in turn.)
w_6 (AX)	100
w_7 (LAT)	100
w_8 (EFL)	80
w_9 (Field Curves)	70

Table 3: GA parameter setting.

Parameter	Parameter value
Population size	5000
Crossover rate	0.8
Mutation probability	0.25
Generation	500

Table 4: Chromatic aberration and field curves data.

	Code V		GA	
	AX	LAT	AX	LAT
Total	0.046982	0.070429	0.028339	0.016186
	x -focus	y -focus	x -focus	y -focus
Total	11.378897	11.361999	1.710281	2.736427

Table 5: Spot size data.

Code V					
	Field 1	Field 2	Field 3	Field 4	Field 5
Total	0.034268	0.031259	0.031645	0.047114	0.077424
GA					
	Field 1	Field 2	Field 3	Field 4	Field 5
Total	0.01416809	0.01531801	0.0227388	0.0305455	0.0306081

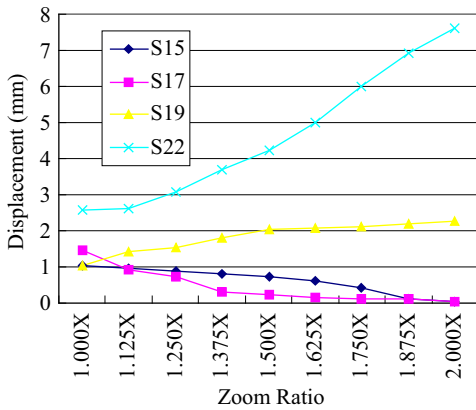


Figure 3: Zoom curve of Code V optimization.

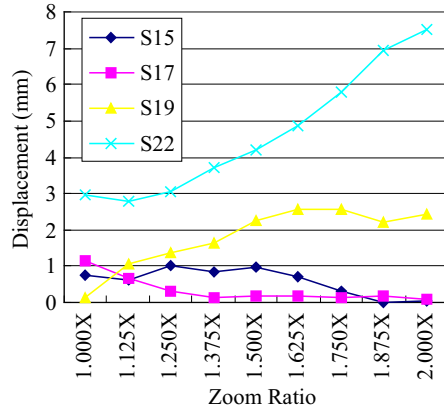


Figure 4: Zoom curve of GA optimization.

aberrations could be further discussed after elimination of chromatic aberration. The 2X optical zoom cell-phone with liquid lens elements is optimized by GA program combined with DLGS. Tables 4–5 show the result of simulation by Code V software versus GA program. Where x -focus is sagittal field curves value and y -focus is tangential field curves value. Figures 3 and 4 shows the lens zoom curve of simulation by Code V software and GA program respectively. From the result of simulation, it is known that the optical system could be optimized by GA program combined with DLGS. MTF almost approach the optical diffraction limit except 1.0 field ray. It will be improved while the aspheric surface lens is added into the optical system. However, the quality of image is great within standard range. Considering the cost, it is decided that aspheric surface lens will be not added into the optical design in this research.

5. CONCLUSIONS AND OUTLOOK

The GA program is employed in this research not only for elimination of chromatic aberrations and field curves during optimization but also find the best solution for digital zoom set for minimization of aberration. The AX of the liquid lens system has 39.68% improvement compared to initials, LAT is 77.02%, sagittal field curves is 84.97%, tangential field curves is 75.92%, spot size is 48.86% improvement as well under the situation of relative illumination are greater than 85%. According to the result of simulation, it is concluded that GA will get better results than conventional LDS method in this case if liquid optics is applied to optical design of miniature zoom optics.

It is concluded that GA program combined with DLGS get the best results in each zoom of optics. On the contrary, when traditional LDS is employed, optimization work is getting strictly and complicated while the liquid lens is used for the purpose of optical zoom. It is not only because the interface curvature of liquid lens is too large in order to gain the enough optical zoom, but also chromatic aberrations of optical zoom camera are the serious problems for liquid lens because of limited optical materials. According to the result of simulation, it is concluded that GA is superior to conventional LDS method in this case if liquid optics is applied to optical design of miniature zoom optics.

ACKNOWLEDGMENT

The authors acknowledge the funding support from Nation Science Council of Taiwan, R.O.C., under Grant NSC 99-2221-E-168-036.

REFERENCES

1. Dickensheets, D. L., B. P. Gogoi, and H. Schenk, "Zoom camera based on liquid lenses," *Proc. of SPIE*, Vol. 6466, 64660F, 2007.
2. Varioptic Web, <http://www.varioptic.com/en/index.php>.
3. Nash, J. N., "Direct torque control, induction motor vector control without an encoder," *IEEE Transactions on Industry Applications*, Vol. 33, No. 2, 333–341, 1997.
4. Rabadi, W., R. Talluri, K. Illgner, J. Liang, and Y. Yoo, "Programming DSP platform for digital still cameras," *IEEE International Convention on Acoustics, Speech, and Signal Processing*, March 1999.
5. Goldberg, D. E., *Genetic Algorithms in Search Optimization and Machine Learning*, 151–159, Addison-Wesley, 1989.
6. Fang, Y. C., T.-K. Liu, C.-M. Tsai, J.-H. Chou, H.-C. Lin, and W. T. Lin, "Extended optimization of chromatic aberrations via a hybrid Taguchi-genetic algorithm for zoom optics with a diffractive optical element," *J. Opt. A: Pure Appl. Opt.*, Vol. 11, No. 4, 045706 (14pp), April 2009.
7. Fang, Y.-C. and C.-M. Tsai, "Miniature lens design and optimization with liquid lens element via genetic algorithm," *J. Opt. A: Pure Appl. Opt.*, Vol. 10, No. 7, 075304, July 2008.
8. Fang, Y.-C., C.-M. Tsai, J. MacDonald, and Y.-C. Pai, "Eliminating chromatic aberration in Gauss type lens design using a novel genetic algorithm," *Applied Optics*, Vol. 16, No. 13, 2401–2410, May 2007.

Adaptive Loading Algorithms Evaluations for IMDD SMF System-based Optical OFDM Transceivers

E. Giacoumidis¹, J. L. Wei², E. Hugues Salas², J. M. Tang², and I. Tomkos¹

¹Networks and Optical Communications (NOC) Group

Athens Information Technology (AIT), Athens, Greece

²School of Electronic Engineering, Bangor University, Bangor, Wales, UK

Abstract— Detailed investigations of the effectiveness of three widely adopted optical orthogonal frequency division multiplexing (OOFDM) adaptive loading algorithms, including power-loading (PL), bit-loading (BL), and bit-and-power loading (BPL), are undertaken, over < 100 km single-mode fibre (SMF) system without incorporating inline optical amplification and chromatic dispersion (CD) compensation. It is shown that the BPL (PL) algorithm always offers the best (worst) transmission performance. The absolute transmission capacity differences between these algorithms are independent of transmission distance and launched optical power. Moreover, it is shown that in comparison with the most sophisticated BPL algorithm, the simplest PL algorithm is effective in escalating the OOFDM SMF links performance to its maximum potential. On the other hand, when employing a large number of subcarriers and a high digital-to-analogue (DAC)/analogue-to-digital (ADC) sampling rate, the sophisticated BPL algorithm has to be adopted.

1. INTRODUCTION

To maximize the optical orthogonal frequency division multiplexing (OOFDM) transmission performance and simultaneously improve the system flexibility and performance robustness, full use can be made of orthogonality among different subcarriers within an OOFDM symbol by applying various adaptive loading algorithms on each individual subcarrier, according to the signal-to-noise ratio (SNR) experienced by the subcarrier [1]. The widely adopted adaptive loading algorithms include power-loading (PL), bit-loading (BL), and bit-and-power loading (BPL), all of which can be implemented using the well-known “water-filling” approach. In the BL algorithm [2, 3], different signal modulation formats are taken on individual subcarriers which have identical electrical powers. In the PL algorithm [4–6] electrical subcarrier powers are manipulated with the same signal modulation format being taken on all those subcarriers. Finally, in the BPL algorithm [4, 5, 7] both the power and signal modulation format of each individual subcarrier are adjusted independently. Each of these adaptive loading algorithms can be utilized to maximize the signal bit rate for a given bit-error-rate (BER) and a fixed power constraint or to minimize the BER for a given signal bit rate in order to increase the system power budget. Throughout this work, the option of employing the adaptive loading algorithms to increase the signal bit rate is considered. Of these three adaptive loading algorithm the BPL algorithm has the ability of achieving the largest signal bit rate [4, 5, 7] but it suffers from the highest level of computational complexity and requires sophisticated OOFDM transceiver designs to accommodate the variations in both the number of bits per symbol and the selective signal modulation formats [4]. On the other hand, as a direct result of the least computational complexity and the simplest OOFDM transceiver architecture, the PL algorithm has been experimentally implemented successfully in end-to-end real-time OOFDM transceivers at 11.25 Gb/s, using low-cost, off-the-shelf electrical and optical components [4]. In addition, the effectiveness of the PL algorithm has been experimentally confirmed recently, showing in end-to-end real-time intensity-modulated and direct detected (IMDD) OOFDM transceivers over < 35 km [8] that it offers transmission capacity degradation of maximum at only 7% compared to the sophisticated BPL algorithm. As the statement that different adaptive loading algorithms offer similar transmission performances, may have huge potential for practical cost-effective OOFDM single-mode fibre (SMF)-based transceiver architecture for various applications scenarios including passive optical networks (PONs) for fibre-to-the-home/cabinet (FTTH/C) which have become very popular recently due the unstoppable bandwidth demand. Detailed explorations of the validity of the above statement in arbitrary SMF-based transmission links are of great importance. This work tenders for the first time a complete study of adaptive loading algorithms evaluations for IMDD OOFDM SMF-based transceivers.

It is shown that over transmission distances of practical interest for IMDD OOFDM signals lower than 100 km, and over a wide range of launched optical powers, in comparison with the most sophisticated BPL algorithm, the simplest PL algorithm is effective in escalating the OOFDM SMF links performance to its maximum potential. The results agree very well with experimental measurements [4]. On the other hand, when employing a large number of subcarriers and a high digital-to-analogue (DAC)/analogue-to-digital (ADC) sampling rate, the sophisticated BPL algorithm has to be adopted.

2. OOFDM MODEL AND TRANSEIVER PARAMETERS

A typical single-channel directly modulated laser (DML)/distributed feedback (DFB)-based OOFDM IMDD transmission system considered here with the PL, BL, and BPL algorithms being conducted via negotiations between the corresponding elements of the transmitter and receiver similarly reported in Ref. [5]. It should also be noted that inline optical amplification and chromatic dispersion (CD) compensation is not included.

In simulating the OOFDM transceivers, the signal generation, transmission, and detection procedures similar to those reported in Refs. [3, 5] are adopted. Here, 64 subcarriers are employed, of which 31 carry real user information, and one contains no power, and the remaining 32 are the complex conjugate of all the aforementioned subcarriers. The DAC/ADC operates at optimum 7-bit resolution and 12.5 GS/s sampling rates. The signal clipping levels are fixed at 13 dB, and the cyclic prefix (CP) parameter is taken to be 25% [3].

A comprehensive standard SMF (SSMF) model used successfully in Ref. [3] is adopted using the split-step Fourier method to model the propagation of the optical signal [3]. It is well known that for a sufficiently small fibre split-step length, this theoretical treatment yields an accurate approximation to the real effects. In the SSMF model, the effects of fibre loss, CD, polarization dependence of Kerr nonlinearity and optical power dependence of the refractive index are included. The effect of fibre nonlinearity-induced phase noise to intensity noise conversion is also considered. To simulate the nonlinear properties of DFB laser-based DML for SMF links, a lumped DFB laser model developed in Ref. [3] is adopted, taking into account a wide range of nonlinear effects such as longitudinal-mode spatial hole burning, linear and nonlinear carrier recombination and ultrafast nonlinear gain compression. In the OOFDM SMF-based receiver, a square-law photo-detector is employed, having a quantum efficiency of 0.8 and a sensitivity of -19 dBm (corresponding to a 10 Gb/s non-return-to-zero with a BER of 1.0×10^{-9}). The adaptive allocation of bit and/or power on each individual OOFDM subcarrier is justified as optical transmission channels remain relatively stable in time. Such adaptive allocation processes also require the knowledge of the channel state information (CSI), which can be easily obtained, both theoretically [3, 9] and experimentally [4, 8], using pilot signals implemented in the OOFDM transceiver design. Through negotiations between the transmitter and the receiver, all the adaptive loading algorithms can thus be implemented according to the total channel and each individual subcarrier BER given in Ref. [3]. The descriptions of the implementation of the three adaptive loading algorithms are described in detailed in Ref. [5]. For fair comparisons between the adaptively loading algorithms it is worth highlighting the following aspects: 1) For a given transmission system, the total electrical signal powers generated by all the algorithms are set to be identical, and comparisons of maximum achievable transmission capacity at a $\text{BER}_T = 1.0 \times 10^{-3}$ are made; 2) Signal modulation formats vary from differential binary phase shift keying (DBPSK), differential quadrature phase shift keying (DQPSK), and 8-quadrature amplitude modulation (QAM) up to 256-QAM; 3) Any subcarrier suffering a very low SNR may be dropped completely if the following condition is met: for the PL algorithm only, the detected errors are too large to achieve the required total channel BER_T ; for the BL and BPL algorithms, the detected errors are too large to achieve the required total channel BER_T even when the lowest signal modulation format is employed.

3. TRANSMISSION DISTANCE AND LAUNCHED OPTICAL POWER IMPACT

In Fig. 1(a), results present signal capacities versus transmission distance at 5 dBm of launched optical power, and in Fig. 1(b) results present signal capacities versus launched optical power over a 40 km SMF link. It is shown, from Fig. 1 that a small signal capacity difference of up to about 7% is observed between the BPL (best) and PL (worst) algorithms. The results agree very well with the real-time experimental IMDD OOFDM SMF-based results reported in Ref. [4], confirming that in comparison with the most sophisticated BPL algorithm, the simplest PL algorithm is effective in escalating the OOFDM SMF links performance to its maximum potential. It is also shown that

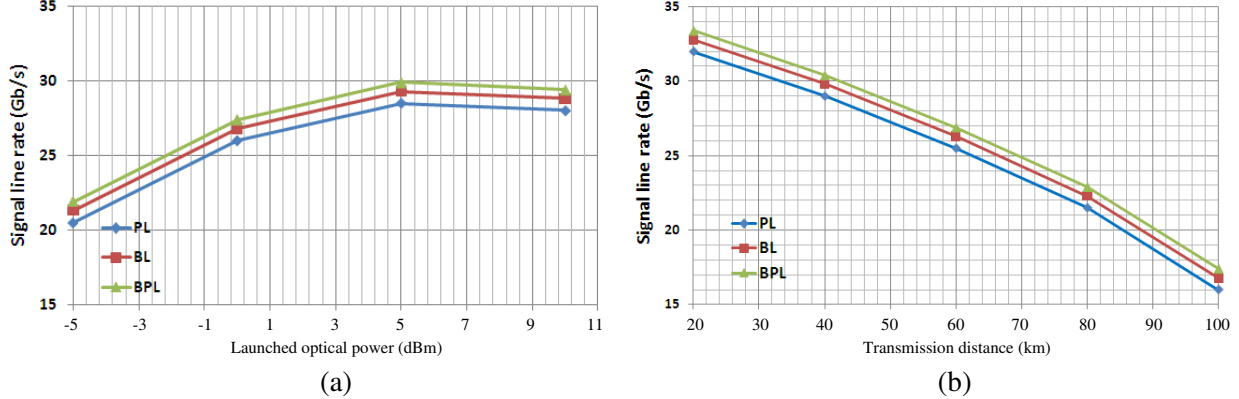


Figure 1: (a) Signal line rate versus launched optical power over a 40 km SMF link for PL, BL and BPL; (b) Signal line rate versus transmission distance over a SMF link at 5 dBm launched optical power for PL, BL and BPL.

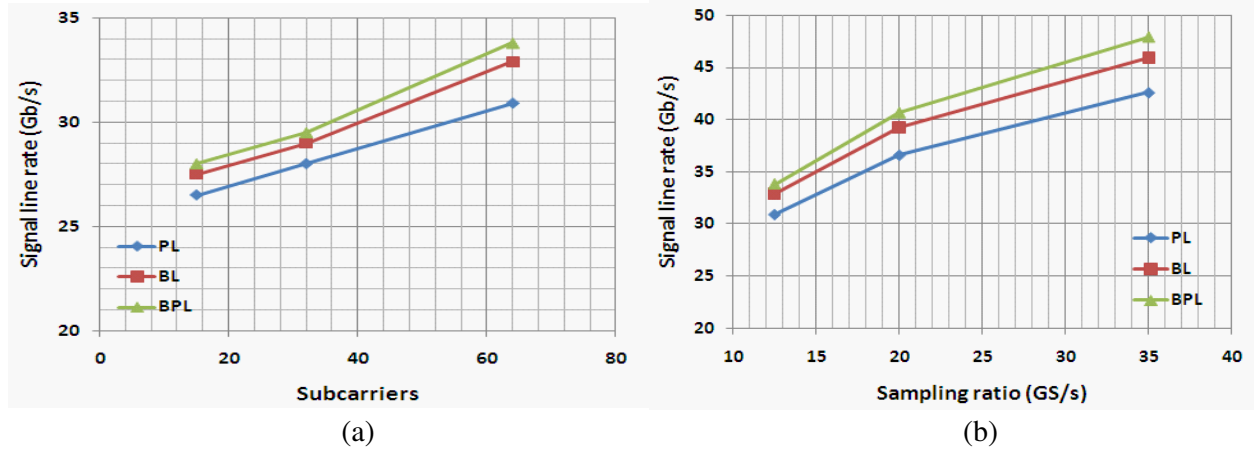


Figure 2: (a) Signal line rate versus number of subcarriers over a 40 km SMF link for PL, BL and BPL; (b) Signal line rate versus sampling ratio, employing 64 subcarriers over a 40 km SMF link for PL, BL and BPL.

the BPL-PL signal capacity difference is independent of both transmission distance and launched optical power. This occurs, because the almost flat response of the SMF bandwidth allows high signal modulation formats to be taken on subcarriers even when the simplest PL algorithm is applied.

4. NUMBER OF SUBCARRIERS AND SAMPLING SPEED IMPACT

The impact of the number of subcarriers and the DAC/ADC sampling ratio on the transmission performance of the three adaptive loading algorithms is presented in Fig. 2, where the signal capacities are plotted as a function of subcarrier number and sampling ratio. It should be noted that, in calculating Fig. 2, use is made of the optical signals emerging at the output facet of a 40 km transmission system at an input optical power of 5 dBm. From Fig. 2, it is revealed that the signal capacity difference between BPL (best) and PL (worst) algorithms increases when a large number of subcarriers are employed. In particular, the BPL-PL signal capacity difference increases up to about 10% when 64 subcarriers are employed while for the case when 15–32 subcarriers are considered the signal capacity difference is at only about 5%. This can be explained by the following phenomenon: For low number of subcarriers the CP length is short producing short OFDM symbols, and in combination with the existence of large noise margins and broad SMF frequency response for distances < 80 km, the subcarriers accommodate high SNR which causes the BPL-PL signal capacity difference to be very small. On the other hand, for a large number of subcarriers the CP length increases, which combat completely the CD effect but enhances the sensitivity to phase noise and frequency offset, as well as the peak-to-average power ratio (PAPR), leading to almost double (10%) BPL-PL signal capacity difference compared to the case with reduced subcarrier number (5%). This indicates that a large number of subcarriers can improve the effectiveness of

the sophisticated BPL algorithm.

Having identified the maximum signal capacity difference between BPL (best) and PL (worst) algorithms when 64 subcarriers are employed, further investigations regarding the DAC/ADC sampling ratio are undertaken. In Fig. 2 the signal capacity versus sampling ratio is depicted, revealing that for high sampling ratio (35 GS/s), the signal capacity difference between BPL and PL is about 12.4%. On the other hand, for low sampling rates (12.5 GS/s) this signal capacity difference drops to about 7%. This is explained by the following phenomenon: a high sampling speed-induced wider SMF spectral bandwidth allows low signal modulation formats to be taken on high frequency subcarriers when the PL algorithm is applied, and hence, a large sampling rate degrades the PL transmission performance.

Numerical investigations reveal that over a large number of subcarriers and sampling speeds, the sophisticated BPL algorithm should be adopted for IMDD OOFDM SMF-based systems over distances < 40 km. Finally, it should be noted that, in contrast to the results reported in Ref. [5] corresponding to the case of MMF links for 35 GS/s sampling rate, here the SMF takes advantage of its vast bandwidth, and thus, higher signal modulation formats on subcarriers can be taken for all adaptive loading algorithms leading to higher signal capacities.

5. CONCLUSIONS

Detailed analytical and numerical investigations over IMDD SMF links without incorporating in-line optical amplification and CD compensation have been undertaken of the effectiveness of three widely adopted OOFDM adaptive loading algorithms including PL, BL and BPL. It was shown that the absolute transmission capacity difference between BPL (best) and PL (worst) algorithms is independent from transmission distance and launched optical power. Numerical results have revealed that, for SMF links lower than 100 km, in comparison with the sophisticated BPL algorithm, the simplest PL algorithm can be considered as an effective means of escalating the OOFDM SMF link performance to its maximum potential. On the other hand, when both the number of subcarriers and the DAC/ADC sampling rate increase, the sophisticated BPL should be adopted. Given the importance of the aforementioned statements for practical cost-effective OOFDM transceiver architecture design such as PONs, experimental verifications of the statements in end-to-end real-time OOFDM SMF-based transmission systems have been pledged.

ACKNOWLEDGMENT

This work is supported from the E.U. FP7 Projects ACCORDANCE and ALPHA.

REFERENCES

1. Li, Y. L. and W. E. Ryan, "Mutual-information-based adaptive bit-loading algorithms for LDPC-coded OFDM," *Wireless Commun.*, Vol. 6, No. 5, May 2007.
2. George, Y. and O. Armani, "Bit loading algorithms for OFDM," *ISIT 2004*, 388, Chicago, IL, 2004.
3. Giacoumidis, E., J. L. Wei, X. Q. Jin, and J. M. Tang, "Improved transmission performance of adaptively modulated optical OFDM signals over directly modulated DFB laser-based IMDD links using adaptive cyclic prefix," *Opt. Express*, Vol. 16, 9480–9494, 2008.
4. Giddings, R. P., X. Q. Jin, E. Hugues-Salas, E. Giacoumidis, J. L. Wei, and J. M. Tang, "Experimental demonstration of a record high 11.25 Gb/s real-time optical OFDM transceiver supporting 25 km SMF end-to-end transmission in simple IMDD systems," *Opt. Express*, Vol. 18, No. 6, 5541–5555, 2010.
5. Giacoumidis, E., X. Q. Jin, A. Tsokanos, and J. M. Tang, "Statistical performance comparisons of optical OFDM adaptive loading algorithms in multimode fiber-based transmission systems," *IEEE Journal of Photonics*, Vol. 2, 130–140, 2010, ISSN: 1943-0655.
6. Krongold, B. S., K. Ramchandran, and D. L. Jones, "Computationally efficient optimal power allocation algorithms for multicarrier communication systems," *IEEE Transactions on Communications*, Vol. 48, No. 1, 23–27, 2000.
7. Duong, T.-N., N. Genay, M. Ouzzif, J. Le Masson, B. Charbonnier, P. Chanclou, and J. C. Simon, "Adaptive loading algorithm implemented in AMOOFDM for NG-PON system integrating cost-effective and low-bandwidth optical devices," *IEEE Photon. Technol. Lett.*, Vol. 21, 790, 2009.

8. Jin, X. Q., R. P. Giddings, and J. M. Tang, "Experimental demonstration of adaptive bit and/or power loading for maximising real-time end-to-end optical OFDM transmission performance," *OSA/OFC/NFOEC*, 2011.
9. Jin, X. Q., J. M. Tang, K. Qiu, and P. S. Spencer, "Statistical investigations of the transmission performance of adaptively modulated optical OFDM signals in multimode fibre links," *J. Lightw. Technol.*, Vol. 26, No. 18, 2008.

Diversity Statistics of Free Space Optical Links Affected by Rain

S. Zvanovec

Department of Electromagnetic Field, Czech Technical University in Prague, Czech Republic

Abstract— Free Space Optical systems introduce prospective technology for fast data transmissions; nevertheless atmosphere radically influences availability of these systems. Between one of the highest affections belongs rain attenuation. The paper discusses several aspects dealing with route diversity utilization in Free Space Optical network. Based on simulations particular link deployment cases were analyzed.

1. INTRODUCTION

Free Space Optics (FSO) bring many advantages to modern communication including larger frequency bandwidth and substantially higher available data rates, immunity to interferences, free license, higher safety of transmission due to narrow optical beams etc. [1]. Most FSO links are nowadays deployed in dense urban areas, where thermal influences (due to building heating, air-conditioning, wind circulation etc.) can be substantial. It would therefore be beneficial to investigate the statistical influence of turbulences on FSO links not only in open areas but also in the vicinity of buildings. First measurement results from initial measurement campaign at CTU in Prague were presented in [2]. The different dependences of the refractive index structure parameter were observed in the case of a FSO link deployed in an urban area compared to results published for links crossing free non built-up areas. Compared to long-normal measurement statistics presented for several maritime links in [3] the normalized scintillation index was not as strictly followed by a fitted lognormal cumulative function in our measurement. For higher scintillation indices the gamma-gamma statistical approach dominates.

As can be seen, there is essential need to use adaptive optics that is able to control the output optical power reaching the detector and therefore compensate for the power fluctuations due to turbulence and other atmospheric phenomena in urban scenario. In order to overcome fades, several techniques were proposed. Spatial transmitter or receiver diversity [4], adaptive beam forming based on the wave front phase error measurement and the setting of the opposite phase aberration on the beam by a deformable mirror [5], wavelength diversity [6], multiple-beam communication [7] or new modulation techniques [8] introduce the state of art of FSO communications. With recent increase of deployed FSO optical systems covering cities (see the recent excellent paper, where diversity in cooperative FSO systems is theoretically analyzed [9]), the complexity and variability of analyses of atmospheric turbulence, fogs, rain attenuation simultaneously affecting accurate measurements dramatically raise. In order to support system performance analyses, a measurement campaign was set up at the Czech Technical University in Prague (CTU)). A free space optical link WaveBridge 500 by Plaintiffree [10] is nowadays placed on roofs of two eight-story buildings in the CTU campus, approximately 30 meters above ground level forming an optical link with a length of



Figure 1: The LightPoint link deployment at CTU.

around 120 meters. The second FSO link consisting of a four-beam free space optical communication systems FlightStrata G by LightPointe (1.25 Gbps of full-duplex, VCSEL at 850 nm [11]) was established in 2010 for educational purposes (students use this link during laboratories to ascertain atmosphere influences, beam wandering, FSO tracking method etc, see Fig. 1). The third optical WaveBridge link is now being configured having common intersecting point (node) with the first two links. This paper brings based on simulations an analysis of route diversity statistics of FSO links (wavelength 850 nm) influenced by rain. The results obtained should form a background to long-term measurement statistics from our three link network.

2. RAIN INFLUENCE

Rain does not introduce the main negative influence affecting optical systems, the fog prevails causing instant drops of links [12]. Nevertheless as it was published in [13] substantial rain attenuations can be observed even under normal conditions. Therefore there is a need to solve rain influence even in the region where raindrops are several orders larger than wavelengths (comparing to millimeter wavelength links). Rain attenuation caused rain rate distribution $R(x)$ along a particular link (with length L) can be generally expressed (regardless of mm or optical region) as:

$$A = \int_0^L kR(x)^\alpha dx \quad (1)$$

where k and α introduce the frequency, polarization and link elevation dependent coefficients. Their exact values were derived from long term worldwide measurements and for frequencies up to 1 THz are given by ITU-R P.838 [14]. See frequency dependence k and α for terrestrial link (zero elevation) and both polarizations depicted in Fig. 2. In the case of optical link, empirical parameters $k = 1.076$ and $\alpha = 0.67$ were then derived from the long term measurement campaign in [13] as to be independent on optical wavelengths.

3. ROUTE DIVERSITY SIMULATIONS

A propagation simulation tool to study a performance of FSO heterogeneous terrestrial networks under different signal propagation conditions and with various configurations has been developed. In order to obtain precise fading statistics, the rain database from a four year period was utilized including $50\text{ km} \times 50\text{ km}$ rain scans from Czech meteorradars (rain rate distributions with 1 km grid resolution and 1 minute time steps). It has to be emphasized that data starting from minimum availability 0.999981 can be determined from simulations with correspondence to 1 minute rain intervals.

For the case of the scenarios employing two optical wireless links affected by time-space variable rain intensities, resulted statistics of diversity gains were compared to statistics of the single link. Focus was given on angular separations and link length dependencies. Example of the simulation results, the comparison of complementary cumulative distribution functions of rain attenuation of

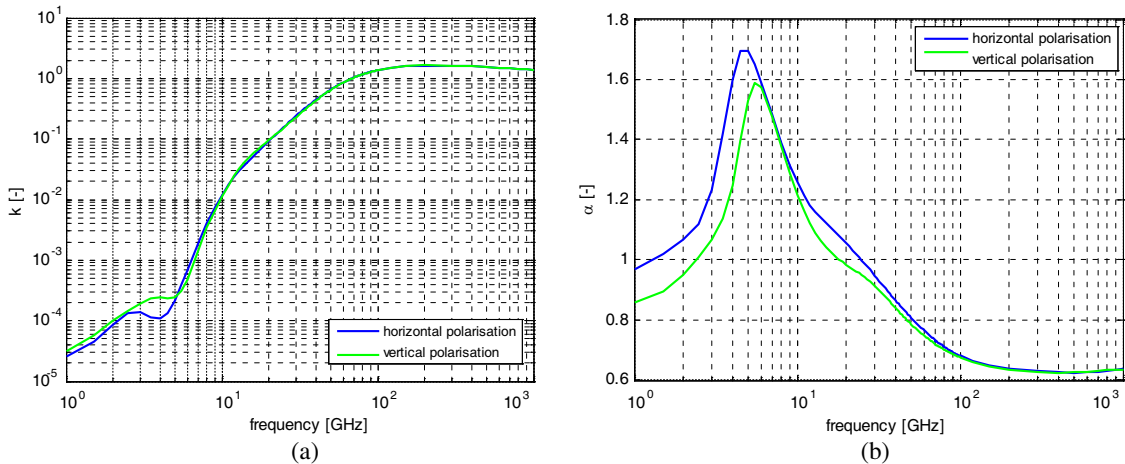


Figure 2: Frequency dependence of (a) coefficient k and (b) coefficient α [14] for both polarizations.

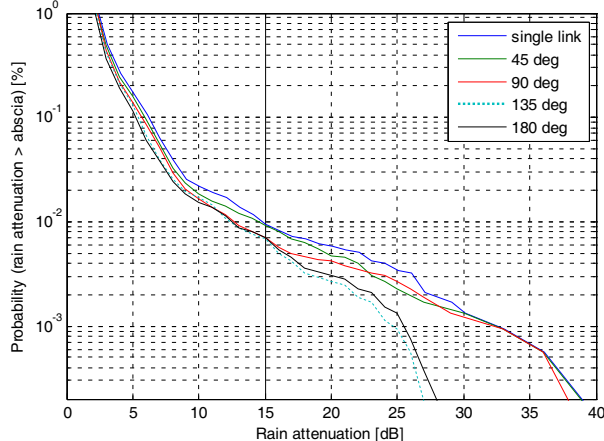


Figure 3: CCDFs of rain attenuation for a single link and two-branch diversity links with equal lengths 2 km for different angular separations.

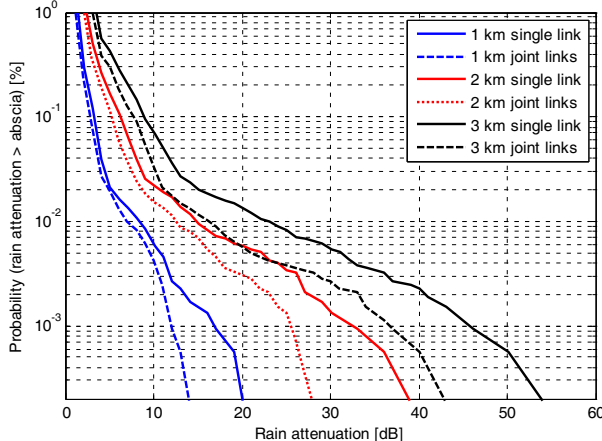


Figure 4: CCDFs of rain attenuation for a single link and two-branch diversity links having different lengths for angular separation 180 deg.

the single FSO link and two-branch diversity links (so called route diversity — i.e., 2 links from one point to 2 different azimuths) is demonstrated in Fig. 3. During route diversity a user was able to connect to two base stations, both distant 2 km. Annual meteoradar data from the year 2005 were utilized for simulations. As it can be seen, for smaller angular separations, diversity gain does not introduce suitable mitigation approach. Contrary to that, utilizing route diversity could be implemented for angular separations between both links higher than approximately 120 degrees. Considering range of high angular separations, diversity gains up to 2.5 dB, 8 dB and 13 dB were observed for the link availability 99.99%, 99.999% and 99.9998%, respectively.

Figure 4 brings comparison of complementary cumulative distribution functions for a single link and two diversity links with different link lengths for the special case when the both joint links are separated by 180 degree (pointing to opposite directions). With increasing link length, rain attenuation of single optical link rises and as it was determined from simulations the utilization of the route diversity is more worth of (higher diversity gains can be yielded).

4. CONCLUSION

The analysis of the statistical variations in spatial organization of precipitation and its influence on Free Space Optical systems were presented. A simulation tool was developed to evaluate various aspects of the FSO system performance. Large rain event database for Czech Republic was built for the simulation using time sequences of rainfall radar images. Derived results of diversity statistics demonstrate that the route diversity is feasible and useful tool to combat rain attenuations. This should be nevertheless clarified by simultaneously performed measurement campaign (measurement of diversity statistics has already started at CTU, but we have no complete annual data at present) will provide us with more sensitive statistics — especially with respects to higher availabilities that could not be reached by 1 minute meteoradar scan steps.

ACKNOWLEDGMENT

This work was supported by the Grant Agency of the Czech Technical University in Prague, grant No. SGS11/065/OHK3/1T/13. Educational utilization of free space optical measurement was supported by FRVS grant 594/2010.

REFERENCES

1. Bouchet, O., et al., *Free Space Optics: Propagation and Communication*, ISTE Ltd, London, 2006.
2. Libich, J. and S. Zvanovec, “Influences of turbulences in near vicinity of buildings on free space optical links,” *IET Microwaves, Antennas & Propagation*, accepted for publication.
3. Henniger, H., et al., “Maritime mobile optical-propagation channel measurements,” *IEEE International Conference on Communications*, Cape Town, South Africa, 2010.

4. Anguita, J. A. and J. E. Cisternas, “Experimental evaluation of transmitter and receiver diversity in a terrestrial FSO link,” *GLOBECOM Workshops (GC Wkshps) 2010*, 1005–1009, 2010.
5. Hashmi, A., et al., “Analysis of optimal adaptive optics system for hybrid RF-wireless optical communication for maximum efficiency and reliability,” *4th International Conference on Emerging Technologies, ICET 2008*, 62–67, 2008.
6. Weerackody, V. and A. R. Hammons, “Wavelength correlation in free space optical communication systems,” *IEEE Military Communications Conference*, 1–6, 2006.
7. Anguita, J. A., et al., “Spatial correlation and irradiance statistics in a multiple-beam terrestrial free-space optical communication link,” *Appl. Opt.*, Vol. 46, 6561–6571, 2007.
8. Chatzidiamantis, N., et al., “Adaptive subcarrier PSK intensity modulation in free space optical systems,” *IEEE Transactions on Communications*, Vol. PP, 1–10, 2011.
9. Abou-Rjeily, C. and S. Haddad, “Cooperative FSO systems: Performance analysis and optimal power allocation,” *Journal of Lightwave Technology*, Vol. 29, 1058–1065, 2011.
10. Plaintree Systems Inc. Available: <http://freespaceoptics.ca>.
11. LightPointe. Available: <http://www.lightpointe.com>.
12. Colvero, C. P., et al., “FSO systems: Rain, drizzle, fog and haze attenuation at different optical windows propagation,” *SBMO/IEEE MTT-S International Microwave and Optoelectronics Conference*, 563–568, 2007.
13. Carbonneau, T. H. and D. R. Wisely, “Opportunities and challenges for optical wireless; the competitive advantage of free space telecommunications links in today’s crowded marketplace,” *Wireless Technologies and Systems: Millimeter-wave and Optical*, Vol. 32, 119–128, 1998.
14. “Specific attenuation model for rain for use in prediction methods,” Recommendation ITU-R P. 838-1, 2005.

Effect of ADC on the Performance of Optical Fast-OFDM in MMF/SMF-based Links

E. Giacoumidis¹, S. K. Ibrahim², J. Zhao²,
J. L. Wei³, J. M. Tang³, A. D. Ellis², and I. Tomkos¹

¹Networks and Optical Communications (NOC) Group
Athens Information Technology (AIT), Athens, Greece

²Photonics Systems Group, Tyndall National Institute and Department of Physics
University College Cork, Cork, Ireland

³School of Electronic Engineering, Bangor University, Bangor, Wales, UK

Abstract— Based on a recently proposed novel technique known as optical fast orthogonal frequency-division multiplexing (FOFDM), which has half the bandwidth occupancy compared to single quadrature based conventional OFDM, investigations are undertaken into the impact of an analog-to-digital converter (ADC) involved in FOFDM signals over unamplified intensity-modulation and direct-detection (IM/DD) multimode fiber (MMF) and singlemode-fiber (SMF) based links. It is evaluated, for the first time, two important issues: 1) The impact of signal quantization and clipping effects for identification of a set of ADC parameters using various FOFDM single-dimensional modulation formats; 2) The FOFDM ADC parameters are compared with the corresponding ADC parameters of a conventional OFDM over both MMF and SMF links. It is shown that FOFDM and conventional OFDM over MMF/SMF links have similar optimum ADC parameters for a targeted BER of 10^{-3} .

1. INTRODUCTION

Over the past several years, as a promising candidate for improving spectral-efficiency in optical communication systems, conventional orthogonal frequency division multiplexing (OFDM) [1] has been rapidly and widely adopted in wireless, wire-line and broadcast systems for efficiently dealing with linear signal distortions encountered when transmitting over dispersive fading channels [2]. In OFDM, multiple subcarriers with equal frequency spacing are utilized to form parallel data transmission, and each separate data stream is modulated over one of the equally-spaced subcarriers [1]. Reducing the spacing between subcarriers in OFDM system, results in improved bandwidth efficiency. For this purpose, optical Fast-OFDM (FOFDM) [3] has been proposed. In contrast to conventional OFDM, FOFDM uses half of the subcarrier spacing with single-dimensional signal modulation formats being used such as M-ary amplitude shifted keying (M-ASK), due to the increased inter-symbol interference (ISI) between adjacent narrowband FOFDM subcarriers [4].

Recently, FOFDM has been effectively implemented experimentally in single-mode fiber (SMF) systems by employing discrete cosine transform (DCT) for double-side band (DSB) signals [5]. Analogue-to-digital converters (ADCs) have been considered as one of the most important devices for a conventional OFDM system limiting the maximum achievable transmission performance, and therefore, in the same manner ADC parameters are also a crucial factor for a FOFDM system.

The present paper presents two important issues: 1) The impact of the signal quantization and clipping effects in order to identify a set of ADC parameters for a targeted bit-error-rate (BER) of 10^{-3} using various FOFDM single-dimensional modulation formats. 2) Having identified the optimum ADC quantization bits from 1), the clipping ratio is evaluated, for the first time, over 500 m MMF for local area networks (LANs) and 50 km SMF for short-reach access networks using FOFDM and conventional OFDM.

2. SYSTEM MODEL AND PARAMETERS

Typical single-channel, un-amplified, intensity-modulation and direct-detection (IM/DD) MMF/SMF links are considered, consisting of a conventional OFDM transceiver using FFT/IFFT, connected by the MMFs/SMFs, similarly to architectures reported in Ref. [6]. The FOFDM system is implemented in a similar way, as shown in Figure 1, only for the subcarrier multiplexing/demultiplexing a fast cosine transform (FCT)/inverse FCT (IFCT) is attached and single-modulation format mapping is generated [3, 5]. In the transceiver, an ADC (DAC) is used to convert an analogue (digital) signal into a digital (analogue) signal, having an automatic gain control unit which sets a finite dynamic amplitude range [6]. Amplitude clipping occurs if the input signal exceeds that

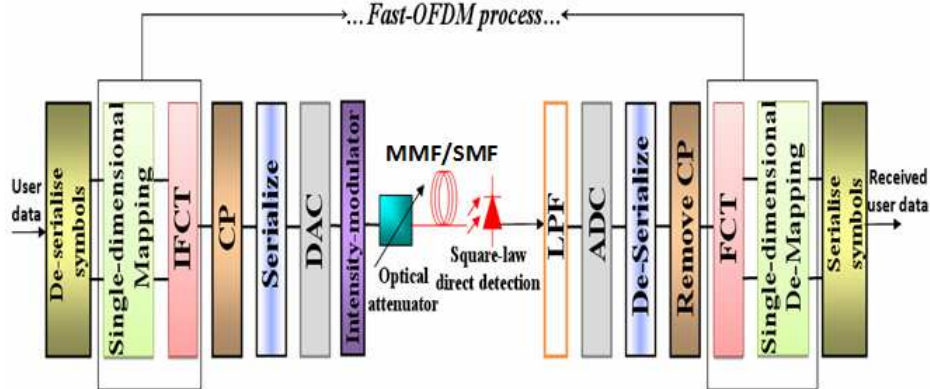


Figure 1: MMF/SMF-based FOFDM transmission link diagram.

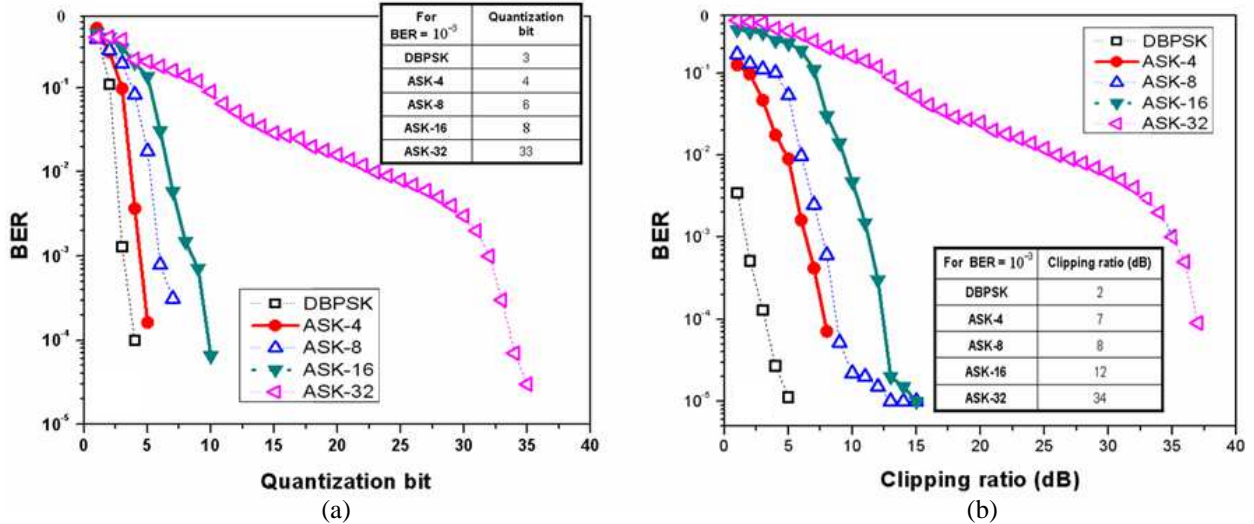


Figure 2: BER versus (a) quantization bit and (b) clipping ratio for a FOFDM system using single-dimensional modulation formats over AWGN channel.

dynamical amplitude range, which will introduce distortions to the input signals. The ADC/DAC impairments are considered in this paper. The 3-dB bandwidths (differential mode delays [DMDs]) of the adopted MMF link are of 202.5 MHz·km (2.0 ns/km) for central launch conditions [6]. The specifications of the SMF link are given in Ref. [6]. For both MMF/SMF FOFDM/OFDM systems, the directly modulated lasers (DMLs) are assumed to be an ideal-intensity modulator at 1550 nm, in order to isolate the ADC parameters from any unwanted laser chirp effects.

3. RESULTS

Initially, simulations for both FOFDM and conventional OFDM models were undertaken over an additive-white-Gaussian noise (AWGN) channel. The purpose of using AWGN channels is to isolate the quantization and clipping effects from other transmission-link impairments to ease the process identifying optimum ADC parameters. In Figure 2, simulations are undertaken for FOFDM for differential binary shift-keying (DBPSK), and amplitude shift-keying (ASK)-8 up to ASK-16, in order to optimize the effects of quantization and clipping for a BER of 10^{-3} , over an AWGN channel. The optimum optical signal-to-noise ratios (OSNRs) for a targeted BER of 10^{-3} are adopted from Ref. [7] (refer to Figure 1(b) of Ref. [7]). It is shown that from DBPSK to ASK-16 the optimum quantization bits and clipping ratios reach to 8-bits and 12 dB respectively, corresponding to the ASK-16. It is noted that for higher modulation format such as ASK-32 the input signal exceeds the ADC dynamical amplitude range, introducing distortions to the signal and therefore unrealistic ADC parameters are defined.

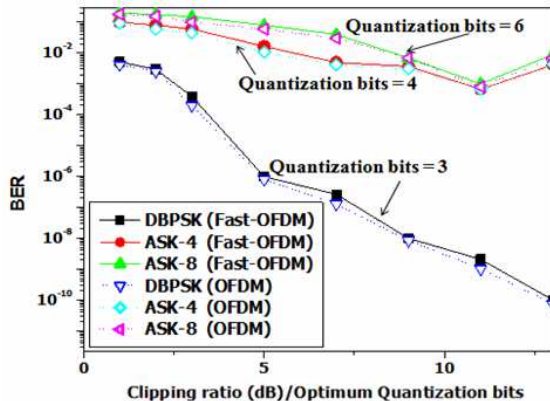


Figure 3: BER versus clipping ratio for a Fast-OFDM/OFDM over 500 m MMF using the optimum quantization bits from the AWGN channel in Figure 2.

Having identified the FOFDM ADC parameters, simulations are undertaken over a 500 m MMF and a 50 km SMF-link respectively. For performance comparisons, the conventional OFDM is also considered. Also for simplicity the employed single-dimensional modulation formats vary from DBPSK up to ASK-8. In Figure 3 results present the BER as a function of clipping ratio for the optimum quantization bits identified previously (see Figure 2) over a 500 m MMF link. It is shown that the BER difference between the FOFDM and the conventional OFDM is almost negligible over the entire range of clipping ratios.

In Figure 4 results present the BER as a function of clipping ratio for the optimum quantization bits identified previously (Figure 2) over a 50 km SMF. The deviation in clipping ratio between FOFDM and conventional OFDM is < 1 dB. Despite the fact FOFDM seems to work slightly better over MMFs due to its capability to improve the tolerance to the DMDs, FOFDM can be very effective for SMFs as well, offering almost the same performance with the conventional OFDM.

4. CONCLUSIONS

In this work it has been concluded that the adopted DAC/ADC quantization bits and clipping ratio for FOFDM are almost similar with these corresponding to the conventional OFDM when using various single-dimensional modulation formats. This statement was valid for scenarios of 500 m MMF links and 50 km SMF links. In particular, it has been shown that < 1 dB deviation in clipping ratio is feasible between FOFDM and conventional OFDM. Having in mind that FOFDM offers twice the bandwidth efficiency compared to conventional OFDM, this work can trigger the implementation of a new generation of very cost-effective and high-speed modems substituting the conventional OFDM technology.

ACKNOWLEDGMENT

This work was supported in part by Science Foundation Ireland (SFI) under grant number 06/IN/I969, and EU FP7 funded projects ALPHA, MODE-GAP and ACCORDANCE.

REFERENCES

- Shieh, W., et al., "Coherent optical OFDM: Theory and Design," *Opt. Express*, Vol. 16, 841–859, 2008.
- Heiskala, J., et al., *OFDM Wireless LANs: A Theoretical and Practical Guide*, Sams, Indianapolis, IN, 2002.
- Zhao, J., et al., "A novel optical fast OFDM with reduced channel spacing equal to half of the symbol rate per carrier," *Proc. OFC/NFOEC*, Anaheim, CA, 2010, Paper OMR1.
- Fuqin, X., "M-ary amplitude shift keying OFDM system," *IEEE Transactions on Communications*, Vol. 51, No. 10, 1638–1642, 2003.
- Ibrahim, S. K., et al., "Demonstration of world-first experimental optical fast OFDM system at 7.174 Gbit/s and 14.348 Gbit/s," *Proc. ECOC*, 2010, PD3.4.

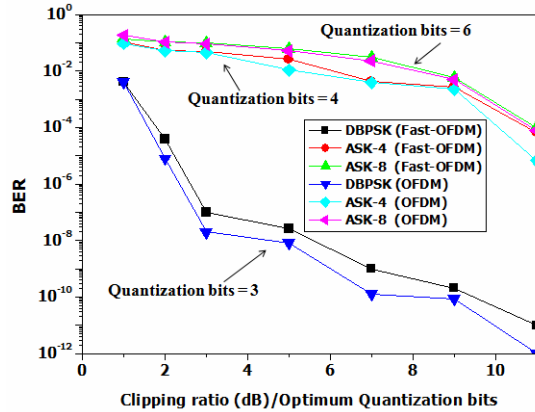


Figure 4: BER versus clipping ratio for a Fast-OFDM/OFDM over 50 km SMF using the optimum quantization bits from the AWGN channel in Figure 2.

6. Giacoumidis, E., et al., “Improved transmission performance of adaptively modulated optical OFDM signals over directly modulated DFB laser-based IMDD links using adaptive cyclic prefix,” *Opt. Express*, Vol. 16, 9480–9494, 2008.
7. Giacoumidis, E., et al., “Performance of optical fast-OFDM in MMF-based links,” *Optical Fiber Communication Conference, OSA Technical Digest (CD)*, Optical Society of America, 2011, paper OWU3.

Improved Transmission Performance of Adaptively Modulated OFDM Signals Using Quantum Dot Semiconductor Optical Amplifier Intensity Modulators

A. Hamié¹, M. Hamze^{1,3}, J. L. Wei², J. M. Tang², and A. Sharaiha³

¹Arts, Sciences, and Technology University of Lebanon (AUL)

Hamra, Commodore Street, Beirut, Lebanon

²School of Electronic Engineering, Bangor University, Dean Street, Bangor LL57 1UT, UK

³Laboratoire RESO, Ecole Nationale d'Ingénieurs de Brest, Brest, France

Abstract— Extensive explorations are undertaken, for the first time, of the feasibility of utilizing quantum dot semiconductor optical amplifier intensity modulators (QD-SOA-IMs) in intensity-modulation and direct-detection (IMDD) SMF-based transmission systems using adaptively modulated optical orthogonal frequency division multiplexing (AMOOOFDM). A theoretical QD-SOA-IM model is developed, of which the performance is compared with previously reported SOA-IMs, and results show that QD-SOA-IMs can not only considerably improve the AMOOOFDM transmission performance but also broaden the optimum operating condition ranges. In particular, for achieving signal bit rates of $> 30 \text{ Gb/s}$ over $> 60 \text{ km}$ SMFs, QD-SOA-IMs allows a 10 dB reduction in CW optical input powers injected into the modulator.

1. INTRODUCTION

To satisfy the increasing end users bandwidth demands, optical orthogonal frequency division multiplexing (OOFDM) has been widely considered as one of the promising enabling technologies for passive optical networks (PONs), because of its high spectral efficiency, excellent resistance to linear impairments, great system scalability and flexibility. The main challenges for practical deployment of OOFDM PON are system cost and flexibility. A recently developed adaptively modulated OOFDM (AMOOOFDM) technique using Semiconductor optical amplifiers (SOA) as intensity modulators (SOA-IMs) have demonstrated over 30 Gb/s for distances up to 60 km using single mode fibers (SMFs) [1] transmission performance. Also colorless transmission has been achieved using SOA-IMs [2] which shows the potential for broadband colorless operation of these devices. Compared with SOA-IMs, QD-SOA-IMs show a faster dynamic gain indicating that these devices could perform better in terms of modulation bandwidth and total system capacity. Detailed numerical simulation results show that, in comparison with SOA-IMs, QD-SOA-IMs can not only considerably improve the AMOOOFDM transmission performance but also significantly lower the required CW optical input powers by approximately 10 dB for transmission distances of up to 140 km. Whilst for transmission distances of $< 20 \text{ km}$, the QD-SOA-IM enabled transmission performance is very similar to that corresponding to an ideal intensity modulator.

2. SYSTEM SETUP AND QD-SOA-IM MODEL

The transmission system is illustrated in Fig. 1, which is composed of an AMOOOFDM transmitter, a single mode fiber (SMF) link, and an AMOOOFDM receiver. The AMOOOFDM transmitter comprises

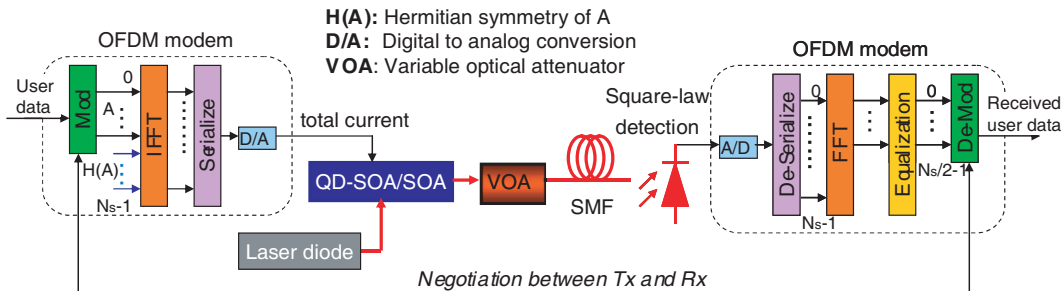


Figure 1: Transmission system diagram together with block diagrams of the AMOOOFDM transmitter and receiver.

an OFDM modem, a SOA/QD-SOA intensity modulator, a laser diode and a variable optical attenuator (VOA). The AMOOFDM receiver consists of a square-law photon detector and an OFDM modem. The work principle of the AMOOFDM system has been described in detail in [1, 2]. The DSP in the OFDM modem including: bit encoding using different modulation format such as DPSK and QAM, IFFT, cyclic prefix insertion, data serialization and digital to analog conversion (DAC). The OFDM modem generated real-valued electrical OFDM signal is added with a DC bias current and then used to directly modulate the optical power injected into the SOA/QD-SOA. A VOA is used before the SMF so as to keep the coupled optical power to the fiber at the desired level. At the receiver side, the OOFDM signal is converted back to the RF domain by a square-law photon detector. Then the original data is recovered by applying the inverse DSP procedure done at the transmitter.

In the QD-SOA-IM model, all the QDs in SOA are assumed to be identical and uniform, and there is only one confined energy level in the conduction and valence band of each dot. This model is a 2LREM model [4–6], where the intermediate (excited) state is replaced by calculating the carrier occupation probability near the band edge of the WL. The wetting layer is populated by the injected current and serves as a reservoir of carriers, as shown in Fig. 2.

In order to gain an in-depth understanding of the effect of the QD-SOA gain saturation on the AMOOFDM system performance, Fig. 3(a) shows the QD-SOA gain versus the optical input power for several values of bias current. It can be seen in Fig. 3(a) that the QD-SOA optical input saturation power increases significantly with increasing bias current. The small-signal gain variation for bias current varying from 100 mA to 300 mA is very small, this is because the QD-SOA charge neutrality defined in [7] is assumed in the ground state (GS) only and not in the whole device as presented in [7]. In Fig. 3(b), comparisons of the gain versus bias current between the SOA and QD-SOA are given for three different optical input powers of 0 dBm, 10 dBm, and 20 dBm. As can be seen in Fig. 3(b), the QD-SOA reaches saturation much faster than the conventional SOA when identical bias current is applied, this is due to the fact that the effective carrier lifetime of the QD-SOA is much smaller than that of the SOA. Generally speaking, the QD-SOA-IM modulation bandwidth is proportional to the inverse of the effective carrier lifetime. As shown in Fig. 4, the

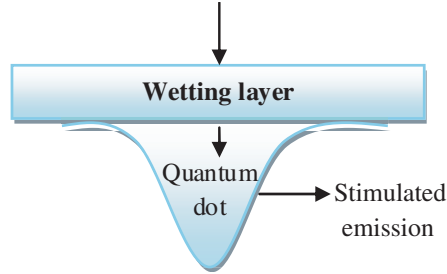


Figure 2: Carrier injection model in the conduction band of a quantum dot. We take into account only the ground state in each dot.

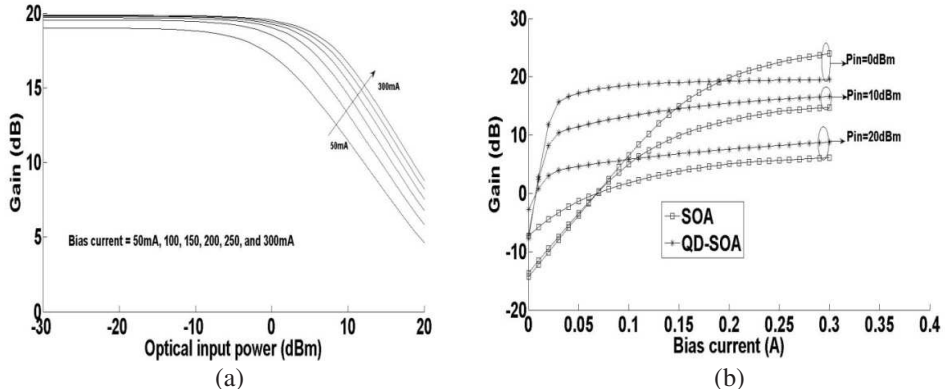


Figure 3: QD-SOA gain saturation characteristics for different operating conditions. (a) QD-SOA gain versus optical input power. (b) Gain versus bias current.

larger the CW optical input power to the QD-SOA is, the wider signal bandwidth is obtained due to reduced effective carrier lifetime and signal spectral distortions, thus leading to improved transmission performance. At the same time, however, the larger CW optical input power also brings about serious signal clipping due to the reduced slope of the gain — current curve, which can be seen in Fig. 3(b).

All the results in Fig. 3 agree well with those obtained in [3–6], indicating the validity of the developed QD-SOA-IM model in this paper.

3. SYSTEM TRANSMISSION PERFORMANCE

Figure 5 shows a contour plot to show the achievable transmission capacity of a 60 km IMDD SMF transmission system for both the SOA-IM and the QD-SOA-IM as function of bias current and CW optical input power, the peak-to-peak (PTP) current is set to 80 mA. As seen from the contour plots in Fig. 5, in comparison with the SOA-IM, the QD-SOA-IM has much broader bias current and CW optical input power dynamic variation ranges, over which a specific signal bit rate is achievable. For example, to achieve signal bit rates of > 30 Gb/s, the SOA-IM requires a CW optical input power to vary in a 3 dB range between 19 dBm to 21 dBm; whilst the QD-SOA-IM allows a CW optical input power to vary in a 20 dB range between 10 dBm and 30 dBm. More importantly, to achieve maximized signal bit rates, the QD-SOA allows the injection of CW input powers as low as 10 dBm, which is more practical since the optical input power to these devices should not exceed 12 dBm. Clearly, the QD-SOA-IM-enlarged dynamic ranges improve the performance robustness. Fig. 5 shows that the optimum CW optical input powers are 20 dBm for both the QD-SOA-IM and SOA-IM. For optical input powers less than the optimum CW optical power value, the degradation of the signal transmission capacity is due to the long effective carrier lifetime. This is seen clearly in Fig. 4, as a relatively small optical input power gives rise to a long effective carrier lifetime and thus a narrower modulation bandwidth.

The numerical results are plotted in Fig. 6, where the identified optimum QD-SOA-IM operating conditions are adopted, i.e., a bias current of 100 mA, a driving current PTP of 80 mA and an optical input power of 20 dBm. Signal bit rate comparisons are also made in Fig. 6 between the QD-SOA-IM, the SOA-IM and the ideal intensity modulator (IM). In simulating the ideal IM, a simple

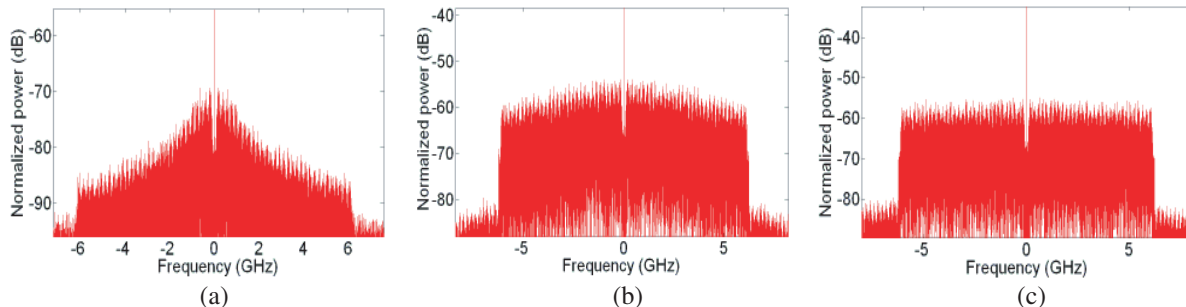


Figure 4: Spectrum of modulated AMOOFDM signal at the output facet of the QD-SOA subject to different CW optical input powers of (a) 0 dBm, (b) 10 dBm and (c) 20 dBm.

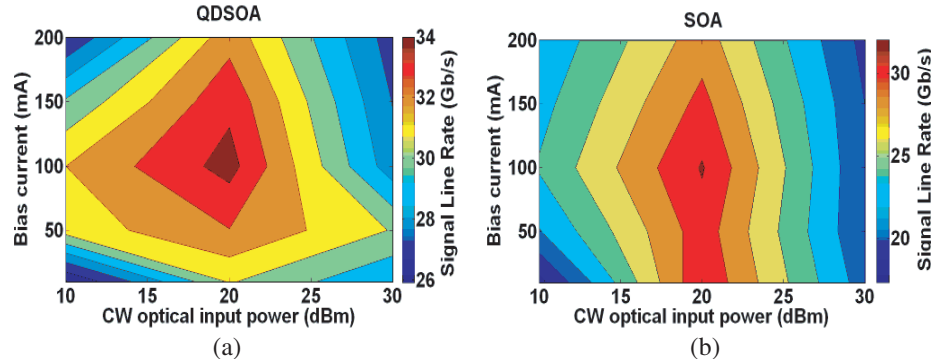


Figure 5: Contour plot of signal line rate as a function of CW optical input power and bias current after transmitting a 60 km SMF IMDD transmission system. (a) QD-SOA and (b) SOA.

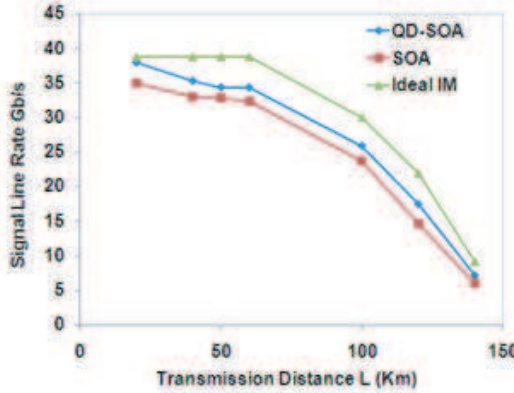


Figure 6: Maximum achievable signal transmission capacity versus reach performance of AMOOFDM signals for various intensity modulators.

square root operation is applied to the driving current. It can be seen in Fig. 6 that, the QD-SOA-IM outperforms the SOA-IM in signal bit rate for all transmission distances of up to 140 km. For transmission distances of 20 km, the QD-SOA-IM offers signal bit rates almost identical to the ideal IM.

4. CONCLUSIONS

Extensive explorations have been undertaken, for the first time, of the feasibility of utilizing QD-SOA-IMs in IMDD SMF-based AMOOFDM transmission systems for applications in PONs. Taking into account the QD and wetting layer effects, a theoretical QD-SOA-IM model has been developed. It has been shown that, in comparison with previously reported SOA-IMs, QD-SOA-IMs can not only considerably improve the AMOOFDM transmission performance but also broaden the optimum operating condition ranges. In particular, for achieving signal bit rates of > 30 Gb/s over > 60 km SMFs, QD-SOA-IMs allows a 10 dB reduction in CW optical input powers injected into the modulator. These results show the potential of using QD-SOA-IMs in future PON systems.

REFERENCES

- Wei, J. L., A. Hamié, R. P. Giddings, and J. M. Tang, "Semiconductor optical amplifier-enabled intensity modulation of adaptively modulated optical OFDM signals in SMF-based IMDD systems," *J. Lightwave Technol.*, Vol. 27, 3679–3689, Aug. 2009.
- Wei, J. L., X. L. Yang, R. P. Giddings, and J. M. Tang, "Colourless adaptively modulated optical OFDM transmitters using SOAs as intensity modulators," *Opt. Express*, Vol. 17, 9012–9027, May 2009.
- Sugawara, M., H. Ebe, N. Hatori, and M. Ishida, "Theory of optical signal amplification and processing by quantum-dot semiconductor optical amplifiers," *Physical Review B*, Vol. 69, 235332-(1-39), Jun. 2004.
- Sun, H., Q. Wang, H. Dong, and N. K. Dutta, "XOR performance of a quantum dot semiconductor optical amplifier based Mach-Zehnder interferometer," *Opt. Express*, Vol. 13, 1892–1899, Mar. 2005.
- Sun, H., Q. Wang, H. Dong, and N. K. Dutta, "All-optical logic performance of quantum-dot semiconductor amplifier-based devices," *Microwave and Optical Technology Letters*, Vol. 48, 29–35, Jan. 2006.
- Berg, T. W., J. Mork, and J. M. Hvam, "Gain dynamics and saturation in semiconductor quantum dot amplifiers," *New Journal of Physics*, Vol. 6, 178, 2004.
- Li, X. and G. Li, "Static gain, optical modulation response, and nonlinear phase noise in saturated quantum-dot semiconductor optical amplifiers," *IEEE J. of Quantum Electronics*, Vol. 45, May 2009.

Bandwidth Efficient Hybrid Wireless-optical Broadband-access Network (WOBAN) Based on OFDM Transmission

Redhwan Q. Shaddad^{1,2}, Abu Bakar Mohammad¹, and Abdulaziz M. Al-Hetar²

¹Photonic Technology Center, InfoComm Research Alliance, Universiti Teknologi Malaysia, Malaysia

²Communication and Computer Engineering Department

Faculty of Engineering and Information Technology, Taiz University, Yemen

Abstract— In this paper, a simple and bandwidth efficient hybrid wireless-optical broadband access network (WOBAN) based on orthogonal frequency division multiplexing (OFDM) is proposed and designed. It is an optimal combination of an optical backhaul and a wireless front-end for an efficient access network. The bandwidth efficient WOBAN based on OFDM provides an effective solution to eliminate intersymbol interference (ISI) caused by dispersive channels. There are two factors considered important here; multipath fading in wireless link and dispersion effects in fiber link. The physical layer performance is analyzed in terms of bit error rate (BER), error vector magnitude (EVM), and signal-to-noise ratio (SNR). An 8 Gb/s data rate has been achieved by the optical backhaul along optical fiber length of 20 km. The wireless front-end access point supports data rate up to 240 Mb/s along an outdoor wireless link.

1. INTRODUCTION

Next generation access network are projected to support high data rate, broadband multiple services, scalable bandwidth, and flexible communications for manifold end-users. A hybrid WOBAN is a promising architecture for next generation access network [1]. The WOBAN is a powerful combination of optical backhaul and wireless front-end. The optical backhaul provides high-bandwidth digital services and long-distance communications. The wireless front-end is ubiquitous and flexible penetration to end-users. This integrated architecture contributes good scalability, cost effectiveness, and high bandwidth efficiency.

The optical backhaul is a tree network connecting the central office (CO) and wireless front-end. The wireless front-end consists of gateway routers and wireless mesh routers are widespread to penetrate an end-user's neighbourhood. In this paper, a new architecture of the WOBAN is proposed and designed based on a wavelength division multiplexing passive optical network (WDM PON) which transport many wireless OFDM signals over fiber at the optical backhaul based a wireless fidelity (WiFi) technology. The front-end is a wireless mesh network (WMN) with several wireless routers and few gateways which are called access points (APs) where the optical unit networks (ONUs) and wireless gateway routers gather. The transport of the wireless signals in the WOBAN is subject to several impairments including dispersion effects in fiber link and multipath fading in wireless link. The bandwidth efficient WOBAN based on OFDM provides an effective solution to eliminate intersymbol interference (ISI) caused by dispersive channels [2]. The WDM PON based on OFDM has been considered as a promising option due to its high bandwidth efficiency, it uses a few wavelengths to multiplex several APs in the frequency domain, and it manages the bandwidth by using modern digital processing hardware [3]. The WMN is implemented by using a multiple-input multiple-output orthogonal frequency division multiplexing (MIMO OFDM) based IEEE 802.11n wireless local area network which has many interesting characteristics such as high coverage, great throughput, high reliability and IEEE 802.11n operates in both the 2.4 GHz and 5 GHz bands [4]. Since the WDM PON based on OFDM and the WiFi network use the same technique OFDM, they provide different levels of bandwidth with good match in capacity scales and high spectral efficiency. The WDM PON supports data rate up to 8 Gb/s in both downstream and upstream along the optical link, which is shared by a group of optical network units (ONUs). Each ONU is connected together with a wireless gateway router to form one AP can provide a data rate up to 240 Mb/s over a wireless channel. Each AP is implemented by using four spatial streams at a channel bandwidth of 40 MHz.

The rest of this paper is organized as follows: in Section 2, the architecture of the WOBAN based on OFDM is presented. The simulation design and concept of the fiber optic and wireless transmission systems are explained in Section 3. Section 4 is dedicated to describe the results and discussion. Section 5 concludes the paper.

2. WOBAN ARCHITECTURE

The proposed WOBAN architecture is shown in Fig. 1 [5]. The optical backhaul of the WOBAN comprises of an optical line terminal (OLT) at the central office (CO), a single mode fiber (SMF), an optical distribution node (ODD), and multiple ONUs which are integrated with wireless gateway routers to form the APs. The OLT converts the data to many corresponding OFDM downstream optical signals based IEEE 802.11n which are then transmitted along the optical fiber. It receives OFDM upstream optical signal from the optical fiber and converts it to the corresponding electrical signal. The ODD demultiplexes the downstream optical signal which is received from the OLT to multiple APs and also multiplexes the upstream traffic from the APs to the OLT. In the wireless

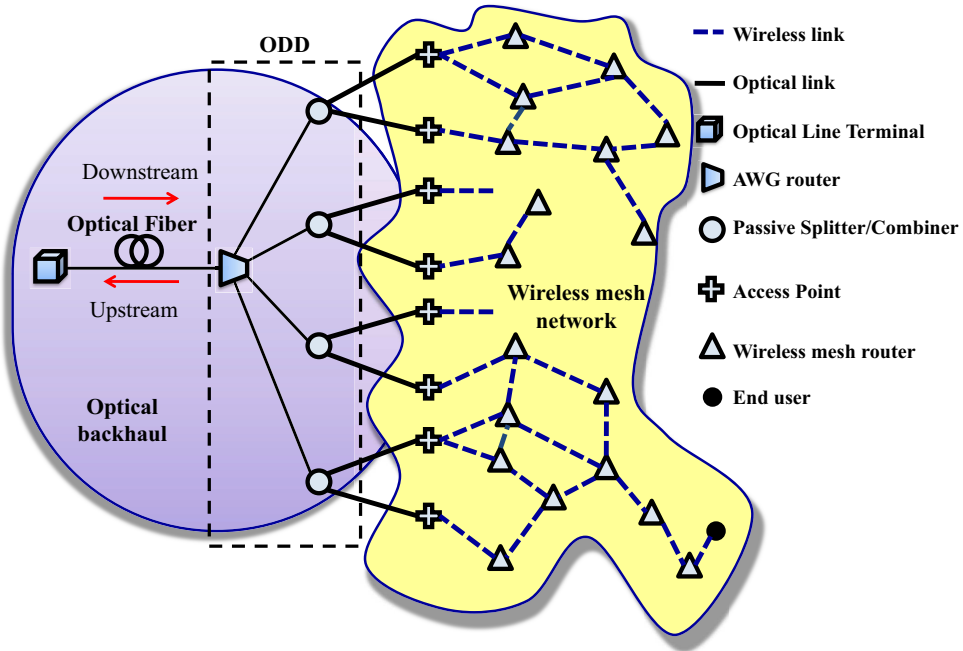


Figure 1: WOBAN architecture.

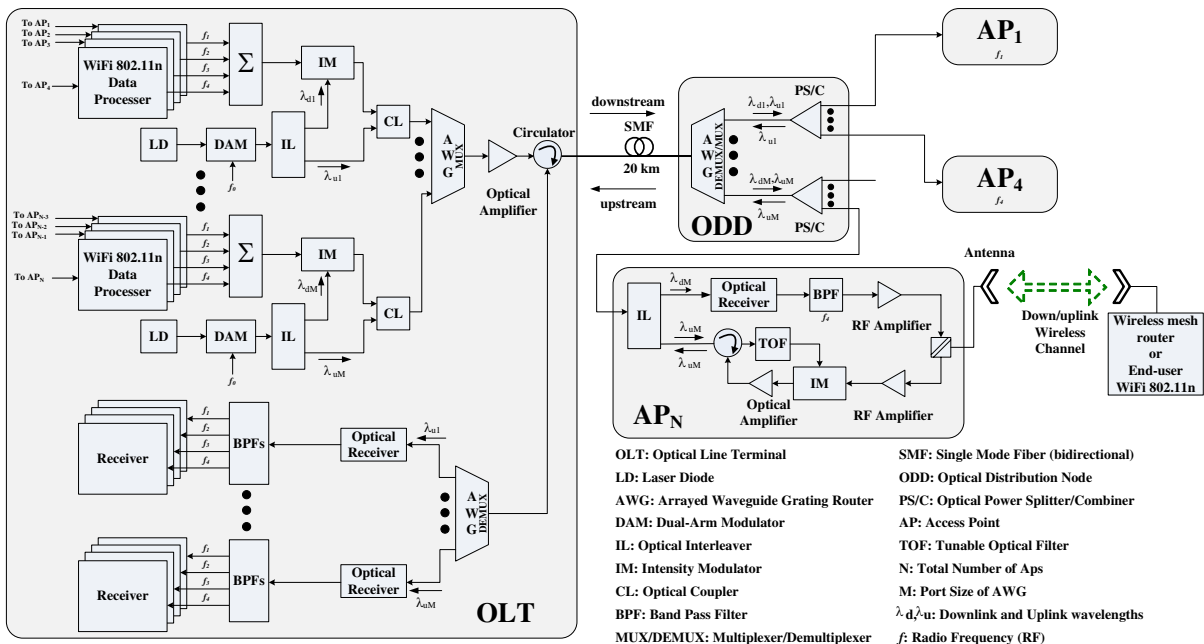


Figure 2: Detail block diagram of the proposed WOBAN.

front-end of WOBAN, WMN is deployed for a ubiquitous and flexible communication to the end-users. Typically, the WMN consists of multiple APs, a group of wireless mesh routers that provide multi-hop wireless communications and a group of wireless end-users [1]. In general, the end-user can send to and receive from its associated mesh router by using specified up/downlink wireless channels.

In this paper, the RF-over-fiber scheme is used to transport radio frequency (RF) wireless signals over fiber. This scheme simplifies the system architecture of the WOBAN by directly conveying high radio frequency broadband signals through optical fibers [6]. In addition, it creates a frequency band guard between the OFDM signal and the optical carrier to reduce the intermodulation distortion [3]. The MATLAB, OptiSystem 8.0 and Advanced Design System (ADS) 2008 software tools are used to accomplish the design and performance analysis of the WOBAN.

3. SIMULATION DESIGN

Design of the WOBAN based on OFDM is shown in Fig. 2. WOBAN design comprises of an OLT connected to multiple APs through 20 km of single mode fiber (SMF). The system uses bidirectional WDM PON with wavelengths assignment and bandwidth allocation done at the OLT. The OLT is designed to implement multiple WiFi 802.11n data processors. Each four WiFi data processors modulates the WiFi signals on different RF frequencies (f_1, f_2, f_3, f_4) in 2.4 GHz band. The WiFi signals are then multiplexed and modulated in external intensity optical modulator (IM) on one assigned wavelength. In the WiFi data processor, the system uses the OFDM technique with Binary Phase Shift Keying (BPSK) and Quadrature Amplitude Modulation (64-QAM). Each processor is designed to provide a data rate of 240 Mb/s for each AP with a channel bandwidth of 40 MHz.

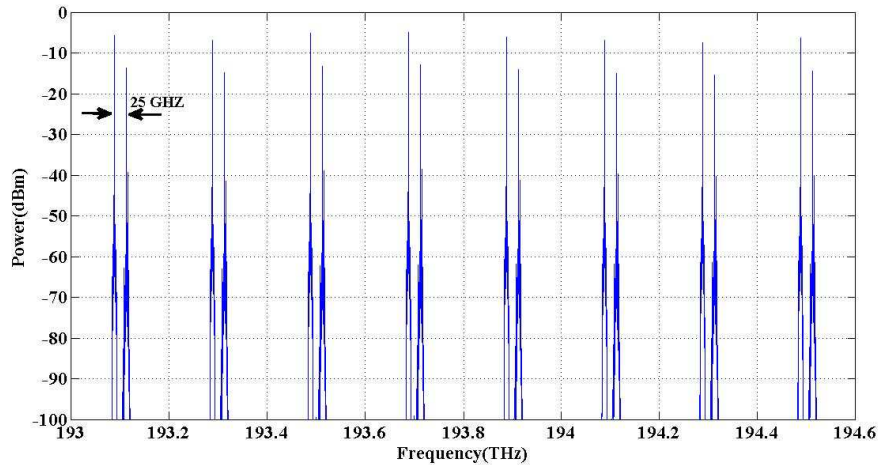


Figure 3: Optical power spectra of the up/downlink channels.

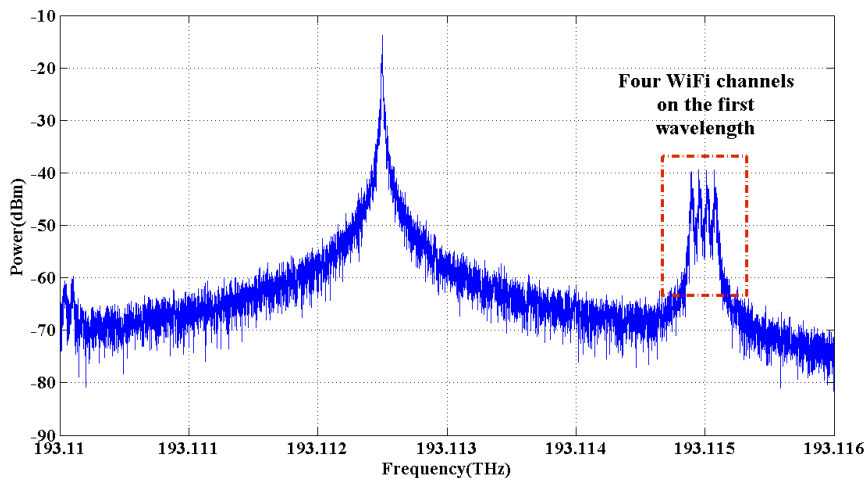


Figure 4: OSSB+C power spectrum of the first downlink channel.

The WDM PON uses the optical carrier suppression and separation (OCSS) technology to generate a wavelength pair from a single laser source at the central office [7] as shown in Fig. 2. The OLT comprises of $M = 8$ laser diodes. Using a dual-arm modulator (DAM), a total of two wavelengths are generated at each LD. The channel spacing of the generated wavelength pairs is determined by twice the frequency of the sinusoidal clock, $f_0 = 12.5$ GHz. An optical interleaver (IL) is used to separate each generated wavelength pair into two channels with downlink wavelength λ_d to modulated the multiplexed RF signals at IM and continuous wave (CW) uplink wavelength λ_u . In downlink, the optical modulated signals are multiplexed at an arrayed waveguide grating router (AWG) and then propagate along 20 km SMF with attenuation of 0.2 dB/km and dispersion coefficient of 17 ps/nm/km. Fig. 3 shows the optical power spectra of the up/downlink channels. There are sixteen ($M = 8$) allocated wavelengths of the up/downlink channels which are selected from conventional band (CB) with 200 GHz (1.6 nm) channel spacing for each link. Also the uplink channels are separated by 25 GHz from the downlink channels. In this design, the wireless signal is externally modulated with the optical carrier resulting in an optical single sideband with carrier (OSSB+C) signal as illustrated in Fig. 4. The single sideband represents four WiFi signals for each wavelength as shown in Fig. 4 for the first downlink optical channel. The OSSB+C modulation method enhances optical spectral efficiency for transporting optically modulated WiFi signals, and overcomes the fiber chromatic dispersion problem. Upon detection at the AP, the wireless signal can be recovered via direct detection using a high-speed photodetector [6].

The WOBAN is designed to operate at data rate of 8 Gb/s in optical backhaul. The downstream is distributed by using ODD to many APs ($N = 32$) according the assigned wavelengths ($M = 8$) and allocated bandwidth (4 frequencies for each wavelength). The ODD comprises of an arrayed waveguide grating (AWG) router and a passive splitter/combiners (PS/Cs). In upstream direction, the APs receive wireless signals from wireless front-end and modulate the wireless signals by external IM using the assigned CW uplink wavelengths based on the wavelength reuse method. The ODD then combines optical modulated signals to send upstream back to the OLT.

In this architecture, the AP has simple design, independence of the air-interface and also enabling multiwireless band operation. The AP receives the optical downstream and transfers it directly to electrical signal which is band-pass filtered according to the allocated RF frequency at the OLT. The wireless signal propagates to an associated wireless mesh router or end-user as demand. The AP supports data rate up to 240 Mb/s along 100 m outdoor wireless link with high spectral efficiency of 6.

4. RESULTS AND DISCUSSION

The received downlink optical signal is detected at the AP and is then amplified and transmitted directly to the associated wireless mesh router or end-user. In this work, the AP is simulated to provide a data rate of 240 Mb/s, since 64-QAM is used in WiFi data processor at the OLT and the end-user. Fig. 5 shows the spectrum of the RF transmitted signal from AP_1 at the carrier frequency 2.4 GHz (f_1) with a bandwidth of 40 MHz. The average of transmitted power is 10 dBm as shown in Fig. 5.

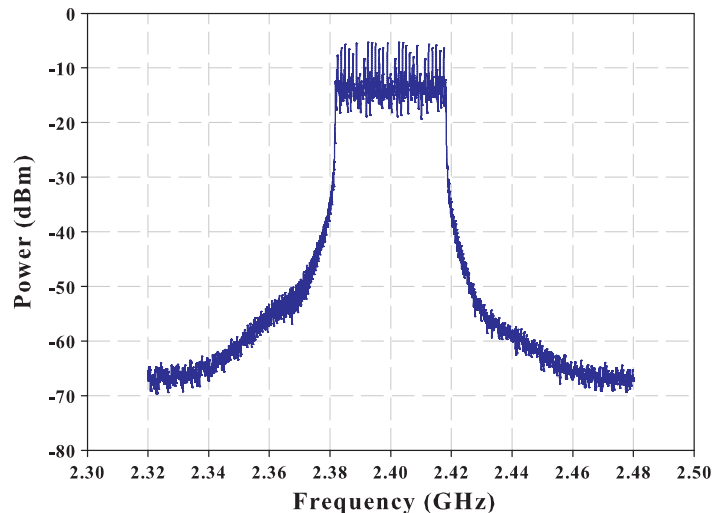


Figure 5: Spectrum of the transmitted power at AP_1 .

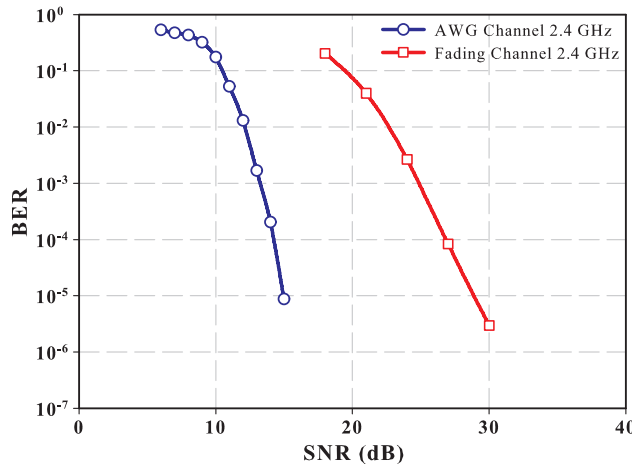


Figure 6: BER versus SNR at the wireless end-user receiver.

The BER at different situations are measured to evaluate system performance. Fig. 6 shows the BER versus the SNR for the received signal at end-user. The additive white Gaussian noise (AWG) channel model and the fading channel model are simulated, since the SMF with dispersion coefficient of 17 ps/nm/km is considered. At a BER less than 10^{-5} , the better performance in wireless communication channel occurs when the SNR is greater than 15 dB and 28.5 dB for the AWG channel and the fading channel respectively. For 64-QAM demodulated OFDM in the WiFi end-user receiver, maximum EVM of -60.8 dB has been estimated. This EVM performance allows perfect symbol detection at the receiver.

5. CONCLUSION

In this paper, the bandwidth efficient WOBAN based on OFDM is proposed and designed as a promising technique for future access network. The physical layer performance in terms of the BER, EVM, and SNR is reported. In conclusion, the proposed WOBAN achieved the data rate of 8 Gb/s for up/downstream over 20 km fiber followed by 100 m outdoor wireless link with a data rate of 240 Mb/s.

ACKNOWLEDGMENT

We greatly appreciate Universiti Teknologi Malaysia and Photonic Technology Center for providing the facilities which enable this work to be done. We would also like to thank the Ministry of Science, Technology and Innovation (MOSTI), Malaysia for sponsoring this work under project vote number 73720.

REFERENCES

1. Sarkar, S., S. Dixit, and B. Mukherjee, "Hybrid wireless-optical broadband-access network (WOBAN): A review of relevant challenges," *J. Lightwave Technol.*, Vol. 25, No. 11, 3329–3340, 2007.
2. Armstrong, J., "OFDM for optical communications," *J. Lightwave Technol.*, Vol. 27, No. 3, 189–204, 2009.
3. Coura, D. J., J. Silva, and M. Segatto, "A bandwidth scalable OFDM passive optical network for future access network," *Photon. Netw. Commun.*, Vol. 18, No. 3, 409–4016, 2009.
4. Perahia E. and R. Stacey, *Next Generation Wireless LANs: Throughput, Robustness, and Reliability in 802.11n*, Cambridge University Press, New York, 2008.
5. Shaddad, R. Q. and A. B. Mohammad, "Performance assessment of a 2 Gb/s hybrid optical-wireless access network," *Proceeding of International Conference on Photonics (ICP 2010)*, Langkawi, Malaysia, July 2010.
6. Lim, C., A. Nirmalathas, M. Bakaul, P. Gamage, K. Lee, Y. Yang, D. Novak, and R. Waterhouse, "Fiber-wireless networks and subsystem technologies," *J. Lightwave Technol.*, Vol. 28, No. 4, 390–405, 2010.
7. Jia, Z., J. Yu, G. Ellinas, and G. Chang, "Key enabling technologies for optical wireless networks: Optical millimeter-wave generation, wavelength reuse, and architecture," *J. Lightwave Technol.*, Vol. 25, No. 11, 3452–3471, 2007.

FDTD Analysis of Signal and Interference Characteristics in Multi-channel Propagation over Forests for WiMAX Communication

Yasumitsu Miyazaki¹, Nobuo Goto², and Koichi Takahashi¹

¹Department of Media Informatics, Aichi University of Technology
50-2 Manori, Nishihamasama-cho, Gamagori 443-0047, Japan

²Institute of Technology and Science, The University of Tokushima
2-1 Minamijosanjima-cho, Tokushima 770-8506, Japan

Abstract— WiMAX wireless communication has been rapidly developed for broadband mobile communication. To design excellent high performance mobile communication systems, accurate evaluation of communication systems is indispensable. Mobile WiMAX wireless communication system uses microwave carrier of 2.5 GHz band and modulation of OFDM mainly. In this paper, propagation characteristics and received electric field distribution of WiMAX wireless data communication system with high bit rate more than 10 Mbps in artificial structures such as buildings, bridge and natural environment such as forest are studied by FDTD simulation. Electric field distributions are studied by changing parameters for material constants size and position of artificial and natural structures. Propagation, reflection, scattering, interference and delay of digital code signal and error bit in received code signals are evaluated to show the environmental characteristics.

1. INTRODUCTION

In recent years, WiMAX wireless communication has been rapidly developed for broadband mobile communication of image and TV transmission. Mobile WiMAX communication system uses microwave carrier of 2.5 GHz frequency band and modulation system is mainly OFDM for transmission of signals. By using OFDM technique, WiMAX provides high speed and reliable communication against the multi pass interference due to the presence of obstacles in communication channels [1]. To design excellent high performance wireless communication systems, accurate evaluation of communication channels is indispensable. By using computer numerical simulation of parallel FDTD method, we studied fundamental microwave propagation and scattering characteristics in urban area [2, 3]. In these analyses, building and street effects on high speed signal propagation have been investigated by computer simulation of FDTD method. However, wave propagation and scattering characteristics by presence of forest and trees are not so much studied. The effects of multiple scattering and attenuation of microwave by forest are severe factors of high speed wireless communications. Size of branches and leaves of trees are comparable with microwave wavelength and yield strong interaction phenomena between microwaves and trees of broadband propagation.

In this paper, propagation and scattering characteristics of microwave over forests in WiMAX wireless communication is numerically analyzed using FDTD method [4, 5]. FDTD method can be applied for signal and noise analysis about several different complex models and inhomogeneous materials such as forests in communication channels. By applying FDTD method for the analysis of communication channels of propagation over trees and forests, numerical simulations of signal propagation for various tree structures at different frequencies and digital signal bit rates are demonstrated. In FDTD simulations, the incident wave is assumed to be a traveling wave from transmission antenna station at a far distance. Numerical results in this paper show and analyze the effects of various structures of forests and beam spot size of incident waves. The shape of forest is assumed to be constructed by random surface and distribution of branches of trees are inhomogeneous. Forest and trees in radio communication channel is considered to be as random surface and inhomogeneous materials. Fig. 1 shows the situation for microwave propagation in mobile WiMAX wireless communication over forests.

The effects of multiple scattering and attenuation due to forests are evaluated using statistical functions, such as average, variance and correlation of conductivities and permittivities for trees. These results may yield important factors for the optimum design of high performance and more reliable WiMAX communication systems.

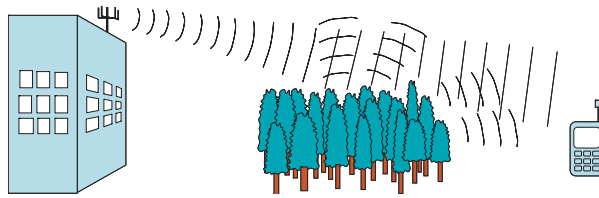


Figure 1: Microwave propagation in mobile WiMAX wireless communication.

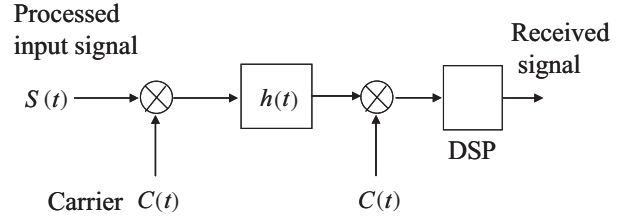
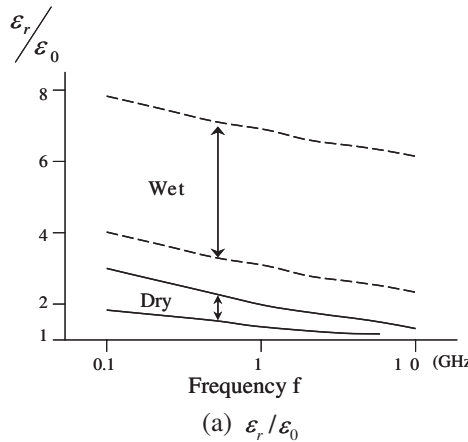
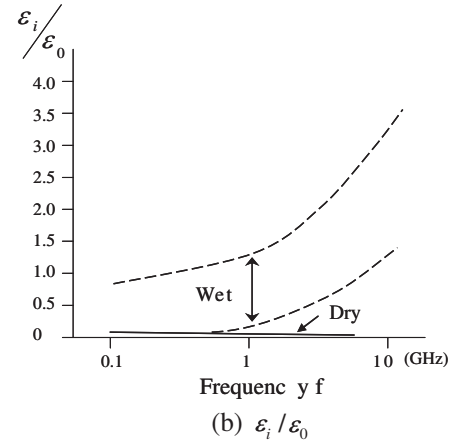


Figure 2: Block diagram of digital communication system for OFDM.



(a) $\varepsilon_r/\varepsilon_0$



(b) $\varepsilon_i/\varepsilon_0$

Figure 3: Complex dielectric constants of trees.

2. WIMAX COMMUNICATION SYSTEM AND FOREST PROPAGATION MODEL

Mobile WiMAX communication system uses OFDM for transmission of signals. OFDM uses multiple sub carrier and provide stable communication against fading effects. OFDM requires much signal processing in transmitter and receiver, and amplifier with wide dynamic range. However, these problems have been resolved gradually by development of recent analog/digital devices and signal processing techniques. WiMAX provides high speed data rate by synthesizing multiple sub carriers. Block diagram of WiMAX communication system is shown in Fig. 2. $S(t)$ is a sequence of transmission codes and $C(t)$ is a carrier of OFDM modulation in Fig. 2.

In urban area, there are a lot of obstacles such as buildings and forest trees and propagation channel becomes very complex. We studied fundamental propagation and scattering of microwaves in urban area, using parallel FDTD computing and showed wave scattering, attenuation and delay due to buildings and roads. In this paper, propagation and scattering characteristics of microwave over forests in WiMAX wireless communication are studied. Fig. 3 shows the frequency characteristics of complex dielectric constant $\varepsilon^* = \varepsilon_r - j\varepsilon_i$ of dry and wet trees. Here, the relation between imaginary part of dielectric constant ε_i and conductivity σ is given by $\varepsilon_i = \sigma/\omega$ when $\omega = 2\pi f$ is angular frequency of electromagnetic waves.

For analysis model of Fig. 1, height of forest $h(y, z)$ is generated as random surface by giving parameters of average height \bar{h} , root mean square of height $\sqrt{\Delta h^2}$ and correlation length ℓ .

$$\sqrt{\Delta h^2} = \sqrt{\frac{1}{\ell_y \ell_z} \int_0^{\ell_y} dy \int_0^{\ell_z} dz (h(y, z) - \bar{h})^2}, \quad \ell = \left\{ \sqrt{y^2 + z^2} |R(y, z)/R(0, 0) = 1/e \right\} \quad (1)$$

where $R(y, z)$ is auto correlation function of $h(y, z)$.

3. COMPUTER SIMULATION BY FDTD

Microwave propagation and scattering by forests are very important phenomena for wireless broadband communication such as mobile WiMAX communication. In WiMAX communication system of complex propagation channel, it is difficult to study accurate propagation characteristics by analytical theory. We study signal and interference characteristics of WiMAX communication signal

in forest model using FDTD method. Computer simulation using FDTD method is very useful to evaluate these characteristics numerically. In FDTD simulations, the incident wave is assumed to be a traveling wave from transmission antenna station at a far distance. Total analysis space model of three-dimensional FDTD is shown in Fig. 4. The size of analysis space is $\ell_x \times \ell_y \times \ell_z$. The incident wave is y -polarized Gaussian beam wave with angular frequency $\omega = 2\pi f$, beam waist $z = z_0$ and beam spot size S . For example, FDTD equation for E_y^n is given by

$$\begin{aligned} E_y^n(i, j, k) &= c_1 E_y^{n-1}(i, j, k) - c_2 J_y^{n-1}(i, j, k) \\ &\quad + c_3 \{ H_x^{n-1}(i, j, k) - H_x^{n-1}(i, j, k-1) - H_z^{n-1}(i, j, k) + H_z^{n-1}(i-1, j, k) \} \quad (2) \\ J_y^n(i, j, k) &= \begin{cases} \neq 0 & (k=1) \\ = 0 & (k \neq 1) \end{cases}, \quad c_1 = \frac{1 - \sigma \Delta t / (2\varepsilon)}{1 + \sigma \Delta t / (2\varepsilon)}, \quad c_2 = \frac{\Delta t / \varepsilon}{1 + \sigma \Delta t / (2\varepsilon)}, \quad c_3 = \frac{c_2}{\Delta s}, \quad c_4 = \frac{\Delta t}{\mu_0 \Delta s} \end{aligned}$$

Here, x , y , z and t are discretized by $x = i\Delta s$, $y = j\Delta s$, $z = k\Delta s$ and $t = n\Delta t$ and $0 \leq i \leq N_x$, $0 \leq j \leq N_y$, $0 \leq k \leq N_z$, $0 \leq n \leq N_t$. The incident wave is a WiMAX communication wave generated by equivalent current density

$$\begin{aligned} J_y^n(i, j, k) &= s(n\Delta t) \sin[(\omega_c + m\omega_0)n\Delta t] \mathbf{J}(i, j, k) = M(n\Delta t) \mathbf{J}(i, j, k) \\ \mathbf{J}^n(i, j, k) &= \exp \left\{ -\left(\frac{i\Delta s - x_0}{S} \right)^2 \right\} \exp \left\{ -\left(\frac{j\Delta s - y_0}{S} \right)^2 \right\} \delta(k - k_0) M(n\Delta t) \quad (3) \end{aligned}$$

where (x_0, y_0, z_0) is the center point of incident beam, S is the beam spot size at $z = z_0$ ($k_0 = 1$), ω_c is the angular frequency of carrier, $\omega_0 = 2\pi f_0$, f_0 is an interval of carrier frequency and $m f_0$ is the frequency of m th sub carrier, $s(n\Delta t) = \exp\{-((n\Delta t - t_0)/T)^2\}$. Here, T is pulse width and t_0 is center of Gaussian pulse envelope $s(n\Delta t)$. Mur's boundary condition is applied to obtain the electromagnetic fields at the boundary of analysis space.

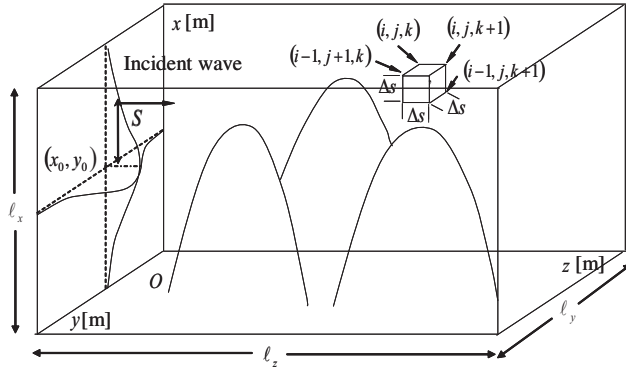


Figure 4: Analysis space of three-dimensional FDTD.

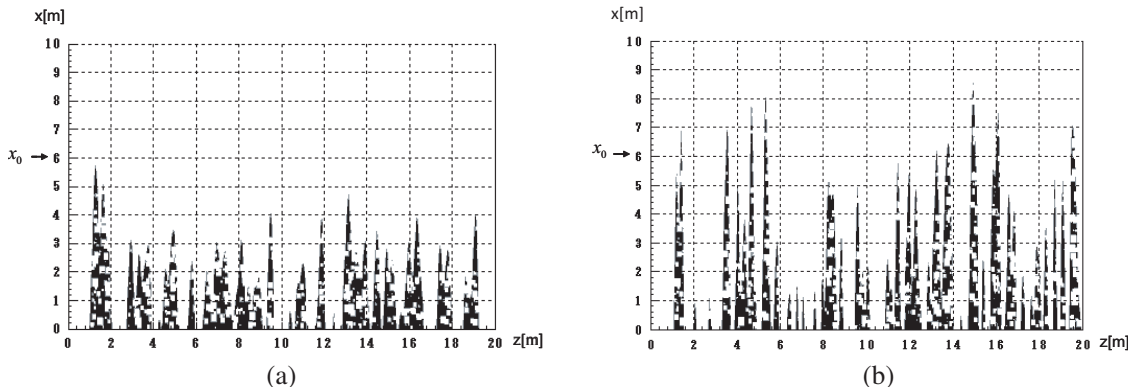


Figure 5: Forest models by random surfaces. (a) Case 1, $\sqrt{\Delta h^2} = 2$ (m), $\ell = 0.2$ (m). (b) Case 2, $\sqrt{\Delta h^2} = 3.4$ (m), $\ell = 0.15$ (m).

4. PROPAGATION AND SCATTERING CHARACTERISTICS

4.1. Twodimensional Analysis

Propagation and scattering characteristics of Gaussian beam waves with microwave frequency are evaluated using FDTD method. In FDTD simulation, $\ell_x = 1000\Delta s = 10$ (m), $\ell_z = 2000\Delta s = 20$ (m), $x_0 = 6$ (m) and $\bar{h} = 1$ (m) are used. For incident wave, $\omega_c = 2\pi f$, $f = 2.5$ GHz, $m = 0$, $T = 2$ (ns) and $t_0 = 5$ (ns) are used. Numerical parameters for FDTD analysis are shown in Table 1. Fig. 5 shows the forest model by random surfaces.

Table 1: Numerical parameters for 2-D FDTD analysis.

Parameters	Values
f : Frequency of incident wave	2.5 GHz
λ : Wavelength of incident wave	0.12 m
ℓ_x : Length of analysis space (x)	10 m (83.3 λ)
ℓ_z : Length of analysis space (z)	20 m (166.7 λ)
x_0 : Center point of the beam (x)	6 m
S : Beam spot size	2.2 m (18.3 λ)
t_0 : Peak time of incident pulse	5 ns
T : Parameter for pulse width	2 ns
ΔS : Length of a cell	0.01 m
Δt : Time increment	0.02 ns
ε_r : Relative dielectric constant of trees	4
σ : Conductivity of forests	10^{-3} S/m
N : Number of air gaps	700 (Case 1-2, 2-2)
a_i : Length of a side of air gaps	$10^{-3} \sim 3 \times 10^{-2}$ m (Case 1-2, 2-2)
\bar{h} : Average height of forests	1.0 m
$\sqrt{\Delta h^2}$: rms height of forests	2.0 m (Case 1) 3.4 m (Case 2)
ℓ : Correlation length of forests	0.20 m (Case 1) 0.15 m (Case 2)

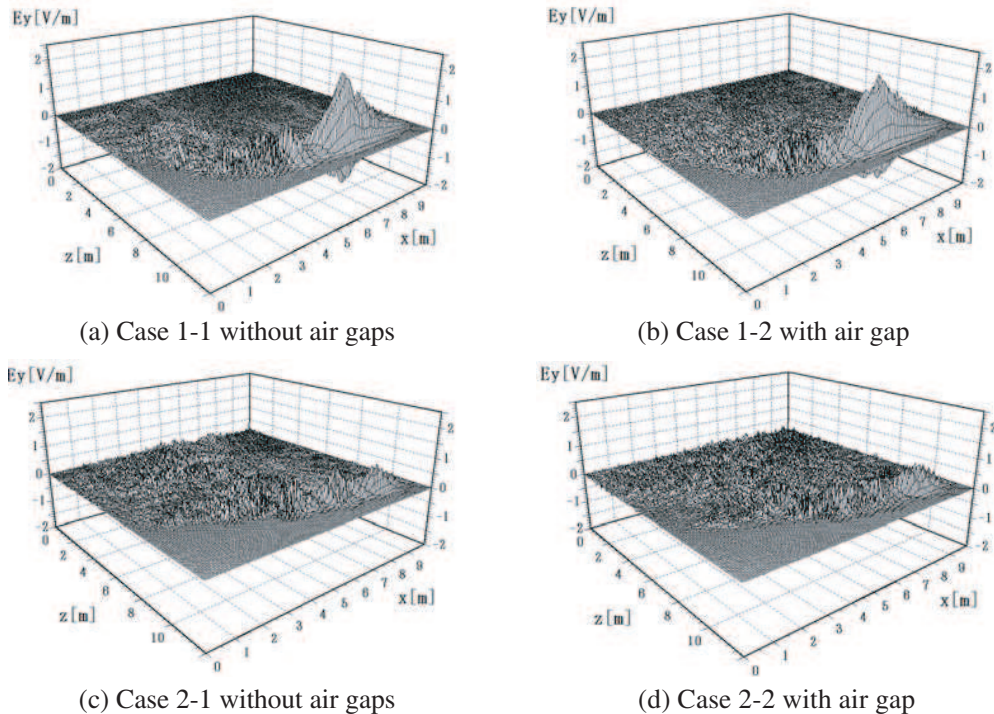


Figure 6: Electric field E_y at $t = 2000\Delta t = 40$ (ns).

Table 2: Numerical parameters for 3-D FDTD analysis.

Parameters	Case 1	Case 2
ℓ_x : Length of analysis space (x)	1.5 m (12.5λ)	
ℓ_y : Length of analysis space (y)	1.5 m (12.5λ)	
ℓ_z : Length of analysis space (z)	1.5 m (12.5λ)	
ΔS : Length of a cell	10^{-2} m ($\lambda/12$)	
Δt : Time increment	0.019 ns ($T_0/20$), $T_0 = 1/f$	
f : Frequency of incident wave	2.5 GHz	
λ : Wavelength of incident wave	0.12 m (c/f)	
t_0 : Peak time of incident pulse	5 ns	
T : Pulse width of incident wave	2 ns	
x_0 : Center point of the beam (x)	0.5 m	
y_0 : Center point of the beam (y)	0.5 m	
S : Beam spot size at $z = 0$	0.12 m (1λ)	
ϵ_r : Dielectric constant of forests	$4\epsilon_0$	
σ : Conductivity of forests	10^{-3} S/m	
\bar{h} : Average height of forests	0.6 m	0.7 m
$\sqrt{\Delta h^2}$: RMS height of forests	0.2 m	0.5 m
ℓ : Correlation length of forests	0.2 m	0.2 m

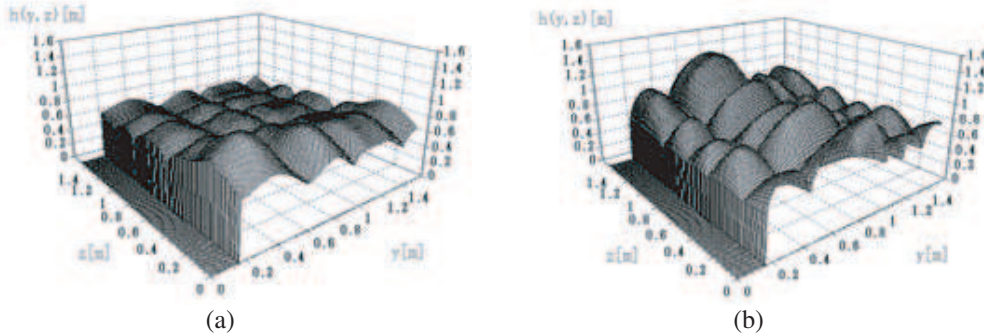
Figure 7: Forest models by 3-D random surfaces. (a) Case 1 ($\sqrt{\Delta h^2} = 0.2$ m, $\bar{h} = 0.6$ m, $\ell = 0.2$ m). (b) Case 2 ($\sqrt{\Delta h^2} = 0.5$ m, $\bar{h} = 0.7$ m, $\ell = 0.2$ m).

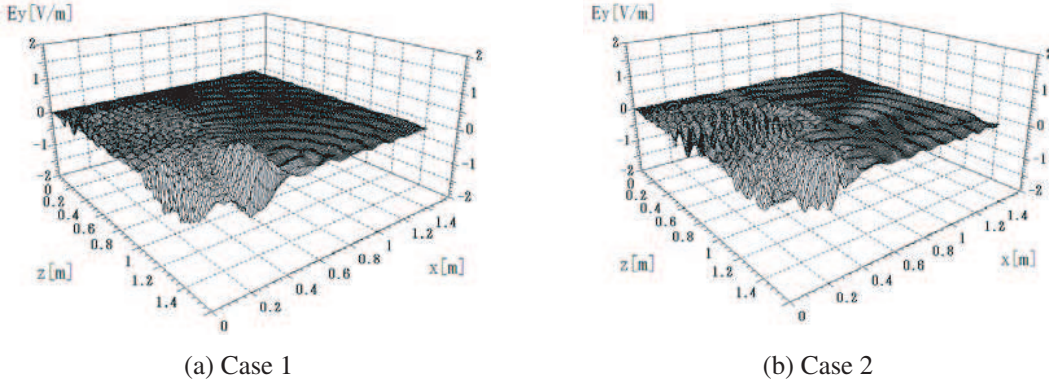
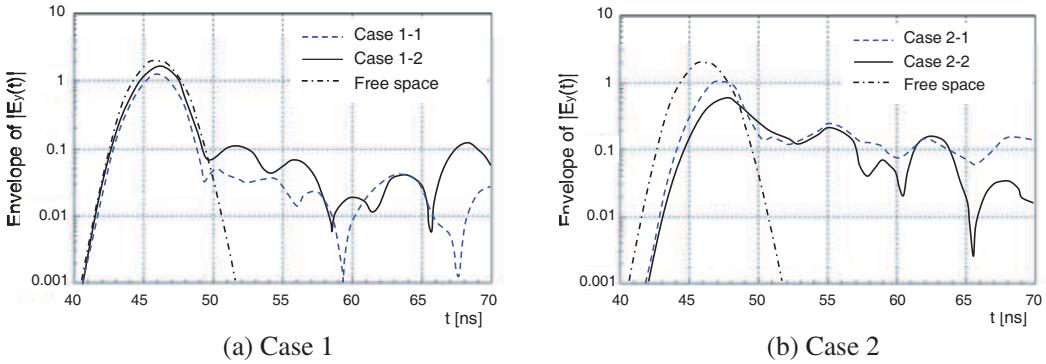
Figure 6 shows numerical results and as shown in Fig. 6, the electromagnetic wave propagated over forest keeps strong intensity with wide beam width when the height of trees is small. However, when there are tall trees higher than beam center, the wave is highly attenuated by scattering and absorption by trees. In these models, two cases are considered for trees with and without airgaps.

4.2. Three-dimensional Analysis

Here, three-dimensional analysis are demonstrated for evaluation actual situation in WiMAX communication, using models of Fig. 7. For incident wave, $\omega_c = 2\pi f$, $f = 2.5$ GHz, $m = 0$, $T = 2$ (ns) and $t_0 = 5$ (ns) are used. Numerical example for three-dimensional analysis is shown in Table 2. Fig. 8 shows results of forest model of Fig. 7. Traveling waves in forest of relative dielectric constant 4.0 delay compared with waves in free space over the forest. Similarly to two-dimensional case, many scattered waves are observed in forest and electromagnetic waves suffer high attenuation.

5. TIME RESPONSE OF WIMAX CHANNEL

Figure 9 shows the envelope of time responses obtained by 2-D FDTD analysis. In WiMAX communication, delayed waves with longer delay time than guard interval may cause serious bit error in receivers. We will study receiving quality in sufficient big area and long observation time by using parallel FDTD computing. Further, we will discuss digitally modulated OFDM signals of $M(n\Delta t)$.

Figure 8: Electric field E_y at $t = 800\Delta t = 15.2$ (ns).Figure 9: Envelope of received electric field at $(x_0, z) = (6 \text{ m}, 12 \text{ m})$ by two-dimensional FDTD analysis.

6. CONCLUSIONS

In this paper, propagation and scattering characteristics of microwave over forests in WiMAX wireless communication is numerically analyzed using FDTD method. Using statistical characteristics, FDTD method can be applied for signal and noise analysis about several different complex models and inhomogeneous materials such as forests in communication channels. By applying FDTD method for the analysis of communication channels of propagation over trees and forests, numerical simulations of signal propagation for various tree structures at different frequencies and digital signal bit rates are shown, using statistical shape parameters and material constants. Next, the interference of signals from multi users at base station is considered for several OFDM modulated signals. For evaluation of transmission characteristics under this environment, SNR, CNR and BER are calculated by time response obtained using FDTD To improve the transmission characteristics, design of digital signal processing and digital filter for recognition and separation of each desired signal from received signals contaminated by noise interference are discussed.

REFERENCES

1. Li, Y., L. J. Cimini, Jr., and N. R. Sollenberger, "Robust channel estimation for OFDM systems with rapid dispersive fading channels," *IEEE Trans. Commun.*, Vol. 46, 902–915, 1998.
2. Selormey, P. and Y. Miyazaki, "Electromagnetic compatibility characteristics of buildings in mobile radio waves propagation channel," *Trans. IEE Japan*, Vol. 119-C, No. 1, 97–104, 1999.
3. Rodriguez, G., Y. Miyazaki, and N. Goto, "Matrix-based FDTD parallel algorithm for big areas and its applications to high-speed wireless communications," *IEEE Trans. Antennas & Propagat.*, Vol. 54, No. 3, 785–796, 2006.
4. Miyazaki, Y., T. Takada, and K. Takahashi, "Attenuation and scattering characteristics of microwaves over forests for WiMAX wireless communications," *Proc. of EMC 2009*, 21P4-4, 225–228, Kyoto, 2009.
5. Miyazaki, Y., T. Takada, and K. Takahashi, "FDTD analysis of propagation and scattering characteristics of microwaves in random forests media for WiMAX communication," *IEEJ Trans. EIS*, Vol. 130, No. 4, 637–643, 2010.

Effect of an External Magnetic Field on Multipactor on a Dielectric Surface

Libing Cai¹, Jianguo Wang^{1,2}, Xiangqin Zhu¹, Yue Wang¹, Chun Xuan¹, and Hongfu Xia¹

¹Northwest Institute of Nuclear Technology, P. O. Box 69-12, Xi'an 710024, China

²School of Electronic and Information Engineering, Xi'an Jiaotong University, Xi'an 710049, China

Abstract— This paper investigates the effect of an external magnetic field on multipactor on a dielectric surface by using PIC simulation. The simulation results show that the drift force of the external magnetic field pulls electrons back to or pushes electrons away from the dielectric surface, which affect the characteristic of multipactor significantly, and if the external magnetic field exceeds a certain value, the multipactor can be suppressed obviously.

1. INTRODUCTION

As the high power microwave (HPM) technology advances, the power and pulse duration of the HPM source increase substantially, the breakdown of the dielectric window of the feed of HPM source has been becoming the major factor of limiting the transmission and radiation of HPM, and hence, it has limited the application of the HPM. It involves many basic physical phenomena, such as the field electron emission, multipactor, and electron-irradiated outgassing, etc. These phenomena cause the further gas breakdown in the gas layer near dielectric surface. The occurrence of the breakdown is the final result of the complicated physical mechanisms mentioned above [1–3]. In the process of the breakdown, the multipactor plays a key role, and it decides the velocity of outgassing and the formation of the gas layer which is the necessary condition of the final gas breakdown [4]. So the suppression of multipactor can delay or avoid the dielectric surface breakdown, and it has been a major concern among researchers on HPM sources.

In most of the past research on multipactor, there have been few studies on the effect of the external magnetic field. At present, the effect of an external magnetic field is studied by using Monte Carlo simulation [5]. And the research of the suppression of multipactor focus on the process of dielectric surface [6]. In this paper, the effect of an external magnetic field on multipactor is studied by particle-in-cell (PIC) simulation, and the suppression of multipactor by the external magnetic field is investigated.

2. MODEL

The geometry for multipactor on a dielectric surface under a rf field and an external magnetic field is shown in Fig. 1. On the dielectric surface there is a dielectric charging electric field, \mathbf{E}_{dc} , a rf electric field, \mathbf{E}_{rf} , a rf magnetic field, \mathbf{B}_{rf} , and an external magnetic field, \mathbf{B}_0 . \mathbf{E}_{rf} , \mathbf{B}_{rf} and \mathbf{B}_0 are parallel to the dielectric surface, \mathbf{E}_{dc} is vertical to the dielectric surface, along the x axis, and \mathbf{B}_0 is vertical to \mathbf{E}_{rf} . Electrons emitted with a random velocity \mathbf{v}_0 and a random angle φ with respect to the positive y axis are subjected to forces imposed by the electric fields. The dc electric field \mathbf{E}_{dc} does not impart any energy to the electrons but simply bends back their trajectory to strike the dielectric surface at a later time. The rf electric field, \mathbf{E}_{rf} imparts energy to the multipactor electrons, as well as translates them along the y axis. The direction of \mathbf{B}_{rf} varies with the direction of \mathbf{E}_{rf} , and the $\mathbf{E} \times \mathbf{B}$ drift of \mathbf{B}_{rf} pulls the electrons back to dielectric surface. The direction of \mathbf{B}_0 is unaltered, and the $\mathbf{E} \times \mathbf{B}$ drift of the external magnetic field \mathbf{B}_0 pulls the electrons back to the dielectric surface in a half rf period and pushes the electrons away from the dielectric surface in the other half rf period. Having gained energy from the rf field, the electron strikes the dielectric surface with much larger energy \mathbf{E} , and therefore, emits δ secondary electrons through the process of the secondary electron emission. The secondary electrons also leave the dielectric surface and strike back at a later time, gaining energy in the process. If $\delta > 1$, there will be an avalanche of the secondary electron emission.

The secondary electron yield coefficient δ is a function of the impact energy of the primary electron and the angle to the normal at which it strikes the dielectric surface. In this paper, Vaughan's empirical formula is adopted to specify the secondary electron yield coefficient δ , as shown in Fig. 2 [7,8]. Two values of impact energy, termed the first and the second crossover point, E_{p1} and E_{p2} respectively, result in a yield of 1, while $\delta > 1$ in between.

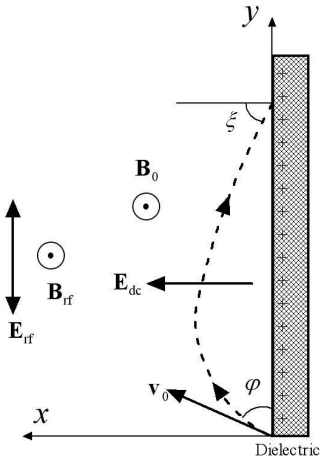


Figure 1: Geometry of multipactor in an external magnetic field.

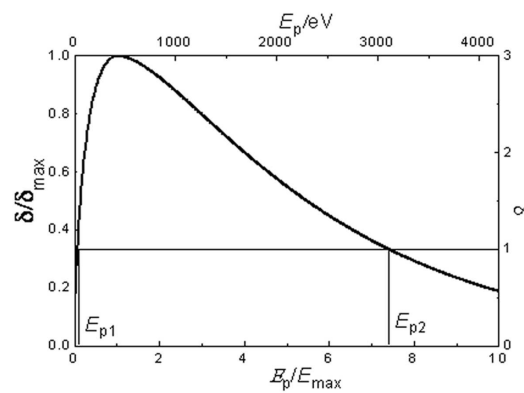
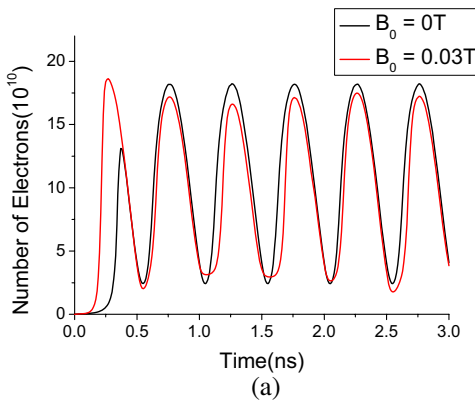
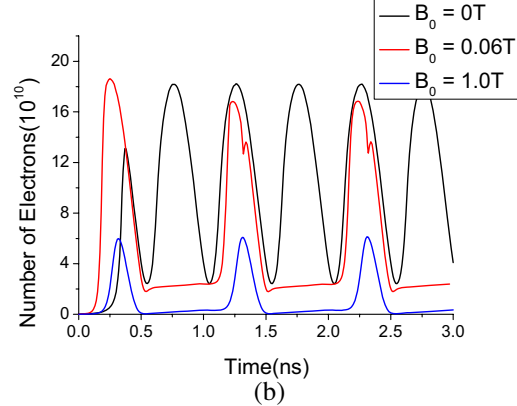


Figure 2: Secondary electron yield vs. impact energy.



(a)



(b)

Figure 3: Temporal evolution of the number of the electrons. (a) at $\mathbf{B}_0 = 0 \text{ T}$ and $\mathbf{B}_0 = 0.03 \text{ T}$, and (b) at $\mathbf{B}_0 = 0 \text{ T}$, $\mathbf{B}_0 = 0.06 \text{ T}$ and $\mathbf{B}_0 = 1.0 \text{ T}$.

3. SIMILATION RESULTS

The direction of the $\mathbf{E} \times \mathbf{B}$ drift of the rf magnetic field is invariant, and the rf magnetic force $qv \times \mathbf{B}_{\text{rf}}$ pulls the electrons back to the dielectric surface. The direction of the $\mathbf{E} \times \mathbf{B}$ drift of the external magnetic changes as the direction of the rf electric field changes. In a half-period, the direction is reverse to that in the other half-period. So the effect of the external magnetic field on the multipactor electrons is different from the rf magnetic field, and the intensity of the effect increase with the external magnetic field. The temporal evolution of the number of the electrons at $\mathbf{B}_0 = 0 \text{ T}$ and $\mathbf{B}_0 = 0.03 \text{ T}$ is shown in Fig. 3(a). In the first half-period of HPM pulse, the direction of the external magnetic force $qv \times \mathbf{B}_0$ is same as the direction of the dc electric force of \mathbf{E}_{dc} , and the external magnetic force pulls the electrons back to the dielectric surface. Therefore the saturation time is shorter than that in case of $\mathbf{B}_0=0 \text{ T}$. But the number of the electrons also oscillates with time at twice the rf frequency after saturation. In the even half-periods, the direction of the external magnetic force is opposite to the direction of the dc electric force of \mathbf{E}_{dc} , and the external magnetic force pushes the electrons away from the dielectric surface.

If the external magnetic force is stronger than the dc electric force, the electrons will go away from the dielectric surface, and there will be no impact with the dielectric surface, which means no secondary electron will be emitted. And the multipactor will be cut off in the even half-periods, as shown in Fig. 3(b). At $\mathbf{B}_0 = 0.06 \text{ T}$ and $\mathbf{B}_0 = 1.0 \text{ T}$, the number of the electrons doesn't increase like that in the case of $\mathbf{B}_0 = 0 \text{ T}$. In the odd half-periods, the external magnetic force pulls the electrons back to the dielectric surface. Therefore the transit time of the electrons decreases with the strength of the external magnetic field, and the energy got from the rf field decreases, too. If the kinetic energy of the electrons is less than the first crossover point, E_{p1} , the secondary electron

yield coefficient will be less than 1. As the increase of the external magnetic field, there will be more and more electrons whose energy are less than E_{p1} . Therefore the peak of the number of the electrons in odd half-periods decreases as the strength of the external magnetic field increases, which can be found in Fig. 3(b). The number of the electrons at $\mathbf{B}_0 = 1.0 \text{ T}$ is less than that at $\mathbf{B}_0 = 0.06 \text{ T}$.

The temporal evolution of the motion of an electron at $\mathbf{B}_0 = 0.06 \text{ T}$ is shown in Fig. 4. Because the direction of the dc electric force of E_{dc} is same to that of the external magnetic force in the odd half-periods, the normal distance is less than 10 μm in most of the even half-periods, and the electrons impact with the dielectric surface continually. So the velocity of the electron is on the order of 10^6 m/s . In the even half-periods, the direction of the dc electric force of E_{dc} is opposite to that of the external magnetic force, and the external magnetic force is greater than the dc electric force of E_{dc} for the electrons, whose velocity exceeds $6.7 \times 10^6 \text{ m/s}$. Therefore the electron moves away from the dielectric surface, and the normal distance increases with time, and can reach 1.0 cm.

The multipactor electrons absorb energy from the rf field, and the energy is deposited on the dielectric surface when the electrons impact with dielectric surface. The power deposited is the rf power absorbed by the dielectric surface through the multipactor electrons, as shown in Fig. 5. The rf peak power is 12 MW, and the peak power deposited is 0.2 MW at $\mathbf{B}_0 = 0 \text{ T}$, which is about 1.6 percent of the rf power. At $\mathbf{B}_0 = 0.06 \text{ T}$, the power deposited is almost zero because there are no or very few electrons impact with the dielectric surface in the even half-periods, and the power deposited is less than that at $\mathbf{B}_0 = 0 \text{ T}$ in the odd half-periods. The gusty peak of deposited power come from the return of the high energy electrons which are push away from the dielectric surface in the even half-periods, and the time band is narrow, so the total energy is not great. Thus the power deposited at $\mathbf{B}_0 = 0.06 \text{ T}$ is less than half of the power deposited at $\mathbf{B}_0 = 0 \text{ T}$.

Once the external magnetic field exceeds a certain value, the multipactor will be cut off in a half-period, and in the other half-period, the intension of the multipactor will decrease versus the strength of the external magnetic field. As shown in Fig. 6, the number of the electrons decreases with the increase of the external magnetic field until the multipactor is suppressed completely. At $E_{rf0} = 3.0 \text{ MV/m}$ and $\delta_{max0} = 3.0$, the multipactor will disappear when the external magnetic field exceeds 1.5 T. And for low rf field and secondary electron yield coefficient, the need external magnetic field to suppress multipactor completely is low, too. At $E_{rf0} = 1.0 \text{ MV/m}$ and $\delta_{max0} = 3.0$ or $E_{rf0} = 3.0 \text{ MV/m}$ and $\delta_{max0} = 2.0$, the need external magnetic field is 0.5 T.

The final gas breakdown of the dielectric surface breakdown is decided by the formation of the gas layer near the dielectric surface, and the formation time is decided by the velocity of outgassing, which is decided by the number of the multipactor electrons. When the multipactor is cut off in the half time of HPM transmission, the formation time of the gas layer will increase to two times. Because the number of the multipactor electrons is linear to the strength of microwave electric field, the breakdown threshold of the HPM power will increase to four times in an external magnetic field with a certain value.

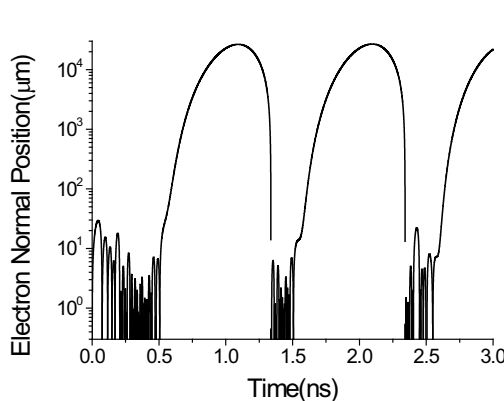


Figure 4: Temporal evolution of the normal position of electrons at $\mathbf{B}_0 = 0.06 \text{ T}$.

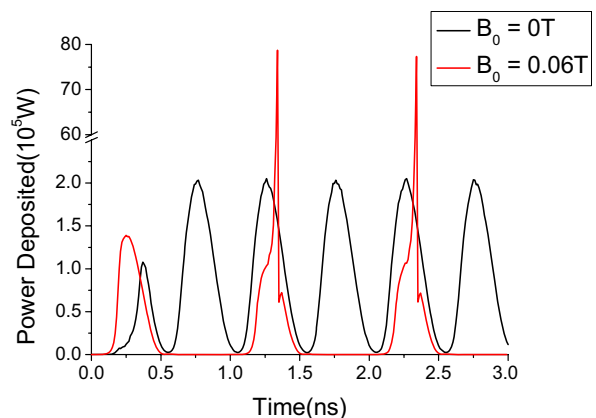


Figure 5: Temporal evolution of the power deposited at $\mathbf{B}_0 = 0 \text{ T}$ and $\mathbf{B}_0 = 0.06 \text{ T}$.

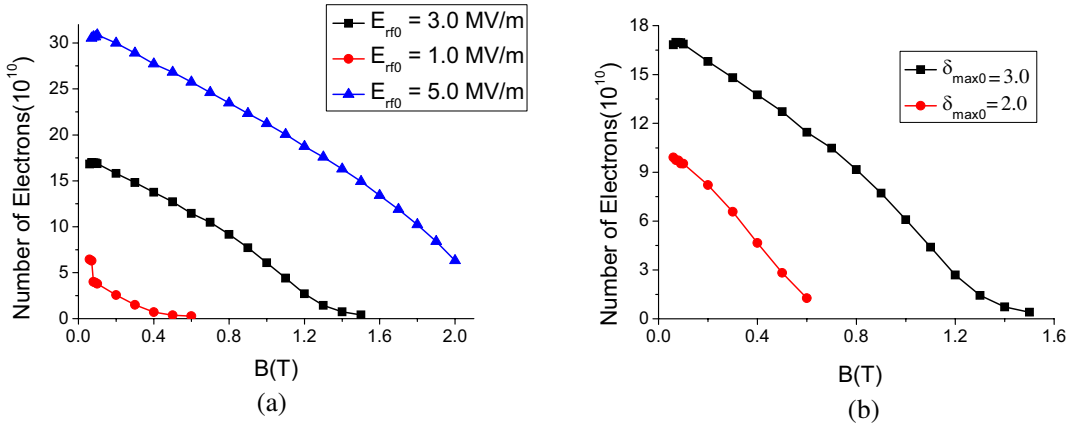


Figure 6: The number of the electrons versus the external magnetic field. (a) at $\delta_{\max 0} = 3.0$, $E_{rf0} = 1.0 \text{ MV/m}$, 3.0 MV/m , and 5.0 MV/m , and (b) at $E_{rf0} = 3.0 \text{ MV/m}$, $\delta_{\max 0} = 2.0$, and 3.0 .

4. CONCLUSIONS

The external magnetic field affects the multipactor by changing the motion of the multipactor electrons. In a half-period, the external magnetic force pulls the electrons back to the dielectric surface, and pushes the electrons away from the dielectric surface in the other half-period. When the external magnetic field exceed a certain value, the multipactor will be cut off in a half-period, which means the velocity of outgassing is half of that in the case of no external magnetic field, and the delay time of breakdown will be increased to twice. For the HPM pulse with the same width, the dielectric window will get fourfold power capability. With the increase of the strength of the external magnetic field, the intension of multipactor will be decreased in the other half-period, which means the dielectric window would get a higher power capability.

REFERENCES

1. Neuber, A., D. Hemmert, H. Krompholz, L. Hatfield, and M. Kristiansen, "Initiation of high power microwave dielectric interface breakdown," *Journal of Applied Physics*, Vol. 86, No. 3, 1724–1728, 1999.
2. Vaughan, J. R. M., "Multipactor," *IEEE Transactions on Electron Devices*, Vol. 35, No. 7, 1172–1180, 1988.
3. Kishek, R. A. and Y. Y. Lau, "Multipactor discharge on a dielectric," *Physical Review Letters*, Vol. 80, No. 1, 193–196, 1998.
4. Wang, J. G., L. B. Cai, X. Q. Zhu, Y. Wang, and X. Chun, "Numerical simulations of high power microwave dielectric interface breakdown involving outgassing," *Physics of Plasma*, Vol. 17, No. 6, 063503, 2010.
5. Valfells, A., L. K. Ang, Y. Y. Lau, and R. M. Gilgenbach, "Effects of an external magnetic field, and of oblique radio-frequency electric fields on multipactor discharge on a dielectric," *Physics of Plasma*, Vol. 7, No. 2, 750–757, 2000.
6. Chang, C., G. Z. Liu, H. J. Huang, C. H. Chen, and J. Y. Fang, "Suppressing high-power microwave dielectric multipactor by the sawtooth surface," *Physics of Plasma*, Vol. 16, No. 8, 083501, 2009.
7. Vaughan, J. R. M., "A new formula for secondary emission yield," *IEEE Transactions on Electron Devices*, Vol. 36, No. 9, 1963–1967, 1989.
8. Vaughan, J. R. M., "Secondary emission formulas," *IEEE Transactions on Electron Devices*, Vol. 40, No. 4, 830, 1993.

An Hybrid MoM-CG Method to Analyze Electromagnetic Scattering

H. Belhadj, S. Mili, and T. Aguili

Sys'Com Lab, National Engineering School of Tunis, Tunisia

Abstract— A hybrid method based on the moment method (MoM) combined to the conjugate gradient (CG) algorithm is presented in this paper to analyze electromagnetic scattering. In fact, the most idea was to exploit the advantages of the CG algorithm, which is an iterative method, and to use it on a conjunction to the direct moment method, when the MoM fails to solve a matrix system due to ill conditioning. The aim was to compute the current density of an iris structure when illuminated by some active modes. It is observed that when using an excessive active modes number, the MoM matrix became ill conditioned and result is inaccurate, so the CG method is incorporated and used in place of matrix inversion in the MoM algorithm. This method is called the hybrid MoM-CG. Simulations results show the relevant impact of this method comparing to the classical moment method.

1. INTRODUCTION

The moment method (MoM) [1] has found widespread use in electromagnetic computational and in practice has been accepted as a stable method. However, in practical terms, as one uses more and more expansion and testing functions per wavelength, the condition number of the resulting moment method matrix increases. In other hand, in the mathematics literature, there is generally a strong preference for iterative methods, especially for large systems, and ill conditioned ones. In fact, iterative methods can easily exploit any sparsity or redundancy in the matrix elements to reduce computer memory requirements, permitting then the treating of more large systems [2]. Also, iterations may be preferable if its convergence is faster and if direct method diverge due to ill conditioning. It is sometimes argued that iteration may be the only stable way to solve ill-conditioned equations [3].

Among the most popular iterative algorithm is the conjugate gradient one [4]. In fact, the conjugate gradient method is sometimes proposed as an alternative algorithm for treating ill-conditioned systems, since, in principle; it insures convergence after a finite number of steps. Unfortunately, in many cases the algorithm does not converges at a sufficiently fast rate to be superior to direct method [3]. Although certain situation may favor use of iteration, other are more interesting when use direct approach. So, resents researches are oriented to hybrid method approach, in order to exploit advantages of each combined method and to circumvent their limits.

In this optic, our work is situated; in fact, the basic idea of this paper was to exploit iterative properties of the conjugate gradient and to use it in conjunction to the moment method.

The structure studied was, the Cantor iris located in the cross section of a parallel-plates waveguide. The aim was to compute the current density of the considered structure when illuminated by some active modes [5]. But, it is observed that from certain active modes number, the moment matrix becomes badly scaled and ill-conditioned and the result is inaccurate. In this case, the MoM-CG method is used in order to solve the matrix equation of the considered problem.

The paper is organized as follows: Section 2 presents the details of the implementation of the CG-MoM to solve scattering from an iris structure on an infinite waveguide. The MGEC method was applied to the structure and the electromagnetic equation to solve using the CG-MoM method has been deducted. Section 3 deals with experimental results. The current density evaluated by the CG-MoM method has been determined and compared to the ones finding by the MoM. The last section draws conclusions and suggests future work.

2. APPLICATION OF THE CG-MOM METHOD

As an example of a scattering problem to be solved using the hybrid MoM-CG method, let us consider the scattering from an iris located in an infinite rectangular waveguide as shown in Figure 1. This structure is excited by some active modes of the rectangular waveguide enclosing it.

The iris of negligible thickness is enclosed by a called EMEM waveguide; it is composed of two perfect electric walls to the top and the bottom, lateral walls are magnetic as shown in Figure 1.

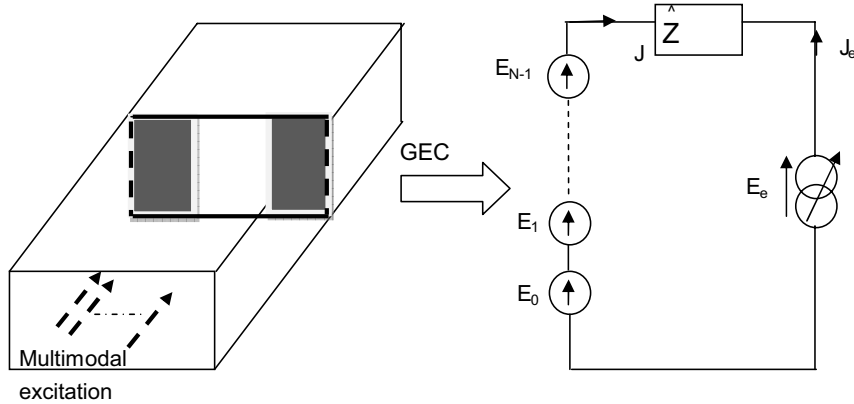


Figure 1: The Cantor iris and its equivalent circuit.

The structure is uniform along the strips axis (oy). Then, the problem is independent of the variable y and only TEM mode and transverse electric modes exist.

The structure is excited by N active modes; the TEM mode and ($N_e - 1$) lower-order evanescent modes. These modes have to be coupled and to respect the structure's symmetry [5].

Boundary conditions are synthetically expressed by the Generalized Equivalent Circuit GEC [6–8] which translates the boundary conditions and the relations between electric and magnetic fields into an equivalent circuit. The considered equivalent circuit of the structure is presented in Figure 1.

Let f_n be the local modal basis of the waveguide used. $E_0, E_1, \dots, E_{N_e-1}$ are the excitation sources, and are expressed as follows:

$$\left\{ \begin{array}{l} E_0 = V_0 f_0 \\ E_1 = V_1 f_1 \\ \vdots \\ \vdots \\ E_{N_e-1} = V_{N_e-1} f_{N_e-1} \end{array} \right.$$

where (f_i) are the N active modes which excite the structure. The impedance operator represents the higher order evanescent modes and is given by:

$$\hat{Z} = \sum_{\substack{n=1 \\ n \neq \text{actif}}}^N |f_n\rangle z_n \langle f_n| \quad (1)$$

where z_n denotes the mode impedance.

J_e is the virtual source defined on the metallic domain and is null on the dielectric, it represents the unknown of the problem: $J_e = \sum_p x_p g_p$.

It is expressed as a series of known test functions g_p used to estimate the current on the metallic domain, x_p are the unknown coefficients, $1 < p < N$. When applying the generalized Ohm and Kirchhoff laws to the equivalent circuit presented on Figure 1, the following system is obtained:

$$\left\{ \begin{array}{l} J = -J_e \\ E_e = E_0 + E_1 + \dots + E_{N_e-1} + \hat{Z} J_e \end{array} \right. \quad (2)$$

So on the metallic domain, the equation to solve is:

$$\hat{Z} J_e = - \sum_{i=0}^{N_e-1} E_i \quad (3)$$

We are trying, on a first step, to solve this equation using the moment method, this method converges perfectly when using a small number of active modes, however it is observed that from

a certain active mode number, the matrix become ill conditioned and result is inaccurate. So, we are thinking to use the conjugate gradient method in conjunction to the moment method, because this method insures convergence in all cases after a finite number of steps. In literature, variants of the conjugate gradient algorithm are used [9], in our case; the moment matrix is a complex one, so the biconjugate gradient algorithm [10] is considered to be the most convenient for this type of matrix. The BiCG algorithm is then incorporated in place of the all matrixes inversion stages on the moment method.

When applying the moment method to the Equation (3), the following system is obtained

$$\begin{aligned}
 & \begin{bmatrix} \langle g_1 | \hat{Z}g_1 \rangle & \langle g_1 | \hat{Z}g_2 \rangle & \dots & \langle g_1 | \hat{Z}g_N \rangle \\ \langle g_2 | \hat{Z}g_2 \rangle & \langle g_2 | \hat{Z}g_2 \rangle & \dots & \langle g_2 | \hat{Z}g_N \rangle \\ \vdots & \vdots & \ddots & \vdots \\ \langle g_N | \hat{Z}g_N \rangle & \langle g_N | \hat{Z}g_2 \rangle & \dots & \langle g_N | \hat{Z}g_N \rangle \end{bmatrix} * \begin{bmatrix} x_{10} & \dots & x_{1N_e-1} \\ x_{20} & \dots & x_{2N_e-1} \\ \vdots & \ddots & \vdots \\ x_{N_e 0} & \dots & x_{NN_e-1} \end{bmatrix} \\
 = & \begin{bmatrix} \langle f_0, g_1 \rangle & \langle f_0, g_2 \rangle & \dots & \langle f_0, g_N \rangle \\ \langle f_1, g_1 \rangle & \langle f_1, g_2 \rangle & \dots & \langle f_1, g_N \rangle \\ \vdots & \vdots & \ddots & \vdots \\ \langle f_{N_e-1}, g_1 \rangle & \langle f_{N_e-1}, g_2 \rangle & \dots & \langle f_{N_e-1}, g_N \rangle \end{bmatrix}^T \quad (4)
 \end{aligned}$$

This system is of the form $[Z][X] = [A]^T$, where $A(i, p) = \langle f_i | g_p \rangle$, $Z(p, q) = [\langle g_p | \hat{Z}g_q \rangle]$ and $[X] = X(p, m)$ designs the matrix of the unknowns, m represents the active mode.

The Biconjugate gradient algorithm is used to solve a system of the form $AX = B$, where A is a complex matrix, X and B are vectors. In this case X and B are matrixes, so in order to solve this system we apply the BiCG algorithm to each column vector of the system (4) which is equivalent to: $[Z]X(m) = A(m)$.

The same procedure is repeated in the computation stage of the matrix input impedance which is in the moment method given by:

$$[Z_{in}] = \frac{1}{2} ([A] [Z]^{-1} [A]^T)^{-1} \quad (5)$$

Remind that the term $[Z]^{-1}[A]^T$ is calculated using the BiCG method, and is noted $[X]$ in (4). The Equation (5) is then written: $[A][X][Z] = id$, and have been solved using the BiCG algorithm.

The current density can be then determined. The following section presents the current distribution using the MoM and the MoM-BiCG method.

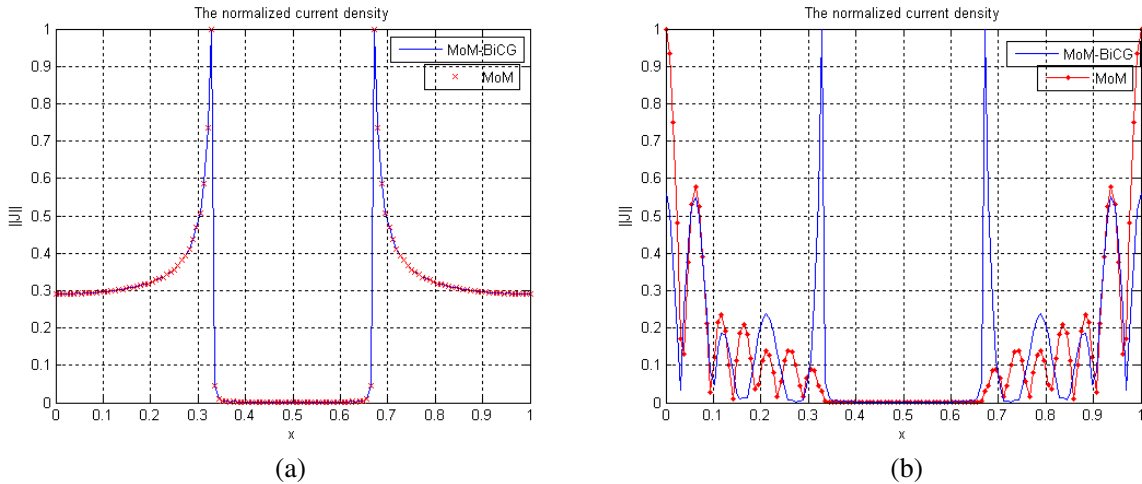


Figure 2: The normalized current distribution depicted by the MoM-CG and the one evaluated by the traditional MoM method (with piecewise sinusoidal function), with $a = 22.910^{-3}$ mm, $d = a/3$ at $F = 2$ GHz, MoM and MoM-BiCG: $f_n = 3000$, $g_p = 200$; (a) 1 active mode; (b) 11 active modes.

3. NUMERICAL RESULTS

The MoM-CG method is used to determine the current distribution corresponding to the iris structure. This method has been tested for some active modes number. Figure 2 presents the current distribution obtained (a) when exciting the iris structure using only the fundamental mode and (b) when exciting the iris using the fundamental TEM mode and 10 active modes. For the first case (a), result is conformed to the one finding using the MoM algorithm, with respect to the boundary conditions. However, it is observed that when raising the active modes number, especially when using an active modes number more than 10 the moment matrix become ill conditioned, so result becomes inaccurate.

Figure 2(b) shows that using the MoM, the current does not satisfy boundary conditions. In fact, at the magnetic wall the current is maximal, and is minimal at the magnetic edges which don't respect the boundary conditions. For the MoM-CG method the current is maximal at the magnetic edges and is decreasing sinusoidally. We can say that the current distribution behavior has been refined; at the magnetic edges it has the same allure as the one obtained using one active mode. But at the magnetic wall the current distribution is raising again.

4. CONCLUSION

The MoM-CG method has been developed and exposed on this work to solve an electromagnetic scattering problem when the MoM fails due to ill-conditioning. This method has been used to determinate the unknown current distribution for an iris structure when illuminated by some active modes. It is observed that when using 11 active modes, the MoM fails to give a reasonable behavior of the current, however result obtained using the MoM-CG method is conforming to boundary conditions on the iris structure and it gives an inaccurate result on the magnetic waveguide walls. As a primarily area for future work to circumvent this problem, we are thinking to use a preconditioning technique and to develop a MoM-PCG method.

REFERENCES

1. Harrington, R. F., "Field computation by moment methods," *IEEE Press Series on Electromagnetic Waves*, Syracuse University, 1993.
2. Peterson, A. F., S. L. Ray, C. H. Chan, and R. Mittra, "Numerical implementation of the conjugate gradient method and the CG-FFT for electromagnetic scattering," *Progress In Electromagnetic Research*, Vol. 5, 241–300, 1991.
3. Sarkar, T. K., K. R. Siarkiewicz, and R. F. Stratton, "Survey of numerical methods for solution of large systems of linear equations for electromagnetic field problems," *IEEE Trans. Antennas Propagat.*, Vol. 29, 847–856, Nov. 1981.
4. Sarkar, T. K., "The conjugate gradient method as applied to electromagnetic field problem," *IEEE Antennas and Propagation Society Newsletter*, 5–13, 1986.
5. Mili, S., C. Larbi Aguili, and T. Aguili, "Study of fractal-shaped structures with pin diodes using multi-scale method combined to the generalized equivalent circuit modeling," *Progress In Electromagnetic Research B*, Vol. 27, 213–233, 2011.
6. Baudrand, H., "Representation by equivalent circuit of the integrals methods in microwave passive elements," *European Microwave Conference*, Vol. 2, 1359–1364, Budapest, Hungary, 1990.
7. Aguili, T., "Modélisation des composantes SFH planaires par la méthode des circuits équivalents généralisée," Thesis manuscript, National Engineering School of Tunis, Tunisia, 2000.
8. Aubert, H. and H. Baudrand, *l'electromagnetisme par les schémas équivalents*, Cepaduès Edition, 2003.
9. Hestenes, M. R. and E. Stiefel, "Methods of conjugate gradient for solving linear systems," *Journal of Research of the National Bureau of Standards*, Vol. 49, No. 6, 409–435, Dec. 1952.
10. Zhang, Y. and Q. Sun, "Preconditioned bi-conjugate gradient method of large-scale sparse complex linear equation group," *Chinese Journal of Electronics*, Vol. 20, No. 1, Jan. 2011.

Effect of the Three-dimensional Wideband Antenna on Plane Wave Distribution

Feng Lu, Li-Yuan Su, Li-Hua Shi, Yan-Xin Li, and Bi-Hua Zhou

Engineering Institute of Corps of Engineers

PLA University of Science and Technology, Nanjing 210007, China

Abstract— In order to measure the electromagnetic field of three-dimensional (3-D), a three-dimensional (3-D) wideband antenna for electric field measurement is designed. In the experiments, we are often concerned with the effect of the antenna on electromagnetic wave distribution. In this paper, the method of moment is used to model the effect of the antenna on plane wave distribution. From the numerical result, we find the law of effects of the antenna on plane wave distribution in the frequency domain.

1. INTRODUCTION

With the development of electronic technique and micro-electronic technique, various of electromagnetic interfere is produced. When electromagnetic interfere is measured, we often want to measure the electric field of three-dimensional at one point. So a three-dimensional(3-D) wideband antenna for transient electric field measurement is designed shown as Fig. 1. In the experiments, we are often concerned with the effect of the antenna on electromagnetic wave distribution. In order to simplify analysis, we assume that the electromagnetic wave is plane wave shown as Fig. 2.

In this paper, the method of moment is used to model the effect of the antenna on plane wave distribution. In the numerical model, the angle of propagation is changed and the size of the antenna is also changed. From the numerical result, we find the law of effects of the antenna on plane wave distribution. At the same time, this work will offer theory direction of the antenna's optimized design.

2. NUMERICAL ANALYSIS OF THE WIDEBAND ANTENNA

The wideband antenna is shown as Fig. 1. And it is used in various of EMC/EMI (electromagnetic compatibility/magnetic inference) experiments. The wideband antenna consists of three dipole

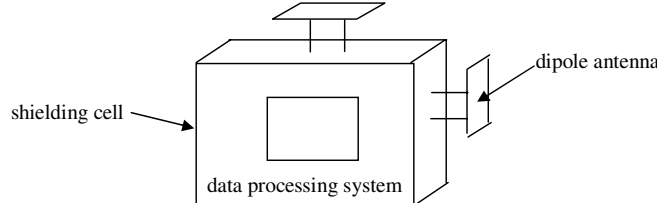


Figure 1: Three-dimensional (3-D) wideband antenna.

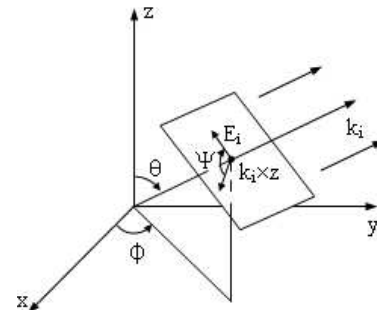


Figure 2: Plane wave.

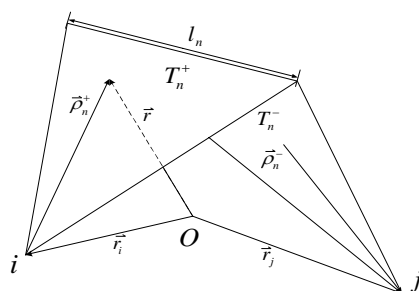


Figure 3: RWG edge element.

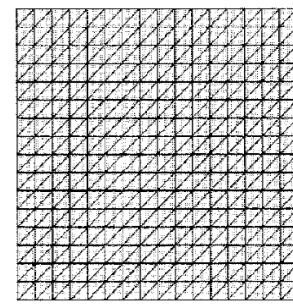


Figure 4: Plane meshes.

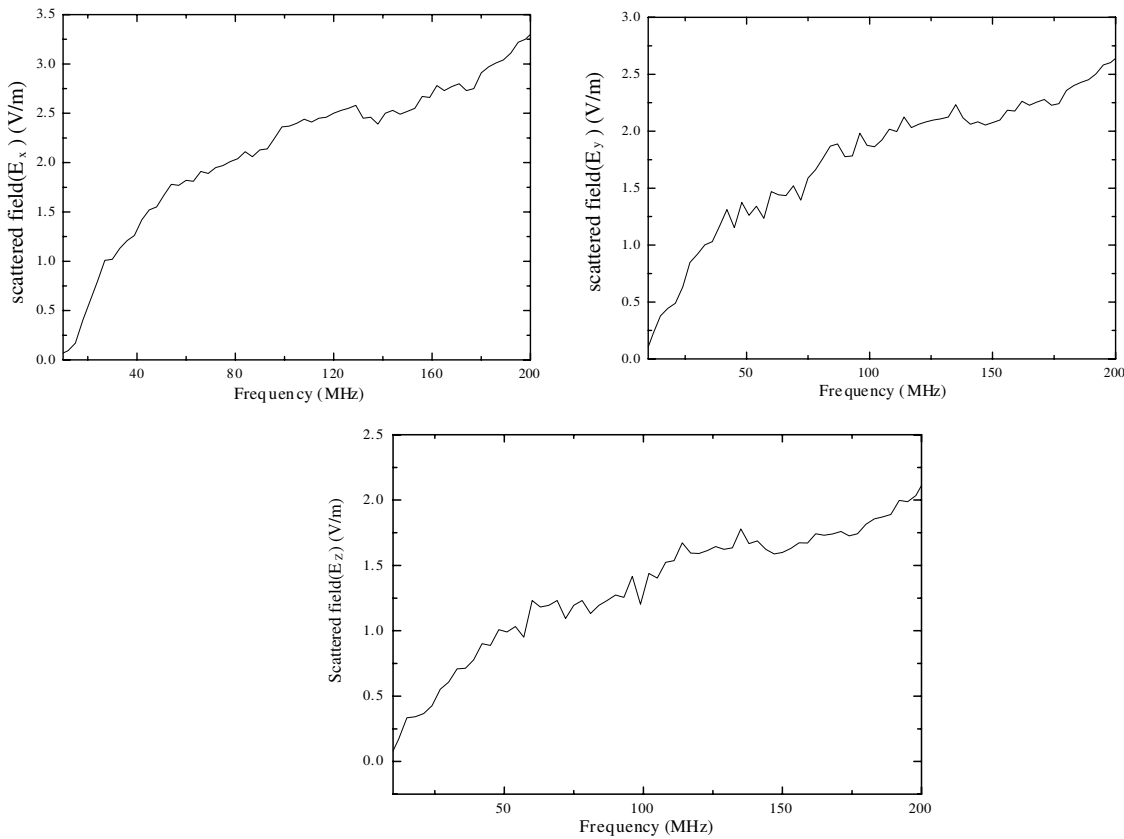


Figure 5: Scattered field of one point which is 0.5 m far form the wideband antenna.

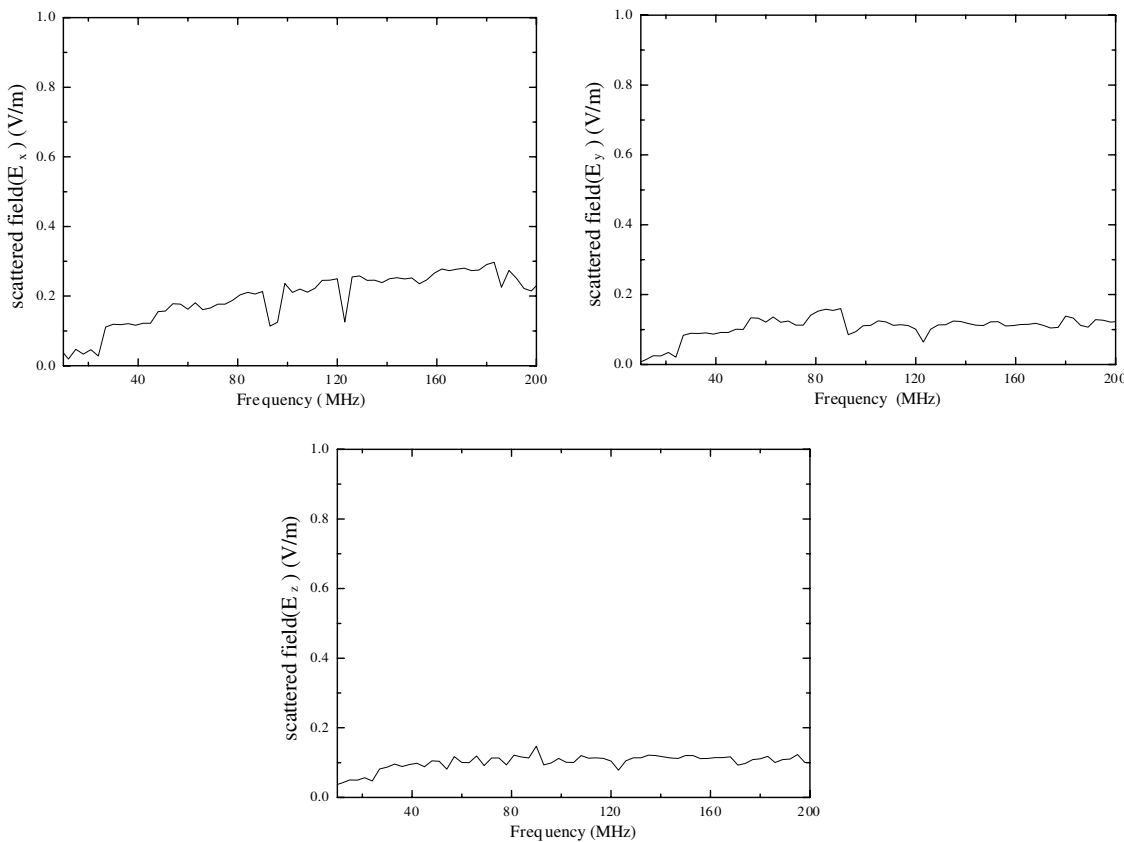


Figure 6: Scattered field of one point which is 1 m far form the wideband antenna.

antennas, data processing system. In the work, electric field is received by three dipole antennas of the wideband antenna. Induction current is transformed into data processing system through electronic circuit. The three dipole antennas is made of metal. And data processing system is often placed in shielding cell. So when we take the effect of the wideband antenna on electromagnetic field into consideration, we often take the effect of surface metal of the wideband antenna into consideration. In order to simplify analysis, we assume that the electromagnetic wave is plane wave whose electric field is 1 V/m.

In this paper, the method of moment [1] is used to model the effect of the wideband antenna on plane wave distribution. And the basis functions — RWG [2] edge element shown as Fig. 3 is used. The scattering algorithm [3, 4] discussed in this paper is based on the use of the electric field integral equation (EFIE). According to the structure of the wideband antenna, the edge elements is created shown as Fig. 4.

3. CONCLUSION

Through several optimized design, the size of the wideband antenna is determined finally: the size of shielding cell is $0.21\text{ m} \times 0.21\text{ m} \times 0.21\text{ m}$, and the size of dipole antenna is $0.09\text{ m} \times 0.09\text{ m} \times 0.002\text{ m}$.

The vector r can be expressed in term of its components as

$$r = xa_x + ya_y + za_z$$

where x , y and z are the scalar projections of r on the x , y and z axes. And a plane wave can also be divided into three plane waves whose electric field polarized direction are parallel to x , y and z axes, respectively. Because of the symmetry of the wideband antenna, we only take one plane wave into consideration in this paper. When $\theta = 90^\circ$, $\phi = 90^\circ$, $\Psi = 0^\circ$, electric field polarized direction is parallel to x -axes.

From Fig. 5 and Fig. 6, we can see that at high frequency (the wavelength is smaller than 2 meters) the wideband antenna has much effect on plane wave distribution, and at low frequency (the wavelength is larger than 2 meters) the wideband antenna has little effect on plane wave distribution.

ACKNOWLEDGMENT

This work was supported by the National Nature Science Foundation of China under Grants 51077133 and the NCET.

REFERENCES

1. Harrington, R. F., *Field Computation by Moment Methods*, McMillan, New York, 1968.
2. Rao, S. M., D. R. Wilton, and A. W. Glisson, "Electromagnetic scattering by surfaces of arbitrary shape," *IEEE Trans. Antennas and Propagation*, Vol. 30, No. 3, 409–418, 1982.
3. Lu, C. C. and W. C. Chew, "Electromagnetic scattering from material coated pec objects: A hybrid volume and surface integral approach," *IEEE Antennas Propagation Symposium*, 1999.
4. Albertsen, N. C., J. E. Hansen, and N. E. Jensen, "Computation of radiation from wire antnnas on conducting bodies," *IEEE Trans. Antennas and Propagation*, Vol. 22, No. 2, 200–205, 1974.

Sensitivity Analysis of Eddy Current Sensors Using Computational Simulation

R. Neugebauer¹, W.-G. Drossel¹, P. Mainda¹, H.-J. Roscher¹, K. Wolf¹, and M. Kroschk²

¹Fraunhofer Institute for Machine Tools and Forming Technology IWU, Chemnitz/Dresden, Germany

²EAAT GmbH Chemnitz, Germany

Abstract— Eddy current sensors can detect the position and movement of metal parts without direct contact. The magnetic fields of these sensors can penetrate protective metal enclosures when designed and applied appropriately. Thus particularly robust solutions for industrial applications are possible, e.g., tracking objects electrically like conductive or ferromagnetic work pieces (device currently being tested) during a treatment process under difficult production conditions.

The disadvantage of a test set up where the sensor and the tested specimen are surrounded by equipment and enclosures is reduced sensor sensitivity, this combined with different test piece material properties and tolerances adversely influences the measurements. In order to evaluate the performance of an eddy current sensor, a sensitivity analysis for selected measurement frequencies are necessary. Experimental studies on the subject of sensor sensitivity under production conditions are difficult and usually not feasible due to the costs involved.

Therefore, using a virtual 3D model such effects were simulated using the finite element program ANSYS. The sensor output is the phase angle between voltage and current of the sensor coil. The use of the magnetic field strength to determine this phase angle yielded results in accordance with the experimental trends. The problem is the large differences in the geometric dimensions, such as the sensor size compared to effective magnetic air gaps.

Magnetic permeability and electrical conductivity are the relevant parameters for the eddy current sensors. In experimental tests, these parameters were determined, also as a function of temperature.

It was followed by the simulation of the sensor characteristics by varying different parameters affecting the sensor signal. The results obtained with element type SOLID117 were highly dependent on finite element meshing.

But requires significantly less computational effort than an element type SOLID236, which was used to verify selected results based on SOLID117 element type.

The result of the simulations is the influence of the considered parameters on the achievable accuracy in the detection of the device under test during the process of machining, individually or in combination.

1. INTRODUCTION

The Fraunhofer Institute for Machine Tools and Forming Technology in Chemnitz, Germany has developed an eddy current sensor including the electronic evaluation mechanism that makes it possible to determine the position of sheet metal [4]. For instance, the flow of material can be regulated by the sheet metal retention force in sheet metal forming based upon the position measured, which has an impact on the quality of production. Eddy current sensors make it possible to detect the position and movement of metallic components without contact. If they are suitably dimensioned, the magnetic field of the sensor can even sufficiently penetrate through a protective housing made of metal. This means that particularly robust solutions are available for industrial applications, for instance when tracking down electrically conducting and/or ferromagnetic workpieces (i.e., the test objects) during the machining process under difficult production conditions. The disadvantage of any protective housing located between the sensor array and the test object is the fact that it drives down measuring sensitivity while the geometric and material tolerances of the test object have a greater impact on the measurement. This is the reason why it is necessary to make a sensitivity analysis for selected measuring frequencies to assess the performance of a sensor array. Experimental tests for analyzing sensitivity are generally difficult under production conditions, which is why they often cannot be undertaken for reasons of expenditures. Therefore, these influences were simulated with the ANSYS finite element program for a model 3-D array.

2. MODEL AND SOLUTION

The eddy current sensor for measuring position (in this case, the delivery path of a piece of sheet metal) is an exploring coil sensor of the parameter type. This means that the excitation coil is simultaneously the measuring coil. Logically, the measuring signal needed is characterized by the change in the coil's impedance.

The magnetic field leaves the coil vertically and the piece of sheet metal running in (the test object) moves vertically to the direction of the coil's magnetic field (refer to Figure 1). This movement changes the surface proportion of the magnetic flow in the board and the air gap. Then, this variable interaction between the board and magnetic field causes a reaction to the sensor coil impedance that varies in intensity. The result is the fact that the impedance (and therefore the phase angle between the current and voltage) constitutes a measure for the delivery path. The phase angle is transformed into voltage with the aid of a synchronous demodulator and downstream filter [5].

We carried out FEM simulation of the eddy sensor with the academic version of ANSYS 12. This FEM analysis is necessary since it is not possible to keep the specific parameters that have an impact on the process separate for our experimental investigation. A 32-bit computer is available for the simulation with an Intel Core2 Quad-Q8200-CPU with 2.33 GHz and the usable working memory was 3.25 GB RAM. Unfortunately, the number of solvable equations is substantially limited since ANSYS needs connected working memory for calculations and it is limited to 2 GB in the 32-bit systems. However, Windows XP offers the possibility of boosting the working memory provided to 3 GB. Although this does not provide continuous memory, ANSYS can utilize it dynamically to boost the number of soluble equations by approximately 15%. The simulation is interrupted if it is in excess of the memory requirements.

The eddy current sensor is modeled for the FEM simulation including its environment. The sensor unit consists of a sensor coil wound on an E-core made of Mu metal with copper-enamel covered wire. Then, the coil and core are surrounded by a U-shaped stainless steel insert that has the purpose of protecting against wear and tear. The positive characteristic of stainless steel is the fact that it acts like air on the magnetic field, which has a linearizing effect on the connection between the phase shift and delivery path. Beyond this, a material with a higher level of permeability would not be sufficiently penetrated by the alternating magnetic field. Finally, this takes advantage of the symmetry of the array in the FEM simulation so that only half of the sensor unit is modeled (refer to Figure 2).

To map reality as precisely as possible, the characteristic values of the materials and the modeled roughness of the piece of sheet metal were tracked experimentally and included in the simulation. The geometry is created in ANSYS 12 Classic. Initially, all of the horizontal sections were drawn in one level for modeling and more complex shapes were combined from various simple forms (such as rectangles and circular segments). In a second step, ANSYS networked these drawn surfaces and volumes. ANSYS 12 has two elementary types available for solving an electromagnetic problem taking eddy currents into account, both of which had their advantages and disadvantages. The first elementary type, Solid117, has jumps in the test simulation findings from time to time that are substantially dependent upon networking. However, with the right networking, the findings were plausible and the tendencies agreed with those experimentally obtained and physically expected. There are no such jumps when using the second elementary type, Solid236, although with the same networking it requires much more working memory to solve this problem because a larger number

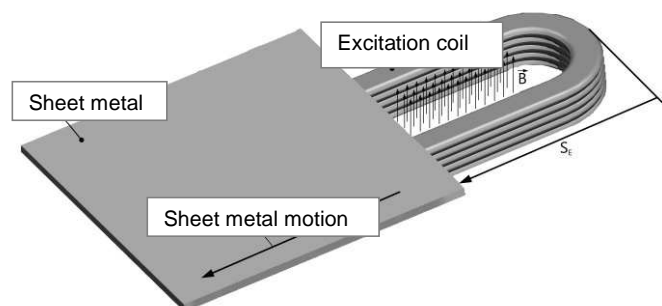


Figure 1: The sensor coil with the piece of sheet metal.

of equations are generated that have to be solved. Therefore, we solved this problem by using the elementary type Solid117.

A current density is defined in the coil as the excitation or load in the system. Local coordinate systems are defined whose y -axis specifies the orientation to indicate the direction of the feeding current density for the specific components of the coil. Logically, Cartesian coordinate systems are introduced that are cylindrical to bending for all straight components of the coil. Finally, the degrees of freedom are limited on the edges to the magnetic vector potential A_Z .

The following step is analysis with a harmonious excitation that corresponds to the operating frequency of the real eddy current sensor. In the original simulation, the real and the imaginary component of the energy stored in the magnetic field and the real and imaginary components of the magnetic flux density B are given as the findings of the simulation. However, the tendencies

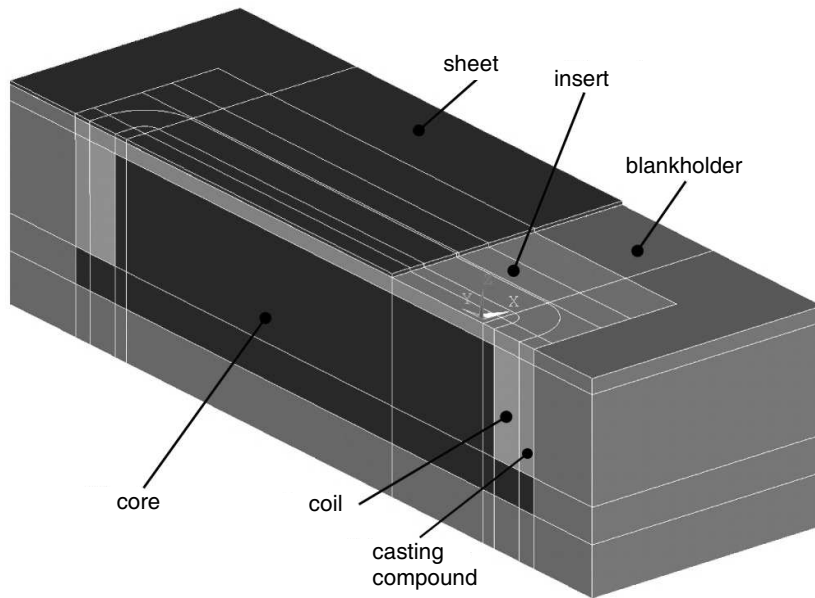


Figure 2: The model-sensor unit.

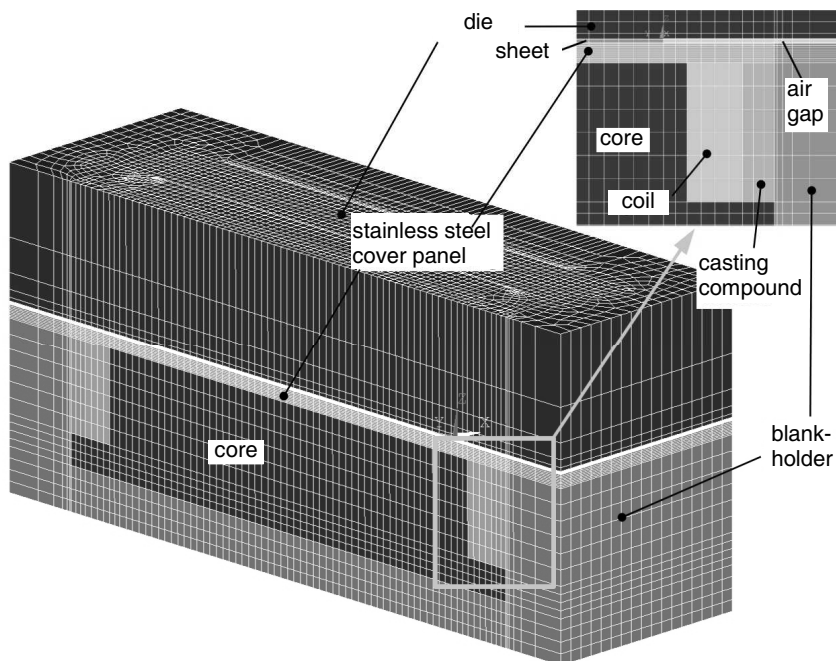


Figure 3: A networked FEM model of the eddy current sensor and its environment.

on the impact of the geometric and material parameters that were obtained with the help of the simulation initially contradicted experimental checks. According to the equation (1) where the relative magnetic permeability is a real number in an analogous fashion to the simulation, the vectors of the magnetic flux density B and magnetic field strength H are parallel to one another. Unfortunately, ANSYS does not confirm this interrelationship.

$$B = \mu H \quad (1)$$

Beyond this, if equation (1) is assumed to be a given fact and the angle of the B -field is obtained through the H -field, we ascertain confirmation of the tendencies obtained experimentally for the impact of the system parameters. We may conclude from these statements that the magnetic field strength H may be used for ascertaining the phase shift between current and voltage. This new method of evaluation not only supplies certain tendencies, but also absolute phase shift values that are on a scale of the phase shifts measured. Finally, the eddy current sensor evaluates the phase shift between current and voltage and, since the resistance of the winding is negligible, the phase angle φ can be calculated with the vector of the magnetic flux density B .

3. RESULTS

To verify results, the results achieved with the elementary type Solid117 were first of all compared with those of the new elementary type Solid236 in ANSYS 12. Unfortunately, it was not possible to use this elementary type due to limited computer capacity since these elements have many more equations to be solved at the same level of networking. Furthermore, the same tendencies become evident when comparing results and there are only slight differences between each of the absolute values [9]. The final points of the sensor characteristic lines calculated are identical, although there is departure of approximately 0.25° in the phase angle at the initial points (Figure 4).

We worked out a system of simulations for the sensitivity of the sensor based upon these initial comparative calculations. The results of these simulations demonstrate:

- the impact of the relative permeability of the sheet metal,
- the impact of the specific resistance of the sheet metal,
- the impact of the sheet-metal thickness (refer to Figure 5) and,
- the impact of the air gaps between the sheet metal and forming tool.

Finally, the speed of the change in the sheet metal's position has a negligible impact on the sensor signal.

Since specific experiments carried out in parallel also tended to confirm the findings of the simulation, we were able to use the insights gained from the calculations to undertake a series of enhancements on the sensory system.

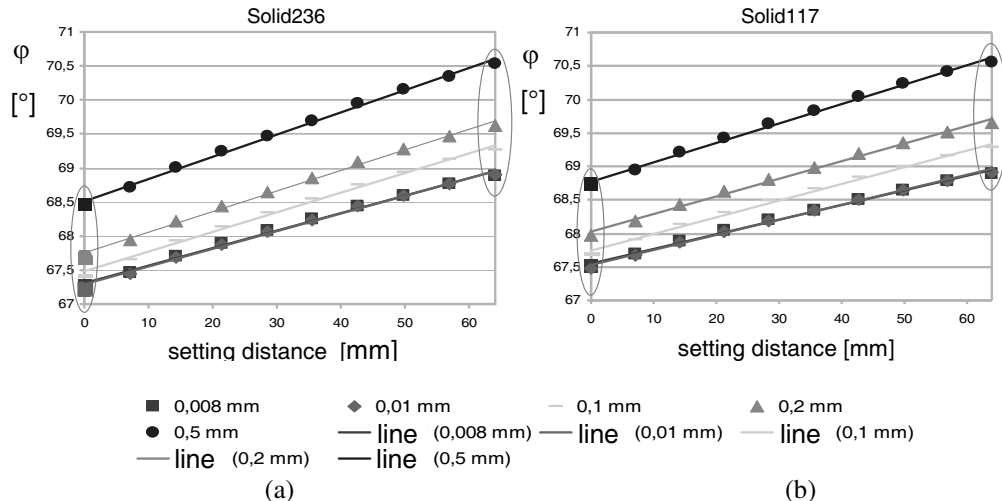


Figure 4: The sensor characteristic lines with differing air gaps with ANSYS elementary types. (a) Solid236. (b) Solid117.

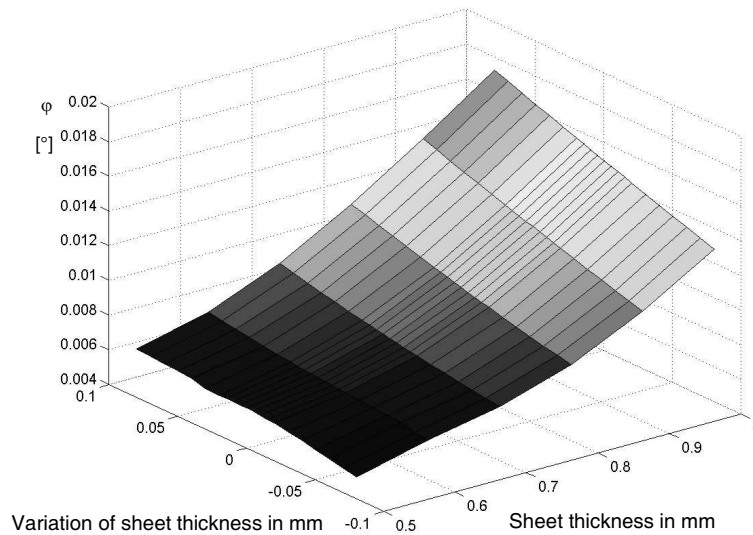


Figure 5: The phase angle φ at various rated sheet metal thicknesses with a fluctuation of ± 0.8 mm in the sheet-metal thickness.

4. CONCLUSION

In conclusion, we carried out an electromagnetic FEM simulation of an eddy current sensor (as shown in Figure 1). This simulation is necessary for assessing the performance of the sensor under production conditions due to the low level of measuring sensitivity and the substantial impact of the test object's geometrical and material tolerances on the measurement. A sensitivity analysis for selected measuring frequencies supplied findings that allowed us to assess the impact of the relative permeability of the sheet metal, the specific resistance of the sheet metal, the sheet-metal thickness and the size of the air gap between the sheet metal and the forming tool. Finally, experiments carried out on this confirmed the tendency of the findings of the simulation.

REFERENCES

1. Nyce, D. S., *Linear Position Sensors: Theory and Application*, John Wiley & Sons Inc., New Jersey, 2003.
2. Wang, Y., *Trennung der Einflussgrößen von Wirbelstromsensoren durch Signalverarbeitung mit Hilfe von Felduntersuchung und Modellierung*, VDI Verlag, Düsseldorf, 1996.
3. Tian, G. and A. Sophian, "Defect classification using a new feature for pulsed eddy current sensors," *NDT & E International*, Vol. 38, 77–82, 2005.
4. Forstmann, U., *Induktive Wegsensoren zur Überwachung und Regelung des Blecheinzugs beim Tiefziehen*, Dissertation, Technische Universität Berlin, Produktionstechnisches Zentrum, Berlin, 2000.
5. Hädrich, J., *Wirbelstromsensor zur Messung des Blecheinzugs Diplomarbeit*, Hochschule Mittweida, 2009.
6. Kroschk, M., *Sensitivitätsanalyse zum serienfähigen Wirbelstromsensor*, Technische Universität Chemnitz, Diplomarbeit, 2010.
7. Kohn, D., *Untersuchung eines induktiven Spiralsensors als Wegaufnehmer und Anwendung des Sensorelementes in Mikroelektronik-Systemen*, VDI Verlag, Düsseldorf, 1968.

An Effective Formulation Based on Approximated Electromagnetic (EM) Mathematic Models of Feed Antennas to Efficient Estimate the Performances of Rotationally Symmetric Parabolic Reflector Antennas

Shih-Chung Tuan¹ and Hsi-Tseng Chou²

¹Department of Communication Engineering, Oriental Institute of Technology, Pan-Chiao, Taiwan

²Department of Communication Engineering, Yuan Ze University, Chung-Li 320, Taiwan

Abstract— In this paper, an effective formulation based on approximated electromagnetic (EM) mathematic models of feed antennas is developed to efficiently estimate the performances of rotationally symmetric parabolic reflector antennas including spillover and aperture efficiencies. The EM mathematic models employ cosine and sine functions with fractional powers to approximate the co-polarized and cross-polarized components of the fields radiated from the antennas to feed the reflectors, where the closed-form solutions of antenna performances are then obtained. In distinguishing from previous works where only cosine tapers with integer powers are employed to model the co-polarized components of feed's radiation with the cross-polarized components ignored, the present work is a broad extension and provides tremendous flexibility in the modeling of realistic feed antennas. Furthermore it allows one to estimate the impact on the antenna performance due to the existence of cross-polarized components, which had been previously ignored for a feed antenna with an ideal radiation pattern. Numerical examples are presented to demonstrate the analysis.

1. INTRODUCTION

Reflector antennas [1–4] have unique features of high directivities and low sidelobe levels, and are widely employed in many applications of point-to-point and satellite communications. In a practical implementation, the antennas' performance and parameters need to be first estimated before a real antenna design is started. An effective and efficient approach with relatively simple formulations to justify the antenna's performance and reveal the information of parameters is very useful and desired for an engineer.

This paper attempted to develop such an effective approach, which allows the engineers to approximately estimate the performance at the initial stage of antenna design. This work can be considered as an extension of a similar effort previously conducted in [2], in which cosine tapers with integer powers were employed to model the co-polarized components of the fields radiated from the antennas [2–4] feeding a reflector. Closed-form formulations of aperture efficiency and gain for a rotationally symmetric parabolic reflector antenna, based on physical optics (PO) approximation [2, 4, 5], were obtained when the reflector was illuminated by the radiation of this modeled feed. The work described in [2] is very convenient in use, but exhibits limitations in practical applications. First of all, the feed's radiations to be modeled are limited to the cases that have rotationally symmetric patterns and can be adequately modeled by the cosine tapers with integer powers. Secondly the cross-polarized components of feed's radiation were ignored in this work. However, in many practical situations these conditions are hard to fulfill especially in the initial stage of antenna design, where the cross-polarized components of feed's radiation can be relatively high, and the co-polarized components are not rotationally symmetric such as in the recent interest to develop co-structure feeds for multi-satellite communications [6, 7].

This paper extends the previous work in [2] and however employs cosine tapers with arbitrary fractional powers to model the co-polarized components of feed's radiation. It further uses cosine and sine functions with also fractional powers to simultaneously approximate the cross-polarized components. Furthermore, the formulation does not restrict the patterns of feed's radiation to be rotationally symmetric. Thus it provides sufficient freedoms to model a classic variety of realistic feed antennas, and allows practical estimations of performance over reflector antennas when the feed antennas do not have ideal radiation patterns at the initial stages of design. In particular, the formulations to estimate many useful parameters including the aperture and spillover efficiencies are obtained in closed forms. In comparison with the previous work in [2], the present solutions appear to have broader applications and advantages. First of all, the radiation patterns of feed

antenna at any stage of design can be properly modeled to estimate their performance when they are used to feed the reflector antenna. Secondly, from a system aspect, the performance of an entire antenna system is most concerned instead of the performance of each component. The proposed models are more flexible in the optimization of the antenna system. Furthermore, the closed form formulations allow one to optimize the feed antenna design with respect to the parameters used in the models.

2. FORMULATIONS DEVELOPMENT

Suppose there is one parabolic dish antenna with a dish diameter D , a focal length of F , and is a rotationally symmetric parabolic surface, its co-pol amount and cross-pol amount in the x -polarized feed field are each approximated as follows:

$$\vec{E}_c(r) = A_c(q_1, q_2) \left[\hat{\theta} \cos^{q_1} \theta \cos \varphi - \hat{\varphi} \cos^{q_2} \theta \sin \varphi \right] \frac{e^{-jkr}}{r} \quad (1)$$

$$\vec{E}_x(r) = A_x(q_3, q_4) \left[\hat{\theta} \sin^{q_3} 2\theta \sin \varphi + \hat{\varphi} \sin^{q_4} 2\theta \cos \varphi \right] \frac{e^{-jkr}}{r} \quad (2)$$

And the y -polarized amount and the circular polarized amount of the feed radiation field can also be obtained through similar method. Under a constant power, the radiation field shape change can be achieved through varied relevant radiation parameters, which is to employ parameter selections in $q_1 \sim q_4$ to simulate the field models in actual applications. Take the radiation fields of horn antennas for example, in particular, the co-polarized field parameters can be represented as follow:

$$A_c(q_1, q_2) = \left[P_t \frac{\eta_0}{\pi} \frac{(2q_1 + 1)(2q_2 + 1)}{q_1 + q_2 + 1} \right]^{\frac{1}{2}} \quad (3)$$

Within the formula, P_t is the possessed radiation power; η_0 is the intrinsic impedance in free space, and the cross-polarized amount in the power calculation is nominal. And $A_x(q_3, q_4)$ is the level of cross-polarized amount relative to co-polarized amount.

2.1. Spillover Efficiency

Spillover efficiency is the value used to describe the energy capture efficiency of a dish antenna, and is defined as follows:

$$\eta_s = \frac{\int_0^{\theta_0} (|F_E|^2 + |F_H|^2) \sin \theta d\theta}{\int_0^{\frac{\pi}{2}} (|F_E|^2 + |F_H|^2) \sin \theta d\theta} \quad (4)$$

Among the parameters, F_E and F_H are the radiation fields of E -plane and H -plane in the feed source of Equation (1) and Equation (2) respectively. The model that is applicable through Equation (4) is a dish antenna with a feed source located on the antenna axis, and is also a rotationally symmetric dish antenna. We can derive the closed form solution from the integrals in Equation (4), and within it, the denominator part can be described through Equation (5) as follows:

$$D = \sum_{m=1}^2 \frac{A_c^2}{2q_m + 1} + \sum_{m=3}^4 \sum_{n_m=0}^{\infty} A_x^2 2^{2q_m} \frac{q_m!}{n_m!(q_m - n_m)!} (-1)^{n_m} \frac{1}{2q_m + 2n_m + 1} \quad (5)$$

And the numerator part can be described through Equation (6) as follows:

$$N = \sum_{m=1}^2 \frac{A_c^2 (1 - \cos^{2q_m+1} \theta_0)}{2q_m + 1} + \sum_{m=3}^4 \sum_{n_m=0}^{\infty} \frac{A_x^2 2^{2q_m} q_m! (-1)^{n_m}}{n_m!(q_m - n_m)!} \frac{[1 - (\cos \theta_0)^{2q_m+2n_m+1}]}{(2q_m + 2n_m + 1)} \quad (6)$$

In the equation, θ_0 is the reflector half angle (Figure 1) observed from the feed source. In Equation (5) and (6), the $n_m = \text{Int}[q_m + 1]$ in the infinite series is taken into calculation so accuracy is maintained. Take notice that under the circumstance when q_m is an integer, “ ∞ ” in Equations (5) and (6) can be replaced by q_m , and the calculation result will still be accurate.

If the cross-polarized part is ignored, we can express the spillover efficiency with the power level alongside $\theta = \theta_0$ (i.e., $\theta = \theta_0$ is the boundary of the rim in a dish antenna). Suppose the power difference with the peak value of the principal beam is $-a$ dB (in general, -10 dB is used for the

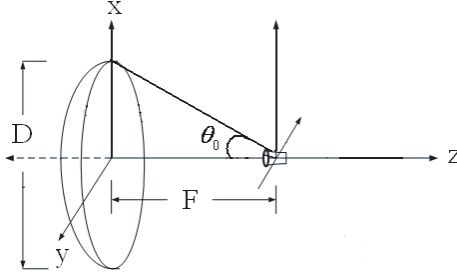


Figure 1: A rotationally symmetric reflector with a feed located along its axis.

difference value), and its field strength is $d = 10^{-a/20}$, the spillover efficiency therefore can be represented as follows:

$$\eta_s = 1 - (\cos \theta_0)^{2q+1} = 1 - d^2 d^{\frac{1}{q}} = 1 - d^2 \cos \theta_0 \quad (7)$$

And as Figure 1 shows, when the feed source is located at the focal point of a parabolic dish antenna, its spillover efficiency can be represented as:

$$\eta_s = 1 - d^2 \left[\frac{(F/D) - \frac{1}{16}(F/D)}{(F/D) + \frac{1}{16}(F/D)} \right] \quad (8)$$

2.2. Aperture Efficiency

The definition of aperture efficiency is the ratio value of the effective radiating surface area of a dish antenna to its physical antenna surface area. From Equations (1) and (2), the aperture efficiency of a rotationally symmetric dish antenna can be expressed as:

$$\eta_I = \cot^2 \frac{\theta_0}{2} \frac{\int_0^{\theta_0} (|F_E| + |F_H|) \tan \frac{\theta}{2} d\theta}{\int_0^{\frac{\pi}{2}} (|F_E|^2 + |F_H|^2) \sin \theta d\theta} \quad (9)$$

Upon deduction, the numerator part in Equation (9) can be represented by Equation (5), and the integral of the denominator can be expressed by:

$$\begin{aligned} A &= B + \left(-\frac{1}{2} \right) [h(q_1, q_4, 1) + h(q_2, q_3, 1)] \\ &\quad + \left(\frac{1}{8} \right) [h(q_1, q_4, 2) + h(q_2, q_3, 2)] + \left(-\frac{1}{16} \right) [h(q_1, q_4, 3) + h(q_2, q_3, 3)] \end{aligned} \quad (10)$$

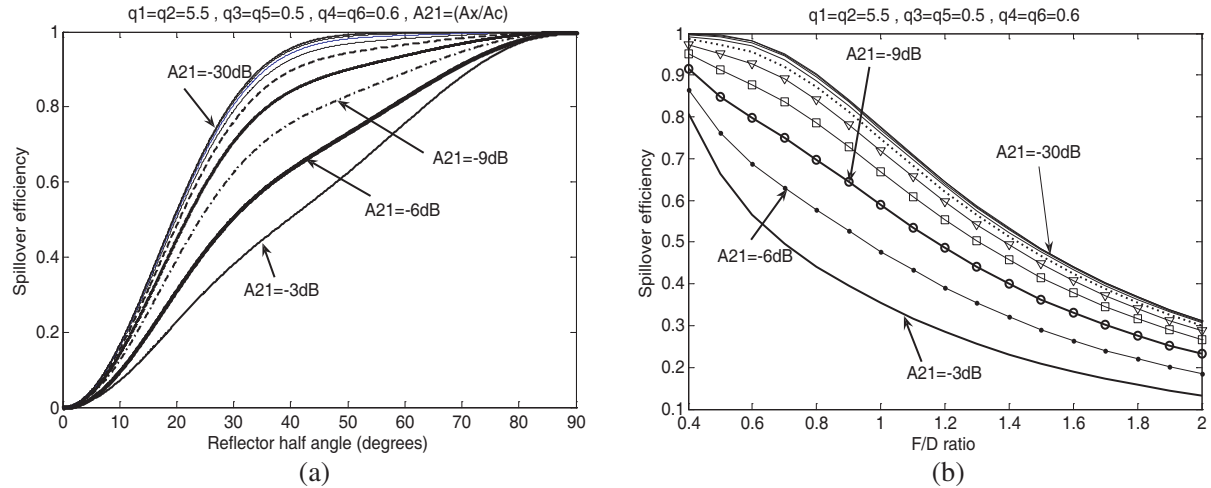
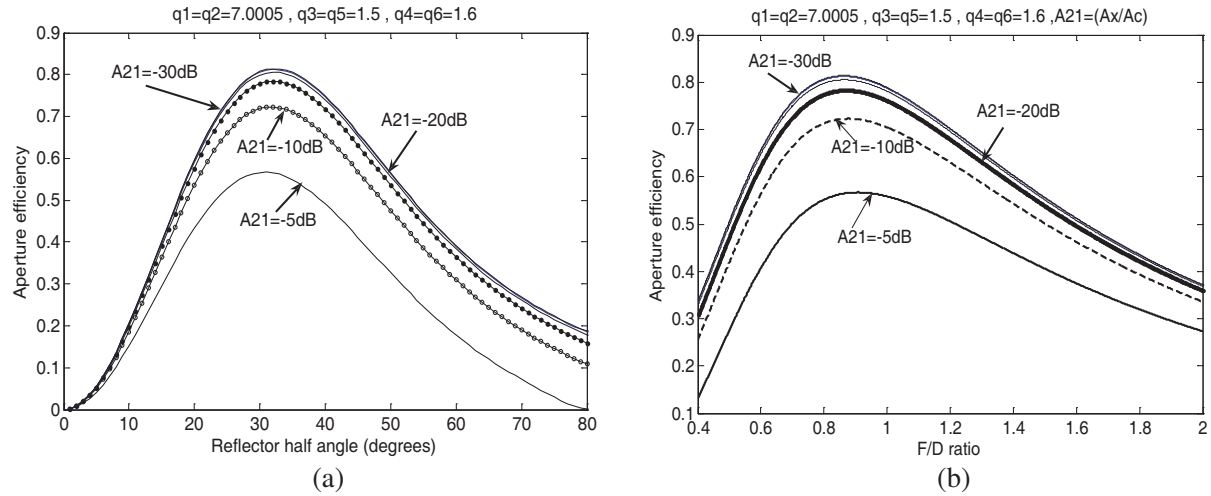
when q_m ($m = 1 \sim 4$) is a non integer, its B and $h(q_m, q_m, t)$ are as follows:

$$B = -A_c \sum_{m=1}^2 \sum_{n_m=0}^{\infty} \frac{q_m!}{n_m!(q_m - n_m)!} \frac{(-1)^{n_m}}{(q_m - n_m)} [(1 + \cos \theta_0)^{q_m - n_m} - 2^{q_m - n_m}] \quad (11)$$

$$\begin{aligned} h(p, q, t) &= 2^{2tq} A_c \left(\frac{A_x}{A_c} \right)^{2t} \\ &\quad \sum_{n_q=0}^{\infty} \left\{ \frac{tq!}{n_q!(tq - n_q)!} (-1)^{2n_q} \frac{Q_a!}{n_q!(Q_a - n_q)!} \frac{1}{(Q_a - n_q)} [(1 + \cos \theta_0)^{Q_a - n_q} - 2^{Q_a - n_q}] \right\} \end{aligned} \quad (12)$$

$$Q_a = 2n_q + 2tq - (2t - 1)p \quad (13)$$

Within the equation, the infinite series need only be calculated up to $n_m = q_m$ to obtain the accurate result. Compared with the theories introduced in the past [1, 2], theories that can only allow integral value of (q_1, q_2) , the Equation (10) of this research can allow a more practical and applicable feed source field shape to be built.

Figure 2: (a) η_s vs θ_o . (b) η_s vs F/D .Figure 3: (a) η_I vs θ_o . (b) η_I vs F/D .

3. RESULTS ANALYSIS AND CONCLUSION

Figure 2 shows spillover efficiency with respect to various feed radiation patterns with the existence of cross-polarization. In the figure, $A_{21} = A_x/A_c$, which range from -3 to -30 dB with -3 dB difference for each curve. Figure 3. shows aperture efficiency with respect to various feed radiation patterns with the existence of cross-polarized component. In the figure, $A_{21} = A_x/A_c$, which range from -5 to -30 dB with -5 dB difference for each curve.

REFERENCES

1. Lashab, M., F. Benabdellaziz, and C.-E. Zebiri, "Analysis of electromagnetics scattering from reflector and cylindrical antennas using wavelet-based moment method," *Progress In Electromagnetics Research*, Vol. 76, 357–368, 2007.
2. Silver, S., *Microwave Antenna Theory and Design*, McGraw-Hill, New York, 1949.
3. Ratmat-Samii, Y. and S.-W. Lee, "Directivity of planar array feeds for satellite reflector applications," *IEEE Trans. Ant. Propag.*, Vol. 31, No. 3, 463–470, May 1983
4. Ratmat-Samii, Y., "Reflector antennas," *Antenna Handbook Theory, Applications and Design*, Chapter 15, Van Nostrand Reinhold Company Inc., 1988.
5. Balanis, C. A., *Antennas Theory Analysis and Design*, 2nd Edition, John Wiley & Sons, Inc, New York, 1997.

Stabilizing the Method of Moments for Dielectrics Using a Combined Charge and Current Formulation of the EFIE

J.-W. De Bleser, E. Van Lil, and A. Van De Capelle
 ESAT, Katholieke Universiteit Leuven, Belgium

Abstract— An alternative, frequency-stable form of the Method of Moments for dielectric materials is presented. By explicitly including both current and charge, a new set of integral equations is derived that remains well-conditioned at all frequencies. The practical implementation of this formulation is discussed, and a number of test results are presented.

1. INTRODUCTION

The *Method of Moments* (MoM), long restricted to the domain of antennas and electrically small scatterers, is quickly breaking through into larger scenarios. One reason for this is the rapid growth in computing power, but at the same time much work has been done on developing new and improving existing algorithms. Multi-level methods, for instance, allow structures thousands to millions of wavelengths in size to be simulated. Large scale scenarios are therefore possible, and as time passes becoming more and more practical.

Unfortunately, the *Electric Field Integral Equation*, (as classically formulated in [6]) is preferred over the *Magnetic FIE* for accuracy but is unstable at low frequencies. This critical flaw hampers its use with small or fine scale models. It is a well-known problem, broadly studied and still actively researched. [1], for example, studies the analytic properties of the EFIE and suggests defining a new, more stable operator, while [2] and [9] propose alternative basis and testing functions to solve the problem. [8] concludes, as we do in [3], that the problem lies in the handling of the charge. We have therefore examined the underlying equations and reformulated the MoM to be stable at all frequencies.

The flaw in the EFIE lies in the relationship between charge and current. By not directly using this (implicit) relationship to simplify the solution of Maxwell's equations, a set of MoM equations can be derived that explicitly contain both charge and current, without containing any frequency singularities. This has been implemented and tested for perfect conductors in [4]. We now seek to extend the PEC method to dielectrics.

In this paper, we will discuss the theory behind the new method, the implementation choices, and some initial results. The solution to Maxwell's equations used for PEC will briefly be reiterated and then expanded to general materials. The resulting theoretical equations will be transformed to a more implementable form and then discretized. The code architecture will then briefly be mentioned, and initial simulation results will be presented.

2. THEORY

The formulation of the equation and the manner of discretization are the two major hurdles faced when implementing the MoM. Formulation has an effect on the algorithm used and the accuracy attained. The discretization, including selecting basis and testing functions and handling singularities, then presents a number of mathematical and practical difficulties. As the goal of this paper is to test the working of a new formulation and algorithm, a fairly simple set of basis and testing functions was chosen in this case.

2.1. Derivation

The standard method of moments [6] makes use of an electric field integral equation derived from Maxwell's equations. The radiated electric field is expressed as a function of surface charges and currents. The Lorenz gauge, $\nabla \cdot \bar{A} = -j\omega\mu\epsilon\phi$ in the frequency domain with \bar{A} the vector potential and ϕ the scalar potential, is used to eliminate charge from this equation. Using this gauge, however, introduces a $1/\omega$ term into the EFIE, leaving the resulting MoM matrix singular at DC. We therefore seek an alternative formulation of the integral equations that does not make explicit use of the Lorenz gauge, or the continuity equation for that matter.

An alternate formulation, given in Equations (1) to (4) from [4], is not singular and can be used for perfect conductors. Here, the Lorenz gauge is avoided by explicitly including the charge density in the EFIE. The MFIE is used first to calculate the electrical surface current $\bar{J}_{s,e}$, and this

is then used with the modified EFIE to calculate the surface charge $\rho_{s,e}$. The scattered field can then easily be calculated.

$$\bar{H}_r = \nabla \times \bar{A}_e \quad (1)$$

$$\bar{E}_r = - \left(j\omega\mu\bar{A}_e + \frac{1}{\epsilon}\nabla\phi_e \right) \quad (2)$$

$$\bar{A}_e(\bar{r}) = \int_S \bar{J}_{s,e}(\bar{r}') G(\bar{r}_n, \bar{r}') dS' \quad (3)$$

$$\phi_e(\bar{r}) = \int_S \rho_{s,e}(\bar{r}') G(\bar{r}_n, \bar{r}') dS' \quad (4)$$

Generalizing this to dielectrics requires a number of changes. Magnetic charges and currents are introduced to increase the degrees of freedom. The radiated fields are then dependent on both currents and on their own respective charge, with magnetic potentials defined in the same way as the electric potentials above. The equivalence principle is then used, together with appropriate boundary conditions, to derive the set of Equations (5) to (8) relating the incident fields to the charges and currents on the outside face of the surface. A complementary set of equations, with flipped normals and the incident fields zero, can be found for the inside face of the surface.

$$\bar{n} \cdot \bar{E}_i = \frac{\rho_{s,e}}{\epsilon} - \bar{n} \cdot \left(\nabla \times \bar{A}_h - \frac{1}{\epsilon}\nabla\phi_e - j\omega\mu\bar{A}_e \right) \quad (5)$$

$$\bar{n} \cdot \bar{H}_i = \frac{-\rho_{s,h}}{\epsilon} - \bar{n} \cdot \left(\nabla \times \bar{A}_e + \frac{1}{\mu}\nabla\phi_h + j\omega\epsilon\bar{A}_h \right) \quad (6)$$

$$\bar{n} \times \bar{E}_i = \bar{J}_{s,h} - \bar{n} \times \left(\nabla \times \bar{A}_h - \frac{1}{\epsilon}\nabla\phi_e - j\omega\mu\bar{A}_e \right) \quad (7)$$

$$\bar{n} \times \bar{H}_i = \bar{J}_{s,e} - \bar{n} \times \left(\nabla \times \bar{A}_e + \frac{1}{\mu}\nabla\phi_h + j\omega\epsilon\bar{A}_h \right) \quad (8)$$

An important difference between this method and that used with perfect conductors is that none of the calculated currents are physical currents. The net surface current of the complete scenario is assumed to be zero, and the surface currents in the above equations are mathematical parameters coupling the internal and external equations. The surface currents calculated with the PEC form, in comparison, will approximate the limit for a skin depth approaching zero of the volume currents in the conductor. These two fundamentally different currents may sometimes be similar for identical scenarios, but will not in general.

2.2. Implementation

Many of the implementation decisions taken for PEC were also used for dielectrics. Point matching, numeric integration, singularity extraction and, where possible, analytic solutions were all used in setting up the MoM matrix. The integrals needed do not differ greatly from those used with PEC, so much of the verification already done remained valid. The greatest difficulty was bringing it all together along with new boundary conditions to now work for general materials.

Equation (9), along with definitions (10) to (14), are the result of transforming the analytical equations from the previous section into matrix form. Only three distinct integrals are needed together with two boundary condition terms, greatly reducing the computation time despite that each must be evaluated in all media. Various structures can be identified, such as the PEC equations in the top left quadrant and the dual perfect magnetic conductor equations in the top right. Eliminating $\bar{\pi}_r$ by setting ω to zero gives two independent sets of equations, corresponding to electrostatics and magnetostatics. $\bar{\pi}_r$ is the term that couples the electric equations to the magnetic, and thus will be worth a closer look when AC signals are considered. The $\bar{\pi}'$ terms are identical to the $\bar{\pi}$ terms except that they, corresponding to the second medium, are calculated with flipped

normals and a different set of material properties.

$$\begin{bmatrix} \bar{E}_i(\bar{r}_n) \\ \bar{H}_i(\bar{r}_n) \\ 0 \\ 0 \end{bmatrix} = \left(\begin{bmatrix} 0 & \frac{\bar{\delta}_b}{\epsilon_1} & \bar{\delta}_c & 0 \\ \bar{\delta}_c & 0 & 0 & \frac{-\bar{\delta}_b}{\mu_1} \\ 0 & \frac{\bar{\delta}_b}{\epsilon_2} & \bar{\delta}'_c & 0 \\ \bar{\delta}'_c & 0 & 0 & \frac{-\bar{\delta}_b}{\mu_2} \end{bmatrix} - \begin{bmatrix} -\mu_1 \bar{\pi}_r & \frac{-\bar{\pi}_b}{\epsilon_1} & \bar{\pi}_c & 0 \\ \bar{\pi}_c & 0 & \epsilon_1 \bar{\pi}_r & \frac{\bar{\pi}_b}{\mu_1} \\ -\mu_2 \bar{\pi}'_r & \frac{-\bar{\pi}'_b}{\epsilon_2} & \bar{\pi}'_c & 0 \\ \bar{\pi}'_c & 0 & \epsilon_2 \bar{\pi}'_r & \frac{\bar{\pi}'_b}{\mu_2} \end{bmatrix} \right) \cdot \begin{bmatrix} J_{s,e} \\ \rho_{s,e} \\ J_{s,h} \\ \rho_{s,h} \end{bmatrix} \quad (9)$$

$$\bar{\pi}_r = j\omega \int_{S_m} \bar{f}_m(\bar{r}') G(\bar{r}_n, \bar{r}') dS' \quad (10)$$

$$\bar{\pi}_c = \int_{S_m} \bar{\nabla}_r G(\bar{r}_n, \bar{r}') \times \bar{f}_m(\bar{r}') dS' \quad (11)$$

$$\bar{\pi}_b = \int_{S_m} \bar{\nabla}_r G(\bar{r}_n, \bar{r}') \Pi_m(\bar{r}') dS' \quad (12)$$

$$\bar{\delta}_c = \bar{f}_n(\bar{r}_n) \quad (13)$$

$$\bar{\delta}_b = \delta_{mn} \bar{n}_n \quad (14)$$

m and n are the basis function and testing function index, respectively. The actual implementation of the $\bar{\pi}$ terms is identical to [4], but will in part be reiterated here:

- \bar{f}_m and Π_m correspond to RWG [7] and uniform block functions respectively. These are tested using point matching in the center of the inscribed circle, \bar{r}_n . The vector surface integral is split into its normal and tangential components, greatly simplifying the handling of the singularity. Each tested triangle therefore produces 3 equations, with a 12 by 5 rectangular matrix as a result.
- Non-singular terms of all three $\bar{\pi}$ functions are integrated using the 7 or 9 point quadrature integration proposed in [5]. The singular tangential terms of $\bar{\pi}_r$ are also computed with routines from [5], and the normal terms are zero due to \bar{f}_m being parallel to the surface.
- The singular terms of $\bar{\pi}_b$ are handled with singularity extraction and an analytic solution for the static term, as with PEC. Results agree closely with an implementation based on [5].
- The singular tangential term of $\bar{\pi}_c$ can be integrated analytically and is equal to $-\bar{J}/2$, analogous to the normal term of $\bar{\pi}_r$. For the normal terms it can be shown that the white areas in Figure 1 balance each other out. The integral needs only be taken over the grey area, does not contain the singularity, and can therefore be performed numerically.

To increase the speed of the test software without becoming buried in optimizations, the code has been parallelized using MPI, BLACS and SCALAPACK. Each thread computes its block of the above matrix, which is divided up such that only one thread needs to compute each $\bar{\pi}$ and $\bar{\delta}$ function for a given area. The least squares solver of SCALAPACK is then used, and the results used to calculate the scattered field. The threads are not restricted to a single machine, as using MPI allows communication, for instance between threads on different nodes of a computing cluster.

3. RESULTS

Verification of the dielectric code will here rely primarily on the scattered field and on an analytic solution for small objects. We examine the computed charge and current densities at various frequencies and for various materials. Making use of the duality of much of the underlying matrix

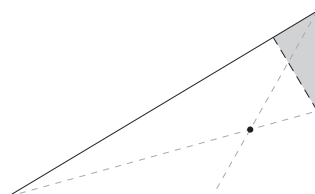


Figure 1: Relevant area for the self term of $\bar{\pi}_c$.

makes it possible to greatly reduce the degree of verification needed. Note that electrostatic results are computed by using the dynamic routines with $f = 0$, which is only possible due to the method's stability.

Figure 2 shows a simple simulation of the scattered field around a sphere made of a material identical to the surroundings at a frequency low enough that the electric and magnetic fields are effectively decoupled. The incident field should be unaffected by the sphere, which can be seen to be the case. This helps verify $\bar{\pi}_c$ and $\bar{\pi}_b$.

Figure 3 shows the static field surrounding a sphere with a relative permittivity and permeability greater than one. The field is now distorted by the presence of the sphere, but the boundary conditions for normal \bar{D} and \bar{B} and for tangential \bar{E} and \bar{H} are satisfied. Note also the duality between the electric and magnetic field.

Verifying that the amplitude of the surrounding static field is correct can more easily be done by verifying the computed charge and current. An analytical solution for the field surrounding a dielectric sphere can be found, and from this the charge and current computed. Figure 4 shows the result, with the black line the analytic solution. The charge matches almost exactly, but the current grows too quickly for large values of ϵ_r . Note that this does not seem to have a significant effect on the scattered field in Figure 3(b), and keep in mind that an identical error is present for $\rho_{s,h}$ and $\bar{J}_{s,e}$.

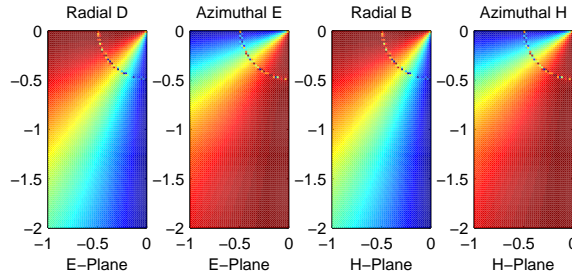


Figure 2: Simulated normalized scattered field around a 1 m sphere with $\epsilon_r = \mu_r = 1$ at 30 kHz.

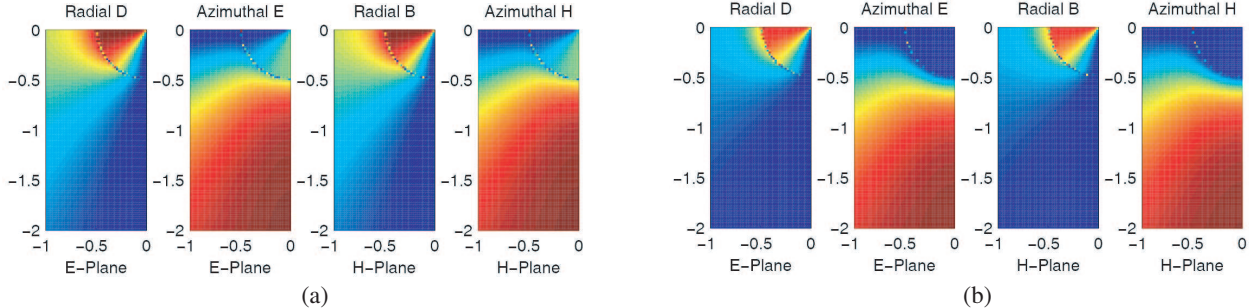


Figure 3: Simulated normalized scattered field around a 1 m sphere at DC. (a) $\epsilon_r = \mu_r = 4$. (b) $\epsilon_r = \mu_r = 64$.

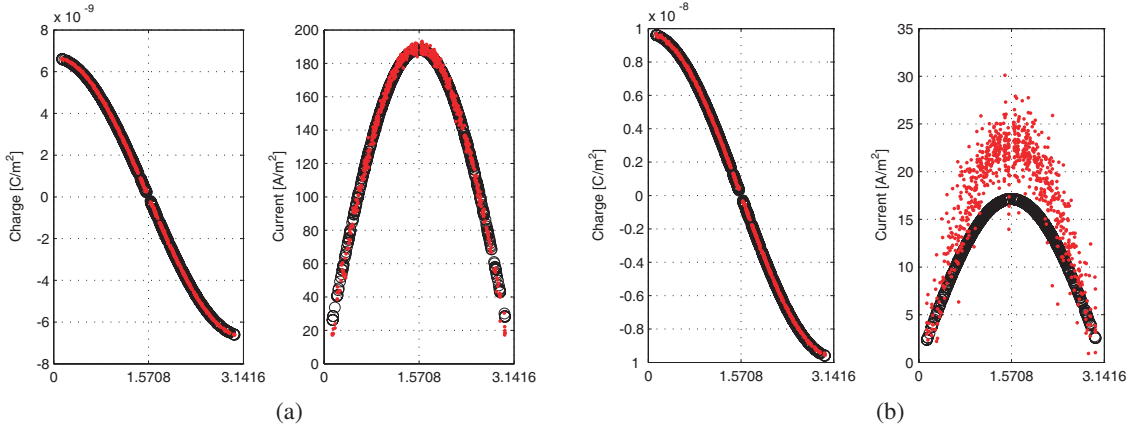


Figure 4: Simulated $\rho_{s,e}$ and $\bar{J}_{s,h}$ compared to the analytic solution. (a) $\epsilon_r = 4$. (b) $\epsilon_r = 64$.

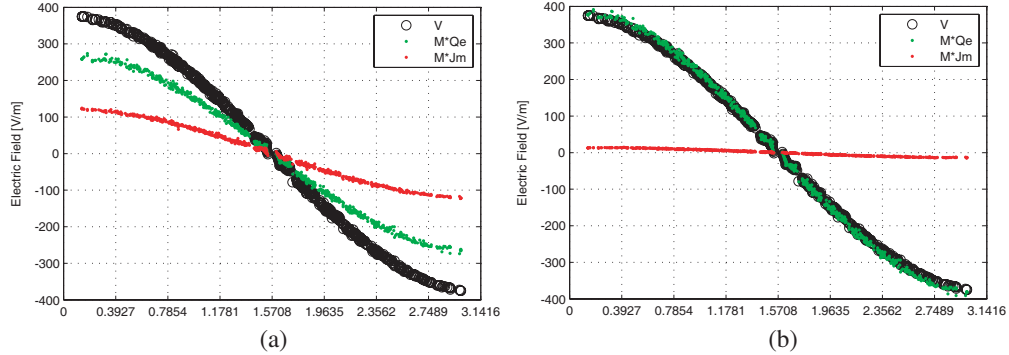


Figure 5: Normally tested incident field, charge contribution and current contribution for a sphere. (a) $\epsilon_r = 4$. (b) $\epsilon_r = 64$.

Figure 5 may help explain the source of the error and why it is not present in the scattered field. It shows the incident field tested with the surface normal (black), compared to the contribution to the tested scattered field from the charge (green) and the current (red), for ϵ_r equal to 4 and 64 respectively. The charge dominates for large values of ϵ_r , implying both that the calculation of the current will be badly conditioned and that errors in the current will likely only result in minimal errors in the scattered field. Therefore, although the current used to calculate Figure 3(b) was erroneous, this is not immediately visible in the scattered field itself.

The algorithm is currently being debugged for frequencies above VLF. Although most integrals have been taken from (and verified by) the PEC simulator, the point matched MFIE and the expanded formulation are new. Results should be available soon.

4. CONCLUSION

We have shown a new formulation of the EFIE and MFIE used for dielectrics. By introducing magnetic charges and currents into a stabilized PEC formulation, we have derived a stable set of dielectric equations. These are discretized with RWG and block functions using point matching. The scattered electrostatic field has been shown to match the expected result closely. The currents show some erroneous behavior, but this has minimal effect on the scattering. Verification is ongoing, so results at resonance and optical frequencies should be available soon.

ACKNOWLEDGMENT

This research was funded by a Ph.D. grant from the IWT, the *Agency for Innovation through Science and Technology*, Belgium.

REFERENCES

1. Adams, R. J., “Physical and analytical properties of a stabilized electric field integral equation,” *IEEE T. Antenn. Propag.*, Vol. 52, No. 2, 362–372, 2004.
2. Cools, K., F. P. Andriulli, F. Olyslager, and E. Michielssen, “Calderón preconditioned time-domain integral equation solvers,” *IEEE Antenn. Propag. Intl. Symp.*, 2007.
3. De Bleser, J.-W., E. Van Lil, and A. Van de Capelle, “An analysis of the low-frequency limit of the boundary integral equations,” *COST2100 MCM*, Valencia, 2009.
4. De Bleser, J.-W., E. Van Lil, and A. Van de Capelle, “A ‘charge and current’ formulation of the electric field integral equation”, *EuCAP*, Rome, Italy, 2011.
5. Graglia, R. D., “On the numerical integration of the linear shape functions times the 3-d Green’s function or its gradient on a plane triangle,” *IEEE T. Antenn. Propag.*, Vol. 41, No. 10, 1448–1455, 1993.
6. Harrington, R. F., D. R. Wilton, C. M. Butler, R. Mittra, and C. L. Bennett, *Lectures on Computational Methods in Electromagnetics*, The Sceee Press, 1981.
7. Rao, S. M., D. R. Wilton, and A. W. Glisson, “Electromagnetic scattering by surfaces of arbitrary shape,” *IEEE T. Antenn. Propag.*, Vol. 30, No. 3, 409–418, 1982.
8. Taskinen, M. and P. Yl-Oijala, “Current and charge integral equation formulation,” *IEEE T. Antenn. Propag.*, Vol. 54, No. 1, 58–67, 2006.
9. Zhao, J.-S., and W. C. Chew, “Integral equation solution of Maxwell’s equations from zero frequency to microwave frequencies,” *IEEE T. Antenn. Propag.*, Vol. 48, No. 10, 1635–1645, 2000.

Electromagnetic Properties at Millimeter Wavelength Range of Diamond Films Grown by DC arc Plasma Jet Technique

B. M. Garin¹, V. V. Parshin², E. A. Serov², Ch. Ch. Jia³, W. Z. Tang³, and F. X. Lu³

¹Institute of Radio Engineering and Electronics of Russian Academy of Sciences, Fryazino Branch
1, Vvedensky Sq., Fryazino, Moscow Region 141190, Russia

²Institute of Applied Physics of Russian Academy of Sciences
46, Ulianov Str., Nizhny Novgorod 603950, Russia

³Beijing University of Science and Technology, 30, College Str., Beijing 100083, China

Abstract— The results of investigation of the diamond sample prepared by using the DC arc plasma jet technique operated under a gas-recycling mode with deposition rate of about 10 mkm/hr is presented.

The measuring methods at the base of high-Q open resonator and cylindrical cavity resonator are discussed.

The absorption mechanism in Diamonds growing by different methods also discussed.

1. INTRODUCTION

Diamond films are a new kind of high quality dielectric material because they possess a combination of novel properties, i.e., high thermal conductivity, high dielectric strength and low dielectric losses. Conventionally, high quality diamond films are exclusively prepared by using microwave plasma chemical vapor deposition (MPCVD) technique. But on the other hand, the deposition rate of diamond films by using the MPCVD technique is rather low. Therefore, the material is very expensive and its application is restricted.

During the last decade, a high power DC arc plasma jet technique has been developed, which shows the advantages of higher deposition rate and lower material cost. Until now, there has been little report on dielectric properties of diamond films prepared by the high power DC arc plasma jet technique. In this paper, preliminary results will be given on such a subject.

2. RESULTS AND DISCUSSION

A diamond film sample has been prepared by using the high power DC arc plasma jet technique, operated under the gas-recycling mode [1]. The flow rates of the gases Ar, H₂ and CH₄ were 2 SLM (standard liter per minute), 8 SLM and 3 SCCM (standard cubic centimeter per minute), respectively, and under the gas recycling mode, the recycled portion of the gases amounted to about 90%. The voltage and current of the DC arc were 100 V and 130 A, respectively, and the deposition rate of the diamond film was about 10 μm/hr which is several times higher than that obtainable by using the ordinary MPCVD technique.

After the deposition, the diamond film was mirror-polished mechanically from the both sides and then it was laser cut into a sample of 18.2 cm in diameter. After polishing the sample is 0.316 mm thick, and it appears transparent but with a little gray color. The in-plane thermal conductivity of the sample measured at room temperature by using a photothermal detection technique [2] is about 19 W/cm K, i.e., very close to the highest value possible for a diamond sample (20–22 W/cm K). This may be explained by the fact that the microstructure of the sample is rather perfect and the sample contains very little microcavities.

The refractive index n and loss tangent $\tan \delta$ of the sample at the short millimeter wavelength range were measured using a Fabry-Perot resonator with a high Q-factor ($Q \sim 10^6$) [3]. The measurements were made at the resonance frequency ($f = 201$ GHz) of the disk when the disk optical thickness is equal to half-wavelength in material ($t \cdot n = \lambda/2$ with t being the thickness of the sample). The plane parallel disk is situated close to the resonator centre, normally to its axis (see Fig. 1). The measurements of loss tangent take place at the two positions of the sample relatively to the standing wave in a resonator, namely when the plate surfaces coincide with the minimum of standing wave in a resonator (upper position in Fig. 1.) and with the maximum (lower position in Fig. 1).

By this way we have three values of the Q-factor of the resonator — two Q-factor values for the resonator with the sample and Q-factor of the empty resonator at the same resonance frequency

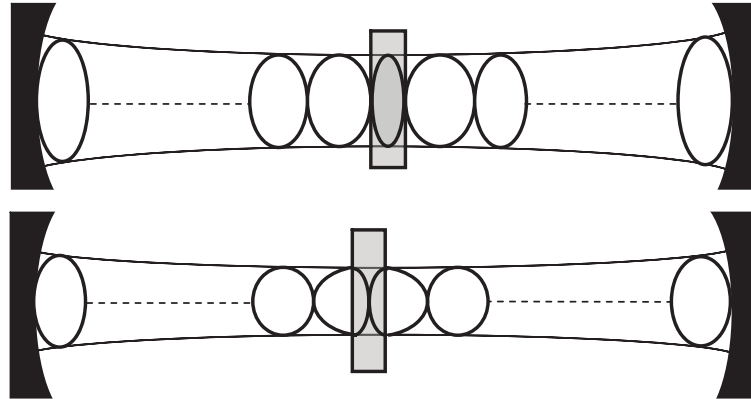


Figure 1: The resonator beam structures with dielectric.

with the same number of half-waves. Using these three values of Q-factor we can calculate the value of loss tangent by three ways combining three pair of Q-factor of empty and loaded resonator [4]. Certainly the results of calculations must be the same.

By this way we have got the loss tangent value $\tan \delta = 3 \cdot 10^{-3}$ (at frequency $f = 201$ GHz). The estimated accuracy of $\tan \delta$ measurements is 10% for the disc thickness of $t = 0.316$ mm. The microwave beam diameter is about 7.5 mm at the level $1/e$ (Gaussian TEM_{00q} mode, $q = 615$), thus the measured parameters are averaged over this area.

The coincidences of these results, measured by three ways means that the diamond surfaces do not have the additional contaminations [4].

The refraction index was found from the measured resonant frequency of the dielectric plate [3], its value $n = 2.354 (\pm 0.002)$. It differs essentially from the refractive index = 2.380 (± 0.001) obtained in our previous measurements of the big set of Microwave Plasma Assistant Chemical Vapor Deposition (MPACVD) diamonds. The later is near to the value for monocrystalline diamond.

The investigated diamond produced by DC arc plasma jet technique has less refractive index value compared to other CVD diamonds. It means that the sample has lesser density.

The loss tangent $\tan \delta$ was measured also at the long millimeter (MM) wavelength range by the cylindrical cavity method [5]. For the measurement, a TM_{015} mode cylindrical cavity with a Q-factor of over 40,000 has been used. It was found that $\tan \delta = (1.5/2.4) \cdot 10^{-4}$ at $f = 35$ GHz (for two sides).

It follows from the measurements that a significant increase of loss tangent with frequency at the MM range is observed in the investigated sample of diamond. It essentially differs from the loss tangent frequency dependence in other CVD diamonds where a decrease of loss tangent with frequency was observed. In that CVD diamonds the dielectric loss is due to electric conductance in the boundaries between crystallites (intergranular regions) [6–8]. The conductance is caused by the thermal excitation of charge carriers from deep levels of forbidden gap at high temperatures [9] and from shallow levels at low temperatures [10].

From the observed increase of loss tangent with frequency in the investigated sample of diamond it follows that the loss mechanism in it is another. Such temperature dependence corresponds to the mechanism of loss induced by lattice disorder [11, 12]. It is also in agreement with the lesser density (compared to usual CVD diamonds) that follows from the measured refraction index.

3. CONCLUSION

The studied sample essentially differs from CVD diamonds studied earlier. In particular:

1. The refractive index is essentially less compared with usual CVD diamonds. It means that the density of sample is less. It combines with absence of big internal cavities. The latest can give additional advantage at terahertz (THz) range due to less scattering of electromagnetic wave.
2. The relative transparency combines with high deposition rate: 10 mkm/hour compared with 2–3 mkm/hour for usual high quality CVD diamonds.

3. The loss tangent increases with frequency whereas it decreases in usual CVD diamonds. It corresponds to the mechanism of loss induced by lattice disorder. Whereas in usual CVD diamonds the loss at MM range is due to electric conductance in the intergranular regions.

Further experiments are needed to explore the reasons why the diamond film sample behaves differently than the samples prepared by MPCVD technique. Such a work is planned for the future.

Such material is perspective for diamond coated copper-diamond composites in the high power electronics at MM and THz ranges.

ACKNOWLEDGMENT

The work was supported by the Russian Foundation for Basic Research (project No. 11-02-91179) and the Chinese Foundation for Natural Sciences.

REFERENCES

1. Lu, F. X., W. Z. Tang, T. B. Huang, J. M. Liu, J. H. Song, W. X. Yu, and Y. M. Tong, "Large area high quality diamond film deposition by high power DC arc plasma jet operating at gas recycling mode," *Diamond and Related Materials*, Vol. 10, 1551, 2001.
2. Bertolotti, M., G. L. Liakhov, A. Ferrari, V. G. Ralchenko, A. A. Smolin, E. Braztsova, K. G. Korotoushenko, S. M. Pimenov, and V. I. Konov, "Measurements of thermal conductivity of diamond films by photothermal deflection technique," *J. Appl. Phys.*, Vol. 75, 7795, 1994.
3. Dryagin, Yu. A. and V. V. Parshin, "A method to measure dielectric parameters in 5–0,5 mm wavelength band," *International Journal of Infrared and Millimeter Waves*, Vol. 13, No. 7, 1023–1032, 1992.
4. Koposova, E. V., S. E. Myasnikova, V. V. Parshin, and S. N. Vlasov, "The absorption investigation in CVD-diamond disks and windows at 50–200 GHz," *Diamond and Related Materials*, Vol. 11, No. 8, 1485–1490, 2002.
5. Guo, G.-F., E. Li, Q.-S. Zhang, and H.-F. Li, "Measurement of temperature dependence of complex permittivity of low-loss dielectric material," *J. of Aeronautical Materials*, Vol. 23, 194, 2003 (in Chinese).
6. Garin, B. M., V. V. Parshin, V. G. Ralchenko, et al., "Losses in diamond in the millimeter range," *Technical Phys. Lett.*, Vol. 25, 288–289, 1999.
7. Garin, B. M., V. V. Parshin, S. E. Myasnikova, and V. G. Ralchenko, "Nature of millimeter wave losses in low loss CVD diamonds," *Diamond and Related Materials*, Vol. 12, No. 10–11, 1755–1759, 2003.
8. Garin, B. M., M. P. Parkhomenko, V. V. Parshin, S. E. Myasnikova, R. Heidinger, I. Danilov, J. Molla, V. G. Ralchenko, V. N. Derkach, and S. I. Tarapov, "Dielectric losses in CVD diamonds at frequencies 1 kHz–200 GHz and temperatures 70–800 K," *Proc. of Seventh Applied Diamond Conf./Third Frontier Carbon Technology Joint Conf. (ADC/FCT 2003)*, Tsukuba, Japan, Aug. 18–21, 2003; M. Murakawa, M. Miyoshi, Y. Koga, L. Schäfer, and Y. Tzeng, editors, Vol. NASA/CP-2003-212319, 297–302, USA, NASA, Aug. 2003.
9. Polyakov, V. I., A. I. Rukovishnikov, B. M. Garin, L. A. Avdeeva, R. Heidinger, V. V. Parshin, and V. G. Ralchenko, "Electrically active defects, conductivity, and MM wave dielectric loss in CVD diamonds," *Diamond and Related Materials*, Vol. 14, No. 3–7, 604–607, 2005.
10. Garin, B. M., V. I. Polyakov, A. I. Rukovishnikov, L. A. Avdeeva, V. N. Derkach, V. V. Parshin, and V. G. Ralchenko, "Dielectric loss and energy distribution of the shallow levels in CVD diamonds," *Diamond and Related Materials*, Vol. 15, No. 11–12, 1917–1920, 2006.
11. Garin, B. M., "One-phonon dielectric losses by excitation of sound," *Sov. Phys. Solid State*, Vol. 32, No. 11, 1917–1920, 1990.
12. Garin, B. M., "Disorder-induced one-phonon absorption of millimeter and submillimeter waves," *SPIE Proc.*, Vol. 2211b, 606–614, USA, 1994.

Design of Waveguide Filter with Rectangular Irises in Cylindrical Cavities

Uma Balaji

Electrical Engineering Technology, Farmingdale State College, Farmingdale, NY 11735, USA

Abstract— The filter described in this paper is composed of rectangular irises of finite thickness as a junction between cylindrical cavities. Mode Matching Method (MMM) has been used to analyze the discontinuities present in the filter and obtain the performance of the filter. The filter has been further optimized to obtain the desired performance.

1. INTRODUCTION

Filters in rectangular and circular waveguides can be designed based on equivalent network theory approach using closed form approximation for susceptance of the apertures [1–3]. Mode matching method to design waveguide filters is a preferred option as accurate design for the desired performance is easily obtained using this approach. A circular waveguide coupled cavity filter with input and output guides that are circular and resonant irises that are also circular has been presented in [4]. This paper presents the design of rectangular irises as coupling elements between cylindrical cavities. The input and output to the filter are rectangular waveguides.

2. THEORY

The input and output to the filter are rectangular waveguides as shown in Figure 1. The irises that couple the input and output rectangular waveguides and the cylindrical cavities are rectangular irises of finite thickness as shown in Figure 2. The axes of all the irises in the filter are concentric with that of the input and output guides. The filter presented here is composed of discontinuities that are from smaller rectangular to larger circular waveguide and, larger rectangular to smaller rectangular waveguide or vice-versa.

The first discontinuity in the filter is from a larger rectangular waveguide to a smaller rectangular waveguide which forms the first iris. This type of discontinuity is easily analyzed using mode matching method. The fields in the rectangular waveguide of this discontinuity are expressed in terms of the fundamental and higher order TE and TM modes of incident and reflected waves with unknown coefficients. The magnitude of power carried by each of these modes is set to unity. The continuity conditions for the tangential components of electric and magnetic fields are imposed at the interface of the discontinuity. Using the principle of orthogonality of modes, the equations of continuity conditions are transformed into matrices relating the unknown coefficients of incident and reflected waves at the discontinuity. The matrices are rearranged and inverted suitably to obtain the generalized scattering matrix which describes the discontinuity in terms of the dominant and higher order modes. Theoretically the generalized scattering matrix is of infinite dimension corresponding to the infinite number of modes. The matrix is truncated to a finite size for numerical computations after testing the convergence of the S-parameters. The method of the analysis for such a discontinuity is available in [5] and a program has been written for the analysis of this discontinuity in the filter.

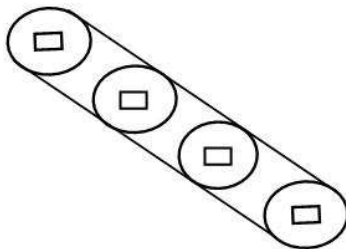


Figure 1: Filter structure — Longitudinal configuration.

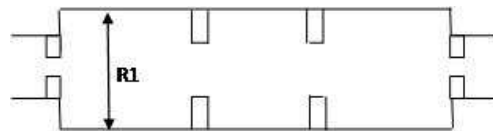


Figure 2: Filter structure showing irises of finite thicknesses.

The next discontinuity in the filter is from the smaller rectangular waveguide to a larger circular waveguide which forms the cylindrical cavity. Mode matching method begins with writing the potential functions on both the sides of the discontinuity. In the circular waveguide the potential functions ψ^h and ψ^e for TE and TM modes are written as,

$$\begin{aligned}\psi^h(\rho, \varphi) &= P_{n,m} J(k_{cn,m}^h \rho) \sin n\varphi \\ \psi^e(\rho, \varphi) &= P_{n,m} J(k_{cn,m}^e \rho) \cos n\varphi\end{aligned}$$

The coefficients P in the above equations are the power normalization constants that set the power carried in each of the modes to a watt. The cutoff wave numbers of the TE_{nm} and TM_{nm} modes are $k_{cn,m}^h$ and $k_{cn,m}^e$.

The potential functions in the rectangular waveguide for TE and TM modes are as follows:

$$\begin{aligned}\Psi_{(m,n)}^{(h)}(x, y) &= T_{m,n}^h \cos(k_{xm} x) \cos(k_{yn} y) \\ \Psi_{(p,q)}^{(e)}(x, y) &= T_{p,q}^e \sin(k_{xp} x) \sin(k_{yq} y)\end{aligned}$$

where, $k_{xm} = m\pi/a$, $k_{yn} = n\pi/b$, $k_{xp} = p\pi/a$ and $k_{yq} = q\pi/b$ are the cut off wave numbers in the rectangular waveguide with dimension of sides being a and b . The values of m and n in the potentials functions correspond to that of various modes. The electric and magnetic field of Transverse Electric (TE) and Transverse Magnetic (TM) for various modes in the region are obtained from these functions.

The discontinuity is symmetric as the longitudinal axes of all the guides are concentric. Due to symmetry it is sufficient to consider only modes that have m and p odd and n and q even for dominant mode namely TE_{10} excitation in the rectangular waveguide. This means that modes that form magnetic wall along y -axis and electric wall along x -axis are alone considered in the analysis.

The symmetry condition in the circular waveguide translate into choosing waveguide modes that have n values that are odd starting from 1 and continuous values of m starting from 1 in determining the values of $k_{cn,m}^h$ and $k_{cn,m}^e$.

The next step in MMM involves writing the continuity condition for the electric and magnetic fields at the interface of the discontinuity. The electric and magnetic fields in circular waveguide are a function of Bessel function in the radial direction and sinusoidal in the angular direction while those in the rectangular waveguide are in Cartesian co-ordinate system. Matching of the fields is done in Cartesian co-ordinate system as the iris is rectangular. In order to transform the continuity condition into linear algebraic equations using the principle of orthogonality of modes, the fields in the circular waveguide are converted as a sum of complex exponential in x and y co-ordinates

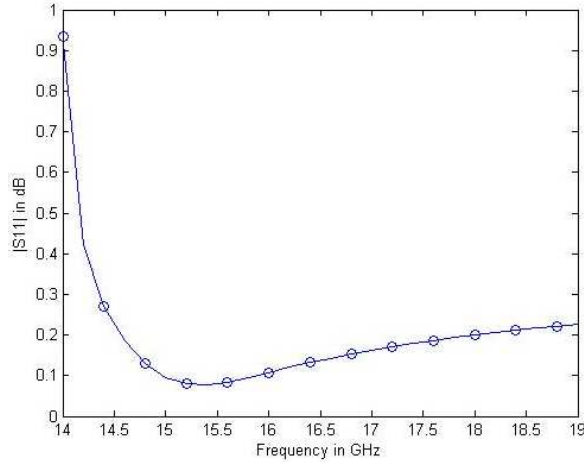


Figure 3: Magnitude of reflection coefficient from rectangular waveguide $10.7 \text{ mm} \times 4.32 \text{ mm}$ to a rectangular waveguide of dimension $15.8 \text{ mm} \times 7.9 \text{ mm}$ — computed, o [5].

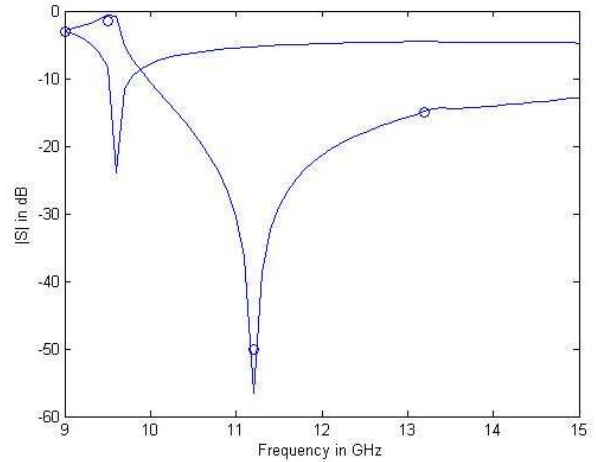


Figure 4: Magnitude of S parameters from WR75 rectangular to circular waveguide with $a = 2b = 0.75"$ = radius of circular waveguide — computed, o [6].

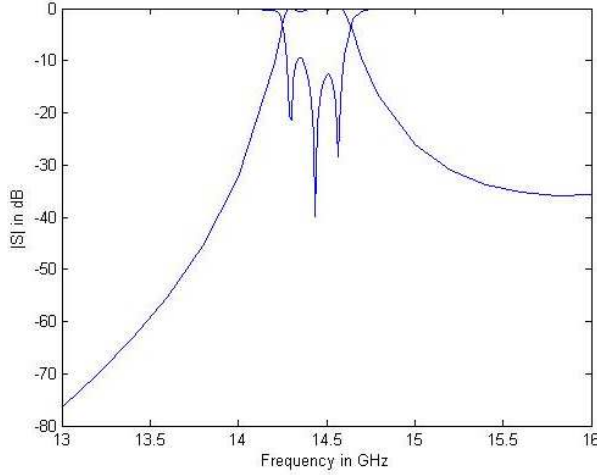


Figure 5: Response of the filter. Input and output rectangular waveguide of dimension 1.58×0.79 cm, Cavity radius = 0.6985 cm, Iris thickness = 0.127 mm, cavity lengths = 1.91, 1.97, 1.91 cm.

using the equations described in the appendix of [6] and given as,

$$J_q(h\rho)e^{jq\varphi} \cong \frac{j^q}{N} \sum_{l=0}^{N-1} e^{j\frac{2lq\pi}{N}} e^{-jh(C_lx+S_ly)}$$

where, $x = \rho \cos \varphi$, $y = \rho \sin \varphi$, $C_l = \cos(\frac{2l\pi}{N})$, $S_l = \sin(\frac{2l\pi}{N})$ and $N - 1 > h\rho + M$, with M being a small integer. Using these equations the fields in circular waveguide which are expressed in cylindrical co-ordinate system are transformed to Cartesian co-ordinate system.

The linear algebraic equations obtained by application of principle of orthogonality are rearranged and manipulated to obtain the generalized scattering matrix of the discontinuity. The generalized scattering matrices of all the discontinuities in the filter are cascaded to obtain the characteristic of the filter. Sufficient higher order modes have been used in the analysis of the discontinuity by testing for convergence of the scattering parameters. The filter has been designed and optimized using a practical quasi-Newton algorithm as described in [7] to obtain the desired performance.

3. RESULTS

The discontinuity from a larger rectangular waveguide to smaller rectangular waveguide was analyzed with 40 TE and TM in larger waveguide. The ratio of the modes from larger to smaller guide was set close to the ratio of the dimensions of the two guides. Convergence of the S-parameters has been observed and the results have been verified with [5] as shown in Figure 3. The analysis of a smaller rectangular to larger circular guide was also performed and a good agreement has been found with [6] as shown in Figure 4. A filter using cylindrical cavities and rectangular coupling irises of finite thickness has been analyzed, designed and optimized further for the desired specifications. The performance and the dimension of the filter are as shown in Figure 5. In comparison to the filter with circular irises as presented in [4] this filter offers improved stop band performance.

4. CONCLUSIONS

The Mode Matching Method has been used for the analysis and design of circular waveguide filters with rectangular irises. The design has been optimized in order to obtaining the desired performance. However further optimization may be necessary to improve the performance to obtain a return loss better than 20 dB.

REFERENCES

1. Collin, R. E., *Foundations for Microwave Engineering*, McGraw-Hill, NY, 1966.
2. Matthaei, G. L., L. Young, and E. M. T. Jones, *Microwave Filters, Impedance-matching Networks and Coupling Structures*, McGraw-Hill, 1964.

3. Eastharn, G. B. and K. Chang, "Analysis and closed form solutions of circular and rectangular apertures in a circular waveguide," *IEEE Trans. Microwave Theory and Techniques*, Vol. 39, No. 4, 718–723, April 1991.
4. Balaji, U., "CAD of resonant circular iris waveguide filter with dielectric filled cavities," *PIERS Proceedings*, 1139–1141, Cambridge, USA, July 5–8, 2010
5. Patzelt, H. and F. Arndt, "Double-plane steps in rectangular waveguides and their applications for transformers, irises and filters," *IEEE Trans. Microwave Theory and Techniques*, Vol. 30, No. 5, 771–776, May 1982.
6. MacPhie, R. H. and K.-L. Wu, "Scattering at the junction of a rectangular waveguide and larger circular waveguide," *IEEE Trans. Microwave Theory and Techniques*, Vol. 43, No. 9, 2041–2045, September 1995.
7. Antoniou, A., *Digital Filters, Design and Applications*, Second Edition, McGraw-Hill, 1993.

A CMOS Doubly Balanced Monolithic Passive Star Mixer with a Compact IF Extraction

Yi-Chang Lee, Shih-Han Hung, Chih-Ming Lin, and Yeong-Her Wang

Department of Electrical Engineering, Institute of Microelectronics

National Cheng-Kung University, No. 1 University Road, Tainan 701, Taiwan

Abstract— A doubly balanced monolithic microwave passive mixers using novel configuration has been designed and fabricated through a $0.18\text{ }\mu\text{m}$ CMOS process. The configuration of the doubly balanced mixer (DBM) can eliminate the use of two dual baluns for application in the conventional star mixer, as well as make the mixer more compact and simplify IF extraction to obtain wider IF bandwidth up to 18 GHz, respectively. From the measured results, the fabricated DBM exhibits wideband performance, superior isolations and high dynamic range.

1. INTRODUCTION

The increasing demand for high-speed data transfer and access has become more prevalent in communication systems. The mixer is one of the important components of communication systems to convert signals from one frequency to another, which demands broadband operation, compact size, low cost, and low-power consumption for high performance transceiver solutions. Doubly balanced mixers (DBM) are usually chosen because of their high dynamic range, even-order mixing product suppression, and inherent port-to-port isolation. The star configuration is commonly used for DBM because of its low IF parasitic inductance, which enables wider IF bandwidth [1]. However, the star configuration in monolithic microwave integrated circuit (MMIC) design is difficult to implement because it uses two rather large half-wavelength Marchand dual baluns and also occupies a larger chip dimension. Moreover, the IF extraction of the MMIC based star DBM is more complicated. This result is in the increase of IF parasitic inductance and the degradation of IF bandwidth. Therefore, it is cost-effective if a star DBM could simplify IF extraction with small-chip-size requirements within the bandwidth.

In order to make a star DBM more compatible with conventional MMICs, many topologies have been proposed [2–6]. However, the configurations of the previous star mixers were mostly based on a pair of symmetrical dual baluns, which may still have large circuit dimensions. To overcome this problem, attention has been drawn to the design of miniature dual baluns. A number of spiral transformer baluns can provide an efficient method for shrinking chip area [7]. Subsequently, three monolithic star DBMs using a new miniature dual balun are proposed [8]. However, the DBM design still has a critical issue of IF extraction. For this reason, a new configuration of DBM is designed and fabricated in $0.18\text{ }\mu\text{m}$ CMOS process. The proposed configuration is more compact in layout design and also more effective in improving the mixer's performance as compared to the conventional DBMs.

2. CIRCUIT DESIGN

Due to configuration of the conventional star DBM, the larger circuit dimension is needed and the complex IF layout will increase additional parasitic inductance to degrade IF bandwidth. In this work, a novel configuration of doubly balanced passive mixer with a compact chip size fabricated in a $0.18\text{ }\mu\text{m}$ CMOS process, as shown in Fig. 1(a), utilizes a LO spiral balun and a meandering RF dual balun to simplify the architecture of the conventional star DBM, while simultaneously satisfy the mixing mechanism of the star mixer.

Particularly, the RF dual balun formed with multiple coupled-line can not only excite the RF signal with a 180° relative phase difference into diodes, but provide an output port for IF extraction. Fig. 1(a) depicts the schematic diagram of the proposed CMOS passive DBM. It can be viewed the overall structure is symmetric, and the terminals of four outside strip-lines were connected together to construct an IF port. A major consideration in the design of the dual balun is the enhancement of the isolation between RF and IF port, which avoids the leak of RF signal from IF port, and vice versa. Owing to the anti-phase relationships of the RF signal, the IF port presents a virtual ground to the RF port. This intrinsic feature leads into the outside coupled-line of the dual balun to form a band-pass filter. Accordingly, it provides a transmission path for the RF signal. The proposed dual balun retains the native property, as well as includes the IF extraction circuit with inherence

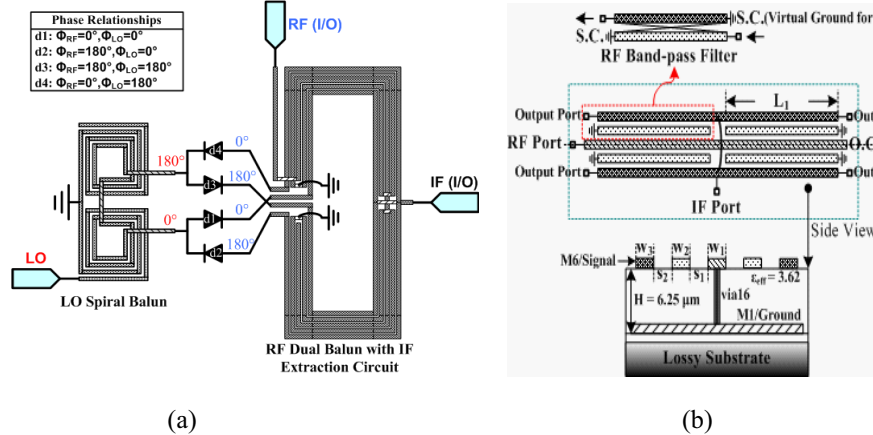


Figure 1: (a) Schematic diagram of the proposed CMOS passive DBM. (b) The cross section structure of the proposed CMOS RF dual balun.

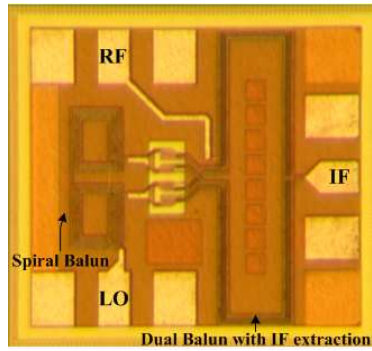


Figure 2: Microphotograph of the fabricated doubly balanced CMOS mixer. The chip dimension is 0.6 mm × 0.54 mm.

isolation. Furthermore, this work presents the meandering RF dual balun and the LO spiral balun, which employ a metal shielded transmission line in CMOS technique so as to surmount the lossy nature of silicon substrate, and achieve the miniaturized necessity.

Figure 1(b) shows the cross sectional view of the proposed CMOS RF dual balun. The sixth metal layer (M6) and first metal layer (M1) are employed to be a signal trace and a ground plane, respectively, and the via16 is used to connect M6 and M1 to form a shorted circuit. To achieve wideband operation, the coupled-line of the dual balun should have high even-mode impedance and closely matched even- and odd-mode phase velocities. Hence, very narrow strip widths were essential to achieve the highest even-mode impedance. The proposed dual balun was fabricated on a silicon-nitride layer of $H = 6.25\mu\text{m}$ with relative permittivity of $\epsilon_{eff} = 3.62$. In this design, Agilent ADS momentum was used in full-wave electromagnetic (EM) simulation to calculate the S -parameters of the passive circuit. The center frequency of this dual balun was designed to be 26 GHz. The designed dimensions, as shown in Fig. 1(b), were $w_1 = 2\mu\text{m}$, $w_2 = 1.8\mu\text{m}$, $w_3 = 3.8\mu\text{m}$, $s_1 = 1.5\mu\text{m}$ and $s_2 = 1.5\mu\text{m}$. The quarter-wave length $L_1 = 1272\mu\text{m}$ was adjusted to achieve the desired center frequency.

The phase relationships of the RF and LO signals at each diode are also presented in Fig. 1(a). It should be noted this new mixing mechanism can be performed like the star DBM [9]. Furthermore, the proposed approach still maintains inherence port-to-port isolations. As the LO^+ and LO^- signals leak through diodes back to the RF dual balun, the LO leakage signals can be cancelled each other out at IF common node. Moreover, the RF dual balun also rejects the in-phase input of LO leakage signals. Consequently, both characteristics result in the enhancement of LO-to-IF and LO-to-RF isolation. According to the proposed RF dual balun, the superior RF-to-IF isolation and wider IF bandwidth ranging from DC to 18 GHz were also achieved.

3. CIRCUIT IMPLEMENTATION AND RESULTS

An Agilent ADS corresponding to TSMC corporation design kit was employed for circuit simulation. These individual components were combined in a harmonic balance simulator to optimize the mixer performance. The fabricated MMIC DBMs were then attached to the carrier plates for testing. The measurement signals were provided by the coplanar 10 μm pitch GSG and GSGSG on a wafer probe measurement system based on the Agilent E4446A spectrum analyzer, which was calibrated with the E44198 power meter. In this case, the gate-drain connected nMOS with a f_T and f_{\max} of better than 60 and 55 GHz, respectively, is used as the diode. In order to achieve good impedance matching, the 16-finger diode with total 26 μm gate width is optimized to ensure minimum conversion loss. A microphotograph of the fabricated doubly balanced CMOS passive mixer is shown in Fig. 2. The core chip dimension, excluding the contact GSG testing pads, is only 0.4 \times 0.54 mm².

Figure 3 represents the measured and simulated conversion loss of the CMOS passive DBM for down-converter mode when IF frequency is fixed at 1 GHz, an LO power level of 11 dBm and RF power level is -10 dBm. The obtained conversion loss is 11 to 14.4 dB within a 3-dB bandwidth from 20 to 34 GHz. Due to high frequency parasitics, the operating bandwidth was slightly decreased from the design goal of 17–34 GHz. Fig. 4 shows the measured and simulated conversion losses versus LO power level with an RF frequency of 24 GHz. A significant mixing effect of an LO drive level of 4 dBm can be seen. The best conversion loss is 10.7 dB at 12 dBm LO power level.

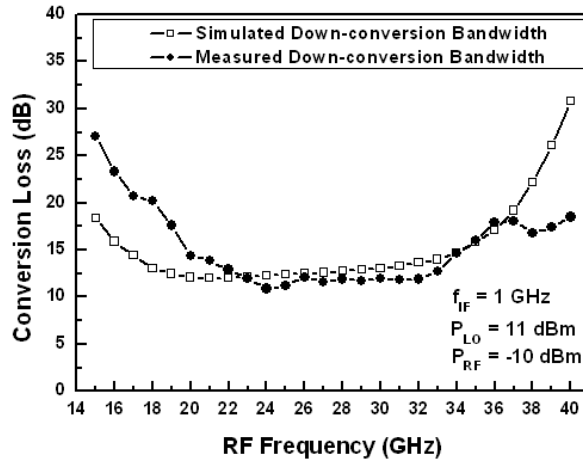


Figure 3: Measured and simulated conversion loss of the mixer as a function of frequency at a fixed LO power of 11 dBm and 1 GHz IF frequency.

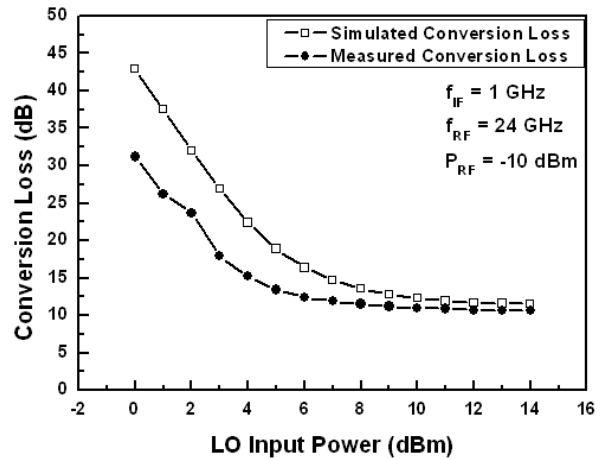


Figure 4: Measured and simulated conversion loss versus the LO power level with a RF input power of -10 dBm.

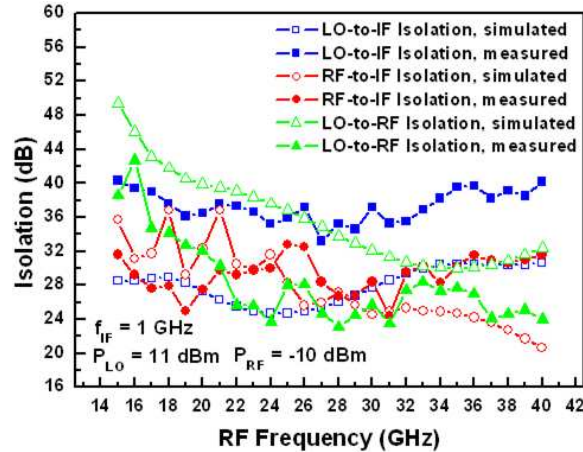


Figure 5: Measured and simulated LO-to-RF, LO-to-IF, and RF-to-IF isolations as a function of the RF frequency.

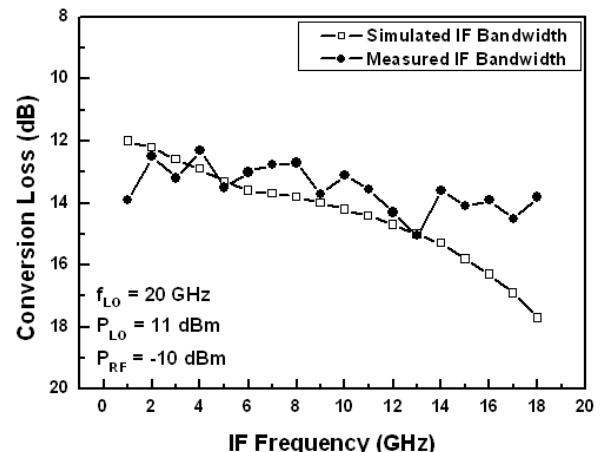


Figure 6: Measured and simulated IF bandwidth from 1 to 18 GHz.

Table 1: Comparison of reported doubly balanced mixers.

Ref.	Technology	RF (GHz)	IF BW (GHz)	CL (dB)	LO power (dBm)	LO-to-RF Iso. (dB)	LO-to-IF Iso. (dB)	P1dB (dBm)	Chip size (mm ²)
[3]	HBT	26–40	DC-11	8–10	16	> 20	N/A	N/A	N/A
[4]	0.1 μm pHEMT	50–75	N/A	13–18	13	35	N/A	3	1.5 × 1.5
[5]	0.15 μm pHEMT	28–36	N/A	11.9–16.2	12	> 46.5	> 31	N/A	1.7 × 1.7
[6]	Package Diode	1–35	DC-1.8	6–18	N/A	15–30	10–20	N/A	N/A
[8]	0.15 μm pHEMT+	25–55	N/A	7–12	13	> 20	> 30	5	1 × 1
[9]	0.15 μm pHEMT	26–38	DC-10	5.4–10.7	12	> 13	> 21	12	2.5 × 1.0
This work	0.18 μm CMOS	20–34	DC-18	11–14.4	11	> 23.1	> 33.2	10	0.6 × 0.54

+ Double spiral transformer

The measured and simulated port-to-port isolations of DBM are shown in Fig. 5. Under the measured conditions shown in Fig. 5, it can be found that the RF-to-IF isolation is between 26.7 and 32.8 dB when RF frequency varies from 20 to 34 GHz. Otherwise, the LO-to-IF isolation exceeds 33.2 dB over the same RF frequency range. Due to the employment of the RF dual balun, both the LO/RF-to-IF isolations have been enhanced without any additional filter. Furthermore, the proposed doubly balanced architecture is a great benefit to the LO-to-RF isolation, which is higher than 23.1 dB from 20 to 34 GHz.

Figure 6 indicates the conversion loss varies with IF frequency. The measured result is accomplished with a fixed LO frequency of 20 GHz and LO power level of 11 dBm. The RF frequency varies between 21 and 38 GHz, corresponding to the IF frequency ranging from 1 to 18 GHz. As the measured results show, the 3-dB IF bandwidth of the mixer is around 18 GHz. This outcome is derived from the utilization of the proposed dual balun. A two tone RF signal was applied at 24 GHz and 24.001 GHz at a fixed LO frequency of 23 GHz and 11 dBm LO drive power to measure the third-order intermodulation intercept point (IIP3). The IIP3 is determined to be approximately 25 dBm. This means high linearity of the proposed DBM can be achieved. Finally, the measured 1 dB compression point is 10 dBm.

The comparisons of the proposed structures with other reported DBMs are summarized in Table 1. This work can simplify IF extraction to expand the IF bandwidth of up to 18 GHz. The proposed work presents some significant advantages such as a broadband operation, an excellent port-to-port isolation and a compact configuration, as compared to previously reported works.

4. CONCLUSIONS

A novel configuration of the DBM has been utilized to simplify IF extractions and scale down overall chip dimensions on the 0.18 μm CMOS process. Performance enhancement and flexible layout design were possible with the proposed baluns as well, including IF extraction techniques. Owing to the utilization of the new 180° hybrid in the CMOS passive DBM provides the widest IF bandwidth of 18 GHz and smallest chip size of 0.4 × 0.54 mm², but maintains superior isolations and high linearity. Finally, it is worth mentioning that the DBMs presented in this paper are amenable to further promote the integration of the RF front end.

ACKNOWLEDGMENT

This work was supported in part by the National Chip Implementation Center, National Applied Research Laboratories, the National Science Council of Taiwan under contracts NSC95-2221-E-006-428-MY3, 98IC05 and the Foundation of Chen Jieh-Chen Scholarship of Tainan, Taiwan.

REFERENCES

1. Maas, S. A., *Microwave Mixers*, 2nd Edition, Artech House, Norwood, MA, 1993.
2. Maas, S. A. and K. W. Chang, "A broadband, planar, doubly balanced monolithic Ka-band diode mixer," *IEEE Trans. Microw. Theory and Tech.*, Vol. 41, No. 12, 2330–2335, 1993.
3. Ryu, Y. I., K. W. Kobayashi, and A. K. Oki, "A monolithic broadband doubly balanced EHF HBT star mixer with novel microstrip baluns," *IEEE MTT-S Int. Microw. Symp. Dig.*, 119–122, 1995.
4. Yeom, K. W. and D. H. Ko, "A novel 60-GHz monolithic star mixer using gate-drain-connected pHEMT diodes," *IEEE Trans. Microw. Theory and Tech.*, Vol. 53, No. 7, 2435–2440, 2005.
5. Lin, C. H., J. C. Chiu, C. M Lin, Y. A. Lai, and Y. H. Wang, "A variable conversion gain star mixer for Ka-Band applications," *IEEE Microw. Wireless Compon. Lett.*, Vol. 17, No. 11, 802–804, 2007.
6. Chang, C. Y., C. W. Tang, and D. C. Niu, "Ultra-broad-band doubly balanced star mixers using planar Mouw's hybrid junction," *IEEE Trans. Microw. Theory and Tech.*, Vol. 41, No. 6, 1077–1085, 2001.
7. Yoon, Y. J., Y. Lu, R. C. Frye, and P. R. Smith, "Modeling of monolithic RF spiral transmission-line balun," *IEEE Trans. Microw. Theory and Tech.*, Vol. 49, No. 2, 393–395, 2001.
8. Kuo, C. C., C. L. Kuo, C. J. Kuo, S. A. Maas, and H. Wang, "Novel miniature and broadband millimeter-wave monolithic star mixers," *IEEE Trans. Microw. Theory and Tech.*, Vol. 56, No. 4, 793–802, 2008.
9. Lin, C. H., C. M. Lin, Y. A. Lai, and Y. H. Wang, "A 26–38 GHz monolithic doubly balanced mixer," *IEEE Microw. Wireless Compon. Lett.*, Vol. 18, No. 9, 623–625, 2008.

A Miniature 18–38 GHz pHEMT MMIC Frequency Doubler

W.-C. Chien¹, C.-H. Liu², S.-H. Hung¹, Y.-C. Lee¹, and Y.-H. Wang^{1,2}

¹Institute of Microelectronics, Department of Electrical Engineering
National Cheng-Kung University, No. 1 University Road, Tainan 701, Taiwan

²Institute of Electro-Optical Science and Engineering
National Cheng-Kung University, No. 1 University Road, Tainan 701, Taiwan

Abstract— A novel MMIC frequency doubler using a GaAs-based pHEMT process is proposed to achieve a miniature area and simplified layout. The circuit configuration is composed of a spiral balun, two common-source transistors, and a band pass filter with a dc-isolated capacitor, for an 18–38 GHz broadband operation. Both the spiral balun and the band pass filter are directly connected to the DC bias. The topology of the frequency doubler can thus be simplified to reduce the use of the bias components, such as the inductor. Thus, this doubler design of the chip size was considerably small and the operating bandwidth was wide. The spiral balun with bias also provide to suppress the fundamental frequency and reduce chip dimension. The fabricated frequency doubler results in a compact core chip size of 0.50 mm^2 , a 0.5–5 dB conversion loss, and an output power of 5 to 9.5 dBm at an input power of 10 dBm.

1. INTRODUCTION

In microwave and millimeter-wave wireless communication systems, high-frequency signals can be achieved by high-frequency oscillators or multipliers from low-frequency signals. As the operation frequency increases, the local oscillator (LO) experiences more difficult in obtaining low phase noise and high output power for the phase-locked loop and mixer at millimeter-wave frequencies. To solve this problem, the use of either the sub-harmonic mixer or the active doubler preceding a local oscillator has been proposed [1–4]. However, there are still some disadvantages of the sub-harmonic mixer or the active doubler, such as low isolation, low bandwidth, and large chip size. Therefore, using the doubler instead of the oscillator at high frequency might result to compact chip size, low power consumption, and high output power.

The balanced doublers employed a rat-race hybrid to achieve broad operating bandwidth have been reported [3, 4]. However, the rat-race hybrid just provided the out-phase signals and occupied large dimension. An ultra-broadband PHEMT MMIC frequency doubler using active balun to reduce chip area has also been proposed [5]. However, the active balun has large DC power consumption and low 1 dB compression point. A frequency double with inherent 180 degrees of phase shift between common gate and common source configurations at the fundamental frequency indicates that the fundamental signals can be cancelled and the second harmonic will be maximized, but this doubler still has high conversion loss [6]. A broadband pHEMT MMIC distributed doubler using high-pass drain line topology was reported [7]. This topology can suppress fundamental signals over broadband without using any balanced structures. Nevertheless, this topology was difficult to match output matching circuit for broadband application. Thus, the conversion loss of the broadband doubler has ripple as high as 4 dB. In references [8] and [9], the doublers used an additional buffer amplifier to enhance the signal power and improve the linearity of the signals; however, the buffer amplifier still suffered from high DC power consumption and large chip dimension.

This paper presents an 18 to 38 GHz MMIC-balanced frequency doubler fabricated using a $0.15\text{ }\mu\text{m}$ GaAs-based pHEMT process. The proposed broadband doubler is composed of one spiral balun, one band pass filter and two common-source (CS) transistors. Both the spiral balun and the band pass filter are integrated directly with the DC bias. The topology of the doubler can thus be simplified to reduce the use of the bias components, such as the inductor. This results in the miniature core chip size as small as 0.5 mm^2 .

2. CIRCUIT DESIGN

The proposed configuration of the frequency doubler is shown in Fig. 1. Two identical common-source configurations, which act as the doubler, and the bias circuits, are integrated with the planar spiral balun and the band pass filter. The planar spiral balun and the band pass filter are connecting to the gate and the drain of the transistor to provide the DC bias path to transistor,

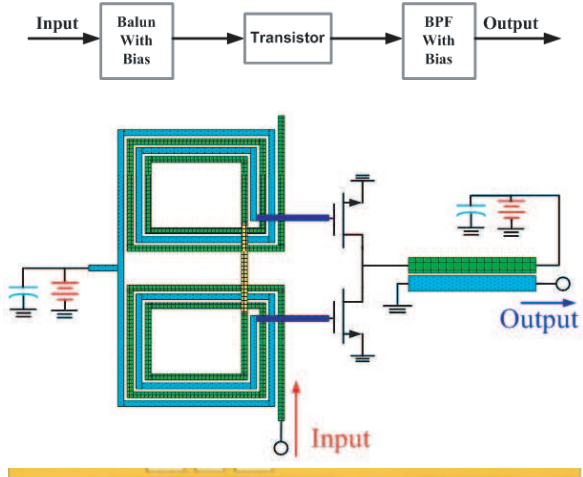


Figure 1: Schematic diagram of the proposed frequency doubler. The corresponding circuit configuration is also shown.

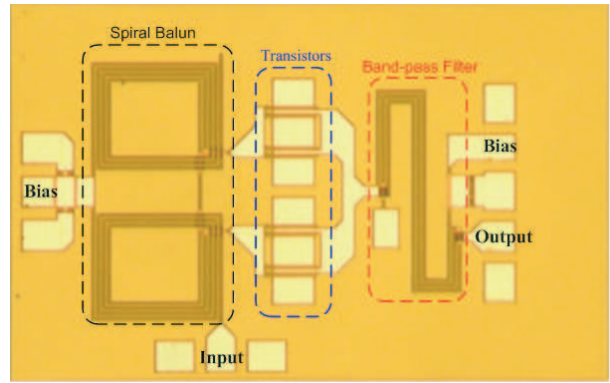


Figure 2: Chip photography of the proposed frequency doubler with a chip size of $1.13 \times 0.729 \text{ mm}^2$, including the contact pads.

respectively. Thus, the topology of the frequency doubler can be simplified to reduce the use of the bias components, and reduce chip dimension.

At the first stage, there is a parallel circuit composed of the gate bias and the grounded dc-isolated capacitor, which are integrated with the planar spiral balun. The input signal through the differential port of the spiral balun is split into two balanced ports and is 180° out of phase, and is fed into two identical transistors and then combined at the point A. The second harmonic signals are in-phase combined and the odd harmonic signals are 180° out-phase and cancelled at the point A. Thus, the spiral balun with bias circuit not only can provide DC bias to gate of transistor, but also can provide characteristic of rejection odd harmonic of doubler. The pHEMTs of the doubler are biased at the class-B region to generate higher second harmonic output power and reduce dc power consumption. In this stage, the planar spiral balun is used to produce balanced signals and to restrain the fundamental frequency because of the balanced configuration. The final stage is a band pass filter with output frequency extraction, which is based on the Lange coupler design. The drain bias of the transistors is directly from the through port of the Lange coupler. The circuit configuration of the band pass filter serves the drain bias of the transistors, and also provides output matching to achieve broad bandwidth and good conversion loss. The chip size of the designed doubler is considerably simplified because of the reduced matching circuit of the passive components. Moreover, this doubler design can exhibit a compact chip size, simple layout, good conversion loss, and broadband operation.

3. CIRCUIT IMPLEMENTATION AND RESULTS

Zeland IE3D software was used in the full-wave EM simulation to calculate the S -parameters of the passive circuits and improve the doubler performance. WIN Semiconductor Corporation design kits were employed in Agilent advanced design system (ADS) for circuit simulation. These individual components were combined in a harmonic balance simulator to optimize doubler performance. The proposed circuit was implemented using a $0.15 \mu\text{m}$ pHEMT technology of the WIN Semiconductor Corporation, with the substrate thickness of $100 \mu\text{m}$ and relative permittivity of 12.9. The realized dimension of the spiral balun with bias was $0.29 \times 0.58 \text{ mm}^2$. A microphotograph of the fabricated circuit is shown in Fig. 2. The chip dimension, including the contact pads, was 1.13×0.729 (0.83) mm^2 . Moreover, the core chip dimension, excluding the contact GSG testing pads, was only 0.847×0.59 (0.5) mm^2 .

The broadband frequency doubler chip, which used AuSn die attached to the moly-made carrier, was measured using on-wafer probing by Cascade RF-1. The measurement signals were provided by the coplanar $100 \mu\text{m}$ pitch GSG and GSGSG on wafer probes measurement system based on the Agilent E4446A spectrum analyzer, which was calibrated with the E44198 power meter. On the other hand, the losses of the probes and the cables were measured separately and were used to correct the measured results.

Figure 3 illustrates the simulated conversion gain and fundamental rejection ratio (FRR) versus

the drain bias V_{DD} at the input frequency of 16 GHz. Obviously, the best conversion gain of -3 dB can be achieved for the V_{DD} in the range of 1.6 to 1.7 V. Also, FRR varies with the bias but within the range of 2 dB. Based on this simulation, the drain bias V_{DD} of 1.6 or 1.7 V was chosen to have best conversion gain. The measurements were performed under the balanced transistors, which were biased for maximum second harmonic output and optimum flatness of output power. The pHEMT device was operated under a drain voltage of 1.7 V, with a drain current of 79 mA, and a gate voltage of -1.1 V. The dc power consumption of the doubler was 134 mW.

The measured output power as a function of input frequency at the input power of 10 dBm is illustrated in Fig. 4. In the input frequency of 9–19 GHz (bandwidth 71.4%), the second harmonic output power is in the range of 5 to 9.5 dBm. It can be found that the best output power is 9.5 dBm at the input frequency of 12.5 GHz. For the fundamental frequency, the output power is about -12.5 to -14 dBm. Due to the limitation of the measurement system, the third harmonic frequency can be measured only up to the input frequency of 14.5 GHz (3rd frequency of 43.5 GHz), the output power is around -5.8 and -14 dBm. The output power of the second harmonic frequency is much higher than those of the fundamental and third harmonic frequency. This indicates the validation of the design concept.

The measured conversion loss and harmonic rejection versus input frequency at input power of 10 dBm is illustrated in Fig. 5. This proposed frequency doubler has about 0.5 to 5 dB conversion loss from 9 to 19 GHz input frequency. The maximum fundamental frequency suppression is 18 dB at 16 GHz while 30.6 dB at input frequency 10.5 GHz for 3rd harmonic frequency. Fig. 6 shows the measured conversion loss and FRR versus input power at input frequencies of 12.5 and 16 GHz, respectively. The better conversion loss is from 9 to 11 dBm of input power. The maximum FRR is 20 dB at 16 GHz input frequency, which increases with increasing in input power. As the results

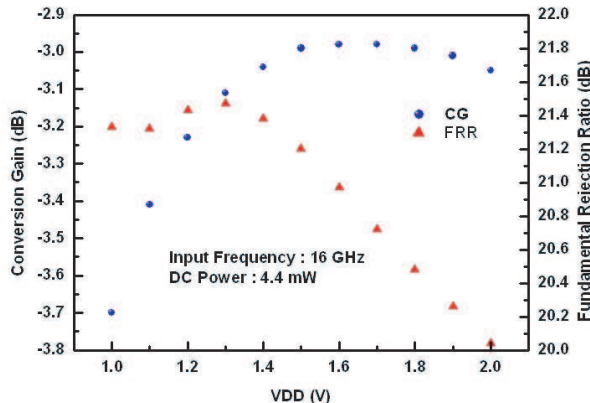


Figure 3: The simulated results of the conversion gain and FRR as a function of drain voltage, V_{DD} , at input frequency of 16 GHz.

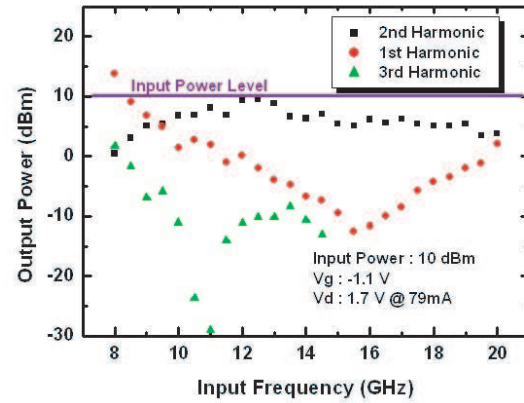


Figure 4: Measured output power versus input frequency at the input power of 10 dBm, with input frequency between 8 to 20 GHz.

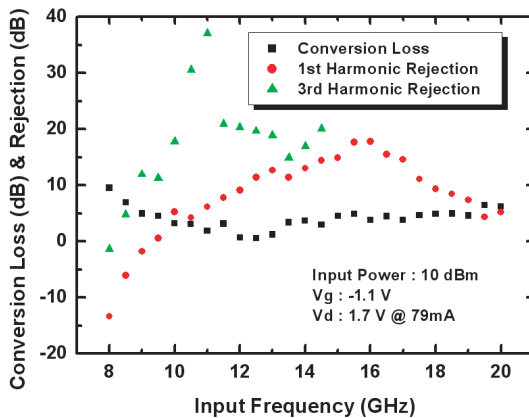


Figure 5: Measured conversion loss and odd harmonic rejection with input frequency between 8 to 20 GHz at an input power of 10 dBm.

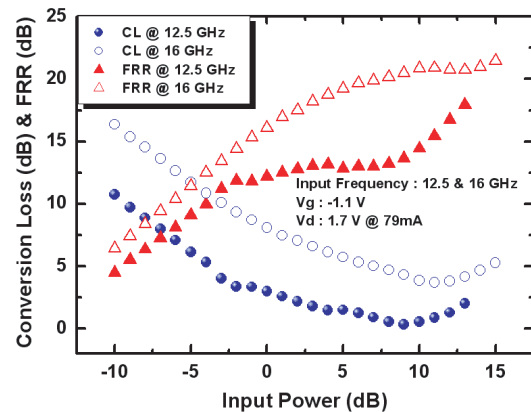


Figure 6: Measured conversion loss and FRR at 12.5 and 16 GHz input frequencies, with input power from -10 to 15 dB.

Table 1: Performance comparison of the reported frequency doublers.

Ref.	Input Freq (GHz)	Bandwidth (%)	CG (dB)	FRR _{max} (dB)	Output Power (dBm)	DC power (mW)	Die Size (mm ²)
[3]	31 ~ 37	17.4	-20 ~ -8.5	48	5.5	50	1
[4]	15 ~ 25	50.0	-6 ~ -3	25	7	132	1.5
[5]	1 ~ 20	181.0	-13 ~ -10	37	0	n.a.	2.2
[6]	5 ~ 9	57.1	-13.5 ~ -9	17	11	n.a.	n.a.
[7]	11 ~ 21	62.5	-10 ~ -2	26	11	n.a.	2
[8]	14 ~ 28	66.7	-2 ~ 1	32	6	275	3
[9]	6 ~ 11	43	-8 ~ -3	20	12	90	2
This work	9 ~ 19	71.4	-5 ~ 0.5	20	9.5	134	0.5*

*Core area

show, the entire band has a conversion gain between -5 to -0.5 dB, has higher output power and a broad bandwidth of 71.4%. Moreover, a miniature size of 1.13×0.729 mm² (0.83 mm²) including the spiral balun and testing pads can be achieved. In a similar frequency range, the pHEMT doubler shows competitive performance as compared with other reported PHEMT MMIC doublers.

Table 1 shows the performance comparison among the presented doubler and the previous reported frequency doublers [3–9]. This pHEMT doubler demonstrates wide-band performance, compact chip size, good FRR, and high output power. The conversion gain is relatively high even without a buffer amplifier.

4. CONCLUSIONS

An 18–38 GHz frequency doubler with the spiral balun and the band pass filter directly connected to the DC bias has been implemented using a 0.15 μ m pHEMT technology. The circuit configuration of the proposed broadband balanced frequency doubler was successfully simplified to reduce the use of the bias components, such as the inductor. The compact configuration with core chip size of 0.5 mm² can be achieved. As the measured results show, the fabricated frequency doubler shows a broadband bandwidth of 71.4%, with the conversion loss between 0.5 to 5 dB at input frequency of 9 to 19 GHz. It is possible for this pHEMT doubler, with smaller chip size, better fundamental rejection ratio, and higher output power as compared with those of previous works, to be fabricated. The conversion gain was relatively high even without a buffer amplifier.

ACKNOWLEDGMENT

This work was supported in part by the National Chip Implementation Center, National Applied Research Laboratories, and the National Science Council of Taiwan under contracts NSC95-2221-E-006-428-MY3, 98IC05, NSC98-2221-E-006-213-MY3 and the Foundation of Chen, Jieh-Chen Scholarship of Tainan, Taiwan.

REFERENCES

- Lin, C.-M., H.-K. Lin, Y.-A. Lai, C.-P. Chang, and Y.-H. Wang, “A 10–40 GHz broadband sub-harmonic monolithic mixer in 0.18 μ m CMOS mechnology,” *IEEE Microw. Wireless Compon. Lett.*, Vol. 19, No. 2, 95–97, 2009.
- Tsai, J.-H., H.-Y. Yang, T.-W. Huang, and H. Wang, “A 30–100 GHz wideband sub-harmonic active mixer in 90 nm CMOS technology,” *IEEE Microw. Wireless Compon. Lett.*, Vol. 18, No. 8, 554–556, 2008.
- Piernas, B., H. Hayashi, K. Nishikawa, K. Kamogawa, and T. Nakagawa, “A broadband and miniaturized V-band PHEMT frequency doubler,” *IEEE Microw. Guided Wave Lett.*, Vol. 10, No. 7, 276–278, 2000.
- Deng, K.-L. and H. Wang, “A miniature broad-band pHEMT MMIC balanced distributed doubler,” *IEEE Trans. Microw. Theory and Tech.*, Vol. 51, No. 4, 1257–1261, 2003.

5. Van Raay, F. and G. Kompa, "Design and stability test of a 2–40 GHz frequency doubler with active balun," *Digest of IEEE MTT-S International Microwave Symposium*, Vol. 3, 1573–1576, Boston, USA, June 2000.
6. Pavio, A. M., S.-D. Bingham, R.-H. Halladay, and C.-A. Sapashe, "A distributed broadband monolithic frequency multiplier," *Digest of IEEE MTT-S International Microwave Symposium*, Vol. 1, 503–504, New York, USA, May 1988.
7. Tang, Y.-L., P.-Y. Chen, and H. Wang, "A broadband PHEMT MMIC distributed doubler using high-pass drain line topology," *IEEE Microw. Wireless Compon. Lett.*, Vol. 14, No. 5, 201–203, 2004.
8. Fager, C., L. Landen, and H. Zirath, "High output power, broadband 28–56 GHz MMIC frequency doubler," *Digest of IEEE MTT-S International Microwave Symposium*, Vol. 3, 1589–1591, Boston, USA, June 2000.
9. Lee, W.-R., S.-F. Chao, Z.-M. Tsai, P.-C. Huang, C.-H. Lien, J.-H. Tsai, and H. Wang, "A high-efficiency, broadband and high output power PHEMT balanced K-band doubler with integrated balun," *Proceeding of Asia-Pacific Microwave Conference*, 763–766, Yokohama, Japan, December 2006.

Investigations on the Design of All-dielectric Frequency Selective Surfaces

F. Yu¹, S. B. Qu^{1,2}, Z. Xu², J. F. Wang¹, Y. M. Yang¹, X. H. Wang¹, H. Zhou¹, and Y. Q. Li¹

¹Department of Mathematics and Physics, College of Science
Air Force Engineering University, Xi'an, Shaanxi 710051, China

²Electronic Materials Research Laboratory, Key Laboratory of the Ministry of Education
Xi'an Jiaotong University, Xi'an, Shaanxi 710049, China

Abstract— Metallic parts are indispensable to traditional frequency selective surfaces. However, for millimeter waves, because of surface wave skin effect, the loss of metal-containing FSS is so large that the performance is badly affected. Besides, metal materials are quite unfavourable for high-temperature resistance and corrosion-resistant requirements. Based on the Mie scattering theory and dielectric resonant characteristics, all-dielectric metamaterials frequency selective surfaces were proposed. The article adopt different dielectric constants and different period dielectric structure to achieve desired frequency selective properties.

1. INTRODUCTION

Frequency selective surfaces (FSSs), generally composed of a two-dimensional (2D), planar array of dipole or slot antennas that are printed on a dielectric substrate, have been used extensively for a variety of millimeter and microwave applications (e.g., filters, polarizers, dplexers in high performance reflector antenna systems, advanced radome designs, smart surfaces for stealth applications and wireless security) [1–4]. According to different structures, especially for their characteristic shapes, sizes, and metal materials of the FSSs unit cell, and also the thicknesses and electromagnetic parameters of the substrates, etc, the FSSs act as first-order band-stop (dipole) or band-pass (slot) spatial filters.

Thanks to the printed circuit technology, metallic Frequency selective surfaces (MFSSs) have been developed rapidly. And MFSSs act satisfactorily in the microwave frequency. However, for millimeter waves, the loss of metal-containing FSS is so large that the performance is badly affected. Besides, metal materials are quite unfavourable for high-temperature resistance and corrosion-resistant requirements. To overcome these problems, all-dielectric metamaterials frequency selective surfaces are proposed. We adopt different dielectric constants and different period dielectric structure to achieve desired frequency selective properties [5].

This paper introduces a new methodology to design all-dielectric metamaterials frequency selective surfaces. The generalized methodology is based on the Mie scattering theory and dielectric resonant characteristics. The design procedure is validated by design examples of all-dielectric metamaterials frequency selective surfaces.

2. THE ANALYSIS OF THE THEORY BASED ON DIELECTRIC RESONANT CHARACTERISTICS

The resonance of all-dielectric materials is based on the Mie scattering theory. In essence, the scattered field originated from the medium of the incident field induction. The media will generate an electric polarization intensity and a magnetic pole strength in the field of action. If the medium response is linear, then the induced polarization and magnetization will also have a concussion, resulting in a new field. According to Lewin research, when the spherical scatterer size and scattering in wavelength can be compared, but far less than the background medium wavelength, μ_e , ε_e Is correlated with the frequency, just like follows:

$$\varepsilon'_e = \varepsilon_{r1} \left(1 + \frac{3\nu_f}{\frac{F(\theta)+2b_e}{F(\theta)-b_e} - \nu_f} \right)$$

$$\mu'_e = \mu_{r1} \left(1 + \frac{3\nu_f}{\frac{F(\theta)+2b_m}{F(\theta)-b_m} - \nu_f} \right)$$

where,

$$b_e = \frac{\varepsilon_{r1}}{\varepsilon_{r2}}, \quad b_m = \frac{\mu_{r1}}{\mu_{r2}}, \quad \nu_f = \frac{4\pi a^3}{3p^3}, \quad F(\theta) = \frac{2(\sin \theta - \theta \cos \theta)}{(\theta^2 - 1) \sin \theta + \theta \cos \theta}, \quad \theta = k_0 a \sqrt{\varepsilon'_{r2} \mu'_{r2}}$$

where μ_{r1} , ε_{r1} is the background material dielectric constant, μ_{r2} , ε_{r2} is the Scattering of dielectric constant, a is the ball radius, and p is the distance between two the ball [10].

Otherwise, from the dielectric resonator (DR) point of view, the resonant characteristics of dielectric spheres come from its internal field. An isolated dielectric resonator in the radiation field is similar to electric or magnetic multi-pole radiation, just like Dipole, quadrupole and etc..

It is worth pointing out that this resonance is not only confined to the ball, the other shapes can also achieve resonance. But the formula is only applicable to the ball because only spherical dielectric resonator can get analytic solution.

For the cylindrical DR which is the most widely used and the easiest processing can stimulate various resonant modes, include: TE (Transverse Electric), TM (Transverse Magnetic), HEM (Hybrid Electromagnetic).

The first resonant frequency to meet $0.5 < a/l < 2$, $30 < \varepsilon_r < 50$ (where a is the ball radius, l is the height), we can use the following formula for estimating:

$$f_{\text{GHz}} = \frac{34}{a\sqrt{\varepsilon_r}} \left(\frac{a}{l} + 3.45 \right)$$

Effect on the resonant of DR frequency is not only dielectric constant, but also radius and height. And the most sensitive factors are the height and radius: increasing height will reduce the resonant frequency; increasing radius, will reduce the resonant frequency as well as generate new models [5–8].

3. THE RESONANCE MODE AND FIELD DISTRIBUTION OF DIELECTRIC RESONATOR

The simulation using CST software for the cylindrical resonator is shown in Fig. 1: Cylindrical dielectric constant $\varepsilon = 70$. In Fig. 1(b), we can see appeared two resonance: 5.161 GHz and 6.13 GHz. We follow the internal electric field and magnetic field distribution (Fig. 2). Obviously

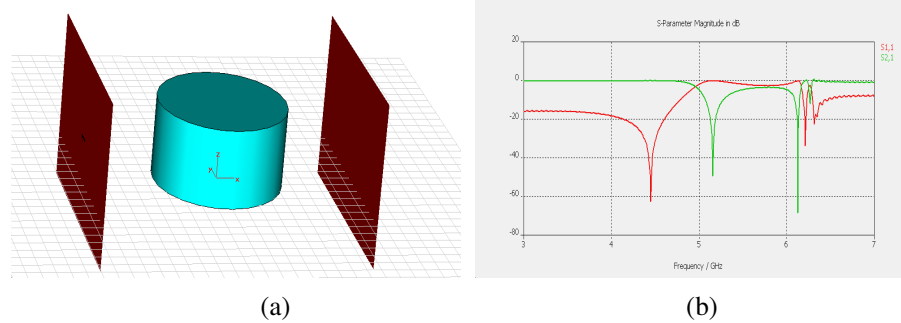


Figure 1: The simulation of cylindrical cal resonator $\varepsilon = 70$.

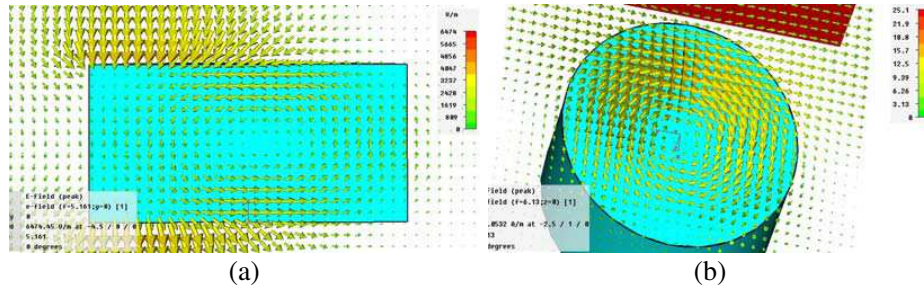


Figure 2: Resonance field distribution (a) in 5.161 GHz for magnetic resonance, (b) in 6.13 GHz for electric resonance.

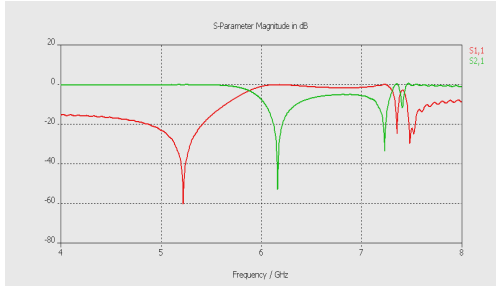


Figure 3: The simulation of cylindrical resonator $\epsilon = 50$.

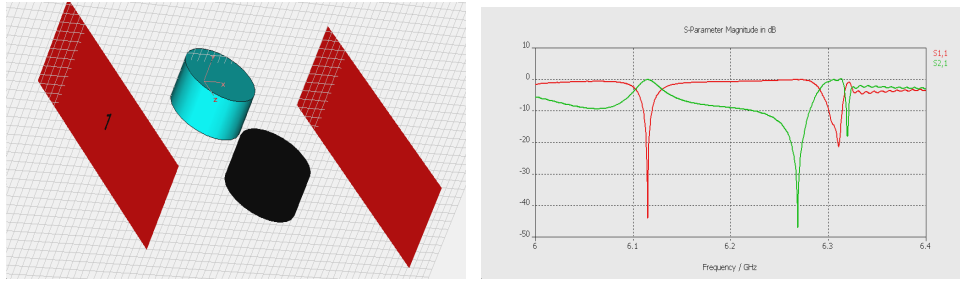


Figure 4: The combination of $\epsilon = 50$ and $\epsilon = 70$ cylindrical dielectric resonator and the combination of simulation.

we can get in 5.161 GHz for magnetic resonance, in 6.13 GHz for electric resonance through the analysis of the figure.

Likewise for the dielectric column $\epsilon = 50$ in 6.164 GHz and 7.232 GHz respectively is magnetic resonance and electric resonance (Fig. 3).

The dielectric constant of respectively 70 and 50 of the two columns were combined, using a dielectric constant of 70 dielectric column electric resonance (6.13 GHz) and a dielectric constant of 50 dielectric column magnetic resonance (6.164 GHz) to realize the frequency selection. We can find in the 6.115 GHz where originally high medium and low dielectric are all stop band emerge a pass band (Fig. 4).

4. CONCLUSION

The realization of frequency selection theory basis is that high dielectric constant dielectric resonator formed electric dipole or magnetic dipole field also appeared electric resonance or magnetic resonance. Electromagnetic waves enter into the dielectric resonator, so that the standing wave which is formed in dielectric resonator produces resonance, and the electric dipole or magnetic dipole is realized. The frequency band-pass due to the combining of different dielectric constants which produce electric dipole and magnetic dipole to the destroy the standing wave formed in dielectric resonators [6]. We can adopt all-dielectric metamaterials frequency selective surfaces The realize frequency selection.

REFERENCES

1. Munk, B. A., *Frequency Selective Surfaces: Theory and Design*, Wiley-Interscience, New York, 2000.
2. Mittra, R., C. H. Chan, and T. Cwik, "Techniques for analyzing frequency selective surfaces — A review," *Proceedings of the IEEE*, Vol. 76, No. 12, 1593–1615, 1988.
3. Pendry, J. B., A. J. Holden, D. J. Robbins, and W. J. Stewart, "Magnetism from conductors and enhanced nonlinear phenomena," *IEEE Transactions on Microwave Theory and Techniques*, Vol. 47, 2075–2084, 1999.
4. Schurig, D., J. J. Mock, B. J. Justice, S. A. Cummer, J. B. Pendry, A. F. Starr, and D. R. Smith, *Science*, Vol. 314, 977, 2006.
5. Liu, R. P., A. Degiron, J. J. Mock, and D. R. Smith, "Negative index material composed of electric and magnetic resonators," *Applied Physics Letters*, Vol. 90, 263504-1–3, 2007.

6. Wang, J. F., S. B. Qu, Z. Xu, J. Q. Zhang, H. Ma, and Y. M. Yang, "The design of left-handed metamaterials composed of magnetic resonators and electric resonators," *Acta. Phys. Sin.*, Vol. 57, 2008 (in Chinese).
7. Marques, R., F. Medina, and R. Rafii-El-Edrissi, "Role of bianisotropy in negative permeability and left-handed metamaterials," *Physical Review B*, Vol. 65, 144440-1–6, 2002.
8. Sauviac, B., C. R. Simovski, and S. A. Tretyakov, "Double split-ring resonators: Analytical modeling and numerical simulations," *Electromagnetics*, Vol. 24, 317–228, 2004.
9. Baena, J. D., R. Marques, and F. Medina, "Artificial magnetic metamaterial design by spiral resonators," *Physical Review B*, Vol. 69, 014402-1–5, 2004.
10. Aydin, K., I. Bulu, K. Guven, M. Kafesaki, C. M. Soukoulis, and E. Ozbay, "Investigation of magnetic resonances for different split-ring resonator parameters and designs," Vol. 7, 168-1–15, 2005.

The Design of A Broad Band Third-order Frequency-Selective Surfaces

Yuqing Li¹, Zhiping Pei¹, Shaobo Qu^{1,2}, Zhuo Xu², Jiafu Wang¹, Hang Zhou¹, Chao Gu¹, and Fei Yu¹

¹College of Science, Air Force Engineering University, Xi'an 710051, China

²Electronic Materials Research Laboratory, Key Laboratory of Ministry of Education
Xi'an Jiao-Tong University, Xi'an 710049, China

Abstract— In view of high order band-pass frequency selective surface(FSS) has the advantages of bandwidth controllable flexibility, stable performance, flat pass band and low insertion loss, we proposed a third-order FSS in this paper. The proposed FSS is composed of four metallic layers separated from one another by three dielectric layers. Simulated results show that such FSS has a third-order response which leads to a quite broad, flat and smooth pass band with very low insertion loss. Its 3dB bandwidth is up to 6.75 GHz and relative bandwidth is as wide as 43%. Moreover, the FSS keep stable performance under different incident angles and polarization states. The FSS owns its advantages to these merits, which is suitable for modern communication, hybrid-radomes, etc.

1. INTRODUCTION

Frequency selective surfaces (FSS) are some periodic surfaces, which are basically assembly of identical elements arranged in one- or two-dimensional infinite arrays but finite arrays in practice. FSS has gained more and more attention in modern communication, hybrid-radomes, etc. These surfaces provide uninhibited transmission in specific frequency bands but suppress transmission in other bands. Usually, the most important step in the design process of a desired FSS is the proper choice of constituting elements for the array, such as the element type and geometry, the presence or absence and the parameters of substrates, and inter-element spacing. These are the most important parameters that will determine the overall frequency response of the structure, including its bandwidth, transfer function, and the dependence of its frequency response on the incidence angle and polarization of the incident electromagnetic wave [1, 2].

Considering high order band-pass frequency selective surface has the advantages of bandwidth controllable flexibility, stable performance, flat pass band and low insertion loss, the FSS with high order characteristic has been the research fashion recently [3, 4]. Traditionally, to achieve a higher-order filter response, several identical first-order FSS panels are cascaded with quarter-wavelength spacing between each consecutive panel. This will result in a bulky structure and high insertion loss. Therefore, FSS design techniques that allow for significantly reducing the overall thickness of an higher-order FSS are highly desirable. In the paper 3, a new technique is presented for designing dual-band frequency selective surfaces with second-order band-pass responses at each band of operation, the unit cell dimensions is considerably smaller than a wavelength, which results in frequency response with stable performance. The paper 4 demonstrated a third-order band pass frequency response FSS with a low-profile and overall thickness of about $\lambda/24$, compared to other third-order band pass FSS, the frequency response is less sensitive to the angle of incidence of the EM waves but only in the TM wave, the polarization sensitive is the main limitation for its further application.

In this letter, we demonstrate a new design of a third-order band pass FSS. The proposed FSS is composed of four metallic layers separated from one another by three dielectric layers. Simulated results show that such FSS has a third-order response, which leads to a broad and quite smooth pass band and very low insertion loss, its 3 dB bandwidth is up to 6.75 GHz and relative bandwidth is as wide as 43%. Moreover, the FSS keep stable performance under different incident angles and polarization circumstance.

2. FSS STRUCTURE

Figure 1 shows the three-dimension topology of the proposed FSS. It is composed of four metallic layers separated from one another by three dielectric layers. The two outside metallic layers are the same structure and commonly have a strip slot width of wa . The two inner metallic layers are

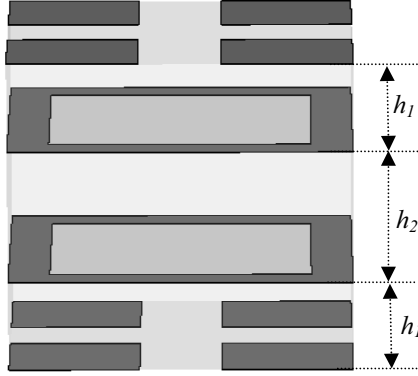


Figure 1: Three-dimension topology of the proposed third-order FSS.

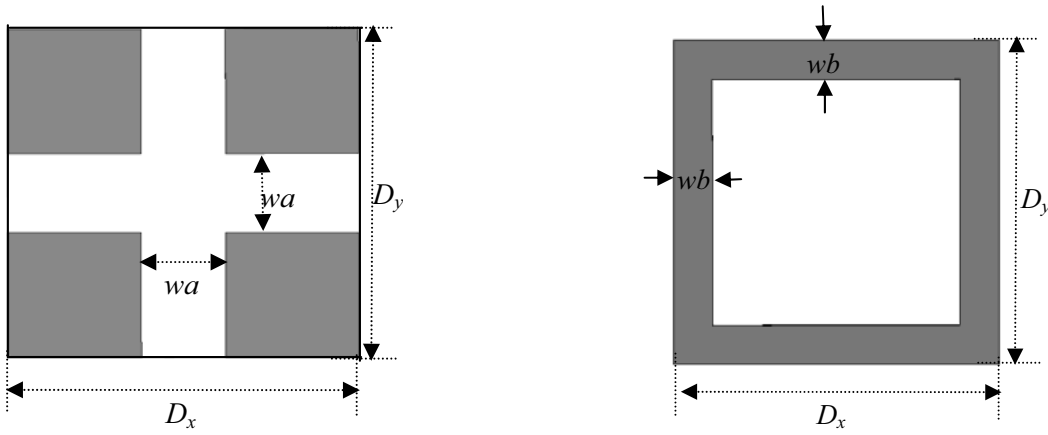


Figure 2: Top view of the two outside layers of the third-order FSS.

Figure 3: Top view of the two inner layers of the third-order FSS.

Table 1: Parameters of the unit cell of the proposed third-order band pass FSS.

Parameter	$D_x = D_y$	wa	wb	h_1	h_2	h_3
Value	5.0 mm	1.2 mm	0.6 mm	0.6 mm	5.2 mm	0.017 mm

metallic wire grid whose width is wb . The detailed configuration of two different metallic layer is shown in Fig. 2 and Fig. 3. The four metallic layers are fabricated on F4B-2 dielectric substrate, with dielectric constant of 2.65 and dielectric loss tangent 0.001. The thickness of three dielectric layer and metallic patches are separately h_1 , h_2 , h_1 , h_3 . The geometrical parameters of the FSS is showed in the Table 1.

3. THE SIMULATED RESULTS

The simulation results are all obtained in CST MICROWAVE STUDIO. Fig. 4 shows the transmission and reflection coefficient of the proposed FSS for normal incidence. From the figure, we can get that the pass band is a third-order band, the three poles rest respectively on the frequency of 13.85 GHz, 15.989 GHz and 17.66 GHz. In virtue of the mutual coupling of the poles, a broad, flat and smooth pass band with low insertion loss is emerged. The 3 dB pass band is from 12.48 GHz to 19.23 GHz, whose bandwidth is up to 6.75 GHz and relative bandwidth is as wide as 43%. The maximum of insertion loss in the pass band is 0.2 dB, which is very low considering the dielectric loss. Outside of the pass band, the transmission coefficient descend down quickly to -20 dB and below, more important is its maintenance.

Figures 5 and 6 show the transmission coefficient of the third-order FSS for different angles of incidence ranging from 0 degree to 40 degree in 10 degree steps under TE polarization wave and TM polarization separately. As observed, regardless of the TE polarization wave or TM polarization

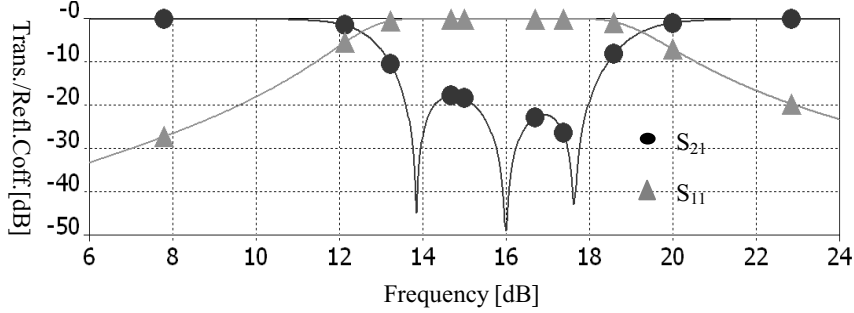


Figure 4: Transmission and reflection coefficient of the FSS for normal.

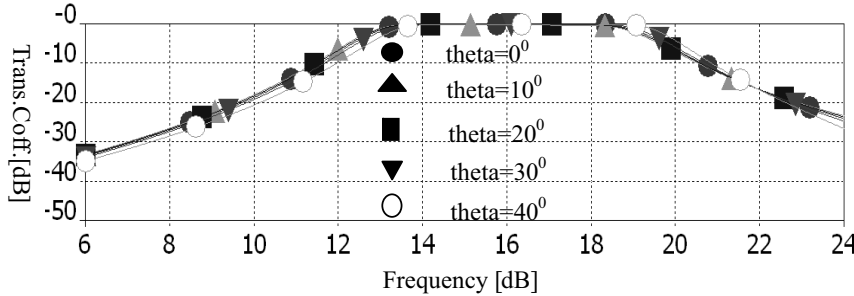


Figure 5: Transmission coefficients of the third-order FSS for various angles of incidence and for the TE polarization.

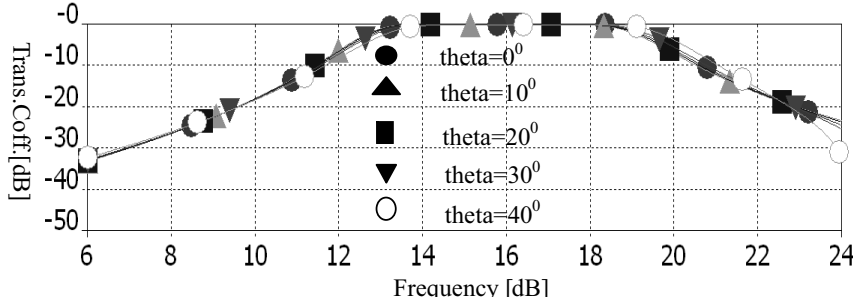


Figure 6: Transmission coefficients of the third-order FSS for various angles of incidence and for the TM polarization.

wave, the structure demonstrates a rather stable response as a function of incidence angle. The pass band deviate only 0.2 GHz, with the maximum insertion loss augmenting slightly, up to 0.4 dB for the 40 degree incidence wave under TE wave. The stable performance is the same occurred for the TM wave, the pass band alter only 0.3 GHz and the 3 dB bandwidth dwindles 0.05 GHz, the maximum insertion loss augment to 0.4 dB. Nevertheless, the structure demonstrates a rather stable frequency response as a function of angle of incidence.

4. CONCLUSIONS

A third-order FSS composed of four metallic layers separated from one another by three dielectric layers has been presented and investigated by numerical simulation. Its frequency performance has been analyzed in detail. Simulated results show that such FSS has a third-order response which leads to a quite broad, flat and smooth pass band with very low insertion loss. Its 3dB bandwidth is up to 6.75 GHz and relative bandwidth is as wide as 43%. Moreover, the FSS keep stable performance under different incident angles and polarization states. The FSS owns its advantages to these merits, which is suitable for modern communication, hybrid-radomes, etc.

REFERENCES

1. Munk, B. A., *Frequency Selective Surfaces: Theory and Design*, Wiley, New York, 2000.

2. Wu, T. K., *Frequency Selective Surface and Grid Array*, Wiley, New York, 1995.
3. Salehi, M. and N. Behdad, "A second-order dual X-/Ka-band frequency selective surface," *IEEE Microwave and Wireless Components Letters*, Vol. 18, No. 12, Dec. 2008.
4. Behdad, N., M. Al-Joumayly, and M. Salehi, "A low-profile third-order bandpass frequency selective surface," *IEEE Transactions on Antennas and Propagation*, Vol. 57, No. 2, Feb. 2009.

Versatile DVCC-based Universal Voltage-mode Biquadratic Filter

Hua-Pin Chen, Yen-Hung Lin, Wen-Hsuan Wu, and Chun-Lin Li

Department of Electronic Engineering, Ming Chi University of Technology, Taiwan, R.O.C.

Abstract— This paper introduces a versatile DVCC-based universal voltage-mode filter with three inputs and three outputs. The proposed circuit employs two differential voltage current conveyors as active elements together with two grounded capacitors and two resistors. Either applications two-input three-output or three-input single-output can be realized in the same configuration. It is more versatile than the universal one with single input and three outputs or the universal one with three inputs and single output. In the operation of two-input three-output, the lowpass, bandpass highpass and bandreject can be realized simultaneously. In the operation of three-input single-output, the lowpass, bandpass, highpass, bandreject and allpass can be realized from the same configuration without any inverting-type voltage input signals or double input voltage signals. The proposed circuit maintains the following advantages: (i) the employment two grounded capacitors ideal for integrated circuit implementation, (ii) no need to impose component choice, (iii) no need to employ inverting-type voltage input signals, and (iv) low active and passive sensitivity performances. HSPICE simulations with TSMC 0.18 μm 1P6M CMOS technology and $\pm 0.9\text{ V}$ supply voltages to verify the theoretical results.

1. INTRODUCTION

As a current-mode active device, the differential voltage current conveyor (DVCC), has the advantages of both the second generation current conveyor (such as large signal bandwidth, great linearity, wide dynamic range) and the differential difference amplifier (such as high input impedance and arithmetic operation capability) [1]. This element is a versatile building block whose applications exist in the literature [2–5]. In 2003, Chang and Chen proposed a universal VM filter with three inputs and a single output [6]. The circuit can realize all five different generic filtering responses but only highpass (HP) and bandpass (BP) responses have the advantage of high input impedance. In 2004, Horng et al. proposed a multifunction filter with a single input and three outputs [7]. The circuit can realize HP, BP and lowpass (LP) responses, simultaneously. However, with the three inputs and single output universal filter can not be used in the same configuration. In 2005, Ibrahim et al. proposed two single DDCC biquads with high input impedance and minimum number of passive elements [8]. The HP, BP or LP filtering responses cannot be realized in the same configuration. In 2007, Chiu and Horng proposed a universal VM filter with three inputs and a single output [9]. The circuit has high-input and low-output impedance advantages but it uses three plus-type DDCCs. In the same year, Chen proposed a universal VM filter based on two plus-type DDCCs [10]. The proposed configuration suffers from high-input impedance. In 2010, Chen proposed another multifunction VM filter with single input and four outputs [11]. The circuit can realize inverting HP, inverting BP, non-inverting LP and non-inverting BP filtering responses, simultaneously. However, with the three inputs and single output universal filter still can not be used in the same configuration. In this paper, a new VM universal biquadratic circuit with three inputs and four outputs is presented. The proposed configuration employs two DVCCs, two grounded capacitors and two resistors. Either three-input single-output or two-input four-output biquadratic filter can be used in the same configuration. When it operates in VM with two-input four-output, the highpass, lowpass bandpass and bandreject responses can be realized simultaneously. When it operates in VM with three-input single-output, all five different generic filtering responses can be realized from the same configuration. It needs neither an inverting-type voltage input signal nor any critical component-matching conditions to realize all five generic filtering responses.

2. CIRCUIT DESCRIPTION

The proposed versatile universal voltage-mode biquadratic filter with three inputs and four outputs employing two DVCCs is shown in Figure 1. By using standard notation, the port relations of a DVCC can be characterized by $I_{Y1} = I_{Y2} = 0$, $V_X = V_{Y1} - V_{Y2}$, $I_{Z+} = I_X$ and $I_{Z-} = -I_X$. The proposed circuit comprises two DVCCs, two grounded capacitors and two resistors. The use of grounded capacitors makes the circuit suitable for integration because grounded capacitor circuit can compensate for the stay capacitances at their nodes. Straightforwardly analyzing the filter in

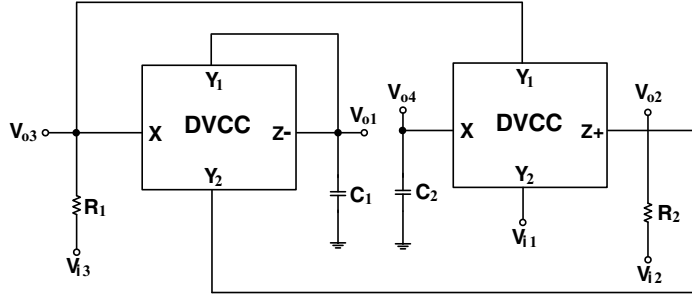


Figure 1: The proposed versatile DVCC-based universal voltage-mode filter.

Figure 1, the following four output voltage signals can be derived as:

$$V_{o1} = \frac{-sC_2R_2V_{i1} + V_{i2} + (sC_2R_2 + 1)V_{i3}}{s^2C_1C_2R_1R_2 + sC_1R_1 + 1} \quad (1)$$

$$V_{o2} = \frac{-(s^2C_1C_2R_1R_2 + sC_2R_2)V_{i1} + (sC_1R_1 + 1)V_{i2} + sC_2R_2V_{i3}}{s^2C_1C_2R_1R_2 + sC_1R_1 + 1} \quad (2)$$

$$V_{o3} = \frac{s^2C_1C_2R_1R_2V_{i1} - sC_1R_1V_{i2} + V_{i3}}{s^2C_1C_2R_1R_2 + sC_1R_1 + 1} \quad (3)$$

$$V_{o4} = \frac{-(sC_1R_1 + 1)V_{i1} - sC_1R_1V_{i2} + V_{i3}}{s^2C_1C_2R_1R_2 + sC_1R_1 + 1} \quad (4)$$

Depending on the status of the biquad input three voltages, V_{i1} , V_{i2} and V_{i3} , numerous filter functions are obtained. There are two cases shown as follows.

Case I. If $V_{i1} = V_{i3} = V_{in}$ (the input voltage signal) and $V_{i2} = 0$, then

$$\frac{V_{o1}}{V_{in}} = \frac{1}{s^2C_1C_2R_1R_2 + sC_1R_1 + 1} \quad (5)$$

$$\frac{V_{o2}}{V_{in}} = \frac{-s^2C_1C_2R_1R_2}{s^2C_1C_2R_1R_2 + sC_1R_1 + 1} \quad (6)$$

$$\frac{V_{o3}}{V_{in}} = \frac{s^2C_1C_2R_1R_2 + 1}{s^2C_1C_2R_1R_2 + sC_1R_1 + 1} \quad (7)$$

$$\frac{V_{o4}}{V_{in}} = \frac{-s^2C_1R_1}{s^2C_1C_2R_1R_2 + sC_1R_1 + 1} \quad (8)$$

Thus, the non-inverting lowpass (LP), inverting highpass (HP), non-inverting bandreject (BR) and inverting bandpass (BP) signals are obtained at the node voltages, V_{o1} , V_{o2} , V_{o3} and V_{o4} , respectively.

Case II. From Equation (3) yield the five types of biquadratic filters with the following specialization.

- (i) lowpass: $V_{i1} = V_{i2} = 0$ and $V_{i3} = V_{in}$
- (ii) bandpass: $V_{i1} = V_{i3} = 0$ and $V_{i2} = V_{in}$
- (iii) highpass: $V_{i2} = V_{i3} = 0$ and $V_{i1} = V_{in}$
- (iv) bandreject: $V_{i2} = 0$ and $V_{i1} = V_{i3} = V_{in}$
- (v) allpass: $V_{i1} = V_{i2} = V_{i3} = V_{in}$

Note that there is also no need of any component matching conditions and inverting type voltage input signal to realize all of the filter responses.

Obviously, from cases I and II, the proposed circuit can act as a multifunction voltage-mode filter with two inputs and four outputs and it can also act as a universal voltage-mode filter with three inputs and a single output, too. Therefore, the proposed circuit is more versatile than those with single input and multiple outputs or with three inputs and single output. The resonance angular frequency ω_0 and quality factor Q are given by

$$\omega_0 = \frac{1}{\sqrt{R_1R_2C_1C_2}} \quad \text{and} \quad Q = \sqrt{\frac{R_2C_2}{R_1C_1}} \quad (9)$$

From (9), it can be seen that the passive ω_0 and Q sensitivities are low and not large than 0.5 in absolute value.

3. SIMULATION RESULTS

Finally, to verify the theoretical prediction of the proposed biquadratic filter, a simulation using HSpice simulation with TSMC 0.18 μm 1P6M process was performed and the CMOS implementation of the DVCC is shown in Figure 2 [7]. The aspect ratios (W/L) of the MOS transistors were taken as 3.6/0.36 for M1, M2, M3, M4; 7.2/0.36 for M5, M6; 5.4/0.36 for all the other NMOS; 14.4/0.18 for all PMOS. The supply voltages are $V_{DD} = -V_{SS} = 0.9\text{ V}$, and the biasing voltages are V_{B1} and V_{B2} are -0.1 V and -0.38 V . Figure 3 shows the simulated amplitude-frequency responses for the LP, HP BP and BR filtering at V_{o1} , V_{o2} , V_{o3} and V_{o4} output terminals in case I, with $R_1 = R_2 = 10\text{k}\Omega$ and $C_1 = C_2 = 15.9\text{ pF}$, leading to a center frequency of $f_o = 1\text{ MHz}$ and quality factor of $Q = 1$. As can be seen, there is a close agreement between theory and simulation.

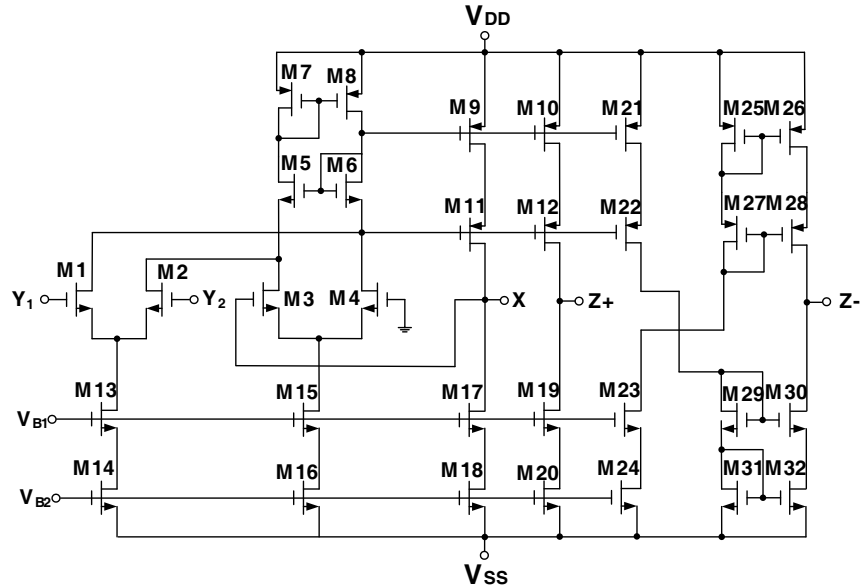


Figure 2: The CMOS implementation of the DVCC.

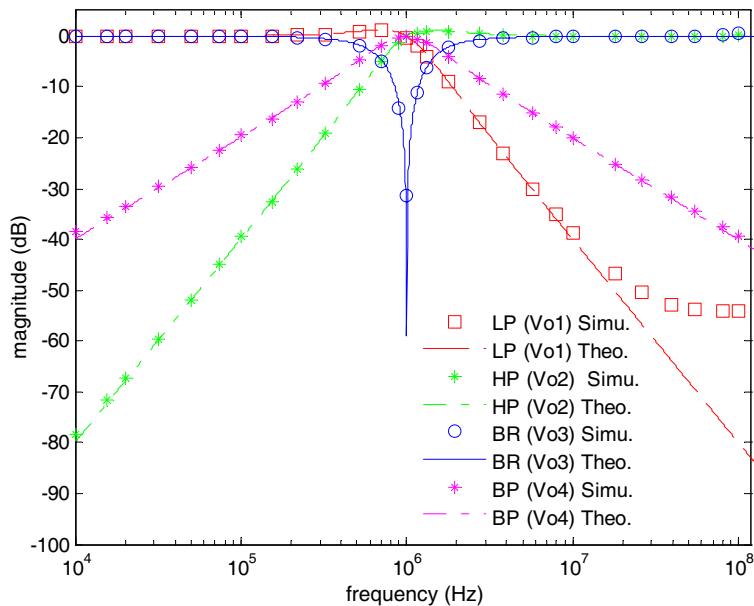


Figure 3: The bandreject, highpass, bandpass and lowpass amplitude-frequency responses in case I.

4. CONCLUSION

In this paper, we presented a new versatile universal VM biquadratic filter with three inputs and four outputs. The circuit can be acted as both a multifunction VM filter with two inputs and four outputs and a universal VM filter with three inputs and a single output. Therefore, the circuit proposed in this paper is more versatile than the multifunction one with a single input and three outputs or the universal one with three inputs and a single output. Besides, the proposed circuit still offers the following advantages: (i) using two grounded capacitors attractive for integration and absorbing shunt parasitic capacitance, (ii) simultaneous realization of lowpass, highpass bandpass and bandreject responses for the two-input four-output filter, (iii) no need to impose component choice to realize all five generic responses for the three-input single-output filter, (iv) no need to employ inverting-type input signals, and (v) low active and passive sensitivity performances. HSPICE simulation results using TSMC 0.18 μm 1P6M CMOS process and $\pm 0.9\text{ V}$ supply voltages validate the theoretical predictions.

ACKNOWLEDGMENT

The author would like to thank the National Science Council and Chip Implementation Center of Taiwan, R.O.C. The National Science Council, Republic of China supported this work under grant number NSC 99-2221-E-131-040.

REFERENCES

1. Elwan, H. O. and A. M. Soliman, "Novel CMOS differential voltage current conveyor and its applications," *IEE Proceedings Circuits, Devices Systems*, Vol. 144, No. 3, 195–200, 1997.
2. Ibrahim, M. A., S. Minaei, and H. Kuntman, "A 22.5 MHz current-mode KHN-biquad using differential voltage current conveyor and grounded passive elements," *International Journal of Electronics and Communications (AEÜ)*, Vol. 59, No. 5, 311–318, 2005.
3. Tsukutani, T., Y. Sumi, and N. Yabuki, "Novel current-mode biquadratic circuit using only plus type DO-DVCCs and grounded passive components," *International Journal of Electronics*, Vol. 94, No. 12, 1137–1146, 2007.
4. Chen, H. P. and S. S. Shen, "A versatile universal capacitors-grounded voltage-mode filter using DVCCs," *Electronics and Telecommunications Research Institute Journal (ETRI)*, Vol. 29, No. 4, 470–475, 2007.
5. Minaei, S. and E. Yuce, "All-grounded passive elements voltage-mode DVCC-based universal filters," *Circuit, Systems, and Signal Processing*, Vol. 29, No. 2, 295–309, 2010.
6. Chang, C. M. and H. P. Chen, "Universal capacitor-grounded voltage-mode filter with three inputs and a single output," *International Journal of Electronics*, Vol. 90, No. 6, 401–406, 2003.
7. Horng, J. W., W. Y. Chui, and H. Y. Wei, "Voltage-mode highpass, bandpass and lowpass filters using two DDCCs," *International Journal of Electronics*, Vol. 91, No. 8, 461–464, 2004.
8. Ibrahim, M. A., H. Kuntman, and O. Cicekoglu, "Single DDCC biquads with high input impedance and minimum number of passive elements," *Analog Integrated Circuits and Signal Processing*, Vol. 43, No. 1, 71–79, 2005.
9. Chiu, W. Y. and J. W. Horng, "High-input and low-output impedance voltage-mode universal biquadratic filter using DDCCs," *IEEE Transactions Circuits Systems — II: Analog Digital Signal Processing*, Vol. 54, No. 8, 649–652, 2007.
10. Chen, H. P., "Universal voltage-mode filter using only plus-type DDCCs," *Analog Integrated Circuits and Signal Processing*, Vol. 50, No. 2, 137–139, 2007.
11. Chen, H. P., "High input impedance voltage-mode multifunction filter with four grounded components and only two plus-type DDCCs," *Active and Passive Electronic Components*, Vol. 2010, June 2010.

High-input Impedance Tunable Voltage-mode Multifunction Biquadratic Filter Using All-grounded Passive Elements

Hua-Pin Chen, Shih-Hsuan Yuan, Wei-Yen Huang, and Yu-Hsin Lin

Department of Electronic Engineering, Ming Chi University of Technology, Taiwan, R.O.C.

Abstract— This paper introduces a high-input impedance tunable voltage-mode multifunction biquadratic filter. The proposed biquadratic filter with single input and five outputs employing two active components and all grounded passive elements. The circuit is very simple, consisting of one single-output differential difference current conveyor (DDCC), one dual-output inverting second-generation current conveyor (ICCII), three grounded resistors and two grounded capacitors. The filter can realize highpass, bandpass and lowpass filtering responses, simultaneously. It is widely used in various parts such as communication, measurement, instrumentation and control system. The proposed circuit offers the following advantages: (i) using grounded capacitors attractive for integration and absorbing shunt parasitic capacitance, (ii) using grounded resistors at X terminal of DDCC/ICCII suitable for the variations of filter parameters and absorbing series parasitic resistances at X terminal of DDCC/ICCII, (iii) high input impedance good for cascability, (iv) no need to change the filter topology, (v) no need to component-matching conditions, (vi) orthogonal tunable of the resonance angular frequency and quality factor, and (vii) low active and passive sensitivity performances. HSPICE simulations with TSMC 0.18 μm 1P6M CMOS technology and $\pm 0.9\text{ V}$ supply voltages to verify the theoretical results.

1. INTRODUCTION

Voltage-mode filters employing current conveyors have been receiving attention nowadays. Moreover, it is good for a circuit to employ only grounded passive elements especially grounded capacitors and not require passive component-matching conditions thus it is convenient for fully integrated circuit technology. As a current-mode active device, the differential difference current conveyor (DDCC), has the advantages of both the second generation current conveyor (such as large signal bandwidth, great linearity, wide dynamic range) and the differential difference amplifier (such as high input impedance and arithmetic operation capability) [1]. Since the addition and subtraction operations of voltage-mode signals need the realization, respectively. The DDCC becomes very attractive to be used in the design of voltage-mode filters. This is due to the fact that the addition and subtraction operations for voltage signals can be performed easily by DDCC [1–7]. Since its presentation by Awad and Soliman [8] the new type of current conveyor, an inverting type second-generation current conveyor (ICCII), has received more attention and its usefulness in the design of active filters and oscillators has been reported [8–10]. In 2003, Chang and Chen proposed a universal VM filter with three inputs and a single output [2]. The circuit can realize all five different generic filtering responses but only highpass (HP) and bandpass (BP) responses have the advantage of high input impedance. In 2004, Horng et al. proposed a multifunction filter with a single input and three outputs [3]. The circuit can realize HP, BP and lowpass (LP) responses, simultaneously. However, with the three inputs and single output universal filter can not be used in the same configuration. In 2005, Ibrahim et al. proposed two single DDCC biquads with high input impedance and minimum number of passive elements [4]. The HP, BP or LP filter responses cannot be realized in the same configuration. In 2007, Chiu and Horng proposed a universal VM filter with three inputs and a single output [5]. The circuit has high-input and low-output impedance advantages but it uses three plus-type DDCCs. In the same year, Chen proposed a universal VM filter based on two plus-type DDCCs [6]. The proposed configuration suffers from high-input impedance. In 2010, Chen proposed another multifunction voltage-mode filter with single input and four outputs [7]. The circuit can realize inverting HP, inverting BP, non-inverting LP and non-inverting BP filtering functions, simultaneously. However, it suffers from orthogonal tunable of the resonance angular frequency ω_o and quality factor Q . In this paper, a new voltage-mode multifunction biquadratic circuit with single input and five outputs is presented. The proposed configuration employs one DDCC, one ICCII, two grounded capacitors and three grounded resistors. The biquadratic filter needs neither an inverting-type voltage input signal nor any critical component-matching conditions to realize LP, BP and HP responses, simultaneously. The input of the circuit exhibits high input impedance so that the synthesized filter can be cascaded

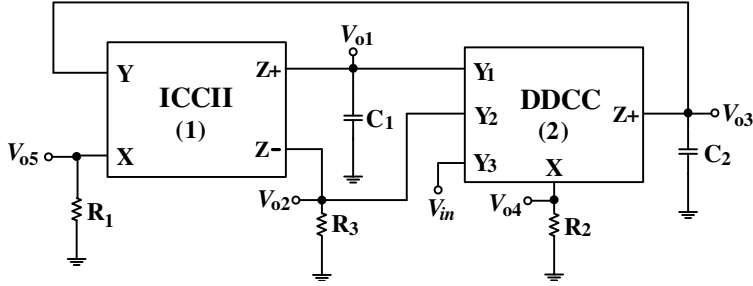


Figure 1: The proposed tunable voltage-mode multifunction filter.

without additional buffers. It permits orthogonal tunability of the resonance angular frequency ω_o and quality factor Q , and enjoys low active and passive sensitivity performances.

2. CIRCUIT DESCRIPTION

The DDCC is a five-terminal analog building block and its terminal relations are given by $I_{Y1} = I_{Y2} = I_{Y3} = 0$, $V_X = V_{Y1} - V_{Y2} + V_{Y3}$ and $I_Z = I_X$ [1]. The DO-ICCII can be characterized by the port relations with $I_Y = 0$, $V_X = -V_Y$ and $I_Z = \pm I_X$ [8]. It is considered to be a special case from the DDCC with single Y_2 input only. The proposed circuit, as shown in Figure 1, employs one DDCC, one ICCII, two grounded capacitors and three grounded resistors. Circuit analysis yields the following voltage-mode filter transfer function:

$$\frac{V_{o1}}{V_{in}} = \frac{-1}{s^2 C_1 C_2 R_1 R_2 + s C_1 R_3 + 1} \quad (1)$$

$$\frac{V_{o2}}{V_{in}} = \frac{s C_1 R_1}{s^2 C_1 C_2 R_1 R_2 + s C_1 R_3 + 1} \quad (2)$$

$$\frac{V_{o3}}{V_{in}} = \frac{s C_1 R_3}{s^2 C_1 C_2 R_1 R_2 + s C_1 R_3 + 1} \quad (3)$$

$$\frac{V_{o4}}{V_{in}} = \frac{s^2 C_1 C_2 R_1 R_2}{s^2 C_1 C_2 R_1 R_2 + s C_1 R_3 + 1} \quad (4)$$

$$\frac{V_{o5}}{V_{in}} = \frac{-s C_1 R_1}{s^2 C_1 C_2 R_1 R_2 + s C_1 R_3 + 1} \quad (5)$$

Thus, we can obtain an inverting LP, two non-inverting BP, a non-inverting HP and an inverting BP filter responses at the output voltages, V_{o1} , V_{o2} , V_{o3} , V_{o4} and V_{o5} , respectively. Due to the input voltage signal is connected directly to the Y_3 port of the DDCC and input current to the Y_3 port is zero, the circuit has the feature of high input impedance. The resonance angular frequency ω_o and quality factor Q are given by.

In all cases, the resonance angular frequency ω_o and quality factor Q are given by

$$\omega_o = \frac{1}{\sqrt{R_1 R_2 C_1 C_2}} \quad \text{and} \quad Q = \frac{1}{R_3} \sqrt{\frac{R_1 R_2 C_2}{C_1}} \quad (6)$$

From (6) it can be seen that the parameter Q of the proposed filter can be varied without changing the pole frequency, but not vice versa. Thus the ω_o and Q can be properly orthogonal tunability by R_1 and/or R_2 and R_3 , in that order. Also, the passive ω_o and Q sensitivities are equal to or smaller than unity.

3. SIMULATION RESULTS

Finally, to verify the theoretical prediction of the proposed biquadratic filter, a simulation using HSpice simulation with TSMC 0.18 μm 1P6M process was performed and the CMOS implementation of the DDCC is shown in Figure 2 [7]. The aspect ratios (W/L) of the MOS transistors were taken as 3.6/0.36 for M1, M2, M3, M4; 7.2/0.36 for M5, M6; 5.4/0.36 for all the other NMOS; 14.4/0.18 for all PMOS. The supply voltages are $V_{DD} = -V_{SS} = 0.9$ V, and the biasing voltages are V_{B1} and V_{B2} are -0.1 V and -0.38 V. Figure 3 shows the simulated amplitude-frequency responses for the LP, HP and two BP filtering at V_{o1} , V_{o2} , V_{o3} and V_{o4} output terminals, with

$R_1 = R_2 = R_3 = 10 \text{ k}\Omega$ and $C_1 = C_2 = 15.9 \text{ pF}$, leading to a center frequency of $f_o = 1 \text{ MHz}$ and quality factor of $Q = 1$. As can be seen, there is a close agreement between theory and simulation.

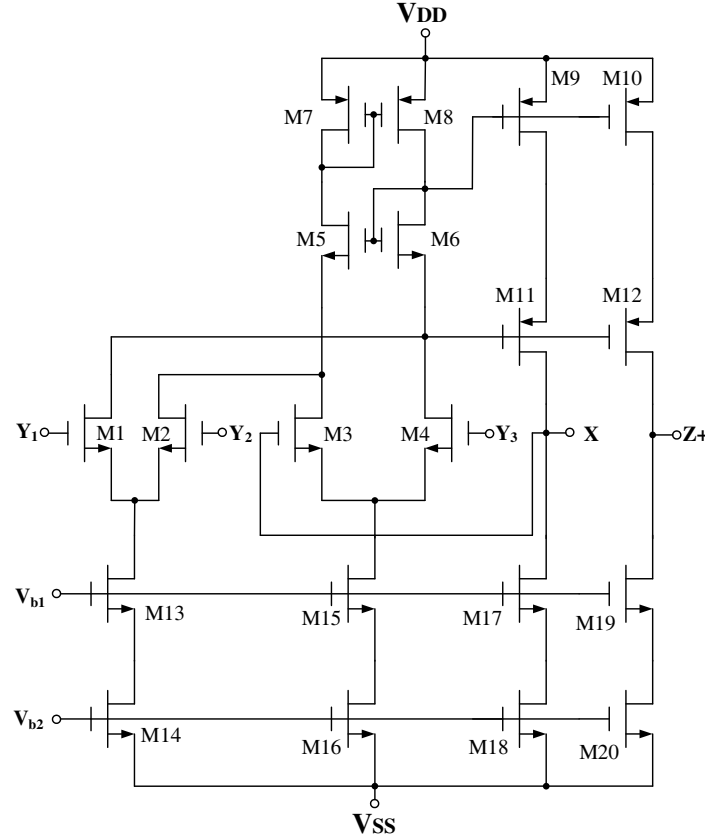


Figure 2: The CMOS implementation of the DDCC.

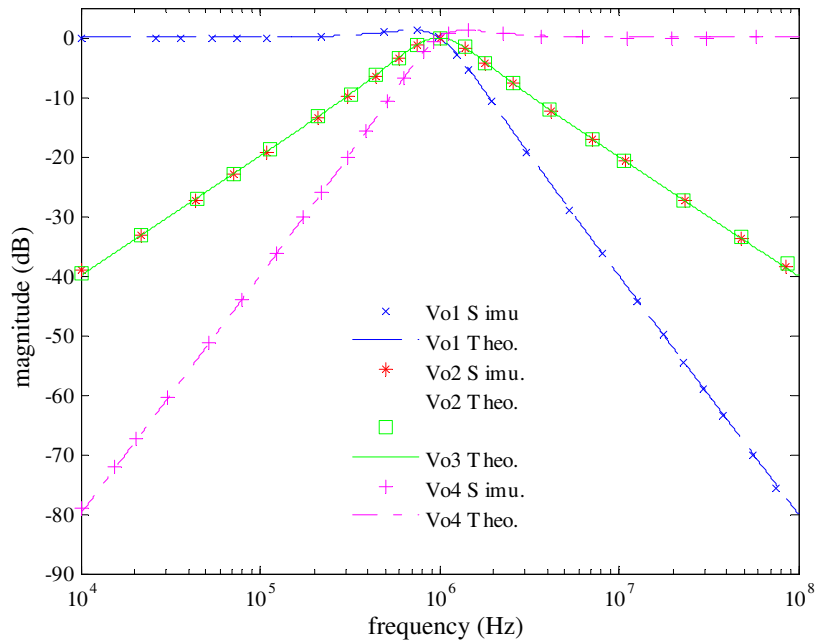


Figure 3: Amplitude responses of the HP, LP and two BP filter.

4. CONCLUSION

In this paper, the authors also propose a new high input impedance voltage-mode multifunction biquadratic filter. This circuit offers several advantages, such as simultaneous realization of LP, BP and HP filtering responses in the same configuration, no requirements for component matching conditions, the use of only grounded passive components, high input impedance, and low active and passive sensitivity performances. The proposed circuit has the same advantages reported by [7] which using two DDCCs, two grounded capacitors and two grounded resistors. Additionally, the proposed circuit has one more important advantage of orthogonal control of resonance angular frequency ω_o and quality factor Q with reported by [7]. HSPICE simulation results using TSMC 0.18 μm 1P6M CMOS process and ± 0.9 V supply voltages validate the theoretical predictions.

ACKNOWLEDGMENT

The author would like to thank the National Science Council and Chip Implementation Center of Taiwan, R.O.C.. The National Science Council, Republic of China supported this work under grant number NSC 99-2221-E-131-040.

REFERENCES

1. Chiu, W., S. I. Liu, H. W. Tsao, and J. J. Chen, “CMOS differential difference current conveyors and their applications,” *IEE Proceeding-circuits Devices and Systems*, Vol. 143, No. 2, 91–96, 1996.
2. Chang, C. M. and H. P. Chen, “Universal capacitor-grounded voltage-mode filter with three inputs and a single output,” *International Journal of Electronics*, Vol. 90, No. 6, 401–406, 2003.
3. Horng, J. W., W. Y. Chui, and H. Y. Wei, “Voltage-mode highpass, bandpass and lowpass filters using two DDCCs,” *International Journal of Electronics*, Vol. 91, No. 8, 461–464, 2004.
4. Ibrahim, M. A., H. Kuntman, and O. Cicekoglu, “Single DDCC biquads with high input impedance and minimum number of passive elements,” *Analog Integrated Circuits and Signal Processing*, Vol. 43, No. 1, 71–79, 2005.
5. Chiu, W. Y. and J. W. Horng, “High-input and low-output impedance voltage-mode universal biquadratic filter using DDCCs,” *IEEE Transactions Circuits Systems — II: Analog Digital Signal Processing*, Vol. 54, No. 8, 649–652, 2007.
6. Chen, H. P., “Universal voltage-mode filter using only plus-type DDCCs,” *Analog Integrated Circuits and Signal Processing*, Vol. 50, No. 2, 137–139, 2007.
7. Chen, H. P., “High input impedance voltage-mode multifunction filter with four grounded components and only two plus-type DDCCs,” *Active and Passive Electronic Components*, Vol. 2010, Jun. 2010.
8. Awad, I. A. and A. M. Soliman, “Inverting second generation current conveyors: the missing building blocks, CMOS realizations and applications,” *International Journal of Electronics*, Vol. 86, No. 4, 413–432, 1999.
9. Minaei, S., E. Yuce, and O. Cicekoglu, “ICCII-based voltage-mode filter with signal input and six outputs employing grounded capacitors,” *Circuit, Systems, and Signal Processing*, Vol. 25, No. 4, 559–566, 2006.
10. Soliman, A. M., “Voltage mode and current mode Tow Thomas biquadratic filters using inverting CCII,” *International Journal of Circuit Theory and Applications*, Vol. 35, No. 4, 463–467, 2007.

Versatile CCII-based Universal Current-mode Biquadratic Filter

Hua-Pin Chen, Kai Chen, Chun-Yeh Chen, and Ming-Shan Chen

Department of Electronic Engineering, Ming Chi University of Technology, Taiwan, R.O.C.

Abstract— New versatile universal current-mode filter with three inputs and three outputs using three multiple-output second-generation current conveyors, two grounded resistors and two grounded capacitors is proposed. Either applications single-input three-output or three-input single-output can be realized in the same configuration. It is more versatile than the universal one with single input and three outputs or the universal one with three inputs and single output. Unlike the previously works, it is highly flexible and easy to design. In the operation of single-input three-output, the lowpass, bandpass and bandreject can be realized simultaneously while the highpass and allpass responses can be easily obtained by connecting appropriated output currents directly without using additional stages. In the operation of three-input single-output, the lowpass, bandpass, highpass, bandreject and allpass can be realized from the same configuration without any inverting-type current input signals or double input current signals. The proposed circuit maintains the following advantages: (i) the employment two grounded capacitors ideal for integrated circuit implementation, (ii) high output impedance good for cascadability for the current-mode circuits, (iii) no need to impose component choice, (iv) no need to employ inverting-type current input signals, and (v) low active and passive sensitivity performances. HSPICE simulations with TSMC 0.18 μm 1P6M CMOS technology and $\pm 0.9\text{ V}$ supply voltages to verify the theoretical results.

1. INTRODUCTION

Current-mode filters using second-generation current conveyors have received considerable attention owing to the fact that their bandwidth, linearity, and dynamic range performances are better than those of their operational amplifiers based counterparts [1]. Several realizations of current-mode biquad filters using dual-output second-generation current conveyors (DOCCIIs) have been proposed [2–7]. However, these configurations cannot be used as either a single-input three-output or three-input single-output without any component matching conditions. The circuits of [2, 3] can simultaneously realize lowpass, bandpass and highpass responses with high output impedance, but these configurations employ four DOCCIIs. The filter of [4] can simultaneously realize lowpass, bandpass, highpass and bandreject responses with high output impedance, but it still employs four DOCCIIs, and employs one capacitor at port X of the DOCCII and hence limits the usage in high frequency range [8]. The circuits of [5, 6] employ three DOCCIIs, two capacitors and two/three resistors. However, with these proposed configurations one of the capacitor still connected at the port X of the DO-CCII. In 2009, Horng et al. [7] proposed a novel CM universal filter with five inputs and two outputs using two multiple-output CCIIIs and five passive elements. However, one of the output currents is not at high impedance output terminal and it still needs a component matching condition to realize the AP response. In this paper, a new configuration for realizing universal current-mode biquadratic filter is proposed. The proposed circuit employs three multiple-output second-generation current conveyors (MOCCIIs) as active elements together with two grounded capacitors and two grounded resistors. It maintains the following advantages: (i) the employment of three MOCCIIs, (ii) the employment of two grounded capacitors, (iii) the employment of all grounded resistors, (iv) no capacitors is connected at the port X of the MOCCIIs, (v) no need to employ inverting-type input current signals or double input current signals, (vi) no need to impose component choice and (vii) either a single-input three-output or three-input single-output can realize in the same configuration.

2. CIRCUIT DESCRIPTION

The CCII can be characterized by the port relations with $I_Y = 0$, $V_X = V_Y$ and $I_Z = \pm I_X$, the sign \pm refers to plus or minus type CCII, respectively. The proposed circuit, as shown in Figure 1, employs three MOCCIIs, two grounded capacitors and two grounded resistors. Straightforwardly

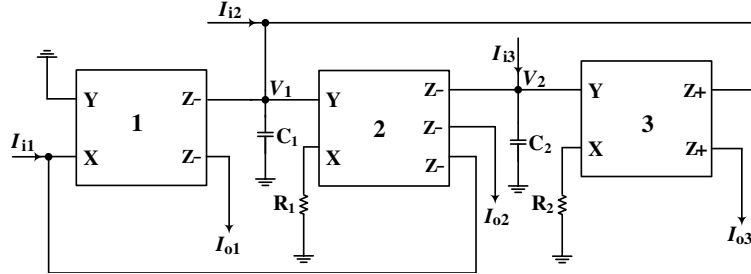


Figure 1: The proposed versatile CCII-Based universal current-mode biquadratic filter.

analyzing the filter in Figure 1, the following three output current signals can be derived as:

$$I_{o1} = \frac{(s^2 C_1 C_2 R_1 R_2 + 1) I_{i1} - s C_2 R_2 I_{i2} - I_{i3}}{s^2 C_1 C_2 R_1 R_2 + s C_2 R_2 + 1} \quad (1)$$

$$I_{o2} = \frac{-s C_2 R_2 I_{i1} - s C_2 R_2 I_{i2} - I_{i3}}{s^2 C_1 C_2 R_1 R_2 + s C_2 R_2 + 1} \quad (2)$$

$$I_{o3} = \frac{-I_{i1} - I_{i2} + (s C_1 R_1 + 1) I_{i3}}{s^2 C_1 C_2 R_1 R_2 + s C_2 R_2 + 1} \quad (3)$$

Depending on the status of the biquad input three currents, I_{i1} , I_{i2} and I_{i3} , numerous filter functions are obtained. There are two cases shown as follows.

Case I. If $I_{i2} = I_{i3} = 0$ (opened) and $I_{i1} = I_{in}$ is given by the input current signal, then the following three current transfer functions are obtained as:

$$\frac{I_{o1}}{I_{in}} = \frac{s^2 C_1 C_2 R_1 R_2 + 1}{s^2 C_1 C_2 R_1 R_2 + s C_2 R_2 + 1} \quad (4)$$

$$\frac{I_{o2}}{I_{in}} = \frac{-s C_2 R_2}{s^2 C_1 C_2 R_1 R_2 + s C_2 R_2 + 1} \quad (5)$$

$$\frac{I_{o3}}{I_{in}} = \frac{-1}{s^2 C_1 C_2 R_1 R_2 + s C_2 R_2 + 1} \quad (6)$$

From Equations (4)–(6), it can be seen that a non-inverting BR response at I_{o1} , an inverting BP response at I_{o2} and an inverting LP response at I_{o3} . Also, a non-inverting HP response is easy obtained by adding the two currents I_{o1} and I_{o3} , yielding a transfer function as follows:

$$\frac{I_{HP}}{I_{in}} = \frac{s^2 C_1 C_2 R_1 R_2}{s^2 C_1 C_2 R_1 R_2 + s C_2 R_2 + 1} \quad (7)$$

Similarly, by connecting the I_{o1} with the I_{o2} output terminals, we obtain the allpass transfer function as follows:

$$\frac{I_{AP}}{I_{in}} = \frac{s^2 C_1 C_2 R_1 R_2 - s C_2 R_2 + 1}{s^2 C_1 C_2 R_1 R_2 + s C_2 R_2 + 1} \quad (8)$$

Obviously, from Equations (4)–(8), it can be seen that the proposed circuit is a universal CM biquadratic filter.

Case II. From Equation (1) yield the five types of biquadratic filters with the following specialization.

- (i) lowpass: $I_{i1} = I_{i2} = 0$ and $I_{i3} = I_{in}$
- (ii) bandpass: $I_{i1} = I_{i3} = 0$ and $I_{i2} = I_{in}$
- (iii) highpass: $I_{i2} = 0$ and $I_{i1} = I_{i3} = I_{in}$
- (iv) bandreject: $I_{i2} = I_{i3} = 0$ and $I_{i1} = I_{in}$
- (v) allpass: $I_{i3} = 0$ and $I_{i1} = I_{i2} = I_{in}$

Note that we do not need critical component matching conditions, inverting-type input current signals, or double input current signals for realizing the above all standard filtering functions in the design. Obviously, it is a three-input and single-output CM universal biquadratic filter.

In all cases, the resonance angular frequency ω_o and quality factor Q are given by

$$\omega_o = \frac{1}{\sqrt{R_1 R_2 C_1 C_2}} \quad \text{and} \quad Q = \sqrt{\frac{R_1 C_1}{R_2 C_2}} \quad (9)$$

From (9) it can be seen that the passive ω_o and Q sensitivities are low and not large than 0.5 in absolute value.

3. SIMULATION RESULTS

Finally, to verify the theoretical prediction of the proposed universal current-mode filter, a simulation using HSPICE with TSMC 0.18 μm process was performed. The CMOS implementation of a DOCCII is shown in Figure 2 [9]. The aspect ratios (W/L) of the MOS transistors were taken

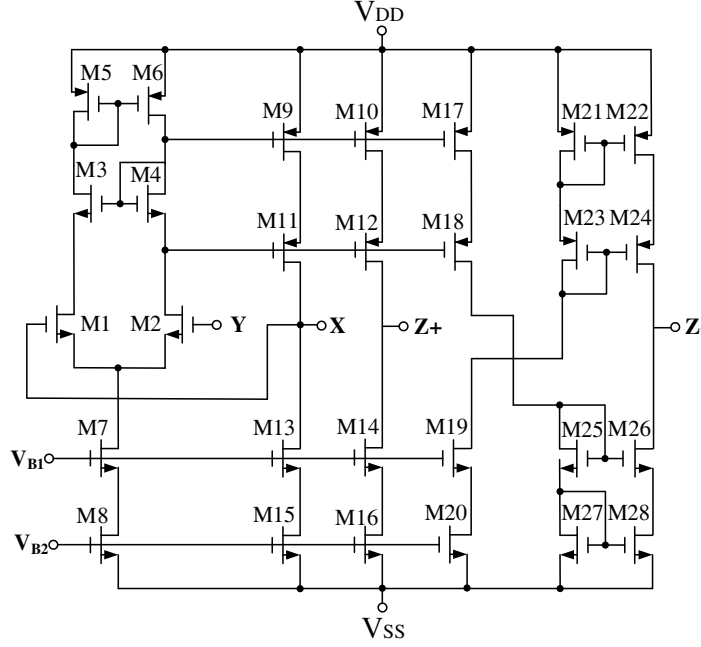


Figure 2: The CMOS implementation of the DOCCII.

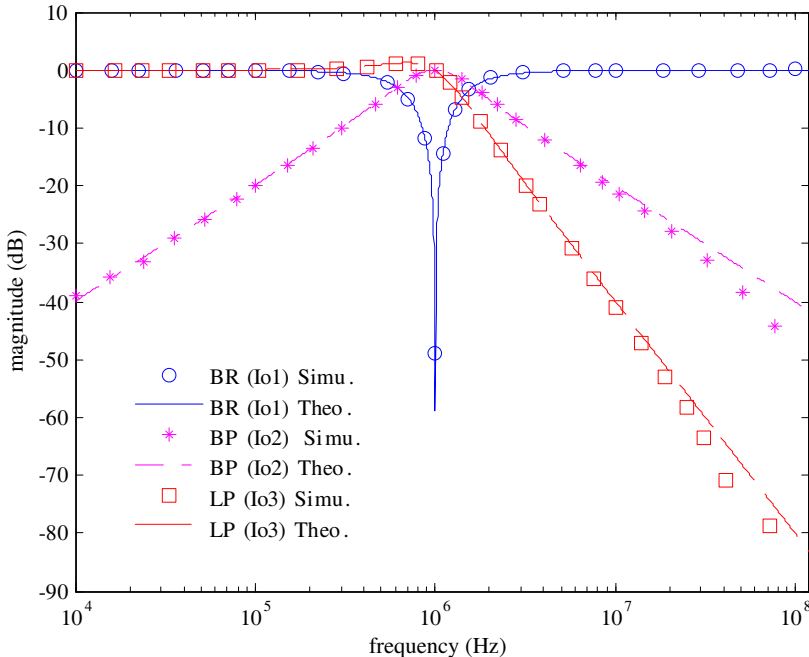


Figure 3: The bandreject, bandpass and lowpass amplitude-frequency responses in case I.

as 3.6/0.36 for M1, M2; 7.2/0.36 for M3, M4; 4.8/0.36 for all the other NMOS; 14.4/0.18 for all PMOS. The supply voltages are $V_{DD} = -V_{SS} = 0.9$ V and the biasing voltages are $V_{B1} = -0.1$ V and $V_{B2} = -0.38$ V, respectively. Figure 3 shows the simulated amplitude responses for the band-reject (BR), bandpass (BP) and lowpass (LP) filtering in case I with $R_1 = R_2 = R_3 = 10\text{ k}\Omega$ and $C_1 = C_2 = 15.9\text{ pF}$, leading to a center frequency of $f_o = 1\text{ MHz}$ and quality factor of $Q = 1$. It appears from Figure 3 that the simulation results agree well with theoretical analysis.

4. CONCLUSION

In 2007, Keskin and Cam proposed a good high output impedance current-mode multifunction filter using three DOCCIs, two grounded capacitors and two resistors [6]. The proposed circuit can simultaneously obtain HP, BP and LP filtering responses. In this paper, the authors propose another high output impedance current-mode universal filter using three MOCCIs, two grounded capacitors and two grounded resistors. The proposed circuit can be used as either a single-input three-output multifunction filter or three-input single-output universal filter with the same topology, which is more versatile than the multifunction one with a single input and three outputs or the universal one with three inputs and single output. Besides, the proposed circuit still offers the following advantages: (i) no capacitor is connected at the port X of the MOCCI, (ii) no need to employ inverting-type input current signals or double input current signals, (iii) no need to impose component choice and (iv) low active and passive sensitivity performances.

ACKNOWLEDGMENT

The author would like to thank the National Science Council and Chip Implementation Center of Taiwan, R.O.C.. The National Science Council, Republic of China supported this work under grant number NSC 99-2221-E-131-040.

REFERENCES

1. Wilson, B., "Recent developments in current conveyor and current-mode circuits," *IEE Proceedings G Circuits, Devices and Systems*, Vol. 137, No. 2, 63–77, 1990.
2. Toker, A. and S. Ozoguz, "Integrable current-mode filter realisation using dual-output current conveyors for low-frequency operation," *International Journal of Electronics and Communications*, (AEÜ), Vol. 55, No. 2, 145–149, 2001.
3. Cicekoglu, O., N. Tarim, and H. Kuntman, "Wide dynamic range high output impedance current-mode multifunction filters with dual-output current conveyors," *International Journal of Electronics and Communications*, (AEÜ), Vol. 56, No. 1, 55–60, 2002.
4. Cicekoglu, O., "High output impedance current-mode four-function filter with reduced number of active and passive elements using the dual output current conveyor," *Analog Integrated Circuits and Signal Processing*, Vol. 28, No. 2, 201–204, 2001.
5. Toker, A. and S. Ozoguz, "Insensitive current-mode universal filter using dual-output current conveyors," *International Journal of Electronics*, Vol. 87, No. 6, 667–674, 2000.
6. Keskin, A. U. and U. Cam, "Insensitive high-output impedance minimum configuration SITO-type current-mode biquad using dual-output current conveyors and grounded passive components," *International Journal of Electronics and Communications*, (AEÜ), Vol. 61, No. 5, 341–344, 2007.
7. Horng, J. W., C. L. Hou, C. M. Chang, W. Y. Chiu, and C. C. Liu, "Current-mode universal biquadratic filter with five inputs and two outputs using two multi-output CCIs," *Circuit, Systems, and Signal Processing*, Vol. 28, No. 5, 781–792, 2009.
8. Fabre, A., O. Saaid, and H. Barthelemy, "On the frequency limitations of the circuits based on second generation current conveyors," *Analog Integrated Circuits and Signal Processing*, Vol. 7, No. 2, 113–129, 1995.
9. Acar, C. and H. Kuntman, "Limitations on input signal level in voltage-mode active-RC filter using current conveyors," *Microelectronics Journal*, Vol. 30, No. 1, 69–76, 1999.

Sensitivity of Fabry-Perot Resonator Based Measurements of Gas Absorptions

P. Piksa, S. Zvanovec, and P. Cerny

Department of Electromagnetic Field, Czech Technical University in Prague, Czech Republic

Abstract— In order to reach maximum sensitivity of gas attenuation measurements and to propose optimal parameters of the new developed spectrometer, the coupling characteristics of several resonator based measurement approaches were analyzed. Three types of resonator feed were investigated the first based on a radial feeding of a resonator cavity, second one using axially alignment feeding with two ports (transmission measurement) and the last having one axial port feeding (reflection measurement method). Based on both analytically derived relations and results from simulations, the optimal setting of coupling is proposed in the paper. Analytical results covering a wide range of couplings were validated by spectroscopic measurements of particular gases attenuations.

1. INTRODUCTION

Microwave high-resolution spectroscopy provides the basic experimental data for molecular physics [1, 2]. The microwave measurements in the frequency domain are in many cases unable to standard resolve the hyperfine structures of rotational lines. Joint research teams of Department of Electromagnetic Field (at the Faculty of Electrical Engineering at the Czech Technical University in Prague) and Laboratory of High-Resolution Molecular Spectroscopy (at the Department of Analytical Chemistry at the Institute of Chemical Technology), are up to date equipped with two millimeter/submillimeter wave spectrometers operating in the spectral intervals from 50 to 600 GHz [3] and from 20 to 110 GHz [1], respectively, for absorption and emission spectra measurements. A new spectrometer based on time-domain Fourier transform is developed within the frame of above mentioned cooperation for a sensitive detection of the rotational free induction decay following polarization by the short pulse.

A Fabry-Perot interferometer is very common tool enabling an enhancement of the sensitivity of the absorption as well as emission measurements in the region of microwave spectroscopy [1] especially due to an apparent lengthening of the optical path length by means of multiple reflections. In the paper, several couplings of the microwave resonators are analyzed.

2. CIRCUIT ANALYSES

In order to reach maximum sensitivity of gas attenuation measurements, the influence between the coupling coefficient and gas attenuation effect within received power was analyzed. Three basic types of resonator feeding were investigated — the first with radial feeding (hereinafter referred to as resonator A), the second with axial two-port feeding (resonator B) and the last one with axial one-port feeding (resonator C). Resonators' deployment and equivalent circuits are depicted in Figure 1.

The unloaded quality factor of a resonator [4] can be defined by equation

$$Q_0 = \frac{\omega_0 L}{R}. \quad (1)$$

The external quality factor, which is only determined by losses due to external impedances of the source and load, can be expressed in the case of resonator A as:

$$Q_v = \frac{\omega_0 L}{\frac{n^2 Z_0}{2}}, \quad (2)$$

whereas in the case of resonators B and C as:

$$Q_v = \frac{\omega_0 L}{n^2 Z_0}. \quad (3)$$

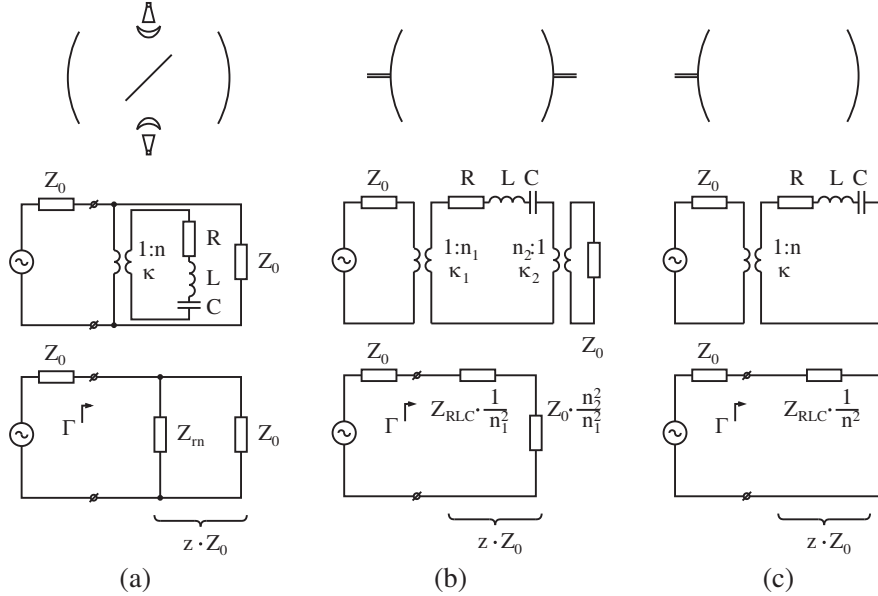


Figure 1: Types of resonator feeding (upper) — (a) with radial feeding (resonator A), (b) with axial two-port feeding (resonator B) and (c) with axial one-port feeding (resonator C) — and their equivalent circuits (bottom).

The relation between unloaded and external quality factors can be determined by the coupling coefficient κ as

$$\kappa = \frac{Q_0}{Q_v}. \quad (4)$$

The serial resonant circuit represents a resonator with electric coupling. On the other hand, a resonator with inductive or slot coupling is represented as the parallel resonant circuit [4] where the admittance and conductance are instead of the impedance Z_{RLC} and the resistance R , respectively. The serial resonant RLC circuit has the impedance given by

$$Z_{RLC} = R \left[1 + j Q_0 \left(\frac{\omega}{\omega_0} - \frac{\omega_0}{\omega} \right) \right]. \quad (5)$$

In the case of ω approaching ω_0 the part of (5) in rounded bracket is for approximately equal to $2 \cdot (\omega - \omega_0)/\omega_0$, which in fact introduces a double of a relative frequency misalignment (2δ).

The impedance Z_{RLC} transformed via the ideal transformer $1:n$ can be expressed in the case of resonator A as

$$Z_{rn} = \frac{Z_{RLC}}{n^2} = \frac{Z_0}{2\kappa} [1 + j Q_0 2\delta]. \quad (6)$$

The power reflection coefficient is generally determined as

$$|\Gamma|^2 = \left| \frac{z - 1}{z + 1} \right|^2 = \frac{P_R}{P_0}, \quad (7)$$

where P_R and P_0 represent reflected and input power, respectively and z stands for a normalized input impedance, which can be expressed for the resonator A as

$$z = \frac{1 + j Q_0 2\delta}{1 + 2\kappa + j Q_0 2\delta}, \quad (8)$$

for the resonator B as

$$z = \frac{1}{\kappa_1} [1 + \kappa_2 + j Q_0 2\delta] \quad (9)$$

and the resonator C as

$$z = \frac{1}{\kappa} [1 + j Q_0 2\delta]. \quad (10)$$

The transmission coefficient T is defined for the resonator A by [5]

$$T = \frac{1 + Q_0^2 (2\delta)^2}{(1 + \kappa)^2 + Q_0^2 (2\delta)^2} \quad (11)$$

and for the resonator B by [6]

$$T = \frac{4 \kappa_1 \kappa_2}{(1 + \kappa_1 + \kappa_2)^2 + Q_0^2 (2\delta)^2}. \quad (12)$$

3. SENSITIVITY OF GAS ABSORPTION MEASUREMENT

The complex permittivity of gas measured in the Fabry-Perot resonator can be described by

$$\varepsilon = \varepsilon' - j \varepsilon'' = \varepsilon' (1 - j \operatorname{tg}\delta). \quad (13)$$

The coupling coefficient of the resonator when influenced by gas attenuation effect can be afterwards defined as [7]

$$\frac{1}{\kappa'} = \frac{1}{\kappa} + \varepsilon'' Q_v = \frac{1}{\kappa} (1 + \varepsilon'' Q_0). \quad (14)$$

Under the assumption the gas medium has the relative permittivity near to 1, the Equation (14) thus can be modified to

$$\kappa' = \frac{\kappa}{1 + Q_0 \operatorname{tg}\delta}. \quad (15)$$

By evaluation of the reflected power change ΔP_R related to the input power

$$\frac{\Delta P_R}{P_0} = \left| |\Gamma(\kappa)|^2 - |\Gamma(\kappa')|^2 \right| \quad (16)$$

and the transmitted power change ΔP_T related to the input power

$$\frac{\Delta P_T}{P_0} = T(\kappa) - T(\kappa'), \quad (17)$$

the sensitivity of the gas absorption measurement associated with the change of the coupling coefficient influenced by gas attenuation effect can be evaluated for all types of the resonator feeding. The Figure 2 depicts this relation for our case of Fabry-Perot resonator (for description of the resonator parameters reader is referred to [1]) with the unloaded quality factor equaled $1.4 \cdot 10^5$ at frequency of 60 GHz and with gas attenuation of 10 dB/km.

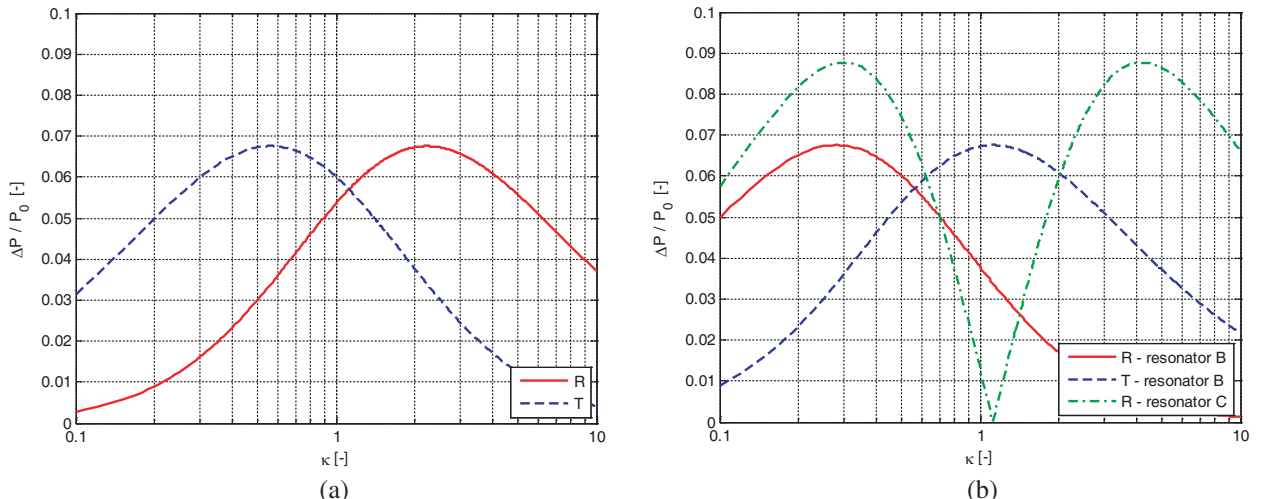


Figure 2: The sensitivity of the gas absorption measurement within reflected power (R) and transmitted power (T) change in relation to the coupling coefficient variation in the case (a) with radial feeding and (b) with axial feeding.

Table 1: Values of couplings for maximal change of reflected and transmitted power due to the gas attenuation and corresponding values of power reflection and transmission coefficients.

	resonator A		resonator B		resonator C
	R	T	R	T	R
κ [-]	2.24	0.56	0.28	1.12	0.30 and 4.19
optimal values of $ \Gamma ^2$, T	-3.2 dB from short	-3.9 dB from T without coupling	-2.3 dB from short	-3.2 dB from P_0	-5.4 dB and -4.2 dB from short

Table 2: Parameters of the radial fed resonator derived from resonant curves measured at the frequency of 55.193 GHz for three different dielectric coupling foils.

foil		reflection (R)			transmission (T)		
material	width [μm]	κ [-]	Q_0 [-]	$\Delta P_R/P_0$ [dB]	κ [-]	Q_0 [-]	$\Delta P_T/P_0$ [dB]
PE ($\varepsilon_r = 2.26$)	100	3.99	$1.79 \cdot 10^5$	-20.44	2.60	$1.01 \cdot 10^5$	-22.29
PTFE ($\varepsilon_r = 2.03$)	100	1.67	$9.9 \cdot 10^4$	-22.42	3.09	$1.69 \cdot 10^5$	-20.22
PP ($\varepsilon_r = 2.3$)	50	0.66	$2.0 \cdot 10^5$	-21.34	0.80	$2.34 \cdot 10^5$	-20.15

In Figure 2 there can be clearly distinguished maxima, when the resonator is the most sensitive on gas attenuation. Their values are then summarized in Table 1.

In next step, measurements of the radial fed Fabry-Perot resonator [5] (resonator A) were performed either of transmission or reflection. When interleaved theoretical Equations (7), (8) and (11) into measured resonant curves for reflection and transmission, following parameters were derived: the unloaded quality factor $Q_0 = 1.79 \cdot 10^5$ and $Q_0 = 1.01 \cdot 10^5$, respectively, and the coupling $\kappa = 3.99$ and $\kappa = 2.6$, respectively. From (16) and (17) sensitivity of the resonator for gas attenuation measurement were determined to be for reflection $\Delta P_R/P_0 = -20.44$ dB and for transmission $\Delta P_T/P_0 = -22.29$ dB. Consequently, several measurements with different coupling foils having different permittivity and widths were accomplished in order to obtain wide scale of coupling coefficients. Results of measurements are summarized in Table 2.

From comparison $\Delta P/P_0$ it is evident, that the resonator with coupling foil PE having width 100 μm reaches the best sensitivity from measurements of gases based on measuring of reflected power while the resonator with coupling foil PP having width 50 μm achieves the best sensitivity when of transmission based measurement approaches.

4. CONCLUSIONS

Sensitivity of the resonator on measured gas attenuation is linearly dependent on the unload quality factor and highly dependent on the coupling coefficient of the resonator with different characteristics for measurement of reflected and transmitted power. In the case of radial fed Fabry-Perot resonator, optimal values of coupling coefficients and quality factors guaranteeing maximal sensitivity of the resonator on measured gas can be reached by the proper choice of a width and permittivity of the coupling foil.

ACKNOWLEDGMENT

The research has been supported by the project of the Ministry of Education, Youth and Sports of the Czech Republic No. LC06071. The measurements and publication were supported by the research project of the Czech Science Foundation P206/10/2182.

REFERENCES

1. Zvárnovec, S., et al., "The use of the Fabry-Perot interferometer for high resolution microwave spectroscopy," *Journal of Molecular Spectroscopy*, Vol. 256, 141–145, 2009.

2. Townes, C. H. and A. L. Schawlow, *Microwave Spectroscopy*, Dover Publications, New York, 1975.
3. Kania, P., et al., “Pressure shifts of acetonitrile ground state parameters,” *Journal of Molecular Structure*, Vol. 795, 209–218, Aug. 21, 2006.
4. Pozar, D. M., *Microwave Engineering*, 2nd Edition, 300–306, Wiley, 1998.
5. Piksa, P., S. Zvanovec, and P. Cerny, “Specific millimeter-wave features of fabry-perot resonator for spectroscopic measurements,” *Microwave and Millimeter Wave Technologies from Photonic Bandgap Devices to Antenna and Applications*, Prof Igor Minin (Ed.), INTECH, 2010.
6. Montgomery, C. G., *Technique of Microwave Measurements*, 290, McGraw-Hill, 1947.
7. Trkal, V. and V. Tysl, “Kvantová elektronika: Mikrovlnná spektroskopie,” 177, Academia, 1968.

Microstrip Diplexer Using High Permittivity Substrate

C.-H. Hsu¹, H.-H. Tung¹, C.-K. Hsu¹, J.-S. Lin², and H.-W. Yang³

¹Department of Electrical Engineering, National United University, Taiwan

²Department of Mechanical Engineering, National United University, Taiwan

³Department of Materials Science and Engineering, National United University, Taiwan

Abstract— A planar microwave diplexer with using cross-coupled compact hairpin filter is proposed. Miniaturization hairpin resonator is realized by using an interdigital structure having parallel coupled lines. The full-wave simulator IE3D is used to design the interdigital hairpin resonator, and to calculate the coupling coefficient of the basic coupling strictures. The response of the fabricated diplexer using $(\text{Mg}_{1/2}\text{Co}_{1/2})\text{Al}_2\text{O}_4$ substrate is designed at a GSM/DSC system. The compact size and the performance of this class of diplexer have been demonstrated.

1. INTRODUCTION

Since microstrip resonators are the basic components of a planar diplexer design, it is necessary to select proper resonator types used in a filter design. A conventional half-wavelength open-line microstrip resonator is too large to be used in the modern communication system such as 900 MHz, 1800 MHz for personal communication systems (PCS) or GSM/DSC systems. Miniaturization of dielectric components for volume efficiency is a major requirement in modern microwave telecommunication systems such as personal communication systems (PCS) or GSM/DSC systems. They can be designed in many different ways and by using different materials. Ceramic material with a high quality factor ($Q \times f$) value (> 10000) and a high permittivity provides a means to create small resonator structures such as coaxial structures that could be coupled to form comb-line bandpass filters [1]. However, further miniaturization becomes more difficult for this filter. Planar microwave components with using high permittivity ceramic substrate provide good miniaturization ability [2–5]. Therefore, there has been much research conducted on planar filters and their components.

On the other hand, the hairpin filters were folded from the open line wavelength microstrip resonator to become U-shaped resonators make progress in circuit size reduction from the parallel-coupled line structure. Since 1989, the miniaturized hairpin resonator was developed by several researchers [7–9]. The interdigital coupled lines at the ends of this structure are used as a capacitor in order to reduce the resonator size. In addition, cross-coupled filter with these attractive characteristics is that of quasi-elliptic function response filters with a pair of attenuation poles at finite frequencies [10, 11]. The capability of placing attenuation poles near the cutoff frequencies of the pass-band improves the selectivity using less resonators. A cross-coupled between a pair of nonadjacent resonators was approached this type filter. The filter employing the cross coupled generally results in a compact topology.

In this design, design of a diplexer with using microstrip four-pole cross-coupled elliptic function filter which using compact interdigital hairpin resonators was presented. In addition, the T-junction was also used to fabricate the diplexer which connected two impact cross-coupled interdigital hairpin bandpass filters. The design approach enables one to use EM simulator to complete the diplexer design with high permittivity ceramic substrate, to determine the physical dimensions of the dplexers.

2. DESIGN MICROSTRIP HAIRPIN FILTER

Figure 1(a) shows the layout and equivalent electrical parameters of an interdigital hairpin resonator. Its fundamental condition is hence the same as that of a conventional miniaturized hairpin resonator [12]. In the case of $Z_s > \sqrt{Z_{io}Z_{ie}}$, the total electrical length of these resonators become shorter than that of conventional. Further miniaturization can be achieved by increasing the coupling between parallel coupled lines and hence decreasing the value of $\sqrt{Z_{io}Z_{ie}}$. In addition, the resonance condition can be calculated from input admittance using $ABCD$ matrices [13].

A four-pole elliptical bandpass filter response can be implemented using the cross coupling between nonadjacent resonators. The cross-couplings give the input signal two paths from the input port to the output. The magnitude and phase of the signal are changed differently though different

Table 1: Dimensions of microstrip hairpin diplexer.

	T	U	V	W	X	Y
(Mg _{1/2} Co _{1/2} Al ₂ O ₄ (mm))	0.4	0.1	0.8	0.6	0.5	0.8
(Mg _{1/2} Co _{1/2} Al ₂ O ₄ (mm)): 55 mm×42 mm						

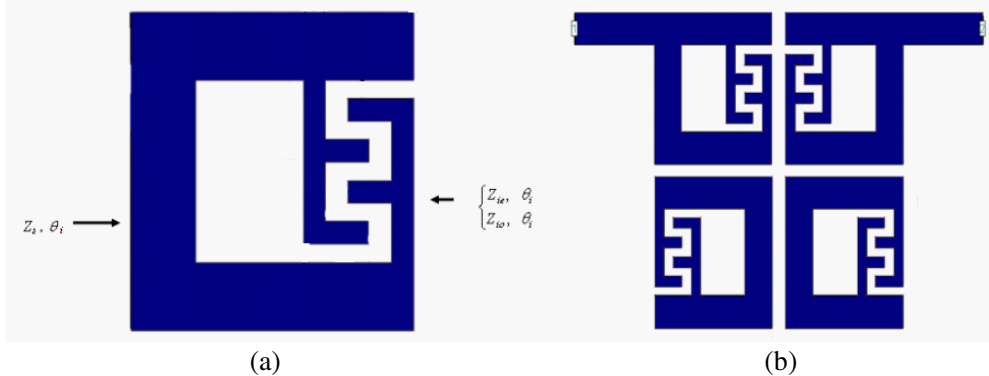


Figure 1: Layout of (a) microstrip interdigital hairpin resonator and (b) microstrip hairpin filter.

paths. As mentioned above, the multi-path effect may cause attenuation poles at finite frequencies if the couplings among the resonators are properly designed. Fig. 1(b) shows the four-pole elliptic function bandpass filter with using miniaturized hairpin resonators. In the configuration, significant couplings exist between any two non-diagonally neighboring miniaturized hairpin resonators. The structure can be extended to form cross-coupled filters of higher orders.

Two kinds of cross-coupled bandpass filters with using compact hairpin resonators are designed to have a fractional at a mid-band frequency $f_o = 900$ MHz and 1.8 GHz. The filter was fabricated on high-permittivity $(\text{Mg}_{1/2}\text{Co}_{1/2})\text{Al}_2\text{O}_3$ ($\epsilon_r = 8.7$) ceramic substrate. A four-pole ($n = 4$) Elliptic function low-pass prototype with a Ω_a value of 1.85 is chosen. The relationships between the bandpass design parameters can the low-pass elements are [14]

$$\left\{ \begin{array}{l} Q_{ei} = Q_{eo} = \frac{C_1}{FBW} \\ M_{1,2} = M_{3,4} = \frac{FBW}{\sqrt{C_1 C_2}} \\ M_{1,4} = \frac{FBW \cdot J_1}{C_1} \\ M_{2,3} = \frac{FBW \cdot J_2}{C_2} \end{array} \right. \quad (1)$$

where FBW denotes the fractional bandwidth of the band-pass filter, C is the capacitance of the lumped capacitor and J is the characteristic admittance of the inverter, and N is the degree of the filter. The cross-coupled structure provides electric, magnetic and mixed coupling. Using a parameter-extraction technique, we carry out EM-simulations to extract the external Q and coupling coefficient M against the physical dimensions [15]. By using the design curves of the coupling coefficient and the external Q , this filter can be realized.

3. DIPLEXER DESIGN

Figure 2 shows the layout and equivalent electrical parameters of a microstrip hairpin diplexer with using two kinds of hairpin filters and T-junction.

Figure 3 shows the calculated filter response of the compact microstrip hairpin diplexer with high-permittivity ($Mg_{1/2}Co_{1/2}Al_2O_3$) ($\epsilon_r = 8.7$) ceramic substrate. The 3-dB fractional bandwidth of the microstrip hairpin diplexer's frequency response was 7.6% (925 MHz) and 7.6% (1.81 GHz). The bandwidth of each filter agrees quite well with the desirable values. It was found that the skirt properties of the cross-coupled filter were sharper. The dimensions of the compact hairpin diplexer with high-permittivity ceramic substrates are provided in Table I. In addition, for high-permittivity ($Mg_{1/2}Co_{1/2}Al_2O_3$) ($\epsilon_r = 8.7$) ceramic substrate, the insertion losses of microstrip hairpin diplexer are about 1.5 dB at the frequency of 925 MHz and 1 dB at the frequency of 1.81 GHz. On the other hand, the return losses of designed diplexer are 21 dB (925 MHz) and 13 dB (1.81 GHz). Finally, the isolations of microstrip hairpin diplexer are 40 dB (9.25 MHz) and 40 dB (1.81 GHz).

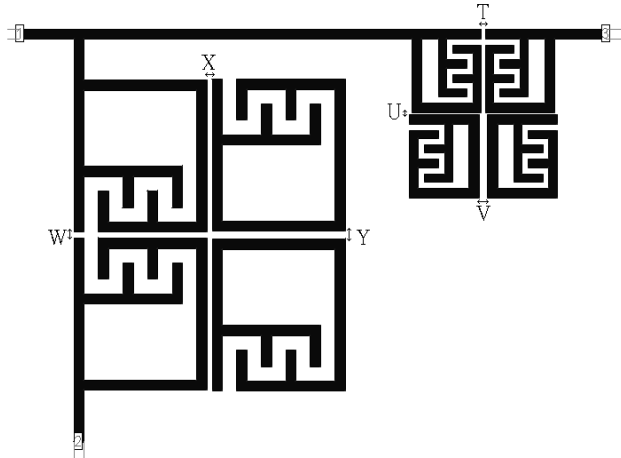


Figure 2: Layout of microstrip hairpin diplexer.

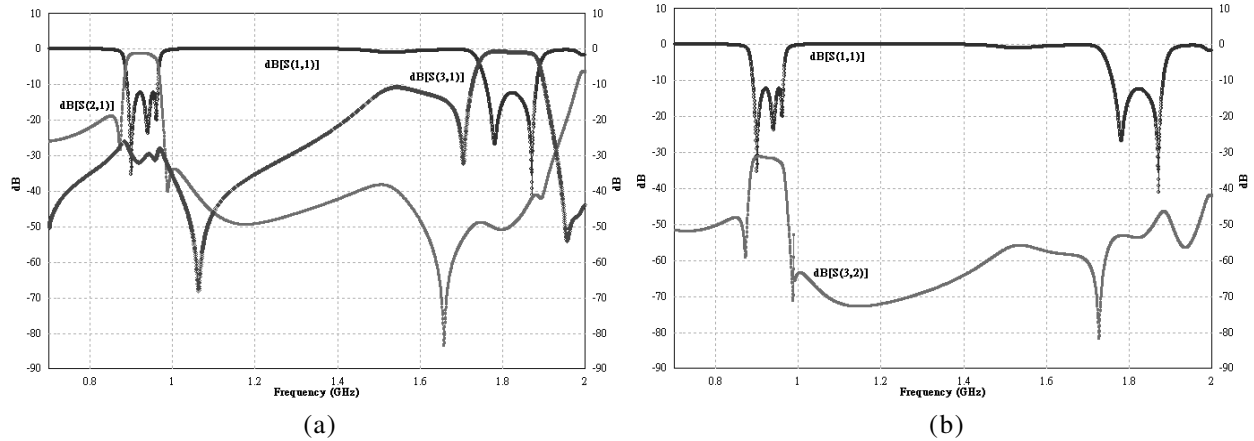


Figure 3: Simulated frequency responses of (a) insertion loss and return loss at 900 MHz and 1.8 GHz (b) isolation at 900 MHz and 1.8 GHz for high-permittivity ($Mg_{1/2}Co_{1/2}$) Al_2O_3 ceramic substrate.

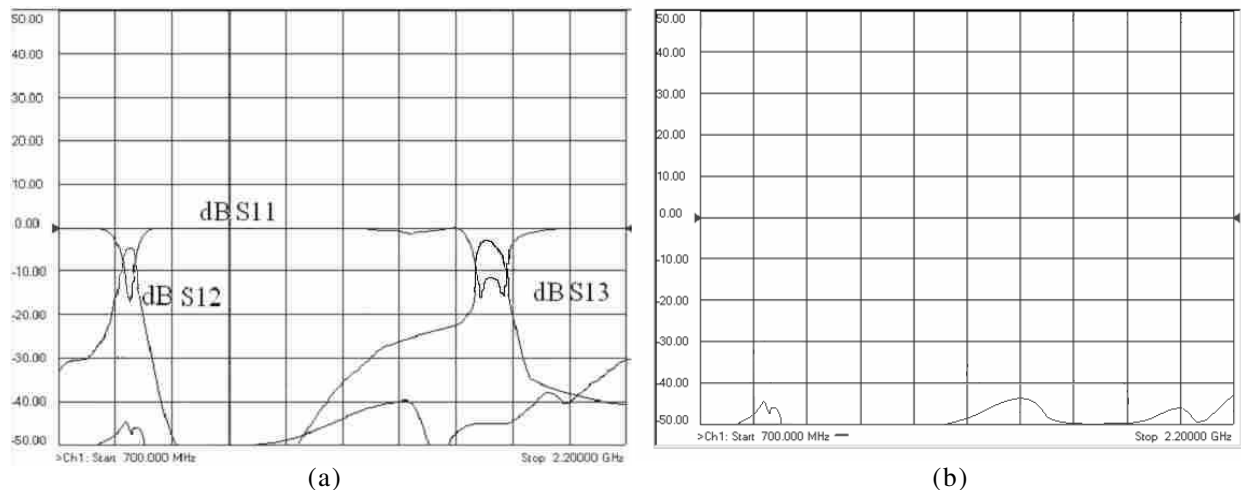


Figure 4: Measured frequency responses of (a) insertion loss and return loss at 900 MHz and 1.8 GHz (b) isolation at 900 MHz and 1.8 GHz for high-permittivity ($Mg_{1/2}Co_{1/2}Al_2O_3$) ceramic substrate.

The measurements are performed with an HP8757D network analyzer. The measured performance is shown in Fig. 4. Using high-permittivity ($Mg_{1/2}Co_{1/2}Al_2O_3$) ($\varepsilon_r = 8.7$) ceramic substrate, the insertion loss is about 4 dB, the return loss is about 17 dB and isolation is 45 dB at the center

frequency of 910 MHz, and the 3-dB passband width is about 5.1%. On the other hand, using high-permittivity ($\text{Mg}_{1/2}\text{Co}_{1/2}\text{Al}_2\text{O}_3$) ceramic substrate the midband insertion loss is about 2.6 dB, the return loss is about 12 dB and isolation is 50 dB at the center frequency of 1.83 GHz, and the 3-dB passband width is 6.8%. The comparison between the measured and simulated results shows that the measured response is strongly influenced by the surface roughness of the ceramic substrate, the conductor thickness, and electric contact.

4. CONCLUSIONS

Miniaturized microstrip hairpin diplexer on high-permittivity ceramic substrate has been implemented. The simple and accurate design technique makes extensive use of EM simulation. The validity of the proposed method was confirmed through the design, fabrication, and measurement of the compact microstrip hairpin diplexer at 900 MHz and 1.8 GHz on high-permittivity ($\text{Mg}_{1/2}\text{Co}_{1/2}\text{Al}_2\text{O}_3$) ceramic substrate. The insertion loss is about 4 dB, the return loss is about 17 dB and isolation is 45 dB at the center frequency of 910 MHz, and the 3-dB passband width is about 5.1%. On the other hand, using high-permittivity ($\text{Mg}_{1/2}\text{Co}_{1/2}\text{Al}_2\text{O}_3$) ceramic substrate, the midband insertion loss is about 2.6 dB, the return loss is about 12 dB and isolation is 50 dB at the center frequency of 1.83 GHz, and the 3-dB passband width is 6.8%. The microstrip interdigital hairpin diplexer with high-permittivity ceramic substrate is an attractive design for further development and applications in modern communication systems.

ACKNOWLEDGMENT

This work was supported by the National United University Foundation under grant 991010-09.

REFERENCES

1. You, C. C., C. L. Huang, and C. C. Wei, "Single-block ceramic microwave bandpass filters," *Microwave J.*, Vol. 37, 24–35, 1994.
2. Cohn, S. B., "Parallel-coupled transmission line resonator filters," *IRE Trans. Microwave Theory Tech.*, 223–231, 1958.
3. Caspi, S. and J. Adelman, "Design of combline and interdigital filter with tapped-line input," *IEEE Trans. Microwave Theory Tech.*, Vol. 36, 759–763, 1988.
4. Matthaei, G. L., "Comb-line bandpass filter of narrow or moderate bandwidth," *IEEE Trans. Microwave Theory Tech.*, Vol. 6, 82–91, 1963.
5. Gysel, U. H., "New theory and design for hairpin-line filters," *IEEE Trans. Microwave Theory Tech.*, Vol. 22, 523–531, 1974.
6. Matthaei, G. L., N. O. Fenzi, R. J. Forse, and S. M. Rohlffing, "Hairpin-comb filters for HTS and other narrow-band applications," *IEEE Trans. Microwave Theory Tech.*, Vol. 45, 1226–1231, 1997.
7. Sagawa, M., K. Takahashi, and M. Makimoto, "Miniaturized hairpin resonator filters and their application to receiver front-end MIC's," *IEEE Trans. Microwave Theory Tech.*, Vol. 37, 1991–1997, 1989.
8. Yabuki, H., M. Sagawa, and M. Makimoto, "Voltage controlled push-push oscillators using miniaturized hairpin resonators," *IEEE MTT-S Int. Microwave Symp. Dig.*, 1175–1178, 1991.
9. Levy, R., "Filters with single transmission zeros at real or imaginary frequencies," *IEEE Trans. Microwave Theory Tech.*, Vol. 24, 172–181, 1976.
10. Kurzok, R. M., "General four-resonator filters at microwave frequencies," *IEEE Trans. Microwave Theory Tech.*, Vol. 14, 295–296, 1966.
11. Lee, S. Y. and C. M. Tsai, "New cross-coupled filter design using improved hairpin resonators," *IEEE Trans. Microwave Theory Tech.*, Vol. 48, No. 12, 2482–2490, 2000.
12. Yabuki, H., Y. Endo, M. Sagawa, and M. Makimoto, "Miniaturized hairpin resonators and their application to push-push oscillators," *Proc. The 3rd Asia-Pacific Microwave Conf.*, 263–266, 1990.
13. Hong, J. S. and M. J. Lancaster, *Microstrip Filters for RF/Microwave Applications*, Wiley, New York, 2001
14. Zeland Software, Inc., IE3D 6.0, New York, 1999.

A Broadband Balun Using Meander Line

C. F. Tseng and S. C. Lu

Department of Electronic Engineering, National United University, Taiwan

Abstract— In this study, a broadband branch-line balun with meander lines is presented. It is implemented by using meander line structure to improve the size and performance of the conventional branch-line balun. The parametric analysis of the proposed balun is carried out using the available electromagnetic solver IE3D. Using the meander line structure, experimental measurements show that the fabricated balun has an amplitude imbalance of 0.09 dB and a phase imbalance of 0.24° operation at 1.98 GHz. Moreover, the proposed balun is found to occupy only 58% of the conventional branch-line balun's area.

1. INTRODUCTION

Baluns are generally used to convert unbalanced input into two balanced outputs and have been widely used in planar microwave integrated circuits, such as balanced antennas, balanced mixers, etc. There are many types of balun [1–3] used in modern wireless communication systems. Among them, the Marchand-type and branch-line-type baluns are very popular for this purpose. The conventional Marchand balun is inherently composed of two quarter-wave length coupled transmission lines, and has a narrow bandwidth [4]. Moreover, its performances depend on the even and odd mode impedances. To develop broadband performance, even and odd mode impedances are equally reduced to half by connecting two baluns in parallel, which have better performance at the expense of increased overall structure size. Therefore, spiral-shaped coupled lines are used to reduce the overall size. Although it is effective to miniaturize size, it increases manufacturing complexity.

The branch-line balun is another well-known design. The conventional branch-line balun is composed of two quarter-wavelength branches and two half-wavelength branches. It has simple structure and can provide low insertion loss. To reduce circuit size, the use of two open stubs in the middle of the two half-wavelength branches has been presented in [5]. This study presents a balun structure based on conventional branch-line balun by introducing meander branches to minimize size. The proposed baluns not only have small size and wider impedance bandwidth advantages, but also have a flat coupling between ports 2 and 3 within a certain frequency, when compared with the conventional one. The designed balun has been successfully implemented and the experimental results have been presented.

2. ANTENNA DESIGN AND EXPERIMENTAL RESULTS

Figure 1 is a conventional branch-line balun. It is composed of a pair of quarter-wavelength transmission lines (Branches 1 and 3) and a pair of half-wavelength transmission lines (Branches 2 and 4). The balun is presumed to fix the voltage and current associated with the outward traveling waves at the two output ports so that they are equal in magnitude and opposite in phase. The conventional branch-line balun can be analyzed using the odd and even mode decomposition method based on the circuit symmetry. The *S*-parameter can be expressed as

$$[S] = \frac{-j}{\sqrt{2}} \begin{bmatrix} 0 & 1 & -1 \\ 1 & 0 & 0 \\ -1 & 0 & 0 \end{bmatrix} \quad (1)$$

By assuming that the characteristic impedances are Z_1 for Branch 1 and Z_2 for Branch 2 to 4, the impedances yield the following solution [6]:

$$Z_1 = \frac{Z_2}{\sqrt{2}Z_2 - Z_0}Z_0 \quad (2)$$

where Z_0 is the system's characteristic impedance. One of them can be chosen freely and then the other one can be determined from (2). In this study, the branch-line impedances are selected as $Z_1 = 0.86 \Omega$ and $Z_2 = 60 \Omega$, respectively.

To reduce the overall size of conventional branch-line balun, the meander branches are employed to substitute for that of conventional balun. The geometry of the proposed balun is shown in

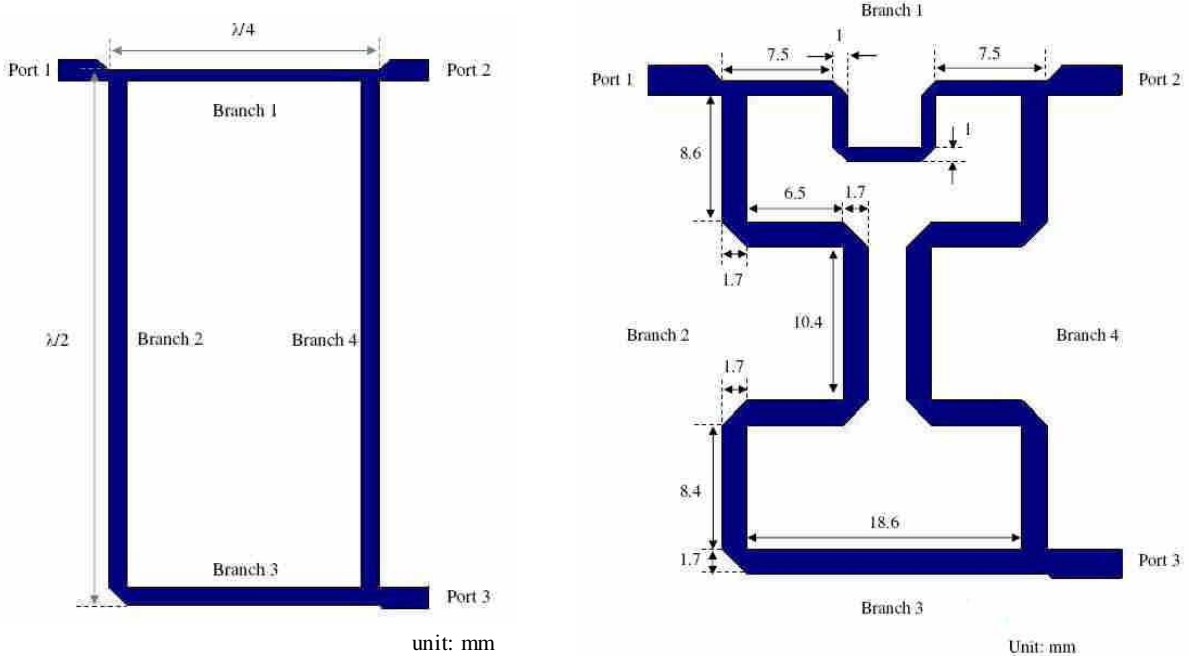


Figure 1: Configuration of conventional branch-line balun.

Figure 2: Configuration of the proposed branch-line balun.

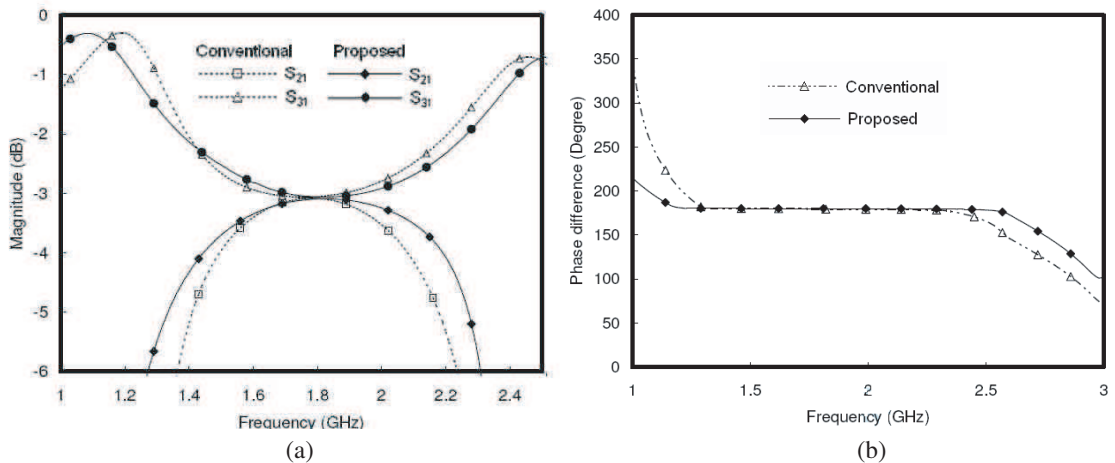


Figure 3: Simulated performance of conventional and proposed balun: (a) Magnitudes of S_{21} and S_{31} ; (b) the phase difference between two output ports.

Figure 2. The above-mentioned prototype designs are fabricated on FR4 substrate with a thickness of 1.6 mm, dielectric constant of 4.4, and loss tangent of 0.002 at the center frequency of 1.8 GHz. The results are measured through SMA connectors attached at the end of the feedline.

Figure 3 presents the analysis results that are compared with those of conventional and proposed branch-line balun of simulated data with insertion loss and phase difference between two output ports (Ports 2 and 3). In addition, the simulated characteristics of the conventional and proposed types are clearly shown in Table 1. Figure 3(a) shows that a wider insertion loss can be obtained between two output ports within a center frequency range, compared with the conventional one. The two insertion losses (S_{21} , S_{31}) at two balanced ports of conventional and proposed balun are $S_{21} = -3.08$ and $S_{31} = -3.05$, and $S_{21} = -3.09$ and $S_{31} = -3.06$ at 1.8 GHz, respectively. Based on ± 0.5 dB magnitude difference at two balanced ports, the simulated bandwidth of the proposed balun is 0.46 GHz from 1.59 to 2.05 GHz (or 25.5% at 1.8 GHz). Figure 3(b) shows that the phase differences between Ports 2 and 3 ($\angle S_{21} - \angle S_{31}$) of conventional and proposed types are 179.7° and 180.2° at 1.8 GHz. With regard to a phase difference of $\pm 10^\circ$, a flat coupling from 1.11 to 2.63 GHz is achieved while the result indicates that a bandwidth over 80% has been implemented.

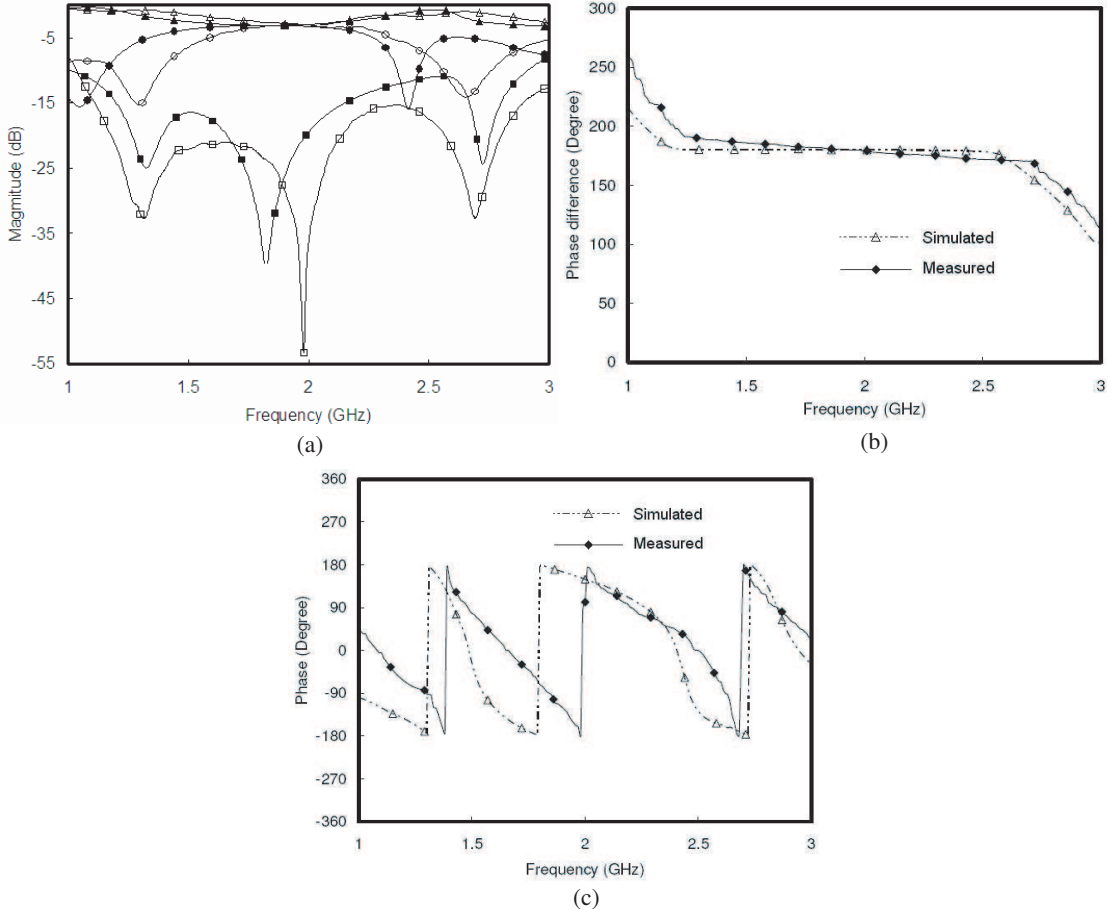


Figure 4: Simulated and measured results of proposed balun: (a) Magnitudes of input return loss (S_{11}) and output insertion loss (S_{21} and S_{31}); (b) the phase difference between two output ports; (c) phase response of input port.

Table 1: Area and performance comparison of conventional balun.

Balun type	Area (mm ²)	Relative area	$S_{21} - S_{31}$ (-3 ± 0.5 dB)	$\angle S_{21} - \angle S_{31}$ ($180^\circ \pm 10^\circ$ dB)
Conventional	25×50	1	1.59–1.97 (GHz)	1.25–2.46 (GHz)
Proposed	22×33	0.58	1.59–2.05 (GHz)	1.11–2.63 (GHz)

for the proposed balun (as shown in Table 1). In addition, the proposed balun has an area of 58% relative to the conventional branch-line balun area.

The proposed balun was fabricated and measured. The simulated and measured results are given in Figure 4. It was found that the measured center frequency shifted from 1.8 to 1.98 GHz. This frequency shift may probably be owing to the variations in the PCB fabrication process. Figure 4(a) shows the Sparameters of the proposed balun. The measured return loss (S_{11}) is below -50 dB at 1.98 GHz and the broad bandwidth is about 90.4% (1.11–2.9 GHz) for $S_{11} < -15$ dB. The measured insertion loss at the two output ports are $S_{21} = -2.93$ and $S_{31} = -3.02$ at 1.98 GHz, respectively. Figure 4(b) plots the phase responses of the designed balun. The simulation and measurement show good agreements. The measured phase difference between the two output ports is 179.75° . Meanwhile, the measured $180^\circ \pm 10^\circ$ phase balance bandwidth of the proposed balun is 1.43 GHz from 1.29 to 2.72 GHz. Figure 4(c) shows the phase of return loss for the proposed balun. According to above-mentioned results, the proposed balun possesses two -3 dB outputs in 180° out of phase near the center frequency.

3. CONCLUSIONS

This study presented a balun structure based on conventional branch-line balun by introducing meander branches. The proposed balun was achieved in 58% of the conventional type's area. The measured return loss of the proposed balun was lower than -15 dB over the frequency of 1.29 to 2.72 GHz, showing a fractional bandwidth of $\sim 72\%$. The measured insertion loss at the two output ports was $S_{21} = -2.93$ and $S_{31} = -3.02$ at 1.98 GHz. The measured $180 \pm 10^\circ$ phase balance bandwidth of the proposed balun was 1.43 GHz from 1.29 to 2.72 GHz.

ACKNOWLEDGMENT

This work was supported by National Science Council of the Republic of China under NSC 97-2221-E-239-006-MY2.

REFERENCES

1. Ghali, H. and T. A. Moseley, "Miniaturized fractal rat-race, branch-line, and coupled-line hybrids," *IEEE Trans. Microwave Theory Tech.*, Vol. 52, 2513–2520, 2000.
2. Ang, K. S., Y. C. Leong, and C. H. Lee, "Multisection impedance-transforming coupled-line baluns," *IEEE Trans. Microwave Theory Tech.*, Vol. 51, 536–541, 2003.
3. Zhang, Z. and S. Xu, "A novel balun structure with a composite right left-handed transmission line," *Microwave Opt. Technol. Lett.*, Vol. 45, 422–424, 2005.
4. Chen, T. H., K. W. Chang, S. B. Bui, H. Wang, G. S. Dow, L. C. T. Liu, T. S. Lin, and W. S. Titus, "Broadband monolithic passive baluns and monolithic double balanced mixer," *IEEE Trans. Microwave Theory Tech.*, Vol. 39, 1980–1986, 1991.
5. Park, M. J. and B. Lee, "Stubbed branch line balun," *IEEE Microwave Wireless Compon. Lett.*, Vol. 17, 169–171, 2007.
6. Li, J. L., S. W. Qu, and Q. Xue, "Miniaturised branch-line balun with bandwidth enhancement," *IEE Electron. Lett.*, Vol. 43, 931–932, 2007.

A Novel Multilayer Dual-mode Substrate Integrated Circular Cavity (SICC) Filter with Power Divider

Zhigang Zhang, Yong Fan, and Yonghong Zhang

Extreme High Frequency Key Laboratory, School of Electronic Engineering
University of Electronic Science and Technology of China, Chengdu, China

Abstract— A novel millimeter-wave multilayer dual-mode filter with power divider is developed based on the substrate integrated waveguide circular cavity (SICC). The novel dual-mode SICC filter/power divider with arc-shaped coupling slots has been designed for Ka-band application. The multilayer dual mode filter/power divider has been firstly realized only by adjusting arc-shaped coupling slots located in metal layers.

Simulated results show that excellent impedance matching at all three ports, amplitude and phase balance at the two output ports, and out-of-band rejection are observed at the operating band. Meanwhile, it is possible to control the return loss, bandwidth and rejection level by adjusting the size of the coupling slots. This novel filter/power divider is very compact and has the advantages of return loss, very low insertion loss, high selectivity.

1. INTRODUCTION

Recently, wireless communication systems are developing gradually towards millimeter wave band. Compact devices with low profile and high performance are required in many millimeter wave systems. Substrate integrated waveguide (SIW) dual mode filter has asymmetry characteristic. Therefore, it can realize very sharp transition by using less number of cavities [1]. However, by taking size, Q-factor and design flexibility into account, SIW filters with circular cavities are reported in [2] and [3].

Power divider is one of the indispensable passive components in many microwave modules and subsystems [4, 5]. As far as we known, the traditional power dividers could not provide distinctive bandpass characteristic at the band edges. If power dividers with a bandpass filter (BPF) function [6, 7] are used for antenna array, it will be advantageous because we can mitigate or eliminate BPF function located after/before the dividers. More recently, special attention has been paid to multilayer cross-coupled substrate integrated waveguide (SIW) filters using low-temperature co-fired ceramic (LTCC) technology [8]. Accordingly, multilayer filter with dual mode character is very attractive candidate to satisfy the requirements in miniaturized circuit [9].

In this paper, a novel millimeter-wave multilayer dual-mode filter with power dividing function is developed based on the substrate integrated waveguide circular cavity (SICC).

The dual mode character has been firstly realized by the coupling aperture located in input/output port and between layers. The position and size of coupling aperture can determine the coupling amount between two degenerate modes. This novel filter/power divider is constructed by introducing multilayer coupling structure, which can not only divide/combine the power of microwave signals, but also reject unwanted frequency signals to better regulate the performance. Additionally, the novel structure is very compact and easily achieved by normal multilayer PCB or LTCC technologies.

2. FILTER ANALYSIS AND DESIGN

2.1. Dual Mode SICC Principle

It is well known that the resonant frequency (unloaded) of mode for circular cavity with solid wall can be calculated by [10]:

$$f_{mnp} = \begin{cases} \frac{c}{2\pi\sqrt{\mu_r\varepsilon_r}} \sqrt{\left(\frac{\mu'_{mn}}{R}\right)^2 + \left(\frac{p\pi}{\Delta h}\right)^2} & \text{TE}_{mnp} \\ \frac{c}{2\pi\sqrt{\mu_r\varepsilon_r}} \sqrt{\left(\frac{\mu_{mn}}{R}\right)^2 + \left(\frac{p\pi}{\Delta h}\right)^2} & \text{TM}_{mnp} \end{cases} \quad (1)$$

where μ_r and ε_r are relative permeability and permittivity of the filling material, μ_{mn} and μ'_{mn} is the n th roots of m th Bessel function of the first kind and its derivative, R is the radius of circular cavity with solid wall, and c is the speed of light in free space. For $m > 0$, each m represents a

pair of degenerate TM and TE modes ($\cos m\varphi$ or $\sin m\varphi$ variation). In circular cavity with dual mode, TM₁₁₀, the lowest higher order mode, has been selected as the working mode. Each different directions represents a different modes ($\cos m\varphi$ or $\sin m\varphi$ variation). This degenerated mode can be used to realize a dual-mode filter. μ_{mn} is 3.832 for the TM₁₁₀ mode. So the corresponding resonant frequency of TM₁₁₀ is derived from formula (1).

$$f_{110} = \frac{c}{2\pi\sqrt{\mu_r\epsilon_r}} \cdot \frac{3.832}{R} = \frac{0.61c}{R\sqrt{\mu_r\epsilon_r}} \quad (2)$$

The radius of the SICC can be obtained according to the formula (2).

$$R = \frac{0.61c}{f_{110}\sqrt{\mu_r\epsilon_r}} \quad (3)$$

And then the solid wall is replaced by metallic vias under guidelines of [8] and [9]. Consequently, using (3), the initial dimensions of the cavity are determined for a desired resonant frequency for the TM₁₁₀ mode and optimized with a full-wave electromagnetic simulator.

2.2. Multilayer Dual-mode SICC Filter with Power Divider

As shown in Figs. 1(a) and (b), there are three substrate layers. The second layer is used for input port, and the first and third layers are used for output ports. Three dual mode cavity resonators are coupled through two arc-shaped slots etched in metal layer 2. By adjusting the size W_S , θ of the arc-shaped slots, the coupling between the three resonators can be controlled. Dual mode character can be easily achieved by changing the angle α between the coupling slot and input/output ports. In addition, it is possible to control the bandwidth and the rejection level by adjusting the size of the two arc-shaped slots.

This novel filter/power divider is constructed by introducing multilayer coupling structure, which can not only divide/combine the power of microwave signals, but also reject unwanted frequency signals to better regulate the performance.

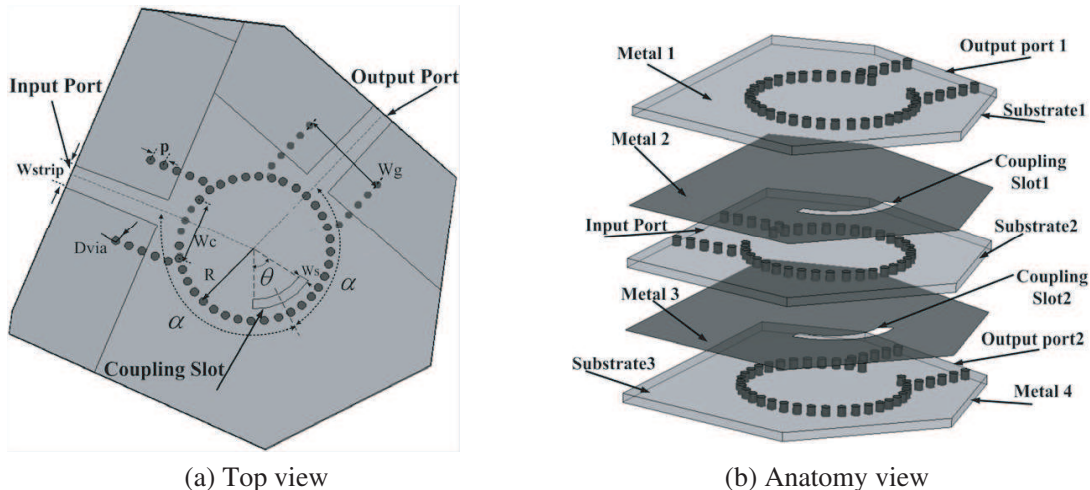


Figure 1: Proposed multilayer dual-mode SICC filter with power divider.

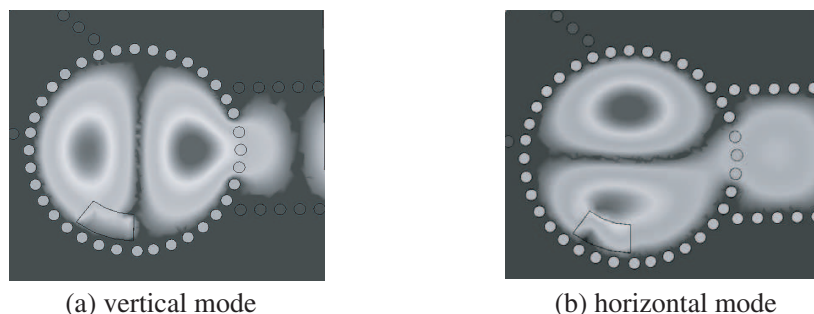


Figure 2: The E -field distribution of the TM₁₁₀ degenerated modes.

Figure 2 shows electrical field distribution of TM₁₁₀ mode in a SICC cavity. There can be two orthogonal degeneration modes, which can be used to realize a dual-mode filter. The coupling apertures and two arc-shaped slots are used to disturb two degenerate modes.

2.3. Design Considerations

Two poles and two transmission zeros can be found in the response of a dual-mode filter with single circular cavity [1]. Two poles below the zero Z_1 are denoted as P_1 and P_2 , respectively, which can be used to control the bandwidth of the passband. The first zero near the passband is denoted as Z_1 , which is approximately equal to the eigenfrequency of the cavity TM₁₁₀ mode. Being so close to the passband, zero Z_1 is very helpful to realize a steeper upper side response. The second pole P_2 is near the zero Z_1 . The space between the zero Z_1 and pole P_2 decides the rolloff slope in the transition band. As shown in Fig. 1, the waveguide located in input/output port can be used to suppress some undesirable response spur and improve the lower stop band characteristic. From the above discussion, the conclusion can be reached that only a few parameters must be concerned, such as the angel α between coupling slots, the position and width of coupling slots d_{slot} and W_C, W_S , θ , the radius of the circular cavity R . According to Fig. 2, for a given angle α , proper parameter W_C/R is limited in a relatively narrow interval. Beyond the limit, either the dual-mode character disappears or the reflection loss worsens. Generally, smaller α and/or smaller W_C/R corresponds to narrower bandwidth and narrower space. In addition, the proper parameter W_C and W_S , d_{slot} assure more poles not to overlap and achieve better response character in passband.

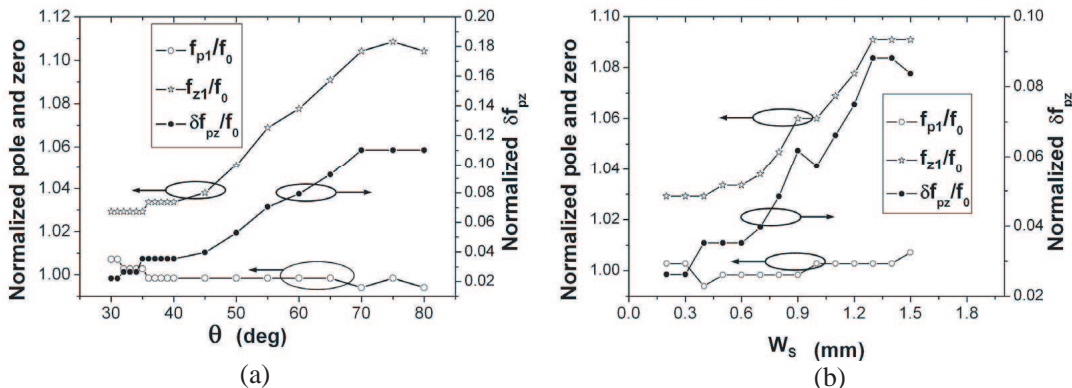


Figure 3: Varying of poles, zero and the distance between pole and zero with W_S or $\theta \cdot f_0 = 27.3$ GHz, $\delta f_{pz} = f_{z1} - f_{p2}$. (a) Varying of P_1 , Z_1 and δf_{pz} with respect to θ , $W_S = 1.2$ mm. (b) Varying of P_1 , Z_1 and δf_{pz} with respect to W_S , $\theta = 37^\circ$.

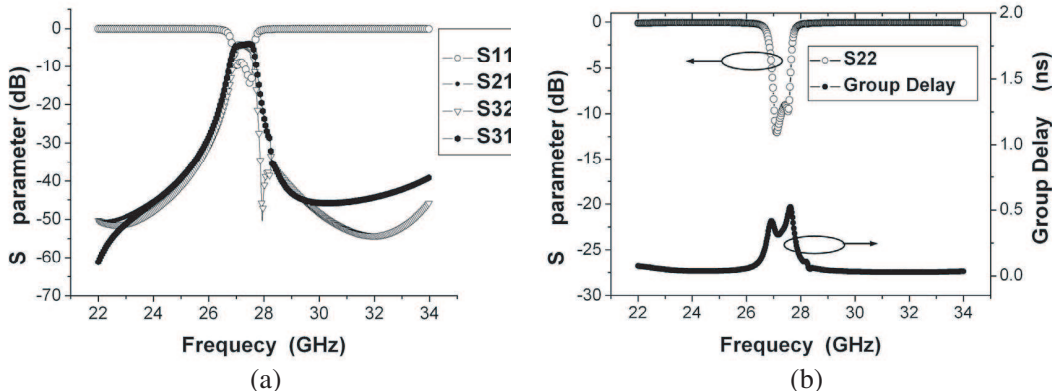


Figure 4: Simulated results of the proposed multilayer dual-mode SICC filter with power divider. (a) Input return loss, insertion loss, isolation. (b) Output return loss, group delay.

Table 1: Parameters of the Filter with Power Divider.

D_{via} (mm)	0.5	W_{strip} (mm)	1.5
p (mm)	0.85	W_g (mm)	6.5
ε_r	2.2	W_c (mm)	3.3
W_s (mm)	1.2	h (mm)	0.508
α (deg)	110	R (mm)	4.55
θ (deg)	37		

2.4. Coupling Aperture

The coupling aperture size determines the amount of coupling for each mode. Fig. 3 illustrate the coupling for the TM₁₁₀ mode when we vary the coupling aperture size W_S and θ . As we can see, the coupling increases when the aperture size is increased. It is then possible to control the bandwidth and the rejection level. When the aperture size is changed, the position of P_1 , P_2 and Z_1 is also modified in frequency because the amount of reactance introduced by the aperture has been changed.

As shown in Fig. 3, the distance between the zero Z_1 and pole P_2 decreases evidently with the width of coupling slots W_s or θ decreased. Meanwhile, small change in the frequency of zero Z_1 . And the more rolloff slope and narrower bandwidth have been obtained in the transition band.

3. SIMULATION RESULTS

To verify the theoretical conclusions above, we designed multilayer dual-mode SICC filter with power divider fabricated with standard PCB process. The proposed filters are designed with the frequency range 22–34 GHz and a center frequency of 27.3 GHz.

After optimization with Ansoft HFSS, the geometry parameters of the proposed filter working in the frequency range 22–34 GHz are listed in Table I. The substrate used for the dual-mode filter is Rogers 5880 with relative permittivity of 2.2 and height of 0.508 mm.

As shown in Fig. 4, the proposed filter/power divider has a center frequency of 27.3 GHz with a bandwidth of 0.85 GHz, and it has a finite transmission zeros at 29.5 GHz. The return loss is greater than 12 dB from 26.8 to 27.6 GHz, while the insertion loss is around 3 dB over the entire band. The insertion loss (the 3 dB power division loss is not included) is less than 0.9 dB from 26.8 GHz to 27.6 GHz. In particular, the out-of-band rejection level is more than 30 dB at the lower stop bands (from 22 to 26 GHz), and more than 45 dB at the upper stopbands (from 29.5 to 34 GHz). The simulated group delays show good linearity within the pass band. The group delay is 0.3 ns at 27.3 GHz within a variation of about 0.2 ns from 26.8 GHz to 27.6 GHz. Obviously, steeper rolloff slope and improved response in the transition band lead to better selectivity in the whole working band.

4. CONCLUSION

A novel multilayer dual-mode SICC filter with power divider has been designed for Ka-band application. Two transmission zeros can be created in this filter, which improve the selectivity of the filter to some extent. Multilayer dual-mode SICC filter/power divider has been firstly realized only by adjusting the coupling aperture located in input/output port and between layers. Meanwhile, it is possible to control the bandwidth and the rejection level by adjusting the position and size of the arc-shaped slots. In addition, the simulated results show that excellent impedance matching at all three ports, amplitude balance at the two output ports, and good out-of-band rejection are observed at the operating band. This novel filter/power divider is very compact and has the advantages of return loss, very low insertion loss, high selectivity.

REFERENCES

1. Tang, H. J., W. Hong, J.-X. Chen, G. Q. Luo, and K. Wu, “Development of millimeter-wave planar dippers based on complementary characters of dual-mode substrate integrated waveguide filters with circular and elliptic cavities” *IEEE Trans. Microw. Theory Tech.*, Vol. 55, No. 4, 776–781, April 2007.
2. Li, R. Q., X. H. Tang, and F. Xiao, “Substrate integrated waveguide dual-mode filter using slot lines perturbation,” *Electron. Lett.*, Vol. 46, No. 12, June 10, 2010.

3. Potelon, B., J. C. Bohorquez, J. F. Favennec, C. Quendo, E. Rius, and C. Person, "Design of ku-band filter based on substrate-integrated circular cavities (SICCs)," *IEEE MTT-S International Microwave Symposium Digest*, 1237–1240, June 2006.
4. Duong, T. H. and I. S. Kim, "Single section Wilkinson type UWB power divider with bandpass filter and DC block characteristics in LTCC technology," *IEEE MTT-S International Microwave Symposium Digest*, 117–120, May 2010.
5. Song, K. and Q. Xue, "Novel ultra-wideband (UWB) multilayer slotline power divider with bandpass response," *IEEE Microwave and Wireless Components Letters*, Vol. 20, No. 1, 13–15, January 2010.
6. Wong, S. W. and L. Zhu, "Ultra-wideband power divider with good in-band splitting and isolation performances," *IEEE Microwave and Wireless Components Letters*, Vol. 18, No. 8, 518–520, August 2008.
7. Shen, W., X. W. Sun, W. Y. Yin, J. F. Mao, and Q. F. Wei, "A novel single-cavity dual mode substrate integrated waveguide filter with nonresonating node," *IEEE Microwave and Wireless Components Letters*, Vol. 19, No. 6, 368–370, June 2009.
8. Wei, Q.-F., Z.-F. Li, L.-S. Wu, W.-Y. Yin, J.-F. Mao, and L. Li, "Compact cross-coupled circular cavity filters using multilayer substrate integrated waveguide," *Electron. Lett.*, Vol. 45, No. 6, March 12, 2009.
9. Deslandes, D. and K. Wu, "Substrate integrated waveguide dual-mode filters for broadband wireless systems," *RAWCON '03, Proceedings*, 385–388, August 2003.
10. Pozar, D. M., *Microwave Engineering*, 2nd Edition, Wiley, New York, 1998.

Design of a Bandpass Filter Using Parallel Coupled Stepped Impedance Resonator Using the Novel Method of Lines

Eman G. E. Ouf¹, Hossam A. Saker¹, Esmat A. F. Abdallah¹, and Hadia M. El-Hennawy²

¹Microstrip Department, Electronics Research Institute, Egypt

²Electronic and Communication Department, Ain Shams University, Egypt

Abstract— The main objective of this paper is to design and analyze a filter at 4 GHz, with bandwidth of 200 MHz to be used in a portable transceiver system. The filter should have short length and suppression of first harmonic to obtain a wide stopband. The analysis is applied using the novel method of line. Also, this analysis is developed by nonequidistant discretization to reduce the discretization window. Based on this algorithm, bandpass filters using parallel coupled stepped impedance resonators are designed and examined. Also, a bandpass filter using the conventional parallel coupled line was designed and examined by this algorithm, to be our reference for comparison. The bandpass filter using parallel coupled stepped impedance resonator was fabricated using thin film technology and photolithographic technique, where good agreement is found between the numerical and experimental results. The filter length is reduced by about 23% compared to the conventional one and the first harmonic was attenuated by about 22 dB.

1. INTRODUCTION

A novel algorithm based on the (GTL) equations and the method of lines was introduced into the EM community in the 1995 to solve waveguide discontinuities in rectangular waveguides and developed in the 1998 to solve planar microstrip circuit discontinuities in the case of isotropic and anisotropic substrates (coplanar) line filter, microstrip line filters, conformal and planar antennas [1, 2]. In this algorithm, the structure is divided into cascaded subsections with respect to the propagation direction and the discretization lines are along the propagation direction of the wave. The advantages of this algorithm are direct evaluation of the scattering parameters, possibility of dealing with open and shielded structures, easy treatment of the excitation, display of all possible modes, higher accuracy, easy treatment of anisotropic materials, and program generalization.

The disadvantages of the coupled line filters are the shift in center frequency arising from the approximations in length calculations, and the increase in longitudinal size of the filter. To overcome these problems, the use of non-uniform transmission line resonators as a filter element was considered.

In this paper, we describe conventional parallel coupled line filters of order one and three and a bandpass filter using parallel coupled stepped impedance resonators with order one and three. Also, the analysis of these filters is applied using the new technique of the method of lines. The bandpass filter using parallel coupled stepped impedance with order three is fabricated and tested, where good agreements is found between the numerical results calculated by the MOL, ready-made software package IE3D Zeland and experimental results.

2. THEORY

2.1. Method of Lines Basic Equations

When dealing with the method of lines, the fields in each region can be expressed as [3]:

$$\vec{H}\eta_o = jk_o^{-1}\vec{\nabla} \times \vec{\Pi}, \quad \vec{E} = \varepsilon_r^{-1}k_o^{-2}\vec{\nabla} \times \vec{\nabla} \times \vec{\Pi} \quad (1)$$

where $\vec{\Pi}$ is the vector potential consisting of two components

$$\vec{\Pi} = \phi_x \vec{e}_x + \phi_y \vec{e}_y \quad \text{And} \quad \varepsilon_r = \varepsilon_r(x, y) \quad (2)$$

The general solution of Equation (1) leads to a consistent system of coupled differential equations of the strum-Liouville type for the potential components ϕ_x and ϕ_y . The coordinates are normalized according to $\bar{X} = k_o X$, $\bar{y} = k_{oy}$, $\bar{z} = k_{oz}$ leading to [3]:

$$\frac{\partial^2}{\partial \bar{z}^2}\phi_x + \frac{\partial^2}{\partial \bar{y}^2}\phi_x + \varepsilon_r \frac{\partial}{\partial \bar{x}} \left[\varepsilon_r^{-1} \left(\frac{\partial \phi_x}{\partial \bar{x}} + \frac{\partial \phi_y}{\partial \bar{y}} \right) \right] + \varepsilon_r \phi_x - \frac{\partial}{\partial \bar{y}} \left(\frac{\partial \phi_x}{\partial \bar{x}} \right) = 0 \quad (3)$$

$$\frac{\partial^2}{\partial \bar{z}^2}\phi_y + \frac{\partial^2}{\partial \bar{x}^2}\phi_y + \varepsilon_r \frac{\partial}{\partial \bar{y}} \left[\varepsilon_r^{-1} \left(\frac{\partial \phi_y}{\partial \bar{y}} + \frac{\partial \phi_x}{\partial \bar{x}} \right) \right] + \varepsilon_r \phi_y - \frac{\partial}{\partial \bar{x}} \left(\frac{\partial \phi_x}{\partial \bar{y}} \right) = 0 \quad (4)$$

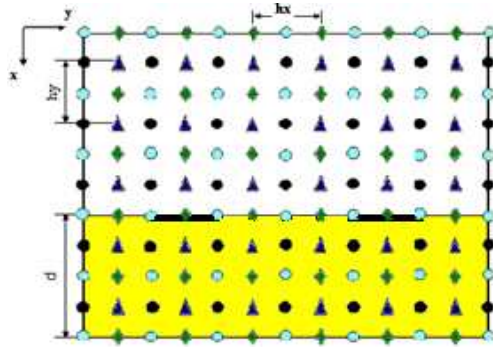


Figure 1: Discretization scheme of the filter cross section.

2.2. Discretization

The area of each section is now subjected to a 2-D discretization under the consideration of the interface and boundary conditions. Fig. 1 shows the planar cross section of the filter at any region with the adequate discretization points. The field components are discretized on different points noting that E_x is discretized together with H_y and E_y together with H_x . The scheme of discretization is executed according to that of [1] resulting in a vector for each field type with a number of elements equals the corresponding discretized lines. The 2-D difference operators and the discretized dielectric constant are constructed by the Kronecker product from the one-dimensional terms; this is described in details in [3, 4] and their symbols are denoted by a hat (^).

The reduced and discretized wave Equations (4) and (5) become:

$$\frac{\partial^2}{\partial \bar{z}^2} \hat{\Pi} - \hat{Q} \hat{\Pi} = 0 \quad \hat{Q} = \begin{bmatrix} Q_{11} & Q_{12} \\ Q_{21} & Q_{22} \end{bmatrix} \quad \hat{\Pi} = \begin{bmatrix} \phi_x \\ \phi_y \end{bmatrix} \quad (5)$$

With Q_{11} , Q_{12} , Q_{21} , and Q_{22} are as defined in [3, 4].

This equation is valid for equidistant discretization scheme. However, nonequidistant discretization is recommended to reduce the discretization window, and consequently the computation time. In this case, the above equation can be used provided that some substitutions are made [4, 5].

2.3. Transformation

Equation (5) represents a system of coupled differential equations, to convert this system to an uncoupled one, we make a transformation by a matrix \hat{T} , where

$$\hat{\Pi} = \hat{T} \hat{\hat{\Pi}}, \quad \hat{T}^{-1} \hat{Q} \hat{T} = \hat{\Gamma}^2 \quad (6)$$

Using (5), (6) we get

$$\hat{\hat{\Pi}}(\bar{z}) = A e^{-\hat{\Gamma} \bar{z}} + B e^{\hat{\Gamma} \bar{z}} \quad (7)$$

A and B denote the amplitudes of the forward and backward going waves and $\hat{\Gamma}$ is a diagonal matrix, containing the normalized propagation constants along the z direction, including the evanescent and propagating modes. Noting that \bar{z} represent a shift of the z co-ordinates as in [1].

2.4. Field Matching

Matching the tangential field components at the interface of each longitudinal section establishes a relation between the amplitudes A and B in all sections. The resulting scattering matrix for one waveguide discontinuity can be carried out as in [6]. For structures with several discontinuities, Equation (7) is used to describe the transformed potential in the inner sections, and the following formulation for the fields in the matching plane.

$$E_t^n = P_e^n \left[\tilde{A}^n \pm \tilde{B}^n \tanh \left(\hat{\Gamma}^n \frac{\pm d^n}{2} \right) \right] \quad \text{And} \quad H_t^n = P_h^n \left[\tilde{B}^n \pm \tilde{A}^n \tanh \left(\hat{\Gamma}^n \frac{\pm d^n}{2} \right) \right] \quad (8)$$

With

$$\tilde{A}^n = A^n \cosh \left(\hat{\Gamma}^n \frac{d^n}{2} \right), \quad \tilde{B}^n = B^n \cosh \left(\hat{\Gamma}^n \frac{d^n}{2} \right)$$

And

$$\mathbf{E}_t = \begin{bmatrix} E_x \\ E_y \end{bmatrix} = P_e \hat{\Pi}, \quad \mathbf{H}_t = \begin{bmatrix} jH_y \\ -jH_x \end{bmatrix} = P_h \hat{\Pi} \quad (9)$$

The different signs in (8) are valued for matching at the right and left sides of the section. The matrices $I_{N\triangleleft}$ are identity matrices [7] of the size of the corresponding reduced line system as shown in Fig. 1.

Different number of lines in neighboring sections caused by different distribution of the metallization require partitioning of the matrices into two submatrices.

The matching procedure of the field components at the interface of any two sections now yields:

$$\mathbf{E}_t^{n-1} = \mathbf{E}_t^n, \quad \mathbf{H}_t^{n-1} = \mathbf{H}_t^n \quad (10)$$

The tangential electric field related to P_e^c at the interfaces should be zero. Solving Equation (10), the transmission factor, A^9 and the reflection factor B^1 are expressed in terms of the incident factor A^1 .

3. NUMERICAL RESULTS

In the uniform coupled microstrip filter, we adjusted its length for a resonance frequency of 4 GHz, the length of coupled lines are adjusted to 7 mm ($\lambda/4$) for ϵ_r (dielectric constant) = 10.2 and h (dielectric height) = 0.635 mm, also the microstrip width and the separation between lines are 0.6 mm and 0.2 mm, respectively to verify 200 MHz bandwidth. A conventional parallel coupled resonator filter with order one is designed and simulated. The resonance frequency occurs at 4 GHz with $S_{11} = -27$ dB, and $S_{21} = -0.53$ dB, also the first harmonic occurs around 8 GHz.

To overcome the first harmonic of the uniform coupled line filter, and also to decrease the size of filter, a stepped impedance resonator (SIR) is used as a nonuniform transmission line resonator. The SIR is symmetrical and has two different characteristic impedance lines Z_1 , Z_2 , of admittance Y_1 and Y_2 . The impedance ratio K is defined as [9]: $K = \frac{Z_2}{Z_1}$

The fundamental resonance condition for the structure can be expressed as [10]:

$$K = \tan \theta_1 \cdot \tan \theta_2 \quad (11)$$

The resonator length

$$\theta_T = 2(\theta_1 + \theta_2) \quad (12)$$

where θ_1 and θ_2 are electrical length of each section. The resonator length has minimum value when $0 < K < 1$ and maximum value when $K > 1$. For practical applications we choose $\theta_1 = \theta_2 = \theta_0$, so that the fundamental resonance frequency is given by:

$$\theta_0 = \tan^{-1} \sqrt{K} \quad (13)$$

The use of a bandpass filter using parallel coupled stepped impedance resonators is considered as shown in Fig. 2. Fig. 3 shows the relation between the scattering parameters (S_{11} , S_{21}) against

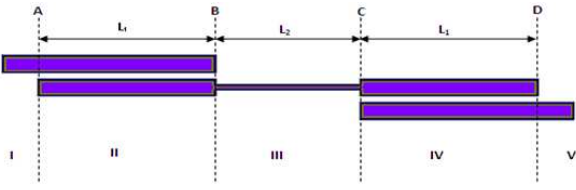


Figure 2: BPF using parallel coupled stepped impedances resonators with $N = 1$.

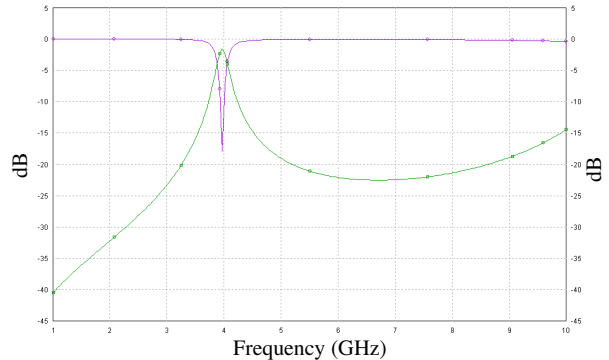


Figure 3: Simulated results (S -parameters magnitude vs. frequency) with $Z_1 = 100 \Omega$, $Z_2 = 50 \Omega$, $\Theta_2 = 43.7^\circ$, $\Theta_1 = 47^\circ$.

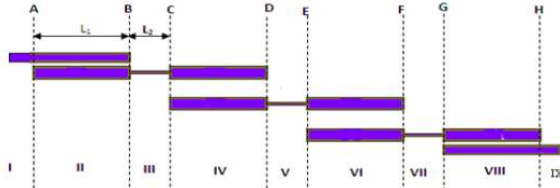


Figure 4: BPF using parallel coupled stepped impedances resonators With $N = 3$.

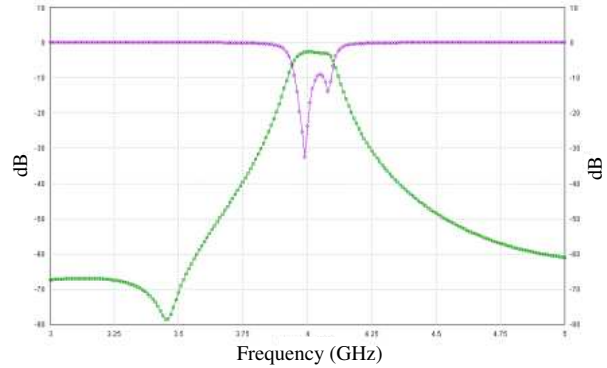


Figure 5: Simulated results (S -parameters magnitude vs. frequency) with $Z_1 = 76.3 \Omega$, $Z_2 = 43 \Omega$, $\Theta_2 = 63^\circ$, $\Theta_1 = 24^\circ$.

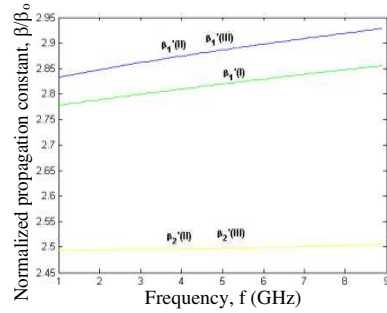


Figure 6: β/β_0 versus f with $L = 7$ mm for first order coupled line filter.

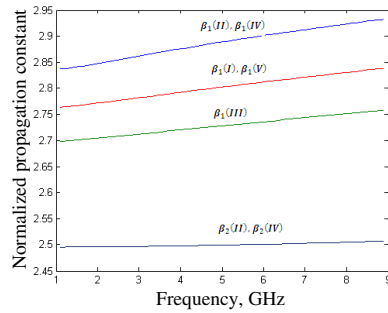


Figure 7: β/β_0 versus f with $L_1 = 4$ mm, $L_2 = 4$ mm, for first order BPF using stepped impedance resonator.

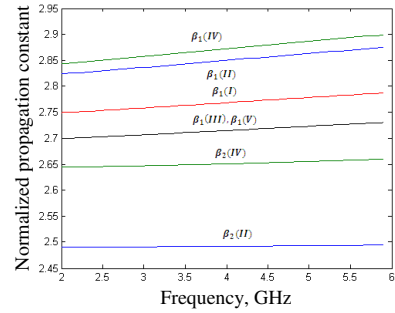


Figure 8: β/β_0 versus f with $L_1 = 5$ mm, $L_2 = 2$ mm, $s_1 = 0.2$ mm $s_2 = 1$ mm $w_1 = 0.6$ mm, $w = 0.8$ mm, or third order BPF using stepped impedance resonator.

frequency for bandpass filter using parallel coupled stepped impedance resonators. It is clear that the resonance frequency at 4 GHz with $S_{11} = -18$ dB, and $S_{21} = -0.53$ dB, also it is clear that the first harmonic is reduced by -22 dB and 23% size reduction is achieved. Fig. 4 shows a parallel coupled stepped impedance filter for $N = 3$, while Fig. 5 shows the simulated S_{11} and S_{21} .

3.1. Propagation Constant

In Figs. 6, 7, and 8, normalized propagation constants of the fundamental mode calculated for different values of input frequencies for each section of the conventional coupled line bandpass filter, and bandpass filter using parallel coupled stepped impedance resonators ($N = 1$, $N = 3$). It is clear that as the frequency increases, the normalized propagation constant increases. In Fig. 6 there are two propagating waves in layers II and III due to the existence of two coupled strip lines while there is only one propagating mode in layer I. In Fig. 7 there are two propagating waves in layers II and IV due to the existence of two coupled strip lines while there is only one propagating mode in layer I and III. In Fig. 8 there are two propagating waves in layers II, IV, VI, and VIII while there is only one propagating mode in layer I, III, V, and VII, for the same reason stated above.

3.2. Filter Performance

In conventional parallel coupled line BPF and BPF using parallel coupled stepped impedance resonators ($N = 1$), the variation of the scattering parameters (S_{21} & S_{11}) against frequency are shown in Fig. 9 and Fig. 10. These results were compared to those obtained by IE3D Zeland and very good agreement of both results was obtained. A BPF with parallel coupled stepped impedance resonators ($N = 3$) was fabricated as shown in Fig. 12, and its performance was measured using HP8719ES vector network analyzer. S_{21} and S_{11} against frequency are plotted together with the results of IE3D and MOL in Fig. 11. It should be noted from the figure that the experimental

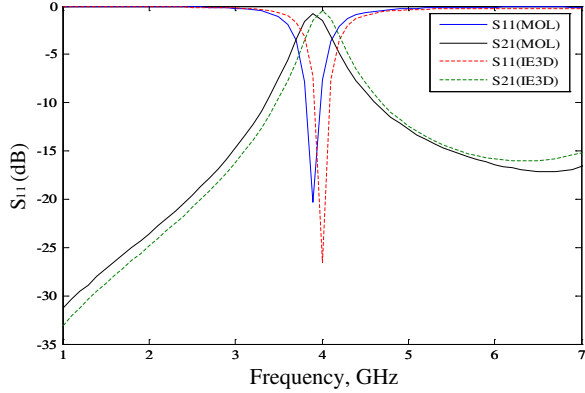


Figure 9: Numerical results using MOL and IE3D Zeland for conventional parallel coupled line BPF ($N = 1$).

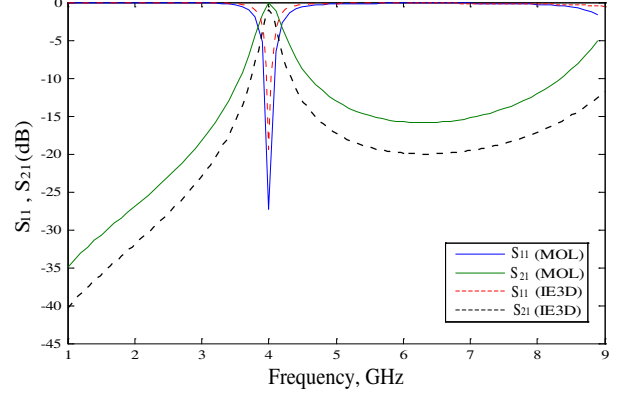


Figure 10: Numerical results using MOL and IE3D Zeland for BPF using parallel coupled stepped impedance resonator ($N = 1$).

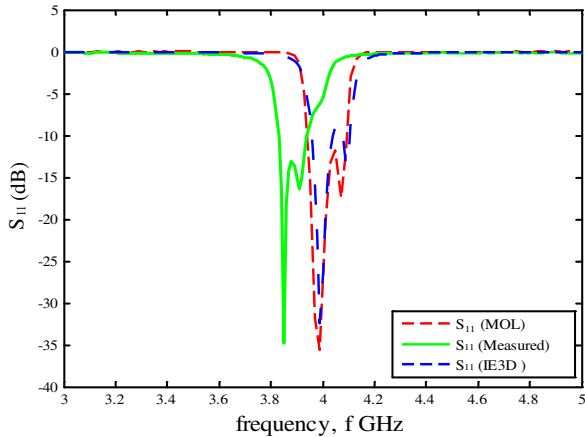


Figure 11: Numerical results using MOL, IE3D zeland, and measurement of S_{11} , S_{21} versus frequency for BPF using parallel coupled stepped impedance resonator ($N = 3$).

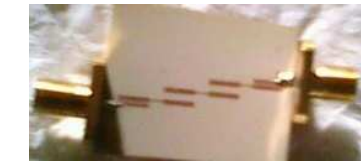


Figure 12: Fabricated BPF using parallel coupled stepped impedance resonator ($N = 3$).

measurements and the numerical results obtained by the MOL are in good agreement. The small difference between the numerical and experimental results can be attributed due to losses from the connecting cables and from the critical dimensions. Also, the soldering of SMA connectors has undetectable effect. It is clear that the resonance frequency of the fabricated BPF filter is 3.85 GHz and scattering parameters $S_{11} = -34$ dB and $S_{21} = -2.9$ dB.

4. CONCLUSION

In this article, the analysis and design of BPF using parallel coupled stepped impedance resonators with $N = 1\&3$, and BPF using the conventional parallel coupled lines were performed using the novel method of lines. Method of lines is developed by the (GTL) equations to find a wide range of longitudinal applications. A ready-made electromagnetic simulator was used to verify the numerical results. The filter is designed and its dimensions are optimized for small size and for first harmonic suppression then it is fabricated and measured. Good agreement is found between the numerical and experimental results.

REFERENCES

1. Vietzorreck, L. and R. Pregla, "Hybrid analysis of 3-d mmic elements by the methods of lines," *IEEE Trans. on Microwave Theory Tech.*, Vol. 44, 2580–2586, 1996.
2. Strassner, B. and K. Chang, "New wide-band DC-block cymbal bandpass filter," *IEEE Trans. on Microwave Theory Tech.*, Vol. 50, 1431–1432, 2002.
3. Pregla, R., "MOL-bpm method of lines based beam propagation method," *Progress In Electromagnetic Research*, Vol. 11, 51–102, 1995.
4. Pregla, R. and W. Pascher, "The method of lines," *T. Itoh (Ed.), Numerical Techniques for Microwave and Millimeter Wave Passive Structures*, 381–446, Wiley, New York, 1989.
5. Diestel, H. and S. Worm, "Analysis of hybrid field problems by the method of lines with nonequidistant discretization," *IEEE Trans. on Microwave Theory Tech.* Vol. 32, 663–638, 1984.
6. Vietzorreck, L. and R. Pregla, "Analysis of discontinuities in microwave circuits with a new eigenmode algorithm based on the method of lines," *25th European Microwave Conference*, 804–808, Bologna, Italy, September 1995.
7. Wilfrid P. and R. Pregla, "Full wave analysis of complex planar microwave structures," *Radio Sci.*, Vol. 22, 999–1002, 1987.
8. Hashish, E. A. and H. A. Saker, "Optimization of microstrip coupled lines bandpass filters using the method of lines and the neural network technique," *Twentieth National Radio Sceince Conference*, 18–20, Cairo, Egypt, March 2003.
9. Mongia, R., I. Bahi, and P. Bhartia, *RF and Microwave Coupled-line Circuits*, 1999.
10. Makimoto, M. and S. Yamshita, "Compact bandpass filters using stepped impedance resonators," *Proc. IEEE*, Vol. 67, 16–19, January 1979.
11. Abas, A. A., H. A. Saker, E. A. Abdallah, and H. M. El-Henawy, "Design of a periodically nonuniform coupled microstrip lines (PNCML) filter using the novel method of lines," *Microwave and Optical Technology Letters*, Vol. 51, 2865–2870, No. 12, December 2009.

A High-Q CMOS Tunable Notch Filter

Sen Wang and Bo-Zong Huang

Department of Electronic Engineering, National Taipei University of Technology, Taipei, Taiwan

Abstract— A high Q CMOS tunable notch filter incorporating a semi-passive inductor is presented in this paper. The semi-passive inductor uses a tapped-inductor feedback to achieve a negative resistance, and then compensate the resistive losses of the inductor. Compared with conventional transformer feedback architectures, the proposed technique not only compensates resistive losses with low-power consumption but also provides a high-inductance inductor. The simulated peak Q of the semi-passive inductor based on a standard 0.18 μm CMOS process is about 150 at 9.7 GHz, and the Q factor at 7 GHz is above 50 which is further applied to a notch filter design. The notch filter can be operated from 6.84 GHz to 7.86 GHz with 1.02 GHz tuning range, and the Q factors of the filter with less than 1.2 mW power consumption are above 240 demonstrating a good notching performance. The feasibility of the proposed semi-passive inductor is believed that it is well suited for further practical RF designs such as bandpass filters or VCOs.

1. INTRODUCTION

Advance in digital and analog circuits makes CMOS technology draws much attention at radio frequencies (RF). The advantages of CMOS RFICs provide not only lower cost, but also a single-chip solution for wireless communication systems. However, poor Q -factor of CMOS inductors limits the applications of RFICs such as filters and VCOs [1, 2]. Recently, many active inductors take advantage of CMOS transistors to realize superior Q factors [3, 4]. The main attributes of the inductors include their small size and high Q factors compared with passive inductors, and can be a tunable design. However, the active inductor is a purely transistor-based technique which consumes high-power consumption. In addition to purely passive and active inductors, many semi-passive inductors consisting of MOS transistors and passive inductors or transformers are presented [5, 6]. The transformer feedback reported in [5, 6] use the magnetic coupling between primary and secondary inductors of the transformer and transistors to compensate the resistive losses of the primary inductor.

In this paper, we present a tunable notch filter which is difficult to be fully integrated into CMOS transceivers. The notch filter using a tapped-inductor feedback technique to achieve a high- Q inductor [7] makes the filter achieve a good frequency rejection, and then can be used as an image rejection filter in a superheterodyne transceiver [8]. The design will be detailed in the following sections. In Section 2, the circuit design of the proposed circuits is discussed. The simulated results are also reported in Section 3. Finally, Section 4 concludes this work.

2. CIRCUIT DESIGN

Figure 1 illustrates schematic of the proposed semi-passive inductor using a tapped-inductor feedback technique. V_G and V_D are the bias for the gate and drain terminals of M_1 , respectively. R is a high-resistive resistor providing RF signal blocking, and eliminating the need for an RF choke. C_1 not only provides a gate bias point but also results a 90° phase difference between i_1 and i_2 . The tapped-inductor is tapped to the source of M_1 and to L_2 resulting in a current flow $i_1 + i_2$ into L_2 . The current flow and the mutual inductance will increase the equivalent inductance of the circuit drastically. Moreover, the 90° phase difference between i_1 and i_2 , and mutual inductance M result in a negative resistance from the feedback loop. Based on the small-signal, the input impedance Z_{in} of the proposed semi-passive inductor can be expressed as

$$Z_{in} = \left(R_1 + R_2 - \frac{Mg_m}{C_3} - \frac{L_2g_m}{C_3} \right) + j\omega \left(L_1 + L_2 + 2M + \frac{g_mR_2}{\omega C_3} \right) \quad (1)$$

The real part of Z_{in} consists of resistive losses of L_1 and L_2 , and negative resistance related to M , L_2 , g_m and C_3 . Conceptually, the overall resistive losses of Z_{in} can be compensated by the proper mutual inductance of M and inductance of L_2 , a high- Q inductor can be achieved equivalently. Typically, L_2 is larger than M with limited coupling coefficient. Therefore, the negative resistance term generated by L_2 is larger than the term generated by M with the same g_m and C_3 . In other

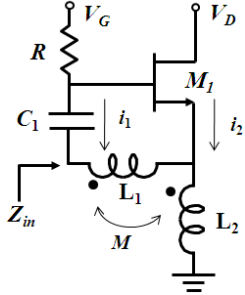


Figure 1: The proposed semi-passive inductor using a tapped-inductor feedback technique.

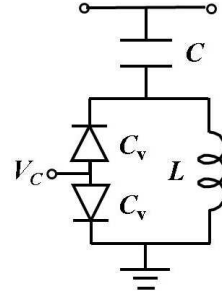


Figure 2: Schematic of the high- Q notch filter using the proposed semi-passive inductor.

words, the proposed technique is believed that the semi-passive inductor is a low-power design compared with conventional transformer feedback architectures.

The semi-passive inductor is a one-port element, or a grounded inductor. The grounded inductor is suitable for a notch filter design. Fig. 2 shows the high- Q CMOS tunable notch filter. The notch filter consists of the grounded inductor L , a pair of varactors, and a capacitor. The L is designed by the semi-passive inductor to achieve a good notch response, and the varactors are added to the resonator to control the notch frequencies. Moreover, the addition of the varactors provides higher rejection response than the pure LC series network. The input impedance (Z) and the notch frequency (f_n) of the notch filter can be expressed as (2) and (3), respectively. Therefore, the notch frequency can be tuned by the capacitance of the varactors (C_v).

$$Z = j \left[\frac{\omega^2 L (C + C_v/2) - 1}{\omega C (1 - \omega^2 L C_v/2)} \right] \quad (2)$$

$$f_n = \frac{1}{2\pi\sqrt{L(C + C_v/2)}} \quad (3)$$

3. SIMULATION RESULTS

The design is based on $0.18\text{ }\mu\text{m}$ TSMC CMOS process which provides single poly layer and six metal (1P6M) layers (from M_1 to M_6 layers.) for interconnection. Capacitors are all designed from M_1 to M_5 , and the tapped-inductor is designed on the top metal layer (M_6) for reducing resistive losses. The R , C_1 , V_D , and aspect ratio of M_1 in Fig. 1 are $10\text{ k}\Omega$, 2 pF , 0.8 V , and $(32\text{ }\mu\text{m}/0.18\text{ }\mu\text{m})$, respectively. And V_G is a bias control for achieving different power consumption. Moreover, the C , L , and tuning range C_v of the notch filter are 0.21 pF , 2.1 nH , and $(0.047\text{ pF}–0.125\text{ pF})$, respectively. Therefore a tunable notch filter around 7 GHz is achieved.

The negative resistance of the inductor could affect the stability of the circuit. Fig. 3 shows the one-port simulation of the semi-passive inductor under different bias condition. The blue line represents the semi-passive inductor consuming 2 mW power locates outside the unit circle of the Smith Chart as shown in Fig. 3. The red line represents the semi-passive inductor consumes 1.2 mW which is operated stably within the unit circle of the Smith Chart to achieve a high- Q factor. The corresponding inductance and Q factor of the red line can be extracted as shown in Fig. 4. The inductance is about 2.2 nH around 7 GHz , and the self-resonant frequency is 11.7 GHz . The peak Q of the semi-passive inductor is about 150 at 9.7 GHz , and the Q factors at 7 GHz are above 50 which are applicable to a good notch filter design.

Figure 5 shows the simulated frequency response of the notch filter. The notch frequency is at 7.1 GHz with 25.5 dB rejection. As shown in Fig. 5, a quality factor (Q_n) of notch filters can be calculated from the following equation.

$$A_{\text{dB}} = 20 \log \left(\frac{Q_n \cdot \Delta f_{3\text{dB}}}{f_n} + 1 \right) \quad (4)$$

where A_{dB} , $f_{3\text{dB}}$, and f_n represent rejection, 3 dB bandwidth, and notch frequency of the filter, respectively. Fig. 6 demonstrates the rejection of the filter under different varactor bias and power consumption, and the corresponding Q_n of each notch frequency are also shown. The Q_n are all more than 240 representing the feasibility of the filter using the proposed high- Q semi-passive

inductor. Moreover, the tuning range of the filter is about 1.02 GHz (from 6.84 GHz to 7.86 GHz). The corresponding current flow at 7.6 GHz, 7.1 GHz, and 6.84 GHz are 1.2 mA, 1.4 mA, and 1.5 mA, respectively. The filter operates at low frequencies consuming more power to maintain high Q_n factors since there are more resistive losses of the inductor at low frequencies. The NF of the filter under different bias conditions is shown in Fig. 7. The NF of each notch frequency is above 35 dB representing a good notching performance. In summary, the high- Q and tunable notch filter incorporating the semi-passive inductor require low-power consumption which is less than 1.2 mW ($0.8 \text{ V} \times 1.5 \text{ mA}$).

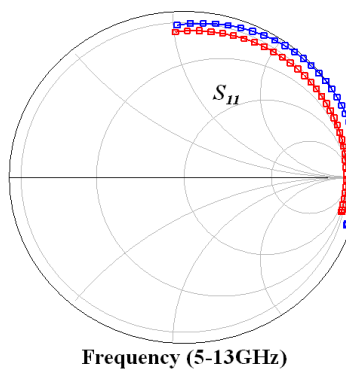


Figure 3: S_{11} of the semi-passive inductor under different bias condition.

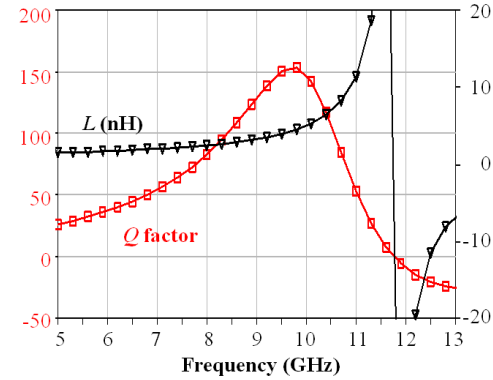


Figure 4: Q factor and inductance of the semi-passive inductor at stable region.

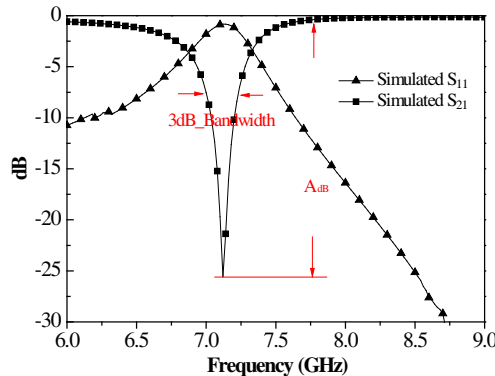


Figure 5: Simulated S_{11} and S_{21} .

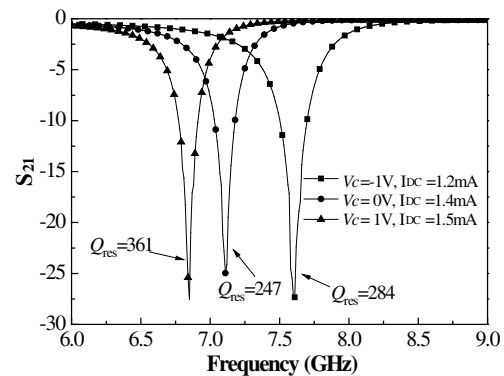


Figure 6: Simulated S_{21} under different bias conditions.

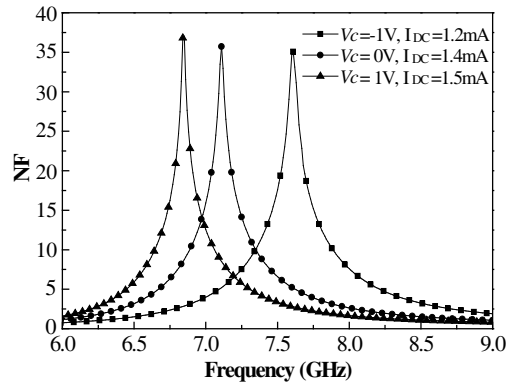


Figure 7: Simulated NF under different bias conditions.

4. CONCLUSION

A frequency-tunable notch filter incorporating a Q -enhanced inductor and a pair of varactors is described in this paper. The semi-passive inductor mainly consists of a NMOS, a capacitor, and a tapped inductor. The tapped-inductor feedback technique not only compensates resistive losses with low-power consumption but also provides a high inductance. The technique is successfully applied to the notch filter design based on a typical $0.18\text{ }\mu\text{m}$ CMOS process. The notch filter demonstrates a good rejection and NF response with low-power consumption. Finally, it is believed that the semi-passive inductor is suitable for further practical applications.

ACKNOWLEDGMENT

The authors would like to thank the National Science Council (NSC) and Chip Implementation Chip (CIC) of Taiwan for financial and technical supports.

REFERENCES

1. He, X. and W. B. Kuhn, "A 2.5-GHz low-power, high dynamic range self-tuned Q -enhanced LC filter in SOI," *IEEE J. Solid-state Circuits*, Vol. 40, 1618–1628, 2005.
2. Wang, T.-P., R.-C. Liu, H.-Y. Chang, L.-H. Lu, and H. Wang, "A 22-GHz pushpush CMOS oscillator using micromachined inductors," *IEEE Microw. Wireless Compon. Lett.*, Vol. 15, 859–861, 2005.
3. Guthrie, B., J. Hughes, T. Sayers, and A. Spencer, "A CMOS gyrator low-IF filter for a dual-mode Bluetooth/ZigBee transceiver," *IEEE J. Solid-state Circuits*, Vol. 40 1872–1879, 2005.
4. Lu, L.-H., Y.-T. Liao, and C.-R. Wu, "A miniaturized Wilkinson power divider with CMOS active inductors," *IEEE Microw. Wireless Compon. Lett.*, Vol. 15, 775–777, 2005.
5. Soorapanth, T. and S. S. Wong, "A 0-dB IL 2140 ± 30 MHz bandpass filter utilizing Q -enhanced spiral inductors in standard CMOS," *IEEE J. Solid-state Circuits*, Vol. 37, 579–586, 2002.
6. Huang, K.-K., S. Wang, and C.-K. C. Tzuang, "Active bandpass filter using transformer feedback in $0.18\text{-}\mu\text{m}$ CMOS for 802.11a wireless LAN," *IEEE Int. Symp. on Circuits and Systems*, 18–21, Seattle, USA, 2008.
7. Wang, S. and R.-X. Wang, "A tunable bandpass filter using Q -enhanced and semi-passive inductors at S-band in $0.18\text{-}\mu\text{m}$ CMOS," *Progress In Electromagnetics Research B*, Vol. 28, 55–73, 2011.
8. Nguyen, T.-K., N.-J. Oh, C.-Y. Cha, Y.-H. Oh, G.-J. Ihm, and S.-G. Lee, "Image-rejection CMOS low-noise amplifier design optimization techniques," *IEEE Trans. Microw. Theory Tech.*, Vol. 53, 538–547, 2005.

Novel Millimeter-wave Power Combining Utilizing Wafer Level Packaging Technology

Yingqian Huang, Xinyi Hu, Jinfang Zhou, Zhiguo Shi, and Kangsheng Chen

Department of Information Science & Electronic Engineering, Zhejiang University, Hangzhou, China

Abstract— It is extremely difficult to obtain high output power with silicon based processes, which presents one of the greatest challenges for realizing fully integrated transceivers, especially at millimeter-wave frequencies. For this reason, various power combining methods have been proposed to achieve higher power levels.

In this paper, a novel power combining method suitable for millimeter-wave applications is presented. The power combining network is synthesized in package utilizing wafer level packaging technology, with an array of power sources of moderate output power capability assumed to be distributed on chip, which means applying further combining in addition to existing on-chip power combining scheme for potentially even higher output power is possible.

The power combining network is composed of more basic power combining units, each consisting of one substrate integrated waveguide (SIW) resonator coupling four $\lambda/4$ standing-wave resonators, which can be synthesized using two quarter-wavelength vertical vias with one end open and the other end shorted. For power combining purpose, the open end of each $\lambda/4$ resonator is connected to the differential output of one on-chip power source, while the shorted end is realized using one of the two metal plates of the SIW resonator. The coupling between the SIW resonator and $\lambda/4$ resonators is through slotting on the metal plate to allow magnetic leakage so that oscillation in $\lambda/4$ resonators will excite the SIW resonator to oscillate. As the quality factor of the SIW resonator is much larger than those of $\lambda/4$ resonators, energy is mainly confined in the cavity of the SIW resonator so that power combining is achieved.

Example design for 60 GHz application is detailed in the paper with simulation results using commercial CST software showing the effectiveness of the power combining method.

1. INTRODUCTION

Obtaining high output power with silicon based processes has remained difficult for circuit designer, especially at millimeter-wave frequencies. With the aggressive scaling of today's nm-scale transistors, achieving sufficient output power has become even more difficult for a power amplifier considering the lower supply voltage, which presents one of the greatest challenges for realizing fully integrated transceivers. To accommodate for the output power requirements of those newest wireless standards, one possibility is to employ various power combining schemes.

In [1], distributed active transformer was invented for power combining and impedance transformation for lower gigahertz applications. Later, a transmission-line transformer based version was proposed to facilitate millimeter-wave applications [2]. In [3], the concept of electrical funnel was used for SiGe BiCMOS 85 GHz power amplifier design. Besides, researchers at UCB have also tried to utilize the classic Wilkinson combiner for designing 60 GHz power amplifier [4]. All these power combining schemes belongs to on-chip power combining.

In this paper, a novel power combining method suitable for millimeter-wave applications is presented. The key feature which distinguishes it from the aforementioned power combining schemes is that power combining is performed in package instead, i.e., the whole power combining structure resides in chip package and can be synthesized utilizing wafer level packaging technology. Comparing to on-chip power combining, in-package power combining scheme has the additional advantages of easier manufacturing, lower loss, and relaxed heat dissipation requirement. Moreover, in-package power combining can be applied in addition to existing on-chip power combining, which provides the possibility to enhance the effective output power even higher.

The system architecture and principle of in-package power combining is depicted in Section 2. Simulation results of example design for 60 GHz applications are presented in Section 3. Finally, some conclusion remarks are provided in Section 4.

2. PRINCIPLES AND CIRCUIT DESIGN

2.1. Architecture and Power Combining Principle

Figure 1 illustrates the system architecture of the in-package power combining scheme. It is assumed that multiple power sources with moderate output power capability are distributed on chip.

Each power source has differential output which is routed to a pair of pads for connecting to a quarter-wavelength ($\lambda/4$) standing-wave resonator in the package. Further, the $\lambda/4$ standing-wave resonators are magnetically coupled to one substrate integrated waveguide (SIW) resonator for power combining. The structure of one SIW resonator coupling multiple $\lambda/4$ standing-wave resonators constitutes the basic power combining unit. In Figure 1, the SIW resonator is shown to be coupling with four $\lambda/4$ standing-wave resonators.

The most compact $\lambda/4$ standing-wave resonator configuration is a differential transmission line of quarter-wavelength with one end open and the other end shorted. The on-chip power sources output is connected to the open end of each $\lambda/4$ standing-wave resonator, while the shorted end is actually one of the two metal plates of the SIW resonator. The coupling between the SIW resonator and the $\lambda/4$ standing-wave resonators is achieved through slotting on the metal plate which allows for magnetic field leakage.

The power combining principle can be explained as follows. Energy from the on-chip power sources is injected to the $\lambda/4$ standing-wave resonators and excites the resonators to oscillate. At the short end, the magnetic field is at its maximum and the electric field minimum. Due to the coupling slots on the metal plate, magnetic field is leaked into the SIW resonator, exciting the SIW resonator to oscillate too. As will be shown later, the quality factor of the SIW resonator is much larger than those of the $\lambda/4$ resonators, so that almost all the energy is focused in the cavity of the SIW resonator. In other words, power combining is achieved. Since the field distribution pattern inside the SIW resonator is the same as that of a conventional TE101-mode waveguide resonator, the basic power combining unit is also called “TE101- $\lambda/4$ power combining unit”.

One of the most notable features of the so-called TE101- $\lambda/4$ power combining unit is that larger power combining network can be composed with ease by coupling the basic units together. As shown in Figure 2, two TE101- $\lambda/4$ power combining units are coupled to enable the combining of power from seven on-chip power sources. However, due to the specific structure of the TE101- $\lambda/4$ power combining unit, all the power sources are required to distribute on chip in an array, so care must be taken when designing the power sources.

In Figure 1, output waveguide is employed for outputting the combined power. Practically, electric probe can be used to output the power directly and excite an antenna. The latter configuration is especially suitable when more than one power combining units are involved and the excitation of an antenna array is needed.

2.2. Structure and Circuit Synthesize

The detailed structure of the proposed power combining network comprising two TE101- $\lambda/4$ power combining units is illustrated in Figure 2. The whole network resides in chip package and wafer level packaging technology is utilized for circuit synthesis and manufacture.

The quarter-wavelength of differential transmission line comprising the $\lambda/4$ standing-wave resonator is actually a pair of vertical metallized vias. As described earlier, at the open end there is

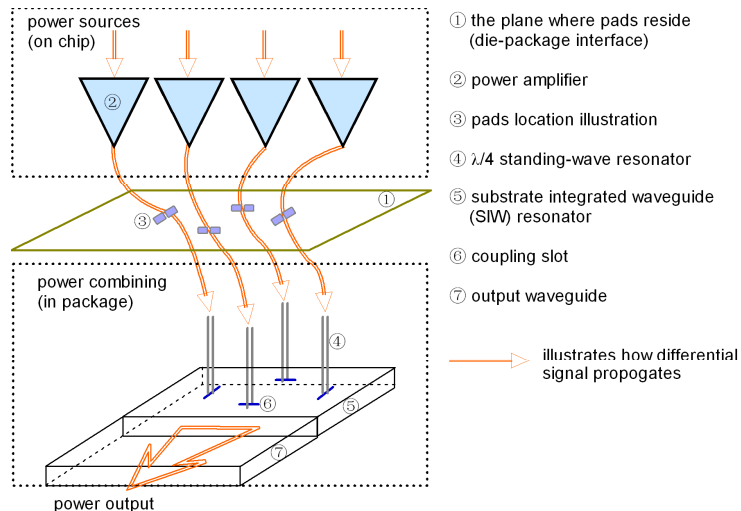


Figure 1: In-package power combining scheme.

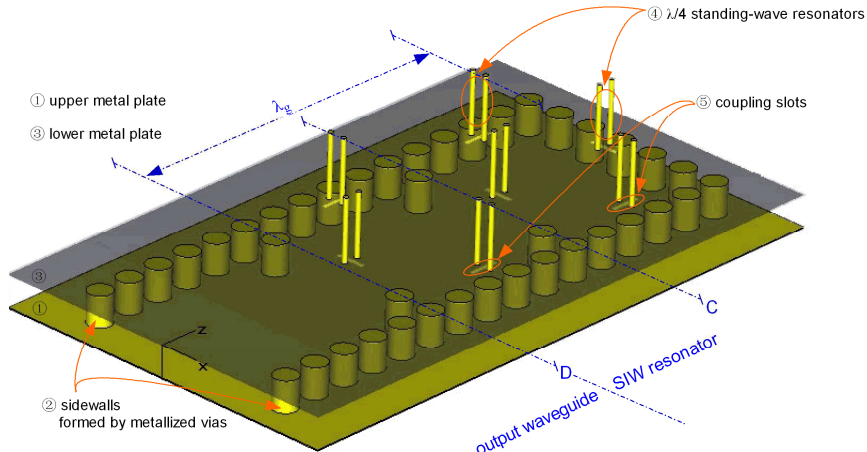


Figure 2: Power combining network comprising two TE101- $\lambda/4$ power combining units.

Table 1: Design parameters for TE101- $\lambda/4$ power combining unit.

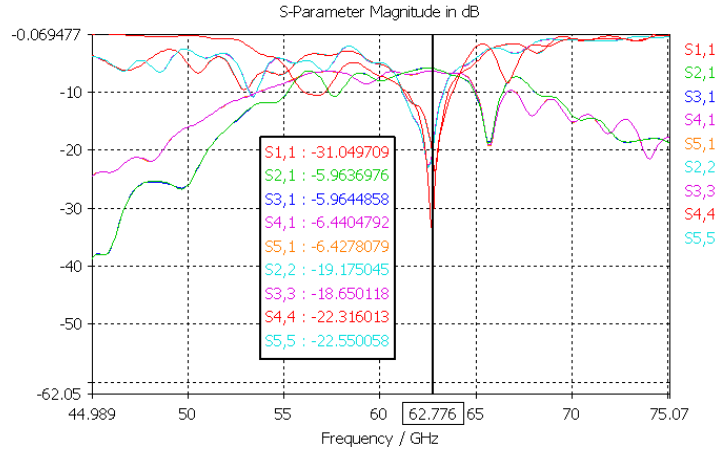
design parameters		value
half-wavelength SIW resonator	cavity width	1768 μm
	cavity length ($\lambda_g/2$)	1768 μm
	cavity height	500 μm
$\lambda/4$ standing-wave resonator	via diameter	20 μm
	via spacing	80 μm
	via length	533 μm
coupling slot	width	30 μm
	length	90 μm
packaging material	dielectric permittivity	4
	dielectric loss tangent	7.49×10^{-5} @60 GHz
	metal	copper

a pair of pads, to which the output of an on-chip power source is connected. Experimental results show that the quality factor of such $\lambda/4$ standing-wave resonator can be almost ten times higher than the on-chip microstrip-based counterpart at 60 GHz. This can be explained largely by the lower loss of packaging material comparing to the chip substrate and the vertical placement of the resonator which eliminates the coupling from the lossy substrate further.

The SIW resonator is composed of the two (upper/lower) metal plates, and array of vertical metallized vias serving as the sidewalls. In Figure 2, the two half-wavelength SIW resonators with each belongs to one power combining unit can also be viewed as one one-wavelength resonator as a whole. The two additional vias placed at the boundary of the two half-wavelength SIW resonators ensure that each resonator excites TE101 mode, or, only TE102 mode exists in the one-wavelength SIW resonator. Results also show that the quality factor of the SIW resonator is more than 1000, which is one order of magnitude higher than that of the $\lambda/4$ standing-wave resonator. So the operating frequency is determined mainly by the size of the SIW resonators, and almost all the energy is confined inside the resonators cavity.

2.3. Example Circuit Design

Example circuit has been designed for verification of the power combining network for 60 GHz applications. Firstly extensive simulations are performed for SIW resonator and $\lambda/4$ standing-wave resonator using commercial CST software to determine the optimal parameters values respectively. Based on the results obtained, the whole TE101- $\lambda/4$ power combining unit is designed. The key design parameters are listed in Table 1.

Figure 3: Simulated S -parameters results.

3. RESULTS

With the parameters values listed in Table 1, the whole structure operates at 62.5 GHz and the quality factor of the SIW resonator alone is simulated to be 1270. When loaded by four $\lambda/4$ standing-wave resonators, the quality factor becomes 642. Field distribution pattern inside the SIW resonator cavity also proves that only TE101-mode is excited. S -parameters results are shown in Figure 3 where port 1 refers the output waveguide and ports 2–5 denote the four open ends of the $\lambda/4$ standing-wave resonators. It can be seen that the reflection coefficients at all ports are below -18 dB, and the transfer coefficients from port 1 to all the other ports are close to the ideal theoretical value of -6 dB, which is in agreement with the design anticipation.

4. CONCLUSION

In this paper, a novel in-package power combining scheme suitable for millimeter-wave applications is presented. Example circuit is designed with simulation results using commercial CST software showing the viability of the proposed method. With the advance of technologies such as wafer level packaging, since in-package power combining provides additional advantages such as easier manufacture, lower loss, and relaxed heat dissipation requirement, further study is deserved.

ACKNOWLEDGMENT

This research is financially supported by National Natural Science Foundation of China with grant Nos. of 60801004 and 61071064.

REFERENCES

1. Aoki I., S. D. Kee, et al., “Distributed active transformer — A new power-combining and impedance-transformation technique,” *IEEE Transactions on Microwave Theory and Techniques*, Vol. 50, No. 1, 316–331, 2002.
2. Niknejad, A. M., M. Bohsali, et al., “Integrated circuit transmission-line transformer power combiner for millimetre-wave applications,” *Electronics Letters*, Vol. 43, No. 5, 290–291, 2007.
3. Afshari, E., H. Bhat, et al., “Electrical funnel: A broadband signal combining method,” *IEEE International Solid-state Circuits Conferences*, 751–760, San Francisco, USA, Feb. 2006.
4. Bohsali, M. and A. M. Niknejad, “Current combining 60 GHz CMOS power amplifiers,” *IEEE Radio Frequency Integrated Circuits Symposium 2009*, 31–34, Boston, USA, Jun. 2009.

Input Signal Distribution Using Coupled $\lambda/2$ Standing-wave Oscillators for Coherent Power Combining

Yingqian Huang, Xi Zi, Jinfang Zhou, and Kangsheng Chen

Department of Information Science & Electronic Engineering, Zhejiang University, Hangzhou, China

Abstract— One of the key challenges to realize a fully integrated transceiver using silicon based processes is the limited output power achievable, especially at millimeter-wave frequencies. Higher output power can be obtained by using various power combining schemes, which typically sum the output power of N identical amplifying stages coherently. Thus to ensure efficient power combining, the input signal must be distributed to all the amplifying stages on the chip with equi-phase and equi-magnitude. While Wilkinson power splitter has been employed for this purpose in the literatures, it becomes bulky and inefficient when N is large, which severely limits the number of outputs that can be combined.

In this paper, a network of coupled $\lambda/2$ standing-wave oscillators is employed to distribute the input signal. Proposed formerly for global clock distribution, theoretically, differential signals of equi-frequency, equi-phase, and equi-magnitude can be obtained by taping onto specific points in the network. It should be noted, however, that the network is especially suited for input signal distribution purpose here, since the specific power combining scheme assumes that a grid of N amplifying stages resides on the chip, which matches to the tap points in a perfect way.

A 30 GHz prototype network comprised of four coupled $\lambda/2$ standing-wave oscillators using TSMC 0.18 μm CMOS process has been design. Post-layout simulation results are presented showing that no distinguishable difference in frequency, phase, and amplitude is observed for the multiple output differential signals. The chip has a total area (including pads) of $800 \times 990 \mu\text{m}^2$ and has been submitted for fabrication.

1. INTRODUCTION

With the recent aggressive scaling of technology, there have been tremendous efforts devoted for the development of radio frequency and even millimeter-wave circuits with silicon-based processes. One of the main challenges for realizing a fully integrated transceiver is the limited output power achievable. To obtain higher output power, miscellaneous power combining schemes have been proposed, which include those based on $N : 1$ transformer [1], utilizing electrical funnel [2], or the classic Wilkinson combiner [3]. However, almost all these schemes employ coherent power combining, which requires that the input power sources are in-phase with each other for combining efficiency. In [4], a 2-to-1 Wilkinson power splitter is used at the input and a combiner at the output for designing a 60 GHz power amplifier with 90nm CMOS process. While presenting much more difficulty in circuit design and layout, the in-phase requirement also highly limits the total number of power sources to be combined.

In [5], a novel in-package power combining scheme suitable for millimeter-wave applications has been proposed, which assumes all the power sources distributed on chip in a grid form. For this purpose, a network of coupled $\lambda/2$ standing-wave oscillators (SWOs) has been designed for input signal distribution. By taping onto specific points in the network, differential signals of equi-frequency, equi-phase, and equi-magnitude can be obtained for further amplification. Moreover, the tap points match the expected power sources locations in a perfect way, which relaxes the routing requirement for the power amplifier units to a large extent. The operation and design of a network of coupled 30 GHz $\lambda/2$ standing-wave oscillators using TSMC 0.18 μm CMOS technology is described in Section 2. Simulation results are presented in Section 3. Finally, some conclusion remarks are drawn in Section 4.

2. NETWORK OF COUPLED $\lambda/2$ STANDING-WAVE OSCILLATORS DESIGN

2.1. $\lambda/2$ Standing-wave Oscillator

In Figure 1, a simplified illustration of $\lambda/2$ standing-wave oscillator is depicted. As shown in Figure 1(a), a signal source in the middle of the $\lambda/2$ resonator generates two incident waves propagating toward both ends of the transmission line. With ideal electrical shorts at both ends, the incident waves are completely reflected with an inverted phase, forming a standing wave which has maximum voltage amplitude in the middle and a minimum voltage swing at the shorted ends. The

standing wave has the same phase regardless of position but amplitude that varies sinusoidally. However, wire losses cause amplitude mismatch between the incident and reflected waves, resulting in a residual traveling wave.

Distributed cross-coupled pair (CCP) can compensate for signal attenuation due to wire loss. The CCPs can be analyzed as distributed transconductance if they are spaced sufficiently close (about $\lambda/10$). Figure 1(b) shows the typical circuit topology of a $\lambda/2$ standing-wave oscillator, where a half-wavelength differential transmission line with both ends shorted together is utilized as the resonator to sustain the standing wave. For circuit implementation, the transmission line is realized by microstrip lines, with CCPs distributed along the lines to compensate for losses. The oscillation frequency is decided as

$$f = \frac{1}{T} = \frac{1}{\lambda/v_p} = \frac{v_p}{2l} = \frac{1}{2l\sqrt{L_{TRAN}(C_{TRAN} + C_{CCP})}} \quad (1)$$

where v_p is the phase velocity of the traveling waves, λ the equivalent wavelength, l the physical length of the half-wavelength transmission line, L_{TRAN} and C_{TRAN} the equivalent inductance and parasitic capacitance of the microstrip lines respectively, and C_{CCP} the CCP's equivalent parasitic capacitance per unit length.

The equivalent lumped model for a transmission line with distributed transconductance is shown in Figure 2(a), where G_{CCP} is the effective transconductance per unit length. The loss is given by

$$\alpha = Re(\gamma) = Re\sqrt{(R + j\omega L_{TRAN})(-G_d + j\omega(C_{TRAN} + C_{CCP}))} \approx \frac{R}{2Z_0} - \frac{G_d Z_0}{2} \quad (2)$$

where $Z_0 = (L_{TRAN}/(C_{TRAN} + C_{CCP}))^{0.5}$ and γ is the transmission-line's propagation constant. Although it is not practical to maintain a precise transconductance over the entire chip, it is possible to design CCPs that will reliably overcome the wire losses ensuring $\alpha < 0$. Since the inherent amplitude saturation of the CCPs will cause them to self-limit, they compensate for wire losses exactly in practical. Shown in Figure 2(b) is the circuit implementation of the CCP, where

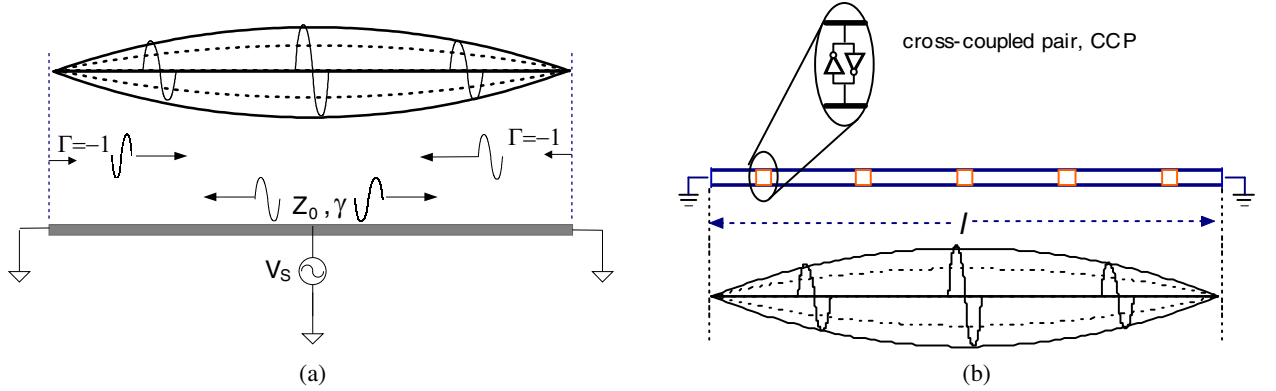


Figure 1: $\lambda/2$ standing-wave oscillator.

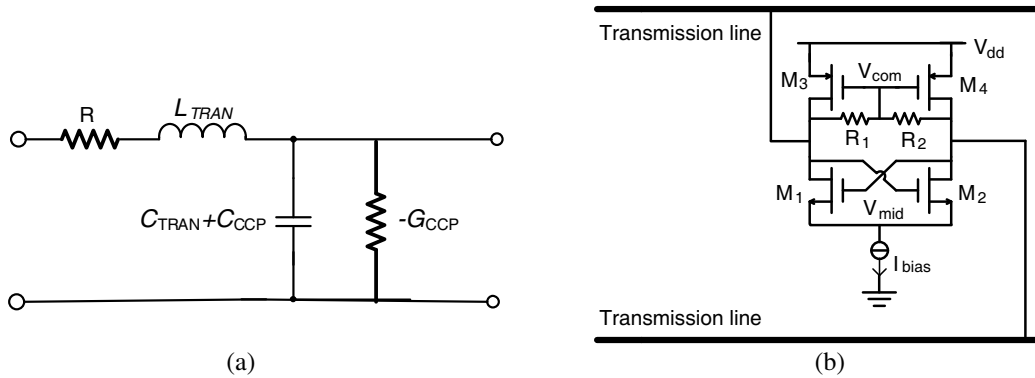


Figure 2: (a) Transmission line model with transconductance. (b) CCP circuit implementation.

the NMOS cross-coupled pair provides enough gain to compensate for wire losses and the PMOS diode-connected loads set the common-mode voltage.

2.2. Coupling $\lambda/2$ Standing-wave Oscillators

The concept of coupling multiple $\lambda/2$ standing-wave oscillators to form a network was formerly proposed in [6] for global clock distribution. As shown in Figure 3(a), four $\lambda/2$ standing-wave oscillators are connected together, with each single oscillator bended at three positions for easy coupling. By taping onto the marked tap points in the network, four differential signals of equi-frequency, equi-phase, and equi-magnitude can be obtained. If rotated 90 degrees, the locations of the tap points match the expected power sources locations for the power combining scheme proposed in [5] in a perfect way.

A network of four coupled 30 GHz $\lambda/2$ standing-wave oscillators using TSMC one-poly six-metal (1P6M) 0.18 μm CMOS technology is designed for prototyping. The half-wavelength transmission lines are realized using microstrip line structure, and for each single $\lambda/2$ standing-wave oscillators, five equally sized and equally spaced cross-coupled pairs are distributed. The choosing of the coupling points is a tradeoff between the size of the grid and the coupling strength. For the transmission lines, the two signal wires run on the top metal layer (metal 6) because it has the lowest resistance, and metal 1 is used as the ground layer because of less attenuation. The width and spacing for the differential microstrip lines are 4 μm and 25 μm , respectively.

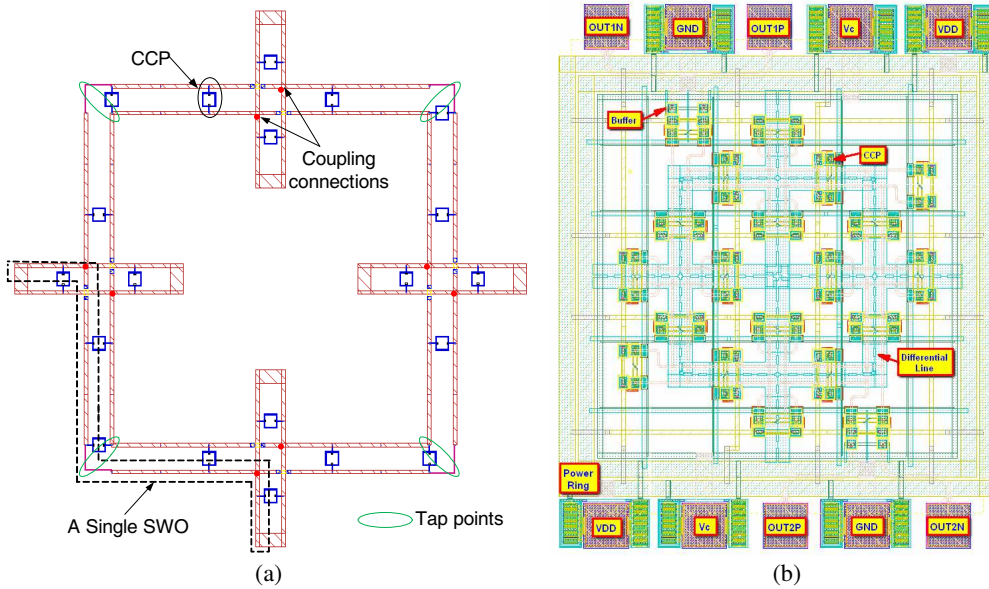


Figure 3: Circuit schematic and layout of the network of four coupled SWOs.

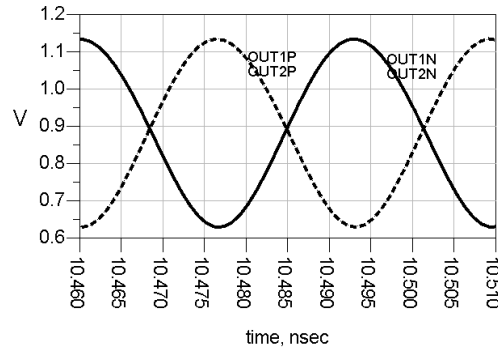


Figure 4: Output waveforms.

3. RESULTS

In Figure 3(b) is the layout for the network of four coupled $\lambda/2$ standing-wave oscillators with a chip area of $800 \times 990 \mu\text{m}^2$ including pads. Post-layout simulation shows that operated at a supply voltage of 1.8 V, the total current consumption is 91mA. The waveform from two diagonal tap locations is outputted using output buffers. As can be seen from Figure 4, the buffers deliver differential signals with equi-phase and equi-magnitude and the operating frequency is found to be 30.35 GHz.

4. CONCLUSIONS

Coherent power combining schemes require that all the input power sources be in-phase with each other, which present great difficulties for circuit design and layout. In this paper, the network of coupled $\lambda/2$ standing-wave oscillators is applied for equi-frequency, equi-phase, and equi-magnitude differential signal distribution. A 30 GHz prototype network comprised of four coupled $\lambda/2$ standing-wave oscillators using TSMC 0.18 μm CMOS process is designed with post-layout simulation results showing the viability of the proposed method. The circuit has been submitted for chip tape-out.

ACKNOWLEDGMENT

This research is financially supported by National Natural Science Foundation of China with grant No. of 61071064.

REFERENCES

1. Niknejad, A. M., M. Bohsali, et al., "Integrated circuit transmission-line transformer power combiner for millimetre-wave applications," *Electronics Letters*, Vol. 43, No. 5, 290–291, 2007.
2. Afshari, E., H. Bhat, et al., "Electrical funnel: A broadband signal combining method," *IEEE International Solid-state Circuits Conferences*, 751–760, San Francisco, USA, February 2006.
3. Bohsali, M. and A. M. Niknejad, "Current combining 60 GHz CMOS power amplifiers," *IEEE Radio Frequency Integrated Circuits Symposium*, 31–34, Boston, USA, June 2009.
4. Reynaert, P., M. Bohsali, et al., "Power combining techniques for RF and mm-wave CMOS power amplifiers," *Analog Circuit Design*, 115–143, Springer Science, 2008.
5. Huang, Y. Q., X. Y. Hu, et al., "Novel millimeter-wave power combining utilizing wafer level packaging technology," *PIERS Proceedings*, Accepted, Suzhou, China, September 12–16, 2011.
6. O'Mahony, F., C. P. Yue, et al., "A 10-GHz global clock distribution using coupled standing-wave oscillators," *IEEE Journal of Solid-state Circuits*, 1813–1820, Vol. 38, No. 11, 2003.

An Investigation of Second-Harmonic Shifting Characteristic of Stepped-Impedance Resonators

S. Theerawisitpong¹, T. Suzuki², and Y. Utsumi²

¹Faculty of Technical Education, Rajamangala University of Technology Thanyaburi
39 Moo 1, Rangsit-Nakorn Nayok Road, Klong Hok, Thanyaburi, Pathumtani 12110, Thailand
²Department of Electrical and Electronic Engineering, Nippon Institute of Technology
4-1 Gakuendai, Miyashiro-machi, Minami Saitama-gun, Saitama-ken 345-8501, Japan

Abstract— This paper reports an investigation of second-harmonic shifting characteristic of SIR technology. In our study, two features of SIR technology including shortened length and second-harmonic shifting characteristic have been investigated with respect to electric current density and equivalent model. It is found that those features are obtained by the effect of equivalent L-C lumped circuits at steps which are confirmed in our study. In addition, proper SIR dimensions enabling second-harmonic frequency at greater than two times of a fundamental frequency ($> 2f_0$) have also been recommended in this paper.

1. INTRODUCTION

The microstrip stepped-impedance line was early proposed by Riblet since 1960 [1], and further studied in later years by well-known pioneers such as Yong, Mattheai, Chang, Horton, Rhodes, and Makimoto [2–7]. Recently, SIR technology is still attracting attention, and is widely applied in various works. Because of two advantages of this technology consisting of shortened length and second-harmonic shifting characteristic, it has therefore been applied for miniaturized filters design having second-harmonic suppression [8–15]. Applying this technology, the length of resonator can be decreased by two times of conventional uniform impedance resonator (UIR) and second-harmonic frequency can also be shifted at more than two times of fundamental frequency ($> 2f_0$). Although these advantages are well recognized, the circumstance of shortened length and second-harmonic shifting characteristic is not clarified yet in any reports.

In our study, SIR technology has been investigated with respect to electric current density and equivalent model, which are also compared with that of UIR. In particular, an investigation of second-harmonic shifting characteristic of SIR has been demonstrated in this paper with ease of understanding in why the length of SIR shorter than the length of UIR and how second-harmonic frequency shifted. Furthermore, we also recommend the proper dimensions of SIR technology.

2. SCHEMATICS OF UIR AND SIR

In our study, SIR technology has been investigated and compared with UIR technology. Their schematics are shown in Figure 1. In this figure, the total length of UIR is defined by L and strip-width W is corresponding to impedance Z_0 . On the other hand, the schematic of SIR consists of two low-impedance and a high-impedance parts. The low-impedance parts are defined on the length L_1 and width W_1 is corresponding to impedance Z_1 . The high-impedance part is defined on the length L_2 and width W_2 is corresponding to impedance Z_2 . Thus, the total length of SIR is $2L_1 + L_2$. It is noted that UIR has only a $50\text{-}\Omega$ impedance (Z_0) while SIR has two low-impedance ($Z_1 < Z_0$) parts and a high-impedance ($Z_2 > Z_0$) part.

These resonators are designed and fabricated on a NPC-F260A laminate having substrate thickness (h) = 1.2 mm, dielectric constant (ϵ_r) = 2.6, tangential loss factor ($\tan \delta$) = 0.0015, and copper-strip thickness (t) = 9 μm . Hence, the total length of UIR (L) corresponding to a fundamental frequency of 2 GHz and strip-width of a $50\text{-}\Omega$ impedance (Z_0) can be calculated at 51.197 mm, and 3.32 mm, respectively [16]. Meanwhile, the dimensions of SIR are designed at W_1 = 6.78 mm (Z_1 = $30\text{ }\Omega$), W_2 = 0.92 mm (Z_2 = $100\text{ }\Omega$), L_1 = 7.32 mm, and L_2 = $2L_1$ = 14.64 mm [17], where the total length of SIR is corresponding to a fundamental frequency of 2 GHz same as that of UIR. The frequency response of these resonators is shown in Figure 2.

Figure 2 shows frequency response of UIR and SIR having the same fundamental frequency f_0 at 2 GHz but second-harmonic frequency of SIR ($f_{s,SIR}$) is greater than that of UIR ($f_{s,UIR}$). The second-harmonic frequency of UIR is at $2f_0$ but second-harmonic frequency of SIR is at $3.2f_0$. Typically, the location of second-harmonic should be better than $2f_0$ because it may harmful

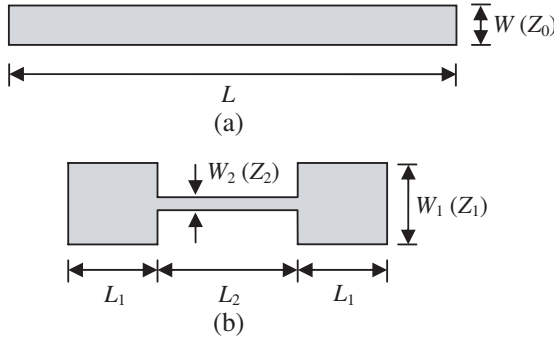


Figure 1: Schematics of (a) UIR having the length L and width W is corresponding to impedance Z_0 , and (b) SIR having two low-impedance parts defined by length L_1 and width W_1 , and a high-impedance part defined by length L_2 and width W_2 .

to fundamental frequency which is an information signal of wireless communication systems. In addition, the length of SIR is also shorter than that of UIR. The shortened length and second-harmonic shifting characteristic mentioned above are two features of SIR technology which have been investigated and demonstrated as detailed in Section 3.

3. INVESTIGATION OF SIR TECHNOLOGY

In this study, the total length of UIR and SIR is designed at the same length and both resonators are analyzed together with respect to electric current density (J) and equivalent model. The electric current density flowed along the resonator length and equivalent model of those resonators are shown in Figure 3.

Figure 3 shows electric current density (J) flowed along the length of UIR and SIR in fundamental and second-resonant modes, which is calculated by IE3D software, and their equivalent models. The total length of UIR and SIR for this case is designed at the same length ($L_{T,UIR} = L_{T,SIR}$). In fundamental mode, maximum electric current density of those resonators is at the center which is a short-circuit position, and minimum electric current density is at the ends which are the open-circuit positions. In second-resonant mode, minimum electric current density is at the open-circuit positions. The maximum electric current density of UIR is at the short-circuit positions while maximum electric current density of SIR is near the short-circuit positions where are on the narrow strip of a high-impedance part, due to current concentration on the narrow-width strip. The equivalent model of UIR consists of a transmission line having an impedance Z_0 and total length $l = \lambda_g/2$ while the equivalent model of SIR consists of two low-impedance transmission lines ($Z_1 < Z_0$) having the length l_1 and a high-impedance transmission line ($Z_2 > Z_0$) having the length $l_2 = 2l_1$. Furthermore, equivalent L-C lumped circuits are also modeled at steps of SIR where L_1 is larger than L_2 . These circuits do not effect to second-resonant mode but they only affect fundamental mode. The electrical length of SIR in fundamental mode is accordingly lengthened. Consequently, fundamental frequency of SIR is shifted down but second-resonant frequency is not change which is same as that of UIR, as shown in Figure 4.

Figure 4 shows the frequency response of UIR and SIR where the total length of these resonators is same. The L-C lumped circuit occurred at steps of SIR effects to fundamental mode and this frequency is therefore shifted down because electrical length of SIR is lengthened, as mentioned above, while second-resonant frequency is not change which is same as that of UIR at approximately 4 GHz. In order to adjust fundamental frequency of SIR same as that of UIR at 2 GHz, the total length of SIR must be shortened. Thus, fundamental and second-resonant frequencies of SIR are shifted up together. The results of UIR and shortened SIR can see in Figures 1 and 2. In those

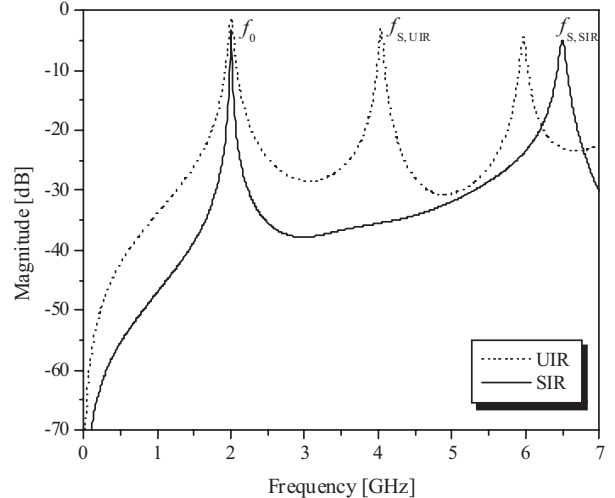


Figure 2: Frequency response of UIR and SIR with the same fundamental frequency at 2 GHz where second-harmonic frequency of UIR is at $2f_0$ and second-harmonic frequency of SIR is at $3.2f_0$.

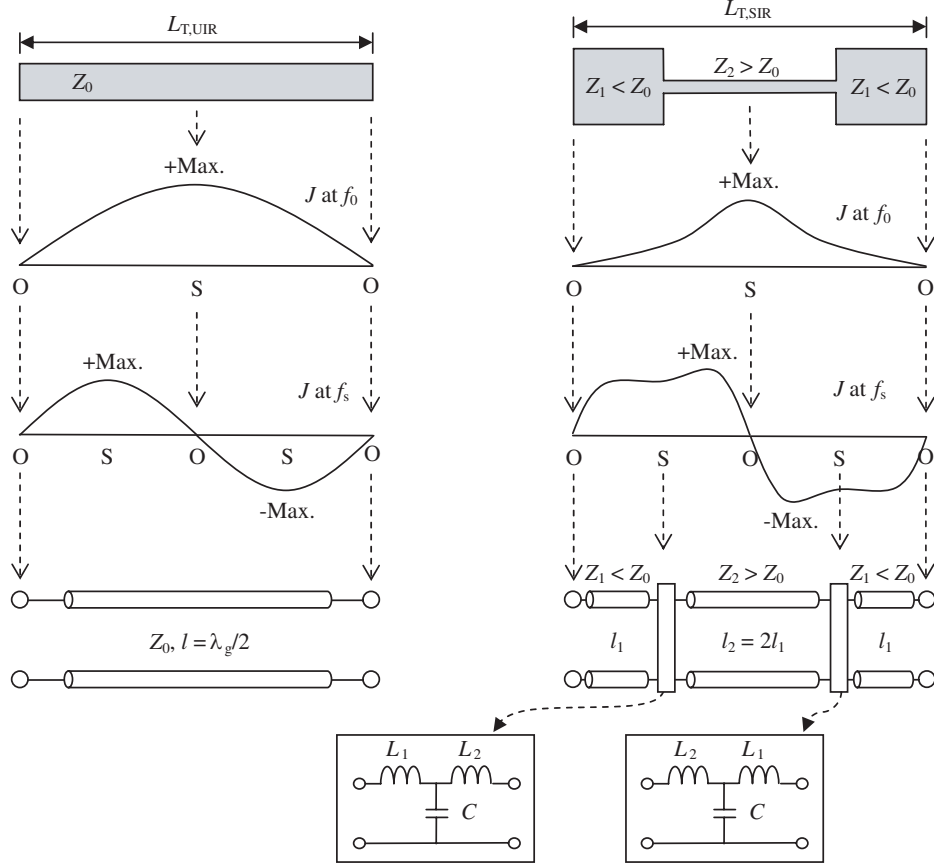


Figure 3: Electric current density (J) flowed along the length of UIR and SIR in fundamental (f_0) and second-resonant (f_s) modes, and their equivalent models, where the total length of these resonators is designed at the same length ($L_{T,UIR} = L_{T,SIR}$). Symbols O and S denote open- and short-circuit positions.

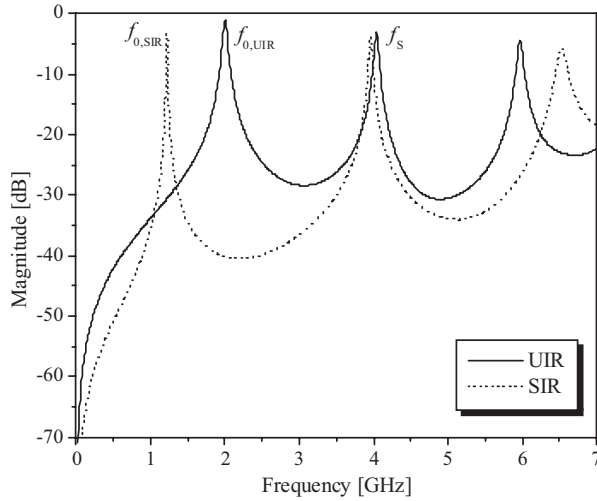


Figure 4: Calculated result of frequency response of UIR and SIR where the total length of these resonators is same. The fundamental frequency of SIR is shifted down while second-resonant frequency of SIR is not change which is same as that of UIR (at approximately 4 GHz).

figures, the fundamental frequency of UIR and SIR is same at 2 GHz but second-resonant frequency of UIR is at $2f_0$ while second-resonant frequency of SIR is at $3.2f_0$, and the total length of SIR is shorter than that of UIR.

4. DIMENSIONS OF SIR

The recommended dimensions of SIR technology are given in [17], where the length ratio $N = L_2/L_1$ is recommended in a range of 1.5 to 2.0 and impedance ratio $R = Z_1/Z_2$ is recommended in a range of 0.2 to 0.3. At those ratios, second-harmonic frequency can be improved at greater than $3f_0$ which is required for high-performance bandpass filters employed in commercial wireless systems. Thus, the proper dimensions of SIR for a NPC-F260A laminate are as follows: $W_1 = 6.78$ mm ($Z_1 = 30 \Omega$), $W_2 = 0.92$ mm ($Z_2 = 100 \Omega$), $L_1 = 7.32$ mm, and $L_2 = 2L_1 = 14.64$ mm, where ratios N and R are respectively 2.0 and 0.3. Second-harmonic frequency can be shifted up to $3.2f_0$ which is satisfactory for further application [17].

5. CONCLUSIONS

An investigation of second-harmonic shifting characteristic of SIR has been demonstrated in this paper. In particular, two features of SIR technology including shortened length and second-harmonic frequency shifted has been investigated with respect to electric current density and equivalent model. Those features are obtained by the effect of equivalent L-C lumped model at steps which are confirmed by our study reported in this paper. This report is beneficial to make sure that why shortened length and how second-harmonic frequency shifted.

REFERENCES

1. Riblet, H. J., "A general theorem on an optimum stepped impedance transformer," *IRE Trans. Microw. Theory Tech.*, Vol. 8, No. 2, 169–170, 1960.
2. Young, L., "Stepped-impedance transformer and filter prototypes," *IRE Trans. Microw. Theory Tech.*, Vol. 10, No. 5, 339–359, 1962.
3. Matthaei, G. L., "Short-step Chebycheff impedance transformer," *IEEE Trans. Microw. Theory Tech.*, Vol. 14, No. 8, 372–383, 1966.
4. Chang, F.-C. and H. Mott, "Exact design of stepped-impedance transformers," *IEEE Trans. Microw. Theory Tech.*, Vol. 20, No. 9, 620–621, 1972.
5. Horton, R., "Equivalent representation of an abrupt impedance steps in microstrip line," *IEEE Trans. Microw. Theory Tech.*, Vol. 21, No. 8, 562–564, 1973.
6. Rhodes, J., "Design formulas for stepped-impedance distributed and digital wave maximally flat and Chebycheff low-pass prototype filters," *IEEE Trans. Circuit and Syst.*, Vol. 22, No. 11, 866–874, 1975.
7. Makimoto, M. and S. Yamashita, "Bandpass filters using parallel coupled stripline stepped-impedance resonators," *IEEE Trans. Microw. Theory Tech.*, Vol. 28, No. 12, 1413–1417, 1980.
8. Kuo, J.-T. and E. Shih, "Microstrip stepped-impedance resonator bandpass filter with an extended optimal rejection bandwidth," *IEEE Trans. Microw. Theory Tech.*, Vol. 51, No. 5, 1554–1559, 2003.
9. Chang, K. F. and K. W. Tam, "Miniaturized cross-coupled filter with second and third spurious responses suppression," *IEEE Microw. Wirel. Co. Lett.*, Vol. 15, No. 2, 122–124, 2005.
10. Wang, H. and L. Zhu, "Aperture-backed microstrip-line stepped-impedance resonators and transformers for performance-enhanced bandpass filters," *IEICE Trans. Eletron.*, Vol. E89-C, No. 3, 403–409, 2006.
11. Lin, S.-C., P.-H. Deng, Y.-S. Lin, C.-S. Wang, and C. H. Chen, "Wide stopband microstrip bandpass filters using dissimilar quarter-wavelength stepped-impedance resonators," *IEEE Trans. Microw. Theory Tech.*, Vol. 54, No. 3, 1011–1018, 2006.
12. U-yen, K., E. J. Wollack, T. A. Doiron, J. Papapolymerou, and J. Lasker, "A planar bandpass filter design with wide stopband using double split-end stepped-impedance resonators," *IEEE Trans. Microw. Theory Tech.*, Vol. 54, No. 3, 1237–1244, 2006.
13. Namsang, A., T. Majang, J. Jantree, S. Chaimool, and P. Akkaraekthalin, "Stepped-impedance hairpin resonators with asymmetric capacitively load coupled lines for improved stopband characteristics," *IEICE Trans. Electron.*, Vol. E90-C, No. 12, 2185–2191, 2007.
14. Hsu, C.-L. and J.-T. Kuo, "A two-stage SIR bandpass filter with an ultra wide upper rejection band," *IEEE Microw. Wirel. Co. Lett.*, Vol. 17, No. 1, 34–36, 2007.
15. Wu, C.-H., C.-H. Wang, and C. H. Chen, "Stopband-extended balanced bandpass filter using coupled stepped-impedance resonators," *IEEE Microw. Wirel. Co. Lett.*, Vol. 17, No. 7, 507–509, 2007.

16. Hong, J.-S. G. and M. J. Lancaster, *Microstrip Filters for RF/Microwave Applications*, John Wiley & Sons, Inc., New York, 2001.
17. Theerawisitpong, S., T. Suzuki, N. Morita, and Y. Utsumi, “Design of microstrip bandpass filters using SIRs with even-mode harmonics suppression for cellular system,” *IEICE Trans. Electron.*, Vol. E93-C, No. 6, 867–876, 2010.

A Novel Bandstop Resonator in Waveguide and Its Application for Suppressing the Spurious Responses with New Advantages to Typical Resonators

S. A. Hassani Gangaraj and M. Tayarani

Department of Electrical Engineering, Iran University of Science and Technology, Iran

Abstract— In this paper a new structure for bandstop waveguide-type resonators is introduced. Because of the similarity between the shape of this resonator and the Greek letter Φ , this resonator is named Φ -shaped resonator. These resonators are located in the cross section of the waveguide. The direction of the electromagnetic waves and the position of these resonators are studied to obtain a good excitation. Various resonances of these structures are determined. Moreover a circuit model is proposed and the parameters of this model are extracted. As a consequence an array of these resonators is used to design a bandstop filter. The results are simulated with CST Microwave Studio 2009 and a rejection level of almost 35 dB is achieved. Finally, these resonators are used as a solution for suppressing the spurious response of inductive post filters. In this case two methods are examined. In the first method an array of these resonators are cascaded with the total structure of the inductive post filter and in the second method these resonators are located in the spaces between the posts. The results verify the performance of these resonators for suppressing the spurious responses.

1. INTRODUCTION

Split Ring Resonators (SRR), originally proposed by Pendry have attracted a great deal of interest for the design of left-handed (LH) media [1]. The properties proposed by left-handed medium have created an extensive investigations due their capability to provide different properties to conventional media [2, 3]. LHM or medium with negative epsilon and negative mu can be realized by SRRs in combination with thin metal wireline [3]. Considering for each propagating mode the waveguide as a transmission line, SRR structures can be used in design of waveguide filters as bandstop resonators [1, 4]. Resonances of SRRs in high frequencies, usually more than 20 GHz, have a low bandwidth and because of their size reduction, they are not achievable very well and the depth of resonances has a significant reduction.

The Φ -shaped resonators proposed in this paper solve the bandwidth problem and size limitation and show deep resonances at high frequencies. Furthermore these resonators can be used for design a band stop filter and they are very effective for suppressing the spurious responses of waveguide filters.

2. Φ -SHAPED RESONATOR

The chiral Φ -shaped resonators are used in waveguide. For a remarkable reduction in waveguide filters volume we will locate these resonators in the cross section of waveguide. Exact position of this resonator is the center of the transverse plane. The dominant mode of the waveguide TE_{10} will excite this resonator. There is no magnetic field in the direction of propagation in the center of the transverse plane and the magnetic field in the transverse direction is not normal to the structure, so only the electric field of TE_{10} will excite this resonator. The model of this resonator is shown in Fig. 1. The CST 2009 has been used for simulation.

The advantage of this resonator from conventional SRRs is in production of high frequency resonances. At high frequencies the amount of coupling with the fields and the dimensions of SRRs will reduce until these resonators are not achievable practically while the Φ -shaped resonators through parallel inductors (left and right arms in Fig. 1) or series capacitors (middle arm in Fig. 1) can produce these resonances without any practical limitation and the resulted bandwidth and depth of resonance is very significant, By the way the structure of Φ -shaped resonators is flexible to form different shapes with the same resonance frequency. Figs. 1, 2.

Figure 1 shows the model of Φ -shaped resonator. Fig. 1 and Fig. 2 shows a same resonance frequency with a different shape or coupling. The waveguide is WR-90.

In Fig. 3, the capability of this resonator for generating high frequency resonances is shown. The resonance is occurred in $f_1 = 21.55$ GHz. This simulation has been done in waveguide WR-51 with frequency limitation [15–22 GHz], where the SRRs are not efficient in these frequencies

because of their size reduction, practical limitation and low depth resonances. Because of electrical excitation of these resonators the resonance frequencies are correspond to frequencies where the physical length $2(A + B)$ of the structure is a multiple of half a wavelength or equivalently the electrical length $\theta = 2\beta(A + B)$ is a multiple of π [5]:

$$2(A + B) = m \frac{\lambda_g}{2} \quad m = 1, 2, 3, \dots \quad (1)$$

$$\lambda_g = \frac{\lambda}{\sqrt{\varepsilon_r - \left(\frac{f_c}{f}\right)^2}} \quad (2)$$

In Equation (2), λ is the free space wavelength and f_c is the cutoff frequency of the waveguide and ε_r is relative permittivity of the substrate of the resonator. For model of Fig. 1, m is approximately 3 as depicted in Table 1 for $\varepsilon_r = 4$.

The bandwidth of the resonances are related to width of the structure (W), Table 2.

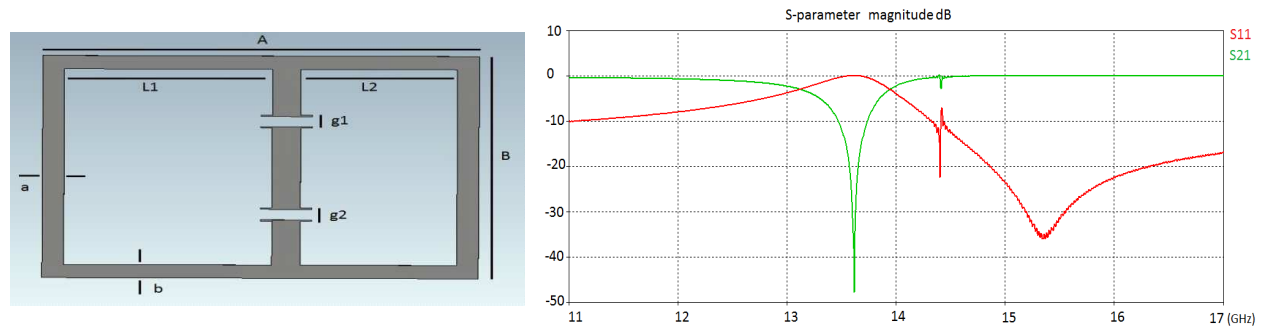


Figure 1. The model of resonator and its response.

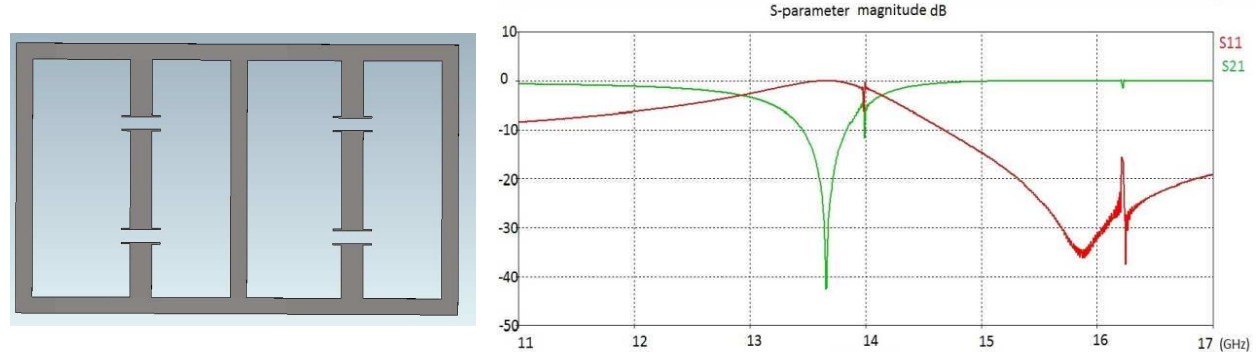


Figure 2. Different shape with same resonance frequency.

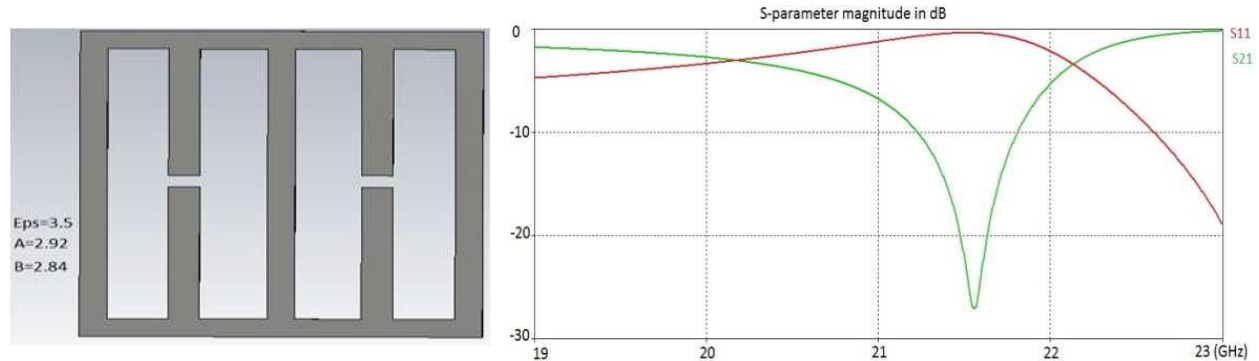


Figure 3. High frequency resonance of resonator.

3. Φ-SHAPED RESONATOR AS A BANDSTOP FILTER

Since the dimensions of resonators are chosen much smaller than the wavelength of an incident electromagnetic wave, resonators can be modeled by a lumped element equivalent circuit [6]. A simple lumped element model is set up for proposed resonator which is shown in Fig. 4. The capacitor for the circuit model can be extracted as follows [7]:

$$R_i = 2Z_0(1/|S_{21}| - 1) \quad (3)$$

$$C_i = \frac{\sqrt{0.5(R_i + 2Z_0)^2 - 4Z_0^2}}{2.83\pi Z_0 R_i B_i} \quad (4)$$

$$L_i = \frac{1}{(2\pi f_i)^2 C_i} \quad (5)$$

where B_i is the -3 dB bandwidth of $S_{21}|_{f=f_i}$, and f_i is the resonance frequency and Z_0 is the characteristic impedance. With respect to bandstop nature of the resonances, we can use an array of these resonators to make a bandstop filter. The resonance frequencies of these chiral structures can be controlled and tuned to provide a wide rejection bandwidth. It should be noted that the resonance frequency of each resonator should be different with the others to yield a good rejection band and for a good passband around the rejection band the distance between the resonators should be $\frac{\lambda_g}{4}$, because such a distance can act as an impedance transformer to make a perfect match between the cascaded resonators. The S -parameter of this band stop filter is depicted in Fig. 5.

As it can be seen in Fig. 5 the resulted band stop filter performance is simulated and a rejection level of almost 35 dB is achieved to confirm the effectiveness of the idea.

Table 1.

$2(A + B)$ (mm)	17.28	17.78	17.98	18.18
f_r (GHz)	13.73	13.43	13.06	12.83
$2(A + B)/\lambda_g$	1.62	1.54	1.51	1.50

Table 2.

W (mm)	0.20	0.23	0.28	0.31
$B.W$ (MHz)	850	870	910	950

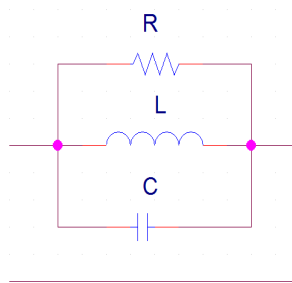
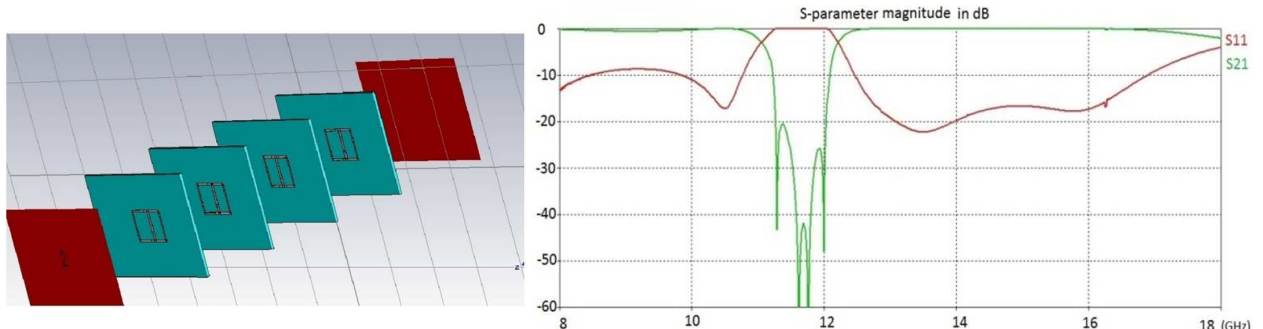


Figure 4. The circuit model.

Figure 5. The array of resonators for bandstop filters and resulted S -parameter.

4. WAVEGUIDE FILTER WITH SUPPRESSED SPURIOUS RESPONSES

Spurious bands and their rejection as a common problem for all transmission line type filters are increasingly notified recently. These undesired frequency bands degrade filter rejection performance specially, for wide band cases. Inwaveguide filters the first spurious band is relatively close to the desired frequency band because of dispersive behavior of waveguides. Using low pass or band reject structures can be considered as a solution for this reason [8]. In this paper, we have used Φ -shaped resonators to suppress the spurious response of inductive post filters. A third order inductive post Tchebychef bandpass filter with a central frequency of 9.2 GHz and 7.5% fractional band width have been designed to evaluate the effectiveness of the presented idea. We will reject the spurious response of this filter by two methods.

In the first method, we have cascaded 8 Φ -shaped resonators with the inductive post filter. The distance between the resonators and inductive post filter is 11.2 (mm) and the distances between the resonators are 6.3 (mm). The resonator's dimensions are as follows: For all resonators $a = 0.249$ mm, $b = 0.209$ mm, $g_1 = 0.1568$ mm, $g_2 = 0.1956$ mm, $g_3 = 0.1868$ mm, $L_2 = 2.2565$ mm, the substrate is Taconic RF-35 tan = 0.0081, $\epsilon_r = 3.5$ the other dimensions are depicted in Table 3:

As it is seen in Fig. 6, with adding the resonators, a rejection more than 40 dB is achieved, while the main passband remains almost unchanged.

In the second method, for a significant reduction in the volume of the total size of the structure the resonators are positioned between the posts of the filter. 8 resonators are used and the dimensions are unchanged with respect to previous method except L_1 and L_2 .

As it is seen in Fig. 7 the spurious response is rejected very well. But the passband has a little shift toward left. It is obvious, because the spaces between the posts of the filter is partially filled with dielectric with $\epsilon_r = 3.5$.

Table 3.

Resonator	L_1 (mm)	Resonator	L_1 (mm)
1	2.521	5	2.091
2	2.341	6	2.011
3	2.251	7	1.931
4	2.172	8	1.781

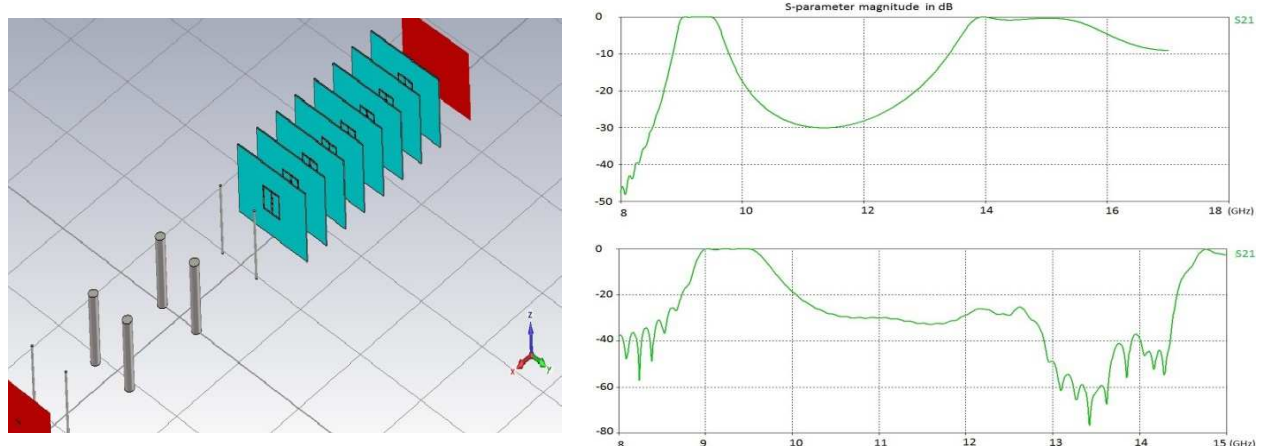


Figure 6. The cascaded resonators with the main filter and the simulated S -parameter for spurious response and suppressed spurious response.

Table 4.

Resonator	L_1 (mm)	L_2 (mm)	Resonator	L_1 (mm)	L_2 (mm)
1	2.821	2.683	5	2.021	2.182
2	2.821	2.782	6	1.821	2.182
3	2.721	2.282	7	1.721	2.182
4	2.321	2.182	8	1.421	2.182

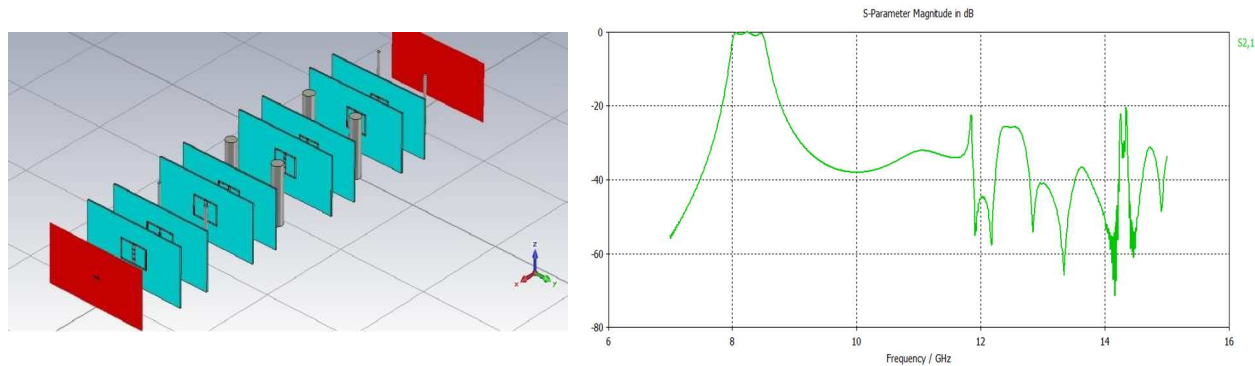


Figure 7. The schematic of total structure and suppressed responses.

5. CONCLUSION

- 1- In this paper we have introduced a special type of resonators that can resonate in a very wide range of frequency and still remain producible.
- 2- The shape of resonator is so flexible for making different shape with a same frequency.
- 3- This resonator can show strongly coupled behavior in the higher resonance frequencies with adding parallel inductors in contrast to conventional SRRs that their coupling will reduce because of their size reduction with increasing their resonance frequency.
- 4- These resonators can be used to design stopband filters with a good level of rejection in its rejection band.
- 5- The stopband filters designed with Φ -shaped resonators are very effective to reduce the spurious responses of waveguide filters that inferred in the Section 4.

REFERENCES

1. Fallahzadeh, S., H. Bahrami, and M. Tayarani, "Very compact bandstop waveguide filters using split-ring resonators and perturbed quarter-wave transformers," *Electromagnetics*, Vol. 30, 482–490, Jun. 2010.
2. Veselago, V. G., "The electrodynamics of substances with simultaneously negative values of ϵ and μ ," *Soviet Phys. Uspekhi*, Vol. 10, No. 4, 509–514, Jan.–Feb. 1968.
3. Smith, D. R., W. J. Padilla, D. C. Vier, S. C. Nemat-Nasser, and S. Schultz, "Composite medium with simultaneously negative permeability and permittivity," *Phys. Rev. Lett.*, Vol. 84, 4184–4187, May 2000.
4. Shelkovnikov, A. and D. Budimir, "Left-handed rectangular waveguide bandstop filters," *Microw. & Optical Technol. Lett.*, Vol. 48, 846–848, 2006.
5. Caloz, C. and T. Itoh, *Electromagnetic Metamaterials: Transmission Line Theory and Microwave Application*, 249, John Wiley & Sons, 2006.
6. Wongkasem, N., A. Akyurtlu, K. Marx, and W. D. Goodhue, "Fabrication of a novel micron scale Y-structure-based chiral metamaterial: Simulation and experimental analysis of its chiral and negative index properties in the Terahertz and microwave regimes," *Microscopy Research Technique*, Vol. 70, 497–505, 2007.
7. Fallahzadeh, S., H. Bahrami, and M. Tayarani, "A novel dual-band stop waveguide filter using split ring resonator," *Progress In Electromagnetics Research Letters*, Vol. 12, 133–139, 2009.
8. Abolhasani, Z. and M. Tayarani "Spurious response suppression in waveguide filter using E-shaped chiral resonator," *IJEEE*, Vol. 5, No. 4, Dec. 2009.

A Low-voltage and Low-power Low Noise Amplifier for Ku-band Application

Cheng-Chi Yu¹, Jiin-Hwa Yang², Lien-Chi Su¹, Heng-Yi Lee¹, and Chang-Chih Chen¹

¹Department of Communications Engineering, Feng-Chia University
100, Wen-Hua Rd., Taichung 407, Taiwan, R.O.C.

²Ph.D. Program in Electrical and Communications Engineering
Feng-Chia University, 100, Wen-Hua Rd., Taichung 407, Taiwan, R.O.C.

Abstract— A low-voltage and low-power low noise amplifier (LNA) for Ku-band (12–18 GHz) application is proposed in this paper. The LNA can be used in receiver front-end for Direct Broadcasting Satellite (DBS) system. In order to decrease the power consumption and provide sufficient power gain at 12–18 GHz, a two-stage wide-band amplifier topology is presented in this circuit. In the first stage, a filter type matching network with an on-chip transformer is used as the input matching network. And this stage is to achieve the required bandwidth and reduce the chip area. In the second stage, a current-reused circuit is used to reduce the power consumption. The proposed LNA chip is fabricated by a TSMC 0.18 μm CMOS process. The chip occupies a die area of 0.67 mm² (0.73 mm * 0.91 mm). The measured results show that maximum power gain (S_{21}) of 12.72 dB, noise figure (NF) of 3.7 ~ 4.8 dB and 1-dB compression points ($P_{1\text{dB}}$) from -17 to -11 dBm between 12–18 GHz are obtained. The total power consumption is only 7.68 mW under 0.8 V power supply voltage.

1. INTRODUCTION

Low-noise amplifier (LNA) is a very important component in RF receiver front-end. Recently, the rapid evolution of wireless communication has resulted in the demand of higher data rates transmission which has increased the desired operation frequency of RFICs and wideband communication applications. The major advantages of CMOS process are low cost and high level of integration. In practical applications power consumption of the LNA becomes an important factor since the receivers are close to continuously power consumption. LNA has to provide sufficient gain and good noise figure to overcome the loss of signal, phase shift and power consumption simultaneously.

This paper proposes a low noise amplifier for Ku-band applications by a standard TSMC 0.18 μm CMOS process. In order to reduce the supply voltage and power consumption while providing sufficient power gain for the LNA at 12–18 GHz operation, a two-stage wide-band amplifier topology is presented. In the first stage, a filter type matching network with an on-chip transformer is used as the input matching network for better noise and power matching. The main goals of this stage are to achieve the required bandwidth and reduce the chip area. In the second stage, a current-reused circuit is used to reduce the power consumption. In addition, a series-peaking inductor between the current-reused circuit and output matching network is adopted to achieve more flat gain.

2. CIRCUIT DESIGN AND ANALYSIS

In this section, we will introduce the topology and analysis of the circuit. Fig. 1 is the schematic of the proposed Low-voltage and Low-power LNA. In the first stage, the filter type matching network is used for input matching. In order to reduce the chip area the inductors L_1 and L_2 are merged into one transformer. The L_2 acts as inductive degeneration in the common-source stage, resulting in the real impedance for better matching to 50 Ohms. The L_1 at the input node also provides the flexibility to further match the imaginary part. When comparing to the two individual spiral inductors (one gate inductor and one source inductor) that usually used for LNA design, the transformer in this design occupies less chip area that can be expected.

In the second stage, we used a current-reused circuit to have the input signal amplify twice without extra power consumptions [1–4]. The current-reused topology consists of the transistors M_1 , M_2 , the capacitors C_1 and C_2 , and the inductor L_3 . The purpose of using C_1 is to create a low impedance path without dc current when the impedance of L_3 is increased with frequency inducing a high impedance path to block the high frequency signal. Therefore, the input signal can be amplified twice under this con-current structure.

For this design, a high gain can be obtained under lower dc power consumptions. In order to balance this gain degradation, a series-peaking inductor L_{sep} is added to make the gain response

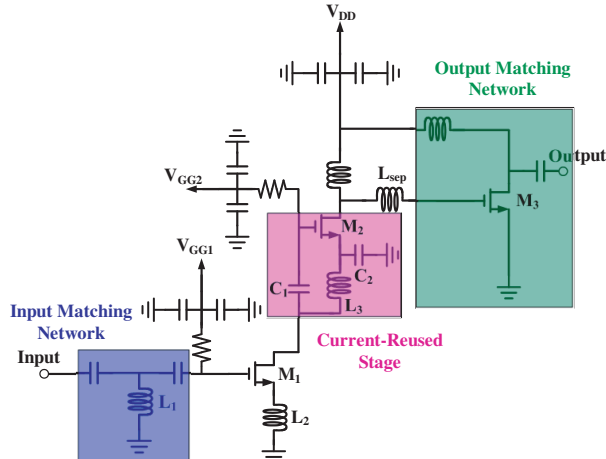


Figure 1: Schematic of proposed Low-voltage and Low-power LNA.

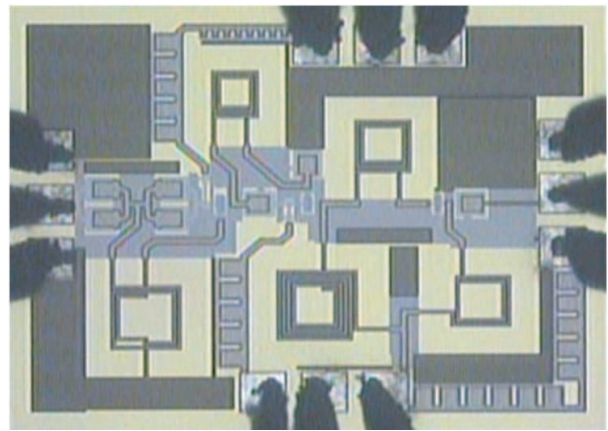


Figure 2: Die photograph of Ku-band LNA.

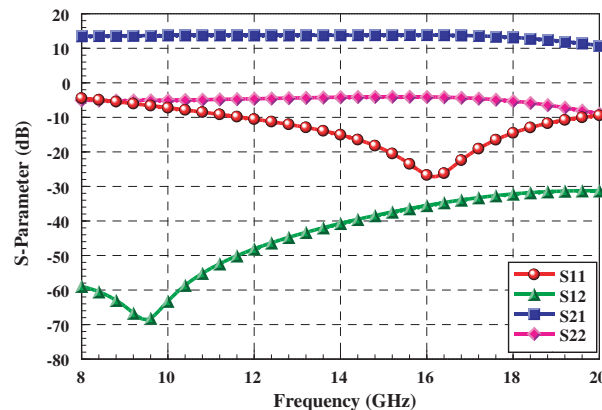


Figure 3: Simulated S -parameters of the Ku-band low noise amplifier.

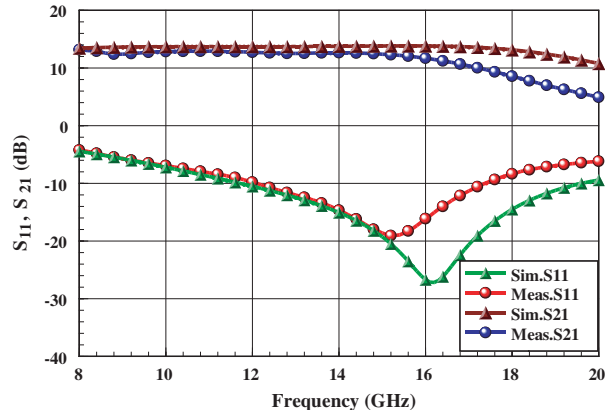


Figure 4: Simulated and measured results of input return loss and power gain of the Ku-band LNA.

Table 1: Performances of the Ku-band LNA.

A Ku-band Low-voltage and Low-power Low Noise Amplifier		
	Simulation	Measurement
$V_{DD} / V_{gg1}/V_{gg2}$ (V)	0.8/ 0.7/1.1	
Operating Frequency (GHz)	12–18	
Gain_Max (dB)	13.83 ± 0.34	12.72
Gain Flatness (dB)	± 0.34 @ 12–18 GHz	± 2.07 @ 12–18 GHz
Input Return Loss (dB)	< -10	< -8.2
Isolation (dB)	< -30	< -35
Noise Figure (dB)	3.4 – 4	3.7 – 4.8
$P_{in,1dB}$ (dBm)	-17 @ 12 GHz -16 @ 15 GHz -15 @ 18 GHz	-17 @ 12 GHz -16 @ 15 GHz -11 @ 18 GHz
Stability	Unconditional Stability	Unconditional Stability
Power consumption (mW)	7.6	7.68
Chip size (mm^2)	$0.73 * 0.91 = 0.67$	

flatter. The series-peaking inductor can also resonate with the parasitic shunt capacitor at the drain of M_2 [5]. Finally, we make the circuit through a buffer stage to match the load 50 Ohms. In

order to reduce the chip area, the voltage supply in the initial design is based on a goal of minimum different supply voltage of 0.7 V, 0.8 V and 1.2 V.

3. EXPERIMENTAL RESULTS

The Ku-band LNA was designed and fabricated by a standard TSMC 0.18 μm CMOS process. The chip occupies a die area of 0.67 mm^2 (0.73 mm * 0.91 mm). The microphotograph of this LNA is shown in Fig. 2. The LNA consumes only 7.68 mW under a voltage supply of 0.8 V. Fig. 3 shows the simulated results of S-parameters. Fig. 4 illustrates the simulated and measured results of input return loss and power gain of the Ku-band LNA. The measured results demonstrate excellent performances of the LNA. They are maximum power gain (S_{21}) of 12.72 dB, reverse isolation below –30 dB, noise figure (NF) of 3.7 ~ 4.8 dB and 1-dB compression points ($P_{1\text{dB}}$) from –17 to –11 dBm between 12–18 GHz. The simulated and measured performances of the LNA are summarized in Table 1.

4. CONCLUSION

A Low-voltage and Low-power LNA for Ku-band application has been proposed. The current-reused topology and transformer in conjunction with series inductive-peaking provide a method for achieving a high performance wideband LNA. The proposed wideband LNA has shown a good agreement between simulation and measured results. Besides, this LNA also has the flattest gains from 12–16 GHz within 1dB and reveals the lowest power consumptions of 7.68 mW.

ACKNOWLEDGMENT

The authors would like to thank National Chip Implementation Center (CIC) for chip implementation and measurement support.

REFERENCES

- Wei, Y.-L., S. S. Hsu, and J.-D. Jin, "A low-power low-noise amplifier for K-band applications," *IEEE Microwave and Wireless Components Letters*, Vol. 19, No. 2, 116–118, Feb. 2009.
- Wang, R.-L., S.-C. Chen, C.-L. Huang, C.-H. Liu, and Y.-S. Lin, "2–6 GHz current-reused LNA with transformer-type inductors," *Asia-Pacific Microwave Conference APMC 2008*, 1–4, Dec. 2008.
- Liu, C.-H., C.-N. Cai, R.-L. Wang, and Y.-K. Su, "A dual-band current-reused low noise amplifier for 2.3 and 5.2 GHz applications," *Asia-Pacific Microwave Conference APMC 2008*, 1–4, Dec. 16–20, 2008.
- Hsieh, H.-H. and L.-H. Lu, "Design of ultra-low-voltage RF frontends with complementary current-reused architectures," *IEEE Transactions on Microwave Theory and Techniques*, Vol. 55, No. 7, 1445–1458, Jul. 2007.
- Hu, J., Y. Zhu, and H. Wu, "An ultra-wideband resistive-feedback low-noise amplifier with noise cancellation in 0.18 μm digital CMOS," *Silicon Monolithic Integrated Circuits in RF Systems SiRF 2008*, 218–221, Jan. 2008.

A Broadband Low Noise Amplifier for X-band Applications

Cheng-Chi Yu¹, Jiin-Hwa Yang², Hsiao-Hua Yeh¹, and Lien-Chi Su¹

¹Department of Communications Engineering, Feng-Chia University
No. 100, Wen-Hua Rd., Seatwen, Taichung 407, Taiwan, R.O.C.

²Ph.D. Program in Electrical and Communications Engineering, Feng-Chia University
No. 100, Wen-Hua Rd., Seatwen, Taichung 407, Taiwan, R.O.C.

Abstract— A broadband low noise amplifier (LNA) for X-band (8–12 GHz) applications is proposed in this study. The proposed LNA circuit is composed of three-stage NMOS transistors which construct a cascade configuration. The design can achieve wide-band matching and higher gain at the same time. The proposed LNA chip is fabricated by TSMC 0.18 μm CMOS process. The chip occupies a die area of 0.45 mm² (0.73 mm * 0.62 mm) only. On-wafer measurement was used to measure the characteristics of the LNA. The measured results show that gain (S_{21}) of 15.15 ~ 20.05 dB, noise figure (NF) of 2.9 ~ 3.1 dB are obtained. The total power consumption is 12.45 mW under a power supply voltage of 0.75 V. The good performances of the LNA make it suitable for X-band applications

1. INTRODUCTION

The high sensitivity X-band (8–12 GHz) receiver is an important device for wireless communication application such as radar and satellite communication. The X-band systems are widely used in military radar and aircraft [1]. Low noise amplifier (LNA) is one of the most important building blocks in front end of communication systems. It is a key component that provides good input return loss, low noise figure and good linearity for the receiver. Low voltage, low power, and good performances are always targets of LNA design, especially for radar applications. At high frequency, the parasitic affect the circuit performance greatly. To find a good architecture is essential that can fit demand and provide a good performance for X-band LNA. This paper demonstrates a three-stage cascade configuration X-band broadband LNA design by TSMC 0.18 μm CMOS process

2. CIRCUIT DESIGN AND ANALYSIS

The complete schematic of the proposed LNA is shown in Fig. 1. This circuit is a three-stage NMOS transistor architecture. It is constructed by a cascade configuration which is adopted to enhance the bandwidth. For producing the 8–12 GHz operating frequency range of the proposed LNA, the operating frequencies of first, second and third stages are designed at 8 GHz, 10 GHz and 12 GHz, respectively. The three-stage architecture can achieve wide-band matching and higher gain at the same time [2]. The source inductor is used to improve impedance matching in this circuit [3].

Furthermore, in order to reduce chip area, the author's self-layout mutual coupled inductor [4] which combines with source inductors of MOS1 and MOS2 is presented in this design to replace the conventional structure of the CMOS process. And the circuit only uses two supply power pads on one side. That can save the area of supply power pad on other side. An obvious size reduction is obtained by these topologies. The proposed LNA chip is fabricated by TSMC 0.18 μm CMOS

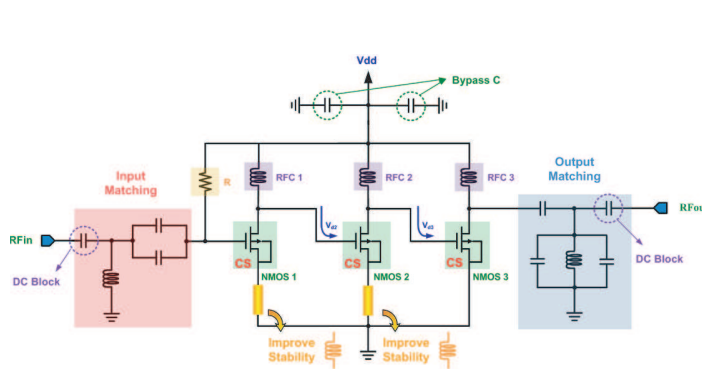


Figure 1: Schematic of the proposed broadband LNA.

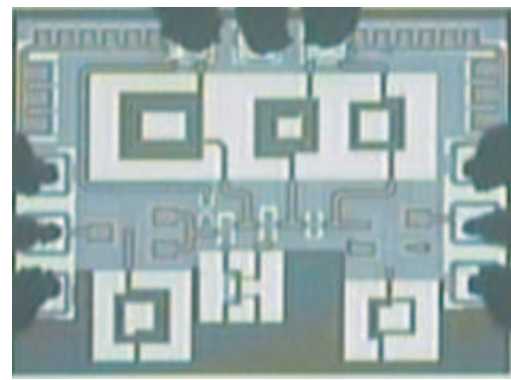


Figure 2: Photograph of the X-band LNA.

process. The die photograph of the LNA is shown in Fig. 2 The chip only occupies a die area of 0.45 mm^2 ($0.73 \text{ mm} * 0.62 \text{ mm}$).

3. EXPERIMENTAL RESULTS

The proposed LNA was simulated by ADS simulator. The simulated S -parameters are shown in Fig. 3. The simulated and measured results of the LNA are summarized in Table 1. The simulated and measured results have a good agreement. The LNA requires only a 0.75 V supply voltage and consumes 12.45 mW powers. The circuit's μ -factor is more than 1 which means that the circuit is unconditional stable in the operating frequency. The simulated and measured power gain is shown in Fig. 4. Between the operating bandwidth of 8–12 GHz, the proposed LNA has power maximum gain of 20.5 dB, noise figure (NF) of $2.9 \sim 3.1$ dB, with input return loss between 10.5 to 9.7 dB and output return loss less than 1 dB. The proposed LNA exhibits a good performance of gain, noise and chip size.

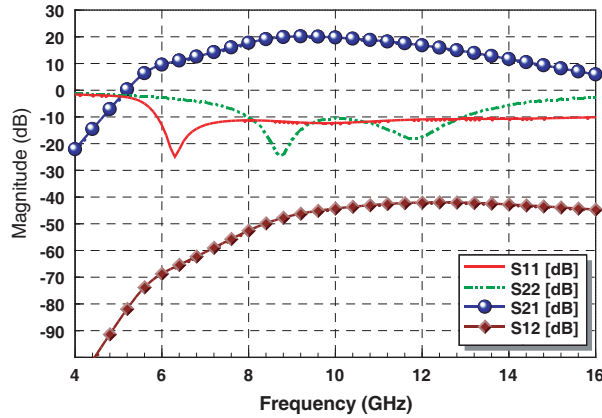


Figure 3: Simulated S -parameters of broadband low noise amplifier.

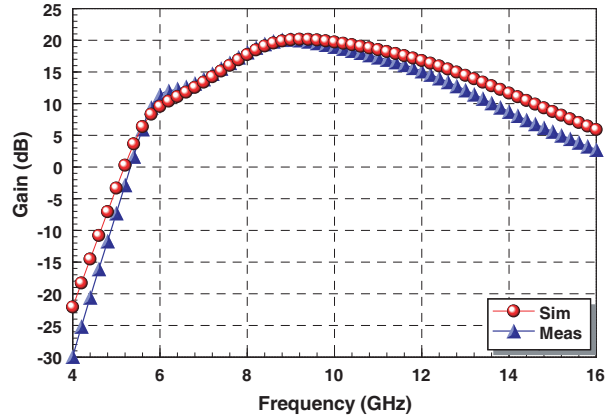


Figure 4: Simulated and measured results for power gain of broadband LNA versus frequency.

Table 1: The performance of proposed broadband LNA.

Broadband Low-Noise Amplifier		
V_{dd1} / V_{dd2} (V)	0.75 / 0.75	
Technology	Simulation	Measurement
Operating Frequency (GHz)	8–12	8–12
Power Gain (dB)	18.5 ± 1.5	17.6 ± 2.45
Input Return Loss (dB)	< -10	$-10.5 \sim -9.7$
Output Return Loss (dB)	< -10	< -10
Isolation (dB)	< -40	< -40
Noise Figure (dB)	$2.8 \sim 3.3$	$2.9 \sim 3.1$
$P_{in,1dB}$ (dBm)	$-24 @ 8 \text{ GHz}$ $-20 @ 10 \text{ GHz}$ $-19 @ 12 \text{ GHz}$	$-27 @ 8 \text{ GHz}$ $-23 @ 10 \text{ GHz}$ $-19 @ 12 \text{ GHz}$
Stability	Unconditional Stability	Unconditional Stability
Power consumption (mW)	12.45	12.45
Chip size (mm^2)	$0.73 * 0.62 = 0.45$	

4. CONCLUSION

A Broadband LNA for X-band application has been proposed. The circuit is composed of a three-stage NMOS transistor architecture which is constructed by a cascade configuration. The three-stage architecture can achieve wide-band matching and higher gain. Using the author's self-layout mutual coupled inductor and two supply power pads on one side of the circuit design can efficiently reduce the chip size. The results of proposed wideband LNA have a good agreement between simulated and measured results.

ACKNOWLEDGMENT

The authors would like to thank National Chip Implementation Center (CIC) for chip implementation and measurement support.

REFERENCES

1. Wang, X. and R. Weber, "Low voltage low power SiGe BiCMOS X-band LNA design and its comparison study with IEEE 802.11a LNA design," *2005 IEEE International Radar Conference*, 27–30, May 2005.
2. Ma, P., M. Racanelli, J. Zheng, and M. Knight, "A novel bipolar-MOSFET low-noise amplifier (BiFET LNA), circuit configuration, design methodology, and chip implementation," *IEEE Transactions on Microwave Theory and Techniques*, Vol. 51, No. 11, 2175–2180, Nov. 2003.
3. Tu, C.-H., Y.-Z. Juang, C.-F. Chiu, and R.-L. Wang, "An accurate design of fully integrated 2.4 GHz CMOS cascode LNA," *2005 IEEE VLSI-TSA International Symposium on VLSI Design, Automation and Test*, 169–172, Apr. 2005.
4. Yeh, H.-H. and C.-C. Yu, "Design and development of CMOS 0.18 μ m low noise amplifiers for commercial radar equipments," The Master's Thesis on Department of Communications Engineering, Feng-Chia University, 89–93, Jun. 2010.

A Tri-band Bandpass Filter Using Short-stub Loaded SIR

Xuehui Guan^{1, 2}, Fang Wen¹, Wei Fu¹, Haiwen Liu¹, Guohui Li², and Lu Zhu¹

¹College of Information Engineering, East China Jiaotong University, Nanchang 330013, China

²Key Laboratory of Specialty Fiber Optics and Optical Access Networks

Shanghai University, Shanghai 200072, China

Abstract— A novel compact triple-passband bandpass filter is presented in this paper. A shorted-stub is loaded to a stepped-impedance resonator (SIR). The resonant frequencies are determined by the length of the loaded-stub and the impedance ratio of the SIR. The input and output port are coupled to the resonator by utilizing pseudo-interdigital structure. A two-pole microstrip triple-passband bandpass filter with central frequencies 1.5 GHz, 2.4 GHz and 5.78 GHz is designed for GPS and WLAN applications.

1. INTRODUCTION

Due to the rapid development of intelligentized wireless communication systems, compact, high performance and low-cost filters are needed. Researches show great interest on bandpass filters (BPFs) with dual- and tri-passband that can work in multiple communication bands. Multi-band bandpass filters with different circuit topology have been reported [1–3]. In [4], tri-band BPF is presented by insetting two narrow stopband in a broadband BPF. In [5], three dissimilar dual-behavior resonators are connected by a transmission line, each dual-behavior resonator creates a passband and two transmission zeros, and triple passband is achieved. However, these kinds of filters suffered from large size. A tri-band BPF based on cascaded three similar uniform impedance resonators (UIRs) is proposed in [6]. In [7], a tri-band BPF is constructed by using three pairs of open-stub loaded open-loop resonators and the parallel coupled microstrip feed lines. In [8], triple passband BPF is realized by two pairs of quarter-wavelength resonators and a pair of half-wavelength resonators. In [9], a triple-band bandpass filter is designed using two pairs of stepped impedance resonators, larger resonator resonant at two different frequencies and two passbands are formed. In [10], a tri-layer tri-band (TLTB) bandpass filter (BPF) is presented. The proposed tri-band BPF is a three-layers structure with two transmission lines on the top layer, open-loop resonators on the middle layer, and a stepped-impedance resonator (SIR) defected-ground structure (DGS) on the bottom layer.

In this paper, a new tri-band BPF based on stub-loaded SIRs and pseudo-interdigital feeding structure is proposed. Three operating bands are designed for commercial applications, i.e., 1.5 GHz for GPS application, 2.4 GHz and 5.78 GHz for WLAN application. Impedance ratio of the SIR and the loaded shorted stub are used to control the operating frequencies of the resonator. Pseudo-interdigital feeding structures are employed to acquire the desired external couplings.

2. DESIGN PROCEDURE

Proposed tri-band resonator is presented in Fig. 1. It is a SIR with a shorted stub loading. The proposed resonators are bended into hairpin structure to reduce the circuit size. Simulated frequency response is shown in Fig. 1. Three resonant frequencies are distributed at 1.5 GHz band, 2.4 GHz band, and 5.78 GHz band. The first resonant frequency is related to the fundamental mode of shorted stub, the second resonant frequency is related to the SIR, and the third resonant frequency is related to the higher order mode of shorted stub.

Proposed resonator that inset in Fig. 1 can be analyzed by using even and odd mode theory, as to the center symmetrical plane. Z_1 , Z_2 , Z_3 and θ_1 , θ_2 , θ_3 are the characteristic impedance and electrical length of the proposed SIR, respectively. When the resonator works at even modes, as shown in Fig. 2(a), the symmetry plane can be seemed as open-ended and the resonant condition can be expressed as:

$$Z_{in} = -jz_3 \frac{\tan \theta_3 (1 - \frac{1}{k_1} \tan \theta_1 \tan \theta_2) + \frac{1}{k_2} \tan \theta_2 + \frac{1}{k_1 k_2} \tan \theta_1}{\tan \theta_3 (k_1 k_2 \tan \theta_1 + k_2 \tan \theta_2) + k_1 \tan \theta_1 \tan \theta_2 - 1} \quad (1)$$

where K_1 and K_2 are the impedance ratio, $K_1 = Z_2/Z_1$, $K_2 = Z_3/Z_2$, $K_1 K_2 = Z_3/Z_1$. Quarter-wavelength resonant mode (Mode-1) and three quarter-wavelength resonant mode (Mode-3) will

produce the passband in 1.5 GHz and 5.78 GHz, respectively. The first passband located at a frequency 1.5 GHz, which is mainly determined by the loaded stub.

When the resonator is excited by odd mode, the symmetrical plane can be seemed as shorted circuit, as shown in Fig. 2(b). Ignoring the phase step discontinuity impact and open-edge capacitance, the impedance Z_{in} can be derived as:

$$z_{in} = jZ_1 \frac{Z_1 \tan \theta_1 + Z_2 \tan \theta_2}{Z_1 - Z_2 \tan \theta_1 \tan \theta_2} \quad (2)$$

It will produce the second passband located at a frequency 2.4 GHz.

3. RESULTS AND DISCUSSION

According to above-mentioned design procedure, bandpass filters with three controllable passbands can be realized by changing the impedance ratio of the SIR and electrical length of the loaded stub. A two-pole tri-band microstrip bandpass filter with central frequencies of 1.5 GHz, 2.4 GHz band, and 5.78 GHz is designed. The schematic of the proposed tri-band BPF is shown in Fig. 3. Pseudo-interdigital and feedline coupling structures are used to obtain the desired external coupling [11, 12].

In this paper, the proposed filter is designed on a 0.8 mm-thick substrate with a dielectric constant of 4.5 and a loss tangent of 0.002. The corresponding structural parameters are $w_1 = 1.8$ mm, $w_2 = 1$ mm, $w_3 = w_4 = 0.2$ mm, $w_5 = w_6 = 1$ mm, $L_1 = 7.35$ mm, $L_2 = 3$ mm, $L_3 = 3.75$ mm, $L_4 = 4.95$ mm, $L_5 = 7.75$ mm, $L_6 = 0.55$ mm. Simulated results of the designed filter are illustrated

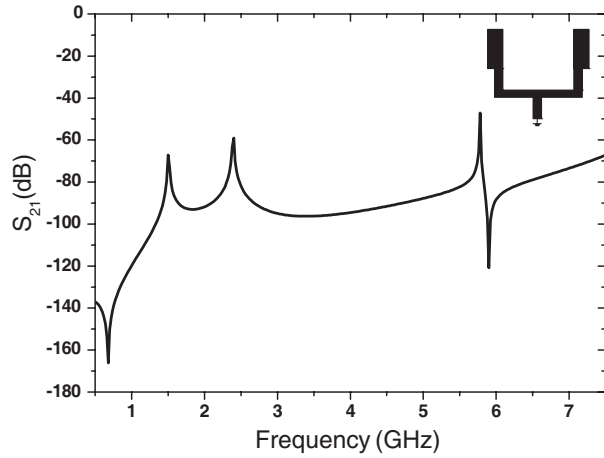


Figure 1: Simulated frequency response of the proposed resonator.

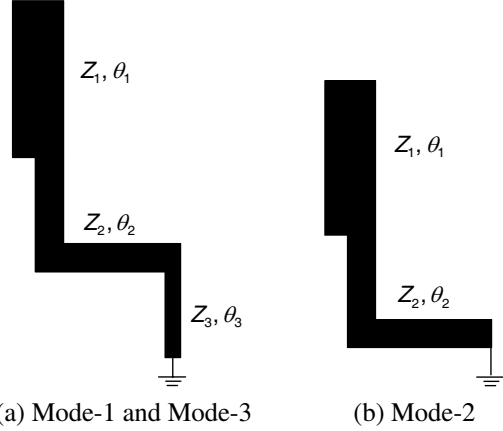


Figure 2: Resonant modes of the resonator.

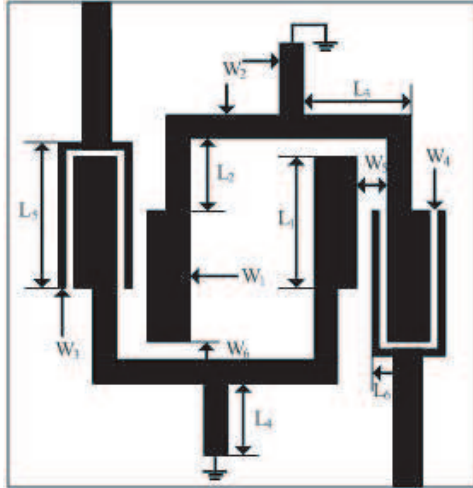


Figure 3: Schematic of the proposed tri-band BPF.

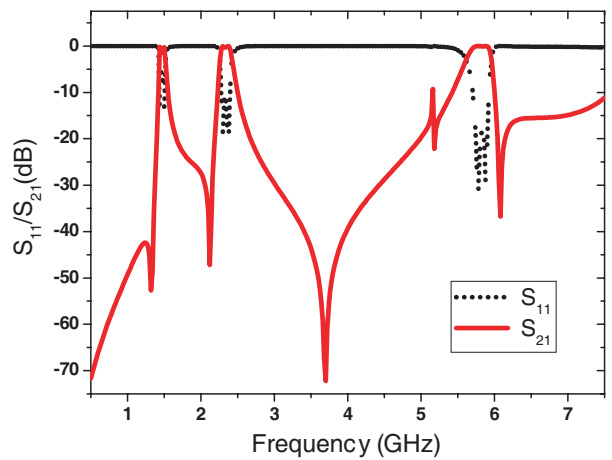


Figure 4: Simulated frequency response of the proposed filter.

in Fig. 4. Obviously, the three resonated frequencies located at 1.5 GHz, 2.4 GHz, 5.78 GHz, respectively. The simulated reflection losses in three passband are about -10.6 dB, -15 dB, and -18 dB. Four transmission zeros are realized at 1.3 GHz, 2.1 GHz, 3.7 GHz, and 6.2 GHz, which improve the selective in the transition band and attenuation in the stopband.

4. CONCLUSION

A novel compact two-order tri-band microstrip BPF with using shorted-stub-loaded SIRs and pseudo-interdigital coupling structure has been proposed. Three passbands with central frequencies of 1.5 GHz, 2.4 GHz and 5.78 GHz for commercially applications are achieved. The circuit structure has exhibited good passband selectivity owing to the transmission zeros produced by the pseudo-interdigital coupled filter configuration.

ACKNOWLEDGMENT

This work is supported by Shanghai Leading Academic Discipline Project and STCSM (S30108 and 08DZ2231100), NSFC of China (No. 61061001), Foundation of Jiangxi Educational Committee (GJJ11437), and the Global Research Network Program of National Research Foundation of Korea (No. KRF-2009-220-D00074).

REFERENCES

1. Fan, J.-W., C.-H. Liang, and X.-W. Dai, "Design of cross-coupled dual-band filter with equal-length split-ring resonators," *Progress In Electromagnetics Research*, Vol. 75, 285–293, 2007.
2. Dai, X.-W., C.-H. Liang, B. Wu, and J. Fan, "Novel dual-band bandpass filter design using microstrip open-loop resonators," *Journal of Electromagnetic Waves and Applications*, Vol. 22, No. 2, 219–225, 2008.
3. Wu, G.-L., W. Mu, X.-W. Dai, and Y.-C. Jiao, "Design of novle dual-band bandpass filter with microstrip meander-loop resonator and CSRR DGS," *Progress In Electromagnetics Research*, Vol. 78, 17–24. 2008.
4. Huang, J.-F., J.-Y. Wen, and Z.-M. Lyu, "A triple broadband microwave filter synthesis using nonuniform lines," *Microwave and Optical Technology Letters*, Vol. 50, 3039–3045, 2008.
5. Rambabu, K., A. E. C. Tan, M. Y. W. Chia, and J. Bornemann, "Printed-circuit filters for wireless dual-and triple-band applications," *Microwave and Optical Technology Letters*, Vol. 50, 1495–1497, 2008.
6. Kung, C.-Y., Y.-C. Chen, C.-F. Yang, and C.-Y. Huang, "Triple-band parallel coupled microstrip bandpass filter with dual coupled length input/output," *Microwave and Optical Technology Letters*, Vol. 51, 995–997, 2009.
7. Lai, X., B. Wu, T. Su, and C.-H. Liang, "A novel tri-band filter using stub-loaded open loop ring resonators," *Microwave and Optical Technology Letters*, Vol. 52, 523–526, 2010.
8. Chen, F.-C., Q.-X. Chu, and Z.-H. Tu, "Design of compact dual-band tri-band bandpass filters using $\lambda/4$ and $\lambda/2$ resonators," *Microwave and Optical Technology Letters*, Vol. 51, 638–641, 2009.
9. Guan, X., Z. Ma, and P. Cai, "A novel triple-band microstrip bandpass filter for wireless communication," *Microwave and Optical Technology Letters*, Vol. 51, 1568–1569, 2009.
10. Hsiao, P.-Y. and R.-M. Weng, "A compact trilayer triband bandpass filter using SIR-DGS and open-loop resonator," *Microwave and Optical Technology Letters*, Vol. 50, 2751–2754, 2008.
11. Chen, F.-C. and Q.-X. Chu, "Compact triple-band bandpass filter using pseudo-interdigital trisection stepped impedance resonators," *Microwave and Optical Technology Letters*, Vol. 50, 2462–2465, 2008.
12. Zhang, Y. P. and M. Sun, "Dual-band microstrip bandpass filter using stepped-impedance resonators with new coupling schemes," *IEEE Trans. Microwave Theory Tech.*, Vol. 54, 3779–3785, 2006.

Waveguide-based Meniscus Thin Lens for Broadband MM-wave Power Combining Applications

Nan Yang, Huaicheng Zhao, Xidong Wu, and Jinfang Zhou

Department of Information Science & Electronic Engineering, Zhejiang University, China

Abstract— A meniscus thin lens integrated in a rectangular waveguide is presented for broadband high-efficiency power combining applications. The combiner structure is composed of ten side-by-side input waveguides, a meniscus thin lens with a matching layer, an *E*-plane sectoral horn, and an output waveguide. Simulation results from CST Microwave Studio show that the choice of the *f/D* number of the meniscus thin lens plays a significant role in achieving high combining efficiency and a matching layer also helps to improve the efficiency. For a ten-way combiner with center frequency of 30 GHz, a broad 80%-efficiency bandwidth of 11.5 GHz (28.5 GHz–40 GHz) has been achieved.

1. INTRODUCTION

Quasi-optical power combining especially with lens is attracting more and more research interest, because of its high efficiency and convenient structure. Some efforts based on waveguide technology such as waveguide lens [1] and waveguide-based dielectric lens [2] have been reported recently. The dielectric lens used in [2] is of relatively higher loss due to its thickness. To overcome this problem, this paper presents another convenient way to realize mm-wave power combining using a meniscus thin lens based on standard rectangular waveguide WR-28. A matching layer is proved with CST Microwave Studio to be useful in improving combining efficiency. The simulation results show a bandwidth of 80% efficiency from 28.5 GHz to 40 GHz can be achieved.

2. THEORY AND STRUCTURE

Figure 1 displays a general diagram of a typical meniscus thin lens. As shown, the focal point of the lens is located at point *F*; *n*, *D* and *f* are the refractive index, diameter and focal length of the meniscus thin lens respectively. The meniscus thin lens has a cylindrical inner surface and an elliptic outer surface, which can be described in Cartesian coordinates as follows [1]:

$$\text{Inner surface: } x^2 + (y + c)^2 = f^2 \quad (1)$$

$$\text{Outer surface: } x^2/a^2 + y^2/b^2 = 1 \quad (2)$$

where

$$b = \frac{n^2 f - n\sqrt{f^2 - D^2/4}}{n^2 - 1} \quad (3)$$

$$a = \frac{\sqrt{n^2 - 1}}{n} b \quad (4)$$

$$c = b/n \quad (5)$$

Figure 2 shows the proposed waveguide-lens-based power combiner. As shown, the combiner consists of ten side-by-side input waveguides, a meniscus thin lens with a matching layer, an *E*-plane sectoral horn, and an output waveguide. All the waveguides used in this design are standard rectangular waveguide WR-28, with a narrow wall *B* = 3.556 mm. The thicknesses of the lens and matching layer are *t* and *tm* respectively, while *d*₁ and *d*₂ denote the length of horn combiner and *E*-plane sectoral horn, which can be expressed as:

$$d_1 = f + t - \frac{B}{D} \sqrt{f^2 - \left(\frac{D}{2}\right)^2} \quad (6)$$

$$d_2 = \frac{D - B}{D} \sqrt{f^2 - \left(\frac{D}{2}\right)^2} \quad (7)$$

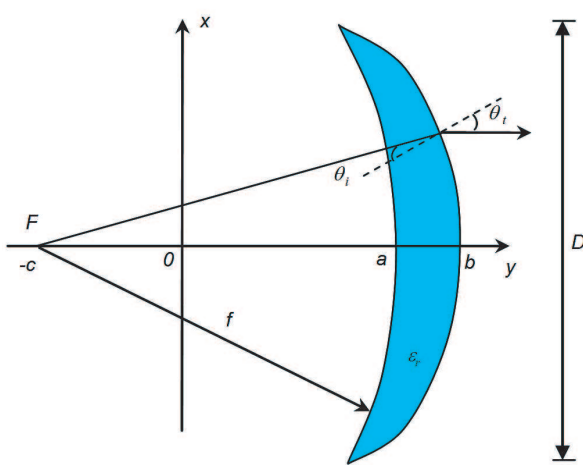


Figure 1: Two-dimensional configuration of a meniscus lens.

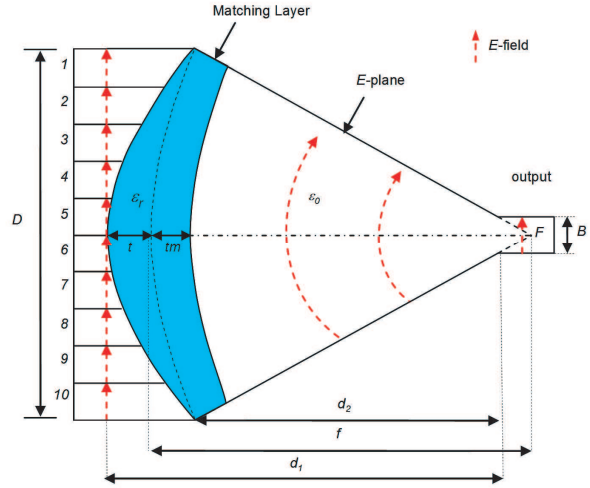


Figure 2: Waveguide-based power combiner using meniscus thin lens with a matching layer.

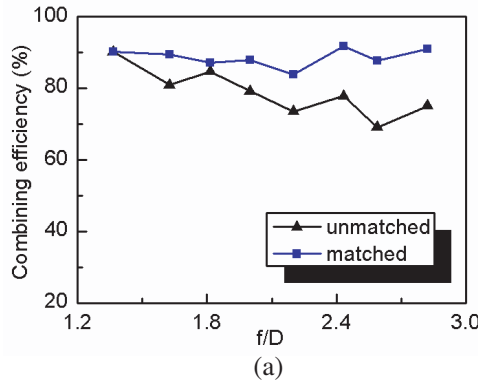
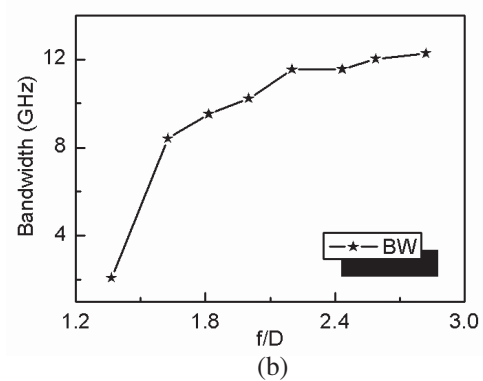


Figure 3: (a) Efficiency comparison between matched and unmatched structure; (b) 80%-efficiency bandwidth vs. the f/D number.



The meniscus thin lens is placed so that its focal point F coincides with the imaginary apex of the E -plane sectoral horn (shown in dash line). The meniscus thin lens transforms the planar wavefront to cylindrical wavefront, which is then converged into the E -plane sectoral horn and collected as output. The matching layer is a partial dielectric filling in the E -plane sectoral horn and its thickness can be optimized to achieve the best matching at the design frequency. One of the most important design objectives is the combining efficiency, which is defined as the ratio of the output power to the total input power when all the ten input waveguide ports are equally excited:

$$\eta = P_{out} / \sum P_i = P_{out} / 10P_1 \times 100\% \quad (8)$$

3. RESULTS

In this paper, Rexolite ($\epsilon_r = 2.54$) is chosen to machine the meniscus thin lens. For a ten-way combiner, the diameter of the lens is fixed to be $D = 10B = 35.56$ mm. Fig. 3(a) shows the simulated combining efficiency at the design frequency of 30 GHz for matched and unmatched structure, respectively. As shown, the combining efficiency can be improved with the optimized matching layer. It should be noted that the optimum combining efficiency does not necessarily increase with the f/D number. However, the efficiency bandwidth is improved with increased f/D number, as shown in Fig. 3(b). The 80%-efficiency bandwidth is more than 8.4 GHz with the f/D number larger than 1.6, but will improve little when the f/D number is larger than 2.4. Finally, the combining efficiency for $f/D = 2.4$ is depicted in Fig. 4, which shows a broad 80%-efficiency bandwidth of 11.5 GHz (28.5 GHz–40 GHz).

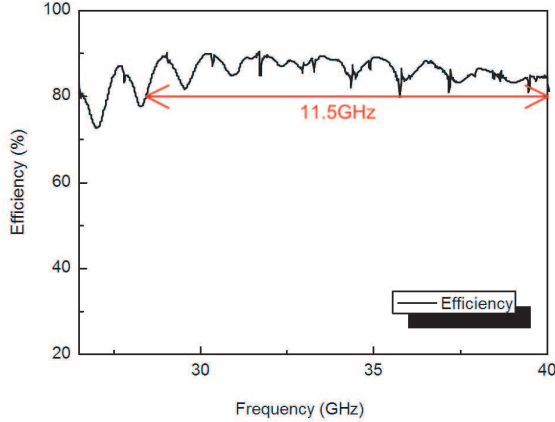


Figure 4: Simulated efficiency of the meniscus thin lens power combiner ($f/D = 2.4$).

4. CONCLUSIONS

This paper demonstrates a broadband power combiner using meniscus thin lens integrated inside a rectangular waveguide. The choice of the f/D number of the meniscus thin lens is critical for achieving high combining efficiency. A matching layer for the meniscus thin lens is introduced to improve the combining efficiency. This structure can be easily extended to higher frequencies or more inputs for higher power applications.

ACKNOWLEDGMENT

This work is supported by Ministry of Science and Technology of China under Project 863 Grant 2009AA01Z226 and by NSFC under grant # 60871010.

REFERENCES

1. Wu, X. D., H. C. Zhao, C. Miao, and W. Wu, "Design on waveguide thin lens quasi-optical power combining," *Asia Pacific Microwave Conference*, 2577–2579, Singapore, December 2009.
2. Wu, X. D., H. C. Zhao, and W. Wu, "Quasi-optical power combining using waveguide-based hyperbolic lens," *Antennas and Propagation Society International Symposium*, 1–4, San Diego, America, July 2008.

Phase Singularities of Focused High-order Hermite-Gaussian Beams

Yongtao Zhang, Chaoliang Ding, Zhiguo Zhao, and Liuzhan Pan

Department of Physics, Luoyang Normal College, Luoyang 471022, China

Abstract— The phase singularities of high-order Hermite-Gaussian beams focused by an aperture lens are studied. Numerical calculation results are given to illustrate the dependence of phase singularities on the truncation parameter and beam order. The reorganization process of phase singularities of focused high-order Hermite-Gaussian beams with increasing truncation parameter is illustrated by numerical examples.

1. INTRODUCTION

In recent years, much interest has been exhibited in singular optics due to its theoretical importance in modern optics and potential applications in practice [1, 2]. There have been some researches focusing on the intensity and phase singularities distribution in the focal region of focused beams [3–8]. In the present paper, we investigate the phase singularities of high-order Hermite-Gaussian beams focused by an aperture lens. Numerical calculation results are given to illustrate the dependence of phase singularities on the truncation parameter and beam order. Hermite-Gaussian beams have been studied extensively in the past decades and have been widely applied in modern optics [9–13].

2. THEORETICAL MODEL

Suppose that a high-order Hermite-Gaussian beam is incident upon an aperture lens at the $z = 0$ plane. The aperture lens system consists of a lens with focal length f and a slit aperture with full width $2a$. The field of the incident beam takes the form

$$E_m(x_0, 0) = S H_m \left(\sqrt{2} \frac{x_0}{w_0} \right) \exp \left(-\frac{x_0^2}{w_0^2} \right), \quad (1)$$

where H_m denotes the Hermite polynomial of order m , w_0 is the waist width of the beam, S is the amplitude at the central position of $x = z = 0$. Within the framework of the paraxial approximation, the field $E_m(x, z)$ of the beam propagating through a paraxial optical $ABCD$ system is expressed as [14]

$$E_m(x, z) = \sqrt{\frac{ik}{2\pi B}} \exp(-ikz) \int_{-a}^a E_m(x_0, 0) \times \exp \left[-\frac{ik}{2B} (Ax_0^2 + Dx^2 - 2xx_0) \right] dx_0, \quad (2)$$

where $k = 2\pi/\lambda = c/\omega$ is the wave number associated with angular frequency ω and wavelength λ . And the transfer $ABCD$ matrix reads as

$$\begin{pmatrix} A & B \\ C & D \end{pmatrix} = \begin{pmatrix} 1 - z/f & z \\ -1/f & 1 \end{pmatrix}. \quad (3)$$

The intensity $I(x, z)$ of focused high-order Hermite-Gaussian beams can be given by

$$I(x, z) = E^*(x, z)E(x, z), \quad (4)$$

On substituting Eqs. (1)–(3) into Eq. (4) and after some algebra, we obtain

$$I(\mu, \Delta z) = I^{(0)} M(\mu, \Delta z), \quad (5)$$

with

$$\begin{aligned} I^{(0)} &= S^* S, \\ M(\mu, \Delta z) &= \frac{N}{a\delta\Delta z} \left| \int_{-a}^a H_m(\sqrt{2}x_1) \times \exp \left[-x_1^2 - \frac{iN\pi(1-\Delta z)x_1^2}{\Delta z\delta^2} \right] \right. \\ &\quad \left. \times \exp \left(-\frac{iN\pi\mu^2}{\Delta z} + \frac{i2N\pi x_1 \mu}{\Delta z\delta} \right) dx_1 \right|^2, \end{aligned} \quad (6)$$

where $N = \frac{a^2}{\lambda f}$ is the Fresnel number, $\delta = \frac{a}{w_0}$ is the truncation parameter, $\mu = \frac{x}{a}$ is the relative transversal coordinate in the x direction, $\Delta z = \frac{z}{f}$ is the relative axial distance.

3. NUMERICAL CALCULATION RESULTS AND ANALYSES

Numerical calculations were performed by using Eqs. (5) and (7) to illustrate the phase singularities of focused high-order Hermite-Gaussian beams, and to stress the influence of truncation parameter δ and beam order m on the behavior of phase singularities. In the following calculations, we have chosen $N = 10$, $\omega = 3 \times 10^{15} \text{ s}^{-1}$ and $a = 1 \times 10^{-3} \text{ m}$.

Figure 1 gives the contour lines of constant intensity of focused high-order Hermite-Gaussian beams with $m = 1$, where $\delta = 1.50$ in Fig. 1(a), $\delta = 1.61$ in Fig. 1(b) and $\delta = 1.75$ in Fig. 1(c). In Fig. 1, contour lines of constant intensity are normalized to 1 in the geometric focal point; adjacent lines differ by a factor of 10. The normalized intensity of A , B , C and D is equal to zero. Therefore, these points are singularities. For $\delta = 1.50$ in Fig. 1(a) there exist four phase singularities labeled A , B , C and D in the focal plane, i.e., $A (1.0000, 0.0985)$, $B (1.0000, 0.1316)$, $C (1.0000, 0.1802)$, $D (1.0000, 0.2290)$. For $\delta = 1.61$, Fig. 1(b) shows that the singularity B is split into three ones labeled B , E , and F , i.e., $A (1.0000, 0.1066)$, $B (1.0000, 0.1312)$, $E (0.9789, 0.1319)$, $F (1.0220, 0.1377)$, $C (1.0000, 0.1811)$, $D (1.0000, 0.2298)$. When we increase the truncation parameter δ to 1.75, the singularities A and B approach each other and annihilate, and the singularities E , F , C and D are located at $E (0.9666, 0.1369)$, $F (1.0358, 0.1467)$, $C (1.0000, 0.1824)$, $D (1.0000, 0.2308)$.

Figure 2 gives the contour lines of constant intensity of focused high-order Hermite-Gaussian beams with $m = 2$ for different values of the truncation parameter δ . From Figs. 2(a) and (b), we see that as the truncation parameter δ is increased from 1.65 to 1.77, the singularity C is split into

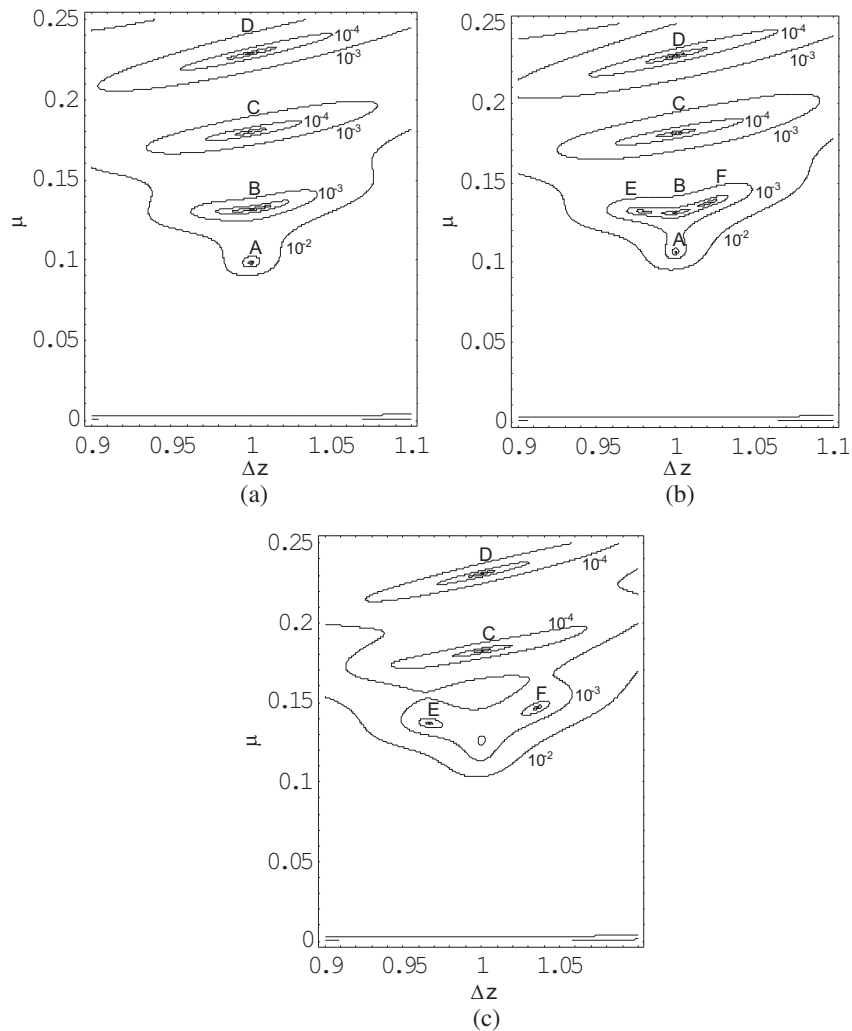


Figure 1: Contour lines of constant intensity of a focused high-order Hermite-Gaussian beam with $m = 1$ for different values of the truncation parameter δ . (a) $\delta = 1.50$, (b) $\delta = 1.61$, and (c) $\delta = 1.75$.

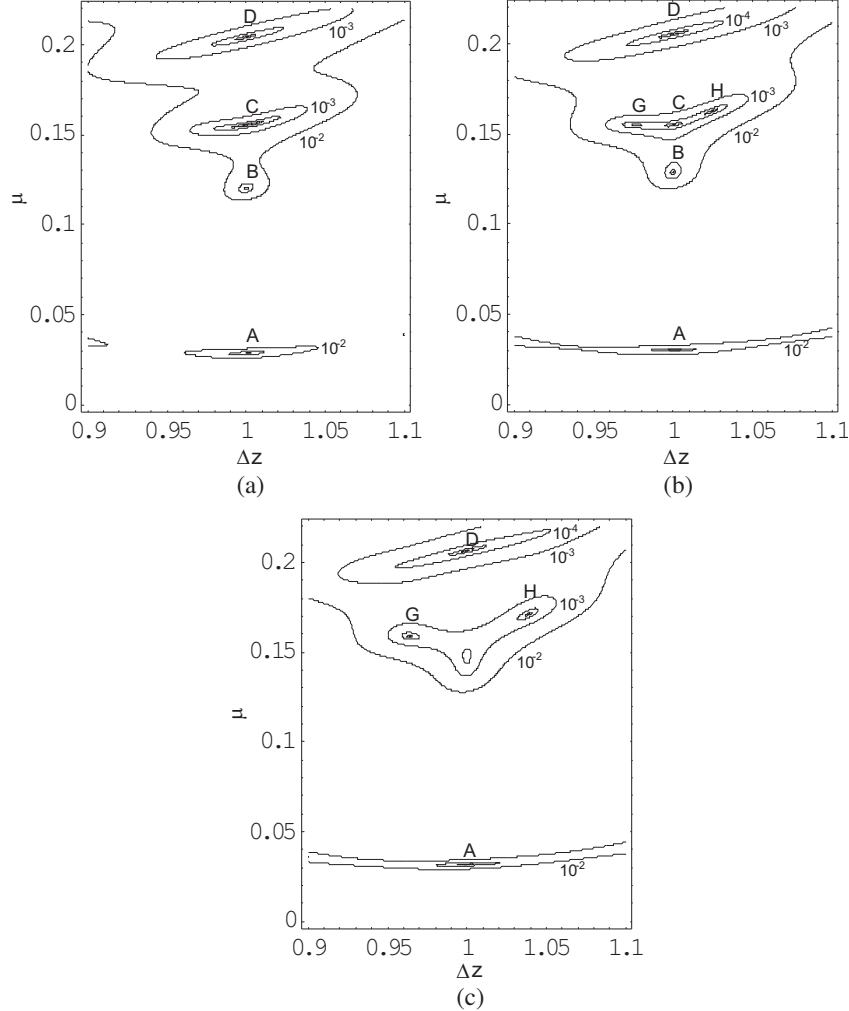


Figure 2: Contour lines of constant intensity of a focused high-order Hermite-Gaussian beam with $m = 2$ for different values of the truncation parameter δ . (a) $\delta = 1.65$, (b) $\delta = 1.77$, and (c) $\delta = 1.90$.

three ones labeled C , G , and H , i.e., A (1.0000, 0.0285), B (1.0000, 0.1202), C (1.0000, 0.1554), D (1.0000, 0.2044) at $\delta = 1.65$, and A (1.0000, 0.0300), B (1.0000, 0.1286), C (1.0000, 0.1550), G (0.9764, 0.1549), H (1.0248, 0.1626), D (1.0000, 0.2055) at $\delta = 1.77$. A further increase of δ to 1.90 in Fig. 2(c) results in an annihilation of singularities B and C , and the singularities A , G , H and D are located at A (1.0000, 0.0317), G (0.9639, 0.1590), H (1.0390, 0.1714), D (1.0000, 0.2067). From Fig. 2, it turns out that as the truncation parameter gradually increases, the singularities B and C approach each other and annihilate, Whereas the singularity A remain in the focal plane. Furthermore, the reorganization process continues with the next pair of phase singularities with increasing beam order m , which is omitted here.

4. CONCLUSIONS

In this paper, the phase singularities of focused high-order Hermite-Gaussian beams have been studied, which depend on the truncation parameter δ and beam order m . Numerical calculation results have been presented to stress the for different values of the on the behavior of phase singularities. As the truncation parameter gradually increases, the singularities A and B approach each other and annihilate for $m = 1$, whereas for $m = 2$ the singularities B and C approach each other and annihilate. With increasing beam order m the reorganization process continues with the next pair of phase singularities. Our study would be useful for understanding the evolution behavior of phase singularities in the presence of astigmatism and for controlling phase singularities.

ACKNOWLEDGMENT

This work was supported by the National Natural Science Foundation of China under Grant No. 60978011 and 61078077, and Natural Science Foundation of Henan Province under Grant No. 112300410062, and the foundation of Luoyang normal college 2010-PYJJ-003.

REFERENCES

1. Soskin, M. S. and M. V. Vasnetsov, "Singular optics," *Prog. in Optics*, Vol. 42, 219–276, 2001.
2. Grier, D. G., "A revolution in optical manipulation," *Nature*, Vol. 424, 21–27, 2003.
3. Karman, G. P., M. W. Beijersbergen, A. van Duijl, and J. P. Woerdman, "Creation and annihilation of phase singularities in a focal field," *Opt. Lett.*, Vol. 22, No. 19, 1503–1505, 1997.
4. Hu, X. and J. Pu, "The effect of spherical aberration on singularities and spectral changes of focused beams," *New J. Phys.*, Vol. 8, No. 6, 93, 2006.
5. Liu, P. and B. Lv, "Phase singularities of the transverse field component of high numerical aperture dark-hollow Gaussian beams in the focal region," *Opt. Commun.*, Vol. 272, No. 1, 1–8, 2007.
6. Chen, J., Z. Chen, and J. Pu, "Singularities and spectral changes of Gaussian beams focused by a lens with spherical aberration," *Opt. and Laser Technol.*, Vol. 40, No. 6, 881–889, 2008.
7. Luo, Y. and B. Lv, "The effect of spherical aberration on the phase singularities of focused dark-hollow Gaussian beams," *Opt. and Laser Technol.*, Vol. 41, No. 4, 441–448, 2009.
8. Zhang, Y. and L. Pan, "The effect of astigmatism on the phase singularities of focused beams," *Opt. and Laser Technol.*, Vol. 42, No. 3, 484–488, 2010.
9. Carter, W. H., "Spot size and divergence for Hermite-Gaussian beams of any order," *Appl. Opt.*, Vol. 19, No. 7, 1027–1029, 1980.
10. Saghafi, S. and C. J. R. Sheppard, "The beam propagation factor for higher-order Gaussian beams," *Opt. Commun.*, Vol. 153, 207–210, 1998.
11. Cai, Y. and Q. Lin, "The elliptical Hermite-Gaussian beam and its propagation through paraxial systems," *Opt. Commun.*, Vol. 207, 139–147, 2002.
12. Cai, Y. and Q. Lin, "Decentered elliptical Hermite-Gaussian beam," *J. Opt. Soc. Am. A*, Vol. 20, No. 6, 1111–1119, 2003.
13. Cai, Y. and C. Chen, "Paraxial propagation of a partially coherent Hermite-Gaussian beam through aligned and misaligned ABCD optical systems," *J. Opt. Soc. Am. A*, Vol. 24, No. 8, 2394–2401, 2007.
14. Collins, S. A., "Lens-system diffraction integral written in terms of matrix optics," *J. Opt. Soc. Am.*, Vol. 60, No. 9, 1168–1177, 1970.

The Effect of Spherical Aberration on the Spectral Stokes Singularities of Tightly Focused Partially Coherent Anomalous Hollow Beams

Yamei Luo¹, Jinhong Li², and Bihua Tang¹

¹Department of Biomedical Engineering, Luzhou Medical College, Luzhou 646000, China

²Department of Physics, Taiyuan University of Science and Technology, Taiyuan 030024, China

Abstract— The spectral Stokes singularities of partially coherent radially polarized anomalous hollow beams focused by a high numerical aperture (NA) objective in the presence of spherical aberration is studied in detail by using the vector Debye formula. It is shown that there exist s_{12} , s_{23} , and s_{31} spectral Stokes singularities. The variation of the spherical aberration, truncation parameter and half angle of the aperture lens will result in the motion, pair creation and annihilation, and changes in the degree of polarization of s_{12} , s_{23} , and s_{31} spectral Stokes singularities, and the handedness reversal of s_{12} singularities (C -points). The creation and annihilation occur for a pair of s_{12} singularities with opposite topological charge but same handedness, and for a pair of oppositely charged s_{23} or s_{31} singularities, which is similar to the aberration-free case. The collision of an s_{12} singularity with an L -line ($s_3 = 0$ contour) leads to a V -point, which is located at the intersection of contours of $s_{12} = 0$ and $s_{23} = 0$ (or $s_{31} = 0$) and is unstable. A small perturbation leads to the handedness reversal and changes in the degree of polarization of the C -point. The results have been illustrated numerically and are compared with the results of previous work.

1. INTRODUCTION

Much interest has been exhibited in the focusing of high numerical aperture (NA) polarized beams due to the applications in confocal microscopy, lithography and electron acceleration etc. Zhan et al. [1] analyzed the focus shaping of generalized cylindricalvector beams and found peak-centered, donut and flat-topped focal shapes under certain conditions. Diehl et al. [2] dealt with the structure of tightly focused radially polarized beams and the existence of phase singularities of the longitudinal and radial electric field components. Schoonover and Visser [3] examined the state of polarization of strongly focused radially polarized fields and showed the evolution of a lemon into a monstar and the presence of a V -point. More recently, we studied the spectral singularities of tightly focused radially polarized beams by introducing spectral Stokes singularities [4]. The aim of the present paper is to illustrate the effect of spherical aberration on the spectral singularities of focused partially coherent high NA radially polarized beams.

2. THEORETICAL MODEL

Assume that a novel type of beam, i.e., anomalous hollow beam is tightly focused by a spherically aberrated aperture lens of the focal length f and aperture radius a . The cross-spectral density of the apodization function of the pupil of such partially coherent radially polarized beam is expressed as [5–8]

$$l_0(\theta_1, \theta_2) = \left[-2 + 8 \left(\frac{\delta \sin \theta_1}{\tan \theta_{\max}} \right)^2 \right] \left[-2 + 8 \left(\frac{\delta \sin \theta_2}{\tan \theta_{\max}} \right)^2 \right] \exp \left[-\frac{\delta^2 (\sin^2 \theta_1 + \sin^2 \theta_2)}{\tan^2 \theta_{\max}} - \frac{f^2}{L_c^2} (\sin \theta_1 - \sin \theta_2)^2 \right], \quad (1)$$

where $\delta = a/w_0$ is the truncation parameter, θ_{\max} is the semi-angle of the aperture lens, w_0 denotes the waist width, L_c specifies the spatial correlation length.

The spherical aberration is described by a phase factor $\exp(ik\phi_R)$, where the spherical aberration function is expressed as [9]

$$\phi_R = \frac{S_1 \delta^4 \sin^4 \theta}{\tan^4 \theta_{\max}}, \quad (2)$$

S_1 is the spherical aberration coefficient, and k is the wave number related to the wavelength λ by $k = 2\pi/\lambda$.

The concept of spectral Stokes singularities can be expressed as [4]

$$\begin{aligned} S_0(\mathbf{r}_1, \mathbf{r}_2) &= \langle E_z^*(\mathbf{r}_1) E_z(\mathbf{r}_2) \rangle + \langle E_\rho^*(\mathbf{r}_1) E_\rho(\mathbf{r}_2) \rangle & S_1(\mathbf{r}_1, \mathbf{r}_2) &= \langle E_z^*(\mathbf{r}_1) E_z(\mathbf{r}_2) \rangle - \langle E_\rho^*(\mathbf{r}_1) E_\rho(\mathbf{r}_2) \rangle \\ S_2(\mathbf{r}_1, \mathbf{r}_2) &= \langle E_z^*(\mathbf{r}_1) E_\rho(\mathbf{r}_2) \rangle + \langle E_\rho^*(\mathbf{r}_1) E_z(\mathbf{r}_2) \rangle, & S_3(\mathbf{r}_1, \mathbf{r}_2) &= i[\langle E_\rho^*(\mathbf{r}_1) E_z(\mathbf{r}_2) \rangle - \langle E_z^*(\mathbf{r}_1) E_\rho(\mathbf{r}_2) \rangle], \end{aligned} \quad (3)$$

where the brackets $\langle \rangle$ denotes the ensemble average, and the asterisk * denotes the complex conjugate.

Using Lommel variables $u = kz \sin^2 \theta_{\max}$, $v = kr \sin \theta_{\max}$, and on substituting Eqs. (1)–(2) into Eq. (3), the generalized Stokes parameters are rewritten as

$$\begin{aligned} S_0(\mathbf{r}_1, \mathbf{r}_2) &= \int_0^{\theta_{\max}} \int_0^{\theta_{\max}} l_0(\theta_1, \theta_2) \sqrt{\cos \theta_1 \cos \theta_2} \\ &\quad \exp \left(-i \frac{u \cos \theta_1}{\sin^2 \theta_{\max}} + i \frac{u \cos \theta_2}{\sin^2 \theta_{\max}} - ik S_1 \delta^4 \frac{\sin^4 \theta_1}{\tan^4 \theta_{\max}} + ik S_1 \delta^4 \frac{\sin^4 \theta_2}{\tan^4 \theta_{\max}} \right) \\ &\quad \times \left[4 \sin^2 \theta_1 \sin^2 \theta_2 J_0 \left(\frac{v \sin \theta_1}{\sin \theta_{\max}} \right) J_0 \left(\frac{v \sin \theta_2}{\sin \theta_{\max}} \right) \right. \\ &\quad \left. + \sin 2\theta_1 \sin 2\theta_2 J_1 \left(\frac{v \sin \theta_1}{\sin \theta_{\max}} \right) J_1 \left(\frac{v \sin \theta_2}{\sin \theta_{\max}} \right) \right] d\theta_1 d\theta_2, \end{aligned} \quad (4a)$$

$$\begin{aligned} S_1(\mathbf{r}_1, \mathbf{r}_2) &= \int_0^{\theta_{\max}} \int_0^{\theta_{\max}} l_0(\theta_1, \theta_2) \sqrt{\cos \theta_1 \cos \theta_2} \\ &\quad \exp \left(-i \frac{u \cos \theta_1}{\sin^2 \theta_{\max}} + i \frac{u \cos \theta_2}{\sin^2 \theta_{\max}} - ik S_1 \delta^4 \frac{\sin^4 \theta_1}{\tan^4 \theta_{\max}} + ik S_1 \delta^4 \frac{\sin^4 \theta_2}{\tan^4 \theta_{\max}} \right) \\ &\quad \times \left[4 \sin^2 \theta_1 \sin^2 \theta_2 J_0 \left(\frac{v \sin \theta_1}{\sin \theta_{\max}} \right) J_0 \left(\frac{v \sin \theta_2}{\sin \theta_{\max}} \right) \right. \\ &\quad \left. - \sin 2\theta_1 \sin 2\theta_2 J_1 \left(\frac{v \sin \theta_1}{\sin \theta_{\max}} \right) J_1 \left(\frac{v \sin \theta_2}{\sin \theta_{\max}} \right) \right] d\theta_1 d\theta_2, \end{aligned} \quad (4b)$$

$$\begin{aligned} S_2(\mathbf{r}_1, \mathbf{r}_2) &= 2i \int_0^{\theta_{\max}} \int_0^{\theta_{\max}} l_0(\theta_1, \theta_2) \sqrt{\cos \theta_1 \cos \theta_2} \\ &\quad \exp \left(-i \frac{u \cos \theta_1}{\sin^2 \theta_{\max}} + i \frac{u \cos \theta_2}{\sin^2 \theta_{\max}} - ik S_1 \delta^4 \frac{\sin^4 \theta_1}{\tan^4 \theta_{\max}} + ik S_1 \delta^4 \frac{\sin^4 \theta_2}{\tan^4 \theta_{\max}} \right) \\ &\quad \times \left[-\sin^2 \theta_1 \sin 2\theta_2 J_0 \left(\frac{v \sin \theta_1}{\sin \theta_{\max}} \right) J_1 \left(\frac{v \sin \theta_2}{\sin \theta_{\max}} \right) \right. \\ &\quad \left. + \sin 2\theta_1 \sin^2 \theta_2 J_1 \left(\frac{v \sin \theta_1}{\sin \theta_{\max}} \right) J_0 \left(\frac{v \sin \theta_2}{\sin \theta_{\max}} \right) \right] d\theta_1 d\theta_2, \end{aligned} \quad (4c)$$

$$\begin{aligned} S_3(\mathbf{r}_1, \mathbf{r}_2) &= -2 \int_0^{\theta_{\max}} \int_0^{\theta_{\max}} l_0(\theta_1, \theta_2) \sqrt{\cos \theta_1 \cos \theta_2} \\ &\quad \exp \left(-i \frac{u \cos \theta_1}{\sin^2 \theta_{\max}} + i \frac{u \cos \theta_2}{\sin^2 \theta_{\max}} - ik S_1 \delta^4 \frac{\sin^4 \theta_1}{\tan^4 \theta_{\max}} + ik S_1 \delta^4 \frac{\sin^4 \theta_2}{\tan^4 \theta_{\max}} \right) \\ &\quad \times \left[\sin 2\theta_1 \sin^2 \theta_2 J_1 \left(\frac{v \sin \theta_1}{\sin \theta_{\max}} \right) J_0 \left(\frac{v \sin \theta_2}{\sin \theta_{\max}} \right) \right. \\ &\quad \left. + \sin^2 \theta_1 \sin 2\theta_2 J_0 \left(\frac{v \sin \theta_1}{\sin \theta_{\max}} \right) J_1 \left(\frac{v \sin \theta_2}{\sin \theta_{\max}} \right) \right] d\theta_1 d\theta_2, \end{aligned} \quad (4d)$$

By letting $\mathbf{r}_1 = \mathbf{r}_2$, we obtain the normalized spectral Stokes parameters $s_1 = S_1/S_0$, $s_2 = S_2/S_0$ and $s_3 = S_3/S_0$. Thus, the complex spectral Stokes fields s_{ij} ($i, j = 1, 2, 3$) can be introduced and are given by

$$s_{12} = s_1 + is_2, \quad s_{23} = s_2 + is_3, \quad s_{31} = s_3 + is_1. \quad (5)$$

The degree of polarization reads as

$$P = \sqrt{s_1^2 + s_2^2 + s_3^2}. \quad (6)$$

s_{12} singularities correspond to the circular polarization (C -points) of nonparaxial partially coherent beams, at which the polarization ellipse reduces to a circle. $s_3 > 0$ ($s_3 < 0$) means right- (left-) handedness. s_{23} and s_{31} singularities must be located on L -lines, where the polarization ellipse degenerates into a line. From Eqs. (1)–(6) it turns out that the spectral Stokes singularities of tightly focused by a spherically aberrated aperture lens depend on the truncation parameter δ , the spherical aberration kS_1 , semi-angle of the aperture lens θ_{\max} (or equally, $NA = \sin \theta_{\max}$) and spatial correlation length L_c .

3. SPECTRAL STOKES SINGULARITIES IN THE FOCAL REGION

From Section 2, we see that the spectral Stokes singularities in the focal region are dynamically variable if a controlling parameter, such as the truncation parameters δ , spherical aberration kS_1 , semi-angle of the aperture lens θ_{\max} and spatial correlation length L_c , is changed which can be illustrated numerically by using Eqs. (4)–(6). In the following numerical calculations $f = 10000\lambda$ is kept fixed, thus the Fresnel number $N = (NA)_2 f / \lambda \gg 1$ to ensure the validity of the Debye theory. Figs. 1(a)–(d) show spectral Stokes singularities in the region ($5 \leq u \leq 12$, $3.5 \leq v \leq 9.5$) for different values of the truncation parameters (a) $\delta = 1.67$, (b) $\delta = 1.65$, (c) $\delta = 1.645$, (d) $\delta = 1.625$. The calculation parameters are $\theta_{\max} = \pi/3$, $kS_1 = 0.03$ and $L_c = 10000\lambda$. The contours of $s_1 = 0$, $s_2 = 0$ and $s_3 = 0$ are represented by solid, dashed and dotted curves, respectively. s_{12} (C -points, labeled by 1, 2, 3, 4, 5, 6), s_{23} (labeled by A, B, C) and s_{31} (labeled by a, b, c) singularities appear at the intersection of $s_i = 0$ and $s_j = 0$, and are represented by circles, triangles and squares, the black and open ones correspond to the topological charges $m_{ij} = -1$ and $+1$, respectively, which are determined by the sign principle [10]. The L -lines ($s_3 = 0$) separate the xy plane into the right- and left-handed regions [3], and the signs \pm of s_3 determine the handedness of C -points and are shown in the figures. As can be seen, at $\delta = 1.67$ in Fig. 1(a) there is a V-point [3] positioned at (11.397, 8.145) marked “★”, at which $s_1 = s_2 = s_3 = 0$, and the degree of polarization $P = 0$. With an increase of the truncation parameter to $\delta = 1.675$, the V-point shifts to (11.387, 8.173), and becomes left-handed whose degree of polarization $P = 0.036$ (not shown). However, with a decrease of the truncation parameter to $\delta = 1.65$ (see Fig. 1(b)), V-point shifts to (11.381, 8.004), and becomes right-handed whose degree of polarization $P = 0.084$. With decreasing truncation parameter a pair of C -points 5 and 6 with opposite charge and same right-handedness approach and annihilate each other $\delta = 1.625$ in Fig. 1(d).

A decrease of δ will result in the motion and change in the degree of polarization of s_{31} and s_{23} singularities. And as a result, a pair of s_{23} singularities A and B in Fig. 1(c), a pair of s_{31} singularities b and c (not shown) annihilate each other, respectively.

Similar behavior of spectral Stokes singularities is present by varying semi-angle of the aperture lens θ_{\max} and spatial correlation length L_c , and is omitted here.

Figure 2 gives the variation of distance between a pair of s_{23} singularities A, B in Fig. 1 versus the spherical aberration kS_1 , $\delta = 1.646$ and the other calculation parameters are the same as in Fig. 1(a). From Fig. 2, we see that the distance between a pair of s_{23} singularities A and B decreases as the spherical aberration decreases. As a result, the annihilation process may take

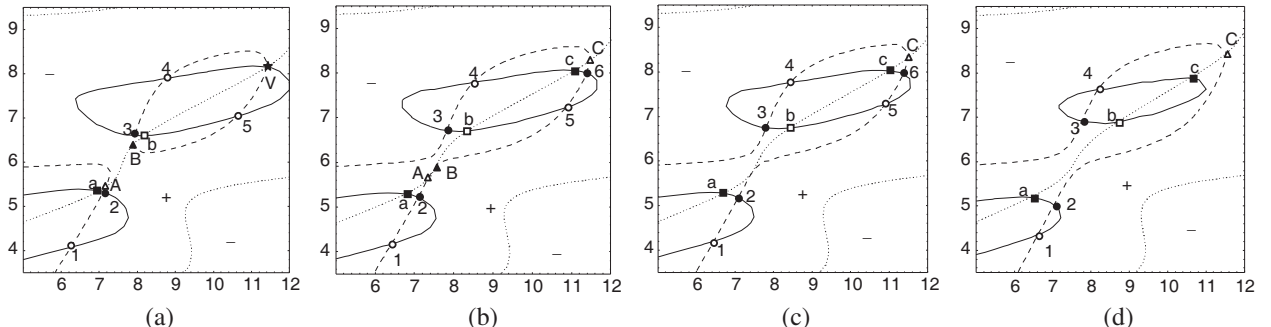


Figure 1: s_{12} , s_{23} and s_{31} singularities for different values of δ (a) $\delta = 1.67$, (b) $\delta = 1.65$, (c) $\delta = 1.645$, (d) $\delta = 1.625$.

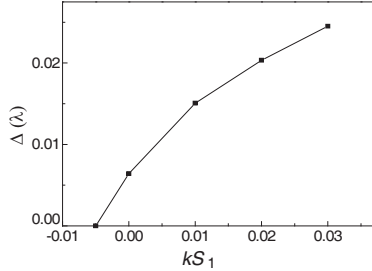


Figure 2: Distance Δ between a pair of s_{23} singularities versus the spherical aberration.

place. Similarly, the change of spherical aberration may result in the annihilation of s_{12} and s_{31} singularities, and not shown here.

4. CONCLUSION

In this paper, the spectral Stokes singularities of focused partially coherent high NA radially polarized beams have been studied, where the spherical aberration has been taken into consideration. It has been shown that there exist s_{12} , s_{23} , and s_{31} singularities, as well as V singularities. s_{12} , s_{23} , and s_{31} singularities may move, create and annihilate, their degree of polarization may change and the handedness reversal of s_{12} singularities may take place by a suitable variation of a controlling parameter, such as the truncation parameter, NA, spherical aberration or spatial correlation length. In comparison with Refs. [3, 4], where the polarization singularities of focused fully coherent and partially coherent high NA radially polarized beams were studied, respectively, in this paper, the spectral Stokes singularities of focused partially coherent high NA radially polarized beams in the presence of spherical aberration have been dealt with and shown that the annihilation process of the spectral singularities will depend on the spherical aberration. The results obtained in this paper would be beneficial to studying of the dependence of spectral Stokes singularities on the spherical aberration, and to controlling of spectral Stokes singularities.

ACKNOWLEDGMENT

This work was supported by the Natural Science Foundation of Luzhou Medical College and the Doctoral Scientific Research Starting Foundation of Taiyuan University of Science and Technology (No. 20102016)

REFERENCES

1. Zhan, Q. and J. R. Leger, "Focus shaping using cylindrical vector beams," *Opt. Express*, Vol. 10, 324–331, 2002.
2. Diehl, D. W. and T. D. Visser, "Phase singularities of the longitudinal field components in the focal region of a high-aperture optical system," *J. Opt. Soc. Am. A*, Vol. 21, 2103–2108, 2004.
3. Schoonover, R. W. and T. D. Visser, "Polarization singularities of focused, radially polarized fields," *Opt. Express*, Vol. 14, 5733–5745, 2006.
4. Luo, Y. and B. Lü, "Spectral Stokes singularities of partially coherent radially polarized beams focused by a high numerical aperture objective," *J. Op.*, Vol. 12, 115703-7, 2010.
5. Cai, Y., "Model for anomalous hollow beam and its paraxial propagation," *Opt. Lett.*, Vol. 32, 3179–3181, 2007.
6. Cai, Y., Z. Zhang, and Q. Lin, "An alternative theoretical model for an anomalous hollow beam," *Opt. Express*, Vol. 16, 15254–15267, 2008.
7. Cai, Y. and F. Wang, "Partially coherent anomalous hollow beam and its paraxial propagation," *Phys. Rev. A*, Vol. 77, 043822, 2008.
8. Zhang, Z., J. Pu, and X. Zhang, "Focusing of partially coherent Bessel-Gaussian beams through a high numerical-aperture objective," *Opt. Lett.*, Vol. 33, 49–51, 2008.
9. Yoshida, A. and T. Asakura, "Propagation and focusing of Gaussian laser beams beyond conventional diffraction limit," *Opt. Commun.*, Vol. 123, 694–704, 1996.
10. Freund, I. and N. Shvartsman, "Wave-field phase singularities: The sign principle," *Phys. Rev. A*, Vol. 50, 5164–5172, 1994.

Propagation of Nonparaxial Gaussian Schell-model Electromagnetic Beams through an Aperture

Haixia Wang, Chaoliang Ding, Yongtao Zhang, and Liuzhan Pan

Department of Physics, Luoyang Normal College, Luoyang 471022, China

Abstract— Based on the generalized Rayleigh-Sommerfeld diffraction integrals, the analytical expression for the 3×3 cross-spectral density matrix of nonparaxial Gaussian-Schell model electromagnetic beams propagating through a rectangle aperture is derived and used to formulate the spectral density and spectral degree of polarization of electromagnetic beams at the z plane. The effect of parameters f , f_σ and truncation parameter δ on the spectral density and spectral degree of polarization of electromagnetic beams are stressed. The results are illustrated by numerical examples.

1. INTRODUCTION

In 2003, Wolf proposed the unified theory of coherence and polarization of stochastic electromagnetic beams [1–3]. Since then, a lot of works has been done on the propagation properties of stochastic electromagnetic beams [4–10]. However, all the above investigations have been restricted to the paraxial regime. With the development and wide application of diode lasers, there exist optical beams with very small spot size that is comparable with the wavelength or with a large divergence angle, for which the paraxial theory is no longer invalid. Recently, some works have been done on the propagation properties of nonparaxial partially coherent beams [11, 12]. In this paper, using the generalized Rayleigh-Sommerfeld diffraction integral, we study the propagation properties of nonparaxial Gaussian Schell-model (GSM) electromagnetic beams through a rectangle aperture.

2. THEORETICAL FORMULATION

For nonparaxial beams the longitudinal component cannot be neglected at any pair of points in the half-space $z \geq 0$ [13], the second-order coherence properties of the field can be studied with the 3×3 cross-spectral density matrix [14]. The cross-spectral-density matrix at the plane $z = 0$ takes the form

$$\vec{W}^0(\rho_{10}, \rho_{20}, 0, \omega) = \begin{bmatrix} W_{xx}^0(\rho_{10}, \rho_{20}, 0, \omega) & W_{xy}^0(\rho_{10}, \rho, 0, \omega) & 0 \\ W_{yx}^0(\rho_{10}, \rho_{20}, 0, \omega) & W_{yy}^0(\rho_{10}, \rho_{20}, 0, \omega) & 0 \\ 0 & 0 & 0 \end{bmatrix}. \quad (1)$$

The cross-spectral density matrix in the half-space $z > 0$ takes the form

$$\vec{W}(\rho_1, \rho_2, z, \omega) = \begin{bmatrix} W_{xx}(\rho_1, \rho_2, z, \omega) & W_{xy}(\rho_1, \rho_2, z, \omega) & W_{xz}(\rho_1, \rho_2, z, \omega) \\ W_{yx}(\rho_1, \rho_2, z, \omega) & W_{yy}(\rho_1, \rho_2, z, \omega) & W_{yz}(\rho_1, \rho_2, z, \omega) \\ W_{zx}(\rho_1, \rho_2, z, \omega) & W_{zy}(\rho_1, \rho_2, z, \omega) & W_{zz}(\rho_1, \rho_2, z, \omega) \end{bmatrix}. \quad (2)$$

The propagation of each of the elements of the cross-spectral density matrix at a pair of points ρ_1 and ρ_2 in the half-space $z > 0$ can be treated by the generalized Rayleigh-Sommerfeld formulas [14]

$$W_{\alpha\beta}(\rho_1, \rho_2, z, \omega) = \left(\frac{z}{\lambda}\right)^2 \iiint W_{\alpha\beta}^0(\rho_{10}, \rho_{20}, 0, \omega) \times \frac{\exp[ik(R_2 - R_1)]}{R_1^2 R_2^2} d^2\rho_{10} d^2\rho_{20}, \quad (\alpha, \beta = x, y) \quad (3a)$$

$$W_{\alpha z}(\rho_1, \rho_2, z, \omega) = -\left(\frac{1}{\lambda}\right)^2 \iiint [W_{\alpha x}^0(\rho_{10}, \rho_{20}, 0, \omega) z(x_2 - x_{20}) + W_{\alpha y}^0(\rho_{10}, \rho_{20}, 0, \omega) z(y_2 - y_{20})] \times \frac{\exp[ik(R_2 - R_1)]}{R_1^2 R_2^2} d^2\rho_{10} d^2\rho_{20}, \quad (\alpha, \beta = x, y) \quad (3b)$$

$$\begin{aligned}
W_{zz}(\boldsymbol{\rho}_1, \boldsymbol{\rho}_2, z, \omega) = & \left(\frac{1}{\lambda} \right)^2 \iiint [W_{xx}^0(\boldsymbol{\rho}_{10}, \boldsymbol{\rho}_{20}, 0, \omega) (x_1 - x_{10}) (x_2 - x_{20}) \\
& + 2W_{xy}^0(\boldsymbol{\rho}_{10}, \boldsymbol{\rho}_{20}, 0, \omega) (x_1 - x_{10}) (y_2 - y_{20}) \\
& + W_{yy}^0(\boldsymbol{\rho}_{10}, \boldsymbol{\rho}_{20}, 0, \omega) (y_1 - y_{10}) (y_2 - y_{20})] \times \frac{\exp[ik(R_2 - R_1)]}{R_1^2 R_2^2} d^2 \boldsymbol{\rho}_{10} d^2 \boldsymbol{\rho}_{20} (3c)
\end{aligned}$$

Let us suppose an electromagnetic Gaussian Schell-model source, the elements of its cross-spectral density matrix at the source plane $z = 0$ are given by the expressions [15]

$$W_{0\alpha\beta}(\boldsymbol{\rho}_{10}, \boldsymbol{\rho}_{20}, 0, \omega) = \begin{cases} \exp\left(-\frac{\boldsymbol{\rho}_{10}^2}{4w_0^2}\right) \exp\left(-\frac{\boldsymbol{\rho}_{20}^2}{4w_0^2}\right) \exp\left(-\frac{|\boldsymbol{\rho}_{10}\boldsymbol{\rho}_{20}|^2}{2\sigma_{\alpha\beta}^2}\right) & \alpha = \beta = x \\ 0 & \text{otherwise} \end{cases} \quad (4)$$

where the variances w_0 and $\sigma_{\alpha\beta}$ are the beam waist and correlation length of the GSM electromagnetic beams.

Assume that a rectangle aperture is located at plane $z = 0$, the cross-spectral density matrix just behind the aperture reads as

$$\overset{\leftrightarrow}{W}^0(\boldsymbol{\rho}_{10}, \boldsymbol{\rho}_{20}, 0, \omega) = \vec{W}_0(\boldsymbol{\rho}_{10}, \boldsymbol{\rho}_{20}, 0, \omega) t(\boldsymbol{\rho}_{10}, \boldsymbol{\rho}_{20}), \quad (5)$$

where $t(\boldsymbol{\rho}_{10}, \boldsymbol{\rho}_{20})$ denotes the window function of the aperture

$$t(\boldsymbol{\rho}_{10}, \boldsymbol{\rho}_{20}) = \begin{cases} 1 & |x_0| \leq a, |y_0| \leq b \\ 0 & \text{otherwise} \end{cases}. \quad (6)$$

On substituting from Eq. (6) into Eq. (5), we obtained the elements of the cross-spectral density matrix of the GSM electromagnetic beam in the output plane as follow

$$\begin{aligned}
W_{xx}(\boldsymbol{\rho}_1, \boldsymbol{\rho}_2, z, \omega) = & -\frac{i\pi w_0^2 z^2}{4s_1 r_1^2 r_2^2 \lambda^2} \int_{-\delta_1}^{\delta_1} \int_{-\delta_2}^{\delta_2} \exp\left[-\frac{k^2(x_1^2 + y_1^2)}{4r_1^2 s_1} + \frac{if_\sigma^2 k^3 (x_1 u + y_1 v) w_0}{2s_1 r_1}\right. \\
& \left. - \frac{ik(x_2 u + y_2 v) w_0}{r_2} + \frac{f_\sigma^4 k^4 (u^2 + v^2) w_0^2}{4s_1} - w_0^2 s_2 (u^2 + v^2)\right] \\
& \times \left(\operatorname{Erf}\left[\frac{-ikx_1 - f_\sigma^2 k^2 r_1 w_0 u - 2r_1 s_1 w_0 \delta_1}{2r_1 \sqrt{s_1}}\right] - \operatorname{Erf}\left[\frac{-ikx_1 - f_\sigma^2 k^2 r_1 w_0 u + 2r_1 s_1 w_0 \delta_1}{2r_1 \sqrt{s_1}}\right] \right) \\
& \times \left(\operatorname{Erfi}\left[\frac{ky_1 - if_\sigma^2 k^2 r_1 w_0 v - i2r_1 s_1 w_0 \delta_2}{2r_1 \sqrt{s_1}}\right] - \operatorname{Erfi}\left[\frac{ky_1 - if_\sigma^2 k^2 r_1 w_0 v + i2r_1 s_1 w_0 \delta_2}{2r_1 \sqrt{s_1}}\right] \right) dudv, \quad (7a)
\end{aligned}$$

$$\begin{aligned}
W_{zz}(\boldsymbol{\rho}_1, \boldsymbol{\rho}_2, z, \omega) = & \frac{\sqrt{\pi} w_0^2}{8\lambda^2 r_1^3 r_2^2 \sqrt{s_1^3 s_2}} \int_{-\delta_1}^{\delta_1} \int_{-\delta_2}^{\delta_2} \exp\left[-\frac{if_\sigma^2 k^3 y_2 w_0 v}{2r_2 s_2} - \frac{ik w_0 (r_1 x_2 u - r_2 y_1 v + r_2 x_1 \delta_1)}{r_1 r_2}\right. \\
& \left. + \frac{f_\sigma^4 k^4 w_0^2 v^2}{4s_2} - w_0^2 (s_1 v^2 + s_2 u^2 + \delta_1^2 s_1) - \frac{k^2 x_1^2}{4r_1^2 s_1} - \frac{k^2 y_2^2}{4r_2^2 s_2} - k^2 f_\sigma^2 \delta_1 w_0^2 u\right] \\
& \times (x_2 - uw_0) \left\{ i2 \exp\left(\frac{k^2 x_1^2}{4r_1^2 s_1}\right) \left[-1 + \exp\left(\frac{1}{r_1} (2k\delta_1 w_0 (ix_1 + f_\sigma^2 kr_1 w_0 u))\right) \right] r_1 \sqrt{s_1} \right. \\
& \left. + i \exp\left[\frac{w_0}{4r_1 s_1} (f_\sigma^2 k^2 u + 2s_1 \delta_1) (i2kx_1 + f_\sigma^2 k^2 r_1 w_0 u + 2r_1 s_1 \delta_1 w_0)\right] \sqrt{\pi} (ikx_1 - 2r_1 s_1 x_1 + f_\sigma^2 k^2 r_1 w_0 u) \right. \\
& \left. \times \operatorname{Erf}\left[\frac{-ikx_1 - f_\sigma^2 k^2 r_1 w_0 u - 2r_1 s_1 w_0 \delta_1}{2r_1 \sqrt{s_1}}\right] \right. \\
& \left. + \exp\left[\frac{w_0}{4r_1 s_1} (f_\sigma^2 k^2 u + 2s_1 \delta_1) (i2kx_1 + f_\sigma^2 k^2 r_1 w_0 u + 2r_1 s_1 \delta_1 w_0)\right] \sqrt{\pi} (kx_1 + i2r_1 s_1 x_1 - if_\sigma^2 k^2 r_1 w_0 u) \right. \\
& \left. \times \operatorname{Erf}\left[\frac{-ikx_1 - f_\sigma^2 k^2 r_1 w_0 u + 2r_1 s_1 w_0 \delta_1}{2r_1 \sqrt{s_1}}\right] \right\} \\
& \times \left(\operatorname{Erfi}\left[\frac{ky_2 + if_\sigma^2 k^2 r_2 w_0 v - i2r_2 s_2 w_0 \delta_2}{2r_2 \sqrt{s_2}}\right] - \operatorname{Erfi}\left[\frac{ky_2 + if_\sigma^2 k^2 r_2 w_0 v + i2r_2 s_2 w_0 \delta_2}{2r_2 \sqrt{s_2}}\right] \right) dudv, \quad (7b)
\end{aligned}$$

$$\begin{aligned}
W_{xz}(\rho_1, \rho_2, z, \omega) = & \frac{i\pi w_0^2 z}{4s_1 r_1^2 r_2^2 \lambda^2} \int_{-\delta_1}^{\delta_1} \int_{-\delta_2}^{\delta_2} (x_2 - uw_0) \exp \left[-\frac{k^2(x_1^2 + y_1^2)}{4r_1^2 s_1} + \frac{if_\sigma^2 k^3 (x_1 u + y_1 v) w_0}{2s_1 r_1} \right. \\
& \left. - \frac{ik(x_2 u + y_2 v) w_0}{r_2} + \frac{f_\sigma^4 k^4 (u^2 + v^2) w_0^2}{4s_1} - w_0^2 s_2 (u^2 + v^2) \right] \\
& \times \left(\text{Erf} \left[\frac{-ikx_1 - f_\sigma^2 k^2 r_1 w_0 u - 2r_1 s_1 w_0 \delta_1}{2r_1 \sqrt{s_1}} \right] - \text{Erf} \left[\frac{-ikx_1 - f_\sigma^2 k^2 r_1 w_0 u + 2r_1 s_1 w_0 \delta_1}{2r_1 \sqrt{s_1}} \right] \right) \\
& \times \left(\text{Erfi} \left[\frac{ky_1 - if_\sigma^2 k^2 r_1 w_0 v - i2r_1 s_1 w_0 \delta_2}{2r_1 \sqrt{s_1}} \right] - \text{Erfi} \left[\frac{ky_1 - if_\sigma^2 k^2 r_1 w_0 v + i2r_1 s_1 w_0 \delta_2}{2r_1 \sqrt{s_1}} \right] \right) dudv, \quad (7c)
\end{aligned}$$

$$s_1 = \frac{k^2}{4} (f^2 + f_\sigma^2) + \frac{ik}{2r_1},$$

$$s_2 = \frac{k^2}{4} (f^2 + f_\sigma^2) - \frac{ik}{2r_2},$$

$$f = \frac{1}{kw_0}, \quad f_\sigma = \frac{1}{k\sigma},$$

$$\delta_1 = \frac{a}{w_0}, \quad \delta_2 = \frac{b}{w_0} \text{ (truncation parameter).}$$

The spectral density and the spectral degree of polarization of the GSM beam are given by [14, 15]

$$I(\rho, z, \omega) = \text{tr} \left[\vec{W}(\rho, \rho, z, \omega) \right] = W_{xx}(\rho, \rho, z, \omega) + W_{yy}(\rho, \rho, z, \omega) + W_{zz}(\rho, \rho, z, \omega), \quad (8a)$$

$$P(\rho, z, \omega) = \sqrt{\frac{3}{2} \left[\frac{\text{tr} (\vec{W}(\rho, \rho, z, \omega)^2)}{\text{tr}^2 (\vec{W}(\rho, \rho, z, \omega))} - \frac{1}{3} \right]}. \quad (8b)$$

On substituting from Eq. (7) into Eq. (8), the spectral density and the spectral degree of polarization at the plane $z > 0$ were obtained. It can be seen that the parameters f , f_σ and δ influence the spectral density and the spectral degree of polarization of nonparaxial GSM electromagnetic beams through a rectangle aperture.

3. NUMERICAL CALCULATION RESULTS AND ANALYSES

To illustrate the dependence of spectral density and spectral degree of polarization on parameters f , f_σ and truncation parameter δ , some numerical calculation results are presented. Fig. 1 and Fig. 2 are the normalized spectral density distributions in the plane $z = 20z_R$ for different parameters f , f_σ , and δ value, $z_R = \pi w_0^2 / \lambda$ is the Rayleigh length. The other calculation parameter are $\delta_1 = \delta_2 = \delta$, $\lambda = 632.8$ nm. From Fig. 1, for the larger values of truncation parameter ($\delta = 2$), the longitudinal component intensity $I_z(x, 0, 20z_R)$ becomes observable with increasing parameters f or f_σ , which are consistent essentially with the obtained results in Ref. [11, 12]. In Fig. 2, with decreasing truncation parameter, the longitudinal component intensity $I_z(x, 0, 20z_R)$ becomes more observable.

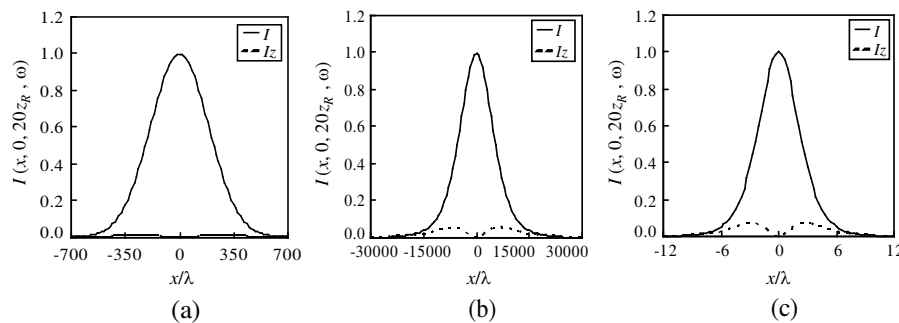


Figure 1: The normalized spectral density distributions in the plane $z = 20z_R$. (a) $f = 0.01$; $f_\sigma = 0.01$; $\delta = 2$; (b) $f = 0.01$; $f_\sigma = 0.3$; $\delta = 2$; (c) $f = 0.5$; $f_\sigma = 0.01$; $\delta = 2$.

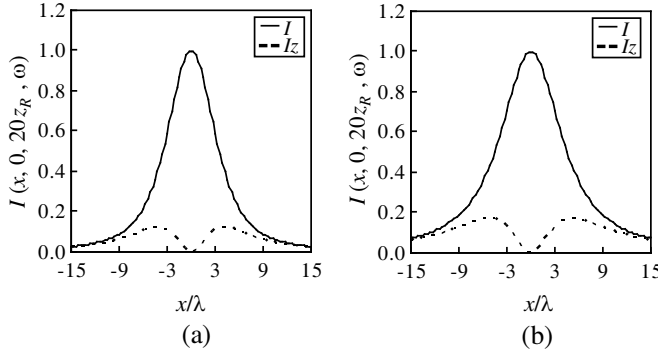


Figure 2: The normalized spectral density distributions in the plane $z = 20z_R$. (a) $f = 0.5$; $f_\sigma = 0.01$; $\delta = 1.2$; (b) $f = 0.5$; $f_\sigma = 0.01$; $\delta = 0.8$.

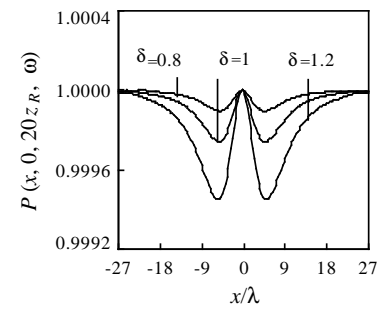


Figure 3: The transverse distribution of the spectral degree of polarization in the plane $z = 20z_R$, $f = 0.5$, $f_\sigma = 0.01$.

Figure 3 is the transverse distribution of the spectral degree of polarization in the plane $z = 20z_R$. As can be seen that, upon propagation, the completely polarization electromagnetic beams can become partially polarized and nonuniform across a typical cross section of electromagnetic beams. Furthermore, the larger the truncation parameter δ is, the smaller the minimum of the spectral degree of polarization $P(x, 0, z, \omega)$ is.

4. CONCLUSION

By using the Rayleigh-Sommerfeld diffraction integral, the propagation properties of nonparaxial Gaussian Schell-model electromagnetic beams through a rectangle aperture are studied. It is shown that the parameters f , f_σ and truncation parameter δ affect the spectral density and the spectral degree of polarization. The truncation parameter δ plays an important role in determining the nonparaxiality of apertured GSM electromagnetic beams. The longitudinal component intensity becomes more observable with decreasing truncation parameter δ . On the cross section of electromagnetic beams, the minimum of the spectral degree of polarization increases with decreasing truncation parameter δ .

ACKNOWLEDGMENT

This work was supported by the National Natural Science Foundation of China under Grant Nos. 60978011 and 61078077, and Natural Science Foundation of Henan Province under Grant No. 112300410062, and the foundation of Luoyang normal college 2010-PYJJ-003.

REFERENCES

- Wolf, E., "Unified theory of coherence and polarization of random electromagnetic beams," *Phys. Lett. A*, Vol. 312, No. 5–6, 263–267, 2003.
- Wolf, E., "Correlation-induced changes in the degree of polarization, the degree of coherence, and the spectrum of random electromagnetic beams on propagation," *Opt. Lett.*, Vol. 28, No. 13, 1078–1080, 2003.
- Wolf, E., *Introduction to the Theory of Coherence and Polarization of Light*, 1st Edition, Cambridge University, Cambridge, 2007.
- Ding, C. L., L. Z. Pan, and B. D. Lü, "Changes in the state of polarization of apertured stochastic electromagnetic modified Bessel-Gauss beams in free-space propagation," *Appl. Phys. B — Lasers Opt.*, Vol. 99, No. 1–2, 307–315, 2010.
- Pan, L. Z., M. L. Sun, C. L. Ding, Z. G. Zhao, and B. D. Lü, "Effects of astigmatism on spectra, coherence and polarization of stochastic electromagnetic beams passing through an astigmatic optical system," *Opt. Express*, Vol. 17, No. 9, 7310–7321, 2009.
- Kanseri, B., S. Rath, and H. C. Kandpal, "Determination of the beam coherence-polarization matrix of a random electromagnetic beam," *IEEE. J. Quantum Elect.*, Vol. 45, No. 9, 1163–1167, 2009.
- Zhao, D. M. and Y. B. Zhu, "Generalized formulas for stochastic electromagnetic beams on inverse propagation through nonsymmetrical optical systems," *Opt. Lett.*, Vol. 34, No. 7, 884–886, 2009.

8. Du, X. Y. and D. M. Zhao, "Polarization modulation of stochastic electromagnetic beams on propagation through the turbulent atmosphere," *Opt. Express*, Vol. 17, No. 6, 4257–4262, 2009.
9. Cai, Y. J., O. Korotkova, H. T. Eyyuboglu, and Y. Baykal, "Active laser radar systems with stochastic electromagnetic beams in turbulent atmosphere," *Opt. Express*, Vol. 16, No. 20, 15834–15846, 2008.
10. Zhao C. L., Y. J. Cai, and O. Korotkova, "Radiation force of scalar and electromagnetic twisted Gaussian Schell-model beams," *Opt. Express*, Vol. 17, No. 24, 21472–21487, 2009.
11. Zhu, Y. B. and D. M. Zhao, "Stokes parameters and degree of polarization of nonparaxial stochastic electromagnetic beams," *Phys. Lett. A*, Vol. 373, No. 17, 1595–1598, 2009.
12. Mei, Z. R., "Generalized Stokes parameters of three-dimensional stochastic electromagnetic beams," *Opt. Express*, Vol. 18, No. 22, 22826–22832, 2010.
13. Chen, C. G., P. T. Konkola, J. Ferrera, R. K. Heilmann, and M. L. Schattenburg, "Analyses of vector Gaussian beam propagation and the validity of paraxial and spherical approximations," *J. Opt. Soc. Am. A*, Vol. 19, No. 2, 404–412, 2002.
14. Mandel, L. and E. Wolf, *Optical Coherence and Quantum Optics*, Cambridge University, Cambridge, 1995.
15. Setälä, T., M. Kaivola, and A. T. Friberg, "Degree of polarization in near fields of thermal sources: Effects of surface waves," *Phys. Rev. Lett.*, Vol. 88, No. 12, 2002.

Spectral Stokes Singularities of Nonparaxial Partially Coherent Elliptical Gaussian Vortex Beams Diffracted at a Half-plane Screen

Shangbin Zheng, Yamei Luo, and Yuan Zhu

Department of Biomedical Engineering, Luzhou Medical College, Luzhou 646000, China

Abstract— Based on the generalized vector Rayleigh-Sommerfeld diffraction integrals, the expression for the cross-spectral density matrix has been derived and used to study the dynamic behavior of spectral Stokes singularities of nonparaxial partially coherent elliptical Gaussian vortex beams diffracted at a half-plane screen. It is shown that the motion, pair creation and annihilation of spectral Stokes singularities are dependent on a controlling parameter, such as spatial correlation length, the off-axis displacement parameter, or the waist width ratio of elliptical Gaussian vortex beams, as well as the propagation distance. The analytical results are illustrated numerically. The results obtained in this paper about studying on some new effects in nonparaxial beam diffraction and propagation provide a method for generating spectral Stokes singularities and are further enrichment and extension of the research range of singular optics, and can be useful for practical applications of optical vortices.

1. INTRODUCTION

Since Nye and Hajnal discovered the polarization singularities for monochromatic electromagnetic wavefields in three dimensions, which were first confirmed experimentally with microwaves, the polarization singularities in vector wavefields have attracted much attention due to their theoretical and applicative aspects [1–4]. However, most of the studies have been made within the frameworks of the paraxial approximation and fully coherent wavefields. Schoonover and Visser showed that with a suitable change in the definition of the Stokes parameters the usual description of the state of the polarization and polarization singularities in the paraxial case can be extended to the nonparaxial regime and explored the polarization singularities of strongly focused radially polarized fields [5]. On the other hand, Yan et al. studied the polarization singularities of paraxial partially coherent electromagnetic beams by introducing spectral Stokes singularities [6]. The purpose of this paper is to study the dynamic behavior of spectral Stokes singularities of partially coherent elliptical Gaussian vortex beams diffracted at a half-plane screen beyond the paraxial approximation. The results are illustrated by numerical examples.

2. THEORETICAL MODEL

Consider a partially coherent elliptical Gaussian vortex beams with topological charge $m = +1$ whose 3×3 cross-spectral density matrix at the source plane $z = 0$ reads as [7, 8]

$$W^0 = \begin{vmatrix} W_{xx}^0(x_{01}, y_{01}, x_{02}, y_{02}, 0) & 0 & 0 \\ 0 & 0 & 0 \\ 0 & 0 & 0 \end{vmatrix}, \quad (1)$$

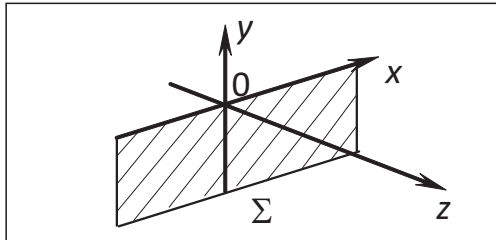


Figure 1: A schematic illustration of a half-plane screen.

where for simplicity we assume that $W_{xy}^0 = W_{xz}^0 = W_{yx}^0 = W_{yy}^0 = W_{yz}^0 = W_{zx}^0 = W_{zy}^0 = W_{zz}^0 = 0$, i.e., the initial beam is linearly polarized in the x direction, and

$$W_{xx}^0(x_{01}, y_{01}, x_{02}, y_{02}, 0) = (x_{01} - b - iy_{01})(x_{02} - b + iy_{02}) \exp\left[-\frac{(x_{01} - x_{02})^2 + (y_{01} - y_{02})^2}{\sigma_0^2} - \frac{1}{2}\left(\frac{x_{01}^2 + x_{02}^2}{w_{0x}^2} + \frac{y_{01}^2 + y_{02}^2}{w_{0y}^2}\right)\right], \quad (2)$$

where w_{0x} , w_{0y} are waist widths in the x and y directions, respectively, b denotes the off-axis distance in the x direction, σ_0 is the spatial correlation length. As shown in Fig. 1, a half-plane screen Σ with transmissivity

$$T(x_0, y_0) = \begin{cases} 1, & y_0 \geq 0 \\ 0 & y_0 < 0 \end{cases}. \quad (3)$$

is positioned at the plane $z = 0$.

The propagation of general beams in the half space $z > 0$ is governed by the vector Rayleigh-Sommerfeld diffraction integrals which for our case are given by [9]

$$W_{xx}(x_1, y_1, x_2, y_2, z) = \left(\frac{1}{2\pi}\right)^2 \iiint_{z=0} W_{xx}^{(0)} \frac{\partial}{\partial z} \left[\frac{\exp(-ikR_1)}{R_1} \right] \frac{\partial}{\partial z} \left[\frac{\exp(ikR_2)}{R_2} \right] dx_{01} dx_{02} dy_{01} dy_{02}, \quad (4a)$$

$$W_{zz}(x_1, y_1, x_2, y_2, z) = \left(\frac{1}{2\pi}\right)^2 \iiint_{z=0} W_{xx}^{(0)} \frac{\partial}{\partial x_1} \left[\frac{\exp(-ikR_1)}{R_1} \right] \frac{\partial}{\partial x_2} \left[\frac{\exp(ikR_2)}{R_2} \right] dx_{01} dx_{02} dy_{01} dy_{02}, \quad (4b)$$

$$W_{xz}(x_1, y_1, x_2, y_2, z) = -\left(\frac{1}{2\pi}\right)^2 \iiint_{z=0} W_{xx}^{(0)} \frac{\partial}{\partial z} \left[\frac{\exp(-ikR_1)}{R_1} \right] \frac{\partial}{\partial x_2} \left[\frac{\exp(ikR_2)}{R_2} \right] dx_{01} dx_{02} dy_{01} dy_{02}, \quad (4c)$$

$$W_{xy}(x_1, y_1, x_2, y_2, z) = W_{yx}(x_1, y_1, x_2, y_2, z) = W_{yy}(x_1, y_1, x_2, y_2, z) = 0, \quad (4d)$$

$$W_{zx}(x_1, y_1, x_2, y_2, z) = W_{xz}^*(x_1, y_1, x_2, y_2, z), \quad (4e)$$

with $*$ denotes the complex conjugate, and $R_\nu = \sqrt{(x_\nu - x_{0\nu})^2 + (y_\nu - y_{0\nu})^2 + z^2}$ ($\nu = 1, 2$).

Setting $x_1 = x_2 = x$, $y_1 = y_2 = y$ in Eqs. (2) and (4), the spectral Stokes parameters are defined as

$$\begin{aligned} S_0(x, y, z) &= W_{zz}(x, y, z) + W_{xx}(x, y, z), & S_1(x, y, z) &= W_{zz}(x, y, z) - W_{xx}(x, y, z), \\ S_2(x, y, z) &= W_{zx}(x, y, z) + W_{xz}(x, y, z), & S_3(x, y, z) &= i[W_{xz}(x, y, z) - W_{zx}(x, y, z)]. \end{aligned} \quad (5)$$

The normalized spectral Stokes parameters are $s_1 = S_1/S_0$, $s_2 = S_2/S_0$ and $s_3 = S_3/S_0$. The complex spectral Stokes parameters s_{ij} ($i, j = 1, 2, 3$) are written as [10]

$$s_{12} = s_1 + is_2, \quad s_{23} = s_2 + is_3, \quad s_{31} = s_3 + is_1, \quad (6)$$

and the degree of polarization reads as

$$P = \sqrt{s_1^2 + s_2^2 + s_3^2}. \quad (7)$$

The spectral Stokes singularities (vortices) of partially coherent beams correspond to the zero points of complex Stokes fields $s_{ij} = 0$, where s_{12} singularities correspond to the circular polarization (C-points), and $s_3 > 0$ ($s_3 < 0$) means right- (left-) handedness, where the orientation of the major and minor axes of polarization ellipse is undetermined. s_{23} and s_{31} singularities must be located on L-lines, where the handedness of the polarization ellipse becomes undefined (linear polarization). From Eqs. (2)–(9) it turns out that the spectral Stokes singularities depend on the spatial correlation length σ_0 , waist width ratio $a = w_{0y}/w_{0x}$, off-axis distance b , as well as on the propagation distance.

3. DYNAMIC BEHAVIOR SPECTRAL STOKES SINGULARITIES

Numerical calculations were made by means of Eqs. (2)–(9) to illustrate the dependence of the spectral singularities on the a , σ_0 , b , and z .

Figure 2 gives the s_{12} , s_{23} and s_{31} singularities within $\{-1.5 \leq x/w_{0x} \leq 0.8, 1.5 \leq y/w_{0x} \leq 2.5\}$ at $z = 10z_{Rx}$, where $z_{Rx} = kw_{0x}/2$ is the Rayleigh length in the x direction, for different values of the waist width ratio (a) $a = 1.6$, (b) $a = 2.1148$, (c) $a = 2.116$, (d) $a = 2.118$, $\sigma_0 = 20\lambda$, $w_{0x} = 0.5\lambda$

and $b = 1.5w_{0x}$. The contours of $s_1 = 0$, $s_2 = 0$ and $s_3 = 0$ are represented by solid, dashed and dotted curves, respectively. s_{12} (C-points), s_{23} and s_{31} singularities appear at the intersection of $s_i = 0$ and $s_j = 0$, and are represented by circles, triangles and squares, the black and open ones correspond to the topological charges $m_{ij} = -1$ and $+1$, respectively, which are determined by the sign principle [10]. The L-lines ($s_3 = 0$) separate the xy plane into the right- and left-handed regions [5], and the signs \pm of s_3 determine the handedness of C-points and are shown in the figures. As can be seen, there are two s_{12} singularities (C-points) with opposite charges $m = \pm 1$ labelled 1 and 2 at $a = 1.6$ in Fig. 2(a). The left-handed C-point 1 and right-handed C-point 2 are positioned at $(-1.419, 1.965)$, and $(-0.996, 1.966)$, whose degree of polarization is $P = 0.643$, and 0.660 , respectively. With increasing waist width ratio to $a = 2.1148$ in Fig. 2(b) C-point 2 moves to the L-line at $(0.707, 2.151)$, and collides with it, resulting in the creation of a V-point marked “★”, at which $s_1 = s_2 = s_3 = 0$, and the degree of polarization $P = 0$, sometimes also called the U-singularity [12]. The V-point is unstable because a small perturbation of a leads to the handedness reversal and change in the degree of polarization. For examples, with an increase of the waist width ratio to $a = 2.115$, C-point 2 shifts to $(0.705, 2.158)$, and becomes left-handed whose degree of polarization $P = 0.013$ (not shown). A further increase of $a = 2.116$ in Fig. 2(c) a pair of C-points 1 and 2 with opposite charge and same left-handedness approach and annihilate each other.

There exist a pair of s_{31} singularities of opposite charge marked a and b whose positions are $(-1.251, 2.252)$, and $(-1.209, 1.798)$, $P = 0.741$, and 0.535 , respectively, in Fig. 2(a). An increase of a results in the motion and change in the degree of polarization of s_{31} singularities a and b . For example, for $a = 2.116$ in Fig. 2(c) s_{31} singularities a and b move to $(0.711, 2.148)$ and $(0.705, 2.110)$, $P = 0.01$ and 0.179 , respectively. For $a = 2.118$ in Fig. 2(d) a pair of s_{31} singularities a and b annihilate each other.

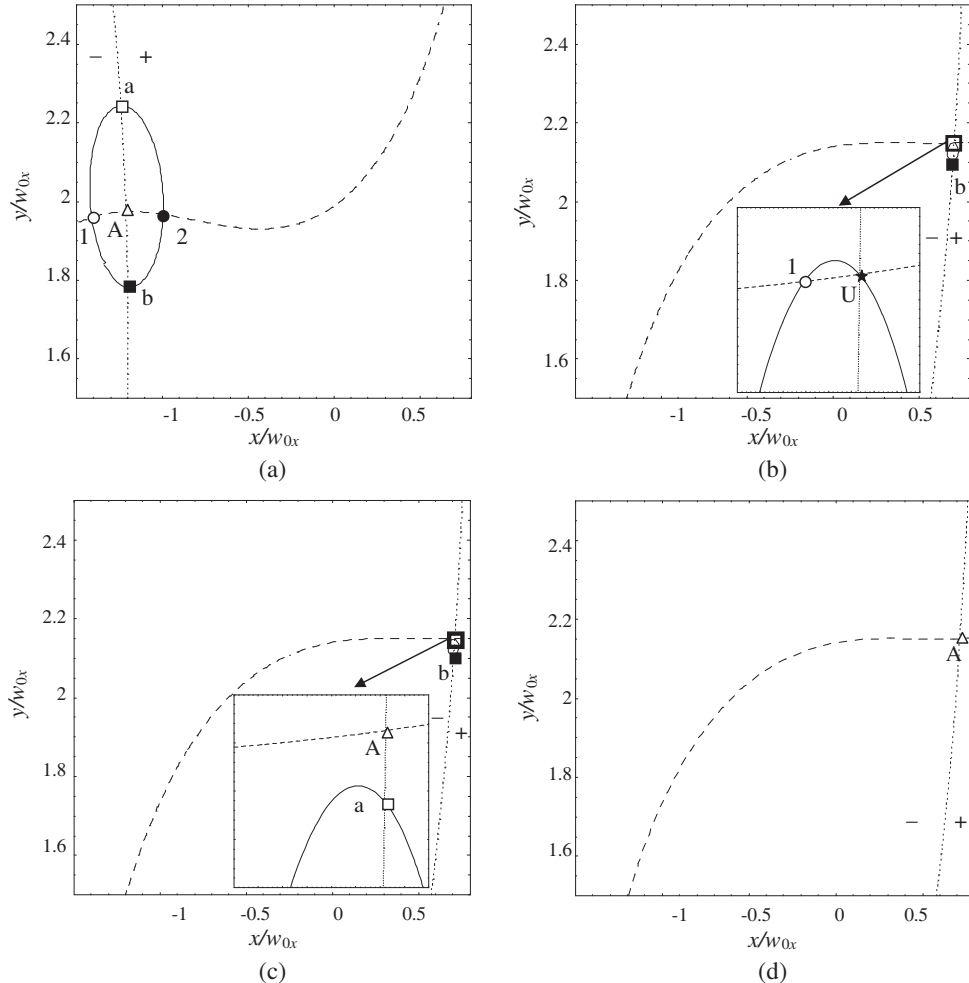


Figure 2: s_{12} , s_{23} and s_{31} singularities at $z = 10Z_{Rx}$ for selected values of the waist width ratio (a) $a = 1.6$, (b) $a = 2.1148$, (c) $a = 2.116$, (d) $a = 2.118$. The other calculation parameters are seen in the text.

There is an s_{23} singularity marked A whose position is $(-1.223, 1.980)$, and $P = 0.268$ in Fig. 2(a). The motion and change in the degree of polarization take place by varying a , e.g., for $a = 2.1148$ and 2.118 in Figs. 2(b), (d), the position of s_{23} singularity A is $(0.707, 2.151)$ and $(0.711, 2.149)$, $P = 0$ and 0.002 , respectively.

Similar behavior of spectral Stokes singularities is present by varying the spatial correlation length σ_0 , off-axis distance a , as well as the propagation distance z , and is omitted here.

4. CONCLUSIONS

In this paper, the spectral Stokes singularities of the nonparaxial partially coherent elliptical Gaussian vortex beams diffracted at a half screen have been studied in detail. It is shown that there exist s_{12} , s_{23} and s_{31} spectral Stokes singularities, which are variable in the variation of a control parameter, such as waist width ratio, the spatial correlation length, or off-axis distance, as well as the propagation distance. The motion, annihilation process, change in the degree of polarization of s_{12} , s_{23} and s_{31} singularities and the handedness reversal of s_{12} singularities may take place. The results obtained in this paper would be beneficial to studying of polarization singularities in nonparaxial diffracted wavefields.

ACKNOWLEDGMENT

This work was supported by the Natural Science Foundation of the Education Department of Sichuan Province (Grant No. 10ZB029).

REFERENCES

1. Nye, J. F. and J. V. Hajnal, “The wave structure of monochromatic electromagnetic waves,” *Proc. R. Soc. Lond. A*, 409, 21–36, 1987.
2. Hajnal, J. V., “Observation of singularities in the electric and magnetic fields of freely propagating microwaves,” *Proc. R. Soc. Lond. A*, Vol. 430, 413–421, 1990.
3. Nye, J. F., *Natural Focusing and the Fine Structure of Light*, IOP Publishing, Bristol, UK, 1999.
4. Dennis, M. R., K. O’Holleran, and M. J. Padgett, “Singular optics: Optical vortices and polarization singularities,” *Progress in Optics*, Vol. 53, 293–363, 2009.
5. Schoonover, R. W. and T. D. Visser, “Polarization singularities of focused, radially polarized fields,” *Opt. Express*, Vol. 14, 5733–5745, 2006.
6. Yan, H. and B. Lv, “Spectral stokes singularities of stochastic electromagnetic beams,” *Opt. Lett.*, Vol. 34, 1933–1935, 2009.
7. Mandel, L. and E. Wolf, *Optical Coherence and Quantum Optics*, Cambridge University Press, Cambridge, 1995.
8. Cai, Y. and U. Peschel, “Second-harmonic generation by an astigmatic partially coherent beam,” *Opt. Express*, Vol. 15, 15480–15492, 2007.
9. Duan, K. and B. Lv, “Partially coherent vectorial nonparaxial beams,” *J. Opt. Soc. Am. A*, Vol. 21, 1924–1932, 2004.
10. Freund, I., A. I. Mokhun, M. S. Soskin, O. V. Angelsky, and I. I. Mokhun, “Stokes singularity relations,” *Opt. Lett.*, Vol. 27, 545–547, 2002.
11. Freund, I. and N. Shvartsman, “Wave-field phase singularities: The sign principle,” *Phys. Rev. A*, Vol. 50, 5164–5172, 1994.
12. Chernyshov, A. A., Ch. V. Felde, H. V. Bogatyryova, P. V. Polyanskii, and M. S. Soskin, “Vector singularities of the combined beams assembled from mutually incoherent orthogonally polarized components,” *J. Opt. A: Pure Appl. Opt.*, Vol. 11, 094010(8), 2009.

Tuning Trapped-mode Resonances in a Planar Metamaterial

J. H. Shi¹, E. Plum², V. A. Fedotov², and N. I. Zheludev²

¹College of Science, Harbin Engineering University, Harbin 150001, China

²Optoelectronics Research Center, University of Southampton, Southampton SO17 1BJ, UK

Abstract— We demonstrate tuning of trapped-mode resonances in a symmetric planar metamaterial both experimentally and theoretically. By controlling the excitation of the Fano-type trapped-mode resonance via the angle of incidence, its quality factor is controlled and the resonance is red-shifted by up to 21%.

1. INTRODUCTION

The asymmetric Fano resonance, which has long been known as a characteristic feature of interacting quantum systems, has more recently been found in plasmonic nanostructures and metamaterials [1, 2]. The steep dispersion of the Fano resonance profile promises applications in slow light [3–9], sensor [10, 11], nonlinear [12] and switching [13] applications. Fano resonances in metamaterials were first observed in arrays of asymmetrically split rings [14], consisting of two wire arcs of different lengths. Incident electromagnetic waves with the electric polarization parallel to these asymmetric wires can excite a high-Q mode formed by counter-propagating currents, i.e., a so-called trapped mode resonance that is associated with an asymmetric Fano-type line shape [14]. The quality factor of such trapped-mode resonances is mainly limited by losses and attempts to compensate or eliminate Joule losses using optically-pumped gain media such as semiconductor quantum dots [15, 16] and superconducting metamaterials [17] have been reported. The tunability of Fano resonances is another key issue. Tuning of a Fano resonance was observed when crossing the superconducting transition temperature of a superconducting metamaterial [17]. Most generally, the properties of Fano resonances can be controlled by the metamaterial design [14, 18–20]. However, it is extremely difficult to change the geometrical size of elements once they are fabricated. Therefore, a practical way of controlling Fano resonances is of great importance for developing metamaterials for real applications [21].

In this paper, we report that trapped-mode Fano-type resonances in a planar metamaterial can be efficiently controlled via the angle of incidence, offering an easy-to-implement way of achieving local field tunability in metamaterials. We demonstrate tuning of the trapped-mode quality factor and its spectral localization experimentally and numerically.

2. EXPERIMENTAL AND SIMULATED RESULTS

We investigate resonance tuning in a meta-surface based on symmetrically split rings (SSR), see Fig. 1. The SSR consists of two identical wire arcs corresponding to 160° and each copper split ring has a radius of 6 mm and a width of 0.8 mm. Due to its high symmetry, this structure does not allow the excitation of anti-symmetric currents at normal incidence. The metamaterial consists of a square meta-molecule array with a period of 15 mm and an overall size of about 200 × 200 mm². It was etched from 35 μm copper cladding covering FR4 PCB substrate of 1.6 mm thickness. Detailed dimensions of the SSR unit cell are given in Fig. 1(b). The SSR metamaterial transmission was measured at angles of incidence from 0° to 50° in the 9–14 GHz frequency range. The experiments were carried out in an anechoic chamber using broadband horn antennas (Schwarzbeck BBHA9120D) equipped with dielectric lens concentrators and a vector network analyzer (Agilent E8364B).

The electromagnetic response of the SSR metamaterial was also simulated using a full three-dimensional Maxwell finite element method solver in the frequency domain, where copper was treated as a perfect electric conductor and a permittivity $\epsilon = 4.05 - i0.05$ was assumed for the lossy dielectric substrate. For the results presented below, both the polarization of the incident wave and the axis around which the metamaterial was tilted to achieve oblique incidence were perpendicular to the SSR wires (i.e., the y -axis), see Fig. 1.

Figures 2 and 3(a) show simulated and measured transmission and reflection spectra of the SSR metamaterial as a function of the angle of incidence α . At normal incidence onto the metamaterial y -polarized electromagnetic waves can only excite one electric dipole resonance at about 11.3 GHz.

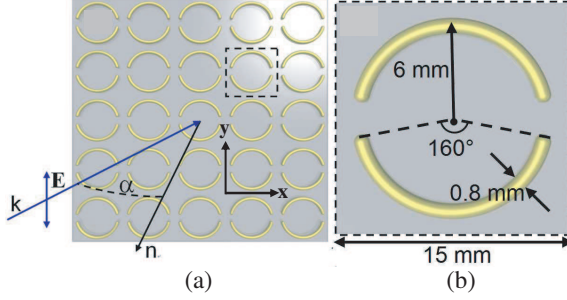


Figure 1: Metamaterial structure. (a) The angle of incidence α is measured between the incident wave vector k and the metamaterial's surface normal n . Here metamaterial transmission and reflection are studied for y -polarized electromagnetic waves at oblique incidence which is realized by tilting the metamaterial around its y -axis. (b) Symmetrically split ring (SSR) unit cell.

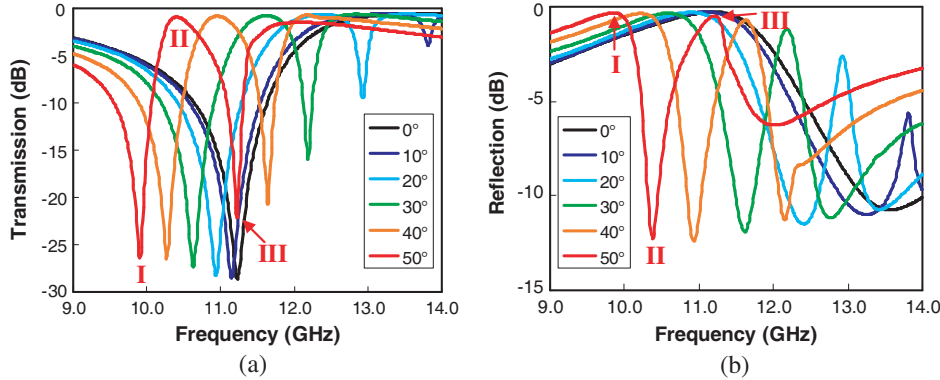


Figure 2: Simulated transmission and reflection of the SSR metamaterial for various angles of incidence. The resonant modes corresponding to resonances I, II, and III are shown in Fig. 4 for $\alpha = 50^\circ$.

The excitation of the trapped mode, which consists of anti-symmetric current oscillations in opposite wire arcs, is prohibited by the high experimental symmetry in this case. However, when the metamaterial pattern is tilted around the y -axis, the trapped-mode resonance appears: a narrow pass band (reflectivity minimum) which may also be discussed in terms of electromagnetically induced transparency (EIT) [3] forms between two transmission minima. It is obvious from Figs. 2 and 3(a) that the SSR metamaterial exhibits large frequency tunability of the trapped-mode resonance. With increasing α , the pass band II becomes more pronounced and as illustrated by Fig. 3(b) its quality factor measured as $Q = f/\Delta f$ increases to about 18 at $\alpha = 50^\circ$ (peak width $\Delta f = 0.6$ GHz at 3 dB below maximum). Simulations [Fig. 2(a)] and experimental results [Fig. 3(a)] agree well with each other, however, the resonant feature II is more pronounced in the simulations. This deviation is linked to scattering from the edges of the experimental sample, which was assumed to be an infinite periodic structure in the simulations.

Oblique incidence leads to a small delay between the excitation of the two arcs of the SSR. This delay is sufficient to allow the excitation of an antisymmetric trapped current mode associated with transmission maximum (reflection minimum) II, which gives rise to a strong magnetic dipole [see Fig. 4(b)]. In contrast to this magnetic dipole mode, resonances I and III are electric dipole resonances with no significant net magnetic field [see Figs. 4(a) and (c)]. At normal incidence, the excited magnetic fields show perfect symmetry with respect to the mirror line of the SSR and completely cancel each other, leading to a vanishing magnetic dipole moment.

The anti-symmetric current oscillations of the trapped-mode resonance II are largely dominated by the x -directional surface currents propagating along the wire arcs. Fig. 5 shows the frequency dependence of the x -directional surface current density at different angles of incidence. At normal incidence, the net x -component of the surface current is zero in each arc. As the angle of incidence increases, currents of equal magnitude oscillating in anti-phase in the two wire arcs appear. In particular the increasing angle of incidence results in a 10-fold enhancement of the magnitude of the excited currents and a remarkably large red-shift of the trapped-mode resonance, which can be tuned from 13.2 GHz to 10.4 GHz. The large magnitude of the anti-symmetric currents results from

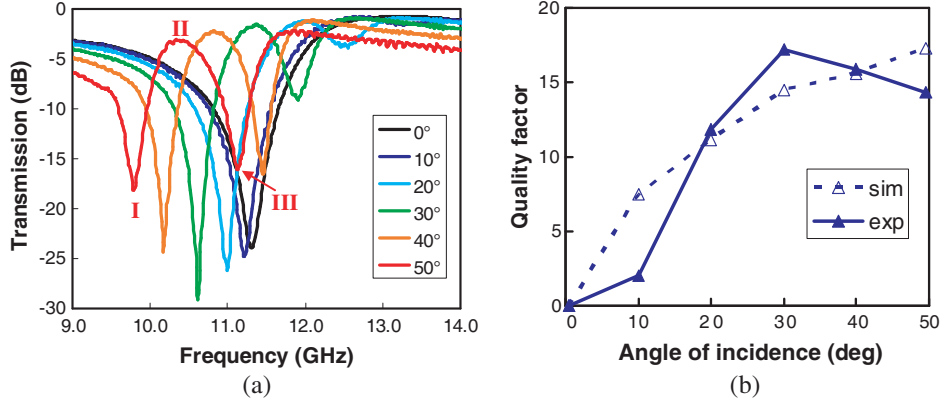


Figure 3: Measured transmission and quality factor. (a) Measured transmission spectra for various angles of incidence. (b) Quality factor for the pass band II as a function of the angle of incidence (dashed line: simulation, solid line: experiment).

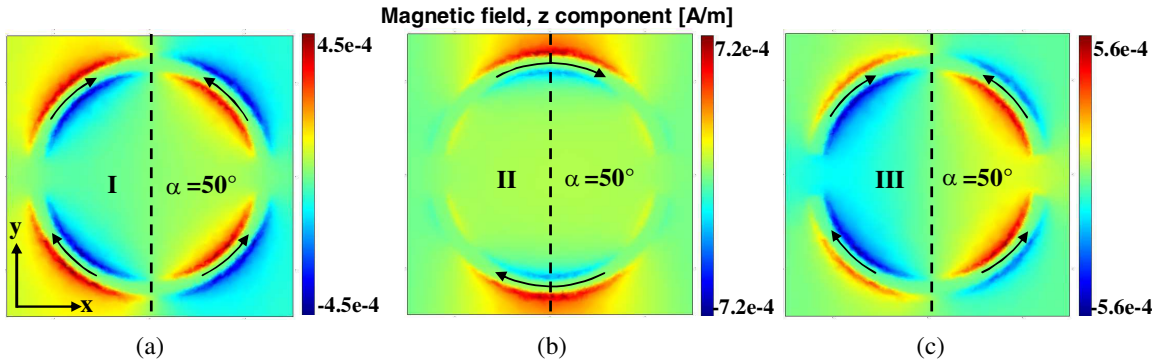


Figure 4: Snapshots of the normal magnetic field at resonances I-III at $\alpha = 50^\circ$, compare Fig. 2. All field maps show the field amplitude at its maximum. The arrows indicate the instantaneous direction of the excited currents and the dashed lines correspond to the SSR mirror line along the y -axis.

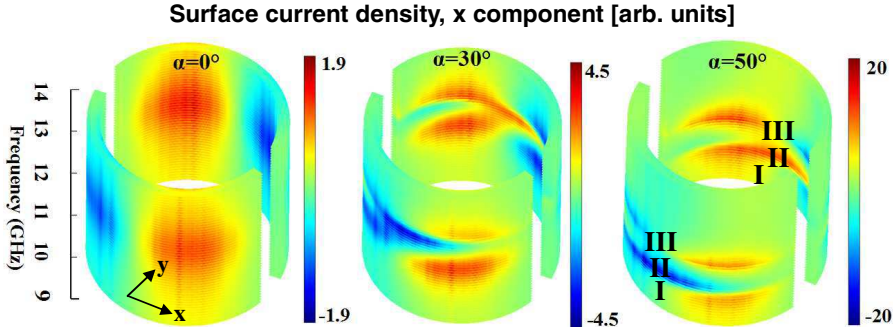


Figure 5: X -component of the instantaneous surface current density as a function of frequency at 0° , 30° and 50° oblique incidence.

the fact that any fields emitted from opposite arcs would destructively interfere in the far-field and therefore the electromagnetic energy is trapped at the meta-surface, ensuring a high quality factor of the pass band.

3. CONCLUSIONS

In summary, we experimentally and numerically demonstrate that the excitation of trapped-mode resonances in SSR metamaterials can be controlled via the angle of incidence. In particular, we have realized trapped mode on/off switching, tuning of the resonance quality factor and a 21% red-shift of the trapped-mode resonance via the angle of incidence for a simple, planar model structure based on symmetrically split rings. The structure is well-suited for existing micro-and nanofabrication technologies and tuning via the incidence angle can be easily applied anywhere in the electromagnetic spectrum. The EIT-like behavior of the SSR metamaterial makes it a promising candidate

for “slow light” applications, while local energy confinement provides an interesting platform for nonlinear and gain metamaterials and the lasing spaser.

ACKNOWLEDGMENT

Financial support of The Leverhulme Trust, The Royal Society and the UK’s Engineering and Physical Sciences Research Council, UK is acknowledged. The author J. H. Shi also thanks for support provided by the Natural Science Foundation of Heilongjiang Province in China under grant LC201006 and in part by the Special Foundation for Basic Scientific Research of Harbin Engineering University under grant HEUCF20111113 and HEUCF20111102.

REFERENCES

1. Fano, U., “Effects of configuration interaction on intensities and phase shifts,” *Phys. Rev.*, Vol. 124, 1866–1878, 1961.
2. Luk'yanchuk, B., N. I. Zheludev, S. A. Maier, N. J. Halas, P. Nordlander, H. Giessen, and C. Chong, “The Fano resonance in plasmonic nanostructures and metamaterials,” *Nat. Mater.*, Vol. 9, 707–715, 2010.
3. Papasimakis, N., V. A. Fedotov, N. I. Zheludev, and S. L. Prosvirnin, “Metamaterial analog of electromagnetically induced transparency,” *Phys. Rev. Lett.*, Vol. 101, No. 25, 253903, 2008.
4. Zhang, S., D. A. Genov, Y. Wang, M. Liu, and X. Zhang, “Plasmon-induced transparency in metamaterials,” *Phys. Rev. Lett.*, Vol. 101, No. 4, 047401, 2008.
5. Tassin, P., L. Zhang, T. Koschny, E. N. Economou, and C. M. Soukoulis, “Low-loss metamaterials based on classical electromagnetically induced transparency,” *Phys. Rev. Lett.*, Vol. 102, No. 5, 053901, 2009.
6. Chiam, S. Y., R. Singh, C. Rockstuhl, F. Lederer, W. L. Zhang, and A. A. Bettoli, “Analogue of electromagnetically induced transparency in a terahertz metamaterial,” *Phys. Rev. B*, Vol. 80, No. 15, 153103, 2009.
7. Liu, N., L. Langguth, T. Weiss, J. Kästel, M. Fleischhauer, T. Pfau, and H. Giessen, “Plasmonic analogue of electromagnetically induced transparency at the Drude damping limit,” *Nat. Mater.*, Vol. 8, No. 9, 758–762, 2009.
8. Papasimakis, N. and N. I. Zheludev, “Metamaterial-induced transparency,” *Opt. Photonics News*, Vol. 20, No. 10, 22–27, 2009.
9. Miroshnichenko, A. E., S. Flach, and Y. S. Kivshar, “Fano resonances in nanoscale structures,” *Rev. Mod. Phys.*, Vol. 82, 2257–2298, 2010.
10. Liu, N., T. Weiss, M. Mesch, L. Langguth, U. Eigenthaler, M. Hirscher, C. Sönnichsen, and H. Giessen, “Planar metamaterial analogue of electromagnetically induced transparency for plasmonic sensing,” *Nano Lett.*, Vol. 10, No. 4, 1103–107, 2010.
11. Lahiri, B., A. Z. Khokhar, R. M. De La Rue, S. G. McMeekin, and N. P. Johnson, “Asymmetric split ring resonators for optical sensing of organic materials,” *Opt. Express*, Vol. 17, No. 2, 1107–1115, 2009.
12. Nikolaenko, A. E., F. De Angelis, S. A. Boden, N. Papasimakis, P. Ashburn, E. DiFabrizio, and N. I. Zheludev, “Carbon nanotubes in a photonic metamaterial,” *Phys. Rev. Lett.*, Vol. 104, 153902, 2010.
13. Sámon, Z. L., K. F. MacDonald, F. DeAngelis, B. Gholipour, K. Knight, C. C. Huang, E. DiFabrizio, D. W. Hewak, and N. I. Zheludev, “Metamaterial electro-optic switch of nanoscale thickness,” *Appl. Phys. Lett.*, Vol. 96, No. 14, 143105, 2010.
14. Fedotov, V. A., M. Rose, S. L. Prosvirnin, N. Papasimakis, and N. I. Zheludev, “Sharp trapped-mode resonances in planar metamaterials with a broken structural symmetry,” *Phys. Rev. Lett.*, Vol. 99, No. 14, 147401, 2007.
15. Plum, E., V. A. Fedotov, P. Kuo, D. P. Tsai, and N. I. Zheludev, “Towards the lasing spaser: Controlling metamaterial optical response with semiconductor quantum dots,” *Opt. Express*, Vol. 17, No. 10, 8548–8551, 2009.
16. Tanaka, K., E. Plum, J. Y. Ou, T. Uchino, and N. I. Zheludev, “Multifold enhancement of quantum dot luminescence in plasmonic metamaterials,” *Phys. Rev. Lett.*, Vol. 105, No. 22, 227403, 2010.
17. Fedotov, V. A., A. Tsiatmas, J. H. Shi, R. Buckingham, P. de Groot, Y. Chen, S. Wang, and N. I. Zheludev, “Temperature control of Fano resonances and transmission in superconducting metamaterials,” *Opt. Express*, Vol. 18, 9015–9019, 2010.

18. Singh, R., I. A. I. Al-Naib, M. Koch, and W. L. Zhang, "Sharp Fano resonances in THz metamaterials," *Opt. Express*, Vol. 19, 6312–6319, 2011.
19. Xiao, X., J. Wu, F. Miyamaru, M. Zhang, S. Li, M. W. Takeda, W. Wen, and P. Sheng, "Fano effect of metamaterial resonance in terahertz extraordinary transmission," *Appl. Phys. Lett.*, Vol. 98, No. 1, 011911, 2011.
20. Plum, E., K. Tanaka, W. T. Chen, V. A. Fedotov, D. P. Tsai, and N. I. Zheludev, "A combinatorial approach to metamaterials discovery," *J. Opt.*, Vol. 13, 055102, 2011.
21. Lu, Y. H., J. Y. Rhee, W. H. Jang, and Y. P. Lee, "Active manipulation of plasmonic electromagnetically-induced transparency based on magnetic plasmon resonance," *Opt. Express*, Vol. 18, 20912–20917, 2010.

The Preliminary Results from Assimilating Rain Rate Derived from Satellite

Q. Lu, X. Yang, R. You, D. Qin, H. Yang, and P. Zhang

National Satellite Meteorological Center of CMA, Beijing, China

Abstract— Inadequate specification of divergence and moisture in the initial conditions of numerical models results in the well-documented “spinup” problem. Observational studies indicate that latent heat release can be a key ingredient in the intensification of extratropical cyclones. As a result, the assimilation of rain rates during the early stages of a numerical simulation results in improved forecasts of the intensity and precipitation patterns associated with extratropical cyclones. Rain observation is the important observation to record the precipitation; fortunately, the precipitation information could be quantitatively estimated from geostationary IR observation, Microwave observation and Radar observation. Here, a technique is described to assimilate the satellite derived rain rate data into a mesoscale model. Compared to the control simulation, assimilation simulation gives rise to a dramatic improvement in forecasts of precipitation patterns and geopotential height fields when assimilating the rain rate.

1. INTRODUCTION

Most NWP models have difficulties in producing realistic weather elements, such as clouds and precipitation, at the beginning of the forecast period (so called “spinup” problem), which is corresponding to an inadequate specification of divergence and moisture during the first hours of the forecast. Results from physical initialization (nudging of rain rate) studies showed an improvement of the moisture analysis and a reduction of the spinup problem. More recent approaches, such as three-dimensional (3DVAR) or four-dimensional (4DVAR) variational assimilations, can explicitly take into account the systematic error of model and satellite-derived precipitation rates to give an optimal initial state, especially humidity [4, 5].

The One-Dimensional VARiational (1DVAR) assimilation of precipitation has already been theoretically researched [2, 3], and the results show that 1DVAR method can adjust the model precipitation rate within the range of realistic background specific humidity errors and rain-rate observation error, and the vertical structure of increments produced by the 1DVAR strongly depends upon convective parameterization.

In this study, to assimilate satellite-derived rain rate in a NWP analysis system, two steps is suggested. First, a 1DVAR assimilation of satellite-derived rain-rate observations is applied. It enables the retrieval of modified temperature and humidity profiles that provide precipitation rates consistent with both observations and a model short-term forecast. Second, 1DVAR analyzed products are introduced in a data assimilation system. The second step can be achieved more easily compared to a direct assimilation of precipitation rates since temperature and humidity variables are already assimilated in 3DVAR or 4DVAR systems.

Section 2 presents the satellite-derived rain rate, forecast/assimilation system, 1DVAR method, observation operator and the experiment design. Numerical simulation results and the sensitivity studies are discussed in Section 3 along with the conclusions at the end.

2. OBSERVATION, FORECAST/ASSIMILATION SYSTEM, 1DVAR, OBSERVATION OPERATOR AND EXPERIMENTS DESIGN

2.1. Satellite-derived Rain Rate

The observations selected for this study are the instantaneous surface rainfall rates estimated from the FY-2C Visible and Infrared Spin Scan-Radiometer (VISSR) by National Satellite Meteorological Center of China Meteorological Administration (NSMC/CMA) and the observed precipitation data by CMA to quantitatively verify the effect of assimilating the FY-2C rain rate. FY-2C rain rate is statistically calculated built on the strong correlation between rain rate with the infrared cloud-top temperature observed by VISSR and the cloud-top temperature gradients. The RMSE of rain rate at each IR temperature level is less than 5.0 mm. The higher the lowest cloud-top temperature, the less the RMSE of the estimated rainfall rate.

2.2. Forecast and Assimilation System

The WRF variational data assimilation system (WRF Var) is modified to assimilate the satellite-derived rain rate and the Advanced Research WRF (ARW) model version 3.1 was used for the OSSE study. Three WRF domains with two-way interactions were configured for the Control and data assimilation experiments, with the resolution horizontally at 10 kM and vertically at 31 levels.

2.3. One-dimensional Variational Method (1DVAR)

Let x be the vector (also denoted control variable) that represents the atmospheric state and R_o the rainfall rate. The 1DVAR retrieval consists of finding an optimum state x that minimizes a distance between the model rainfall rate and R_o , given a background constraint provided by the error covariances of a short-term forecast profile xb . If the background and observation errors are uncorrelated and each has a Gaussian distribution, the maximum likelihood estimator of the state vector x is the minimum of the following cost function:

$$J(x) = \frac{1}{2} (x - x^b)^T B^{-1} (x - x^b) + \frac{1}{2} \left(\frac{R(x) - R_o}{\sigma_o} \right)^2 \quad (1)$$

where B is the background error covariance matrix and σ_o the standard deviation of observation error. In addition, $R(x)$ is a calculation of surface rain rate from the atmospheric state x at the observation location. The minimization module uses a limited memory quasi-Newton optimization routine, requiring an iterative estimation of the gradient of the cost function. The gradient of $J(x)$ is given by

$$\nabla J(x) = B^{-1} (x - x^b) + R'^T \left(\frac{R(x) - R_o}{\sigma_o^2} \right) \quad (2)$$

The operator $R'^T(x)$ is the transpose of the Jacobian vector of the partial derivatives of rainfall rates with respect to the input profile x .

2.4. Observation Operator

The observation operator $R(x)$ includes two components that are the moist-convective parameterization and the stratiform precipitation parameterization. A diagnostic parameterization of stratiform precipitation based on a moist-local adjustment process is used, in which, the excess of moisture with respect to saturation at a given level is converted into nonconvective precipitation. The adjusted values of temperature and specific humidity correspond to a saturation state and are obtained by keeping the moist static energy constant.

A modified Kuo scheme is used in the numerical model for cumulus convection. Following the discussion in Chang and Holt (1994), the convective latent heating at a grid point in the model is

$$\frac{\delta T}{\delta t} = \frac{bgLM_t(T_c - T)}{C_p P_s \int_{\sigma} (T_c - T) d\sigma}, \quad \text{if } M_t > 0 \quad (3)$$

where b is a partitioning parameter set equal to the vertical mean relative humidity; T_c , the cloud temperature; L , the specific latent heat; C_p , the specific heat at constant pressure of air; and P_s the surface pressure. Here, M_t is the total moisture convergence defined as:

$$M_t = \frac{P_s}{g} \int_{\sigma} -\nabla \cdot V q d\sigma \quad (4)$$

where q is the specific humidity. The rain rate ($\delta R / \delta t$ cm s⁻¹) in the model, which is related to the vertically integrated heating rate, is then defined at each grid point as:

$$\frac{\delta R}{\delta t} = \frac{P_s C_p}{g \rho_w L} \int_{\sigma} \frac{\delta T}{\delta t} d\sigma \quad (5)$$

where ρ_w is the density of liquid water.

The coupling of moist-convective and stratiform precipitation schemes follows the fractional-stepping approach [1], i.e., the convective precipitation operator is applied first and then the stratiform precipitation parameterization acts on an atmospheric state already affected by the convective precipitation operator.

2.5. Experiment Design

Control and assimilation experiment were designed to understand the impact of assimilation after retrieved FY-2C rain rate data on the meteorological fields and rainfall. The FY-2C rain rate data was assimilated with the assumption of the observational error in 6 mm/h. The experiments were run from 00 8 to 06 30 September 2008 for about 20 days to catch several different typhoon events occurred in September 2008.

3. NUMERICAL SIMULATION RESULTS

The 24 hr accumulated rainfall from FY-2C was geo-matched to in-situ observed 24 hr accumulated rainfall from CMA observing system and the comparison of averaged rainfall from all available stations each day between FY-2C and in-situ observation is shown in Figure 1. Generally the FY-2C is in good agreement with in-situ observation, except that the typhoon events were occurred frequently, i.e., Kammuri, Nuri, Sinlaku, Hagupit and Higos were taken place one by one. Since that, the 90-day STD containing those typhoon events is 6.446 larger than the other 90-day average.

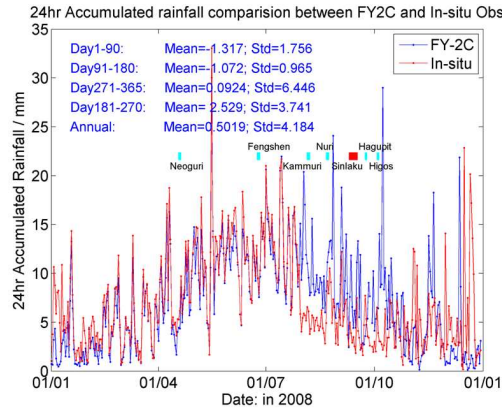


Figure 1: 24 hr Accumulated rainfall comparison between FY2C and In-situ Obs from all available stations each day of 2008.

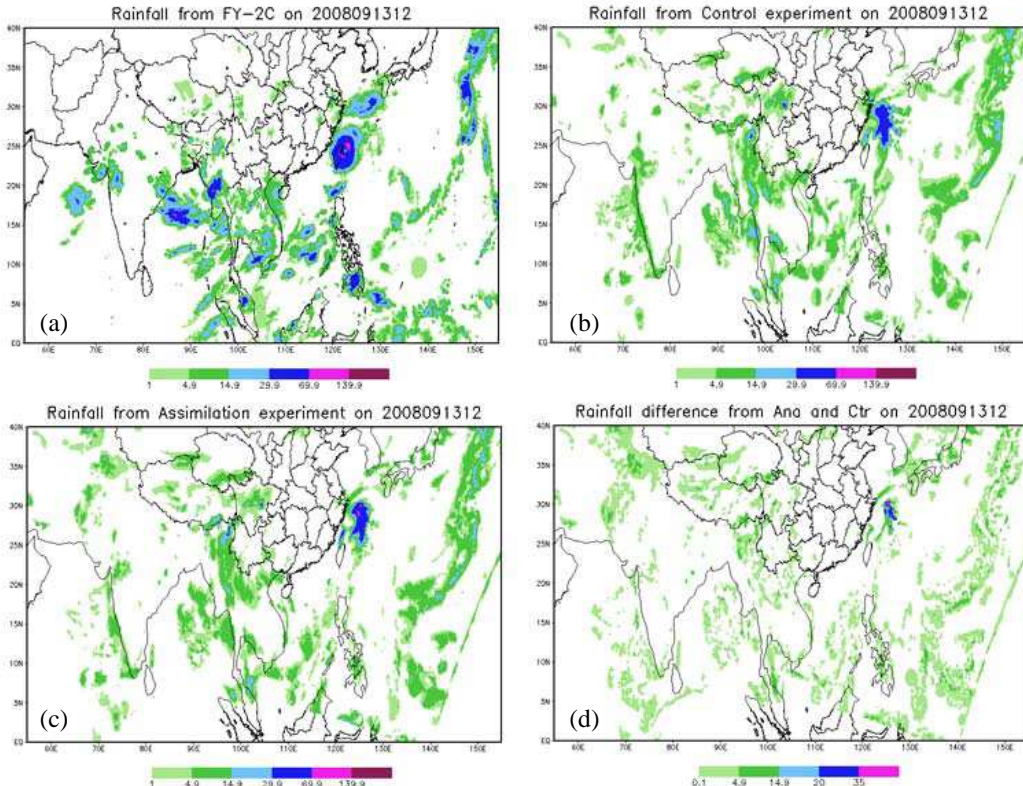


Figure 2: Comparison of Six-hour accumulated rainfall (mm) from assimilating rainfall on 2008091312, (a) FY-2C observation, (b) the control run, (c) rain rate assimilation and (d) difference from assimilation and control.

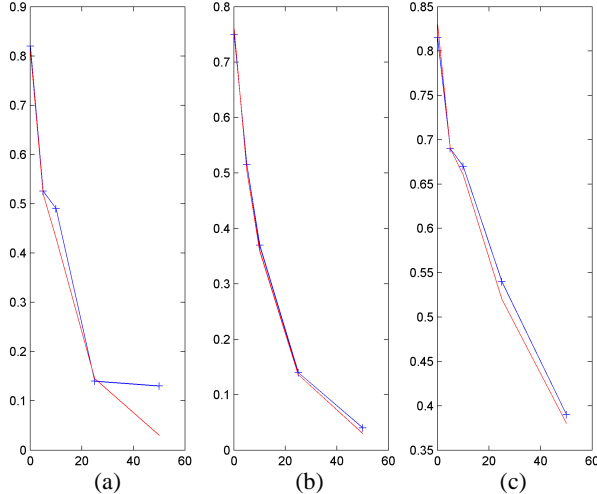


Figure 3: Six-hour accumulated precipitation forecast skill measured from Control and Rain rate assimilation experiments at different thresholds for: (a) 6–12 h, (b) 12–18 h, (c) 0–24 h.

By comparing the rainfall from control and assimilation in Figure 2, the strengthened rainfall center in assimilated experiment is significantly observed in better agreement with FY-2C than Control. The difference figure further confirms it and makes it clearer.

To quantitatively evaluate precipitation, threat scores (TSs) for the 6-h accumulated rainfall (over land only) were calculated (Figure 3) using the formula:

$$TS = \frac{NH}{NA + NB - NH} \quad (6)$$

where NH is the number of hits for a given rainfall threshold. NA and NB are the numbers of grid boxes whose rainfall amounts were greater than or equal to the given rainfall threshold from the nature run and data assimilation experiments, respectively.

In general, the threat scores decreased when the rainfall threshold increased (Figure 3). After assimilating FY-2C rain rate data, the TS has improvement, especially for 0–24 h.

4. CONCLUSION

But applying 1DVAR algorithm in the WRF-VAR system, the FY-2C retrieved rain rate data is assimilated. Some useful conclusions and lesson is summarized as follows:

The rainfall information can be physically assimilated by a 1DVAR system with a cloud convective model; the meteorological fields can be improved, but with the main impact on the humidity fields; The forecasted rainfall within the assimilation window could be improved greatly and better redistributed after observed rainfall is directly assimilated into the model.

ACKNOWLEDGMENT

This work was supported by the National Natural Science Foundation of China (Grant No. 40705037) and also by China's Research and Development Special Fund for GRAPES model (No. 22005051).

REFERENCES

1. Beljaars, A. C. M., "Numerical schemes for parameterizations," *Proceedings of ECMWF Seminar on Numerical Methods in Atmospheric Models*, 1–42, Reading, United Kingdom, European Centre for Medium-Range Weather Forecasts, 1991.
2. Fillion, L. and R. Errico, "Variational assimilation of precipitation data using moist convective parameterization schemes: 1D-Var study," *Mon. Wea. Rev.*, Vol. 125, 2917–2942, 1997.
3. Fillion, L. and J.-F. Mahfouf, "Coupling of moist-convective and stratiform precipitation processes for variational data assimilation," *Mon. Wea. Rev.*, Vol. 128, 109–124, 2000.
4. Treadon, R. E., *Assimilation of Satellite Derived Precipitation Estimates with the NCEP GDAS*, Ph.D. Dissertation, The Florida State University, Tallahassee, Florida, 1997.
5. Tsuyuki, T., "Variational data assimilation in the Tropics using precipitation data. Part III: Assimilation of SSM/I precipitation rates," *Mon. Wea. Rev.*, Vol. 125, 1447–1464, 1997.

An Initial Study on Assimilating Satellite-derived Total Precipitable Water in a Variational Assimilation System

Q. Lu, X. Yang, C. Wu, J. Zheng, D. Qin, H. Yang, and P. Zhang

National Satellite Meteorological Center of CMA, Beijing, China

Abstract— A variational assimilation system was used to examine the comparative impact of including satellite derived total column water vapor from MODIS NIR and IR observations (observed reflectance or radiance). The results show that the initial humidity field was improved by assimilating the satellite derived total column water vapor, especially over the rainfall areas, at the same time, the initial temperature field and the geopotential height field were also improved. The precipitation forecast difference between including and excluding the total column water vapor experiments was obvious during the assimilation time-window, and the precipitation forecast was also improved in the twenty-four hours precipitation forecast. More precipitation information can be obtained by introducing the satellite derived total column water vapor information into the variational assimilation system.

1. INTRODUCTION

Numerical weather prediction is an initial and boundary value problem [2], the more accurate initial conditions could result in the improvement of forecast skill. Over the past two decades, considerable progress has been made in satellite technology, which is significantly increasing the atmospheric information in data-sparse areas. With proper and effective assimilation of satellite data, on the current condition of assimilating more temperature information, the forecasted fields have been much improved, but with greater improvement on the temperature structure than the moisture structure.

Moderate Resolution Imaging Spectrometer (MODIS) instruments, on board the NASA Earth Observation System Terra and Aqua satellites, have channels observing atmospheric moisture and temperature: near-infrared (NIR) and infrared (IR). The retrieved total precipitable water (TPW) from NIR and IR algorithms contain valuable moisture information, it could be expected that the analyzed and forecasted moisture structure would be improved by assimilating the MODIS NIR and IR TPW. The Weather Research and Forecasting (WRF) model is a new generation advanced mesoscale (10 km–1 km) model for both operational numerical weather prediction (NWP) and atmospheric research and it is the successor of the MM5, Eta, and RUC model system. And in this study, its three-dimensional variational data assimilation system (3D-Var) was extended to assimilate the MODIS TPW data.

The primary objectives of this study are: to investigate the impact of the assimilating MODIS NIR and IR Total Precipitable Water using WRF-3DVAR system on moisture structure. This paper is organized as follows. The TPW features from MODIS the numerical modeling system, including the WRF model and its variational data assimilation component, and the experiment design are described in Section 2. Numerical simulation results and three sensitivity studies are discussed in Section 3 along with concluding remarks at the end.

2. OBSERVATION, FORECAST/ASSIMILATION SYSTEM, OBSERVATION OPERATOR AND EXPERIMENTS DESIGN

2.1. Satellite-derived Precipitable Water

The resolutions of the MODIS total precipitable water (TPW) retrieved from NIR and IR algorithms are 1 and 5 km, respectively, enough describing detailed horizontal gradients of moisture and temperature.

The accuracy of TPW would influence its assimilation impact. Many validations have been done to understand the error characteristics of TPW retrievals to improve the assimilation in NWP. For MODIS NIR TPW over ocean, the Root Mean Square Error (RMSE) is about 5.0 mm with an underestimate in a dry atmosphere [3], while for MODIS NIR TPW over land, the RMSE is about 3.3 mm, with an slight underestimate by less than 1 mm in a dry atmosphere and overestimate by up to 7 mm in a moist atmosphere [1]. In contrast, MODIS IR TPW over land is overestimated (underestimated) in a dry (moist) atmosphere, with the maximum deviation of up to 5 mm and an RMSE of 4.1 mm over sea [1, 4].

For MODIS IR TPW, data over cloudy areas were excluded in the original data set. Therefore no more data screening was performed during the preprocessing stage. For MODIS NIR TPW, data over clear-sky and cloudy regions were available in the data set. Since the TPW data over the cloudy region is the vertical integral of water vapor only above the cloud top, in general, one prefers not to use those data in 3D-Var. In processing MODIS NIR TPW, the resolution of data was reduced from 1 to 5 km by averaging data from cloud-free pixels in 5×5 matrices, with a required minimum of 10 clear sky pixels identified using the cloudiness flag provided in the data set. Consequently, many MODIS NIR TPW data near the cloudy area were discarded.

2.2. Forecast and Assimilation System

The Advanced Research WRF model version 3.1 and its three-dimensional variational data assimilation system (3D-Var) were used [5]. The domain configuration included a domain of 10 km horizontal resolutions. The grids extended vertically to 50 hPa and were resolved by 31 unevenly spaced sigma levels with the finest resolution in the boundary layer. The physics parameterization schemes that were applied to the simulations included the Purdue-Lin microphysics, the new Kain-Fritsch cumulus parameterization, the Yonsei University boundary layer parameterization, the Dudhia shortwave parameterization, and the Rapid Radiative Transfer Model longwave parameterization. The initial and lateral boundary conditions and sea surface temperature data were from the National Centers for Environmental Prediction Global Forecast System (GFS) with spatial and temporal resolutions of $1^\circ \times 1^\circ$ and 6 h, respectively.

A data screening process was performed hourly for 6 h, starting from 18 UTC 7 September 2008. The model was then integrated for 48 h starting from 00 UTC 8 September 2008. Following the gross-error quality control used for most of the observations in WRF 3D-Var, satellite TPW data that differed from the model's background by more than 5 times the observation-error variance were removed. An observation error of 5 mm was used for MODIS TPW data.

2.3. Observation Operator

The incremental approach is utilized in WRF 3D-Var system and the analysis state, x_a , is obtained by

$$x^a = x^b + \delta x^a \quad (1)$$

where x^b is the background state and δx^a is the analysis increment of TPW obtained by minimizing the following cost function:

$$J(\delta x) = \frac{1}{2} \delta x^T B^{-1} \delta x + \frac{1}{2} (\text{TPW}_{model} - \text{TPW}_{obs})^T O^{-1} (\text{TPW}_{model} - \text{TPW}_{obs}) \quad (2)$$

where B is the covariance matrix of background errors, O is the covariance matrix of observational errors, and N is the total number of available observations. TPW_{Obs} stands for the MODIS TPW retrieved from NIR and IR algorithms. TPW_{model} represents TPW from the background state that was computed using a forward operator in the 3D-Var system, and the formula is as follows:

$$\text{TPW}_{model} = \frac{p^*}{g} \sum_{k=1}^{KX} q(k) \Delta \sigma(k) \quad (3)$$

where p^* is defined as the difference in the pressure between the model surface and top, $q(k)$ the model specific humidity at the k th layer, $\Delta \sigma(k)$ is the layer thickness of the model at the k th layer, and KX is the total number of layers. After the minimization of the cost function, the adjoint TPW operator and the spatial correlations (from the background covariance matrix) project two-dimensional TPW increments onto 3-D moisture increments.

2.4. Experiment Design

The horizontal resolution in the WRF simulation is 10 km for the research domain with 31 vertical levels. Control and assimilation experiment were designed to understand the impact of assimilation after MODIS NIR and IR TPW data on the meteorological fields and rainfall. Over land, the MODIS NIR TPW data was assimilated with the assumption of the observational error in 3.5 mm, while over sea, MODIS IR TPW data was assimilated with the assumption of the observational error in 4.5 mm. The experiments were run from 00 8 to 06 30 September 2008 for about 20 days.

3. NUMERICAL SIMULATION RESULTS

Generally when the temperature information is assimilated into NWP model, the temperature profile will be modified significantly, and then the geo-potential, but smaller impact on the humidity profile is observed. What will happen after assimilating humidity information?

To understand this question and demonstrate the effect of assimilating the MODIS NIR and IR data to meteorological fields and rainfall, the profiles in $2^\circ \times 2^\circ$ square area are averaged to get the averaged profile and three typical averaged profiles with heavy rainfall occurred in September 2008 are calculated. The three averaged profiles are located at 88E & 25N (over land), at 126E & 26N (over coastal water), and at 147E & 33N (over sea), designed to demonstrate what effect will be different from over land, to over coastal water (interface of land and sea) and then to over sea. The NCEP reanalysis is taken as the observation for Figures 1 and 2.

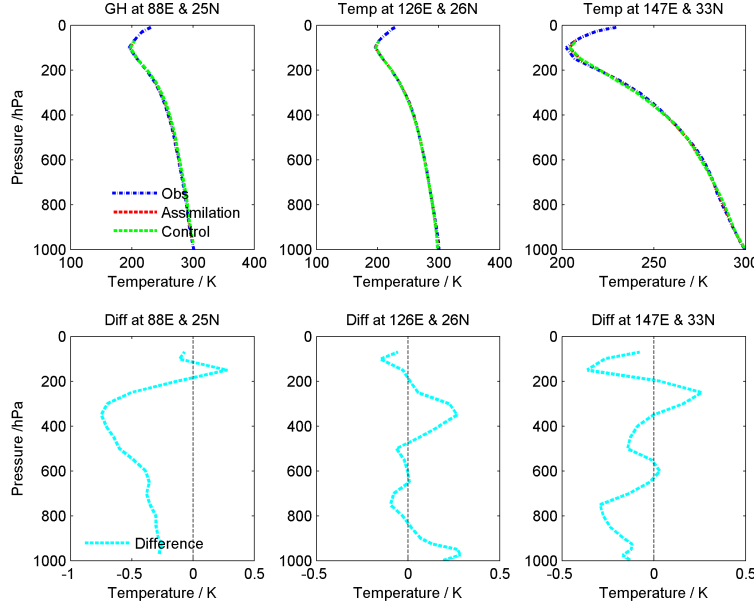


Figure 1: Comparison of temperature profile at different places. The top panels are temperature itself and the bottom panels are the differences between assimilation and Control, with the left column located at 88E & 25N, with the middle column located at 126E & 26N, and with the right column located at 147E & 33N.

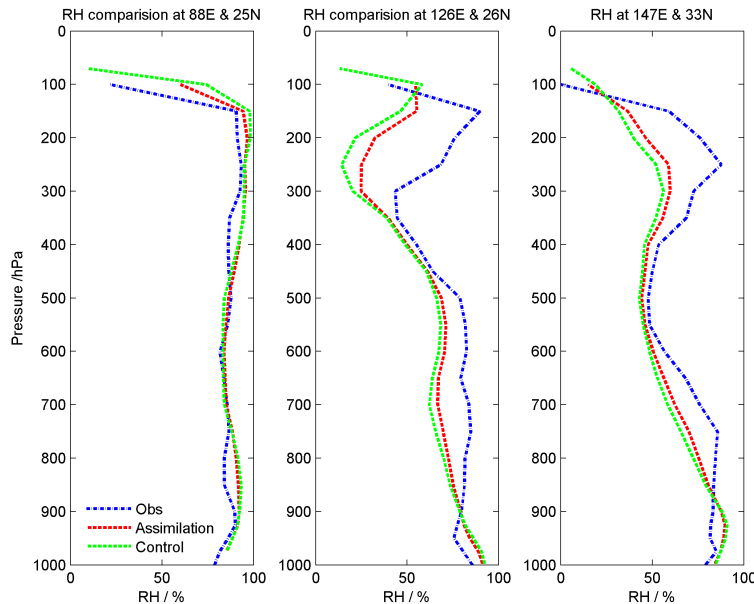


Figure 2: Comparison of relative humidity profile at different places, with the left column located at 88E & 25N, with the middle column located at 126E & 26N, and with the right column located at 147E & 33N.

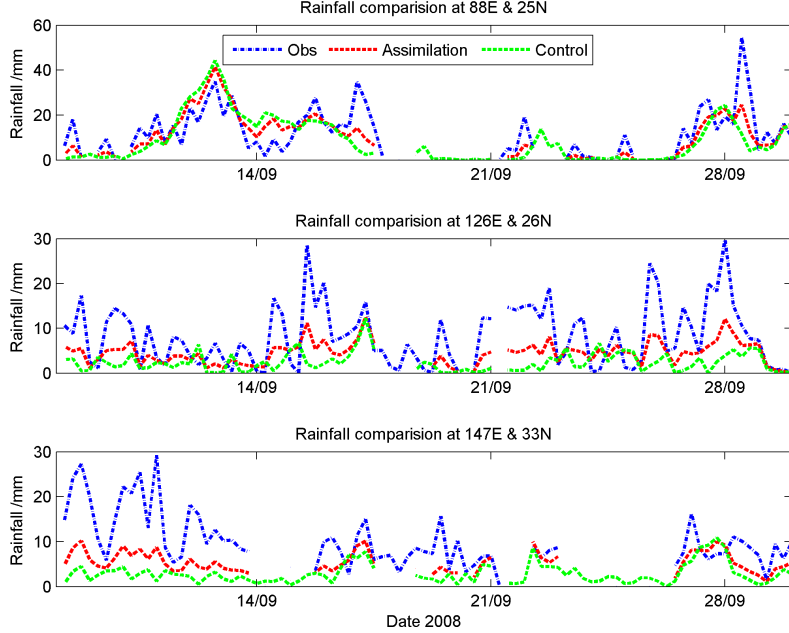


Figure 3: The evolution of forecasted rainfall against time, with the top panel located at 88E & 25N, with the middle panel located at 126E & 26N, and with the bottom panel located at 147E & 33N.

Figure 1 shows the comparison of temperature profile at different places. It indicates that the temperature profile at three places all has been well predicted against the obs. The departure between Assimilation and Control is generally within 0.5 K. Over land, the negative departure is observed, while over sea, the positive departure near 200–500 hPa and the negative departure below 500 hPa are observed. The temperature profile is less improved and it is the same case for the geo-potential height (figure omitted).

Figure 2, showing the comparison of relative humidity profile at different places, demonstrates that the significant modification and improvement to the relative humidity profile are observed after assimilating the MODIS NIR and IR TPW data containing humidity information at different palaces, especially over sea.

Figure 3 shows the evolution of forecasted rainfall against time displaying the impact of assimilating the FY-2C rain rate data on the forecasted rainfall. Simulated rainfall from Control and Assimilated experiment is generally small than the observation, especially during the period of typhoon events. The bias over coastal water and over sea is larger than over land. After assimilating the FY-2C rain rate data, the larger bias during the period of typhoon events is reduced closer to the observation and the tendency of rainfall evolution is also improved in better agreement with the observation (FY-2C rain rate).

4. CONCLUSION

The impact of satellite-derived TPW from MODIS near-infrared (NIR) and infrared (IR) was assessed and compared using the Weather Research and Forecasting model and its three-dimensional variation data assimilation (3D-Var) system. Some useful conclusions and lesson is summarized as follows:

The MODIS TPW information can be physical assimilated in a variational system; the assimilation reduces the difference in TPW between the model and observations; the meteorological fields can be improved, but more improvement is achieved on the humidity field and forecasted rainfall after assimilating the MODIS NIR and IR TPW data.

ACKNOWLEDGMENT

This work was supported by the National Natural Science Foundation of China (Grant No. 40705037) and also by China's Research and Development Special Fund for GRAPES model (No. 22005051).

REFERENCES

1. Chen, S. H., Z. Zhao, J. S. Haase, A. Chen, and F. Vandenberghe, “A study of the characteristics and assimilation of retrieved MODIS total precipitable water data in severe weather simulations,” *Mon. Wea. Rev.*, Vol. 136, 3608–3628, 2008.
2. Kalnay, E., *Atmospheric Modeling, Data Assimilation and Predictability*, Cambridge University Press, Cambridge, UK, 2003.
3. Kleidman, R. G., Y. J. Kaufman, et al., “Remote sensing of total precipitable water vapor in the near-IR over ocean glint,” *Geophys. Res. Lett.*, Vol. 27, 2657–2660, 2000.
4. Seemann, S. W., J. Li, W. P. Menzel, and L. E. Gumley, “Operational retrieval of atmospheric temperature, moisture, and ozone from MODIS infrared radiances,” *J. Appl. Meteorol.*, Vol. 42, 1072–1091, 2003.
5. Skamarock, W. C., J. B. Klemp, J. Dudhia, et al., “A description of the advanced research WRF version 3,” Technical Note NCAR/TN-475+STR, National Cener for Atmospheric Research, Boulder, Colo, 2008.

The Web Site for Retrieving the Microwave Complex Permittivity Spectra of Moist Soils

V. L. Mironov¹, A. M. Epikhin², S. V. Fomin¹, and L. G. Kosolapova¹

¹Kirensky Institute of Physics, SB, RAS, Krasnoyarsk, Russia

²Digital Mind Development Ltd., Krasnoyarsk, Russia

Abstract— This web site was set up to facilitate remote access to practical usage of moist soil dielectric models in process of developing and testing remote sensing software to be designed for radar and radiometry microwave techniques. In case of thawed soils, it provides a user on line with numerical values of both the relative dielectric constant and loss factor of moist soils as a function of water content, frequency, temperature, and soil texture. The algorithm used for calculating complex dielectric constant is based on the most reliable dielectric data, on the one hand, and the temperature and mineralogy dependable dielectric model, on the other hand, recently developed, which proved to ensure the least error of dielectric predictions as compared with those provided by the other models being used in radar and remote sensing retrieving algorithms. In case a set of dielectric data is available for a user, the site allows comparing on line these data with the values retrieved from the site and estimating standard deviation from each other regarding these two data sets. The services provided on line with this site are deemed to be extended in the nearest future.

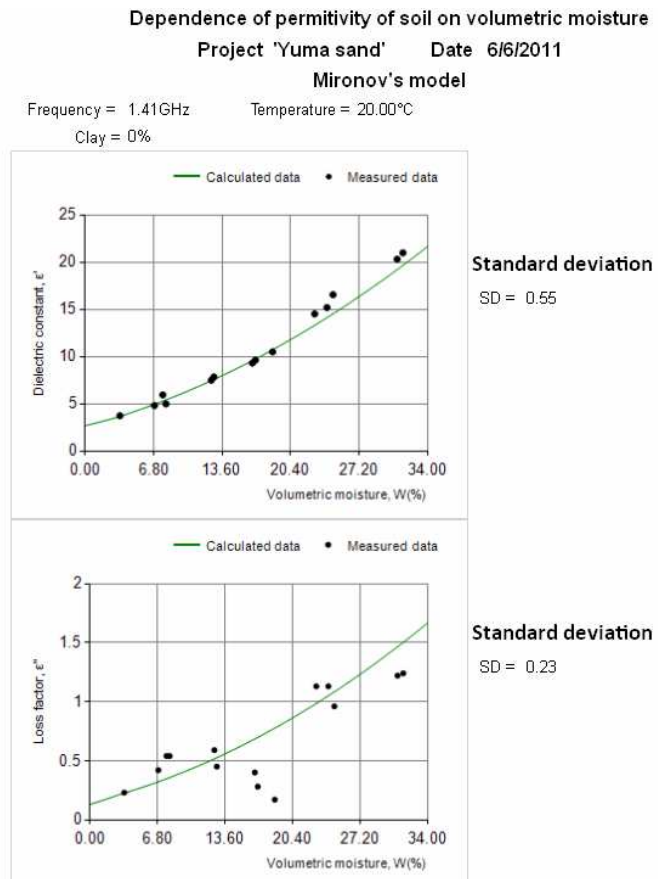


Figure 1: An example of retrieving the dielectric constant and loss factor as a function of soil moisture. The data retrieved on line (solid lines) are compared with the data measured in [1] for the Yuma Sand soil (symbols). The standard deviations are 0.55 for ϵ' and 0.23 for ϵ'' .

1. INTRODUCTION

Moist soil dielectric models (MSDMs) in the microwave band are an essential part of the software used in radar and radiometer remote sensing. These models are also needed for interpreting the data attained by Time Domain Reflectometers (TDRs) and Ground-penetrating radars (GPRs). The software developed for this site is based on the measured permittivity data that are recognized as most reliable and have been used for developing the MSDMs employed in the contemporary radar and radiothermal remote sensing algorithms [1–4]. It provides moist soil complex permittivity values as a function of soil moisture (from dry to field capacity), electromagnetic frequency (from 0.3 to 26.5 GHz), soil temperature (from 10°C to 40°C), and percentage of clay in soil (from about zero to 76%). The MSDM software covers the soil types containing less than 5–7% of organic matter and classified as not saline. The software for calculating the complex permittivity employs the temperature and mineralogy dependable soil dielectric model [5, 6]. The error of predictions attained by these models is substantially decreased as compared with that of the well known in remote sensing Dobson model [2, 3] and is on the same order regarding the renowned Schmugge model [1]. Besides that, the Dobson and Schmugge models are valid in the narrower temperature range from 22°C to 24°C, and the Schmugge model accounts only for two frequencies, that is, 1.4 and 5.0 GHz.

2. THE WEBSITE DESCRIPTION

The website is available at <http://rsl.dmddevelopment.ru/>. At the Homepage of the website, a brief description of the deliveries and the basics of the algorithm used for dielectric predictions are given. Three functional web pages are available for users: 1) Calculation, 2) Downloads, 3) Publications, and 4) Comments. At the Calculation page, the complex dielectric constant can be retrieved on line as a function of soil moisture, with the frequency, temperature and clay content (in accordance with the USDA classification) fixed as parameters. The data retrieved are displayed in a form of graphs and tables. The site users can also add a set of dielectric data available for them from

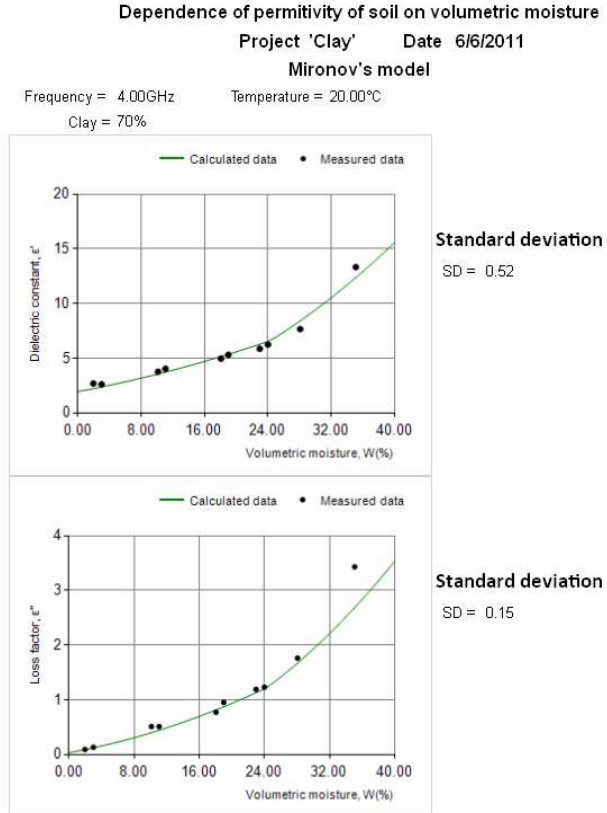


Figure 2: An example of retrieving the dielectric constant and loss factor as a function of soil moisture. The data retrieved on line (solid lines) are compared with the data measured in [8] for the Irving Clay soil (symbols). The standard deviations are 0.52 for ϵ' and 0.15 for ϵ'' .

other sources to be graphically displayed together with those calculated on line. The standard deviation value (between the two sets of dielectric data) is shown in additional box placed next to the graphical representation. Projects developed by the users can be saved on their computers. In the same way, the users can retrieve: 1) the complex dielectric constant spectra, with the soil moisture, temperature and clay content being fixed; 2) the temperature dependences of the complex dielectric constant, with the moisture, frequency, and clay content being fixed as parameters.

At the web page Publications, a user can find the list of references as to the dielectric data measured and the dielectric models used to develop the site. Finally, the web page Comments was deemed to set up feedback service with the users, which is needed, first, to learn about applicability of the dielectric model used as a site basic element and, second, to evaluate the usefulness of and need for such tools in the process of creating the algorithms of remote sensing using radars and radiometers. Besides that, we will be grateful to the users for their suggestions to improve the site.

In Figs. 1 and 2, are shown the examples of products retrieved with the use of the web site. The data for the dielectric constant and loss factor measured are taken from the papers [1] and [8]. They relate to extreme soil types in terms of content of clay fraction, namely, the Yuma Sand (with no clay fraction, collected in USA, see Fig. 1) and the Irving Clay (with 70% clay fraction, collected in Australia, see Fig. 2). As seen from the results presented in Figs. 1 and 2, the data calculated using the web site and the data measured are in good agreement with each other. The standard deviation of the retrieved data from those measured are about 0.55 for ϵ' and 0.23 for ϵ'' , which lies in the limits of error related to soil samples measurements. It should be noted that the data measured in [1] and [8] have not been used in the process of developing the dielectric models employed in the web site algorithm.

3. CONCLUSIONS

The internet site developed is available at <http://rsl.dmdevelopment.ru/>. The deliveries of the site are presented in the form of tables and plots for the relative dielectric constant and loss factor as a functions of soil moisture, frequency, or temperature, with the rest variables being fixed. The results provided can be downloaded from the site. In addition, the users can enter their own values of complex permittivity in order to quantitatively compare them with those displayed on the site graphs. Moreover, the users can download the dynamic linked library file “CalculationMethods.dll” to use it as a ready-made software library in their applications, if the environment Microsoft.NET Framework 4.0 is installed. The evolution of this site is planned to include other dielectric models and use the initial dielectric data measured over a broader assemblage of soils, frequencies, and temperatures, with frozen soils being considered as well.

ACKNOWLEDGMENT

This research was supported by the Siberian Branch of the Russian Academy of Sciences under Project II.10.1.6 and by the Russian Foundation for Basic Research and Centre National de la Recherche Scientifique (France) under Grant 09-05-91061.

REFERENCES

1. Wang, J. and T. Schmugge, “An empirical model for the complex dielectric permittivity of soils as a function of water content,” *IEEE Trans. Geosci. Remote Sensing*, Vol. 18, No. 4, 288–295, 1980.
2. Dobson, M. C., F. T. Ulaby, M. T. Hallikainen, and M. A. El-Rayes, “Microwave dielectric behavior of wet soil — Part 1,” *IEEE Trans. Geosci. Remote Sensing*, Vol. 23, No. 1, 25–34, 1985.
3. Dobson, M. C., F. T. Ulaby, M. T. Hallikainen, and M. A. El-Rayes, “Microwave dielectric behavior of wet soil — Part 2,” *IEEE Trans. Geosci. Remote Sensing*, Vol. 23, No. 1, 35–46, 1985.
4. Curtis, J. O., C. A. Weiss, Jr., and J. B. Everett, “Effect of soil composition on dielectric properties,” *U.S. Army Corps of Engineers Waterways Experiment Station, Vicksburg, MS Technical Report EL-95-34*, December 1995.
5. Mironov, V. L., L. G. Kosolapova, and S. V. Fomin, “Physically and mineralogically based spectroscopic dielectric model for moist soils,” *IEEE Trans. Geosci. Remote Sensing*, Vol. 47, No. 7, 2059–2070, 2009.
6. Mironov, V. L. and S. V. Fomin, “Temperature and mineralogy dependable model for microwave dielectric spectra of moist soils,” *PIERS Online*, Vol. 5, No. 5, 411–415, 2009.

7. Mironov, V. L., M. C. Dobson, V. H. Kaupp, S. A. Komarov, and V. N. Kleshchenko, "Generalized refractive mixing dielectric model for moist soils," *IEEE Trans. Geosci. Remote Sensing*, Vol. 42, No. 4, 773–785, 2004.
8. Sabburg, J., J. A. R. Ball, and N. H. Hancock, "Dielectric behavior of moist swelling clay soils at microwave frequencies," *IEEE Trans. Geosci. Remote Sensing*, Vol. 35, No. 3, 784–787, 1997.

Temperature Dependable Microwave Dielectric Model for a Pine Litter Thawed and Frozen

V. L. Mironov and I. V. Savin

Radiophysics of Remote Sensing Laboratory, Kirensky Institute of Physics
SB, RAS, Krasnoyarsk, Russia

Abstract— Dielectric measurements of a pine litter of Siberia boreal forest over the range from 0.5 to 15 GHz and from -30 to $+25^{\circ}\text{C}$ are presented. The measurements were fitted to the Temperature Generalized Refractive Mixing Dielectric Model (TD GRMDM) recently proposed by Mironov et al. This TD GRMDM predicts the dielectric for this soil in the whole range of moistures, frequencies, and temperatures measured. The model prediction errors are on the same order as that of dielectric measurements. The model proposed is the first of its kind to provide a physical basis for radar and radiothermal remote sensing algorithms that retrieve the freeze/thaw state and the volumetric moisture in the upper layer of an Siberia forest soil.

1. INTRODUCTION

Forest floor strongly influences the radiobrightness temperature of forest land territories. Consequently, complex dielectric constant of the layer of leaf or needle debris must be taken into account in remote sensing algorithms to retrieve the moisture content of forest topsoil [1]. So far, the dielectric constant models for litter have not been developed to such an extent as the dielectric models of moist soils have. In this area of research, there are published only a few papers. In particular, semi-empirical models of the complex permittivity are proposed for two types of litter which samples were taken from the leaf [2] and pine [3] forest floors. These models provide for the dielectric properties of thawed only litter, which limits their usage, particularly for the northern territories, where the topsoil is in the frozen state for a long time during the year.

In this paper, we developed a physically substantiated temperature dependable spectroscopic dielectric model (TD GRMDM) of pine litter collected in the East Siberia boreal forest. The model covers the range of frequencies and temperatures stretching from 500 MHz to 15 GHz and from -30°C to $+25^{\circ}\text{C}$, respectively.

2. TEMPERATURE DEPENDABLE SPECTROSCOPIC DIELECTRIC MODEL

The theoretical basis of this model has been developed in the case of shrub tundra soil, which contains at least 90% of organic matter [4]. According to [4], the relationship between the complex refractive index (CRI) of moist litter and the gravimetric moisture contained in the litter is expressed as follows:

$$\frac{n_s^* - 1}{\rho_d(m_g)} = \frac{(n_m^* - 1)}{\rho_m} + \frac{(n_b^* - 1)}{\rho_b} [m_g + (m_{g1} - m_g)u(m_g - m_{g1})] + \frac{(n_t^* - 1)}{\rho_t} [(m_g - m_{g1})u(m_g - m_{g1}) \\ + (m_{g2} - m_g)u(m_g - m_{g2})] + \frac{(n_\mu^* - 1)}{\rho_\mu} (m_g - m_{g2})u(m_g - m_{g2}). \quad (1)$$

In formula (1), $n_{*j} = \varepsilon_j^{(1/2)}$ stands for the CRI, with $\varepsilon_j = \varepsilon'_j + i\varepsilon''_j$ being the complex relative dielectric constant, ρ_j is the mass density. The subscripts s , d , m , b , t , and μ , are used to designate the moist litter, dry litter, litter solids, bound water, transient bound water, and unbound water ($\mu = u$) in a thawed litter sample or moistened ice water ($\mu = wi$) in a frozen one, respectively. m_g is the gravimetric moisture (ratio of mass of water to mass of dry matter), and m_{g1} is the maximum gravimetric fraction of bound water (MGFBW). m_{g2} is the transition moisture which separates the range of liquid water or moistened ice water, $m_g > m_{g2}$, from that of transient bound water, $m_{g1} < m_g < m_{g2}$. $u(x)$ denotes the Heaviside step function: $u(x) = 1$ if $x > 0$, and $u(x) = 0$ if $x \leq 0$. Furthermore, we presume that $\rho_b = \rho_u = \rho_t = 1 \text{ g/cm}^3$, and $\rho_{iw} = 0.917 \text{ g/cm}^3$. Let us consider the value of m_{g2} as a maximal gravimetric fraction of the bound and transient bound water (MGFBTW), which is characteristic to a given individual type of the soil. $\rho_d(m_g)$ is a function of initial water content, m_g , in a sample to be dried. The term $(n_m^* - 1)/\rho_m$ is a reduced CRI of the litter solids, and we consider this entire term as a single material property of the litter solids. The

real, $\text{Re}n^*=n$, and imaginary, $\text{Im}n^*=\kappa$, parts of the CRI are further referred to as the refractive index (RI) and normalized attenuation coefficient (NAC), which is a proportion of the standard attenuation coefficient to the free space propagation constant.

The dielectric measurements of moist litter samples were conducted according to the methodology given in [4]. The litter samples were prepared with the use of material collected from the topsoil layer at the depth from 3 to 7 cm located in a pine forest, which is 50 km far from the city of Krasnoyarsk East Siberia. The technique to process the samples before placing in a measurement coaxial container was similar to that used in [4]. So was the method to obtain the moisture content and mass density of the samples measured.

The Equation (1) was fitted to the reduced RIs, $(n_s - 1)/\rho_d$, and NACs, κ_s/ρ_d , measured as a function of gravimetric moisture. An example of such fitting to the RI measured is shown in Fig. 1. As seen from Fig. 1, the model (1) is quite satisfactory. Indeed, the RI and NAC measurements are piecewise linear in certain moisture ranges, indicating contributions of particular forms of water. As a result of fitting, the values of $(n_m - 1)/\rho_m = 0.52$ and $\kappa_m/\rho_m = 0.000834$ can be obtained as the values of $(n_s - 1)/\rho_d$ and κ_s/ρ_d at $m_g = 0$. The variations of these values with frequency and temperature were found to be negligible, and the numerical values given above are their averages of all measured values. The MGFBW, m_{g1} and the MGFBTW, m_{g2} are determined as a point of transition from one linear segment of the fit to another.

The dependencies of the MGFBW, m_{g1} , and the MGFBTW, m_{g2} , on the temperature are presented in Fig. 2. The values shown in Fig. 2 are the result of averaging of all values measured over all the frequencies.

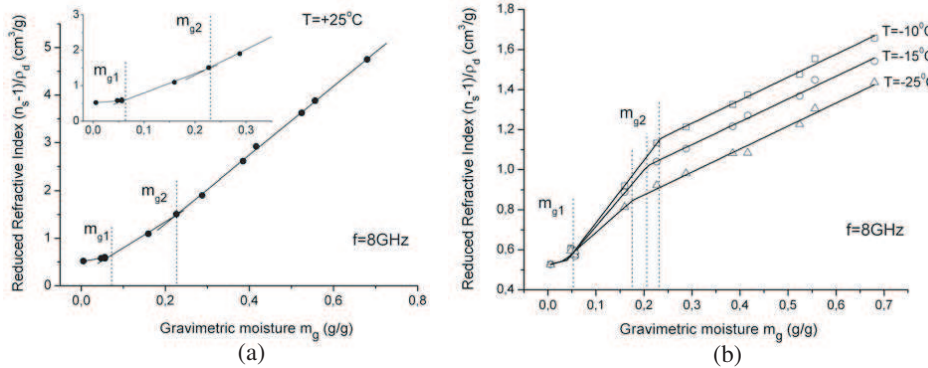


Figure 1: Behavior of the reduced characteristics for the RI, $(n_s - 1)/\rho_d$ vs. gravimetric moisture as a function of frequency in the case of (a) thawed litter, at the temperature of 25°C , frequency of 8.0 GHz and (b) frozen litter, at the temperatures of -10 , -15 , -20°C , frequency of 8.0 GHz .

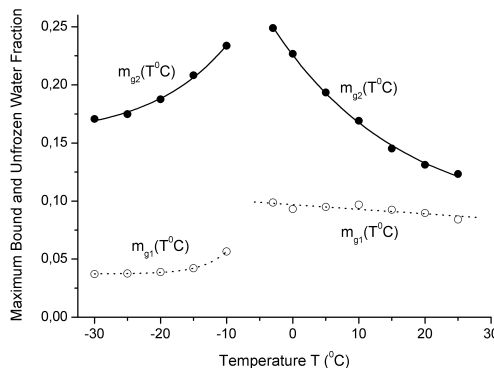


Figure 2: The maximum gravimetric fraction of bound water m_{g1} , and maximum gravimetric fraction of transient water, m_{g2} , as a function of temperature.

The fits related to these dependences are expressed in the form:

$$m_{g1} = \begin{cases} 0.097 - 3.96 \cdot 10^{-4} \cdot T, & -5^\circ\text{C} \leq T \leq 25^\circ\text{C}, \\ 0.082 + 0.144 \cdot \exp(-T/19.31), & -30^\circ\text{C} \leq T \leq -7^\circ\text{C} \end{cases} \quad (2)$$

$$m_{g2} = \begin{cases} 0.037 + 0.297 \cdot \exp(T/3.66), & -5^\circ\text{C} \leq T \leq 25^\circ\text{C}, \\ 0.155 + 0.189 \cdot \exp(T/11.47), & -30^\circ\text{C} \leq T \leq -7^\circ\text{C} \end{cases} \quad (3)$$

where T is the temperature of the sample in centigrade. The samples were observed to get frozen at the freezing temperature of $T_f = -6^\circ\text{C}$.

Finally, the values of CRIs for all the categories of litter water, that is, bound litter water, n_b^* , transient bound litter water, n_t^* , and unbound litter water, n_u^* , in the case of thawed samples ($T > T_f$), or moistened ice water, n_{iw}^* , in the case of frozen samples ($T < T_f$), were derived from the slopes of the linear segments in formula (1), the latter having been expressed through the respective RIs and NACs. Further, the values of RIs, n_p , and NACs, κ_p , were converted into the relative dielectric constants (DC), $\varepsilon'_p = n_p^2 - \kappa_p^2$, and loss factors (LF), $\varepsilon''_p = 2n_p\kappa_p$. Here the subscript p can be substituted by any of the subscripts b , t , u , and iw designating the forms of the water in litter. Similar to [4], the DCs and LFs for all the forms of water in litter were shown to follow the Debye equation as a function of electromagnetic frequency, f , that is:

$$\varepsilon'_p + i\varepsilon''_p = (n_p^*)^2 = \varepsilon_{\infty p} + \frac{\varepsilon_{0p} - \varepsilon_{\infty p}}{1 - i2\pi f\tau_p} + \frac{i\sigma_p}{2\pi f\varepsilon_0} \quad (4)$$

where ε_{0p} and $\varepsilon_{\infty p}$ are the low- and high-frequency limit dielectric constants, τ_p is the relaxation time (the inverse of the relaxation frequency), and σ_p is the ohmic conductivity, each specific to the different forms of litter water. Finally, $\varepsilon_0 = 8.854 \text{ pF/m}$ is the permittivity of vacuum.

Like in [4], at each fixed temperature, formula (4) was fitted to the measured spectra for all categories of litter water to yield the spectroscopic parameters measured as a function of temperature: $\varepsilon_{0p}(T)$, $\varepsilon_{\infty p}(T)$, $\tau_p(T)$, and $\sigma_p(T)$. Following [4], the temperature dependences measured for both the low and high frequency limits were fitted with the Clausius-Mossotti equation

$$\varepsilon_{qp}(T) = \frac{1 + 2 \exp[F_{qp}(T_{seqp}) - \beta_{vqp}(T - T_{seqp})]}{1 - \exp[F_{qp}(T_{seqp}) - \beta_{vqp}(T - T_{seqp})]}, \quad F_{qp}(T) = \ln \left[\frac{\varepsilon_{qp}(T) - 1}{\varepsilon_{qp}(T) + 2} \right], \quad (5)$$

with $q = 0$ and $q = \infty$, standing for the low and high frequency limit dielectric constants, to derive the volumetric expansion coefficients, β_{vqp} , starting temperature T_{seqp} , for which any measured one can be taken, and the values of $\varepsilon_{qp}(T_{seqp})$ at the starting temperatures as the parameters of the TD GRMDM of pine litter. The numerical values of all these parameters are given in Table 1.

Table 1: TD GRMDM parameters for all forms of water in litter in the temperature range $-30^\circ\text{C} \leq T \leq +25^\circ\text{C}$.

Parameter	Units	Bound water		Unbound water	Transient bound water		Moistened Ice Water
p (subscript)		b		u	t		Iw
Temperature Range		$T < T_f$	$T > T_f$	$T > T_f$	$T < T_f$	$T > T_f$	$T < T_f$
$\varepsilon_{0p}(T_{seqp})$	-	7.61	14.05	78.69	35.82	65.45	5.7
β_{v0p}	1/K	-7.45×10^{-3}	-3.32×10^{-3}	-1.55×10^{-4}	-1.17×10^{-3}	-2.31×10^{-4}	-4.23×10^{-3}
T_{seqp}	°C	-20	+20	+20	-20	+20	-20
$\varepsilon_{\infty p}(T_{seqp})$	-	4.25	5.26	10.18	8.17	17.05	5.09
$\beta_{v\infty p}$	1/K	-3.48×10^{-3}	-3.98×10^{-3}	-3.33×10^{-3}	-8.65×10^{-3}	-2.13×10^{-3}	-1.38×10^{-3}
T_{seqp}	°C	+20	-20	20	-20	+20	-20
$\Delta H_p/R$	K	216	386	2160	2026	1518	328
$\Delta S_p/R$	-	4.81	4.2	3.27	1.88	0.16	3.88
$\sigma_p(T_{seqp})$	S/m	0.15	0.21	0.33	0.25	0.8	0.071
$\beta_{\sigma p}$	(S/m)/K	$+2.6 \times 10^{-3}$	$+3.79 \times 10^{-3}$	$+2.08 \times 10^{-3}$	$+12.4 \times 10^{-3}$	$+5.72 \times 10^{-3}$	$+1.15 \times 10^{-3}$
T_{seqp}	°C	-20	+5	+20	-20	+20	-20

The next spectroscopic parameter needing a temperature dependence is the relaxation time. For this purpose, the Debye relation was applied like in [4]:

$$\tau_p(ps) = \frac{48}{T_K} \exp \left[\frac{\Delta H_p}{R} \frac{1}{T_K} - \frac{\Delta S_p}{R} \right]. \quad (6)$$

where ΔH_p is the activation energy of the relaxation process, R is the universal gas constant ($8.314 \times 10^3 \text{ J K}^{-1} \text{ kmol}^{-1}$), and ΔS_p is the entropy of activation. T_K is the temperature in Kelvin. The relaxation time in (6) is given in picoseconds. The ratios $\Delta H_p/R$ and $\Delta S_p/R$, which are proportional to the activation energy and entropy of activation, respectively, were determined through fitting formula (6) to the measured values of $\tau_p(ps)$. The values of $\Delta H_p/R$ and $\Delta S_p/R$ thus determined are given in Table 1.

According to [4], we suggest for the conductivity, $\sigma_p(T)$ to have a linear dependence on the temperature, which is characteristic to ionic solutions:

$$\sigma_p(T) = \sigma_p(T_{s\sigma p}) + \beta_{\sigma p}(T - T_{s\sigma p}). \quad (7)$$

Here, $\beta_{\sigma p}$ is the derivative of conductivity with respect to temperature and $\sigma_p(T_{s\sigma p})$ is the value of conductivity at an arbitrary starting temperature, $T_{s\sigma p}$. Formula (8) was fitted to the conductivities, $\sigma_p(T)$, measured as a function of temperature to yield more TD GRMDM parameters of pine litter, which are shown in Table 1.

As a result of consideration conducted in this section, the TD GRMDM can be defined as an assembly of the following steps in the TD GRMDM algorithm procedure.

1. The temperature, T , has to be assigned; and a determination made as to whether the litter is frozen or thawed.

2. The values of the Debye parameters, namely the low and high frequency limits, relaxation time, and conductivity, for all types of soil water are to be calculated with the use of formulas (5), (6), (7) and the data in Table 1.

3. Once the values, $\varepsilon_{0p}(T)$, $\varepsilon_{\infty p}(T)$, $\tau_p(T)$, and $\sigma_p(T)$, and are known, the values of dielectric constant, $\varepsilon'_p(f, T)$, and loss factor $\varepsilon''_p(f, T)$ for all the types of soil water can be calculated as a function of frequency at a given temperature using formula (4).

4. The translation from the values $\varepsilon'_p(f, T)$ and $\varepsilon''_p(f, T)$ to the RI, n_p , and NAC, κ_p , regarding all the types of soil water, have to be made with the formulas

$$n_p(f, T) = \frac{1}{\sqrt{2}} \sqrt{\sqrt{\varepsilon'^2_p(f, T) + \varepsilon''^2_p(f, T)} + \varepsilon'_p(f, T)}, \quad (8)$$

$$\kappa_p(f, T) = \frac{1}{\sqrt{2}} \sqrt{\sqrt{\varepsilon'^2_p(f, T) + \varepsilon''^2_p(f, T)} - \varepsilon'_p(f, T)}.$$

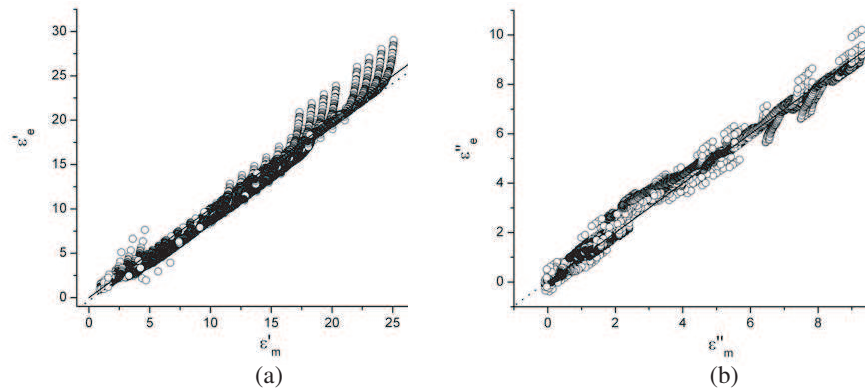


Figure 3: Correlation of the TD GRMDM predictions for (a) dielectric constant, ε'_{sp} , and (b) loss factor, ε''_{sp} , of moist litter with the measured ones, ε'_{sm} , ε''_{sm} . Dotted and solid lines represent bisectors and linear fits, respectively. Correlation coefficients are equal to: $R_{\varepsilon'} = 0.994$. $R_{\varepsilon''} = 0.996$. The standard deviations are: $SD_{\varepsilon'} = 0.669$. $SD_{\varepsilon''} = 0.201$. The data shown relate to the following 10 temperatures, $T = 25, 20, 15, 10, 5, 0, -5, -7, -15, -25^\circ\text{C}$, with the 6 values of gravimetric moisture at every temperature being equal to $m_g = 0.048, 0.159, 0.287, 0.416, 0.556, 0.68 \text{ g/g}$ and the frequencies ranging from 0.5 to 15 GHz, for a total of about 400 data points.

5. The gravimetric soil moisture, m_g , has to be assigned, and MGFBW, m_{g1} , and MGFUW, m_{g2} are determined with (2) and (3).

6. The dry soil bulk density, ρ_d , has to be assigned and formulas (1) applied to make calculations for the soil RI, $n_s(\rho_d, m_g, f, T)$, and NAC, $\kappa_s(\rho_d, m_g, f, T)$, using the litter water RIs and NACs calculated with (8).

7. Finally, the values $n_s(\rho_d, m_g, f, T)$ and $\kappa_s(\rho_d, m_g, f, T)$ are translated to the soil dielectric constant, $\epsilon'_s(\rho_d, m_g, f, T)$, and loss factor, $\epsilon''_s(\rho_d, m_g, f, T)$, with the formulas $\epsilon'_s = n_s^2 - \kappa_s^2$ and $\epsilon''_s = 2n_s\kappa_s$.

In the following section, the TD GRMDM for the shrub tundra soil will be evaluated in terms of prediction error by correlating the moist soil dielectric data predicted with those measured in the multidimensional domain of temperature, frequency, and moisture.

The error of the dielectric model with respect to the experimental data was determined using correlation analysis. In this case, the correlation coefficient (R) and standard deviation (sd) for the dielectric constant and loss factor were found to be: $R = 0.994$, $sd = 0.699$ and $R = 0.996$, $sd = 0.201$, respectively. The visual results of correlation analysis are presented in Fig. 3.

3. CONCLUSIONS

A physically substantiated temperature dependable spectroscopic dielectric model of pine litter, which is characteristic for the pine forests in Siberia, has been developed. The model covers the range of frequencies and temperatures stretching from 500 MHz to 15 GHz and from $+25^\circ\text{C}$ to -30°C , respectively. The intrinsic variables in this model, on which the complex dielectric constant depends, are the litter moisture, electromagnetic frequency, temperature, and density of dry litter sample. Among the parameters of the model are included the parameters of the linear temperature dependence for the reduced complex refractive index of sample solids. The latter are supplemented by the parameters related to the exponential temperature dependences of water contents in a litter sample, regarding bound, film, and capillary types of litter water. In addition, the number of parameters of the model includes some physical characteristics for each type of litter water. This group of parameters consists of the low-frequency and high frequency limits of dielectric constant and ohmic conductivity, temperature coefficient of volume expansion, activation energy, activation entropy and the temperature coefficient of the increment of ionic conductivity.

The error of the dielectric model with respect to the experimental data was determined using correlation analysis. In this case, the correlation coefficient (R) and standard deviation (sd) for the dielectric constant and dielectric loss factor were found to be: $R = 0.994$, $sd = 0.699$ and $R = 0.996$, $sd = 0.201$, respectively.

Next, we plan to develop the TD GRMDM for other types of litter.

ACKNOWLEDGMENT

This research was supported by the Siberian Branch of the Russian Academy of Sciences under Project II.10.1.6 and by the Russian Foundation for Basic Research and Centre National de la Recherche Scientifique (France) under Grant 09-05-91061.

REFERENCES

- Grant, J. P., A. A. Van de Griend, M. Schwank, and J.-P. Wigneron, "Observations and modeling of a pine forest floor at L-band," *IEEE Transactions on Geoscience and Remote Sensing*, Vol. 47, No. 7, Part 1, 2024–2034, 2009.
- Schwank, M., M. Guglielmetti, C. Matzler, and H. Fluhler, "Testing a new model for the L-band radiation of moist leaf litter," *IEEE Transactions on Geoscience and Remote Sensing*, Vol. 46, No. 7, 1982–1994, 2008.
- Demontoux, F., B. Le Crom, G. Ruffi, J.-P. Wigneron, J. P. Grant, and V. L. Mironov, "Electromagnetic characterization of soil-litter media — Application to the simulation of the microwave emissivity of the ground surface in forests," *European Physical Journal — Applied Physics*, Vol. 44, 303–315, 2008.
- Mironov, V. L., R. D. De Roo, and I. V. Savin, "Temperature-dependable microwave dielectric model for an arctic soil," *IEEE Transactions on Geoscience and Remote Sensing*, Vol. 48, No. 6, 2544–2556, June 2010.

SMOS First Results Successes and Issues: Towards Global Soil Moisture and Sea Salinity Maps

**Y. H. Kerr¹, P. Waldteufel², F. Cabot¹, P. Richaume¹, A. Mahmoodi³,
S. Delwart⁴, J.-P. Wigneron⁶, S. Mecklenburg⁴, N. Reul⁵, and J. Boutin⁷**

¹CESBIO (CNES CNRS UPS IRD), Toulouse, France

²IPSL, Verrières le Buisson, France

³Array Systems, Toronto, Canada

⁴ESA ESRIN, Frascati, Italy

⁵IFREMER, Brest, France

⁶INRA EPHYSE, Bordeaux, France

⁷LOCEAN, Paris, France

Abstract— SMOS, a L Band radiometer using aperture synthesis to achieve a good spatial resolution, was successfully launched on November 2, 2009. It was developed and made under the leadership of the European Space Agency (ESA) as an Earth Explorer Opportunity mission. It is a joint program with the Centre National d'Etudes Spatiales (CNES) in France and the Centro para el Desarrollo Tecnológico Industrial (CDTI) in Spain.

SMOS carries a single payload, an L band 2D interferometric, radiometer in the 1400–1427 MHz h protected band. This wavelength penetrates well through the vegetation and the atmosphere is almost transparent enabling to infer both soil moisture and vegetation water content over land and sea surface salinity over the oceans. SMOS achieves an unprecedented spatial resolution of 50 km at L-band maximum (43 km on average) with multi angular-dual polarized (or fully polarized) brightness temperatures over the globe and with a revisit time smaller than 3 days.

SMOS as been now acquiring data for over one year after the end of the commissioning phase. The data quality exceeds what was expected, showing very good sensitivity and stability. The data is however very much impaired by man made emission in the protected band, leading to degraded measurements in several areas including parts of Europe and of China. However, many different international teams are now addressing cal val activities in various parts of the world, with notably large field campaigns either on the long time scale or over specific targets to address the specific issues. These campaigns take place in various parts of the world, in different environments from the Antarctic plateau to the deserts, from rain forests to deep oceans. Actually SMOS is a new sensor making new measurements paving the way to new applications. However it also requires a very fine analysis of the data so as to validate both the approach and the retrieval quality, as well as for monitoring the evolution of the sensor. To achieve such goals it is very important to link efficiently ground measurement to satellite measurements through field campaigns and related airborne acquisitions as well as with other existing sensors.

This paper thus gives an overview of the science goals of the SMOS mission, a description of the main mission elements, and a foretaste of the first results including performances at brightness temperature as well as at geophysical parameters. It will include how the grond campaigns were elaborated to address the main cal Val activities accounting for SMOS specificities, in what context they were organized as well as the most significant results.

1. INTRODUCTION

The SMOS (Soil Moisture and Ocean Salinity) satellite was successfully launched in November 2009. This ESA led mission for Earth Observation is dedicated to provide soil moisture over continental surface (with an accuracy better than $0.04 \text{ m}^3/\text{m}^3$) and ocean salinity. These two geophysical features are important as they control the energy balance between the surface and the atmosphere. Their knowledge at a global scale is of interest for climatic and weather researches in particular in improving models forecasts.

2. OBJECTIVE

The purpose of this communication is to present the mission results after more than one year in orbit as well as some outstanding results already obtained. A special attention will be devoted to level 2 products and in particular to soil moisture.

3. METHODOLOGY

3.1. SMOS Data

The SMOS instrument measures the passive microwave emission of the Earth surface at a frequency of 1.4 GHz (L-band). It has been demonstrated that this frequency is well adapted to monitor surface soil moisture (first 5 cm). The instrument is an interferometer and provides brightness temperatures with an average resolution of 40 km, at several angle and dual polarizations (H and V). It means that a point at the surface is seen several times with different incidence angles. Data are acquired at two times in a day at 6 am and 18 pm (local time) and insure a complete coverage of the Earth surface in 3 days.

3.2. Modeled Brightness Temperature and Soil Moisture Retrievals

Modeling multi-angular brightness temperatures is not straightforward. The radiative model transfer model L-MEB (L-band Microwave Emission) is used over land. It is based on semi-empirical relationships, adapted to different type of surface. It computes a dielectric constant leading to surface emissivity. Surface features (roughness, vegetation) are also considered in the models. However, considering SMOS spatial resolution a wide area is seen by the instrument with strong heterogeneity. The L2 soil moisture retrieval scheme takes this into account. For each node, a wide area is defined (~ 123 km) referred to as a working area. A complete knowledge of the surface is necessary (soil texture, surface classification of the vegetation). The surface types are gathered in 10 main classes: Nominal surface, Forest, Wetlands, Pure Water, Saline Water, Barren ground, Urban, Ice, Frozen soil, Snow. The soil moisture retrieval is run over the nominal surface, which is a scene covered by low vegetation. Forest areas are also of interest if they are not too opaque (in terms of radiative penetration).

For each of these classes a decision tree determines the dielectric model to be used and its configuration (parameterization) according to the surface. For the nominal and forest, Dobson's law is used to get a dielectric constant.

Brightness temperatures are computed for every class composing a working area. A weighted function is applied for the incidence angle and the antenna beam. Once the brightness temperature is computed for the entire working area, the minimizing process starts. Different cases are then possible. The retrieval process succeeds a soil moisture is derived along with vegetation optical thickness, and effective surface temperature. If no soil moisture is derived (not attempted or process failed) a dielectric constant is still derived from a simplified modeled (the cardioid model).

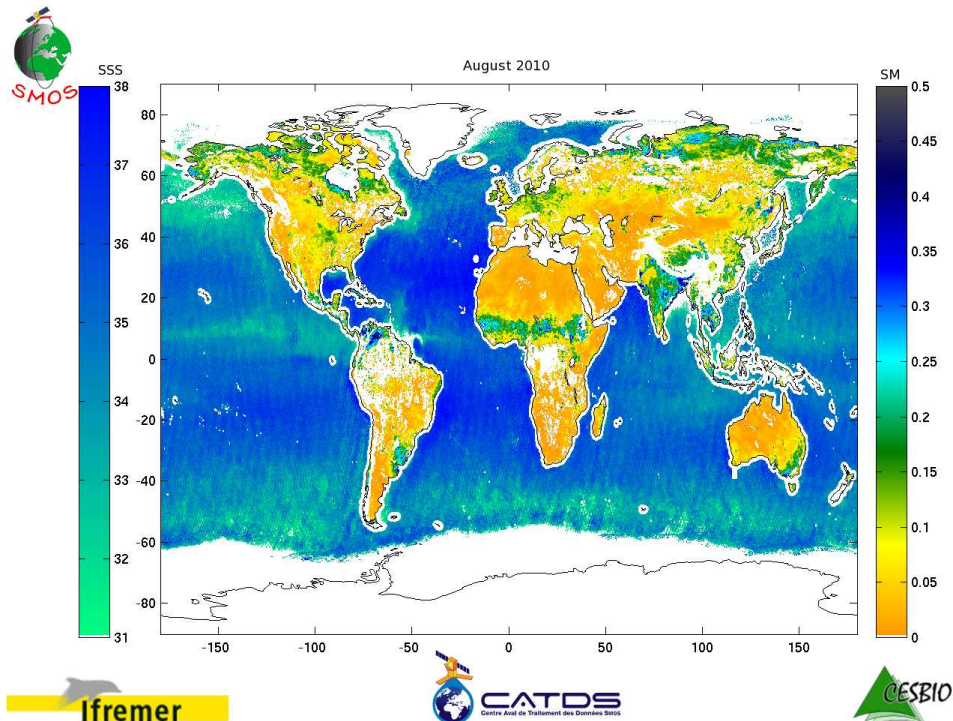


Figure 1: Global map of soil moisture and sea surface salinity obtained from SMOS for August 2010.

3.3. Sea Surface Salinity and Sea Ice

SMOS data enabled very quickly to infer Sea surface salinity fields. As salinity retrieval is quite challenging, retrieving it enable to assess very finely the characteristics of the complete system

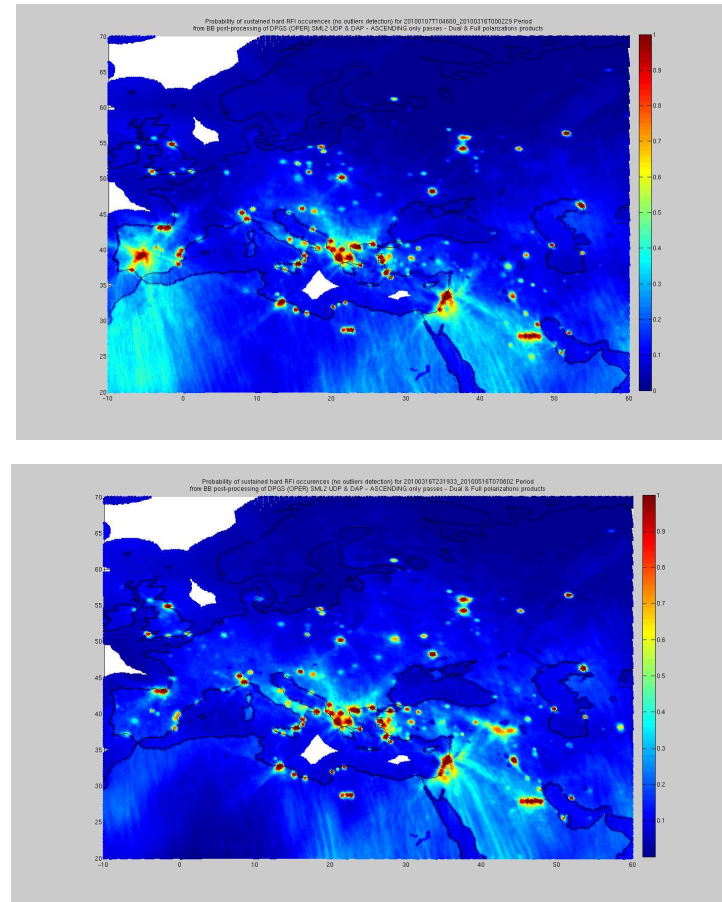


Figure 2: Probability of RFI over Europe for the first 3 months of SMOS life (top panel) and the following summer (bottom panel).

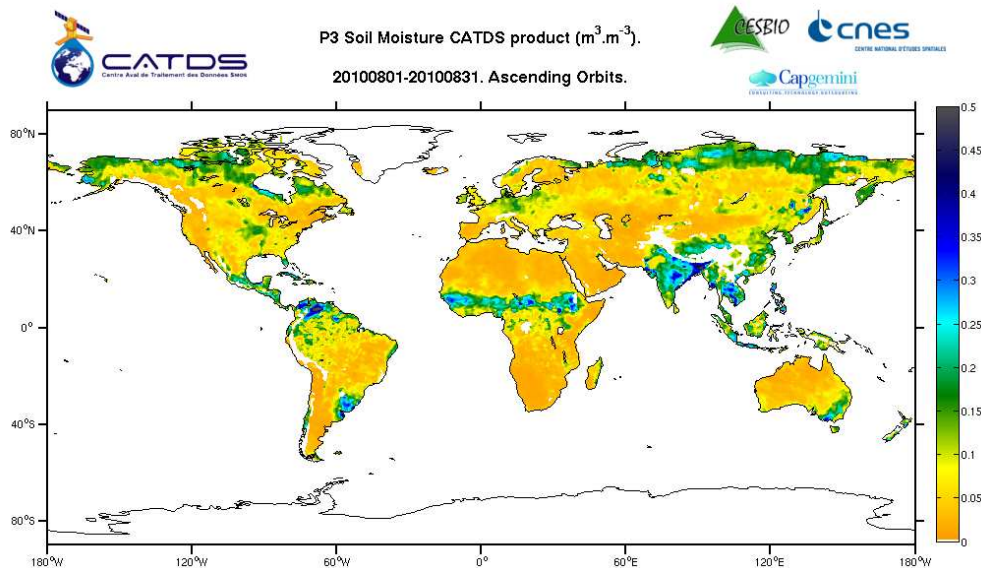


Figure 3: Monthly SMOS soil moisture retrieval.

in terms of stability, drift etc. Some anomalies such as the ascending descending temperature differences, temporal drifts or land sea contamination were used to infer issues and improve data quality.

3.4. RFI

SMOS is affected by RFI. Careful analysis of the perturbations enabled to start legal activities against unlawful emitters as well as finding methods to quantify them. Several approaches were tested and implemented in the algorithms to flag such data. In parallel some actions were taken to reduce the number of sources and this is particular obvious over Europe where over 100 sources in 19 countries were switched off as shown in Figure 2.

4. CONCLUSION AND PERSPECTIVES

This presentation shows in detail the first SMOS in flight results. The retrieval schemes have been developed to reach science requirements, that is to derive the surface soil moisture over continental surface with an accuracy better than $0.04\text{m}^3/\text{m}^3$. Over the ocean the goals are not yet satisfied but results are already getting close to the requirements.

The first results obtained as of today are thus very encouraging as can be seen on Figure 3. It is expected to have an even more significant yield in July.

During the presentation we will show SMOS results and present details analysis of retrieval quality together with main issues encountered.

REFERENCES

1. Kerr, Y. H., "Soil moisture from space: Where are we?," *Hydrogeology Journal*, Vol. 15, 117–120, 2007.
2. Kerr, Y. H., P. Waldteufel, J. P. Wigneron, J. Font, and M. Berger, "Soil moisture retrieval from space: The Soil Moisture and Ocean Salinity (SMOS) mission," *IEEE T. Geosci. Remote*, Vol. 39, No. 8, 1729–1735, 2001.
3. Kerr, Y., P. Waldteufel, P. Richaume, J. P. Wigneron, P. Ferrazzoli, and R. Gurney, "SMOS level 2 processor for soil moisture — Algorithm Theoretical Based Document (ATBD)," *CBSA*, Technical Note SO-TN-ESL-SM-GS-001, No. 2, 212, 2006.
4. Wigneron, J.-P., Y. Kerr, P. Waldteufel, K. Saleh, M.-J. Escorihuela, P. Richaume, P. Ferrazzoli, P. de Rosnay, R. Gurney, J.-C. Calvet, J. P. Grant, M. Guglielmetti, B. Hornbuckle, C. Mätzler, T. Pellarin, and M. Schwank, "L-band Microwave Emission of the Biosphere (L-MEB) model: Description and calibration against experimental data sets over crop fields," *Rem. Sens. Environ.*, Vol. 107, 639–655, 2007.
5. Hornbuckle, B. K., A. W. England, R. D. De Roo, M. A. Fischman, and D. L. Boprie, "Vegetation canopy anisotropy at 1.4 GHz," *IEEE Transactions on Geoscience and Remote Sensing*, Vol. 41, No. 10, Part 1, 2211–2223, 2003.

Method of Moment Simulation of Noise Correlation in Antenna Arrays

Choon Hock Niow¹, Hon Tat Hui¹, and Yantao Yu²

¹Department of Electrical and Computer Engineering, National University of Singapore, Singapore

²College of Communication Engineering, Chongqing University, Chongqing, China

Abstract— A new noise modeling method is proposed to calculate the correlated noise covariance matrix in antenna arrays using Method of Moments (MoM). This noise modeling method models the antenna array performing under a noisy environment in a more accurate manner. By obtaining the correlated noise covariance matrix from the proposed noise modeling method, compensation can be carried out more accurately to achieve better direction finding in a noisy environment.

1. INTRODUCTION

Multiple Signal Classification (MUSIC) is a high resolution, eigenstructure-based direction finding algorithm that is used in antenna arrays to determine the direction-of-arrival (DOA) of a number of wavefronts [1]. The performance of the MUSIC algorithm is dependent on the accuracy of the signal and noise subspaces which are affected by the presence of mutual coupling in antenna arrays. Several methods such as mutual coupling compensation [2, 3] and spatial smoothing [4] are developed to improve the MUSIC algorithm performance. However, these methods assume uncorrelated noise which is valid only for antenna arrays with sufficiently large antenna spacing. The MUSIC algorithm performance deteriorates as the antenna spacing reduces due to the presence of noise coupling [5] caused by mutual coupling effects which produces correlated noise [6].

In this paper, we proposed a new noise modeling method using MoM to obtain the correlated noise covariance matrix. By incorporating the correlated noise covariance matrix into the MUSIC algorithm, accurate direction finding can be achieved even under low signal-to-noise ratio (SNR).

2. NOISE MODELING METHOD

Consider the signal model where $\mathbf{X}(t)$ is the complex voltage received at time t . Then

$$\mathbf{X}(t) = \mathbf{S}(t) + \mathbf{N}_T \mathbf{N}(t) \quad (1)$$

where $\mathbf{S}(t)$ is the complex voltage across the antenna terminals due to the incoming signals as well as mutual coupling effects from other antenna elements [2], and $\mathbf{N}(t)$ is the *uncoupled* complex voltage due to the Gaussian noise. This model is inconsistent because only signal is affected by mutual coupling. In reality, both signal and noise are affected by mutual coupling. To make the model consistent and realistic, the mutual noise matrix \mathbf{N}_T is added to make $\mathbf{N}(t)$ coupled due to mutual coupling effects. $\mathbf{N}_T \mathbf{N}(t)$ is the *coupled* complex voltage due to the Gaussian noise and mutual coupling effects.

To find the mutual noise matrix \mathbf{N}_T , consider s plane waves with equal amplitude and phase impinge evenly on n -dipole array at directions θ_k ($k = 1, 2, \dots, s$) [7]. The dipoles are $\lambda/2$ in length and spaced d apart, and λ is the wavelength of the incident wave. Each dipole is divided into 63 segments of length $\lambda/125$ [5]. The diameter of each dipole is $\lambda/500$ [5]. Each dipole is terminated with terminal load Z_L . Using FEKO, the plane waves are impinged t times to obtain the $s \times t$ matrix \mathbf{V}_i at the i -th dipole. Next, \mathbf{V}_i is multiplied by $t \times s$ matrix \mathbf{G} to obtain the $s \times s$ noise matrix \mathbf{N}_i at i -th dipole. The matrix \mathbf{G} is spatially uncorrelated along s columns and temporally distributed zero mean, circular complex white Gaussian noise along t rows. All the noise matrices have the same matrix \mathbf{G} . The noise matrix \mathbf{N}_i at i -th dipole can be described in the matrix form:

$$\mathbf{N}_i = \mathbf{V}_i \mathbf{G} \quad (2)$$

where

$$\mathbf{V}_i = \begin{bmatrix} \mathbf{V}_{11}^i & \dots & \mathbf{V}_{1t}^i \\ \vdots & \ddots & \vdots \\ \mathbf{V}_{s1}^i & \dots & \mathbf{V}_{st}^i \end{bmatrix} \quad (3)$$

$$\mathbf{G} = \begin{bmatrix} \mathbf{G}_{11} & \dots & \mathbf{G}_{1s} \\ \vdots & \ddots & \vdots \\ \mathbf{G}_{t1} & \dots & \mathbf{G}_{ts} \end{bmatrix} \quad (4)$$

The normalized noise covariance matrix $\mathbf{N}_T \mathbf{N}_T^H$ can be easily obtained by finding the covariance of all the noise matrices \mathbf{N}_i ($i = 1, 2, \dots, n$) as follows,

$$\mathbf{N}_T \mathbf{N}_T^H = \text{norm} \begin{bmatrix} \text{cov}(\mathbf{N}_1, \mathbf{N}_1) & \dots & \text{cov}(\mathbf{N}_1, \mathbf{N}_n) \\ \vdots & \ddots & \vdots \\ \text{cov}(\mathbf{N}_n, \mathbf{N}_1) & \dots & \text{cov}(\mathbf{N}_n, \mathbf{N}_n) \end{bmatrix} \quad (5)$$

The mutual noise matrix \mathbf{N}_T is obtained by taking the square root of $\mathbf{N}_T \mathbf{N}_T^H$ as follows,

$$\mathbf{N}_T = \sqrt{\mathbf{N}_T \mathbf{N}_T^H} \quad (6)$$

3. CORRELATED NOISE COVARIANCE MATRIX

Spatial smoothing is required if the signals are coherent [4]. Hence, the n -dipole array can be divided into overlapping arrays with p dipoles in each subarray ($p < n$). The number of subarrays required is k where $k = n - p + 1$. To detect q coherent signals, the array is divided into at least q arrays. The covariance matrix of $\mathbf{X}(t)$ can be written as:

$$\mathbf{R} = E\{\mathbf{X}(t)\mathbf{X}^H(t)\} = E\{\mathbf{S}(t)\mathbf{S}^H(t)\} + E\{\mathbf{N}_T \mathbf{N}(t) \mathbf{N}^H(t) \mathbf{N}_T^H\} = \mathbf{SS}^H + \sigma^2 \mathbf{N}_T \mathbf{N}_T^H \quad (7)$$

where σ^2 is the noise power. The term $\sigma^2 \mathbf{N}_T \mathbf{N}_T^H$ is the correlated noise covariance matrix which is different from the uncorrelated noise covariance matrix $\sigma^2 \mathbf{I}$ mentioned in [1–4].

To counteract the mutual coupling effects, (7) can be written as:

$$\mathbf{R}' = \mathbf{Z}_T \mathbf{R} \mathbf{Z}_T^H = \mathbf{U} \mathbf{U}^H + \sigma^2 \mathbf{Z}_T \mathbf{N}_T \mathbf{N}_T^H \mathbf{Z}_T^H \quad (8)$$

where \mathbf{U} is the uncoupled voltage due to the incoming signals alone and \mathbf{Z}_T is the receiving mutual impedance matrix [2]. Both the noise and signal subspaces are compensated by \mathbf{Z}_T . This is different from [3] where only the signal subspace is compensated. To account for k subarrays, the average covariance matrix can be written as:

$$\overline{\mathbf{R}'} = \frac{1}{k} \sum_{i=1}^k \mathbf{R}'_i \quad (9)$$

The generalized eigenvalues and eigenvectors of $\overline{\mathbf{R}'}$ becomes:

$$\overline{\mathbf{R}'} \mathbf{V}_k = \lambda_k \mathbf{Z}_T \mathbf{N}_T \mathbf{N}_T^H \mathbf{Z}_T^H \mathbf{V}_k \quad (10)$$

where λ_k and \mathbf{V}_k are the generalized eigenvalues and eigenvectors of $\overline{\mathbf{R}'}$ respectively. Using the eigenstructures, the MUSIC search function can be written as:

$$P(\varphi) = \frac{\mathbf{a}^H(\varphi) \mathbf{a}(\varphi)}{\mathbf{a}^H(\varphi) \mathbf{W} \mathbf{W}^H \mathbf{a}(\varphi)} \quad (11)$$

where \mathbf{W} is $p \times (p - q)$ matrix whose column vectors are the eigenvectors \mathbf{V}_k corresponding to the noise subspace and $\mathbf{a}(\varphi)$ is the search vector of the dipole array.

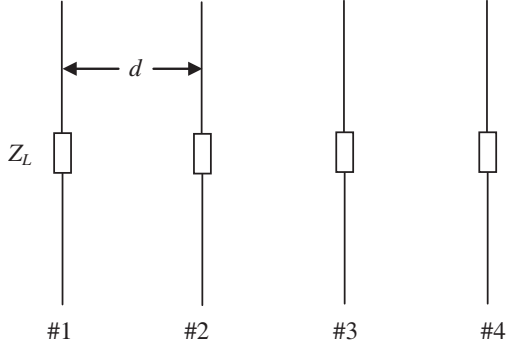
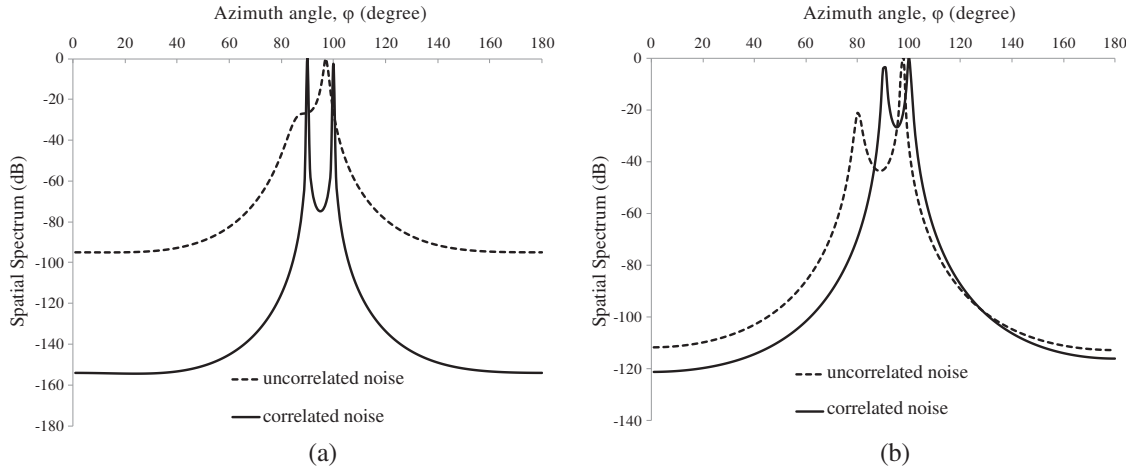


Figure 1: A four-dipole array.

Figure 2: (a) MUSIC performance at $d = 0.5\lambda$ and DOA = 90°, 100° under SNR = 3 dB. (b) MUSIC performance at $d = 0.3\lambda$ and DOA = 90°, 100° under SNR = 3 dB.

4. SIMULATION EXAMPLES

To demonstrate the effectiveness of the correlated noise covariance matrix in the MUSIC algorithm, a 4-dipole array is used, as shown in Fig. 1. Each antenna is terminated with a load impedance $Z_L = 50 \Omega$. Two incoming coherent signals at $\varphi = 90^\circ$ and 100° are simulated using (1). A comparison is made between the conventional MUSIC algorithm in [3] and the improved MUSIC algorithm in (10) using the correlated noise covariance matrix at $d = 0.3\lambda$ and 0.5λ under SNR of 3 dB.

From Fig. 2, it is clear that the conventional MUSIC algorithm fails to work when the correlated noise covariance matrix is used. However, the improved MUSIC algorithm is able to resolve the two signals at 90° and 100° even at close element separation and low SNR.

5. CONCLUSIONS

It is possible to obtain the correlated noise covariance matrix accurately using the proposed noise modeling method. The improved MUSIC algorithm is also able to compensate both the signal and noise subspaces accurately such that the antenna array is able to resolve the incoming signals even at low SNR and close antenna spacing.

ACKNOWLEDGMENT

This work was supported in part by the US ONR research project under the project number PR No. 09PR03332-01.

REFERENCES

1. Schmidt, R. O., "Multiple emitter location and signal parameter estimation," *IEEE Trans. Antennas Propagat.*, Vol. 34, No. 3, 276–280, 1986.
2. Hui, H. T., "Improved compensation for the mutual coupling effect in a dipole array for direction finding," *IEEE Trans. Antennas Propagat.*, Vol. 51, No. 9, 2498–2503, 2003.

3. Yeh, C. C., M. L. Leou, and D. R. Ucci, "Bearing estimation with mutual coupling present," *IEEE Trans. Antennas Propagat.*, Vol. 37, No. 10, 1332–1335, 1989.
4. Shan, T. J., M. Wax, and T. Kailath, "On spatial smoothing for estimation of coherent signals," *IEEE Trans. Acoust. Speech Signal Processing*, Vol. 33, No. 4, 806–811, 1985.
5. Kisliansky, A., R. Shavit, and J. Tabrikian, "Direction of arrival estimation in the presence of noise coupling in antenna arrays," *IEEE Trans. Antennas Propagat.*, Vol. 55, No. 7, 1940–1947, 2007.
6. Torrieri, D. and K. Bakhru, "The effects of nonuniform and correlated noise on superresolution algorithms," *IEEE Trans. Antennas Propagat.*, Vol. 45, No. 8, 1214–1218, 1997.
7. Qi, C., Z. Chen, Y. Wang, and Y. Zhang, "DOA estimation for coherent sources in unknown nonuniform noise field," *IEEE Trans. Aerosp. Electron. Syst.*, Vol. 43, No. 3, 1195–1204, 2007.

A Compact Printed Array with Increased Port Isolation

Yantao Yu

Chongqing University, China

Abstract— Strong mutual coupling between closely spaced elements in compact antenna arrays may cause significant system performance degradation, such as reduction in gain and signal-to-noise ratio. In this paper, an efficient technique to increase the isolation between the antenna ports is proposed. It utilizes the electromagnetic band-gap structure to reduce the mutual coupling between antenna elements. Examples of printed monopole arrays are designed. Computational results are presented.

1. INTRODUCTION

Antenna arrays with multiple ports are widely used in modern wireless communication systems, such as MIMO system, direction finding, etc. In mobile applications, the small physical sizes of the platform restrict the volume for the antennas [1] and thus the use of compact arrays is required. In such cases, strong mutual coupling between closely spaced elements in compact antenna arrays may cause significant system performance degradation [2, 3], such as reduction in gain and signal-to-noise ratio (SNR). Therefore, it is important to find ways to removed or reduced the mutual coupling effect from antenna arrays.

The effect of mutual coupling has been studied intensively [4, 5] in the past years and many mutual coupling compensation methods have been suggested [6–13]. In [6, 7], decoupling is achieved by changing the geometry of the antenna. The relation of the isolation and the array configuration of two nearby antennas in a cellular handset was studied in [8]. Signal processing techniques using different coupling matrices [9, 10] may be applied to the received signal vectors from adaptive arrays to counter the effects of mutual coupling. In addition, there are also methods using passive and lossless decoupling and matching networks to transform coupled antenna ports into independent and matched ports. Various implementations of decoupling networks have been suggested, for example, the design of decoupling network for two-element arrays can be found in [11, 12] and for three-element arrays in [13]. In recent years, another important approach proposed is to use electromagnetic bandgap (EBG) structures to suppress the surface wave in microstrip substrates. The mushroom-like EBG structure in [14] has been implemented to reduce the mutual coupling effect between elements of a microstrip array. Some nonperiodic EBG structures, known as defected ground structures (DGS) [15, 16], are also used to produce the band rejection characteristics. In this paper, a Chinese character Wang-shaped DGS structure is proposed. The design is applied to a printed monopole array to reduce the mutual coupling effect between array elements.

2. THE DEFECTED GROUND STRUCTURE

The proposed Wang-shaped defected ground structure is shown in Figure 1. The structure is etched on the ground plane of a dielectric substrate with a dielectric constant of ϵ_r and a thickness of h . The dimensions of the structure can be optimized in order to obtain a good band rejection performance at design frequencies. This Wang-shaped structure has a total dimension of 19 mm × 4.8 mm. Figure 2 shows the simulated electrical performance of the proposed DGS on a FR4 substrate with $\epsilon_r = 4.4$ and $h = 1.6$ mm.

3. DESIGN OF PRINTED MONPOLE ARRAY

A monopole array with two elements is printed on the same FR4 substrate, as shown in Figure 3. Each monopole operates at 2.4 GHz and has a width of 1 mm and a length of 22.5 mm. The center-to-center distance of the two printed monopoles is 15 mm, which is about 0.12λ . The substrate has a dimension of 35 mm × 45 mm. Figure 4 shows the simulated S -parameters of the two-monopole array. It can be seen that the mutual coupling between the two monopoles is very strong in the operating frequency band. Then, the DGS designed in Section 2 is used to reduce the mutual coupling of the array.

As shown in Figure 5, the proposed defected ground structure is etched on the ground plane of the monopole array. Figure 6 shows the coupling coefficient, S_{12} , of the array with DGS, compared with the case without DGS. It can be seen that the mutual coupling effect has been significantly reduced across the operating band.

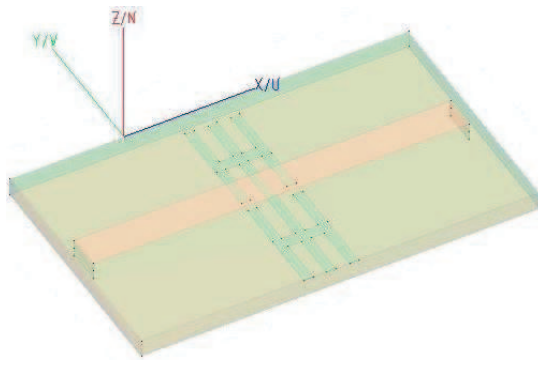


Figure 1: The Wang-shaped defected ground structure.

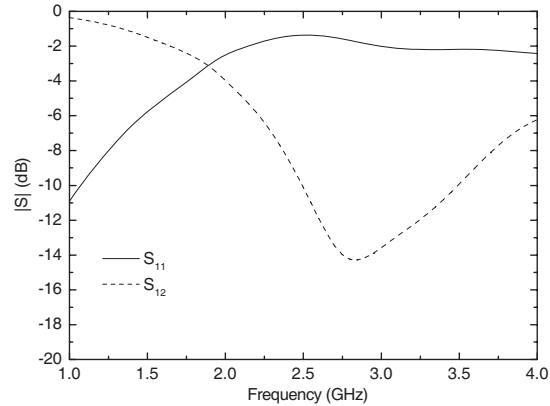


Figure 2: Simulated S -parameters of the microstrip line with the proposed DGS.

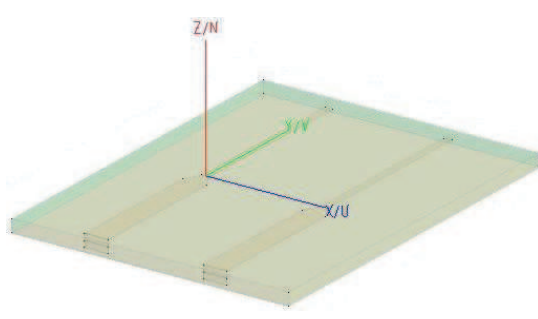


Figure 3: The two-element monopole array printed on FR4 substrate.

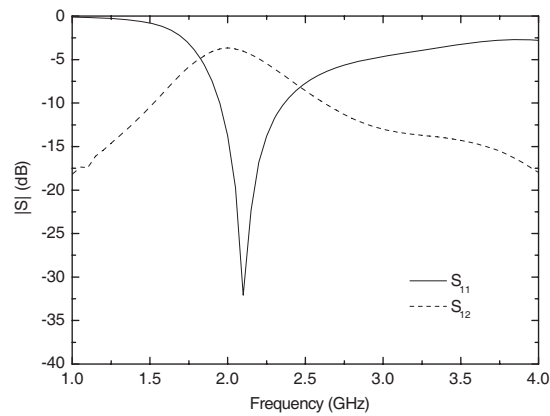


Figure 4: Simulated S -parameters of the two monopole array.

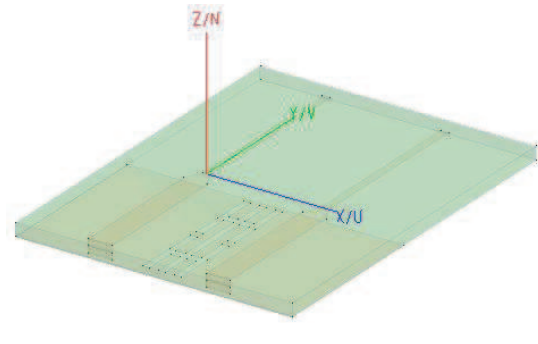


Figure 5: The printed monopole array with DGS etched on the ground plane.

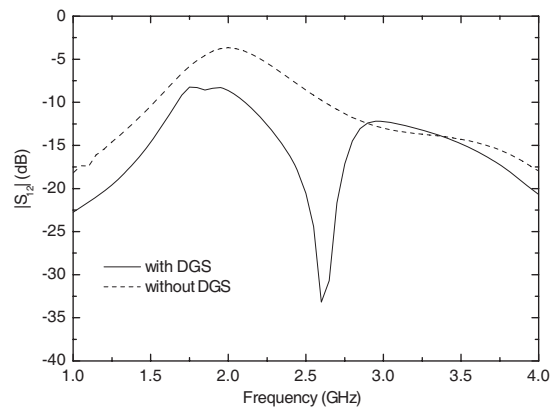


Figure 6: The coupling coefficient of the printed monopole array with and without DGS.

4. CONCLUSIONS

Mutual coupling in compact antenna arrays causes significant system performance degradation. It is very important to remove or reduce the mutual coupling effect. In this paper, the method using electromagnetic band-gap structure to increase the isolation between the antenna ports is studied. A Wang-shaped defected ground structure is proposed to achieve band rejection at design frequencies. This structure is used in a two-element printed monopole array and simulation result shows that the mutual coupling effect of this compact array is significantly reduced.

ACKNOWLEDGEMENT

This work was supported by the Fundamental Research Funds for the Central Universities (Grant No. 0214005300001).

REFERENCES

1. Gupta, I. J. and A. A. Ksieński, "Effect of mutual coupling on the performance of adaptive arrays," *IEEE Trans. Antennas Propaga.*, Vol. 31, No. 5, 785–791, 1983.
2. Friel, E. M. and K. M. Pasala, "Effects of mutual coupling on the performance of STAP antenna arrays," *IEEE Trans. Aerosp. Electron. Syst.*, Vol. 36, No. 2, 518–527, 2000.
3. Yong, S. K. and J. S. Thompson, "Effect of channel conditions and antenna parameters on the performance analysis of compact antenna arrays," *IET Proc. Communications*, Vol. 151, No. 4, 394–400, 2004.
4. Akyel, C., S. I. Babic, and M.-M. Mahmoudi, "Mutual inductance calculation for non-coaxial circular air coils with parallel axes," *Progress In Electromagnetics Research*, Vol. 91, 287–301, 2009.
5. Ravaud, R., G. Lemarquand, V. Lemarquand, S. I. Babic, and C. Akyel, "Mutual inductance and force exerted between thick coils," *Progress In Electromagnetics Research*, Vol. 102, 367–380, 2010.
6. Esser, D. and H. J. Chaloupka, "Design approach for a class of compact multiport antennas," *Proc. IEEE Int. Symp. Microwave Antennas Propaga. EMC Tech. for Wireless Comm.*, Vol. 1, 144–147, Beijing, 2005.
7. Yousefzadeh, N., C. Ghobadi, and M. Kamyab, "Consideration of mutual coupling in a microstrip patch array using fractal elements," *Progress In Electromagnetics Research*, Vol. 66, 41–49, 2006.
8. Li, Z. and Y. R. Samii, "Optimization of PIFA-IFA combination in handset antenna design," *IEEE Trans. Antennas Propaga.*, Vol. 53, No. 5, 1770–1778, 2005.
9. Steyskal, H. and J. S. Herd, "Mutual coupling compensation in small array antennas," *IEEE Trans. Antennas Propaga.*, Vol. 38, No. 12, 1971–1975, 1990.
10. Segovia-Vargas, D., R. Martin-Cuerdo, and M. Sierra-Perez, "Mutual coupling effects correction in microstrip arrays for direction-of-arrival (DOA) estimation," *IEE Proc. Microwaves Antennas Propaga.*, Vol. 149, No. 2, 113–118, 2002.
11. Diallo, A., C. Luxey, P. Le Thuc, R. Staraj, and G. Kossiavas, "Study and reduction of the mutual coupling between two mobile phone PIFAs operating in the DCS1800 and UMTS bands," *IEEE Trans. Antennas Propaga.*, Vol. 54, No. 11, 3063–3074, 2006.
12. Dossche, S., S. Blanch, and J. Romeu, "Optimum antenna matching to minimize signals correlation on a two-port antenna diversity system," *Electronics Letters*, Vol. 40, No. 19, 1164–1165, 2004.
13. Hong, T. and Y. Yu, "A compact monopole array with increased port isolation," *Journal of Electromagnetic Waves and Applications*, Vol. 25, Nos. 8–9, 1213–1220, 2011.
14. Yang, F. and Y. Rahmat-Samii, "Microstrip antennas integrated with electromagnetic bandgap (EBG) structures: A low mutual coupling design for array applications," *IEEE Trans. Antennas Propaga.*, Vol. 51, No. 10, 2936–2946, 2003.
15. Mandal, M. K. and S. Sanyal, "A novel defected ground structure for planar circuits," *IEEE Microw. Wirel. Compon. Lett.*, Vol. 16, No. 2, 93–95, 2006.
16. Kim, C.-S., J.-S. Lim, S. Nam, K.-Y. Kang, and D. Ahn, "Equivalent circuit modeling of spiral defected ground structure for microstrip line," *Electronics Letters*, Vol. 38, 1109–1111, 2002.

Study on the Decoupling of Stacked Phased Array Coils for Magnetic Resonance Imaging

Dandan Liang¹, Hon Tat Hui¹, Tat Soon Yeo¹, and Yantao Yu²

¹Department of Electrical & Computer Engineering, National University of Singapore, Singapore

²College of Communication Engineering, Chongqing University, Chongqing 400044, China

Abstract— It has been suggested that multi-coil solenoids, which consist of an array of stacked surface coils, can be used in magnetic resonance imaging (MRI) applications to increase the signal-to-noise ratio (SNR) and consequently improve the image quality. However, due to the physical stacked design, mutual coupling effect occurs and distorts the array signals. A new compensation method has been proposed to remove the mutual coupling effect. It employs a set of newly defined mutual impedances to establish a compensation matrix through which the decoupled signals can be obtained. In this paper, the design of stacked phased array coils for MRI is described in details, and the decoupling method between the coil elements is clearly explained. Moreover, workbench experiments were conducted in a mimic MRI system with a cylindrical phantom acting for the loading purpose. A two-element stacked phased coil array has been designed as the receive-only coils under the radiation of a source coil placed above the cylindrical phantom. With the scattering parameters measured by a network analyzer, the new mutual impedances and compensation matrix were determined, and thereby decoupled signals were obtained. To demonstrate the robustness of the decoupling method, measurements were performed over a power deviation from -10 dBm to 10 dBm , a frequency deviation from 84.9 MHz to 85.1 MHz , and a deviation of the distance between the two coil elements from 0.5 cm to 3 cm . In each case, the derived decoupled signals were then compared with the ideally measured coupling free signals. From the comparison results, it is concluded that the new decoupling method can decouple the coupled signals effectively. Because of the robustness and flexibility in all the different experimental scenarios, the stacked phased array coil design together with the new decoupling method is proved to have a potential application in MRI.

1. INTRODUCTION

Magnetic resonance imaging (MRI) is a widely used medical imaging technique to visualize the internal structures of human body. It makes use of the property of nuclear magnetic resonance (NMR) to image nuclei of atoms inside the body. The basic physical effect at work in NMR is the interaction between nuclei with a nonzero magnetic moment and an external uniform static magnetic field. The NMR phenomenon is observed when a system of nuclei in a static magnetic field experiences a perturbation by an oscillating magnetic field at a specific frequency. Since the discovery of nuclear magnetic resonance (NMR), it has found a number of applications in the fields of biology, engineering, medical imaging and material science.

In MRI system, radio frequency (RF) coils constitute the key hardware component for the transmission of RF signal pulses to the tissues being interrogated and provide the means of collecting returning MR signals information to construct the image [1]. One of the vital factors that determine the image quality is the signal-to-noise ratio (SNR), which is influenced by the choice of receiver coil positioned within the imaging volume. The problem of increasing SNR has attracted great attention from academic and clinical research [2, 3], which is also the motivation for the design of stacked phased array surface coils introduced in this paper.

2. DESIGN OF STACKED SURFACE COILS AND THE DECOUPLING METHOD

The signal strength of an RF coil can be increased by putting n turns for the coil, thereby increasing the magnetic field of the coil by a factor of n . Even though this may increase the coil resistance by a factor of n , the noise is only proportional to its resistance by \sqrt{R} . Therefore, the SNR will be increased by \sqrt{n} . However, this method is deemed impractical due to phase cancellation. The coils have many turns in them and the length of wire is a wavelength at the frequency of interest. As the current travels down the coil, the current will suffer the progressive phase shift of 360° . Thus the contributions to the field at the center of the coil will have all phases, and the resultant field will be rather small. From the principle of reciprocity, it makes a very poor receiving coil [4]. While a surface coil provides high SNR reception over a small geometric area immediately adjacent to the

coil, phased array surface coils can extend the high SNR characteristic of a single surface coil to a larger field-of-view without phase cancellation problem, and therefore will possibly work as a good receiver in MRI system.

We introduce an array of stacked surface coils which consists of a number of surface coils positioned one over another. The configuration of stacked surface coils is a mimic of the n -turn coil to achieve an increase of \sqrt{n} in SNR for every random number of consecutive stacked coils without the phase cancellation problem. The array which consists of two square surface coils is shown in Fig. 1. The only problem of this stacked surface coil configuration working as the receiver in MRI system is the mutual coupling effect that exists between the stacked coils, but it can be minimized by the new measured mutual impedance and compensation matrix [5, 6], thus obtaining decoupled signals.

Unlike the conventional mutual impedance which is defined with the requirement that one of the elements works in the transmitting mode, the new mutual impedance is defined when all the antenna elements are in receiving mode, being excited by external source, which is really the case for a receiving array. Hence, it is possible that the new mutual impedance can measure the coupling effect more accurately. To explain the definition of new mutual impedance, we simply consider an array of two parallel dipoles in receiving mode, where dipole #2 is excited by the incident field coming from horizontal direction so that a current distribution is induced on it. The value of the current distribution at the terminal load is indicated as I_2 . This induced current distribution then re-radiates and induce a current distribution on dipole #1, and produce voltage V_{12} across the load. The new mutual impedance which depends on the direction of the incident field is then defined as

$$Z_t^{12} = \frac{V_{12}}{I_2} \quad (1)$$

and Z_t^{21} is defined in the same way. With the calculated new mutual impedance Z_t^{12} and Z_t^{21} , the decoupled signal can be obtained using the following compensation method

$$\begin{bmatrix} U_1 \\ U_2 \end{bmatrix} = \begin{bmatrix} 1 & \frac{Z_t^{12}}{Z_L} \\ \frac{Z_t^{21}}{Z_L} & 1 \end{bmatrix} \begin{bmatrix} V_1 \\ V_2 \end{bmatrix} \quad (2)$$

where U_1 , U_2 are the resultant decoupled signals, and V_1 , V_2 are the measured coupled signals.

3. EXPERIMENTAL MEASUREMENTS AND CALCULATED RESULTS

3.1. Experimental Setup

As shown in Fig. 2, the experimental setup is a simulated MRI system, where the source coil is supported by four supporting stands, and a two-element array of stacked phased surface coils works as the receiver coil. The resonance frequency in a 2 Tesla MRI system, which is the Lamour frequency, is calculated as $f_0 = \gamma B_0 = 85.16$ MHz, where γ represents the Gyro-magnetic ratio

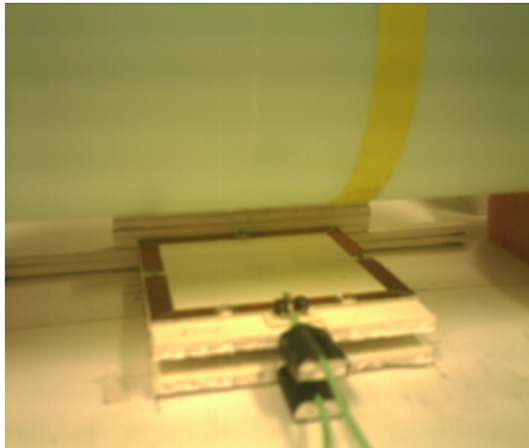


Figure 1: The configuration of the array of two stacked square surface coils.

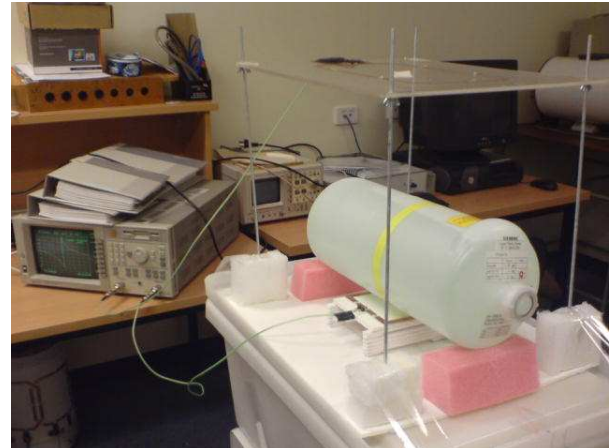


Figure 2: Experimental setup with a loading condition.

and is 42.58 MHz/T for hydrogen atom, so the source coil was tuned to operate at 85 MHz when doing the experiment. A cylindrical phantom that consists of a solution mixture with the dielectric properties of $\epsilon = 48.6$, $\sigma = 0.6 \text{ S/m}$, which are very close to those of human brain tissues, is placed above the stacked phased array coils for loading purpose. The network analyzer in the setup is used to measure the scattering parameter S_{21} , as it can be converted into voltage [7] by

$$S_{21} = \frac{\beta}{\alpha} \quad (3)$$

where α is the square root of the power output from the transmitting port of the network analyzer, which can be set and β is given by

$$\beta = \frac{V}{\sqrt{Z_L}} \quad (4)$$

where V is the voltage received by the coil and Z_L is the system impedance of 50Ω .

3.2. Measurement Procedure

Three experimental scenarios were conducted over the power variation from -10 dBm to 10 dBm , the frequency variation from 84.9 MHz to 85.1 MHz, and the variation of the distance between the two stacked surface coils from 0.5 cm to 3 cm. For each scenario, the following four measurements for scattering parameter S_{21} were taken to determine the new mutual impedances.

- (1) The receiving port of the analyzer is connected to coil 1 with coil 2 connected to a 50Ω load. The measured S -parameter S_{21} , denoted as S_{21_1} , contains both the actual signal from the source coil as well as the coupled signal from coil 2.
- (2) The receiving port of the analyzer is connected to coil 2 with coil 1 connected to a 50Ω load. The measured S -parameter S_{21} , denoted as S_{21_2} , contains both the actual signal from the source coil as well as the coupled signal from coil 1.
- (3) The receiving port of the analyzer is connected to coil 1 with coil 2 removed. The measured S -parameter S_{21} , denoted as S'_{21_1} , contains only the actual signal from the source coil.
- (4) The receiving port of the analyzer is connected to coil 2 with coil 1 removed. The measured S -parameter S_{21} , denoted as S'_{21_2} , contains only the actual signal from the source coil.

By considering (3) and (4), together with the relationship of coupled signals and coupling-free signals [5], the new mutual impedance is calculated as

$$Z_t^{12} = \frac{S'_{21_1} - S_{21_1}}{S_{21_2}} Z_L \quad (5)$$

$$Z_t^{21} = \frac{S'_{21_2} - S_{21_2}}{S_{21_1}} Z_L \quad (6)$$

Thus, the compensation matrix in (2) is determined, and thereby decoupled signals can be obtained.

3.3. Comparison of the Results

Firstly, in the experimental scenario of power variation from -10 dBm to 10 dBm with the step of 5 dBm , the measurements were done with the operating frequency of 85 MHz, and during the decoupling calculation, the compensation matrix was calculated based on the measurement data in the case with the power of 0 dBm . The comparison of calculated decoupled signals and the measured coupling-free signals in the case with the separation distance of 1.5 cm is shown in Fig. 3(a), where Cal_U1 and Meas_U1 correspond with coil 1, and Cal_U2 and Meas_U2 correspond with coil 2.

Similarly, Fig. 3(b) shows the comparison of results in the experimental scenario of frequency variation from 84.9 MHz to 85.1 MHz with the step of 0.05 MHz when the separation distance between the two stacked surface coils was 1.5 cm. The source power was fixed at 0 dBm , and the compensation matrix was calculated from the data at 85 MHz. Fig. 3(c) illustrates the comparison of results in the experimental scenario of distance variation from 0.5 cm to 3 cm with the step of 0.5 cm , when the system was working at the resonant frequency of 85 MHz and power level of 0 dBm , and the compensation matrix was determined by the data in the case with the separation distance of 2 cm.

From the three figures, it is clear that the coupled signals were successfully recovered despite the minor difference in comparison, and especially in the cases of 0 dBm in Fig. 3(a), 85 MHz in

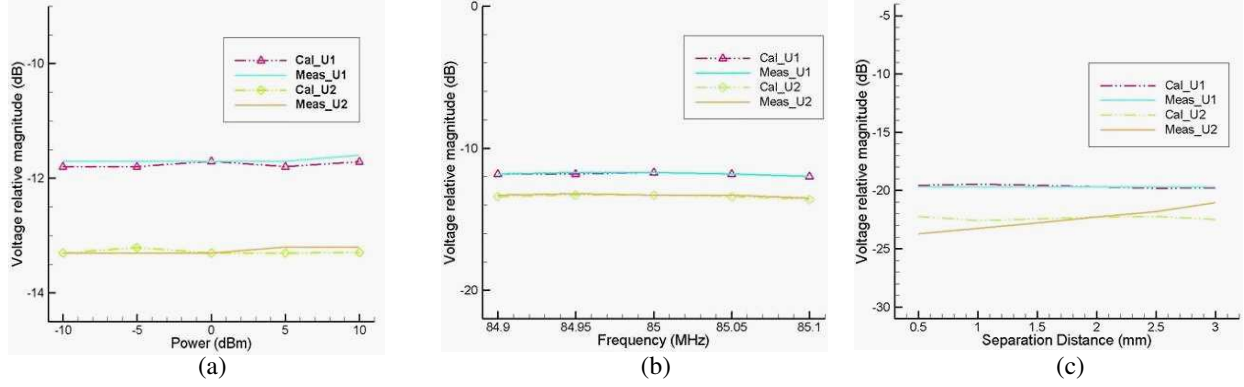


Figure 3: Comparison of results in the experiment scenario of (a) power variation, (b) frequency variation, and (c) distance variation.

Fig. 3(b), and 2 cm in Fig. 3(c), from which the compensation matrix used in their respective experimental scenario was calculated, the coupling was totally removed. Moreover, it can be seen that the separation distance between the two surface coils can influence the decoupling results more than power level and operating frequency. In Fig. 3(c), the disagreement of the results for coil 2 at the separation distance of 0.5 cm and 3 cm might be caused by the extra strong coupling when the coils were placed too close to each other or one coil was too close to the phantom.

4. CONCLUSIONS

To increase the SNR in MRI system, stacked phased array surface coils can be used, and the problem of mutual coupling can be effectively minimized by using a new compensation method. Therefore, it is concluded that the design of stacked phased array coils together with the new decoupling method will have a potential application in MRI to achieve a higher SNR and consequently improve the image quality.

REFERENCES

1. Young, S. W., *Magnetic Resonance Imaging: Basic Principles*, Raven Press, New York, 1988.
2. Vesselle, H. and R. E. Collin, "The signal-to-noise ratio of nuclear magnetic resonance surface coils and application to a lossy dielectric cylinder model — Part I: Theory," *IEEE Trans. Biomed. Eng.*, Vol. 42, No. 5, 497–506, May 1995.
3. Vesselle, H. and R. E. Collin, "The signal-to-noise ratio of nuclear magnetic resonance surface coils and application to a lossy dielectric cylinder model — Part II: The case of cylinder window coils," *IEEE Trans. Biomed. Eng.*, Vol. 42, No. 5, 507–520, May 1995.
4. Chen, C. N. and D. I. Hoult, *Biomedical Magnetic Resonance Technology*, Adam Hilger, Bristol and New York, 1999.
5. Hui, H. T., "A new definition of mutual impedance for application in dipole receiving antenna arrays," *IEEE Antennas Wireless Propag. Lett.*, Vol. 3, No. 1, 364–367, 2004.
6. Hui, H. T., "Improved compensation for the mutual coupling effect in a dipole array for direction finding," *IEEE Trans. Antennas Propagat.*, Vol. 51, No. 9, September 2003.
7. Pozar, D. M., *Microwave Engineering*, John Wiley, 2005.

Novel Wideband Microstrip Antenna Array with Double U-slots

Hong-Jun Wu¹, Jie-Feng Xu¹, Xiao Hua¹, Shi-Lei Zhang¹, and Ying Wang²

¹Wenzheng College, Soochow University, Suzhou 215006, China

²School of Electronics and Information, Soochow University, Suzhou 215006, China

Abstract— A novel 2×2 microstrip patch antenna array is presented in this paper. With two cross-coupled slots etched in the radiating element, the proposed structure achieves wide band and high gain. Simple fabrication techniques can be used, since the radiating elements and the feeding network are placed on the same layer. Good agreement between the simulated and measured responses has been obtained. An impedance bandwidth of 23.1% and a maximum gain of 11.34 dBi are achieved.

1. INTRODUCTION

Microstrip antenna arrays are widely used in many applications, such as satellite communications, radar, missiles and so on. Microstrip antennas possess advantages such as simple structure and compact size. Besides these, the feeding network and the microstrip radiating elements of the array could be placed on the same layer for easy fabrication [1]. However, microstrip antennas generally exhibit narrow impedance bandwidth, typically only a few percent [2, 3]. In order to overcome this problem, researchers have adopted different techniques recently [4–6]. In [7], a 2×2 microstrip wideband antenna array with U-slot has been proposed. The impedance bandwidth of this typical antenna array is 18% [7].

In this paper, a novel microstrip radiating patch with double U-slots is proposed. A 2×2 antenna array using this element is designed and optimized. The impedance bandwidth of 23.1% ranging from 5.78 to 7.29 GHz and a maximum gain of 11.34 dBi has been achieved.

2. DESCRIPTION OF ANTENNA ARRAY

The geometry of the proposed antenna array with double U-slots and probe feed are shown in Fig. 2 and Fig. 3. The detailed dimensions of the radiating element and the feeding network are given as following: $w_1 = 3.9$ mm, $w_2 = 3.6$ mm, $w_3 = 0.5$ mm, $w_4 = 0.8$ mm, $w_5 = 31.6$ mm, $w_6 = 8.6$ mm, $w_7 = 2.5$ mm, $h_1 = 0.7$ mm, $h_2 = 10.4$ mm, $h_3 = 12$ mm, $h_4 = 5$ mm, $h_5 = 21.3$ mm and $h_6 = 2.9$ mm. The dielectric substrate is with a relative permittivity ϵ_r of 2.7 and a thickness h of 3.5 mm. The centre frequency of the proposed antenna array is around 6.53 GHz. The design procedure of the antenna array can be summarized as following:

- (1) Decide the initial width and the length of the patch based on the specified centre frequency for a practical application.
- (2) Design the double U-slots. The double U-slots consist of four paralleled vertical rectangular slots and two horizontal rectangular slots. U-slot plays an important role to control the wideband behavior of the coupled patch antenna.

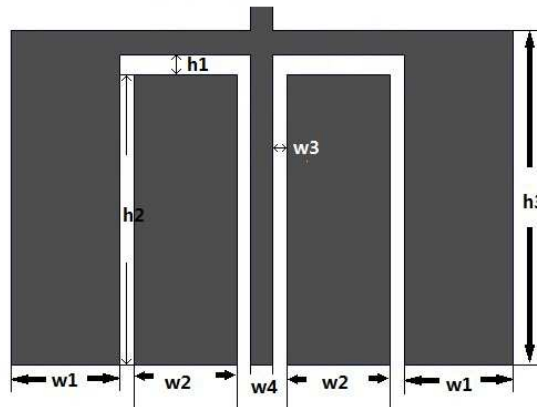


Figure 1: The geometry of single radiating element with double U-slots (units: mm).

- (3) Implement the optimization of the radiating element using simulation software.
- (4) Initial design of the feeding network.
- (5) Implement of the optimization to the whole antenna array using simulation software.

3. RESULTS AND DISCUSSIONS

The simulated S_{11} of the proposed 2×2 microstrip array is shown in Fig. 3. The bandwidth of 23.1% ranging from 5.78 to 7.29 GHz has been achieved. The gain of the proposed array is shown in Fig. 4. A maximum gain of 11.34 dBi is obtained.

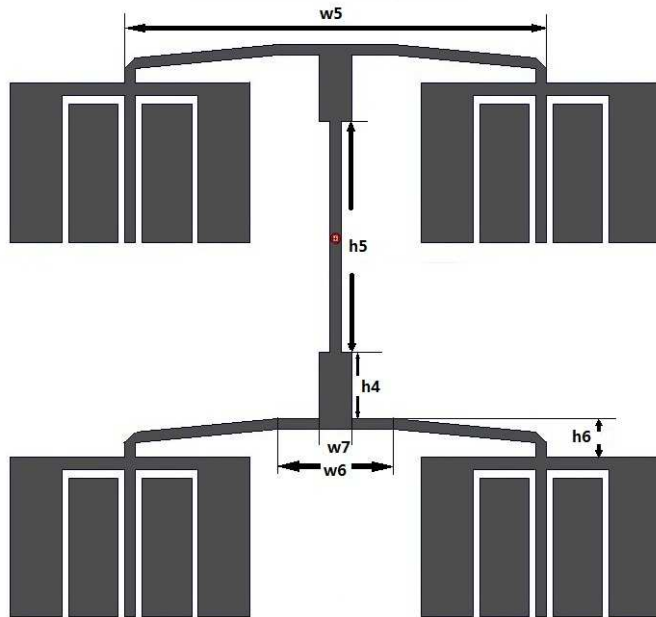


Figure 2: The geometry of the proposed 2×2 antenna array (units: mm).

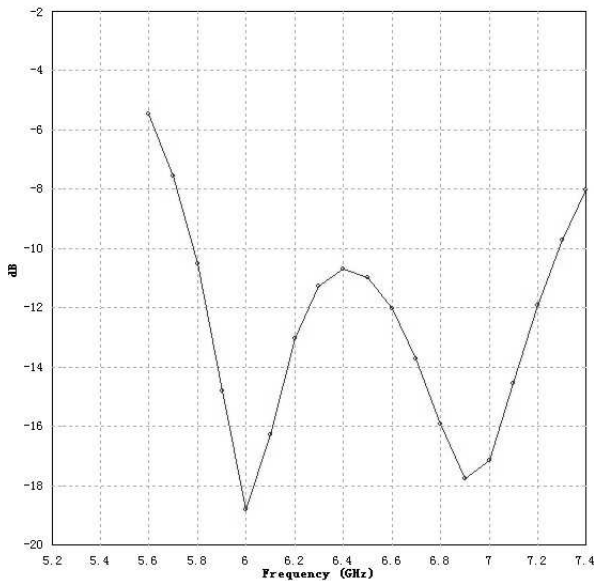


Figure 3: The simulated S_{11} of the proposed antenna array.

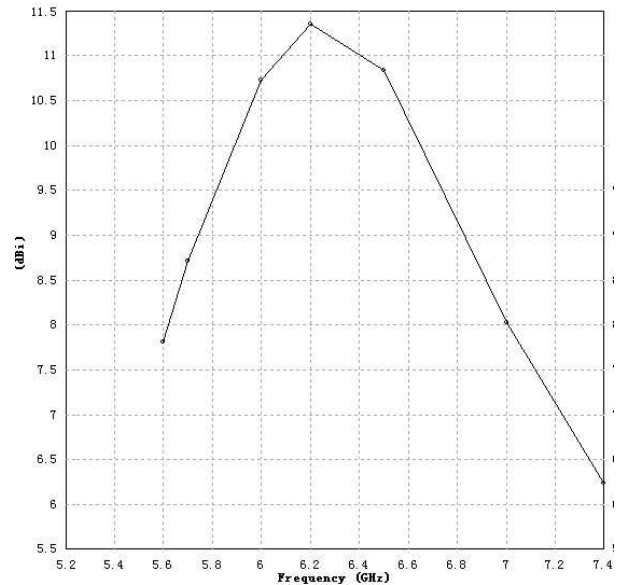


Figure 4: The simulated gain of the proposed microstrip antenna array.

4. CONCLUSION

In this paper, a novel microstrip radiating patch with double U-slots is proposed. The double U-slots of the element help to solve the problem of narrow bandwidth for traditional microstrip antennas. The proposed 2×2 antenna array exhibits broad bandwidth and high gain. The impedance bandwidth of 23.1% ranging from 5.78 to 7.29 GHz and a maximum gain of 11.34 dBi has been achieved.

REFERENCES

1. Li, L., *Antennas and Radio Propagation*, Sience Press.
2. Lin, C. L., *Modern Antenna Design*, Posts & Telecom Press.
3. Chen, Y. L., *Optimization Study on Linear Arrays with Rectangular Patch Elements*.
4. Wang, H., X. B. Huang, and D. G. Fang, “A microstrip antenna array formed by microstrip line fed tooth-like-slot patches,” *IEEE Trans. Antennas Propag.*, Vol. 55, No. 4, 1210–1214, Apr. 2007.
5. Huynh, T. and K. F. Lee, “Single-layer single-patch wideband microstrip antenna,” *Electron Lett.*, Vol. 31, No. 16, 1310–1312, 1995.
6. Lau, K. L., K. M. Luk, and K. F. Lee, “Wideband U-slot microstrip patch antenna array,” *Inst. Elect. Eng. Proc. Microw. Antennas Propag.*, Vol. 148, No. 1, 41–44, 2001.
7. Wang, H., X. B. Huang, and D. G. Fang, “A single layer wideband u-slot microstrip patch antenna array,” *IEEE Antennas and Wireless Propag. Letters*, Vol. 7, 9–12, 2008.

Dual-band Microstrip Antenna Array with EBG Structures

Jian-Jian Gu and Ying Wang

School of Electronics and Information, Soochow University, Suzhou 215006, China

Abstract— In this paper, a novel dual-band microstrip antenna array with electromagnetic band gap (EBG) structures is presented. The ring-type EBG structures between the two radiating patches help to separate the feed lines for the two bands, thus the two patches could operate individually at their particular frequencies, simultaneously.

1. INTRODUCTION

As we know, dual band antenna can be used to transmit and receive signals simultaneously for wireless communication systems. Various multiband antennas have been reported recently [1–3]. However, when two radiating patches working at different frequencies, the mutual coupling between the two patches leads to degradation of the performance of the antennas. Thus these two radiating element should be separated electrically, while keeping the size of the antenna arrays as small as possible [4]. In [4], a single-port dual-band microstrip antenna array with EBGs is reported. EBG structures operate like a band rejecter, separating the branch of feed lines feeding two different groups of arrays of patch antennas. Different kinds of EBG structures are discussed also in [4].

In this paper, a novel EBG structure has been adopted between the 2.4 GHz and 5.8 GHz radiating elements for better mutual coupling reduction.

2. PRELIMINARY STRUCTURE OF THE ANTENNA ARRAY

The preliminary geometry of the antenna array is shown in Fig. 1. The dielectric substrate is with a relative permittivity of 4.2 and a thickness of 3.2 mm. The design procedure of the antenna array can be summarized as follows:

- 1) Decide the initial width and the length of the patches working at the specified frequencies of 2.4 GHz and 5.8 GHz.
- 2) Initial design of the feeding network.
- 3) Optimize the circuit using simulation software.

The simulated S_{11} of the preliminary structure is shown in Fig. 2. It is noted that an extra resonance appears between the two desired bands and the centre frequency of the 2nd band is shifted from 5.8 GHz to 6.0 GHz. This is due to the coupling between the two radiating patches. In order to overcome this problem, the proposed antenna array with EBG structures between the two radiating patches is shown in Section 3.

3. PROPOSED ANTENNA ARRAY WITH EBG STRUCTURES

The Electromagnetic Bandgap (EBG) structures are well known due to their compact size and special EM characteristics such as bandgap, surface wave suppression and in-phase reflection coefficient properties [5–9]. In this paper, ring-type EBG structures are adopted for mutual coupling reduction and harmonic suppressions. This type of EBG structures with height of 1.6 mm from the GND consists of an open-ended ring and three vias connected to the ground. Those rings are of different dimensions based on their bandgap characteristics, which correspond to 2.4 GHz and 5.8 GHz accordingly. The proposed antenna array is shown in Fig. 3. It is noted that better performance of the antenna array between the two desired bands has been achieved as shown in Fig. 4.

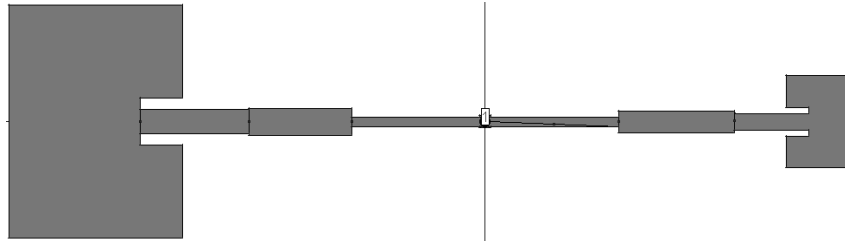


Figure 1: Preliminary geometry of the antenna array.

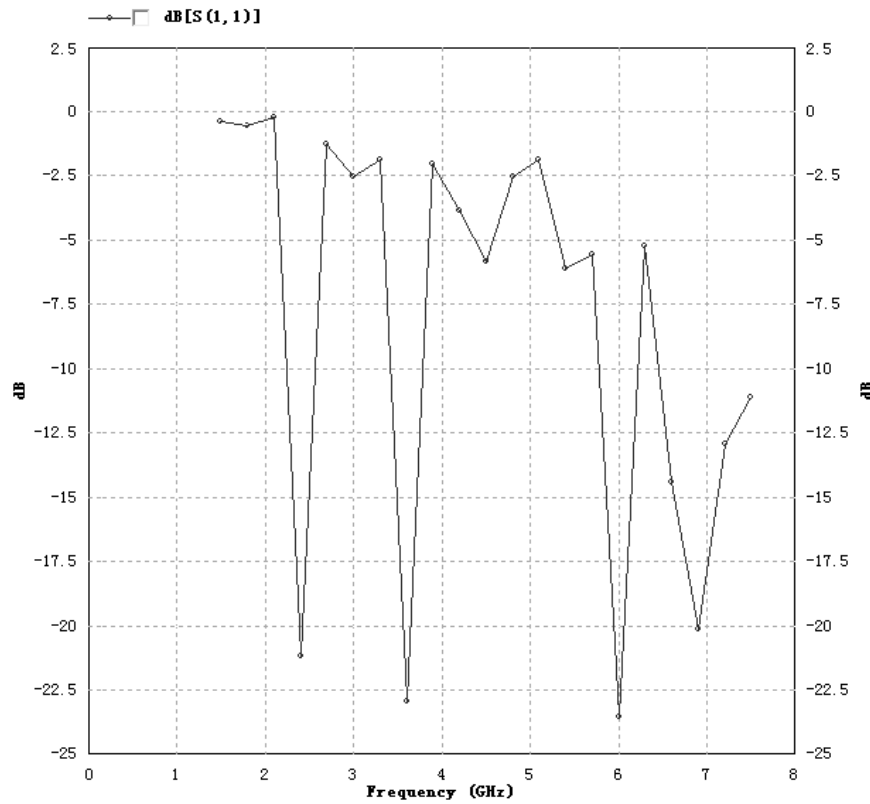
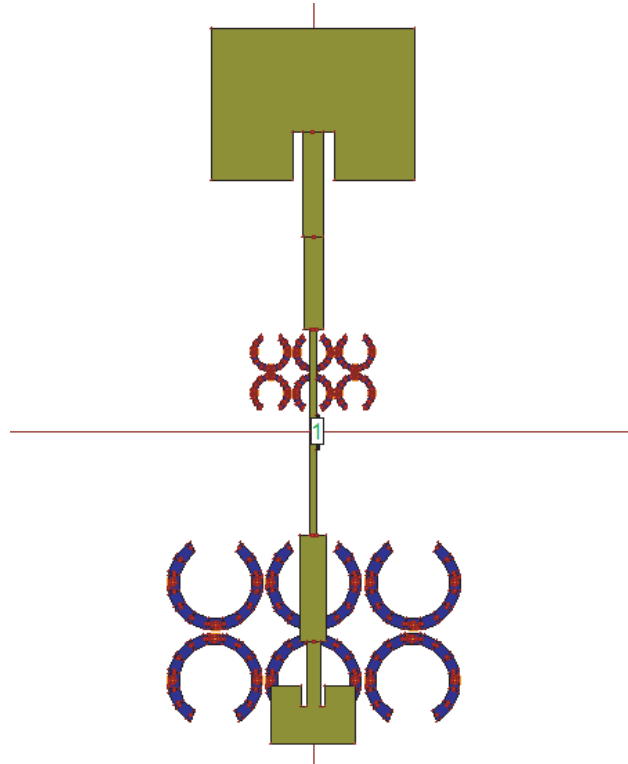
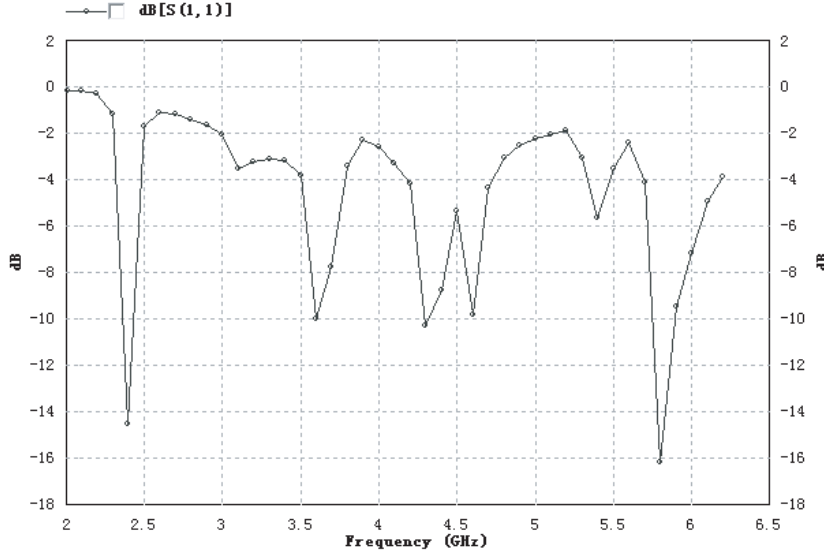
Figure 2: Simulated S_{11} of the preliminary antenna array.

Figure 3: Proposed antenna array with EBG structures.

Figure 4: Simulated S_{11} of the antenna array.

4. CONCLUSION

In this paper, a novel antenna array with EBG structures has been proposed. Ring-type EBG structures with three vias connected to the ground has been adopted between the 2.4 GHz and 5.8 GHz radiating patches for better mutual coupling reduction.

REFERENCES

- Shin, Y.-S., K.-B. Kong, and S.-O. Park, "A compact multiband PIFA with the modified ground plane and shorting plate for wireless communications applications," *Microw. Opt. Technol. Lett.*, Vol. 50, No. 1, 114–117, 2008.
- Wu, Y. J., B. H. Sun, J. F. Li, and Q. Z. Liu, "Tripleband omnidirectional antenna for LAN application," *Progress In Electromagnetic Research*, Vol. 76, 477–484, 2007.
- Zulkifli, F. Y., H. Halim, and E. T. Rahardjo, "A compact multiband microstrip antenna using U and S slots," *IEEE Int. Symp. on Antennas and Propagation*, San Diego, USA, July 5–11, 2008.
- Masri, T. and M. K. A. Rahim, "Dual-band microstrip antenna array with a combination of mushroom, modified Minkowski and Sierpinski electromagnetic band gap structures," *IET Microw. Antennas Propag.*, Vol. 4, No. 11, 1756–1763, 2010.
- Rajo-Iglesias, E., L. Inclan-Sanchez, J. L. Vazquez-Roy, and E. Garcia-Muoz, "Size reduction of mushroom-type EBG surfaces by using edgelocated vias," *IEEE Microw. Wireless Compon. Lett.*, Vol. 17, No. 9, 670–672, Sep. 2007.
- Yang, F. and Y. Rahmat-Samii, "Microstrip antennas integrated with electromagnetic band-gap (EBG) structures: A low mutual coupling design for array applications," *IEEE Trans. Antennas Propag.*, Vol. 51, No. 10, 2936–2946, Oct. 2003.
- Folayan, O. and R. Langley, "Dual frequency band antenna combined with a high impedance band gap surface," *IET Microwaves, Antennas Propag.*, Vol. 3, No. 7, 1118–1126, 2009.
- Yangm F. and Y. Rahmat-Samii, *Electromagnetic Band-gap Structures in Antenna Engineering*, Cambridge Univ. Press, Cambridge, UK, 2008.
- Goussetis, G., A. P. Feresidis, and J. C. Vardaxoglou, "Tailoring the AMC and EBG characteristics of periodic metallic arrays printed on grounded dielectric substrate," *IEEE Trans. Antennas Propag.*, Vol. 54, No. 1, 82–89, Jan. 2006.

A Compact Printed Multi-band Antenna for Laptop Applications

Cheng-Chi Yu¹, Jiin-Hwa Yang², Chang-Chih Chen¹, and Wen-Chao Hsieh¹

¹Department of Communications Engineering, Feng-Chia University
No. 100, Wen-Hua Rd., Seatwen, Taichung 407, Taiwan, R.O.C.

²Program in Electrical and Communications Engineering, Feng-Chia University
No. 100, Wen-Hua Rd., Seatwen, Taichung 407, Taiwan, R.O.C.

Abstract— This study proposes a compact printed multi-band antenna, which has the advantages of simple structure, small size, easy fabrication, and making integration within thin laptop. The main operating frequencies of the proposed antenna are at GPS (1.575 GHz), WLAN (2.4, 5.8 GHz), Bluetooth (2.45 GHz) and WiMAX (2.5, 3.5, 5.5 GHz) bands. The main structure of the antenna is composed of T-shaped monopole and grounded inverted L-shaped branch. The T-shape monopole excites 2.4 GHz operating frequency band. And, the grounded inverted L-shaped branch not only can excite 3.5 GHz operating band but also can be used for impedance matching, which can tune the bandwidth of each operating band. A branch is added on the left part of T-shaped monopole which can excite GPS band (1.575 GHz). Finally, the 5.5 GHz operational frequency of WiMAX can be excited by adding a stub on the T-shaped monopole branch. Therefore, a multi-band antenna for laptop applications is achieved.

The antenna occupies a small area of $9 \times 47 \text{ mm}^2$ only. This antenna is fed on the T-shaped monopole by a 50Ω coaxial cable. The measured result shows that the 10 dB return loss is satisfied at each operating band, and has a good agreement with simulated result. Moreover, the gain, radiation efficiency and radiation pattern of each operating center frequency were also simulated and measured. They demonstrate very good performances. The gain is about $1.25 \sim 6.38 \text{ dBi}$ and radiation efficiency ranges from 67% to 95% at each band. The measured radiation pattern is similar to general monopole antenna. The characteristics of the antenna make it attractive for practical application in laptops.

1. INTRODUCTION

In recent years, with the rapid progress in wireless communication, the demands for multi-band antenna are increasing. In order to realize multi-band WLAN/WiMAX operations, several schemes had been proposed, such as planar inverted F antenna, inverted L antenna and T-type monopole antenna structure [1, 2]. These types of antenna have simple structure and small size and suit for internal laptop planar antenna. There are many ways to design multi-band antenna such as adding radiation branch, using coupling or open slot to achieve the design specifications [3, 4].

In this paper, we propose a compact printed multi-band antenna for laptop applications. The main operating frequencies of the proposed antenna are at GPS (1.575 GHz), WLAN (2.4, 5.8 GHz), Bluetooth (2.45 GHz) and WiMAX (2.5, 3.5, 5.5 GHz) bands.

2. ANTENNA DESIGN

Figure 1(a) shows the geometry of the proposed multi-band antenna. The detailed dimension of the antenna is shown in Fig. 1(b). In the figure, the point A denotes feeding point and the point B denotes grounding point. The antenna is fabricated on a FR4 substrate with a thickness of 1.6 mm and a relative permittivity of 4.4. This antenna is fed on the T-shape monopole by a 50Ω coaxial cable.

The operating principle is analyzed as following. At first, four types of antenna are defined that are called antenna A, antenna B, antenna C and proposed antenna, as shown in Fig. 2(a). The structure of antenna A can be seen as a T-shaped monopole which can excite 2.4 GHz resonant mode, and the simulated result of return loss is shown in Fig. 2(b). The antenna A can't achieve the desired results of proposed antenna. Hence, the grounded inverted L microstrip line was added to adjust the impedance matching, and the new structure is called antenna B. The Fig. 2(b) shows that the antenna B not only has a good impedance matching at the 2.4 GHz resonant mode and also excites 3.5 GHz resonant mode. In order to design the GPS band (1.575 GHz), a branch was added on the left part of T-shaped monopole (antenna C). Finally, to achieve a proposed multi-band antenna, a stub was added on the right part of T-shaped monopole which can excite 5.5 GHz operating frequency band of WiMAX. From the above design processes, a multi-band antenna for laptop applications is achieved.

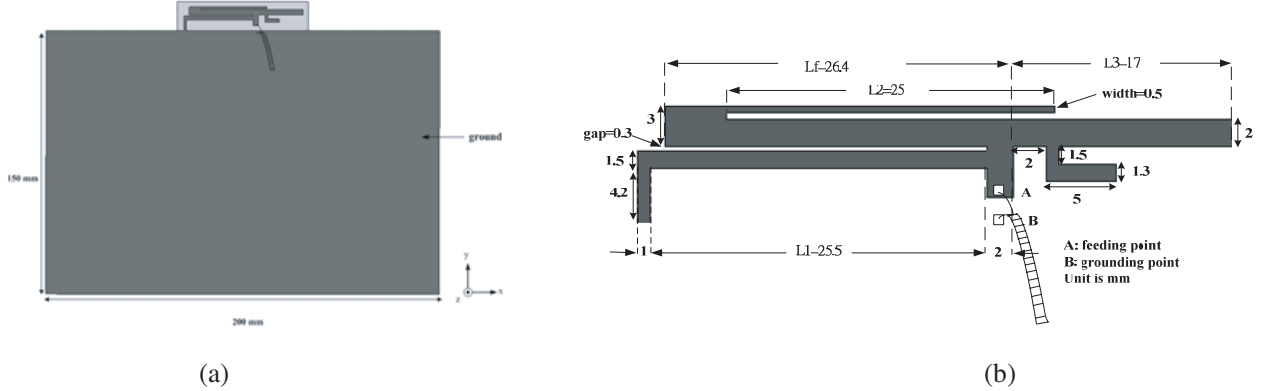


Figure 1: (a) Geometry of the proposed multiband antenna, (b) detailed dimensions of the proposed antenna.

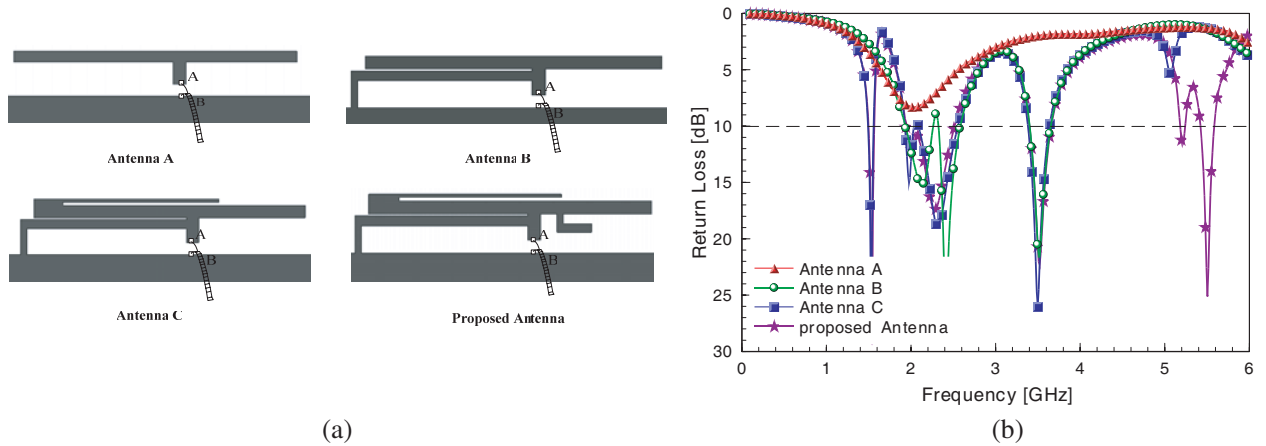


Figure 2: Antenna design: (a) Four types of antenna, (b) simulated results of each type antenna.

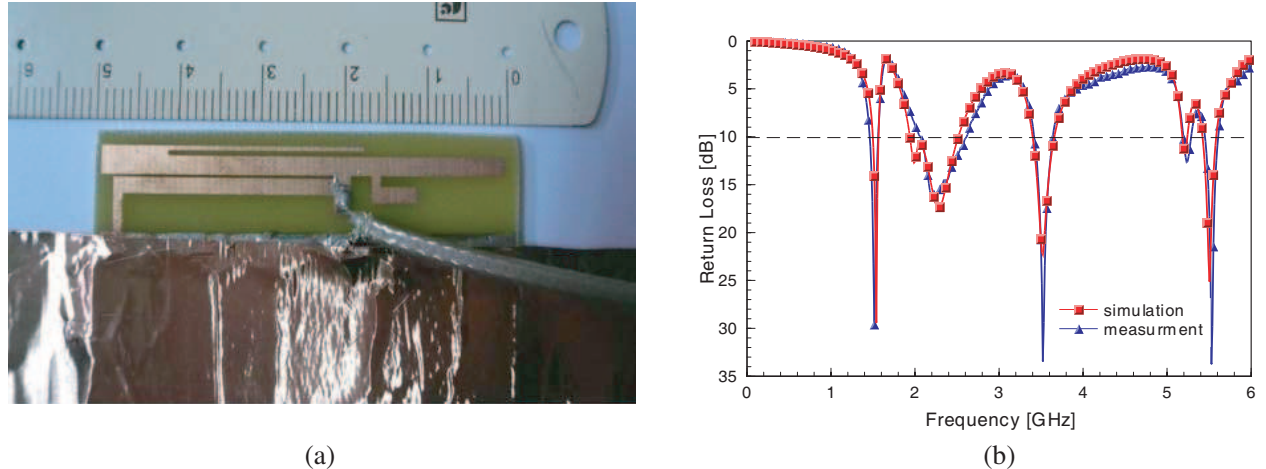


Figure 3: (a) Photo of the fabricated prototype of the proposed antenna, (b) simulated and measured return loss of the proposed antenna.

3. RESULTS AND DISCUSSION

The proposed antenna was fabricated and shown in Fig. 3(a). The measured and simulated return loss of the proposed antenna is shown in Fig. 3(b). The measured result shows that the 10 dB return loss is satisfied at each operating band, and has a good agreement with simulated result. From the results, four resonant modes at about 1.575, 2.4, 3.5 and 5.5 GHz are successfully excited. The first resonant mode at 1.575 GHz can be used for GPS operation. The second resonant mode at about 2.4 GHz can cover the operations of 2.4GHz WLAN, Bluetooth (2.45 GHz) and 2.5 GHz

WiMAX. The third resonant mode can be applied to 3.5 GHz WiMAX operation, and the fourth resonant mode satisfies 5.8 GHz WLAN and 5.5 GHz WiMAX operations.

For actual application, antenna must be integrated with a LCD screen of laptop. Fig. 4(a) is the photo of the proposed antenna integrated with a LCD screen of notebook. Fig. 4(b) depicts the measured return loss of the antenna with/without LCD screen.

Figures 5(a)–(d) exhibit the measured far-field radiation patterns on the x - z and x - y planes for four frequencies at 1.575, 2.4, 3.5 and 5.5 GHz, respectively. On the horizontal plane (x - z plane), nearly omnidirectional patterns in all frequencies are obtained. Fig. 6 shows the simulated radiation efficiency and peak gain of the proposed antenna for all bands. The peak gain is about $1.25 \sim 6.38$ dBi and radiation efficiency ranges from 67% to 95%.

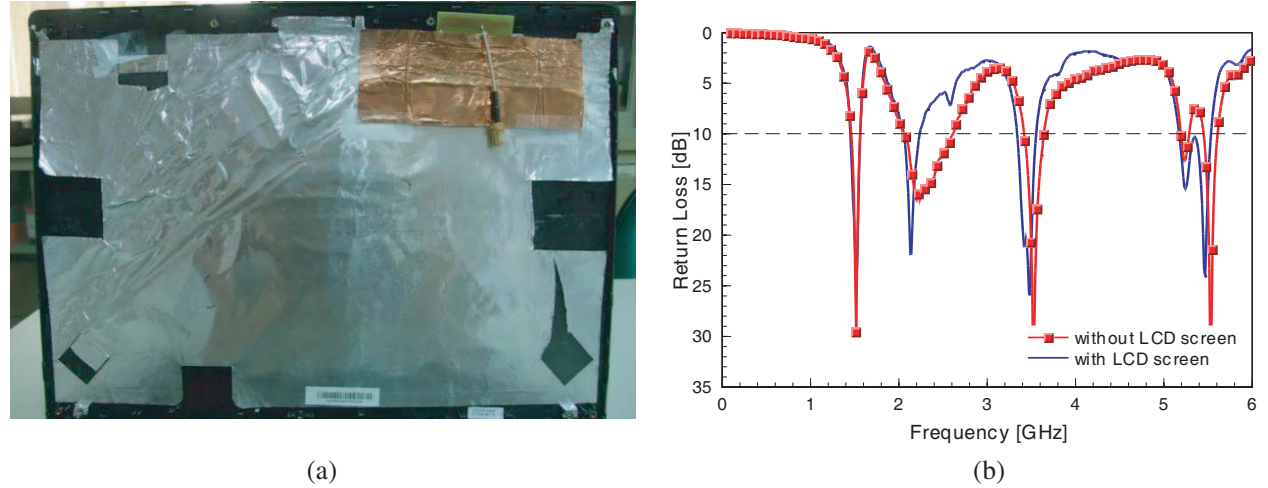


Figure 4: (a) Photo of the proposed antenna integrated with a LCD screen, (b) measured return loss of the antenna with/without LCD screen.

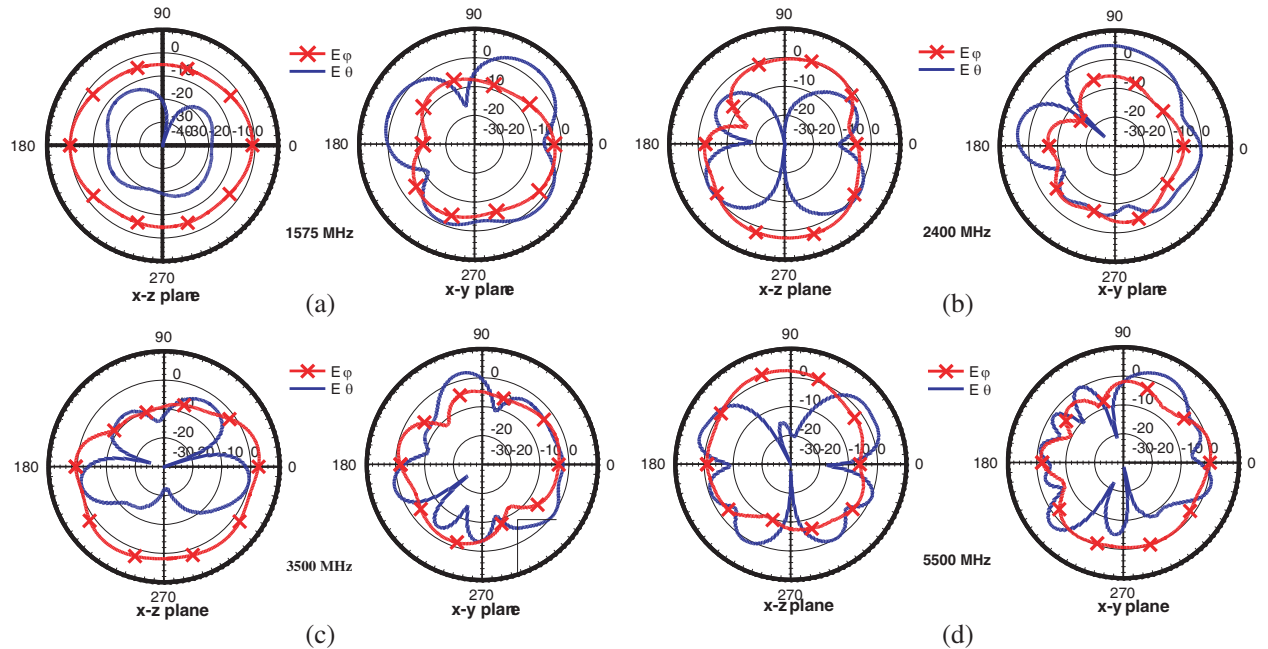


Figure 5: Measured radiation patterns (a) 1.575 GHz, (b) 2.4 GHz, (c) 3.5 GHz, (d) 5.5 GHz.

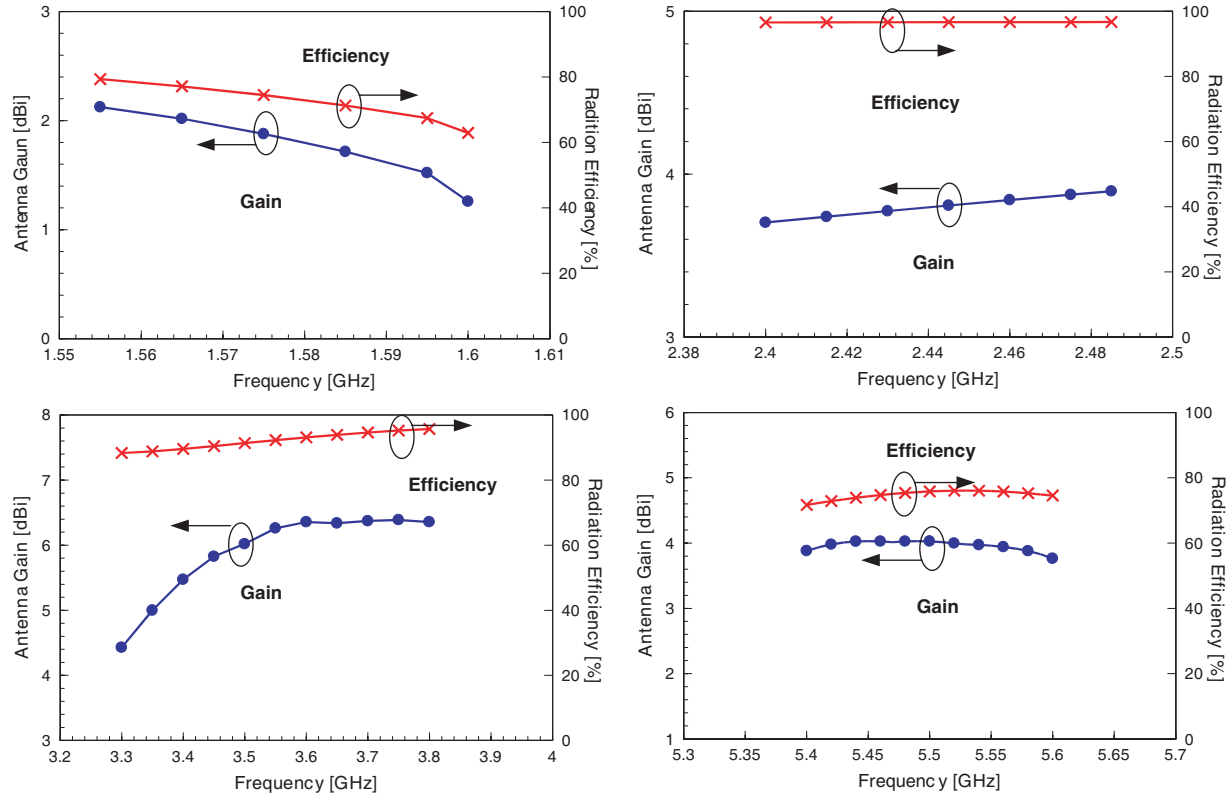


Figure 6: Simulated radiation efficiency and peak gain.

4. CONCLUSION

A compact printed multi-band antenna for laptop applications has been presented in this article. This antenna has the advantages of simple structure, small size, easy fabrication, and making integration within thin laptop. The measured results are satisfied at each operating band, and demonstrate good agreements with simulated results.

REFERENCES

1. Liu, D. and B. P. Gaucher, "A new multiband antenna for WLAN/cellular applications," *Proc. IEEE Veh. Technol. Conf.*, Vol. 1, 243–246, Sep. 2004.
2. Su, C., M. W. S. Chen, Y. T. Cheng, and K. L. Wong, "Shorted T-shaped monopole antenna for 2.4/5 GHz WLAN operation," *Microwave and Optical Technology Letters*, Vol. 41, 202–203, May 2004.
3. Lee, C. T. and K. L. Wong, "Uniplanar printed coupled-fed PIFA with a band-notching slit for WLAN/WiMAX operation in the laptop computer," *IEEE Trans. Antenna & Propagation*, Vol. 57, No. 4, 1252–1258, Apr. 2009.
4. Hosoe, T. and K. Ito, "Dual-band planar inverted F antenna for laptop computers," *Proc. 2003 IEEE Antennas Propagation Society International Symposium*, Vol. 3, 87–90, Jun. 2003.

A Novel Compact EBG Structure for Mutual Coupling Reduction in a Patch Array

Haoyun Fei, Huipin Guo, Xueguan Liu, and Ying Wang

School of Electronic and Information Engineering, Soochow University, Suzhou 215021, China

Abstract— This paper presents a novel and compact C-shape electromagnetic band-gap (EBG) structure and arrangement for mutual coupling reduction. For the proposed antenna array, the reduction of mutual coupling between the two radiating elements reaches 10 dB. The size of the C-shape EBG array is only $0.064\lambda_0$ at the operating frequency. Due to the use of EBG structures, the front-back ratio of the antenna is increased by 5.4 dB. Simulated and measured results are given to verify the improvement of the performance of the antenna array.

1. INTRODUCTION

Electromagnetic BandGap (EBG) structures consist of periodic dielectric or metal elements which exhibit band-stop characteristics. EBG can be used to block surface wave excitation [1] reduce mutual coupling, reduce cross polarization [2] and enhance the performance of antennas in terms of gain, direction pattern [3], side lobe, back lobe and so on.

High resistance electromagnetic surface structure [4] as one kind of EBG structures is widely used, which is convenient for design, easy for fabrication. Various EBG structures have been adopted for different applications. For example, Fangming Zhu [6] placed mushroom-like EBG structure [5] between antenna elements and the mutual coupling at the resonant frequency is reduced nearly 12 dB. Hence the overall performance of the antenna array is improved greatly. However, the size of this kind of EBG structure nearly equals to half of the stop-band wavelength, which cannot meet the requirement of compact circuit size nowadays. In this paper, a novel C-shape EBG structure is proposed. Compared with mushroom-like EBG structure in [5], C-shape EBG structure has compact size, more adjustable parameters, and more ways of arrangement.

2. C-EBG STRUCTURE CONFIGURATION

Figures 1 and 2 show the proposed C-shape EBG structure and its combined structure. It consists of a periodic array of metal via holes within a host dielectric grounded substrate. The main parameters are the outer and inner radius, R_1 and R_2 , of the ring, the diameters of the via and the distance between the adjacent patches, rr and g . The radian of the ring is chosen to be π and the effect of the radian of the circle will not be discussed in this paper. The theoretical analysis of the C-shape EBG is given in [7]. The equivalent circuit is shown in Fig. 3. The inductor L results from the current flowing through the vias and the capacitor C is due to the gap effect between the adjacent EBG patches. The bandgap of such structure can be predicted as

$$\omega = \frac{1}{\sqrt{LC}} \quad (1)$$

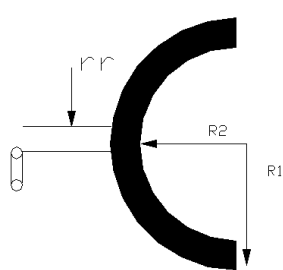


Figure 1: Geometry of the C-shape EBG structure.

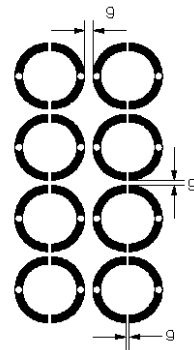


Figure 2: Reverse symmetric C-shape EBG.

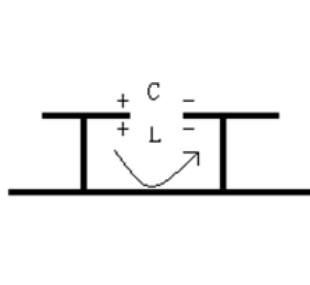


Figure 3: Equivalent circuit of C-shape EBG structure

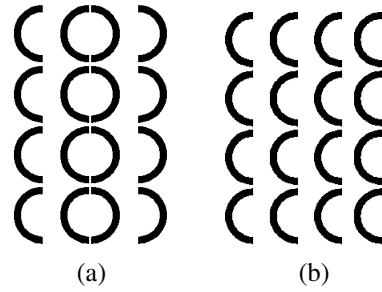


Figure 4: Various arrangements of EBG structures.

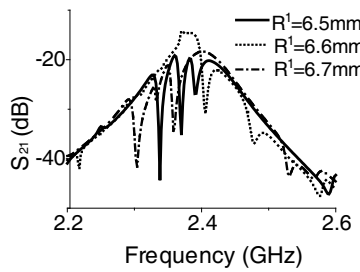


Figure 5: Simulated S_{21} of the C-EBG with different R_1 .

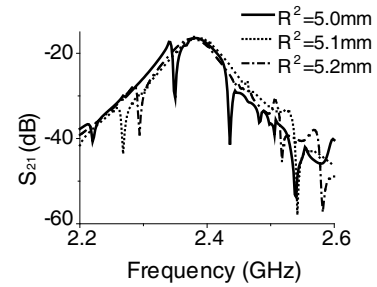


Figure 6: Simulated S_{21} of the C-EBG with different R_2 .

When the LC circuit resonate the circuit reactance tends to infinity, the electromagnetic wave of the resonance frequency cannot propagate, which forms the bandgap [8].

The C-shape EBG structure can be placed in different orientations, thus the array of C-shape EBG structures could be arranged in different ways, such as reverse symmetric shape as shown in Fig. 2, symmetrical brackets shape as shown in Fig. 4(a) and asymmetric C-form structure as shown in Fig. 4(b). Different layout of the EBG arrays results in different bandgap characteristics. In this paper, reverse symmetric shape of the EBG array is adopted due to its better performance at the operating frequency (2.4 GHz) and its compact size.

The geometry of the proposed antenna array with C-shape EBG structures placed between the two patches is shown Fig. 11. The dielectric substrate is with a relative permittivity ϵ_r of 10.2 and a thickness h of 2.54 mm. The overall size of the antenna array is 130 mm * 70 mm. The patch antenna is designed to operate at 2.4 GHz, and its parameters are: Antenna length $L = 17.8$ mm, width $W = 26$ mm [9]. The distance between the two antenna elements is $0.7\lambda_0$, C-shape EBG patches are placed between the two radiating patches to reduce the mutual coupling, The distance between the radiating patch and the C-shape EBG structure is 19.6 mm.

3. BANDGAP CHARACTERIZATION

The characteristics of C-shape EBG array are mainly controlled by the following parameters: the number of the C-shape EBG structures, the size of the EBG unit, the inner and outer radius of the C-shape, the arrangement of the EBG unit, the relative dielectric constant and thickness of the substrate and so on. In order to study the performance of the EBG arrays, the outer ring radius R_1 , inner radius R_2 , unit spacing rr and radius of the via g are varied for analysis while remain other parameters unchanged.

Case 1

$R_2 = 5.0$ mm, $rr = 0.5$ mm, $g = 1.5$ mm, R_1 varies from 6.5 mm to 6.7 mm. When R_1 is increased, the position of the vias changes, thus affect the equivalent inductance L and capacitance C . L and C determine the bandgap characteristics. The simulation results are shown in Fig. 6. When R_1 is gradually increased, the total circuit reactance is reduced first, and then increased [10]. Thus the centre frequency of the bandgap is increased first and then reduced accordingly.

Case 2

$R_1 = 6.5$ mm, $rr = 0.5$ mm, $g = 1.5$ mm, R_2 varies from 5.0 mm to 5.2 mm. The simulation results are shown in Fig. 7. When R_2 is increased, the total circuit reactance is increased first and

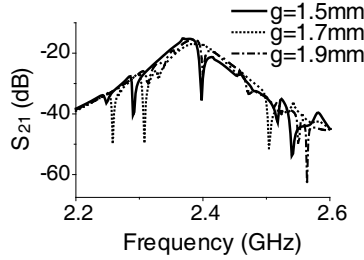


Figure 7: Simulated S_{21} of the C-EBG with different g .

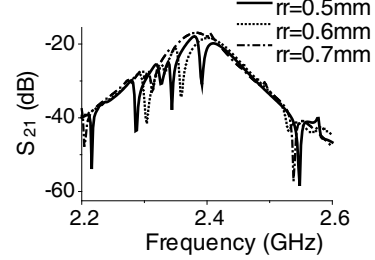


Figure 8: Simulated S_{21} of the C-EBG with different rr .

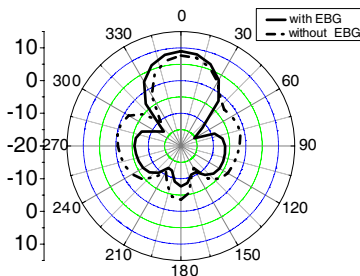


Figure 9: E -plane radiation pattern.

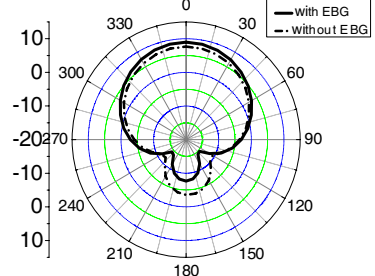


Figure 10: H -plane radiation pattern.

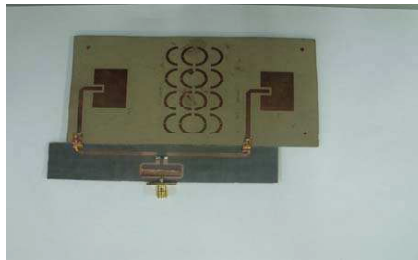


Figure 11: Photograph of the fabricated antenna array.

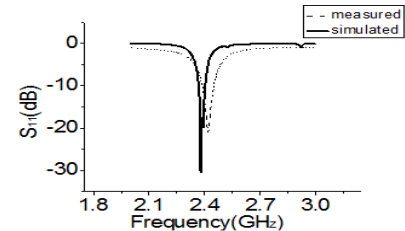


Figure 12: Simulated and measured S_{11} .

then reduced, thus the centre frequency is decreased first and then increased.

Case3

$R_1 = 6.5\text{ mm}$, $R_2 = 5.0\text{ mm}$, $rr = 0.5\text{ mm}$, g varies from 1.5 mm to 1.9 mm. The simulation results are shown in Fig. 8. When g is increased, the total circuit reactance is reduced first and then increased, thus the centre frequency is increased first and then decreased.

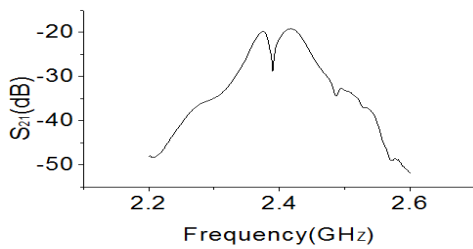
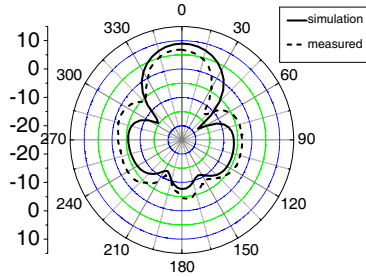
Case 4

$R_1 = 6.5\text{ mm}$, $R_2 = 5.0\text{ mm}$, $g = 1.5\text{ mm}$, rr varies from 0.5 mm to 0.7 mm. The simulation results are shown in Fig. 9. When rr is increased, the coupling capacitance between EBG unit basically remains unchanged and the coupled inductance L is reduced, thus the centre frequency is increased.

The parameters mentioned above are optimized using simulation software. These parameter are chosen to be $R_1 = 6.5\text{ mm}$, $R_2 = 5.0\text{ mm}$, $rr = 0.5\text{ mm}$, $g = 1.5\text{ mm}$. The simulation results of the E - and H -plane radiation patterns of the antenna array with EBG and without EBG at 2.4 GHz are shown in Fig. 9 and Fig. 10. With EBG structures adopted, the gain of the antenna array is increased from 7.6 dB to 8.9 dB. The gain of the side lobe is decreased from -3.5 dB to -4.1 dB , and the main-side lobe ratio of the antenna is increased by 5.4 dB.

The photograph of the fabricated antenna array is shown in Fig. 11. The measured S_{11} and S_{21} of the proposed antenna array are shown in Fig. 12 and Fig. 13. It is noted from Fig. 13 that the mutual coupling between the two radiating patches is reduced for 10 dB at 2.4 GHz.

The simulated and measured E -plane radiation pattern of antenna array is shown in Fig. 14. The measured gain is lower than the simulated results due to the losses of the power dividers and

Figure 13: Measured S_{21} .Figure 14: Simulated and measured E -plane radiation pattern.

the radiating elements. The maximum simulated gain is 8.9 dB and the maximum measured gain is 6.86 dB as shown in Fig. 14.

4. CONCLUSION

In this paper, a novel compact C-shape EBG structure has been adopted between two radiating patches to reduce the mutual coupling. A 10 dB mutual coupling reduction is obtained at the resonant frequency (2.4 GHz). This C-shape EBG structure, with the advantages of compactness, flexibility and various layout arrangement, is attractive for many applications in different areas, such as compact antennas, surface wave suppression and antenna arrays.

REFERENCES

1. Huff, G. H. and J. T. Bernhard, "Improvements in the performance of microstrip antennas on finite ground planes through ground plane edge serration," *IEEE Transactions on Microwave and Wireless Components Letters*, Vol. 12, No. 8, 308–310, 2002.
2. Fishler, E., A. Haimovich, R. S. Blum, et al., "MIMO radar: An idea whose time has come," *Proc. IEEE Radar Conference*, 71–78, 2004.
3. Deng, H., "Polyphase code design for orthogonal netted radar systems," *IEEE Transactions on Signal Processing*, Vol. 52, No. 11, 3126–3135, 2004.
4. Klemm, R., "Space-time adaptive processing principles and applications," *The Institution of Electrical Engineers*, London, 1998.
5. Scalora, M., et al., "Generalized non linear schrodinger equation for dispersive susceptibility and permeability: Application to negative index materials," *Phys. Rev. Lett.*, Vol. 95, No. 1, 3902–3905, 2005.
6. Zhu, F., Y. Xia, and J. Ye, "Performance improvement of microstrip patch antenna and array with electromagnetic bandgap structure," *IEEE Microwave and Millimeter Wave Technology*, 1602–1605, 2008.
7. Liang, C., "The equivalent model of the square high impedance surface of PBG structure," Xidian University, Xi'an, 2004 (in Chinese).
8. Sievenpiper, D., *High Impedance Electromagnetic Surfaces*, Dissertation, Department of Electrical Engineering, University of California, Los Angeles, CA.
9. Liu, X. and H. Guo, *Microwave Technology and Antenna*, Publishing Company of Xidian University, Xi'an, 2006 (in Chinese).
10. Shen, J., *The Analysis and Design of the Microstrip Phased Array Antenna*, Soochow University, Suzhou, 2010 (in Chinese).

Simulation of a Conformal Reconfigurable Fractal Tree Antenna with Adaptive Multi Beam and Frequency Characteristics

Huseyin Altun¹, Erdal Korkmaz¹, and Bahattin Turetken²

¹Department of Electrical and Electronics Engineering, Fatih University, Istanbul, Turkey

²The National Research Institute of Electronics and Cryptology (UEKAE), Tubitak, Gebze, Turkey

Abstract— This paper presents the design and the analysis of a conformal fractal tree reconfigurable antenna having adaptive multi beam radiation patterns and adaptive operation frequency characteristics. The proposed antenna covers some service bands such as: WiMAX (2.400–2.483) GHz, m-WiMAX (3.4–3.6) GHz and WLAN (5.15–5.825) GHz and operates some other frequencies between 2.24 GHz to 9.87 GHz. The designed antenna is reconfigured by using PIN diode switches. For biasing the diodes, influences on the antenna characteristics is presented in the results. The optimization in biasing and integration of these switches into the antenna is also discussed.

1. INTRODUCTION

In radar and modern communication systems the demand on multi-functional antennas is increasing. The requirements for these antennas are the abilities to have multi radiation patterns, adapting the operation frequency and polarization, keeping the physical dimensions and positioning unaltered. Reconfigurable antennas with switching capability used as a multiple input multiple output (MIMO) system have been used in recent years to fulfill these requirements. By means of switches with compatible antenna elements the antenna and its feed structure can be physically reconfigured to provide radiation pattern, frequency band and polarization diversity so they have more advantage to compare with conventional antennas [1]. The most prevalent implementation about reconfigurable antenna is related to the operation frequency [2] since it might be the easiest feature to alter. Polarization and pattern reconfigurable antennas are also attractive since they can provide diversity features which leads to an increased signal to noise ratio and therefore a higher quality of service of whole systems [3–5].

PIN diodes are generally used more than transistors and switches as switching devices for RF and microwave front-end communication systems since they have several crucial properties such as low insertion loss, good isolation, low power handling and low cost [6].

Although a reconfigurable antenna can take many shapes we will focus on fractal tree antennas in this work. In terminology, fractal means broken or irregular fragments which were originally entitled by Mandelbrot [7] to describe a family of complex shapes that possess an inherent self-similarity in their geometric structure. As a result of small investigation in the environment a lot of example for fractal shapes can be seen as trees, clouds, galaxies, leaves, snowflakes and much more. Fractal tree structures can be applied into antenna design to produce multiband characteristics [8–10].

A conformal antenna is an antenna that conforms to something or it conforms to prescribed shape. The shape can be some part of a train, airplane or other vehicle. The purpose in conformal antenna is to make surface matched structure so that it becomes integrated with the structure and does not extra drag. Since they have very low profile and can be applied on flexible substrates they can behave “hidden” antennas [11].

The target in this paper is showing the design of a new shape of fractal tree antenna for multiband and multi radiation pattern applications. PIN diodes are used as switches for multi frequency and multi beam reconfiguration. By switching PIN diodes, the resonant frequency and radiation pattern variation simulation by using CST is presented.

2. ANTENNA DESIGN

A designed reconfigurable fractal tree antenna schematic is presented from its top view in Figure 1(a) and perspective view in Figure 1(b). Antenna is designed on a substrate with a Rogers RT5880 (lossy) material which has 2.2 relative permittivity. The height of the substrate is 70 mm and the width is 64.7 mm and with a 1.6 mm thickness. The ground has been chosen from PEC material with a thickness of 0.2 mm. Substrate and ground made conformal on the cylinder with a radius of 50 mm. The antenna is fed by a 50 ohm round coax. The inner conductor of the coax has diameter

of 0.689 mm with a material PEC and the shield is 2.13 mm Rogers RT5880. The feeding line is 5 mm long from end to top.

As shown in Figure 1(a) some parts at the antenna are numbered for the description. The numbered parts are called trunks and they make the connection from source to branches. For switching, PIN diodes are used. The connection between feed line and trunks are established by the diodes namely, D1t, D2t, D3t, D4t while the connection between trunks and branches are established by diodes D1b, D2b, D3b, D4b. In our structure totally eight PIN diodes are deployed to alter the electrical length of the antenna to operate at different resonant frequencies.

Dimension of the trunks (part 1, 2, 3, 4) are 20×2 mm and branches are 10×2 mm with the rotation angle of 45 degree and with the rotation angle of 90 degree at the middle. Fractal structure has thickness of 0.1 mm. PIN diodes are 0.5 mm.

The PIN diodes are modeled as a series RL circuits for ON state, and a combination of series-parallel RLC circuits for the OFF state which can be seen in Figure 2. As a result of searching for suitable PIN diodes, MACOM-MA4AGBLP 912 was chosen for the simulation since it has high switching cut off frequency, low series inductance and small forward resistance [12]. The equivalent circuit of the PIN diode, shown in Figure 2, is used in the simulation.

The values of the elements of the equivalent circuits for simulation are given in Table 1. Lumped elements are used in modeling the PIN diode within CST Microwave Studio.

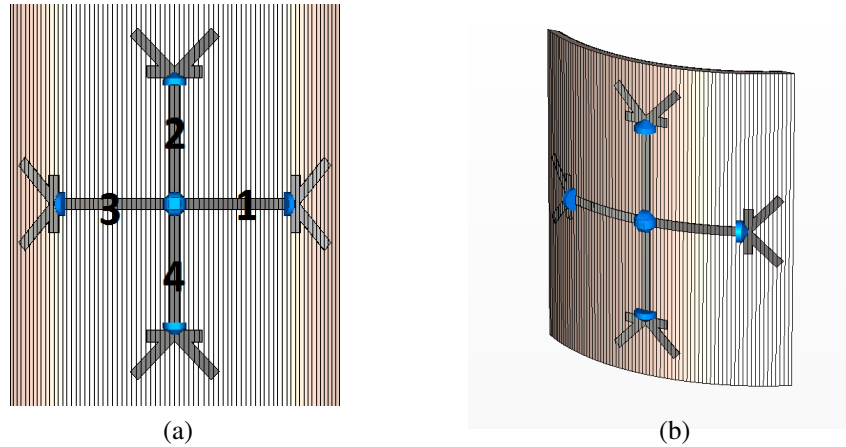


Figure 1: Designed antenna schematic. (a) Top view and (b) perspective.

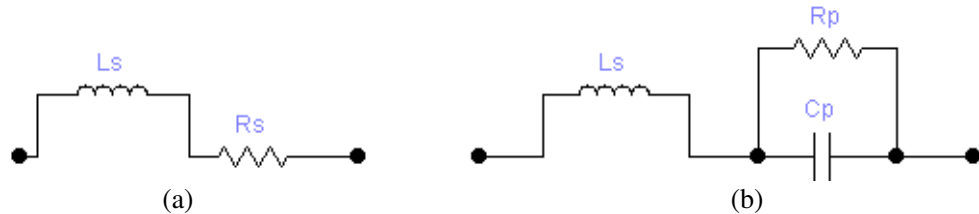


Figure 2: The equivalent circuits of the pin diode. (a) ON state, (b) OFF state.

Table 1: The values of the elements of the PIN diode simulation equivalent circuit.

Element	Value
Serial Inductance (L_s)	0.5 nH
Serial Resistance (R_s)	5 Ω
Parallel Resistance (R_p)	1 k Ω
Parallel Capacitance (C_p)	0.02 pF

3. SIMULATION RESULTS

The desired conformal reconfigurable fractal tree antenna is designed and simulated by using CST Microwave studio. By changing the diodes conditions, we alter on the characteristic of antenna and it results shifting in operating frequency and radiation pattern. By different combinations of diodes ON state or OFF state we have many different radiation patterns with different operating frequencies. When all eight diodes are ON state, antenna starts to operate at 2.89 GHz, 6.25 GHz and 8.17 GHz and return loss and radiation pattern ($\phi = 0$, turning about theta) is shown in Figure 3. In Figure 4, the diodes on the vertical axis become ON state and horizontal axis become OFF state, then opposite condition of this is shown ($\theta = 90$, turning about phi). In Figure 5, radiation patterns sequentially are shown while diodes are ON state between source to trunk and trunk to branch is showing separately for each trunk-branch couple. It can be seen that while the trunk is becoming ON or OFF state with branch, radiation direction is changing with 90 degree since there are 90 degree angles between trunks. In order to notice this situation we had a two-

Table 2: Compilation of results.

Mode	ON State Diodes	Resonant Frequency (GHz)	Max. Peak Gain (dBi)
I	D1t, D1b, D3t, D3b	2.52, 5.89, 8.4, 9.3	6.64
II	D3t, D3b, D4t, D4b	2.58, 5.7, 8.02, 9.5	4.51
III	D1t, D2t, D3t, D4t	4.32, 4.63, 7.59, 8.2	9.91
IV	D2t, D2b	2.29, 5.44, 8, 9.58	4.63
V	D1t	3.49, 4.91, 7.5, 8.33	6.09
VI	ALL	2.89, 6.25, 8.17	4.47

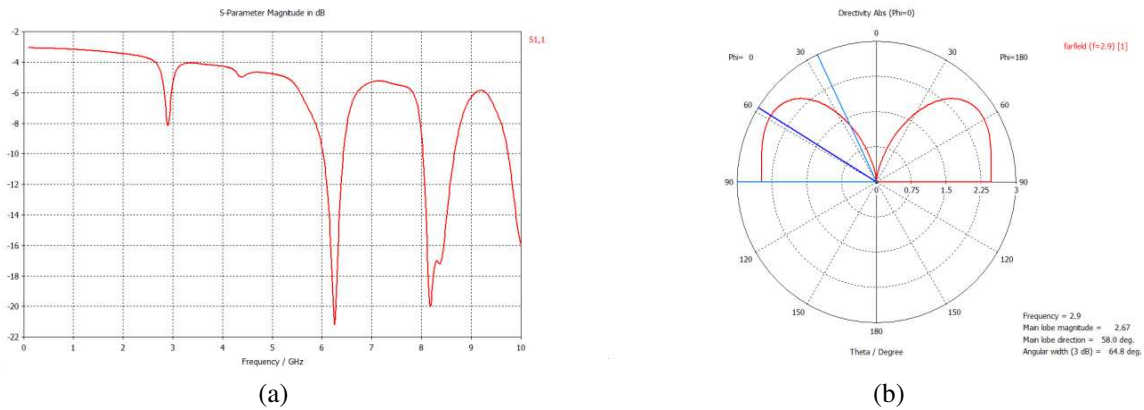


Figure 3: When all diodes are ON state. (a) Return loss and (b) radiation pattern at 2.9 GHz.

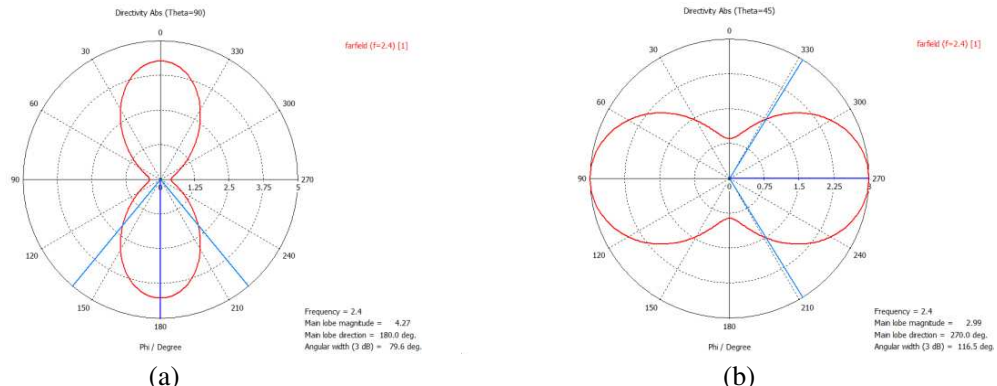


Figure 4: (a) Vertical diodes are ON and others are OFF state. (b) Horizontal diodes are ON state at 2.4 GHz.

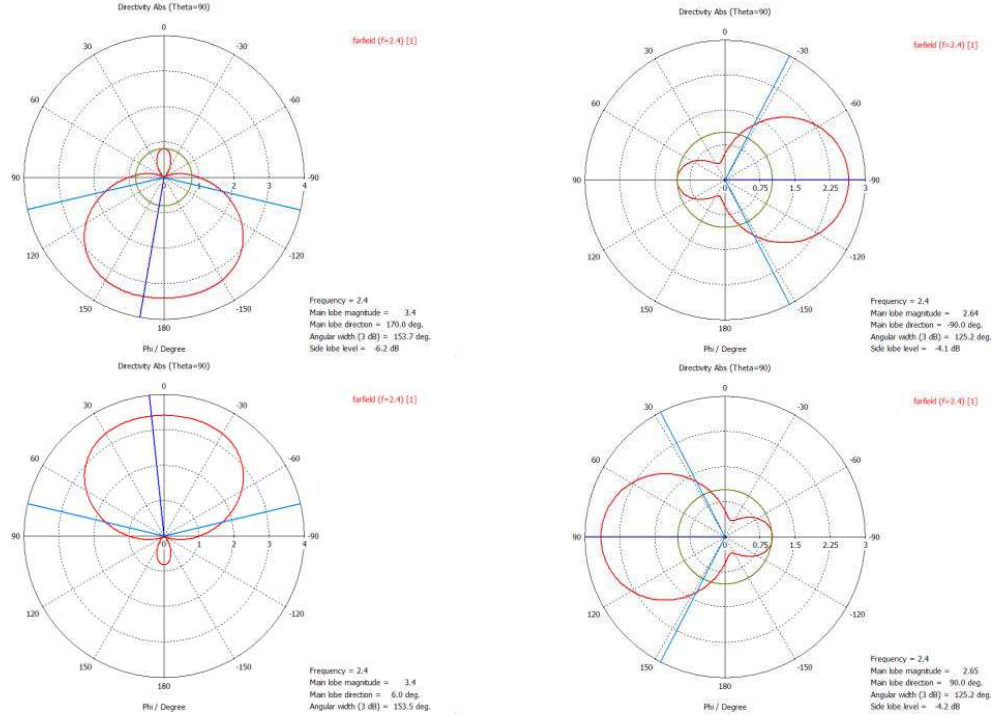


Figure 5: When diodes are ON between source to trunk and trunk to branch for each trunk-branch couple at 2.4 GHz.

dimension result which has the theta = 45 angle by turning about phi. By using this specification the radiation pattern side can be easily controlled by diodes. This feature can work properly in WiMAX (2.400–2.483) GHz and WLAN (5.15–5.825) GHz bands. Also, a detailed compilation of the results by using different combination are shown in Table 2.

4. CONCLUSIONS

In this paper a multiband frequency reconfiguration is studied by using of a conformal fractal tree antenna controlled by PIN diodes. The effect of the biasing lumped elements on the antenna performance is discussed based on the simulation results. PIN diodes reconfiguration causes frequency shift in the resonance frequency of the antenna and radiation pattern (side) can be controlled by changing PIN diodes state ON or OFF.

REFERENCES

1. Langoni, D., M. H. Weatherspoon, E. Ogunti, and S. Y. Foo, "An overview of reconfigurable antennas: Design, simulation, and optimization," *IEEE 10th Annual Wireless and Microwave Technology Conference 2009, WAMICON '09*, 1–5, 2009.
2. Zhang, J., A. Wang, and P. Wang, "A survey on reconfigurable antennas," *Microwave and Millimeter Wave Technology*, Vol. 3, 1156–1159, 2008.
3. Godara, L. C., *Handbook of Antennas in Wireless Communications*, CRC Press, New York, 2002.
4. Zhang, S., G. H. Huff, J. Feng, and J. T. Bernhard, "A pattern reconfigurable microstrip parasitic array," *IEEE Trans. Antennas Propag.*, Vol. 52, 2773–2776, Oct. 2004.
5. Dietrich, C. B., K. Dietze, J. R. Nealy, and W. L. Stutzman, "Spatial, polarization, and pattern diversity for wireless handheld terminals," *IEEE Trans. Antennas Propag.*, Vol. 49, No. 9, 1271–1281, Sept. 2001.
6. Nikolaou, S., B. Kim, and P. Vryonis, "Reconfiguring antenna characteristics using PIN diodes," *3rd European Conference on Antennas and Propagation 2009, EuCAP 2009*, 3748–3752, 2009.
7. Mandelbrot, B. B., *The Fractal Geometry of Nature*, W. H. Freeman, New York, 1983.
8. Petko, J. S. and D. H. Werner, "Miniature reconfigurable three-dimensional fractal tree antennas," *IEEE Transactions on Antennas and Propagation*, Vol. 52, No. 8, 1945–1956, 2004.

9. Puente, C., J. Claret, F. Sagües, J. Romeu, M. Q. Lopez-Salvans, and R. Pous, "Multiband properties of a fractal tree antenna generated by electrochemical deposition," *IEE Electron. Lett.*, Vol. 32, No. 25, 2298–2299, Dec. 1996.
10. Balanis, C. A., *Antenna Theory*, Wiley publications, 2005.
11. Lars, J. and P. Patrik, *Conformal Array Antenna Theory and Design*, Wiley-Interscience Publication, 2006.
12. Available: <http://www.alldatasheet.com/datasheet-pdf/pdf/301066/MA-COMCOM/MA4AGBLP912.html>.

Convergence and Sidelobe Suppression Properties of Array Antenna

James Jen, Meng Qian, Zekeriya Aliyazicioglu, and H. K. Hwang
 Electrical and Computer Engineering, California State Polytechnic University-Pomona
 3801 W. Temple Ave., Pomona, CA 91768, USA

Abstract— This paper investigates the performance of beam pattern forming employing the Minimax algorithm. The antenna beam pattern and its convergence rate depend on the relative weight and step size. The simulation results show the converging time of the array antenna is relatively insensitive to the relative weight and a fast step size decay rate speeds up the converging time. A 244 element nonuniformly spaced array antenna is used in this simulation study.

1. INTRODUCTION

One of the important antenna design criteria for communication application is to design a well defined antenna mainlobe and to suppress sidelobes as much as possible. For RF image mapping or radar applications, large sidelobes may result in unacceptable sidelobe clutter. For communication application, a low sidelobe helps to reduce the radio frequency interference (RFI). The antenna (as shown in Figure 1) used in this study is a non-uniformly spaced array with 244 elements. The inter-element spacing of this antenna equal 0.8λ , 1.6λ and 3.2λ respectively where λ is the signal wavelength. Since the inter-element spacing greater than half wavelength, this antenna has many grating lobes. For geo-synchronous application, the edge of the earth only corresponds to elevation angle of 8.7° . For elevation angle less than 9° , there are no grating lobes.

If all elements are weighted by the same constant, its antenna pattern is shown in Figure 2. The center of this plot corresponds to elevation angle equal to 0° . The edge of the plot corresponds to an elevation angle equal to 9° . The peripheral numbers around correspond to the azimuth angle. The 3 dB mainlobe beamwidth (MLBW) is 2.4° . The sidelobes decay slowly. It may create co-channel interference for the other users.

One way to speed up the sidelobe decay rate is to impose a window function to the element weights. For example, if the Hamming window applies to the weight tapering, its antenna pattern is shown in Figure 3. The 3 dB MLBW of this antenna is 3.3° . The sidelobe decay rate is still not fast enough.

Apply other window function does not significantly improve the sidelobe suppression. The sliced antenna plot at 0° azimuth angle for uniform weight Hamming and Chebyshev tapering weight are shown in Figure 4.

Figure 4 shows that the sidelobe level is not effectively reduced when applying the weight tapering. This is due to the fact that the array size is finite and we are only interested in elevation angles less than 9° .

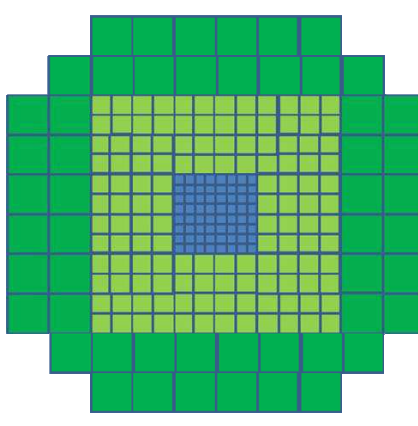


Figure 1: 244 Non-uniformly spaced array antenna.

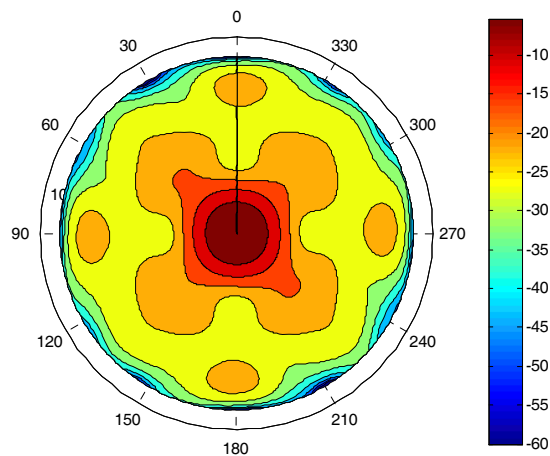


Figure 2: Antenna pattern with constant element weight.

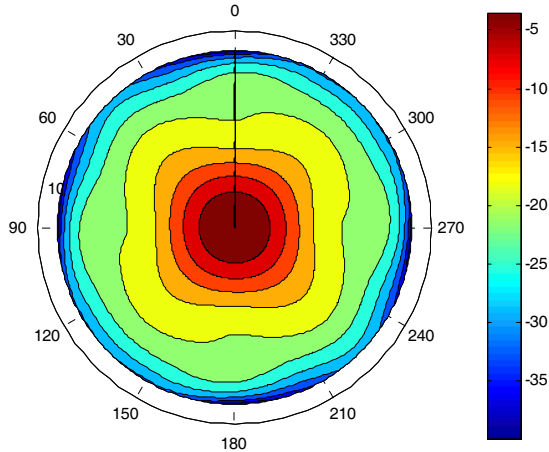


Figure 3: Antenna pattern with hamming tapering.

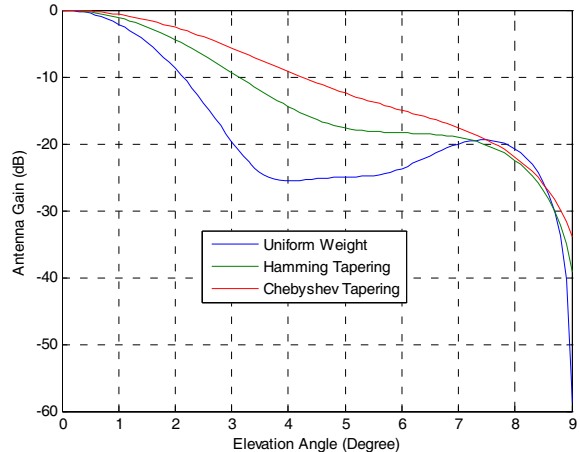


Figure 4: Sliced antenna pattern at 0° azimuth Angle.

There are many array antenna design algorithms [1–7]. One method to improve the antenna pattern is design the antenna using the Minimax algorithm [6–8]. The Minimax algorithm starts the element weight from a random state. It iteratively updates the element weights by reducing the maximum value of the cost function. The cost function is defined as the weighted difference of the antenna pattern for a given weights to the ideal antenna pattern. Details of the algorithm were discussed in [6].

2. COMPUTER SIMULATIONS

The antenna beam pattern and its convergence rate depend on the relative weight and step size. The relative weight is the ratio of weight for the cost function in the rejection and gain regions. Higher relative weight further suppresses the gain in the rejection region and increases the ripple in the gain region. To ensure the algorithm is properly convergent, Equation (1) defines the step size $\alpha(n)$ at the n th iteration.

$$\alpha(n) = \alpha(0)d^{n-1} \quad (1)$$

where d is the decay rate and $\alpha(0)$ is the initial step size. Initial step size $\alpha(0)$ is chosen to be 0.004.

Suppose that the ideal circular antenna MLBW is defined as 2°, and suppression as much as possible for elevation angle greater than 3°. Using the step size decay rate $d = 0.999$, and the relative weight = 100, the steady state antenna pattern is shown in Figure 5. Comparison of Figure 1 to Figures 2 and 3, it is clear that the Minimax algorithm provides a significantly improved antenna pattern.

The convergent curve is defined as the absolute maximum weighted cost as a function of iteration time. Figure 6 is the convergent curve for relative weight = 100 and $d = 0.999$. This curve shows that it takes approximately 6000 iteration for the algorithm to reach a steady state.

Table 1 summarizes the convergent time in number of iterations, the maximum and minimum gain in the mainlobe, and the maximum sidelobe gain as function of different step size decay factor d for relative weight = 100.

Antenna pattern performance for relative weights equaling 30 and 1 are shown in Table 2 and Table 3.

Tables 1, 2, 3 show that the best sidelobe rejection can be achieved by using a large relative weight and slow step size decay factor. However, with a large relative weight and slow step size decay factor, it takes longer iterations for the pattern to reach the steady state. One might suspect that further increasing the relative weight can further reduce the sidelobe gain. Table 4 shows the result of using the step size decay factor equal 0.999 and relative weight equal 100, 200 and 500.

Table 4 shows that with further increases in the relative weight beyond 200, additional sidelobe suppression is marginal. If one desires to have uniform gain within the antenna mainlobe, a large relative weight will introduce a higher ripple in the mainlobe. Proper choice of the relative weight depends on the tradeoff of allowable mainlobe ripple and the amount of sidelobe suppression. Figure 7 shows the sliced antenna plot as function of elevation angle. This is the sliced antenna

plot along the azimuth angle 0° . This plot shows that better sidelobe suppression can be achieved by using a larger relative weight; it also introduce a larger ripple in the mainlobe region.

Table 1: Antenna pattern performance for relative weight = 100.

d	Maximum Mainlobe Gain	Minimum Mainlobe Gain	Maximum Sidelobe Gain	Convergence Time
0.9	-0.10 dB	-2.71 dB	-28.41 dB	100
0.99	-0.16 dB	-3.10 dB	-32.44 dB	600
0.999	-0.13 dB	-2.81 dB	-35.30 dB	6000

Table 2: Antenna pattern performance for relative weight = 30.

d	Maximum Mainlobe Gain	Minimum Mainlobe Gain	Maximum Sidelobe Gain	Convergence Time
0.9	-0.25 dB	-3.20 dB	-27.11 dB	100
0.99	-0.11 dB	-2.90 dB	-30.03 dB	600
0.999	-0.07 dB	-2.90 dB	-32.92 dB	6000

Table 3: Antenna pattern performance for relative weight = 1.

d	Maximum Mainlobe Gain	Minimum Mainlobe Gain	Maximum Sidelobe Gain	Convergence Time
0.9	-0.05 dB	-3.11 dB	-19.58 dB	100
0.99	-0.02 dB	-3.05 dB	-23.00 dB	800
0.999	-0.01 dB	-3.02 dB	-26.75 dB	9000

Table 4: Antenna pattern performance for step size decay rate = 0.999.

Relative Weight	Maximum Mainlobe Gain	Minimum Mainlobe Gain	Maximum Sidelobe Gain	Convergence Time
100	-0.13 dB	-2.81 dB	-35.30 dB	6000
200	-0.02 dB	-3.05 dB	-45.92 dB	6000
500	-0.04 dB	-3.09 dB	-46.23 dB	5000

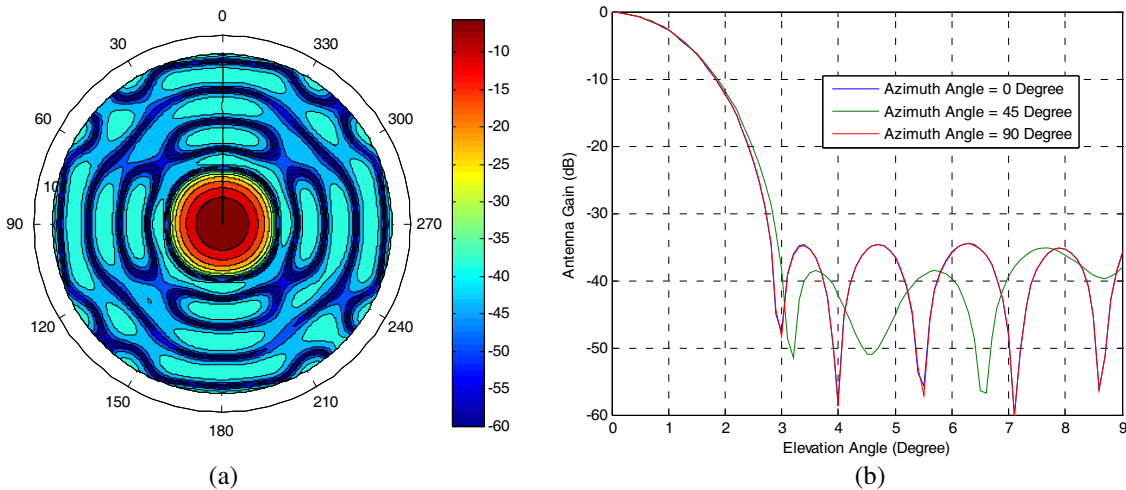


Figure 5: (a) Steady state antenna pattern. (b) Sliced antenna pattern.

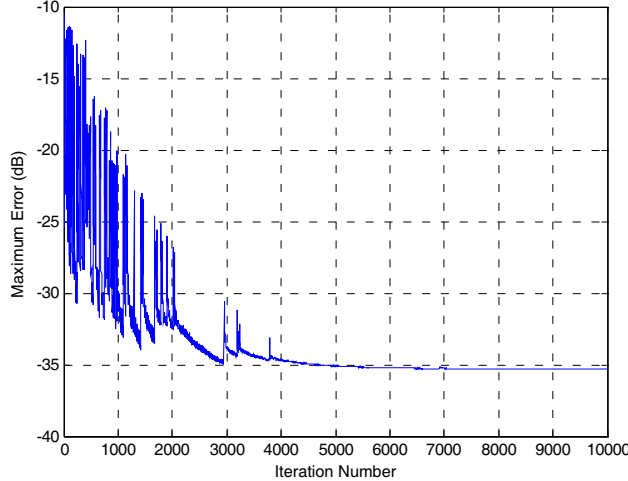
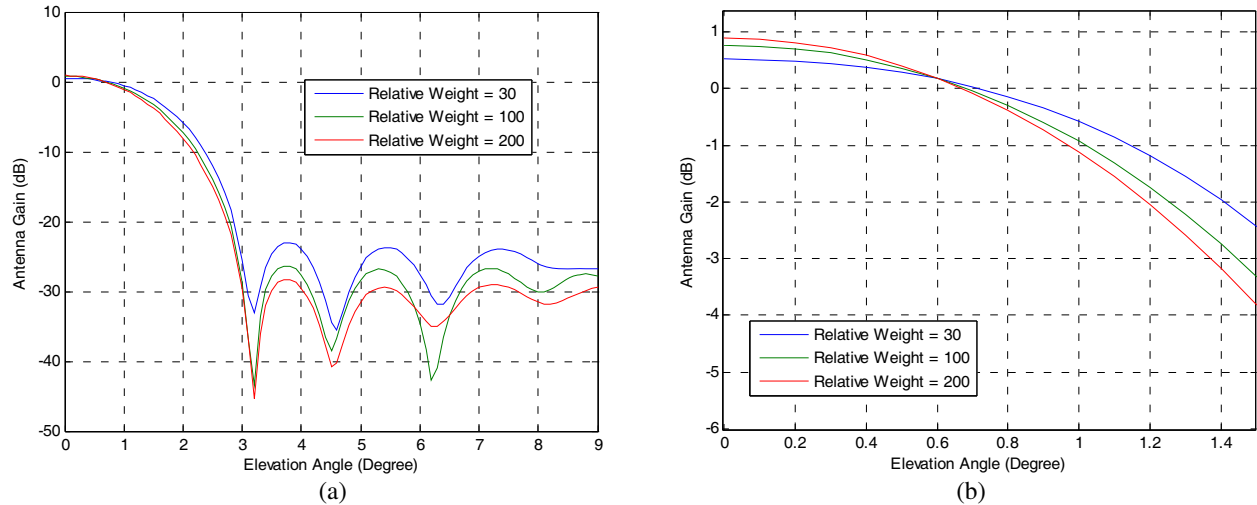
Figure 6: Convergent curve for $r_w = 100$, $d = 0.999$.

Figure 7: (a) Sliced antenna plot. (b) Sliced antenna mainlobe plot.

3. CONCLUSIONS

The conclusions based on the results of this simulation study are summarized as follows:

1. The converging time of the array antenna is relatively insensitive to the relative weight.
2. A fast step size decay rate speeds up the converging time.
3. Sidelobe rejection capability suffers either by reducing the relative weight or by using a faster step size decay factor.
4. For a 3 dB circular beam, sidelobe rejection improvement is marginal if the relative weight is greater than 200.
5. For an antenna mainlobe with uniform gain, the sidelobe rejection improvement also increases mainlobe ripple.

REFERENCES

1. Stutzman, W. L. and E. L. Coffey, "Radiation pattern synthesis of planar antennas using the iterative sampling method," *IEEE Transactions on Antenna and Propagation*, 1975.
2. Ares, F., S. R. Rengarajan, A. Vieiro, and E. Moreno, "Extension of orchards pattern synthesis technique for overdetermined systems," *IEEE*, 1995.
3. Schjaer-Jacobsen, H. and K. Madsen, "Synthesis of nonuniformly arrays using a generalized nonlinear minimax optimization method," *IEEE Transactions on Antenna and Propagation*, 1976.

4. Peters, T. J., "Application of conjugate gradient method to the synthesis of planar arrays," *Aerospace Technical Report*, No. TR-0090 (5925-05)-1, 1991.
5. Bhattacharyya, A. K., "Projection matrix method for shaped beam synthesis in phased arrays and reflectors," *IEEE Transactions on Antennas and Propagation*, March 2007.
6. Hwang, H. K. and R. Grados, "Antenna pattern design based on minimax algorithm," *AIAA International Communications Satellite Systems Conference*, 2008.
7. Hwang, H. K. and R. Grados, "Multibeam antenna and antenna beam shaping using the minimax algorithm," *AIAA International Communications Satellite Systems Conference*, 2008.
8. Madsen, K., "An algorithm for minimax solution of overdetermined systems of non-linear equations," *J. Inst. Matjs Applics*, 1975.

Stacked Coupled Circular Microstrip Patch Antenna for Dual Band Applications

Pradeep Kumar and Nitasha Bisht

Department of Electronics and Communication Engineering

Jaypee University of Information Technology, India

Abstract— In this paper, the design of stacked coupled circular microstrip antenna is presented for dual frequency operations. The two circular patches are isolated by a substrate. The lower patch is the feed patch and the upper patch is excited by the stacked coupling. The designed antenna is simulated and optimized using CST Microwave Studio simulator. The designed antenna produces two resonances at 3.4233 GHz and 3.7395 GHz. The radiation pattern of the designed antenna is also shown. The designed antenna produces the broadside radiation pattern.

1. INTRODUCTION

For light weight applications, such as in missiles, aircraft, aerospace, mobile handset, etc., microstrip antennas are the most suitable antennas [1, 2]. Microstrip antennas have various advantages and disadvantages over other antennas such as small size, low cost, easy to fabricate, and low gain, narrow bandwidth respectively [3]. In various applications, dual-frequency bands are desirable [4]. Dual-frequency microstrip antennas have the advantages for doubling the system capacity of transmission and reception [5]. In [6], using E-shape patch and U-shape patch, the antenna is designed for dual band applications. The dual operation frequencies are 4.7 GHz and 5.4 GHz. In [7], a dual band microstrip antenna has been proposed; the proposed antenna consists of a microstrip patch with a U-shaped slot that is fed by a broadband electromagnetic coupling probe, known as L-probe. In [8], authors have designed a U-shaped dual frequency microstrip antenna for wireless communication. In [9], the concept of slot loading along with a superstrate is used and the microstrip antenna is designed for dual frequency operation. In [10], authors have presented the cavity-model based simulation tool along with the genetic optimization algorithm for the design of dual-band microstrip antennas. Multiple slots in the patch or multiple shorting strips between the patch and the ground plane are used. The optimization of the positions of slots and shorting strips is performed via a genetic optimization algorithm, to achieve an acceptable antenna operation over the desired frequency bands.

In this paper, stacked coupled microstrip antenna is designed for dual band applications. The designed antenna generates two resonances at 3.4233 GHz and 3.7395 GHz. The radiation and the total efficiency of the designed antenna are 0.9784 and 0.9481 respectively. The organization of the rest of the paper is as follows: The geometrical configuration of the designed antenna is discussed in Section 2. Section 3 discusses the simulated results with discussion. Finally, Section 4 concludes the work.

2. ANTENNA CONFIGURATION

The geometrical configuration of the proposed stacked coupled microstrip antenna is depicted in Fig. 1. Two microstrip circular patches are isolated by the substrate as shown in Fig. 1. The lower microstrip circular patch is the feed patch and excited by the probe feeding technique. The upper circular metallic patch is excited by the coupling. The radius of both patches is ‘ r ’. The thickness, the dielectric constant of the lower and upper substrate are ‘ $H1$ ’, $\epsilon r1$ and ‘ $H2$ ’, $\epsilon r2$ respectively.

Table 1: Dimensions of the proposed antenna.

Radius of upper patch (mm)	Radius of lower patch (mm)	Thickness of upper the substrate (mm)	Dielectric constant of the upper substrate	Thickness of the lower substrate (mm)	Dielectric constant of the lower substrate	Thickness of the upper patch (mm)	Thickness of the lower patch (mm)
15	15	1.4	2.2	1.59	2.2	0.01	0.01

3. RESULTS AND DISCUSSION

The designed stacked coupled circular microstrip antenna is simulated using Finite element based CST microwave studio software. The designed stacked coupled microstrip antenna is optimized

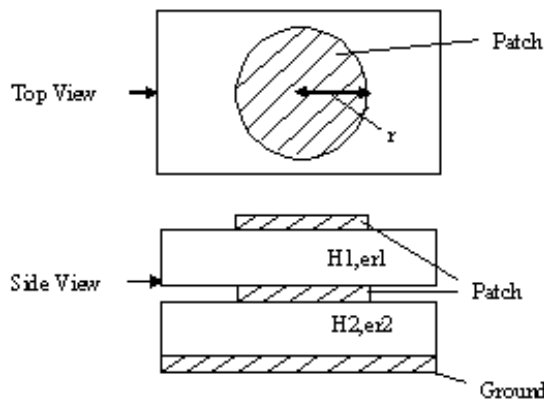


Figure 1: Geometrical configuration of stacked coupled circular microstrip antenna.

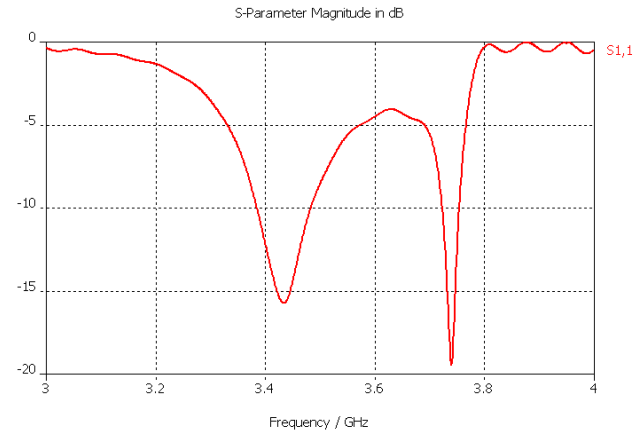


Figure 2: Return loss of the proposed antenna.

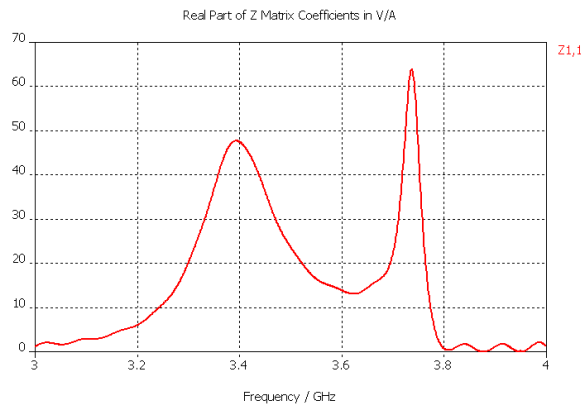


Figure 3: Real part of the input impedance.



Figure 4: Imaginary part of the input impedance.

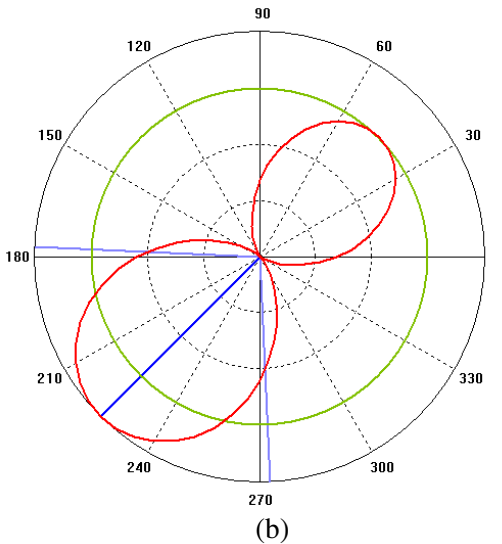
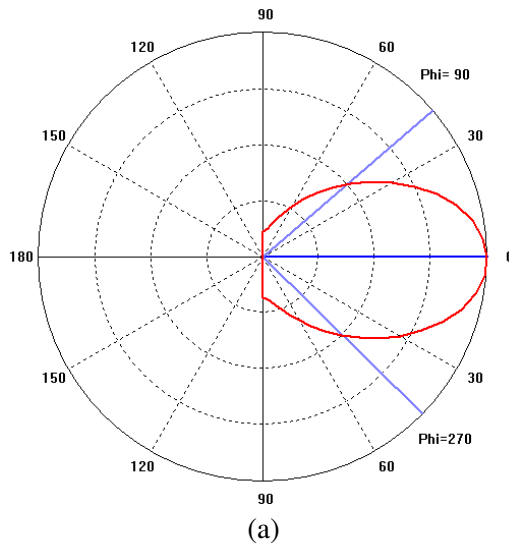


Figure 5: Radiation pattern of the designed antenna at 3.4233 GHz, (a) theta plane, (b) phi plane.

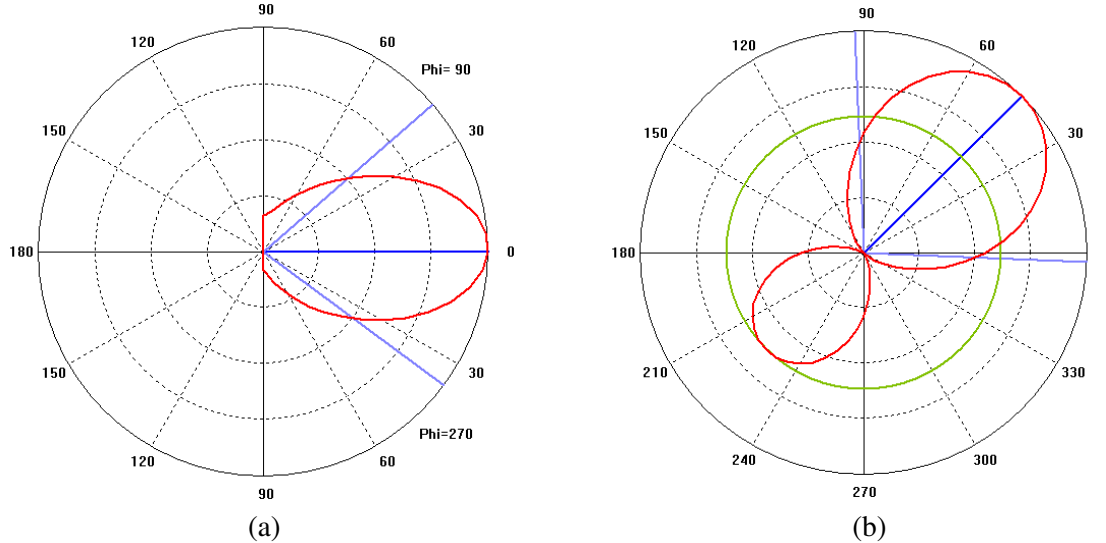


Figure 6: Radiation pattern of the designed antenna at 3.7395 GHz, (a) theta plane, (b) phi plane.

using CST microwave studio. The dimensions of the optimized simulated model is given in Table 1. The return loss of the designed stacked coupled microstrip antenna is shown in Fig. 2. From this figure, it can be observed that the designed antenna produces two resonances at 3.4233 GHz and 3.7395 GHz. For both resonances the return loss is less than -10 dB, so the designed antenna can be used for both bands. The real and imaginary part of the input impedance of the designed antenna is shown in Fig. 3 and Fig. 4 respectively.

The simulated radiation pattern of the designed antenna for first resonance, i.e., at 3.4233 GHz is shown in Fig. 5. The designed antenna produces broadside radiation pattern. The radiation and the total efficiency is very high, i.e., 0.9764 and 0.9481 respectively. The directivity of the antenna at 3.4233 GHz is 5.073 dB. The simulated radiation pattern of the designed antenna for second resonance, i.e., at 3.7395 GHz is shown in Fig. 6. The designed antenna produces broadside radiation pattern. The radiation and the total efficiency is 0.7960 and 0.7867 respectively. The directivity of the antenna at 3.7395 GHz is 5.563 dB.

4. CONCLUSION

In this paper, a stacked coupled circular microstrip antenna has been designed. The designed microstrip antenna is optimized using FDTD based CST Microwave simulator. The designed stacked coupled microstrip antenna produces two resonances at 3.4233 GHz and 3.7395 GHz respectively. The designed stacked coupled circular microstrip antenna generates broadside radiation pattern. The efficiency of the designed antenna is very high. The radiation efficiency up to 0.9764 and the total efficiency upto 0.9481 is achieved. The designed stacked coupled circular microstrip antenna can be used for dual frequency applications.

REFERENCES

1. Garg, R., P. Bhartia, I. Bahl, and A. Ittipiboon, *Microstrip Antenna Design Handbook*, Artech House Publishers, Boston, London, 2001.
2. Balanis, C. A., *Antenna Theory: Analysis and Design*, Wiley, 2005.
3. Kumar, P., A. K. Singh, G. Singh, T. Chakravarty, S. Bhooshan, S. K. Khah, and A. De, "Numerical computation of resonant frequency of gap coupled circular microstrip antennas," *Journal of Electromagnetics and Applications*, Vol. 21, No. 10, 1303–1311, 2007.
4. Islam, M. T., N. Misran, and A. T. Mobashsher, "Compact dual band microstrip antenna for Ku-band application," *Information Technology Journal*, Vol. 9, No. 2, 354–358, 2010.
5. Shynu, S. V., G. Augustin, C. K. Aanandan, P. Mohanan, and K. Vasudevan, "Design of compact reconfigurable dual frequency microstrip antennas using varactor diodes," *Progress In Electromagnetics Research*, Vol. 60, 197–205, 2006.

6. AbuTarboush, H. F. and H. S. Al-Raweshidy, "A connected E-shape and U-shape dual-band patch antenna for different wireless applications," *The Second International EURASIP Workshop on RFID Technology (EURASIP'08)*, Budapest, Hungary, July 7–8, 2008.
7. Ghalibafan, J., A. R. Attari, and F. H. Kashani, "A new dual-band microstrip antenna with U-shaped slot," *Progress In Electromagnetics Research C*, Vol. 12, 215–223, 2010.
8. Singh, V. K. and Z. Ali, "Dual band U-shaped microstrip antenna for wireless communication," *International Journal of Engineering Science and Technology*, Vol. 2, No. 6, 1623–1628, 2010.
9. Krishna, D. D., M. Gopikrishna, C. K. Aanandan, P. Mohanan, and K. Vasudevan, "Compact dual band slot loaded circular microstrip antenna with a superstrate," *Progress In Electromagnetics Research*, Vol. 83, 245–255, 2008.
10. Ozgun, O., S. Mutlu, M. I. Aksun, and L. Alatan, "Design of dual-frequency probe-fed microstrip antennas with genetic optimization algorithm," *IEEE Trans. on Antennas and Propagation*, Vol. 51, No. 8, 2003.

The Use of RBF Based on Ant Colony Algorithm and Fisher Ratio for Eddy Current Nondestructive Detecting System

Xiaoyun Sun¹, Donghui Liu², and Aihua Li³

¹College of Electrical and Electronics Engineering, Shijiazhuang Tiedao University, Shijiazhuang, China

³College of Electrical Engineering and Information Science, Hebei University of Science and Technology
Shijiazhuang 050018, China

²Department of Electrical Engineering, Mechanical Engineering College, Shijiazhuang 050003, China

Abstract— The RBF network based on ant colony algorithm and Fisher ratio algorithm is used for eddy current nondestructive detecting. Due to the singleness of traditional center algorithm of RBF, it's hard to obtain a simply structure and precise results. A new algorithm which combines ant colony algorithm and Fisher ratio algorithm is adopted to optimize RBF network. The simulation result shows that the RBF structure is simplified strongly, the robustness is improved. Contrast with single ant colony algorithm, this method has much better recognition effect.

1. INTRODUCTION

Owing to the advantages of quick detecting and sensitive to surface defects, eddy current nondestructive detecting technology has been widely used in axis pressure instruments, nucleus equipments, pipelines and so on. At present, eddy current nondestructive detecting based on electromagnetic induction theory has developed greatly. It can be used for many parameters detecting which can change impedance. Because not all the defects are dangerous to the equipment running, so it's necessary to evaluate hazard. Now the shape and position of defects are widely used to solve these problems [1].

Due to the difficulty of recognizing defect, an inverse problem which is quantitative of eddy current nondestructive detecting is also difficult in this area. Many artificial intelligence methods show many advantages in recognizing defects, RBF network is one of them [1–3]. To a large extent, the center neurons determine the network performance. Now the algorithm to ascertain centers is so single that the converge speed and the training accuracy are difficult to keep balance. And it's hard to obtain the most optimal centers and width. So a new algorithm which combines ant colony algorithm with Fisher ratio is adopted to optimize RBF network.

2. RBF NEURAL NETWORKS

RBF includes input layer, hidden layer and output layer. It is a forward network based on the approaching theory of function. The training process is to find the optimal fitting model of training samples in multidimensional space. It's a regularization method. RBF neural network training is divided into two parts: First, the selection of RBF centers and width. Second, the estimation of the weight [3]. The center function is Gaussian function:

$$v(x) = \exp \left[-\frac{\|x - c_i\|^2}{2\sigma_i^2} \right] \quad i = 1, 2, \dots, k, \dots, N \quad (1)$$

where, x is d dimension input vector. c_i denotes network center, σ_i^2 denotes width, N refers to number of hidden nodes, $v_i(x)$ is output of i th node. σ_i^2 denotes width.

The output is

$$y[x(k)] = \sum_{i=1}^N \omega_i v_i(k) + b \quad (2)$$

where, ω_i is weight. b is a constant.

3. RBF CENTER SELECTION BASED ON ANT COLONY ALGORITHM AND FISHER RATIO ALGORITHM

3.1. Ant Colony Algorithm

Ant colony algorithm (ACA) is a novel bionic evolutionary algorithm inspired by the foraging behavior of real ant colonies. The positive feedback mechanism is adopted. It has good characteristics

of greed searching, robustness, distributed computing and Combining with other algorithms easily. These ants deposit pheromone on the ground in order to mark some favorable path that should be followed by other members of the colony. In the search process, it is easy to obtain the global optimization [4, 5].

The basic idea of ant colony algorithm is as follows: An ant leaves some pheromone on ground when it travels and marks the path by a trail of this substance. The pheromone would evaporate at a certain rate as time goes on. The next ant will smell the pheromone remained on different paths and chooses one with a probability proportional of the pheromone. The ant that follows the path will leave its own pheromone. This pheromone is considered as a positive feedback process which could be treated as knowledge sharing through collaborative efforts. Based on previous knowledge, ants progressively construct their paths. The best path reported by this algorithm is a shortest or optimal path [6, 7].

3.2. Fisher Ratio Algorithm

Fisher ratio linear discrimination algorithm designs a map from low dimension to high dimension using classification information of training samples [8]. It not only simplifies classification procession, but also can get especially penetrating cognition to every class separation. Now it widely applies in pattern recognition [9]. Fisher ratio algorithm can be consulted in reference [3].

3.3. RBF Center Selection Based on Ant Colony Algorithm and Fisher Ratio Algorithm

The basic idea of RBF center selection divides into two parts. At first, obtain initial centers using ant colony algorithm [10]. Then, optimize RBF network using Fisher ratio algorithm [3, 8]. Take the centers obtained from step 1 as the initial centers of Fisher ratio algorithm. Then train RBF network. At last a simplified and optimal RBF network structure is obtained.

The center selection procedure using ant colony algorithm and fisher ratio algorithm is summarized as follows.

Step 1: Take all the training examples as candidate centers (c_1, c_2, \dots, c_N). The number of ants is N . The empirical value of transfer probability is $p_0 = 0.7$. Initial iterative times is $NT = 0$, the maximum iterative times is NT_{\max} .

Step 2: Calculate the distance d_{ij} between class c_i and class c_j .

$$d_{ij} = \left\| \overline{X^{(c_i)}} - \overline{X^{(c_j)}} \right\| = \sqrt{\sum_{k=1}^n (\overline{X^{(c_i)}} - \overline{X^{(c_j)}})^2} \quad (3)$$

$$\overline{X^{(c_i)}} = \frac{1}{N} \sum_{k=1}^{N_i} X_k (X_k \in c_i) \quad (4)$$

$X^{(c_i)}$ is the clustering center vectors. c_i includes N_i samples.

Step 3: Calculate pheromone $\tau_{ij}(t)$. Assuming the initial pheromone on the path from x_i to $c_j(k)$ is

$$\tau_{ij} = \begin{cases} 1, & d_{ij} \leq r \\ 0, & d_{ij} > r \end{cases}$$

where, $r = d_{\min} + (d_{\max} - d_{\min}) * 0.5$, $d_{\max} = \min(d_{ij})$, $d_{\min} = \max(d_{ij})$.

Step 4: Calculate transfer probability from x_i to x_j .

$$P_{ij} = \frac{\tau_{ij}}{\sum_{j=1}^n \tau_{ij}} \quad (5)$$

If $P_{ij}(t) \geq P_0$, x_i mergers to class x_j . The class number subtracts 1.

Step 5: Computing d_{ij} between each sample and new centers, renovate ρ_t according to formula (6)

$$\rho_t = \begin{cases} 0.9\rho_{t-1}, & 0.9\rho_{t-1} \geq \rho_{\min} \\ \rho_{\min}, & \rho_{\min} \end{cases} \quad (6)$$

ρ is attenuation coefficient, in order to avoid the pheromone from increasing infinitely, usually $\rho < 1$. Here $\rho_{t0} = 0.9$, ρ_{\min} is the minimum of ρ .

Table 1: Structure comparasion between ACA and ACA & fisher ratio.

Parameters	ACA	ACA & Fisher
Center numbers	21	10

Renovate $\tau_{ij}(t)$ using new ρ ,

$$\tau_{ij}^{new} = \rho\tau_{ij}^{old} + \frac{Q}{1 + d_{ij}} \quad (7)$$

Step 6: The procedure continues until no merger or attain the maximum iterative times. Otherwise return to step 4.

Step 7: Take the centers got by ant colony algorithm as initial cluster centers for Fisher ratio algorithm, the optimal centers M is gotten according to reference [3].

Step 8: Computing the width $\sigma_i = \frac{d_m}{\sqrt{2M}}$, d_m is the maximum distance among all the centers.

Step 9: Solving w_{ij} using least mean square (LMS) algorithm.

4. APPLICATION IN EDDY CURRENT NONDESTRUCTIVE DETECTING

The samples derived from defect of plate crack in eddy current nondestructive detecting system. Take length training as an example, RBF input vector are amplitude and phase of the crack impedance increment [3]. There are 45 groups of training samples. Length range is 16 ~ 30 mm. 11 groups of testing samples is 4 mm deep with different length. There are no same samples between testing samples and training samples.

Ant colony algorithm/fisher ratio algorithm together (ACA&Fisher) and single ant colony algorithm (ACA) are used respectively to simulate the problems above (shown in Table 1).

In ant colony algorithm, the network structure is $8 \times 21 \times 1$; In ACA&Fisher algorithm, the network structure is $8 \times 1 \times 1$. In Fisher ratio algorithm, the given value is 1% of the sum of class separability of all previous selected neurons. From Table 1, we can see that, the network structure is simplified by ACA & Fisher algorithm, it has better robustness.

5. CONCLUSION

An improved RBF network based on ant colony algorithm and Fisher ratio algorithm is applied in eddy current quantitative detecting. First, compute RBF initial centers and basis function width according to the advantages of ant colony algorithm such as the parallel optimization characters and self-adaptive changing attenuation coefficient; second Optimizing RBF network with the advantages of Fisher ratio algorithm such as quick training and better clustering. The results show that the network structure is simplified strongly, the robustness is improved. Contrast with ant colony algorithm, this method has much better recognition effect.

REFERENCES

1. Zhang, S., T. Chen, G. Liu, et al., "Natural crack profile reconstruction using eddy current technique and neural network," *Nondestructive Testing*, Vol. 30, No. 5, 280–284, 2008.
2. Zhang, S., T. Chen, G. Liu, et al., "Reconstruction of natural crack shapes from the ECT signals by using an artificial neural network based forward model and ant colony optimization algorithm," *Science Technology and Engineering*, Vol. 8, No. 6, 1545–1549, 2008.
3. Sun, X., D. Liu, and A. Li, "The use of RBF based on fisher ratio for eddy current nondestructive detecting system," *Nondestructive Testing*, Vol. 12, No. 30, 892–894, 905, 2008.
4. David, M., M. de Backer, R. Haesen, et al., "Classification with ant colony optimization," *IEEE Transactions on Evolutionary Computation*, Vol. 5, 651–665, 2007.
5. Marco, D., B. Mauro, and S. Thomas, "Ant colony optimization," *IEEE Computational Intelligence Magazine*, Vol. 1, No. 4, 28–39, 2006.
6. Dorigo, M. and L. M. Gambardella, "Ant colony system: A cooperative learning approach to the traveling salesman problem," *IEEE Transactions on Evolutionary Computation*, Vol. 1, No. 1, 53–66, 1997.
7. Wu, F. and Y. Zhao, "Radial basis function neural network based on ant colony clustering," *Journal of Xi'an Jiaotong University*, Vol. 40, No. 4, 386–389, 2006.
8. Mao, K. Z., "RBF neural network center selection based on fisher ratio class separability measure," *IEEE Trans. Neural Networks*, Vol. 13, No. 5, 1211–1217, 2002.

9. Yin, J., M. Yang, and J. Wan, "A kernel fisher linear discriminated analysis approach aiming at imbalanced data set," *Pattern Recognition and Artificial Intelligence*, Vol. 23, No. 3, 2010.
10. Lin, X., X. Wang, Z. Wang, et al., "Traffic flow forecasting based on ant colony clustering algorithm and RBF neural network," *Journal of Hebei University of Technology*, Vol. 39, No. 3, 42–45, 2010.

Multi-sensor Data Fusion System for Enhanced Analysis of Deterioration in Concrete Structures

Othman Sidek, Shahid Kabir, and S. A. Quadri

Collaborative μ -electronic Design Excellence Centre (CEDEC)
Engineering Campus, Universiti Sains Malaysia (USM), Penang, Malaysia

Abstract— Multisensor data fusion provides significant advantages over single source data. The use of multiple types of sensors plays an important role in achieving reasonable accuracy and precision. A novel integrated heterogeneous multi sensor data fusion approach in structural health monitoring is proposed. The study concerns to find a simple and affordable monitoring strategy for Alkali-aggregate reaction (AAR), which is one of the root causes for structural deterioration in concrete. Many researchers have stated the process of gradual structural deterioration to be very complicated because of the random distribution of aggregate, the arising and growth of concrete crack shows remarkable abnormality and discontinuity. Although researchers have developed several test methods to identify potential reactivity of aggregate. There is no universally valid standard testing method for all cases of AAR. The conventional methods namely petrographic examinations, expansion tests, and chemical analyses are cost expensive and require high skilled person to carry out tests. More over they qualitatively determine the possibility of AAR presence but least quantitatively predict whether the AAR will be deleterious. In order to develop a monitoring strategy for AAR in small size concrete structures, it is necessary to simulate the AAR expansion and cracking within reasonable laboratory timescale. A standard method to accelerate AAR expansion is employed on four samples which are prepared with different level of alkali concentrations. Different sensor systems are used at surface and internal level. Acoustic sensor system, electro-mechanical system, optical systems are employed to obtain surface level damage. The internal level of damage is obtained by embedded sensors within the structure. Features extracted from heterogeneous sensors are fed to Decentralized Kalman filter. The fused global estimates and individual source estimates are fed to artificial neural network (ANN), which characterize and quantify the level of damage. The research is focused on establishing correlation among surface damage level, internal damage level and the amount of gel concentration in the structure. To emphasize the expected improved accuracy using data fusion, evaluations are done on efficiency and accuracy of single source data system comparing with the fused heterogeneous data.

1. INTRODUCTION

In recent years, structural health monitoring (SHM) has been an important research area for designing and evaluating reliability of civil engineering structures. SHM is a system, where different kinds of sensors are put in a structure to make it have the ability to sense its structural integrity under various load and environmental conditions. To investigate both local and global damage, a dense array of sensors is anticipated to be required for large-scale civil engineering structures. The type of the sensors is chosen according to the objective of the specific SHM system, and these sensors are then mounted in the structure to measure the static or dynamic structural response.

The study is focused on developing efficient, reliable and affordable monitoring strategy for aging concrete structures which are suffering deterioration from AAR reaction.

Alkali-aggregate reaction is a chemical reaction between the alkali in Portland cement and reactive minerals in aggregate and additives that takes place when moisture is present. This reaction results in the formation of a hygroscopic gel that absorbs water and expands, causing significant expansion and characteristic cracking of the concrete and ultimately failure of the concrete in worst cases.

Mass concrete hydraulic structures such as dams, weirs, locks, and canals come directly in contact with water and water pressure which acts as catalyst in AAR expansion process. AAR problems in mass concrete of hydraulic structures may be considered more serious as they exclusively suffer from AAR problem; moreover they are usually expected to be operational for a long time, owing to their importance, extent, high costs, and long construction periods. Many concrete dams and other hydraulic structures worldwide have suffered from AAR [1]. Construction engineers and real estate owners are demanding better methods of assessing the AAR reaction in structures in order to provide preventive maintenance.

Failures are often addressed after they occur, i.e., by reactive maintenance. This approach is undesirable based on health and environmental considerations, but is often the default practice due to economic and technical considerations. Preventive maintenance, rehabilitation, and replacement are practiced where feasible; however, this is hampered by the difficulty of accessing the system and efficiently inspecting it.

These difficulties can potentially be addressed through the implementation of smart systems. Smart Systems are defined as miniaturized devices that incorporate functions of sensing, actuation and control. They are capable of describing and analyzing a situation, and taking decisions based on the available data in a predictive or adaptive manner, thereby performing smart actions. An ideal, smart system has capability to detect, locate and quantify any change in the structural integrity of the object under study.

With the development of the technologies in sensing, Micro-Electro-Mechanical Systems (MEMS) researchers and developers have demonstrated an extremely large number of micro sensors for almost every possible sensing modality. MEMS based sensors having low installation costs; more reliability and reasonable accuracy have attracted more attention in SHM of civil structures. The paper proposes an affordable monitoring strategy for AAR affected concrete structures using integrated heterogeneous multi sensors.

2. PREVIOUS WORK

In recent years, multi-sensor data fusion method attracts increasing interest to SHM due to its inherent capabilities in extracting information from different sources and integrating them into a consistent, accurate and intelligible data set [2, 3]. Data fusion techniques can combine data from multiple information sources and related information from associated databases to achieve improved accuracies and more specific inferences than by the use of a single source alone. Researchers are engaging in the study of damage identification methods using data fusion techniques to achieve improved accuracies and more specific inferences.

Guo and Zhang [4] and Guo [5] regarded the changes of frequencies and mode shapes as two different information sources and used the data fusion method to detect the damage of two-dimensional truss structures. Basir and Yuan [6] described a multi-sensor implementation of an evidence theory based engine diagnostic system. Bao and Li [7] employed the D-S evidence theory and Shannon entropy to decrease the uncertainty and improve the accuracy of damage identification. Yang and Kim [8] presented an approach for fault diagnosis in induction motors using D-S theory. Guo and Li [9] presented a two-stage method of determining the location and extent of multiple structural damages by using the data fusion technique and genetic algorithm. Shao-Fei Jiang et al. [10] presented 5-phase complex structural damage detection method by integrating data fusion and probabilistic neural network (PNN). In order to demonstrate the capability of the proposed method, a 4-story benchmark framed structure proposed by the American Society Of Civil Engineers (ASCE) Task Group on Health Monitoring was validated by numerical simulation [11]. To extract feature parameters and produce the samples for training and testing, wavelet base function $\psi(t)$ was employed.

Zhao et al. [12] proposed weighted fusion damage index, based on the D-S evidence theory. Weighted fusion damage indices were calculated from data of piezoceramic-based smart aggregates used in the structural health monitoring. Transducers' location information is considered into the approach to improve the damage identification results. A two-story concrete frame instrumented with piezoceramic-based smart aggregates is fabricated as the object for the structural health monitoring test. The experimental result showed that the proposed weighted fusion damage index can detect the severity of the cracks.

The proposed approach is novel of its kind as heterogenous sensors are employed at surface and internal level to study the damage phenomena and evaluate the changes in structural integrity due to AAR reaction. The evaluation of single source damage sensor will be inferior as compared to fused data from heterogeneous damage sensors as it obtains maximum information from multiple sources regarding defect location and characterization. Acoustic sensor system, electro-mechanical system, optical systems are employed to obtain surface level damage. The internal level of damage is obtained by embedded sensors within the structure.

3. RESEARCH METHODOLOGY

3.1. NBRI Test

In order to study the affect of AAR on concrete structures it is necessary to simulate the AAR expansion and cracking within reasonable laboratory timescale. A large number of ultra-accelerated test procedures, for determining the potential alkali reactivity of aggregates, have been developed, particularly in the past 15 years. An ultra-accelerated test method is defined as one which yields results within a few days or; at most, a few weeks. There are two possible selecting criteria for testing aggregates. In the first, testing should be done under severe conditions that will hopefully detect any potentially expansive aggregate. The other is testing under moderate accelerating conditions. We are adopting the second testing criteria as the former method is expensive and requires experts to carry out the procedure. Because of the lengthy lead time required to evaluate adequately aggregate sources for potential alkali-aggregate reactivity, we are using National Building Research Institute (NBRI) standard accelerated method proposed by Oberholster and Davies [13]. Four different samples of concrete bars measuring $160 \times 40 \times 40$ mm are prepared using NBRI standard testing method. Depending on the mixture of alkali concentrations, the four samples prepared are 1) Non reactive 2) Marginal reactive 3) Moderately reactive and 4) Very reactive.

3.2. Integrated Multi Sensor Data Fusion Approach

The methodology adopted is to obtain data from four different systems namely acoustic system, electro mechanical, optical system and embedded sensors and fuse them in order to get more accuracy as compared with the conventional single source sensor systems.

Pulse-echo is one of the simple and oldest acoustic methods for nondestructive evaluation of concrete and masonry. In pulse-echo technique the pulse propagates through the medium and is reflected by material defects or by interfaces between regions of different densities. Thus the deterioration of test object is estimated by change in the velocity of reflected wave. These reflected waves, or echoes, are monitored by a second transducer coupled to the surface of the test object near the pulse source. The transducer output is displayed on an oscilloscope or similar device.

To obtain information from electro mechanical system, low cost and simple, linear variable displacement transformer (LVDT) and an analog data logger were selected for the experiments. Two LVDT sensors are fixed at either side of the specimen. The expansion in terms of displacement is calibrated as change in voltage at the data logger output device. In order to obtain optical information, charge coupled device (CCD) camera is used. CCD is an apparatus which is designed to convert optical brightness into electrical amplitude signals.

In order to obtain the internal dynamic changes due to AAR expansion in the specimen, two PZT piezoelectric sensors are embedded into the mortar specimens. Polymer based waterproof material is used for encapsulation. Impedance analyzer is used to test the electric impedance of PZT piezoelectric sensor. The local rigidity of the mortar specimen decreases with increase in the crack depth, which causes decrease in systemic resonance frequency and increases systemic impedance value. Systemic impedance value under different frequency ranges is collected and analyzed by impedance analyzer.

The challenge for data fusion is to merge heterogeneous data from acoustic system, electro-mechanical system, optical system and embedded sensors in an efficient way to increase the accuracy and consistency of the acquired data. After the data-acquisition step in these four systems, the data is subjected to data cleansing process. Data cleansing is the process of selectively choosing data to accept for, or reject from, the feature selection process. The data-cleansing process is usually based on knowledge gained by individuals directly involved with the data acquisition. Local Kalman filter is used to accomplish the data-cleansing process. The area of the structural damage-detection process that receives the most attention in the technical literature is the identification of data features that allow one to distinguish between the undamaged and damaged structure. The data is condensed and various samples of features are obtained. The various feature vectors sets are analyzed and the features which are redundant and convey least information are discarded and thus the best feature vector sets are retained. Decentralized Kalman filter is used to fuse data to find the global estimates.

3.3. Artificial Neural Network

Further investigation on extracted global estimates is carried out by integrating data fusion technology with ANN approach. ANN is ideally suited to identify non linear system dynamics [14]. A well trained ANN network characterizes and quantifies level of deterioration of the specimen

under study. Thus total amount of cracking, total length and width of cracks are evaluated. In depth analysis of damage phenomena at various levels in different alkali concentration samples is made to find correlation among overall surface damage level, internal damage level and AAR gel concentration in the structure.

Artificial neural network (ANN) classifiers are used to obtain damage information such as total amount of cracking, total length and width of cracks. The most popular multi-layer perceptron (MLP) network is used which is having three layers: an input layer, a hidden layer and an output layer. In the input layer, the number of nodes corresponds to the number of input features and the number of nodes in the output layer corresponds to the number of target classes. The number of hidden nodes, however, depends on the type of data. As ANN is ideally suited to identify non linear system dynamics, a well trained ANN network characterizes and quantifies level of deterioration of the specimen under study. Two sets of input and output are used to train MLP network, the first set comprises of feeding the best selected fused features from decentralized Kalman filter to MLP classifier. The second set comprises of individual systems feeding from single source data to MLP.

Finally the results obtained from individual source sensor system and data fusion system are analyzed and compared. The expected improved accuracy using multi sensor data fusion approach is estimated. The integrated approach of damage detection using multi sensor data fusion technique at surface level and impedance spectra of sensors at internal level for four different specimens characterizes and quantifies the level of damage at surface level and at internal level and provides a correlation between them which can render the information on concentration of gel in the structure.

4. CONCLUSIONS

Multisensor data fusion is establishing significant advantages in structural health monitoring application by improving accuracy and precision in evaluation process. The paper proposes a novel heterogeneous sensor based setup which uses data fusion technology and artificial neural network classifier to find an affordable monitoring strategy for Alkali-aggregate reaction, which is one of the root causes for structural deterioration in concrete. The future work using the proposed experimental setup is focused on establishing correlation among surface damage level, internal damage level and the amount of gel concentration in the structure. To emphasize the expected improved accuracy using data fusion, evaluations of single source data system will be compared with fused heterogeneous data.

REFERENCES

1. <http://www.renewableenergyworld.com/re/a/news/print/article/2010/08/dealing-with-alkali-aggregate-reaction-in-hydraulic-structures>.
2. Gros, X. E., J. Bousigue, and K. Takahashi, "NDT data fusion at pixel level," *NDT & E International*, Vol. 32, 283–292, 1999.
3. Hall, D.L., *Mathematical Techniques in Multi-Sensor Data Fusion*, Artech House, Boston, USA, 1992.
4. Guo, H. and L. Zhang, "A weighted balance evidence theory for structural multiple damage localization," *Computer Methods in Applied Mechanics and Engineering*, Vol. 195, 6225–6238, 2006.
5. Guo, H. Y., "Structural damage detection using information fusion technique," *Mechanical Systems and Signal Processing*, Vol. 20, 1173–1188, 2006.
6. Basir, O. and X. Yuan, "Engine fault diagnosis based on multi-sensor information fusion using Dempster-Shafer evidence theory," *Information Fusion*, Vol. 8, 379–386, 2005.
7. Bao, Y. and H. Li, "Application of information fusion and Shannon entropy in structural damage detection," *Proceedings of Health Monitoring of Structural and Biological Systems*, 1–9, San Diego, California, USA, April 2007.
8. Yang, B.-S. and K. J. Kim, "Application of Dempster-Shafer theory in fault diagnosis of induction motors using vibration and current signals," *Mechanical Systems and Signal Processing*, Vol. 20, 403–420, 2006.
9. Guo, H. Y. and Z. L. Li, "A two-stage method to identify structural damage sites and extents by using evidence theory and micro-search genetic algorithm," *Mechanical Systems and Signal Processing*, Vol. 23, 769–782, 2009.
10. Jiang, S., C.-M. Zhang, and C. G. Koh, "Structural damage detection by integrating data fusion and probabilistic neural network," *Advances in Structural Engineering*, Vol. 9, No. 4, 445–459, 2006.

11. Johnson, E. A., H. F. Lam, L. S. Katafygiotis, and J. L. Beck, "A benchmark problem for structural health monitoring and damage detection," *Proceedings of International Symposium on Engineering Mechanics*, 317–324, Austin, Texas, USA, 2000.
12. Zhao, X., H. Gu., G. Song, Y. L. Mo, and J. Xu, "Structural health monitoring with data fusion method," *Proceedings of Earth and Space 2010: Engineering, Science, Construction, and Operations in Challenging Environments*, 2509–2517, Honolulu, Hawaii, March 2010.
13. Oberholster, R. E. and G. Davies, "An accelerated method for testing the potential alkali reactivity of siliceous aggregates," *Cement and Concrete Research*, Vol. 16, 181–189, 1986.
14. Adeli, H., "Neural networks in civil engineering: 1989–2000", *Computer-Aided Civil and Infrastructure Engineering*, Vol. 16, 126–142, 2001.

Fiber Optic-based Sensing Approach for Corrosion Detection

Othman Sidek, Shahid Kabir, and Muhammad Hassan Bin Afzal

Collaborative μ -electronic Design Excellence Centre (CEDEC)

Engineering Campus, Universiti Sains Malaysia (USM), Penang, Malaysia

Abstract— Fiber optic based sensing technology has shown remarkable progress and accuracy level in structural health monitoring of civil structures especially in concrete structures. In this work, a FOS based Enhanced Fiber Optic Corrosion Sensor is being applied in the concrete structures to sense, measure and obtain the corrosion in concrete structures and also quantify the corrosion level. A basic half cell method is being applied on the similar accelerated concrete structures as a benchmark to evaluate and analyze the accuracy level of proposed EFOCS method of corrosion detection. Finally, a unique and special coating material (PDMS) is being applied on the EFOCS sensor for performance and accuracy enhancement. All data from three different methods has been collected, analyzed and evaluated and further scope of improvement also been discussed.

1. INTRODUCTION

The durability and practicability of reinforced concrete structures is one of the primary concerns in the present day science. Because, majority of modern physical infrastructures are being constructed of reinforced concrete structures. These concrete structures can be degraded or deteriorated for various reasons such as low funding, population growth, tighter health and environmental needs, substandard installation, insufficient inspection and maintenance, and lack of uniformity in design, construction and operation practices usually have adverse effects on reinforced concrete structures [1]. There are various types of concrete degradation but steel corrosion is one primary cause for concrete deterioration. Naturally, inside concrete structures, steel is surrounded by the alkaline environment and also in a passive condition with a negligible corrosion rate. Nevertheless when the concrete cover of the steel is being infiltrated by carbon dioxide and chlorides to get in touch with the steel, the corrosion rate also gets accelerated. To avoid such situation, a proper, effective and accurate steel corrosion detection method is highly required to be developed [2]. In this paper, a new fiber optic based sensing method for detecting the onset of steel corrosion inside reinforced concrete structure with particular application on concrete structures has been studied, developed and experimented in the laboratory. The physical principle is first discussed. Then, this specific sensing method was tested in various conditions and also embedded in cement mortar to demonstrate the feasibility of corrosion sensing. Then, sensor covering for practical application was discussed for applying in practical applications. Further assessments were also being carried out on the covered sensors to examine its durability and overall performance.

2. PROBLEMATIC AREAS

In reinforced concrete infrastructure, the steel corrosion occurs due to penetration of chloride ions or carbon dioxide. This is one of the most important causes of deterioration of reinforced concrete structures and usually has a very negative effect on modern science both in safety issues and economically. The objective of the present investigation is to develop a low-cost FOS based sensing technology for detecting steel corrosion inside reinforced concrete infrastructures and also measure the level of the corrosion occurred in the specific section so necessary steps can be taken effectively. Over the time, different type of approaches is being studied, applied and tested to detect the steel corrosion effectively and also measure the corrosion rate appropriately. Table 1 gives brief overviews of some prominent and useful steel corrosion detection techniques and also their specific advantages and disadvantages in details [2].

All the above proposed method and technology certainly lacked in three most important areas while detecting steel corrosion inside concrete structures.

- First, installations of all this sensing methods are very complicated and often required professional assistance.
- Second, most of these methods are only applicable in newly constructed concrete structure. That means, these sensing methods need to be installed while constructing the structure which is a huge limitation.

Table 1: Summary of some prominent and useful steel corrosion detection.

Proposed Method & Time	Advantages	Disadvantages
Chemical Analysis on cored samples, by J. P. Broomfield, 1997 [3].	1. A straight-forward procedure. 2. Can detect carbonation effectively and immediately.	1. Have some problems detecting chloride concentration, less accurate results. 2. Very expensive and time-consuming method, since taking core sample from a very large concrete structure is very problematic.
Embeddable corrosion sensor also known as ladder sensor, by P. Schiessl and M. Raupach, 1992 [4].	1. Compact and properly embedded inside new concrete structure. 2. Corrosion can be determined by comparing the potential of each rod with the help of a reference electrode. 3. Genuine and direct assessment of the corrosion activity.	1. Extremely high installation cost. 2. Only applicable for new concrete structures.
Application of cylindrical sensor based on “ladder” sensor technique, by M. Raupach, 2002 [5].	1. A specific hole is cored inside the concrete structure for sensor embedding purpose. 2. Corrosion can be determined by comparing the potential of each rod with the help of a reference electrode. 3. Genuine and direct assessment of the corrosion activity.	1. The cost is still high. 2. Problems in detecting chloride based penetration and corrosion.
FIBER Optic based sensing method for chloride detection, D. L. Huston and P. L. Fuhr, 1998 [6].	1. No electro-magnetic interference. 2. Very creative and useful installation technique has been developed which supports longevity and accuracy.	1. Very large in size. 2. Not applicable in existing concrete structure. 3. Installing and monitoring in various places simultaneously is highly problematic.
A special FOS based detection method with special polymer cladding, M. Ghandehari, 2001 [7].	1. Optical fiber's cladding is made of surrounding-sensitive special polymer for elevated response. 2. Changes in chloride concentration immediately affect the fiber cladding.	1. Though it is a very effective method, but it is very complicated and often requires professional's assistance. 2. Limited to chloride detection and does not support one-to-one corrosion detection procedure.
FOS based pH sensor for corrosion detection in Concrete structure, W. R. Habel and D. Hoffmann, 2007 [8].	1. An effective and accurate method to detect corrosion by evaluating pH range.	1. For certain environment, chloride-induced corrosion cannot be detected properly.

- Third, excessive high cost is needed for designing and fabricating these methods. So to overcome these problematic areas, a new FOS based sensing method to detect corrosion inside concrete structures has been studied and presented in this paper [9].

3. OBJECTIVES

1. To fabricate and design a novel and unique FOS based sensing technology to detect and measure the level of corrosion inside concrete structures.
2. Can be applied both in new and used concrete structure.
3. Application of PDMS as a coating of optical fiber cable and analysis of overall performance.
4. Making sure of overall performance by verifying the output results with provided data.
5. Overcome the durability and feasibility issue.
6. Enhancement of proposed sensor with PDMS coating and output analysis.

4. FABRICATION OF FOS BASED ENHANCED FIBER OPTIC CORROSION SENSOR (EFOCS)

An Enhanced Fiber Optic Corrosion Sensor (EFOCS) is being applied here [9]. It is manufactured of one FBG sensor and two specific sized identical reinforcing bar and then it is essential to package up with the sample concrete slab in a particular method. These two rebars are a special type of screw-thread steel. First, rebar 1 is split in to R1-1 and R1-2, and rebar 2 is split in to R2-1 and R2-2. Second, a FBG sensor is set vertically to the twin rebar axis and bonded on their planed surface after R1-2and R2-2 are placed alongside. Third, R1-1 and R2-1 are attached to R1-2 and R2-2, respectively. Last, the FBG sensor and twin rebar elements are installed together with concrete structure. Usually, the output of the corrosion of the twin rebar represents in the shift of the maximum wavelength of the grating because of their volume growth. With the purpose of balancing this specific temperature effect, a fiber optic temperature sensor (FOTS) is applied here [9]. Here Figure 1 represents the standard schematic diagram of enhanced fiber optic corrosion sensor [9].

5. FABRICATION OF PDMS COATED FBG SENSOR & FUTURE WORK

In the recent years, FOS based fiber Bragg grating (FBG) sensors have been studied, researched and experimented extensively for sensing and measuring several types of physical parameters such as strain, bending, pressure, temperature, and chemicals [11–16]. By applying FBG sensors, the environmental perturbations on the FBG sensors, such as strain, temperature, and pressure, can be straightforwardly calculated by monitoring the degree of the Bragg wavelength shift induced by the amount of the FBG bend. Nonetheless, for chemical sensing purpose, ordinary FBGs are not entirely suitable for practical applications because optical fibers do not respond to chemical solutions. Furthermore, traditional FBGs are intrinsically not sensitive to a surrounding-medium refractive index (SRI) variation because optical fields are well-bound within a fiber core and a light coupling with the SRI is screened by a thick cladding layer. So to overcome these problems, long-period fiber gratings (LPFGs) are generally used for chemical sensing applications, where the light couplings between the core and the cladding modes are present, associated an optical interaction linking the cladding and an external medium [13, 16–18]. Here, the Figure 2 represents the standard schematic diagram of PDMS coated FBG sensor [19].

So, to effectively determine the corrosion level of a concrete structure, here a special FBG sensor has been applied with specific PDMS coating for enhanced sensing and measuring the concrete

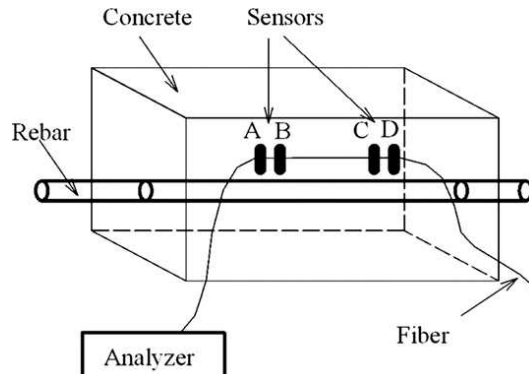


Figure 1: A standard schematic diagram of enhanced fiber optic corrosion sensor.

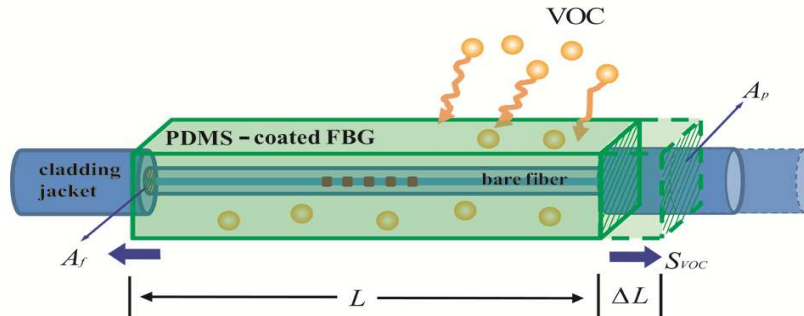


Figure 2: A standard schematic diagram of PDMS-coated FBG sensor.

corrosion. After applying the special PDMS coating on the FBG sensor, it will be introduced into the EFOCS. After that, the output results from half cell method, standard EFOCS method and enhanced PDMS coated EFOCS method will be observed, analyzed and verified. Then the accuracy of these three proposed methods will be compared and further scope of improvements will be discussed.

6. CONCLUSIONS

There are different types of concrete degradation but steel corrosion is one of the major reasons for severe concrete deterioration. Traditional detection methods are not very effective and user-friendly comparing to the modified sensor based technologies. Especially, FOS based technology is very easier to operate and durable. Here a unique coating of PDMS material for the fiber optic sensor has been proposed and with appropriate research and further study, the detection accuracy enhancement will be analyzed.

REFERENCES

1. Kabir, S., P. Rivard, D.-C. He, and P. Thivierge, "Damage assessment for concrete structure using image processing techniques on acoustic borehole imagery," *Construction and Building Materials*, Vol. 23, 3166–3174, 2009.
2. Christopher, K., Y. Leung, K. T. Wan, and L. Chen, "A novel optical fiber sensor for steel corrosion in concrete structures," *Sensors*, Vol. 8, 1960–1976, 2008.
3. Broomfield, J. P., *Corrosion of Steel in Concrete*, E & FN SPON, London, 1997.
4. Schiessl, P. and M. Raupach, "Monitoring system for the corrosion risk for steel in concrete," *Concrete International*, Vol. 14, No. 7, 52–55, 1992.
5. Raupach, M., "Corrosion behaviour of the reinforcement under on-site-conditions," *Proceedings of 15th International Corrosion Congress, Frontiers in Corrosion Science and Technology*, Art. 096, Granada, 2002.
6. Huston, D. R. and P. L. Fuhr, "Distributed and chemical fiber optic sensing and installation in bridges," *Fiber Optic Sensors for Construction Materials and Bridges*, edited by F. Ansari, 79–88, 1988.
7. Ghandehari, M., "Ingress monitoring in concrete structures," *Proceedings of the 15th ASCE Conference on Engineering Mechanics*, New York, 2001.
8. Habel, W. R. and D. Hofmann, "Fibre optic sensors for long-term SHM in civil engineering and geotechnique," *Proceedings of International Society for Structural Health Monitoring of Intelligent Infrastructure Conference*, Vancouver, Canada, Nov. 2007.
9. Gao, J., J. Wu, J. Lia, and X. Zhao, "Monitoring of corrosion in reinforced concrete structure using bragg grating sensing," *NDT&E International*, Vol. 44, 202–205, 2011.
10. Kersey, A. D., M. A. Davis, H. J. Patrick, M. Le Blanc, K. P. Koo, C. G. Askins, M. A. Davis, and E. J. Friebel, "Fiber grating sensors," *Journal of Lightwave Technology*, Vol. 15, No. 8, 1442–1463, 1997.
11. Othonos, A. and K. Kalli, *Fiber Bragg Gratings Fundamentals and Applications in Telecommunications and Sensing*, Artech House, Boston, 1999.
12. Rao, Y. J., "Recent progress in applications of in-fiber Bragg grating sensors," *Optical Lasers Engineering*, Vol. 31, No. 4, 297–324, 1999.

13. Zhang, L., W. Zhang, and I. Bennion, *In-fiber Grating Optic Sensors in Fiber Optics Sensors*, Chaper 4, Dekker, New York, 2002.
14. Shu, X., K. Chisholm, I. Felmeri, K. Sugden, A. Gillooly, L. Zhang, and I. Bennion, “Highly sensitive transverse load sensing with reversible sampled fiber Bragg gratings,” *Applied Physics Letters*, Vol. 83, No. 15, 3003–3005, 2003.
15. Bhatia, V. and A. M. Vengsarkar, “Optical fiber long-period grating sensors,” *Optical Letters*, Vol. 21, No. 9, 692–694, 1996.
16. Shu, X. and D. X. Huang, “High sensitive chemical sensor based on the measurement of the separation of dual resonant peaks in a 100-mm period fiber grating,” *Optical Communication*, Vol. 171, Nos. 1–3, 65–69, 1999.
17. Shu, X., L. Zhang, and I. Bennion, “Sensitivity characteristics of long-period fiber gratings,” *Journal of Lightwave Technology*, Vol. 20, No. 2, 255–266, 2002.
18. Barnes, J. A., R. S. Brown, A. H. Cheung, M. A. Dreher, G. Mackey, and H.-P. Loock, “Chemical sensing using a polymer coated long-period fiber grating interrogated by ring-down spectroscopy,” *Sensors and Actuators B Chem.*, Vol. 148, No. 1, 221–226, 2010.
19. Park, C.-S., Y. Han, K.-I. Joo, Y. W. Lee, S.-W. Kang, and H.-R. Kim, “Optical detection of volatile organic compounds using selective tensile effects of a polymer-coated fiber Bragg grating,” *Optics Express*, Vol. 18, No. 24, 24754, 2010.

Artifact Mitigation in High Energy CT via Monte Carlo Simulation

Xuemin Jin and Robert Y. Levine
Spectral Sciences, Inc., USA

Abstract— The high energy (< 15 MeV) incident polychromatic γ -ray spectrum and energy-resolved photon attenuations in steel, obtained via EGS/BEAM Monte Carlo, were applied to derive beam hardening correction in steel cylinders and pipes. Monte Carlo simulated pencil beam projections were processed using latch bit filters to isolate exiting primary photons. The beam hardening correction was applied to these projections, which were then interpolated to a uniform grid. Filtered back projections of the raysums with and without the beam hardening correction were compared. It was demonstrated that beam hardening artifacts can be successfully removed for steel structures.

1. INTRODUCTION

CT artifacts resulting from preferential absorption of lower energy photons in a polychromatic beam are known as beam hardening effects, and have been a focus of intense research [1, 2]. The beam hardening correction (BHC) involves a renormalization of each measured intensity with a correction factor that depends on the measured intensity, the polychromatic input spectrum, an energy-dependent attenuation, and a reference monoenergetic photon beam energy [1]. Steel is a high-Z dense material upon which accelerator-based high energy (> 1 MeV) photon sources are applied for nondestructive testing (NDT) CT [3]. In this paper, we apply the Monte Carlo simulated incident polychromatic γ -ray spectrum and the energy-resolved attenuation [3] to compute the BHC, and demonstrate procedures necessary to obtain corrected images with steel cylinders and pipes. Cylinders will have more beam hardening and scattering disparity along a projection, whereas the thin pipe boundaries are more easily masked by artifacts.

2. BEAM HARDENING CORRECTION OVERVIEW

Formally, the measured raysum, r_0 , from a polychromatic source with normalized incident spectral density $S_n(E)$ through a homogeneous material of attenuation $\mu(E)$ and thickness d is modeled as

$$r_0 = -\ln \left[\int S_n(E) e^{-\mu(E)d} dE \right] \quad (1)$$

The BHC in CT converts r_0 to an equivalent raysum $\mu(E_0)d$ for a monoenergetic source of reference energy E_0 [1]. For N_0 incident photons and N detector particle counts, the raysum estimate r_0 results from $\ln(N_0/N)$. The appropriate BHC for this measurement converts r_0 to

$$r = \ln(N_0/N) + \mu(E_0)d + \ln \left[\int S_n(E) e^{-\mu(E)d} dE \right]. \quad (2)$$

Monte Carlo simulation has a significant role in determining the BHC via calculation of the input attenuation $\mu(E)$ and spectral density $S_n(E)$ in Eq. (2).

2.1. Polychromatic Sources

The accelerator that creates a bremsstrahlung-generated photon flux for high-Z NDT is similar to a radiotherapy medical accelerator, except the flattening filter and ion chamber have been removed to increase photon yields. In the accelerator head a 15 MeV electron beam is incident on a 1 cm thick tungsten slab to create bremsstrahlung photons with a continuous spectrum in the range 0–15 MeV. Primary photon fluence is defined as γ -rays created via target bremsstrahlung that do not interact anywhere further in the beam line to the scoring plane.

Monte Carlo simulations were performed for 100 million input 15 MeV electrons and simulated interactions, trajectories, and particle showers using the EGS/BEAM code [4] with 20 processors on a Beowulf cluster. A scoring plane was placed at the end of the accelerator head to compute the ~ 2 GB phase space file for the emerging 18° beam. The spectral density of the phase space particles in the central 1 cm of the beam, an area that defines a pencil beam for raysum measurements, was calculated. Figure 1 shows the spectral density for the pencil beam in which the primary photon

spectrum is separated from electrons and positrons. There are energy cutoffs for photon (10 keV) and electron (0.7 MeV) transport which force the spectrum to zero. The cutoffs are chosen based on the extremely short range of these particles in solids in order to speed-up the Monte Carlo simulation [4]. The charged particle cutoff is higher, but as can be seen in Figure 1, represents a very small percentage of the particles in the beam (and also would not have a significant range in steel). In order to compute the BHC in Eq. (2) an explicit expression for the normalized spectrum $S_n(E)$ is required, which was obtained from a six order polynomial fit to the spectrum shown in Figure 1.

2.2. Steel Spectral Attenuation

The energy-resolved steel spectral attenuation, $\mu(E)$, is also employed in Eq. (2). This was derived using a series of EGS/BEAM Monte Carlo slab simulations with incident monoenergetic photons. Figure 2 contains the resulting primary photon attenuation $\mu(E)$ for steel, which is appropriate if scatter has been removed via collimation. Also shown is a third order exponential fit to the data that is applied to the BHC calculation in Eq. (2).

2.3. BHC Estimation

The steel BHC versus thickness d is derived from the following equation

$$\text{BHC}(d) = \mu(5.6 \text{ MeV})d + \ln \left[\int S_n(E)e^{-\mu(E)d} dE \right], \quad (3)$$

where $S_n(E)$ and $\mu(E)$ are given in Figures 1 and 2. The reference energy $E_0 = 5.6 \text{ MeV}$ is somewhat arbitrary. Procedures for choosing E_0 are discussed in the literature [1]. Figure 3 shows the resulting steel BHC and an exponential fit to the function $\text{BHC}(d)$, which is used for the applications to tomographic reconstructions in the next section.

3. APPLICATION OF BHC TO TOMOGRAPHIC RECONSTRUCTION

In this section we apply the steel BHC in Figure 3 to tomographic reconstruction of steel cylinders and pipes. In order to obtain the necessary projection data via Monte Carlo simulation, we use a polychromatic photon pencil beam with the spectrum in Figure 1. The incident pencil beam had square areal dimensions with $\Delta x = \Delta y = 0.01 \text{ cm}$ half maxima. Projection data was obtained through a series of EGS/BEAM simulations with different incident offsets on the steel target. A scoring plane was placed behind a 19 cm lead collimator nearly two meters downstream from the steel targets. Latch bits were set to distinguish primary and scattered particles.

The specific steps in generating projection data, applying the BHC, and performing CT reconstructions were as follows: 1) obtain projection data via independent multiple-offset pencil beam simulations using the phantom model, 2) apply spline interpolation of projection data onto an equally spaced 256 sample grid to create a 256×256 reconstructed image, and 3) perform filtered

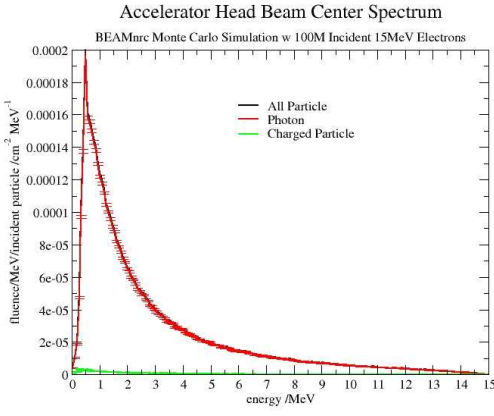


Figure 1: EGS/BEAM Monte Carlo simulation of 15 MeV accelerator head pencil beam spectral densities.

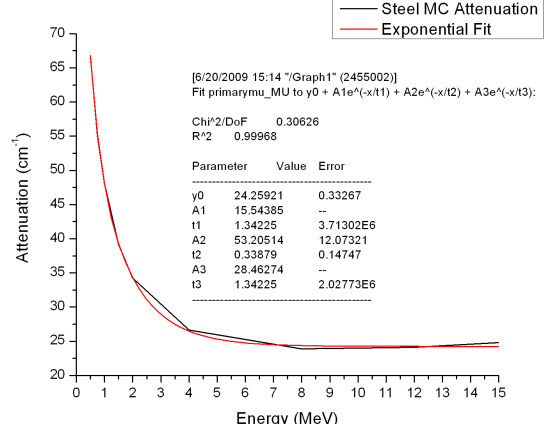


Figure 2: Steel spectral attenuation in the range 0.5–15 MeV via EGS/BEAM Monte Carlo slab calculations.

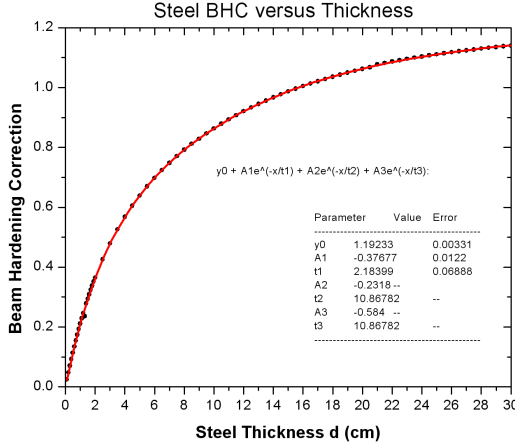


Figure 3: Steel BHC versus thickness.

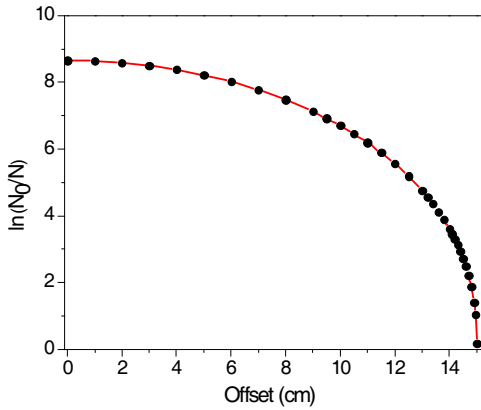


Figure 4: Projection from EGS/BEAM simulations on steel cylinder with radius of 15 cm.

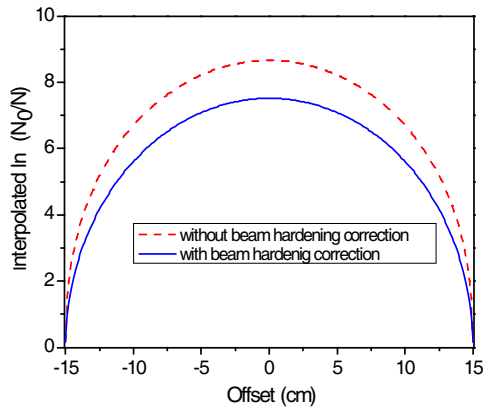


Figure 5: Interpolation of projection data to uniform 256 point grid with and without the steel BHC.

back projection using the Siddon algorithm [5] with 180 one-degree separated beams for the uncorrected reconstruction. Alternatively, after step 2, we apply the BHC in Eq. (3) to projection data, and perform the same filtered back projection reconstruction to the BHC-processed projections to obtain corrected reconstructions. The results of these procedures for the steel cylinder and pipe are shown in the following sections.

3.1. Steel Cylinder

The steel cylinder of 15 cm radius was constructed as an EGS/BEAM Monte Carlo phantom. For each offset $0.01 \times 0.01 \text{ cm}^2$ pencil beam, a total of $N_0 = 200$ million incident photons were chosen from the polychromatic spectrum in Figure 1. The offsets of the incident pencil beams in centimeters for the EGS/BEAM simulations were 0, 1, 2, 3, 4, 5, 6, 7, 8, 9, 10, 10.5, 11, 11.5, 12, 12.5, 13, 13.2, 13.4, 13.6, 13.8, 14, 14.1, 14.2, 14.3, 14.4, 14.5, 14.6, 14.7, 14.8, 14.9, 14.95, 15. In order to isolate beam hardening from scatter effects, latch bits were employed to count primary photons [4]. This count of exiting photons N at the scoring plane was obtained for each pencil beam. Figure 4 shows the count plotted as $\ln(N_0/N)$ versus offset that defines the projection data. The interpolation of this function to a uniform grid is shown in Figure 5 with and without the application of the BHC in Eq. (3) using the appropriate thickness d of the steel cylinder at the corresponding offset. The magnitude of the BHC is significant, nearly a factor of 7.4 at the center of the cylinder. The filtered back projection reconstructions are shown in Figures 6 and 7. The beam hardening artifact is prominent in Figure 6(a), and is completely removed in Figure 6(b) after the application of BHC. This is further illustrated in Figure 7 with a horizontal slice through the reconstructed images in Figure 6.

3.2. Steel Pipe

The second example we considered was a steel pipe of 13 cm inner radius and 15 cm outer radius. In order to boost photon yields and isolate beam hardening effects, the pipe phantom was set in a vacuum. Consequently, only $N_0 = 5$ million photons were needed for each pencil beam simulation. This allowed dense beam offset sampling near the inner and outer edges of the pipe. The offsets

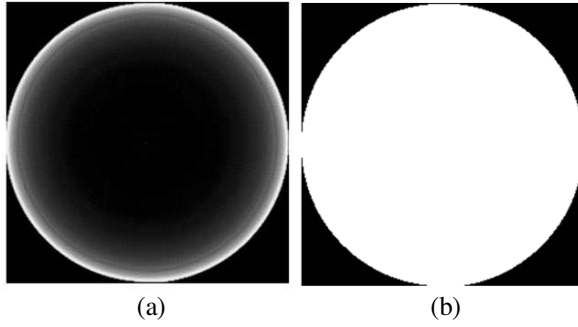


Figure 6: Tomographic reconstructions of steel cylinder from EGS/BEAM simulated projection in (a) without the BHC and (b) with the BHC.

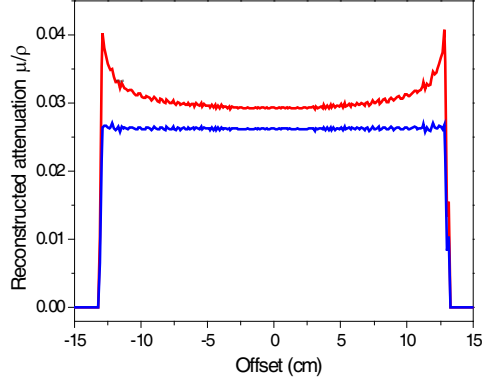


Figure 7: The red curve is from Figure 6(a) (without BHC) and the blue curve is from Figure 6(b) (with BHC).

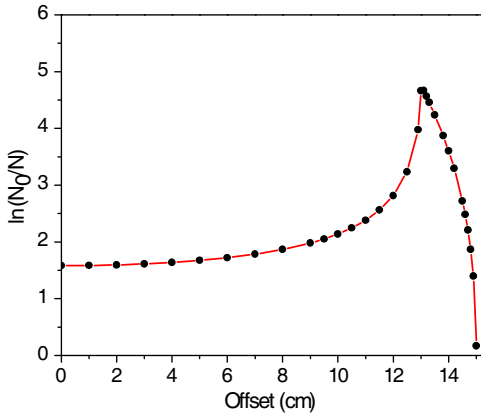


Figure 8: Primary photon fluence projection from EGS/BEAM simulations on steel pipe of inner radius 13 cm and outer radius 15 cm.

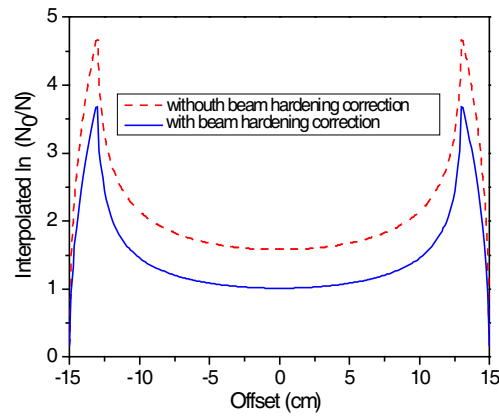


Figure 9: Projections interpolated onto equally spaced grid of 256 samples with and without the steel BHC.

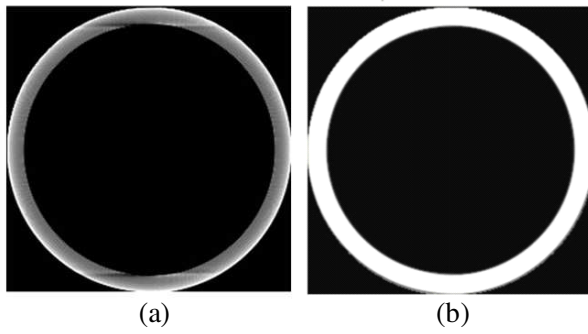


Figure 10: Tomographic reconstructions of steel pipe from EGS/BEAM projections.

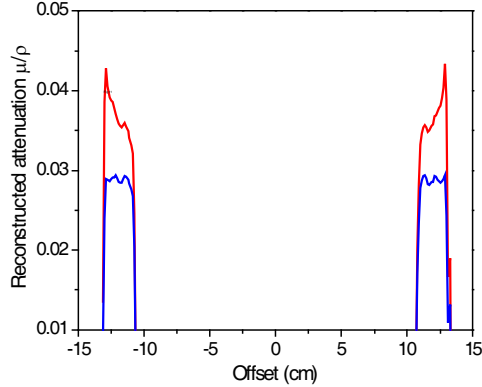


Figure 11: Horizontal slices through the reconstructions in Figure 10. The red curve is from Figure 10(a) (without BHC) and the blue curve is from Figure 10(b) (with BHC).

in centimeters were given by 0, 1, 2, 3, 4, 5, 6, 7, 8, 9, 9.5, 10, 10.5, 11, 11.5, 12, 12.5, 12.9, 13, 13.1, 13.2, 13.3, 13.5, 13.8, 14, 14.2, 14.5, 14.6, 14.7, 14.8, 14.9, and 15. We computed primary photon numbers at the scoring plane using appropriate latch bit filters. The resulting function $\ln(N_0/N)$ versus offset is plotted in Figure 8. Spline interpolation to a uniform grid was applied to the projection data, and the BHC in Eq. (2) was implemented for steel thickness d at the corresponding offset. The results shown in Figure 9 indicate a large correction in the pipe center and at the rim where the reconstruction is most delicate.

Filtered back projection reconstructions from 180 one-degree views with the raysum estimates in Figure 9 are shown in Figure 10. The beam hardening artifact is apparent in Figure 10(a) and completely removed via the (Eq. (3)) BHC application in Figure 10(b). Figure 11 shows horizontal slices through the reconstructions in Figure 10 without (red) and with (blue) the BHC. Beam hardening is observed in the cupped signature towards the edge of the pipe image.

4. CONCLUSIONS

The key inputs to high energy (> 1 MeV) beam hardening correction for nondestructive testing, incident photon spectral density and material spectral attenuation, were derived via first-principles Monte Carlo simulation. In this paper, the Monte Carlo-derived BHC was shown to remove beam hardening effects for steel cylinders and pipes. The overall reconstruction corrections were remarkably successful, but required dense edge sampling and interpolation via pencil beams. These may not be available in CT measurements and processing. Nevertheless, if there is prior knowledge of the accelerator head configuration and expected materials, it is possible to derive spectra from Monte Carlo simulation for BHC calculation. In our future research, we will fully simulate the BHC procedure by including simulated calibration curves that correlate the BHC factor with measured particle counts at the detector.

REFERENCES

1. Kak, A. C. and M. Slaney, *Principles of Computerized Tomographic Imaging*, IEEE Press, New York, 1988.
2. Gao, H., L.Zhang, Z. Chen, Y. Xing, and S. Li, “Beam hardening correction for middle-energy industrial computerized tomography,” *IEEE Trans. Nuclear Science*, Vol. 53, 2796–2807, 2006.
3. Jin, X., R. Y. Levine, and D. Reiss, “Spectral feature of high energy photon scatter in high-Z materials,” *IEEE Trans. Nucl. Sci.*, 2011 (submitted for publication).
4. Rogers, D. W. O., B. A. Faddegon, G. X. Ding, C.-M. Ma, J. We, and T. R. Mackie, “BEAM: A Monte Carlo code to simulate radiotherapy treatment units,” *Med. Phys.*, Vol. 22, 503–524, 1995.
5. Siddon, R. L., “Fast calculation of exact radiological path for a three-dimensional CT array,” *Med. Phys.*, Vol. 12, 252–255, 1985.

Analysis of Depolarized Electromagnetic Waves Propagated through Random Media

Yukihisa Nanbu¹, Mitsuo Tateiba², and Hosam El-Ocla³

¹Sasebo National College of Technology, Sasebo, Nagasaki 857-1193, Japan

²Ariake National College of Technology, Omuta, Fukuoka 836-8585, Japan

³Department of Computer Science, Lakehead University
955 Oliver Road, Thunder Bay, Ontario P7B 5E1, Canada

Abstract— When the optical path-length becomes large in long propagation through random media, then we have to consider the effect of depolarization of EM waves. In this paper, to solve this depolarization problem, we have derived an integral equation using the dyadic Green's function on the assumption that there exists a random medium screen of which the dielectric constant is fluctuating randomly, and modified the integral equation on the assumption that the observation point is very far from the screen. Form this modified integral equation, the analytic expression of the depolarized EM wave has been given by using the perturbation method.

1. INTRODUCTION

Studies of the electromagnetic (EM) wave propagation through random media have been continued into the important development of remote sensing, various measurements, and satellite communications. It is mainly assumed in the studies that the fluctuating intensity of continuous random medium is so weak and the fluctuating scale-size is much larger than the wave length of EM wave [1]. Therefore the scalar approximation has been used. When the optical path-length becomes large in long propagation through random medium, however, then we have to consider the effect of depolarization of EM waves. In previous studies, quantitative analysis of the depolarization has not been investigated sufficiently.

In this paper, to solve this depolarization problem, we first have derived an integral equation using the dyadic Green's function on the assumption that there exists a random medium screen of which the dielectric constant is fluctuating randomly. Next we have modified the integral equation on the assumption that the observation point is very far from the screen. Form this modified integral equation, the analytic expression of the depolarized EM wave has been given by using the perturbation method. Finally we have shown the first order perturbation of the depolarized EM wave; and will be able to discuss quantitatively the depolarization of EM wave propagated through the random medium screen.

2. FORMULATION

Let us consider the problem of electromagnetic (EM) wave scattering by a random medium with volume V . When we designate an incident EM wave by $\mathbf{F}_{in} = [\mathbf{E}_{in}, \mathbf{H}_{in}]_t$, the scattered EM wave by $\mathbf{F}_s = [\mathbf{E}_s, \mathbf{H}_s]_t$, and the total EM wave by $\mathbf{F} = [\mathbf{E}, \mathbf{H}]_t$, then \mathbf{F} satisfies the Maxwell's equations in overall region $(V + \bar{V})$. Therefore we obtain

$$\bar{\bar{L}}\mathbf{F} = \begin{cases} 0 & \text{in } \bar{V} \\ \bar{T}j\omega \left[\begin{array}{c|c} \{\varepsilon(\mathbf{r}) - \varepsilon_0\}\bar{\bar{1}} & \bar{\bar{0}} \\ \bar{\bar{0}} & \{\mu(\mathbf{r}) - \mu_0\}\bar{\bar{1}} \end{array} \right] \mathbf{F} & \text{in } V \end{cases} \quad (1)$$

where $\varepsilon(\mathbf{r})$ and $\mu(\mathbf{r})$ are the dielectric constant and magnetic permeability of the random medium, respectively, and

$$\bar{\bar{L}} = \left[\begin{array}{c|c} \nabla \times & -j\omega\mu_0\bar{\bar{1}} \\ \hline j\omega\varepsilon_0\bar{\bar{1}} & \nabla \times \end{array} \right], \quad \bar{T} = \left[\begin{array}{c|c} \bar{\bar{0}} & -\bar{\bar{1}} \\ \hline \bar{\bar{1}} & \bar{\bar{0}} \end{array} \right], \quad \bar{\bar{1}} = \left[\begin{array}{ccc} 1 & 0 & 0 \\ 0 & 1 & 0 \\ 0 & 0 & 1 \end{array} \right] \text{ and } \bar{\bar{0}} = \left[\begin{array}{ccc} 0 & 0 & 0 \\ 0 & 0 & 0 \\ 0 & 0 & 0 \end{array} \right], \quad (2)$$

in which

$$[\nabla \times] \equiv \left[\begin{array}{ccc} 0 & -\partial/\partial z & \partial/\partial y \\ \partial/\partial z & 0 & -\partial/\partial x \\ -\partial/\partial y & \partial/\partial x & 0 \end{array} \right].$$

By applying the difference of material parameters between \bar{V} and V :

$$\varepsilon_d(\mathbf{r}) = \begin{cases} \varepsilon(\mathbf{r}) - \varepsilon_0 & \text{in } V \\ 0 & \text{in } \bar{V} \end{cases} \quad \mu_d(\mathbf{r}) = \begin{cases} \mu(\mathbf{r}) - \mu_0 & \text{in } V \\ 0 & \text{in } \bar{V} \end{cases}, \quad (3)$$

Equation (1) can be rewritten in overall space: $V + \bar{V}$ as

$$\bar{\bar{L}}\mathbf{F} = -\bar{T}\bar{T}\bar{\bar{M}}\mathbf{F}; \quad \bar{\bar{M}}(\mathbf{r}) = j\omega \begin{bmatrix} \bar{0} & -\mu_d(\mathbf{r})\bar{1} \\ \varepsilon_d(\mathbf{r})\bar{1} & \bar{0} \end{bmatrix} \quad (4)$$

Using the dyadic Green's function \mathbf{G} , we can express solutions of Eq. (4) with \mathbf{F}_{in} as these of the following integral equation:

$$\mathbf{F} = \mathbf{F}_{in} + \int_V \mathbf{G}(\mathbf{r} - \mathbf{r}') \odot \bar{T}\bar{\bar{M}}(\mathbf{r}') \mathbf{F}(\mathbf{r}') d\mathbf{r}' \quad (5)$$

Let us define a vector \mathbf{A} as $\mathbf{A} = [\mathbf{A}_e, \mathbf{A}_m]_t$ where $\mathbf{A}_e = [A_{ex} A_{ey} A_{ez}]_t$ and $\mathbf{A}_m = [A_{mx} A_{my} A_{mz}]_t$. Then, using $\mathbf{G} = \mathbf{G}_e + \mathbf{G}_m$ where \mathbf{G}_e , \mathbf{G}_m , respectively, are due to electric and magnetic point source, we define the operator \odot as follows:

$$\mathbf{G} \odot \mathbf{A} = \sum_{\alpha=x,y,z} (\mathbf{G}_{e\alpha} A_{e\alpha} + \mathbf{G}_{m\alpha} A_{m\alpha}) \quad (6)$$

where \mathbf{G}_e is expressed as

$$\mathbf{G}_e = \sum_{\alpha} \mathbf{G}_{e\alpha} = \sum_{\alpha} \begin{bmatrix} \mathbf{G}_{e\alpha}^e \\ \mathbf{G}_{e\alpha}^m \end{bmatrix}; \quad \mathbf{G}_{e\alpha}^e = \sum_{\alpha} \begin{bmatrix} G_{e\alpha}^{ex} \\ G_{e\alpha}^{ey} \\ G_{e\alpha}^{ez} \end{bmatrix}, \quad \mathbf{G}_{e\alpha}^m = \sum_{\alpha} \begin{bmatrix} G_{e\alpha}^{mx} \\ G_{e\alpha}^{my} \\ G_{e\alpha}^{mz} \end{bmatrix} \quad (7)$$

and \mathbf{G}_m is expressed by changing the subscript of \mathbf{G}_e from e to m . Here it should be noted that $G_{e\alpha}^{\beta}$, $G_{e\alpha}^{m\beta}$, respectively, are the β -directional electric and magnetic wave fields radiated from the α -directional electric point source. The scattering EM wave is written as

$$\mathbf{F}_s = \int_V \mathbf{G}(\mathbf{r} - \mathbf{r}') \odot \bar{T}\bar{\bar{M}}(\mathbf{r}') \mathbf{F}(\mathbf{r}') d\mathbf{r}' = - \int_V \mathbf{G}(\mathbf{r} - \mathbf{r}') \odot \mathbf{J}_d(\mathbf{r}') d\mathbf{r}' \quad (8)$$

3. ANALYSIS OF DYADIC GREENS' FUNCTION

Figure 1 shows the Geometry of the problem. Assuming $\mu_d = 0$, we obtain

$$\mathbf{J}_d = -\bar{T}\bar{\bar{M}}\mathbf{F} = j\omega\varepsilon_d \begin{bmatrix} \mathbf{E} \\ \mathbf{0} \end{bmatrix} \quad (9)$$

Assuming TE-wave incidence shown in Fig. 1 and applying Eq. (6) on \mathbf{A} with $A_{m\alpha} = 0$, we have

$$\begin{bmatrix} \mathbf{E}(\boldsymbol{\rho}, z) \\ \mathbf{H}(\boldsymbol{\rho}, z) \end{bmatrix} = \begin{bmatrix} \mathbf{E}_{in}(\boldsymbol{\rho}, z) \\ \mathbf{H}_{in}(\boldsymbol{\rho}, z) \end{bmatrix} - j\omega \int_V \sum_{\alpha=x,y,z} \mathbf{G}_{e\alpha}^e(\boldsymbol{\rho} - \boldsymbol{\rho}', z - z') \varepsilon_d(\boldsymbol{\rho}', z') E_{\alpha}(\boldsymbol{\rho}', z') d\mathbf{r}' \quad (10)$$

where $\boldsymbol{\rho} = (x, y)$ and $\int_V d\mathbf{r}' = \int_0^{z_0} dz' \int_{S_{\infty}} d\boldsymbol{\rho}'$. Consequently, $\mathbf{E}(\boldsymbol{\rho}, z)$ can be expressed as

$$\begin{bmatrix} E_x(\boldsymbol{\rho}, z) \\ E_y(\boldsymbol{\rho}, z) \\ E_z(\boldsymbol{\rho}, z) \end{bmatrix} = \begin{bmatrix} E_{ix}(\boldsymbol{\rho}, z) \\ E_{iy}(\boldsymbol{\rho}, z) \\ E_{iz}(\boldsymbol{\rho}, z) \end{bmatrix} - j\omega \int_V \sum_{\alpha} \begin{bmatrix} G_{e\alpha}^{ex}(\boldsymbol{\rho} - \boldsymbol{\rho}', z - z') \varepsilon_d(\boldsymbol{\rho}', z') E_{\alpha}(\boldsymbol{\rho}', z') \\ G_{e\alpha}^{ey}(\boldsymbol{\rho} - \boldsymbol{\rho}', z - z') \varepsilon_d(\boldsymbol{\rho}', z') E_{\alpha}(\boldsymbol{\rho}', z') \\ G_{e\alpha}^{ez}(\boldsymbol{\rho} - \boldsymbol{\rho}', z - z') \varepsilon_d(\boldsymbol{\rho}', z') E_{\alpha}(\boldsymbol{\rho}', z') \end{bmatrix} d\mathbf{r}' \quad (11)$$

The dyadic Green's function $\mathbf{G}_{e\alpha}^e$ is expressed as

$$\begin{aligned} \mathbf{G}_{e\alpha}^e(\mathbf{r}, z) &= j\omega\mu_0 [\mathbf{i}_{\alpha} + (\mathbf{i}_{\alpha} \cdot \nabla) \nabla] G(\mathbf{r}, z) \\ &= j \frac{1}{\omega\varepsilon_0} \left[\left(-k^2 + \frac{jk}{r} + \frac{1}{r^2} \right) (\mathbf{i}_{\alpha} \times \mathbf{i}_r) \times \mathbf{i}_r + 2\mathbf{i}_r (\mathbf{i}_{\alpha} \cdot \mathbf{i}_r) \left(\frac{jk}{r} + \frac{1}{r^2} \right) \right] G(\mathbf{r}, z) \end{aligned} \quad (12)$$

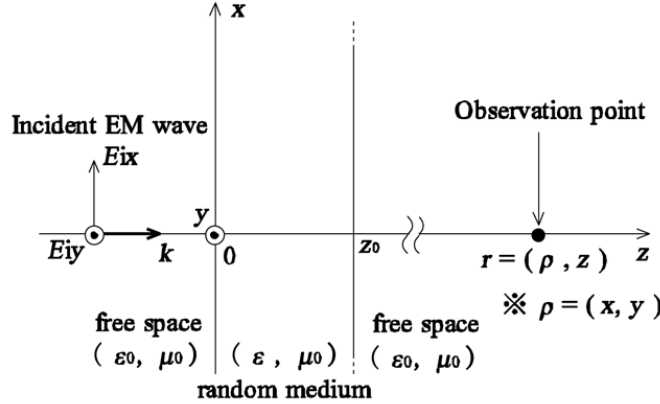


Figure 1: Geometry of the problem.

where $G(\mathbf{r}, z)$ is the scalar Green's function in free space, $k = \omega\sqrt{\epsilon_0\mu_0}$ is the wavenumber in free space and \mathbf{i}_α ($\alpha = x, y, z$), \mathbf{i}_r are the α - and r -directional unit vector, respectively.

When $kr \gg 1$, then $\mathbf{G}_{e\alpha}^e$ is approximated by

$$\mathbf{G}_{e\alpha}^e(\mathbf{r}, z) = j \frac{1}{\omega\epsilon_0} [-k^2(\mathbf{i}_\alpha \times \mathbf{i}_r) \times \mathbf{i}_r] G(\mathbf{r}, z) \quad (13)$$

Here we assume a far field of which the observation point is in the neighborhood of the z -axis; i.e., $z \gg \rho, x, y$, and $r \approx z \rightarrow \infty$. Then we obtain

$$\mathbf{G}_e^e = \begin{bmatrix} G_{ex}^{ex} & G_{ey}^{ex} & G_{ez}^{ex} \\ G_{ex}^{ey} & G_{ey}^{ey} & G_{ez}^{ey} \\ G_{ex}^{ez} & G_{ey}^{ez} & G_{ez}^{ez} \end{bmatrix} = \frac{k^2 G(\mathbf{r}, z)}{j\omega\epsilon_0} \begin{bmatrix} R_{ex}^{ex} & R_{ey}^{ex} & R_{ez}^{ex} \\ R_{ex}^{ey} & R_{ey}^{ey} & R_{ez}^{ey} \\ R_{ex}^{ez} & R_{ey}^{ez} & R_{ez}^{ez} \end{bmatrix} = \frac{k^2 G(\mathbf{r}, z)}{j\omega\epsilon_0} \mathbf{R}; \quad (14)$$

$$\mathbf{R} = \frac{1}{r^2} \begin{bmatrix} x^2 - r^2 & yx & zx \\ xy & y^2 - r^2 & zy \\ xz & yz & z^2 - r^2 \end{bmatrix} = \frac{1}{r^2} \begin{bmatrix} -(y^2 + z^2) & yx & zx \\ xy & -(x^2 + z^2) & zy \\ xz & yz & -(x^2 + y^2) \end{bmatrix} \quad (15)$$

4. EXPRESSION OF EM WAVE USING PERTURBATION METHOD

Here we use a perturbation method to estimate effects of depolarization due to the propagation in the random medium. Equation (11) can be expressed by the following formal equation.

$$\mathbf{E} = \mathbf{E}_{in} + \mathbf{L}\mathbf{E} \quad (16)$$

where $\mathbf{E} = [E_x, E_y, E_z]_t$, $\mathbf{E}_{in} = [E_{ix}, E_{iy}, E_{iz}]_t$, and $\mathbf{L} = -j\omega \int_V d\mathbf{r}' \cdot [\sum_\alpha \mathbf{G}_{e\alpha}^e(\mathbf{r} - \mathbf{r}') \epsilon_d(\mathbf{r}')] \cdot \mathbf{E}$. Here, \mathbf{L} is divide into

$$\mathbf{L} = \mathbf{L}_0 + \Delta\mathbf{L} \quad (17)$$

where \mathbf{L}_0 and $\Delta\mathbf{L}$ are the unperturbed and perturbed operators, respectively. In this case, \mathbf{E} can also be defined as follows:

$$\mathbf{E} = \sum_{n=0}^{\infty} \Delta^n \mathbf{E}^{(n)} \quad (18)$$

According as the power of Δ , the field equations may be expressed by

$$\Delta^0 : \mathbf{E}^{(0)} = \mathbf{E}_{in} + \mathbf{L}_0 \mathbf{E}^{(0)} \quad (19)$$

$$\Delta^1 : \mathbf{E}^{(1)} = \Delta\mathbf{L}\mathbf{E}^{(0)} + \mathbf{L}_0 \mathbf{E}^{(1)} \quad (20)$$

$$\Delta^2 : \mathbf{E}^{(2)} = \Delta\mathbf{L}\mathbf{E}^{(1)} + \mathbf{L}_0 \mathbf{E}^{(2)} \quad (21)$$

:

$$\Delta^n : \mathbf{E}^{(n)} = \Delta\mathbf{L}\mathbf{E}^{(n-1)} + \mathbf{L}_0 \mathbf{E}^{(n)} \quad (22)$$

:

In above equations, $\mathbf{E}^{(0)}$ is the unperturbed field which is not depolarized through propagation in the random medium. Therefore, \mathbf{E} can be expressed as the following equation by putting $\Delta^{(n)} = 1$.

$$\mathbf{E} = \sum_{n=0}^{\infty} \mathbf{E}^{(n)} = \mathbf{E}^{(0)} + \mathbf{E}^{(1)} + \mathbf{E}^{(2)} + \dots + \mathbf{E}^{(n)} + \dots \quad (23)$$

On the other hand, \mathbf{E} can be expressed by

$$\begin{aligned} \mathbf{E} &= \mathbf{E}_{in} + [\mathbf{L}_0 \mathbf{E}^{(0)} + \Delta \mathbf{L} \mathbf{E}^{(0)}] + [\mathbf{L}_0 \mathbf{E}^{(1)} + \Delta \mathbf{L} \mathbf{E}^{(1)}] + \dots \\ &= \mathbf{E}_{in} + (\mathbf{L}_0 + \Delta \mathbf{L})(\mathbf{E}^{(0)} + \mathbf{E}^{(1)} + \mathbf{E}^{(2)} + \dots) = \mathbf{E}_{in} + \mathbf{L}\mathbf{E} \end{aligned} \quad (24)$$

Because $\mathbf{E}_{in} = [E_{ix}, E_{iy}, 0]_t$ shown in Fig. 1, the unperturbed wave is given as the solution of the following equation.

$$\begin{aligned} E_{\alpha}^{(0)}(\boldsymbol{\rho}, z) &= E_{i\alpha}^{(0)}(\boldsymbol{\rho}, z) - k^2 \int_0^{z_0} dz' \int_{S_{\infty}} d\boldsymbol{\rho}' \\ &\quad \cdot \left[G(\boldsymbol{\rho} - \boldsymbol{\rho}', z - z') R_{e\alpha}^{e\alpha}(\boldsymbol{\rho} - \boldsymbol{\rho}', z - z') \delta\varepsilon(\boldsymbol{\rho}', z') E_{\alpha}^{(0)}(\boldsymbol{\rho}', z') \right] \end{aligned} \quad (25)$$

where $\delta\varepsilon(\mathbf{r}) = [\varepsilon(\mathbf{r}) - \varepsilon_0]/\varepsilon_0$. From Eq. (25), we obtain the unperturbed operator \mathbf{L}_0 .

$$\mathbf{L}_0 = L_0 \mathbf{D}_{L_0}; \quad (26)$$

$$L_0 = -k^2 \int_0^{z_0} dz' \int_{S_{\infty}} d\boldsymbol{\rho}' \cdot [G(\boldsymbol{\rho} - \boldsymbol{\rho}', z - z') \delta\varepsilon(\boldsymbol{\rho}', z')] , \quad (27)$$

$$\mathbf{D}_{L_0} = \frac{-1}{|\mathbf{r} - \mathbf{r}'|^2} \begin{bmatrix} (y - y')^2 + (z - z')^2 & 0 & 0 \\ 0 & (x - x')^2 + (z - z')^2 & 0 \\ 0 & 0 & (x - x')^2 + (y - y')^2 \end{bmatrix} \quad (28)$$

On the other hand, using Eqs. (14) and (15), we can express Eq. (16) as

$$\mathbf{E}(\boldsymbol{\rho}, z) = \mathbf{E}_{in}(\boldsymbol{\rho}, z) - k^2 \int_0^{z_0} dz' \int_{S_{\infty}} d\boldsymbol{\rho}' \cdot [G(\boldsymbol{\rho} - \boldsymbol{\rho}', z - z') \mathbf{R}(\boldsymbol{\rho} - \boldsymbol{\rho}', z - z') \delta\varepsilon(\boldsymbol{\rho}', z') \mathbf{E}(\boldsymbol{\rho}', z')] \quad (29)$$

From above equation, we obtain the operator \mathbf{L} in Eq. (17).

$$\mathbf{L} = L_0 \mathbf{D}_L; \quad (30)$$

$$\begin{aligned} \mathbf{D}_L &= \mathbf{R}(\boldsymbol{\rho} - \boldsymbol{\rho}', z - z') \\ &= \frac{1}{|\mathbf{r} - \mathbf{r}'|^2} \begin{bmatrix} -(y - y')^2 - (z - z')^2 & (x - x')(y - y') & (x - x')(z - z') \\ (x - x')(y - y') & -[(x - x')^2 + (z - z')^2] & (y - y')(z - z') \\ (x - x')(z - z') & (y - y')(z - z') & -[(x - x')^2 + (y - y')^2] \end{bmatrix} \end{aligned} \quad (31)$$

Because $\Delta \mathbf{L} = \mathbf{L} - \mathbf{L}_0$, we can obtain the perturbed operator $\Delta \mathbf{L}$.

$$\Delta \mathbf{L} = L_0 \Delta \mathbf{D}; \quad (32)$$

$$\Delta \mathbf{D} = \frac{1}{|\mathbf{r} - \mathbf{r}'|^2} \begin{bmatrix} 0 & (x - x')(y - y') & (x - x')(z - z') \\ (x - x')(y - y') & 0 & (y - y')(z - z') \\ (x - x')(z - z') & (y - y')(z - z') & 0 \end{bmatrix} \quad (33)$$

If $z_0 \ll z$, then $R_{ex}^{ex} \approx -1$, $R_{ey}^{ey} \approx -1$ and $R_{ez}^{ez} \approx 0$ in Eq. (25). In this case, we have obtained $\mathbf{E}^{(0)}$: The solution of Eq. (25) approximately in a compact form [1]. Therefore we can discuss quantitatively the depolarization through the analysis of Eq. (20).

5. CONCLUSION

We derived an integral equation using the dyadic Green's function on the assumption that there exists a random medium screen of which the dielectric constant is fluctuating randomly. To solve the depolarization problem, we modified the integral equation on the condition that the observation point is very far from the screen. Form this modified integral equation, the analytic expression of the depolarized EM wave has been given by using the perturbation method. This result is useful for the analysis of the depolarization of EM wave propagated through a random medium screen.

REFERENCES

1. Tateiba, M., "Theoretical study on wave propagation and scattering in random medium and its application (invited)," *IEICE Transactions on Electronics*, Vol. E93-C, No. 1, 3–8, 2010.

Electromagnetic Analysis of an in-car Complex Channel of Propagation by Means of Non Invasive Measurements and FDTD Based EM Simulations

J. G. Tartarin¹, M. Cheikh², J. David³, and A. Morin²

¹LAAS-CNRS & Universite de Toulouse, 7 av. du Col. Roche, Toulouse 31077, France

²Continental Automotive France SAS, 1 rue Paul Ourliac, Toulouse 31036, France

³LAPLACE, 2 rue Camichel, Toulouse 31000, France

Abstract— Wireless communication systems are now largely deployed to secure human activities: sensors can alert from different dangers indoor (house fire or gas leak, alert and prevent from intrusion) or outdoor (civil and military applications). The development of sensors in transport (aircrafts, trains, trucks, cars, ...) is a crucial and sensitive area for security purposes (radar, driver vigilance system, ...). Among these solutions, tire pressure monitoring systems (TPMS) measure in real time the pressure of tires to increase safety, reduce tire wear and save gas. However, the wireless communication between the four emitting wheel sensor modules and the receiver usually suffer from important data losses. These losses can be attributed to the profile of the radio frequency (RF) channel of propagation (rotating wheel, ground effects, ...). As the RF channel is not operating in free space conditions, many propagation effects corrupt the propagation between the sources and the receiver. Moreover, the emitting sources are close to metallic frames (rim, chassis of the car, ...), and far field condition is rarely satisfied. It is thus necessary to propose reliable models of the radiating source and of the propagation effects to establish efficient solutions and to improve the rate of the received frames. This work presents results on the electromagnetic (EM) simulations of the transmitting source, and of the overall channel for different car models; these simulations are confronted to non-invasive measurements to analyze the root causes of failing transmissions. This method, melting EM simulations with RF measurements, shortens the roadmaps for setting new wireless systems working in harsh environments.

1. INTRODUCTION

Automotive security requirements make use of different RF systems. Among these systems, tire pressure monitoring systems (TPMS) allow a real time evaluation of the pressure for each tire of the car, by sending frames of data over a RF signal (next, the carrier frequency is given @ $F_{RF} = 434\text{ MHz}$). The system can locate each tire around the vehicle, and a display screen on the dashboard close to the receiver alerts the driver when the pressure is lower or higher than the expected value (Figure 1, right caption). It is well established that RF propagation in a complex structure can be sensitive to local RF signal losses. In a car structure, the medium of propagation is made of 3D multi-scale modules, and the transmitters (sensors+RF module) are moving around the rim as a function of the speed of the vehicle. As the structure of the car is made with many different dielectric or metal parts sizing from some wavelengths ($\lambda_{RF} = 69\text{ cm}$) to less than $\lambda_{RF}/20$ (i.e., lumped pieces), the RF channel of propagation is perturbed by a combination of dense multipath processes due to diffraction, diffusion, reflection (diffuse or specular), and waveguide transmission. The development of TPMS modules needs an accurate knowledge of the involved propagation phenomena, so that matched strategies can be developed to improve the reception rate of the sent frames [1]. A fully experimental approach is not suited to develop optimized modules: this technique is time consuming, and cannot easily authorize studies versus variable parameters to understand the underlying phenomena managing the propagation channel performance. Electromagnetic (EM) simulations stand as an efficient tool to shorten times of development, and to understand how the RF channel is established (or perturbed) between the transmitter and the receiver [2]. Moreover, EM simulation allows to determine the impact of the car design, or to test the robustness of the TPMS versus different options (rim size, number of passengers, ...). TPMS communications are affected by signal losses when the RF received power is lower than a given value (depending on the signal to noise S/N ratio): this RF power is approximately -90 dBm for the receiver of this study (Figure 1, left caption). It is well known that the angular position of the emitting source plays a deterministic role in the appearance of black spots. But other parameters (such as the position

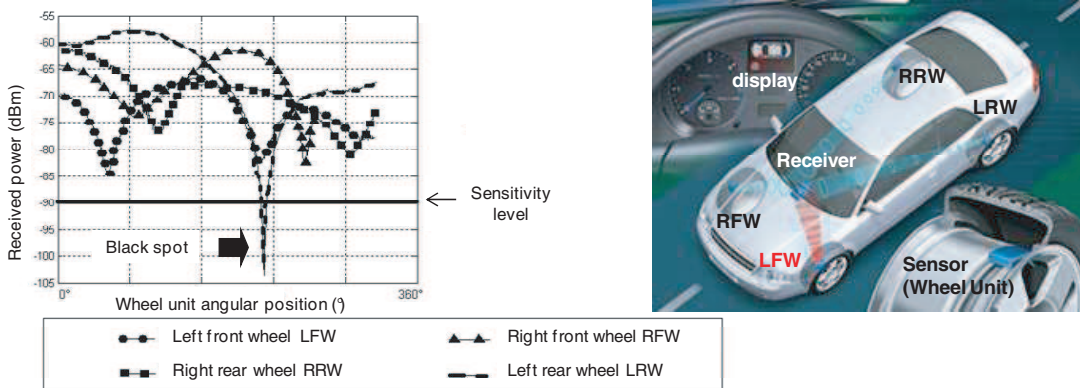


Figure 1: Tire Pressure Monitoring System (TPMS) involving four wheel units and a receiver on the dashboard (right caption). The received power varies according the angle of the wheel unit, with different signatures for each module (left caption). Each received frame on a black spot angular position is lost.

of the receiver on the dashboard, the manufacture of the tires, the type of car, ...) also have an impact on the angular position of some of these black spots.

The first paragraph is dedicated to the study of the radiated power at the vicinity of the emitting source around the wheel. The second paragraph presents simulations and measurements of the electromagnetic field distribution in and out of the car structure for two different structures. A conclusion synthesizes the final results.

2. NEAR FIELD MEASUREMENTS AND SIMULATIONS OF THE RF SOURCE

Electromagnetic simulations are performed using Finite Difference Time Domain method (FDTD software EMPIRE from IMST). FDTD method is based on the resolution of Maxwell's equations, and is suitable for the simulation of multi-scale environment operating in Rayleigh zone as well as in Fresnel zone. A large set of simulations has been performed to calibrate the simulation tools and to establish the exactness of the following studies. Moreover, a specific non-invasive measurement method is used, which does not interact with the EM fields to measure [3]. This method is also particularly suitable for measurements of complex systems (cf. Section 3). The emitting module radiation pattern is usually analyzed using two dimensions (2D) or three dimensions (3D) representation in far field simulations or measurements. This method is not fully relevant for automotive embedded systems as far field conditions are not generally satisfied. We have proposed an accurate method for characterizing the source module with different configurations (wheel unit alone, with rim, with tire, with ground effects). It is shown that the presence of the rim and tire affects the radiation pattern, as well as the ground effect: several sources are then located between tire and rim according to a $\lambda_{RF}/2$ distribution law. Measurements match with EM simulations trends (even if the metallic or dielectric constants and design of the tire are not accurately instructed) [4]. It is clear that the increase in the frequency carrier (for example from 434 MHz to 2.45 GHz) generates a larger distribution around the wheel, and thus can penalize the RF transmission efficiency: this is relevant with experimental results from TPMS tests at $F_{RF} = 2.45$ GHz. From measurements and EM simulation (Figure 2), it is evidenced that the relative angular position of the wheel unit referred to the ground changes the power distribution, and thus the RF radio link efficiency. From now, the TPMS unit cannot be considered like a lumped source.

3. WIRELESS COMMUNICATION IN CAR STRUCTURES: SIMULATIONS AND MEASUREMENTS

The scanning measurement of the EM field inside the full car environment is not a convenient strategy to understand which parameter impacts the RF losses between the four emitters and the source: then, measurements have been focused around the dashboard using 3-axis representation, with a measurement resolution of 3 cm for the horizontal plan ($x-y$), and of 5 cm for the vertical axis (z) (cf. Figure A for $x-y-z$ axis representation). Figure 3 represents the variation of the received power for two different locations near the dashboard (@ two y -positions).

From the numerous sounding records versus $x-y-z$ axis, no strong correlation can be found between power data records with $x-y-z$ parameters to get out a generic rule for the receiver's

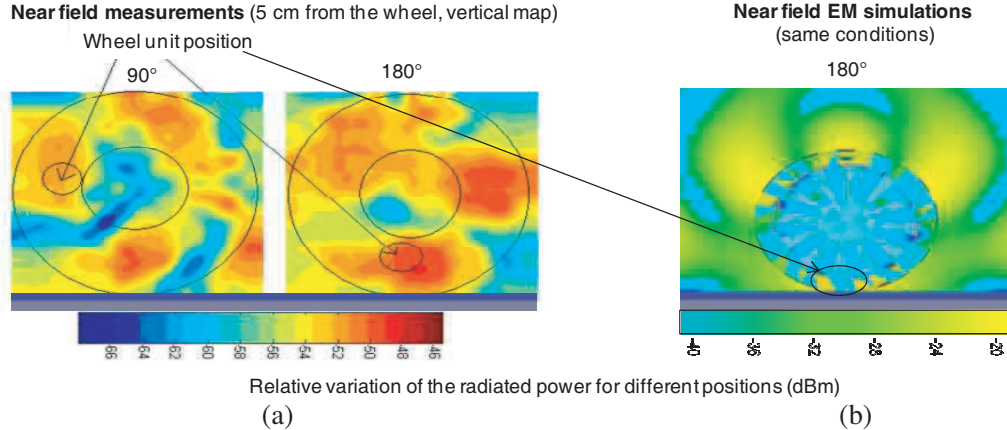


Figure 2: (a) Measurements and (b) simulated relative power distribution in near field condition of the wheel unit embedded with the rim, the tire and considering ground effects (flat grey zone under the wheel).

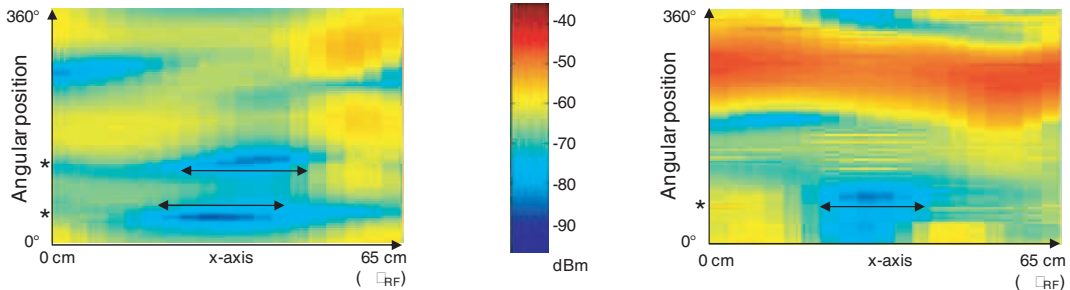


Figure 3: Measurements of the received power versus x -axis of the car for different angular positions of the wheel unit. The two plots are given for 2 y -positions spaced by 10 cm from rear to front part of the dashboard).

location (as far as the optimum location differs from a wheel unit to another one). However, it is obvious that some angular positions (angular width less than 10°) are error-prone (RF signal losses noticed by * and arrows in Figure 3), on a large x -axis range (over some 20 cm). Mostly, for a given angular position, power variation with x -axis is very smooth. The variation versus the y -axis is larger than that versus x -axis. This can be attributed to an RF channel mostly perturbed by the y -position (i.e., channel length), whereas the x -location does not play a strong role if avoiding given sensitive zones (angular black spots *). These results compare favorably with EM simulations. Different structures of cars have been investigated. Two car structures are proposed in this paper (Figure 4): the first one is convenient for evaluating the impact of the size of the car (just by varying one parameter length at a time), the impact of the glasses (no glass-replaced by metal, up to 4 or 6 glasses). The second car structure has been used for realistic complex structures simulations.

Figure 5 presents a lateral simulation of the RF signal propagation inside the car. If the RF signal between the ground and the chassis seems to be guided (with a $\lambda_{RF}/2$ periodicity on the magnitude of the electrical field), the propagation in direct link (Line Of Sight, LOS) between the sensor and the receiver is largely perturbed by the many metallic-dielectric parts constituting the car. The meshing structure close to the emitting antenna is important (step $\lambda_{RF}/150$), and decreases in the tire ($\lambda_{RF}/50$) and at all other simulated zones ($\lambda_{RF}/20$). Increasing the meshing definition should improve the accuracy of the EM simulation, however the proposed simulated results are in good agreement with the measurement trends.

The angular variation of the wheel sensor's position is given in Figure 6 for a fixed position of the receiver on the dashboard. The trend of the simulated magnitude of the signal is in good agreement with measurements, despite reduced variation range due to the simulator's power resolution (20 dB). From our studies, the embedded contributions of the car structure has been computed (chassis, engine, lateral metallic frames, glasses,). The overall car design statistically impacts of more than 30 dB the RF budget link in comparison with free space propagation context. This study has been used to set the different strategies of diversity to improve the efficiency of the reception of data (time diversity, polarization and space diversity) [5].

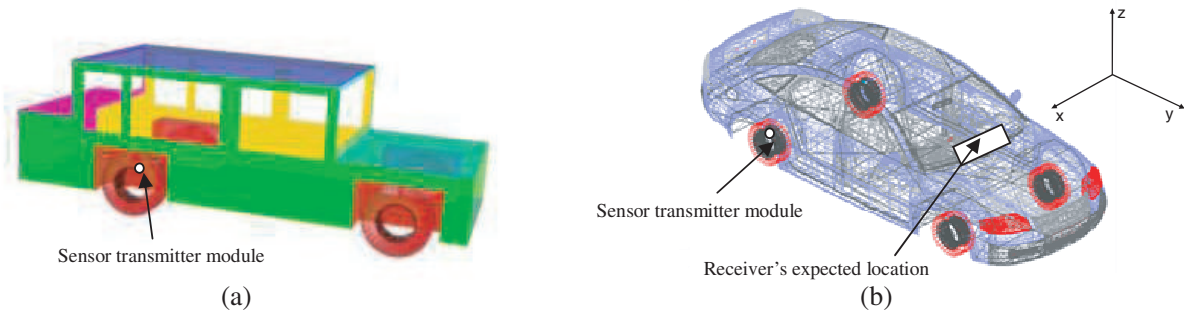


Figure 4: Design of car structures for EM simulations: (a) simplified tunable car's structure and (b) realistic models (meshing and EM simulations are next performed @ $F_{RF} = 434$ MHz).

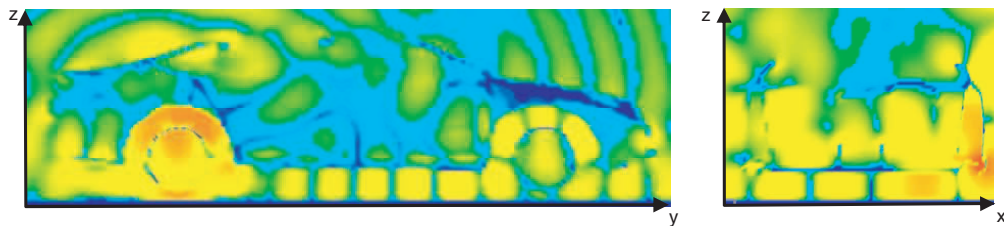


Figure 5: EM field in vertical lateral cut (left caption y - z cross-section) and vertical cut (right caption x - z cross-section at the dashboard): the simulated car structure is a berline (Figure 4(b)) RF waves are mainly guided between the ground and the chassis, whereas the EM field is largely perturbed inside the car.

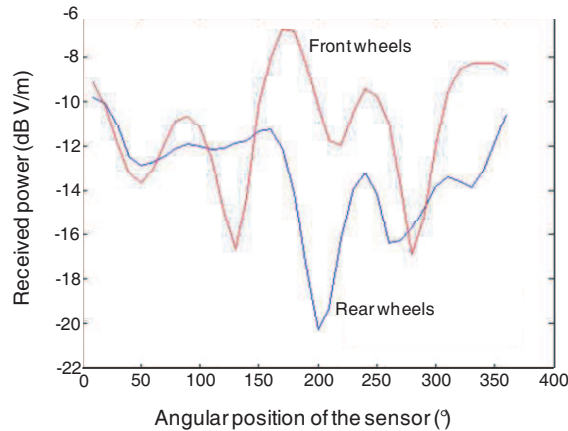


Figure 6: Simulated received power variation versus the angular position of the transmitter wheel unit. Black spot positions can be evidenced for given angular positions (rear wheels @ 200 degrees).

4. CONCLUSIONS

This paper is a contribution to the analysis of wireless radio link in complex embedded environments. The wheel unit is accurately investigated, and it is shown that the source is distributed around the tire. The EM field distribution of the complete car structure is characterized and simulated. From EM simulations, it is possible to discriminate the impact of each element constituting the car from the overall RF signal losses: less than 7 dB are associated with the chassis alone, and more than 20 dB are attributed to the rest of the car structure.

REFERENCES

1. Cheikh, M., J. G. Tartarin, J. David, S. Kessler, and A. Morin, "Transmission quality evaluation of tire pressure monitoring systems," *12th International IEEE Conference on Intelligent Transportation Systems — ITSC 2009*, 6, Saint-Louis, USA, October 2009.

2. Blocher, H. L., K. Beilenhoff, and J. Wenger, "Simulation of the electromagnetic wave propagation in cars," *European Microwave Conference*, 1151–1154, Munich, 2003.
3. Cheikh, M., J. David, J. G. Tartarin, S. Kessler, and A. Morin, "Channel characterization techniques for wireless automotive embedded systems," *PIERS Proceedings*, 1391–1395, Marrakesh, Morocco, March 20–23, 2011.
4. Cheikh, M., J. David, J. G. Tartarin, S. Kessler, and A. Morin, "RF source characterization of tire pressure monitoring system," *European Wireless Technology Conf., (EuWiT'2009)*, 4, Roma, September 2009.
5. Cheikh, M., J.-G. Tartarin, J. David, S. Kessler, and A. Morin, "Efficient time diversity evaluation for direct tire pressure monitoring system," *Vehicular Technology Conference VTC*, Taipei, 5, 2010.

A Neural Network-ray Launching Technique for Coverage Prediction

Juan Pascual-García, José Víctor Rodríguez-Rodríguez, María Teresa Martínez-Inglés,
 José María Molina-García-Pardo, and Leandro Juan-Llácer
 Department of Information and Communication Technologies (TIC)
 Technical University of Cartagena (UPCT), Spain

Abstract— Wireless communication systems require accurate coverage prediction to achieve an appropriate deployment. Ray launching is one of the most precise techniques to calculate path loss for urban outdoor and indoor environments. Nevertheless, it is a very time consuming method. In previous works an efficient mechanism to evaluate the path loss in a limited area from a one point ray launching simulation was presented. This technique was two hundred times faster than the original ray launching method.

In order to use this fast technique in the whole area of interest is necessary to select the simulation points in a suitable way. Otherwise, large errors will occur in the coverage prediction. To allow fast and accurate prediction coverage in large areas the one simulation technique is incorporated into a neural network structure. The neural structure has three layers. The main layer is composed of several one simulation units. Each unit (neuron) is able to calculate the path loss everywhere in the whole area, but is accurate only in a certain region of the area. For this reason, another layer groups the input points in different regions and connects each region to the appropriate neurons. Finally, the output layer performs a linear combination of the main layer neuron outputs. The neural network-ray launching technique was tested in a 60 GHz indoor environment. The simulation results show that the proposed method is precise and allows a drastic time reduction with respect to the original ray launching tool.

1. INTRODUCTION

Nowadays, wireless and mobile communication systems need accurate coverage prediction tools. This is especially important for the design of high frequency systems that operate in microcell and indoor environments. Ray launching is a deterministic technique that permits a precise calculation of the path loss [1]. The main handicap of ray-launching techniques lies on the slowness of the calculation. Even in simple indoor scenarios, the time needed to compute the path loss in all points of interest could make ineffective this accurate technique.

In [2], a very fast propagation model, based on a ray launching technique, was presented. A traditional ray launching method determines the direct, reflected and diffracted rays that arrive to each reception point. In [2] the path loss is evaluated in a spatial region using only the rays corresponding to a reception point which was placed at the center of the mentioned region. We call this approximation method the one simulation technique. The results showed that the one simulation technique was up to 200 times faster than the exact ray launching model [2].

The approximation error in the one simulation technique grows as the region area is increased. Thus, more simulation points must be added to reduce the error. The selection of these points is essential to achieve a correct performance in the whole area of interest. In the present work, the desired point selection is efficiently achieved by means of a neural network structure. The neural network is composed of three layers. Each neuron of the main layer is a one simulation unit which is able to calculate the path loss in the whole area. Another layer, called the selection layer, separates the neurons in different groups. Each group is accurate in certain area of the original region. Finally, the output layer combines linearly the outputs of the neurons that belong to one specific group. The final output is very accurate since is a linear combination of precise one simulation path loss calculations.

2. THE ONE SIMULATION TECHNIQUE

In this section, the one simulation technique is briefly explained. The method is similar to the technique developed in [2]. The technique assumes that the rays impinging to one point are similar to the rays impinging to points placed near that point. In order to evaluate the path loss is necessary to make a phase and module correction. If r is the position of the new point, where we want to calculate the path loss, and r_o is the position of the original point, the correction for the direct ray is:

$$H_{LOS}(\vec{r}) = H_{LOS}(\vec{r}_o) \cdot e^{-j\frac{2\pi}{\lambda}(R_{Tx-N} - R_{Tx-o})} \cdot \frac{R_{Tx-o}}{R_{Tx-N}}, \quad (1)$$

where R_{Tx-o} is the distance between the transmitter and the original point and R_{Tx-N} is the distance between the transmitter and the new point. The reflected rays are reconstructed using the image theory. The image of the reflection position is calculated as:

$$\vec{r}_I = \vec{r}_o + \tau c \cdot (\cos(\varphi_{Rx}) \hat{x} + \sin(\varphi_{Rx}) \hat{y}), \quad (2)$$

where φ_{Rx} is the angle of arrival of the multiple reflected ray. The image is employed to evaluate the reconstructed multiple reflected ray:

$$H_{REFL}(\vec{r}) = H_{REFL}(\vec{r}_o) \cdot e^{-j\frac{2\pi}{\lambda}(R_{I-N} - R_{Tx-o})} \cdot \frac{R_{I-o}}{R_{I-N}}, \quad (3)$$

where R_{I-o} is the distance between the image and the original point and R_{I-N} is the distance between the image and the new point. It is assumed that the reflection coefficient does not change. Finally, the diffracted ray is reconstructed with the next equation:

$$H_{DIF}(\vec{r}) = H_{DIF}(\vec{r}_o) \cdot \frac{\psi(s_N, s'_N, \phi_N, \phi'_N)}{\psi(s_o, s'_o, \phi_o, \phi'_o)}, \quad (4)$$

where $\Psi(s_N, s'_N, \phi_N, \phi'_N)$ and $\Psi(s_o, s'_o, \phi_o, \phi'_o)$ are the variable part of the electric field expression for the new and original points respectively. More details of this diffraction term can be found in [2]. The more similar the rays of the original and new point are the better the path loss approximation is.

3. THE NEURAL NETWORK-RAY LAUNCHING TECHNIQUE

The neural network has three layers, as depicted in Figure 1. The input data is the position of the point where the path loss is going to be evaluated. The selection layer assigns the input point to one of the regions in which the whole area of interest is divided. This layer is obviously a classifier. The classification criterion is based on the similarity between the rays of two distinct points. The selection layer is also an activation layer since it activates only one group of neurons of the main layer. Each neuron of the main layer is a one simulation calculation unit. Therefore it is able to evaluate the path loss of the input point. The final output is the linear combination of all output neurons of the region activated by the selection layer. The selection layer assures that the main rays of the input point are similar to the main rays of the region neurons. Thus, the approximation of the path loss is precise. The complete neural network can be viewed as a neural network that incorporates knowledge about the problem in order to achieve a better approximation [3].

The design and train of the neural network comprises various steps:

- Simulation of several points inside the area of interest. The simulation produces a set of rays for each point. Each of these points (class points) defines a region in the whole area (a class of points).
- Simulation of a training set. The utility of this set is twofold. It is used to determine the regions limit (training of the selection layer). Furthermore, the points that define the neurons of the main layer are extracted from this set.
- Simulation of a testing set. This set is used to test the classification quality and the approximation performance.
- Training of the selection layer. We have chosen as classifier a Radial Basis Neural Network (RBFNN).
- In each class, the points that permit the best proximation performance of the path loss in their class are added as neurons of the main layer.
- Computation of the approximation error in the whole area. If the training and testing threshold errors are satisfied then the training ends. If not, more neurons are added in those regions where the threshold errors have been exceeded. Each region is allow to possess a different number of neurons, i.e., in Figure 1 region number 1 has p neurons and region number 2 has q neurons.

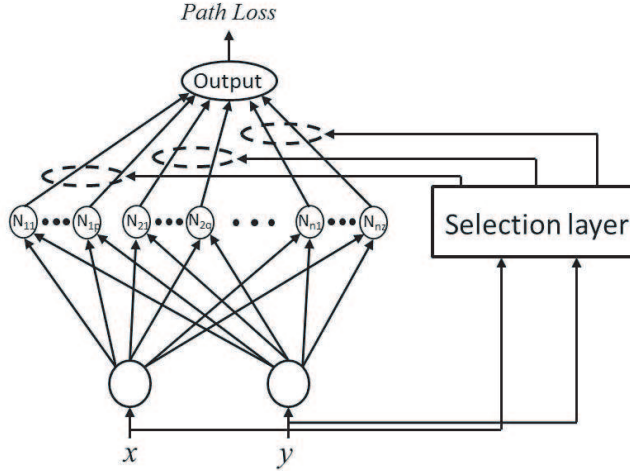


Figure 1: Neural network structure.

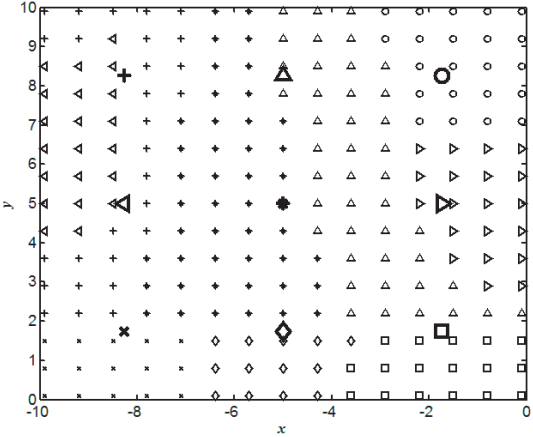


Figure 2: Classes (regions) in the room. Big symbols correspond to the reference points used to define the classes (class points).

4. RESULTS

The neural network-ray launching technique was tested in an indoor environment at 60 GHz. This frequency is inside the band of 57–66 GHz, which is a very promising candidate to provide high speed data services for WLAN applications [4]. The indoor scenario is a room of $10 \text{ m} \times 10 \text{ m}$. $[-10 \leq x \leq 0; 0 \leq y \leq 10]$. The transmitter is placed at the position $[-6, 8]$. The room walls are constructed with plasterboard. This material has a relative dielectric constant of 2.81 and a conductivity of 0.15 at 60 GHz [4]. The maximum number of rays to obtain the path loss with the ray launching tool at each reception point was 10000.

The number of classes (regions) was set to 9. Therefore 9 class points were simulated in a regular grid as depicted in Figure 2. To define the limits of each region a training set must be defined. A 15×15 regular grid was selected as shown in Figure 2. Each training point must be assigned to one of the 9 classes. To carry out this task a comparison between the two main rays (direct and first reflection rays) of each training point and each class point was performed. Each training point is assigned to the class point whose rays show the higher similarity to the training point rays. To measure the similarity between two rays a Gaussian function is utilized:

$$G_{similarity} = \frac{1}{2\pi\sqrt{\sigma}} e^{-\frac{1}{2\sigma^2} \|r_c - r_t\|^2}, \quad (5)$$

where r_c is the position of the class point ray and r_t is the position of the training point ray.

Once the class definition step ends, main layer neurons are added to each one of the 9 classes. The number of neurons ranges from 3 to 5, depending on the difficulty in the approximation. A testing set composed of 100 random points was simulated in order to test the classification ability and the approximation error (set 1). Furthermore, to show the quality of the new procedure an additional testing set of 10000 points distributed in a regular grid was simulated (set 2). This last set was not used to design the neural network.

The classification error measured with the random testing set was 6%. The neural network method was compared with the technique developed in [2]. The Table 1 shows that our method clearly outperforms the previous work. When only one point is selected as simulation unit, huge errors appear. More one simulation units must be used. Nevertheless, as shown in Table 1, if the 225 points of the training set are employed with the old method, large errors still appear. Therefore, the neural network method provides an appropriate assignation, based on the similarity between rays, and a linear combination of the best units that assures the lowest errors as seen in Table 1.

Once trained, the neural network computes the path loss very fast. The neural network spends only 1.45 seconds to evaluate the path loss of 10000 points whereas the ray launching technique consumes 4132 seconds. The total time spent in the neural design is 162 seconds. Thus, the neural method becomes profitable. All simulations were performed with an I5 3.5 GHz Intel processor computer.

Table 1: Error data corresponding to the three methods. The error is the absolute value of the difference between the path loss calculated with the ray launching technique and the path loss evaluated with the approximated method.

	Error Mean (dB)		Error Variance (dB)		Maximum Error (dB)	
	Set 1	Set 2	Set 1	Set 2	Set 1	Set 2
1 one simulation units [2]	0.615	0.638	0.640	0.607	4.787	10.644
225 one simulation units	0.167	0.256	0.114	0.292	2.121	5.567
Neural network	0.217	0.259	0.045	0.076	1.042	2.753

5. CONCLUSIONS

In this paper, a neural network technique for the calculation of path loss in wireless environments is presented. The neurons of the structure are units that calculate the path loss by means of a ray launching based method. The neural network performs two main operations to compute the path loss. Firstly, it assigns an input point to the proper region. Secondly, the path loss corresponding to the input point is calculated with a linear combination of the best one simulation units of the selected region (class). The simulation results show the ability of the neural method to calculate the path loss, even for large sets, with precision. The larger error is less than 3 dB. Furthermore, the mean is only 0.259 dB and the variance is very small (0.076 dB). The neural method fulfills its main purpose because it is very fast and precise. Thus, the method becomes profitable with only one execution.

ACKNOWLEDGMENT

This work is funded by the Ministerio de Educación y Ciencia. Ref. TEC2010-20841-C04-03 project and the Fundación Séneca CARM Ref. 08818/PI/08 project.

REFERENCES

1. Lawton, M. C., R. L. Davies, and J. P. McGeehan, “A ray launching method for the prediction of indoor radio channel characteristics,” *IEEE International Symposium on Personal, Indoor and Mobile Radio Communications*, 104–108, London, UK, September 1991.
2. Ibernon-Fernandez, R., J.-M. Molina-Garcia-Pardo, J.-V. Rodriguez, and L. Juan-Llácer, “Predicting coverage in an area from a single simulation,” *IEEE Antennas and Propagation Society International Symposium*, 727–730, Washington, USA, July 2005.
3. Wang, F. and Q. J. Zhang, “Knowledge-based neural models for microwave design,” *IEEE Transactions on Microwave Theory and Techniques*, Vol. 45, No. 12, 2333–2343, 1997.
4. Correia, L. M. and P. O. Frances, “Estimation of materials characteristics from power measurements at 60 GHz,” *Proceedings of 5th IEEE International Symposium on Indoor and Mobile Radio Communications*, 510–513, The Hague, Holland, September 1994.

A Robust Indoor Wireless Localization

Hermawan Raharjo, Si Wen Chen, and Pengty Ngor

School of Electrical and Electronic Engineering, Nanyang Technological University, Singapore

Abstract— This paper presents a robust 3D positioning method based on Line-of-Sight (LOS) and Non-Line-of-Sight (NLOS) paths' Time of Arrival (TOA) and Angle of Arrival (AOA) measured at both mobile and reference devices in an indoor environment. Selection process by using a novel two-step weighting approach is proposed to reduce uncertainties in mobile device's location. In this process, Gaussian neighborhood function is constructed and used to calculate weighted centroid of adjacent points. Additionally, with the knowledge of ceiling height, we are able to use only one path to estimate mobile position. The proposed localization scheme is shown to be robust and outperforms previous bidirectional NLOS localization scheme.

1. INTRODUCTION

Wireless localization is an important area that receives significant research interest recently. It is required in many sensor network applications, such as transportation systems, personal tracking and navigation [1–3]. Conventional LOS schemes fail to work when there are insufficient RDs in LOS with the MD or when the signals are dominated by NLOS paths [4, 5]. Several NLOS mitigation techniques [6–12] have been suggested to identify and discard NLOS signals. These techniques are, however, will not perform satisfactorily as they generally require the number of LOS RDs to be more than the number of NLOS RDs.

Non Line of Sight localization (NLOS) techniques have been proposed to tackle the problem of insufficiency of LOS path. In NLOS schemes, NLOS information, like those of one bounce scattering, is not discarded but used to complement LOS information in determining MD position. So far, NLOS information that is contained within one bounce scattering paths can be used to assist LOS paths [13–15]. However, these methods do not work well in environments when multipath becomes too dominant and distances travelled by multiple-bounce reflection paths become comparable with those of one-bounce reflection, causing weighting factors of multiple-bounce LPMDs to be comparable with those of one-bounce.

In this paper, we formulate a novel technique to improve the robustness of the method presented in [13, 14]. Method of eliminating multiple-bounce reflection paths is proposed. We also extend the problem into 3-D environments in order to be beneficial for indoor mobile localization. In indoor environments with abundant of low-height scatterers [16], LOS path may be blocked by the scatterers but in most cases the signal can reach the receiver through ceiling reflected path. Thus, it is advantages to make use of such ceiling reflected path for localization. If the ceiling height is known, we can make use of such ceiling reflected path to estimate the mobile position. Moreover, robustness and accuracy of the algorithm is also greatly enhanced by our proposed Gaussian neighborhood weighting method. The rationale of the method is that since each measurement metric contains noise, each proximate point will also contain error. The method will then construct a Gaussian weighting function of each proximate point using the calculated variance, and assign weights to neighborhood proximate points based on how close these points are to the proximate point of interest by using Gaussian weighting function. Proximate points that have smaller variances will assign less weight to their neighbors and more weight to themselves and vice versa. Our simulation results show good accuracy and robustness of the proposed algorithm even in a dense multipath environment and for large AOA and TOA measurement noise.

2. THEORY AND FORMULATION

2.1. Concept of Line of Possible Mobile Device Location

The concept of Line of Possible Mobile Device (LPMD) in a 2-D environment has been introduced in [13, 14]. It uses LOS and one-bounce reflection paths to find possibilities of MD's position. Intersection points of LPMD serve as the estimator of MD's position. However if the problem is to be extended into 3-D, LPMDs will not intersect with each other. In this case, proximate points which are defined as points on each LPMD in a LPMD pair between which the distance between those 2 points is minimized [20].

2.2. Location Approximation Using Neighborhood Weighting

To enhance the localization accuracy, a weighting factor is assigned to each of the LPMDs. The weighting factor of each LPMD is chosen to be inversely proportional to the square of the distance traveled of that particular LPMD. Each weighting factor is also normalized with respect to other weighting factors. It is formulated as follows:

$$W'_{j,n} = \frac{1/d'_{j,n}^2}{\sum_{j=1}^N \sum_{m=1}^M 1/d'_{j,n}^2} \quad (1)$$

After assigning weights to each LPMD path, the next step is to find proximate points of all possible combinations of LPMD pairs and to calculate their corresponding weighting factors. The weighting factor of each proximate point depends on the weighting of each LPMD in the LPMD pair and the angle between the two LPMDs as given below

$$Wp'_a = \left(\frac{W'_{j,n} \times W'_{i,\ell}}{W'_{j,n} + W'_{i,\ell}} \right) \times \sin \Psi, \quad (j \neq k) \cup (\ell \neq n), \quad (2)$$

where $i, j = 1, 2, \dots, N$ where N is the total number of RD in the environment, $\ell, n = 1, 2, \dots, L$ where L is the total number of paths that can be traced from a particular RD, $\alpha = 1, 2, \dots, A$ where $A = {}^N C_2$ the number of proximate points existing in the environment. Ψ is the angle between the LPMD pair.

The next step is to calculate the neighborhood weighting factor. It is calculated by taking into account proximate point's individual weighting factor and weighting factors of its surrounding proximate points. The weighting factor of neighborhood proximate points is inversely proportional to their distances to the proximate point of interest. It is formulated as follows:

$$Wn'_a = \sum_{b=1}^K \frac{Wp'_b}{\sigma_{p_a} \sqrt{2\pi}} \times \exp \left(-\frac{\|\vec{p}_b - \vec{p}_a'\|}{2\sigma_{p_a}^2} \right) \quad (3)$$

where σ_{p_α} : Error standard deviation of the position of proximate point a . \vec{p}_b , Wp_b : Coordinate and weighting factor of proximate point b respectively.

The neighborhood weighting function takes the form of a Gaussian distribution function. Given the variance of a proximate point, the likelihood of that proximate point lying within a certain distance from the mean can be modeled and calculated by a Gaussian distribution function, with \vec{p}_a assumed to be the mean of the Gaussian distribution. The approximate mobile device position can be finally calculated as follows:

$$\hat{P}'_m = \frac{1}{K} \sum_{a=1}^K (\hat{P}'_a \times Wn'_a) \quad (4)$$

where $\hat{P}'_a = (X_a, Y_a, Z_a)$: Coordinate of a -th proximate point. \hat{P}'_m = Estimated MD position.

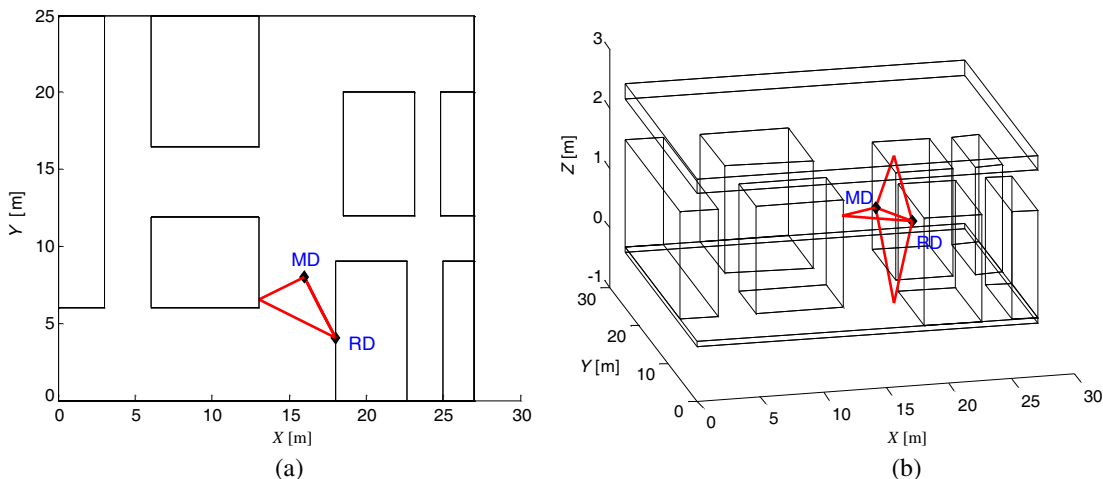


Figure 1: RD is in LOS with the MD. (a) Plan view. (b) 3-D view.

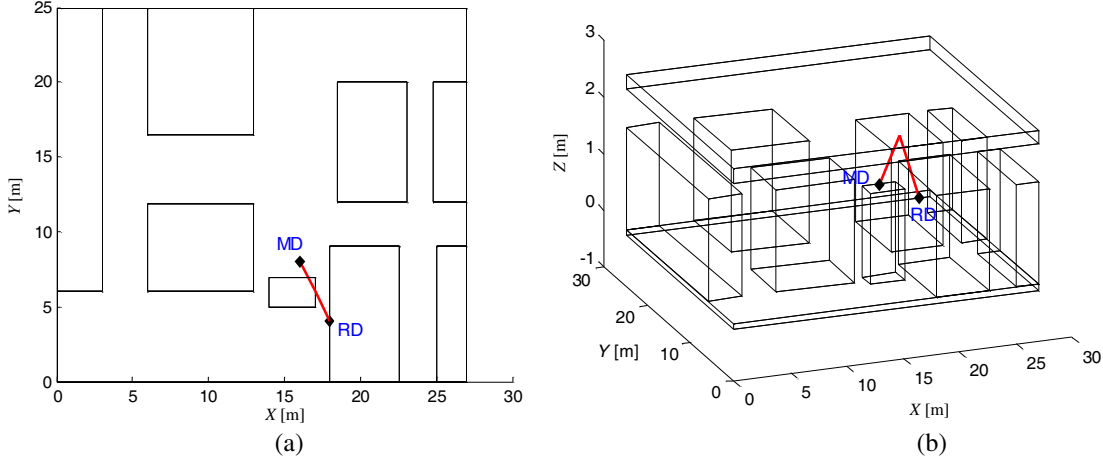


Figure 2: Case B: No RD is in LOS with the MD. (a) Plan view. (b) 3-D view.

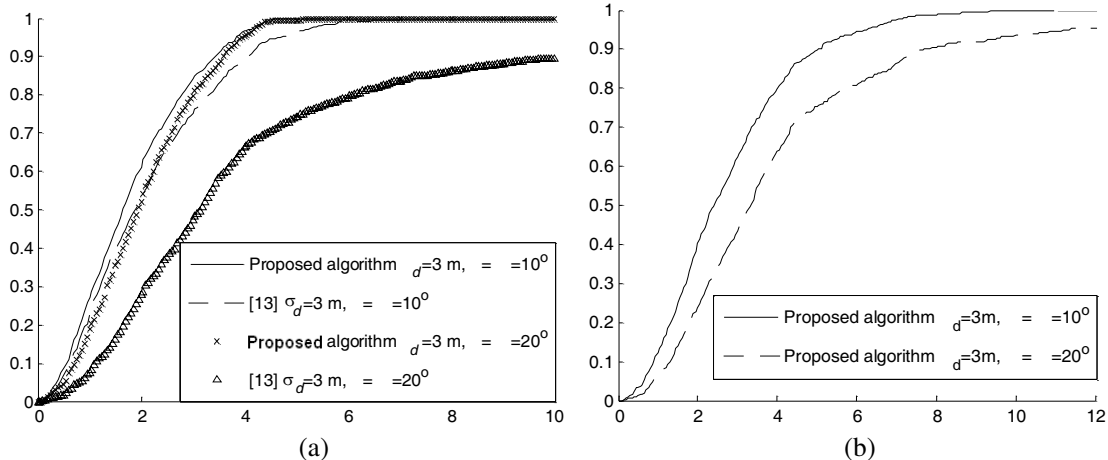


Figure 3: (a) Comparison of the CDF performance for an actual MD located at (16, 8, 1.5). RD is in LOS with MD. (b) Comparison of CDF performance for an actual MD located at (16, 8, 1.5). No RD is in LOS with MD.

3. RESULT AND DISCUSSION

To test the applicability and accuracy of our proposed localization scheme, we compare our simulation results with those presented in [13]. The authors in [13] presented the accuracy of their algorithm by selecting only the 2 best LOS and NLOS paths based on their weighting factor of LPMD paths. Here, RD and MD were positioned at the same height with ground and ceiling reflectors so that the environment is a 3-dimensional scene. Measurement data metrics (AOA and TOA) were measured by using ray tracing methodology proposed in [17–19]. RD and MD were put in the environment at (18, 4, 1.5) and (16, 8, 1.5).

For case A, MD is at position (16, 12, 1.5) in the layout as shown in Figure 1(a). In this position, RD is in LOS with MD. For case B, there is one scatterer placed between RD and MD to block LOS path so that RD is in NLOS with MD. Simulation results for case A and B are shown in Figures 3(a) and 3(b).

It is observed from the simulation results as depicted in Figure 3 that the proposed algorithm has much better accuracy. For example, in Figure 3(a), under condition 1: $\sigma_d = 3 \text{ meter}$, $\sigma_\phi = \sigma_\theta = 100$, the proposed algorithm has about 3.5 meter accuracy 90% of the time as compared to 4.1 meters of algorithm in [13]. Under condition 2: $\sigma_d = 3 \text{ meter}$, $\sigma_\phi = \sigma_\theta = 200$, our proposed algorithm has about 3.6 meters accuracy as compared to 10.5 meters of algorithm in [13]. This shows that our algorithm outperforms algorithm in [13] and improve the localization accuracy by up to 66%. In Figure 3(b), because of known ceiling height, we can get the image point of RD according to the ceiling plane. Then we are able to change the ceiling reflection to LOS path to estimate mobile position. Whereas [13] fails to work in this kind of situation.

4. CONCLUSIONS

A novel approach to improve the accuracy and robustness of NLOS bidirectional localization using neighborhood weighting method has been proposed. The proposed algorithm was tested and shown to be accurate and robust under various operating conditions. Moreover, the proposed algorithm also significantly outperforms the current NLOS localization algorithm.

REFERENCES

1. Patwari, N., J. N. Ash, S. Kyperountas, A. O. Hero III, R. L. Moses, and N. S. Correal, “Locating the nodes: Cooperative localization in wireless networks,” *IEEE Signal Processing Mag.*, Vol. 22, 54–69, Jul. 2005.
2. Sayed, A. H., A. Tarighat, and N. Khajehnouri, “Network-based wireless location: Challenges faced in developing techniques for accurate wireless location information,” *IEEE Signal Processing Mag.*, Vol. 22, 24–40, Jul. 2005.
3. Reed, J. H., K. J. Krizman, B. D. Woerner, and T. S. Rappaport, “An overview of the challenges and progress in meeting the E-911 requirement for location services,” *IEEE Commun. Mag.*, 30–37, Apr. 1998.
4. Jiang, L. and S. Y. Tan, “A simple geometrical-based AOA model for mobile communication systems,” *IEE Electronics Letters*, Vol. 40, No. 19, 1203–1205, Sep. 2004.
5. Jiang, L. and S. Y. Tan, “Geometrical-based statistical channel model for outdoor and indoor propagation environments,” *IEEE Trans. Veh. Tech.*, Vol. 56, No. 6, 3587–3593, Nov. 2007.
6. Wang, X., Z. X. Wang, and B. O’Dea, “A TOA-based location algorithm reducing the errors due to non-line-of-sight (NLOS) propagation,” *IEEE Trans. Veh. Tech.*, Vol. 52, 112–116, Jan. 2003.
7. Khajehnouri, N. and A. H. Sayed, “A non-line-of-sight equalization scheme for wireless cellular location,” *Proc. ICASSP 2003*, Vol. 6, 549–552, Apr. 2003.
8. Chen, P. C., “A non-line-of-sight error mitigation algorithm in location estimation,” *Proc. IEEE Wireless Communications Networking Conf.*, Vol. 1, 316–320, 1999.
9. Cong, L. and W. H. Zhuang, “Nonline-of-sight error mitigation in mobile location,” *IEEE Trans. Wireless Commun.*, Vol. 4, 560–572, Mar. 2005.
10. Xiong, L., “A selective model to suppress NLOS signals in angle of arrival (AOA) location estimation,” *Proc. IEEE Int. Symp. Personal, Indoor and Mobile Radio Commun.*, Vol. 1, 461–465, 1998.
11. Chan, Y. T., W. Y. Tsui, H. C. So, and P. C. Ching, “Time-of-arrival based localization under NLOS conditions,” *IEEE Trans. Veh. Tech.*, Vol. 55, 17–24, Jan. 2006.
12. Borras, J., P. Hatrack, and N. B. Mandayam, “Decision theoretic framework for NLOS identification,” *Proc. IEEE Veh. Tech. Conf.*, Vol. 2, 1583–1587, 1998.
13. Seow, C. K. and S. Y. Tan, “Non line of sight localization in multipath environment,” *IEEE Trans. Mobile Computing*, Vol. 7, No. 5, 647–660, May 2008.
14. Seow, C. K. and S. Y. Tan, “Localization of omni-directional mobile device in multipath environments,” *Progress In Electromagnetic Research*, Vol. 85, 323–348, 2008.
15. Miao, H. L., K. Yu, and M. J. Juntti, “Positioning for NLOS propagation: Algorithm derivations and cramer-rao bounds,” *Proc. ICASSP 2006*, Vol. 4, 1045–1048, Jun. 2006.
16. Tan, S. Y. and H. S. Tan, “Modelling and measurements of channel impulse response for an indoor wireless communication system,” *Proceedings IEE, Part H, Microwaves, Antennas and Propagation*, Vol. 142, No. 5, 405–410, Oct. 1995.
17. Ang, T. W., S. Y. Tan, and H. S. Tan, “Analytical methods to determine diffraction points on multiple edges and cylindrical scatterers in UTD ray tracing,” *Microwave and Optical Technology Letters*, Vol. 22, No. 5, 304–309, Sep. 1999.
18. Sun, Q., S. Y. Tan, and K. C. Teh, “Analytical formulae for path loss prediction in urban street — Grid microcellular environments,” *IEEE Trans. Veh. Tech.*, Vol. 54, No. 4, 1251–1258, USA, Jul. 2005.
19. Tan, S. Y., M. Y. Tan, and H. S. Tan, “Multipath delay measurements and modelling for inter-floor wireless communications,” *IEEE Trans. Veh. Tech.*, Vol. 49, No. 4, 1334–1341, Jul. 2000.
20. Raharjo, H., S. Y. Tan, and C. K. Seow, “Non-line-of-sight localization scheme using two-steps weighting process,” *7th International Conference on Information, Communications and Signal Processing, ICICS 2009*, Macau, China, Jan. 2010.

Neural Model for Modeling of Dumbbell Shape Defected Ground Structure

Hamid Reza Dalili Oskouei and Jafar Khalilpour
 University of Aeronautical Science & Technology, Tehran, Iran

Abstract— In recent years, neural networks have gained a lot of attention as fast and flexible tools for modeling, simulation, optimization and design of military microwave device. In this paper, a new approach of neural networks is proposed to model the Dumbbell Defected ground structure (DGS). This structure is used in different parts of military weapons such as filters, oscillators and power amplifiers.

It should be noted that the obtained results are in excellent agreement with simulation and measurement results.

1. INTRODUCTION

Recently, there has been much interest in various kinds of defected ground structures (DGS), realized by etching a defected pattern on the ground plane [1, 4]. These structures that are used in periodic [5, 7] and non-periodic [1–4] states have two main properties:

- 1- Slow wave propagation in pass band.
- 2- Band stop characteristic.

Slow wave propagation phenomenon in pass band is used for compacting microwave structures, whereas the stop band is useful to suppress the unwanted surface waves. Because of these two properties, these structures have found many applications in military microwave circuits such as filters [1, 2], power amplifiers [8], dividers [9], microwave oscillator [10] and harmonic control in microstrip antennas [11].

Modeling of these structures is a major problem among military researchers. Several equivalent circuits for these structures have been presented in the literature [1, 10, 12, 13]. The circuit parameters for these equivalent circuits should be extracted from the simulation results. Hence, there is not direct correlation between the physical dimensions of the DGS and equivalent *LC* parameters [1, 11, 12]. A new, simple, and accurate model based on artificial neural network is suggested for Dumbbell DGS in this paper. By using this model, value of *L* and *C* can be obtained easily without any need to the simulation result.

The artificial neural network (ANN) techniques have been employed in modeling numerous RF/microwave circuits, antenna and systems [14–16]. The main characteristics of neural network techniques are generality, adaptability, and generalization ability. Because of that artificial neural network (ANN), techniques are able to properly handle electromagnetic problems such as the analyses of planar transmission lines, waveguide filters, CPW lines, microstrip antenna, FET transistors, and planar spiral inductors. Every year, more and more RF and microwave problems are modeled with Neural Networks. ANNs can be used even when component formulas are not available. The neural networks commonly used in applications in microwaves, are MLP, RBF, and wavelet networks. Nevertheless, in some particular microwave applications, these conventional techniques do not offer good outputs or the large amount of training database is needed to ensure model accuracy. Hence, some new ANNs are proposed in the literature. One of these new types of ANNs is Sampling Function ANN [17].

2. DUMBBELL DGS CONFIGURATION

Figure 1 displays the geometry of a dumbbell shaped DGS etched on the ground plane of a conventional 50 microstrip transmission line with a dielectric constant of 10.5 and thickness of 50 mil. This kind of DGS, that is a combination of two square cells with a thin slot, has been used in as a low-pass filter in [1].

This DGS is modeled by a parallel LC resonator in series with the transmission line, as shown in Fig. 2. The equivalent circuit and extraction of the circuit parameters from simulation result is discussed in detail by Ahn et al. [1]

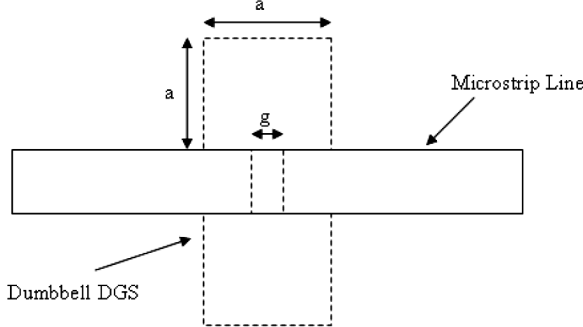


Figure 1: Dumbbell DGS configuration.

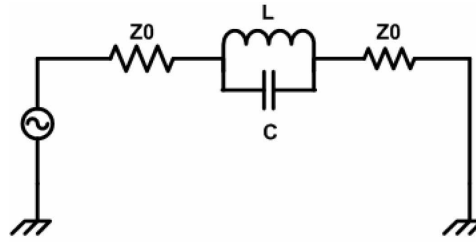


Figure 2: Equivalent circuit for Dumbbell DGS [1].

For this structure, the inductance and capacitance level depend upon to aperture area and gap width, respectively; And can be expressed as follows [1]

$$C = \frac{\omega_c}{2Z_0(\omega_0^2 - \omega_c^2)} \quad (1)$$

$$L = \frac{1}{4c\pi^2 f_0^2} \quad (2)$$

where f_c is the 3-dB cutoff frequency and f_0 is resonance frequency which can be obtained from EM simulation results. In this paper, we suggest Sampling Function ANN model for this structure, which yields L and C parameters without usage of EM simulation results.

3. SAMPLING FUNCTION ANN

This ANN is a combination of the sample Function in signal processing theory [5] and Radial Base Function (RBF) neural network configuration. The sample function is

$$\text{sample}(t) = \sin c(t/\pi) = \sin(t)/t \quad (3)$$

In this ANN, sample function is used instead of Gaussian function in RBF Neural Networks. Therefore, the activation functions of the hidden layer are defined with a set modified sample function, given by

$$g_i(t_i, c_{ji}) = \text{sample}\left(\sigma^2 \|t_i - c_{ji}\|^2\right) = \frac{\sin\left(\sigma^2 \|t_i - c_{ji}\|^2\right)}{\left(\sigma^2 \|t_i - c_{ji}\|^2\right)} \quad (4)$$

where t is the input vector that includes the input variables (DGS Dimension); c and σ are the centers (Translations) and the widths (dilatations) of sample functions, respectively.

The choice of a sample function is based on the signal processing theory. We know from this theory that the reconstructed signal $x_r(t)$ is equivalent to a linear combination of $\sin c$ functions [18],

$$x_r(t) = T \cdot \frac{\omega_c}{\pi} \sum_{-\infty}^{\infty} x(nT) \sin c\left(\frac{\omega(t - nT)}{\pi}\right) \quad (5)$$

From expression (5) for the finite number of samples, we can reach suitable accuracy for $x_r(t)$. Using this simple definition in neural networks, results in a more efficient training algorithm. For instance, sigmoid (MLP) and Gaussian (RBF) functions need more complex gradient calculations, naturally slowing down the training algorithm. On the other side, authors have shown in a previous study of microwave modeling with AAN [17], that the combination of sample function are more efficient than combination of sigmoid or Gaussian functions. The configuration of the sampling function artificial neural network (SF-ANN) used in modeling Dumbbell DGS is shown in Fig. 3.

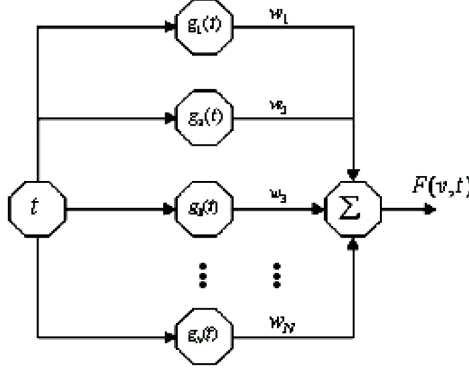


Figure 3: Configuration of the SF-ANN.

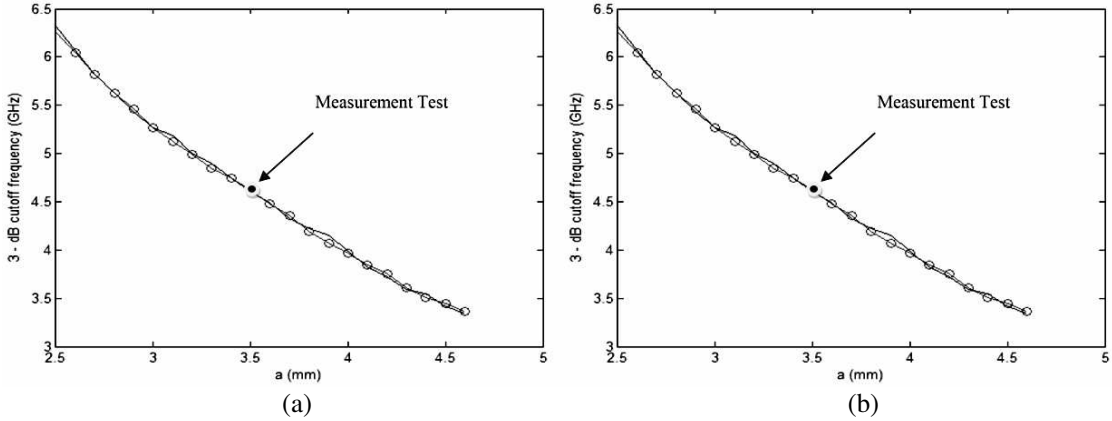


Figure 4: (a) Comparison between the neural model and simulation (3-dB cutoff frequency). (b) Comparison between the neural model and simulation (Resonance Frequency).

The direct computation of the SF-ANN is defined by the following expression:

$$net_n = \sigma_n \|t - c_n\|^2 = \sigma_n (t - c_n)^T \cdot (t - c_n) \quad (6)$$

$$y_n = g(t, c_n) = \text{sample}(net_n) \quad (7)$$

$$F(v, t) = \sum_{n=1}^N \omega_n y_n + \omega_0 \quad (8)$$

where net_n is the n th internal activation potential, y_n is the n th hidden neuron output, w_n is the n th weight between n th neuron and output layer, $F(v, t)$ is the neural model output, and N is the number of hidden units. In the supervised training process of the SF-ANN techniques, and measurement results for test data. Solid line is the SF-ANN model, circle line is simulation result and · is a measurement test for verification of simulation and ANN model.

The free parameters of the NN model $v = [w, \sigma, c]$ should be adjusted so as to diminish the following error function:

$$E(v, t) = \frac{1}{2} e^2 = \frac{1}{2} [f(t) - f(v, t)]^2 \quad (9)$$

This was accomplished by using the gradient method:

$$\Delta \omega = -\eta \nabla E \quad (10)$$

4. SIMULATION RESULT

In the neural network model of Dumbbell DGS, the input variables are DGS dimensions and the outputs of the ANN model are 3-dB cutoff frequency (f_c) and resonance frequency (f_0). We used the three layer SF-ANN, in which, the hidden layer has 50 neurons. In the training process, 50 examples were used, corresponding to simulation results with HFSS software and measurement

results presented in [1]. The final average error, after 2000 epochs of teaching, and learning rates ($\eta_w = 0.01$, $\eta_\sigma = 0.1$ and $\eta_c = 0.01$) was lower than 1.0×10^{-4} .

In order to validate the neural models for DGS, the test results obtained from this model are compared with results of simulation and a measurement data. One of these comparisons is presented graphically in Figs. 4(a) and 4(b). These figures show the resonant frequency of dumbbell DGS and 3 dB cutoff frequency, respectively, for various values of a . In this example g is fixed at 0.4 mm.

It is apparent from these figures that results of the SF-ANN are in excellent agreement with simulation and measurement results.

5. CONCLUSION

A new, efficient, and accurate ANN model was presented and used in the modeling of Dumbbell Defected ground structure. This model is useful for achieving circuit parameter without any need to the EM simulation. The SF-ANN model outputs have shown excellent agreement with the corresponding a measured result and EM simulation.

REFERENCES

1. Ahn, D., et al., "A design of the low-pass filter using the novel microstrip defected ground structure," *IEEE Trans. Microwave Theory Tech.*, Vol. 49, No. 1, 86–91, Jan. 2001.
2. Kim, J. P. and W. S. Park, "Microstrip low pass filter with multislots on ground plane," *Electronics Letters*, Vol. 37, No. 25, 1525–1526, Dec. 2001.
3. Sharma, R. Y., T. Chakravarty, S. Bhooshan, and A. B. Bhattacharyya, "Design of a novel 3 dB microstrip backward wave coupler using defected ground structure," *Progress In Electromagnetics Research*, Vol. 65, 261–273, 2006.
4. Radisic, V., Y. Qian, R. Caccioli, and T. Itoh, "Novel 2-D photonic bandgap structure for microstrip lines," *IEEE Microwave and Guided Wave Letters*, Vol. 8, No. 2, 69–71, Feb. 1998.
5. Oskouei, H. D., K. Forooraghi, and M. Hakkak, "Gauded and leaky wave characteristics of periodic ground structures," *Progress In Electromagnetics Research*, Vol. 73, 15–27, 2007.
6. Lim, I.-S., C.-S. Kim, Y.-T. Lee, D. Ahn, and S. Nam, "Vertically periodic defected ground structure for planar transmission lines," *Electronics Letters*, Vol. 38, No. 75, 803–804, Jul. 2002.
7. Kim, C.-S., J.-S. Park, D. Ahn, and J.-B. Lim, "A novel 1-D periodic defected ground structure for planar circuits," *IEEE Microwave and Guided Wave Letters*, Vol. 10, No. 4, 131–133, Apr. 2000.
8. Radisic, V., Y. Qian, and T. Itoh, "Broadband power amplifier using dielectric photonic bandgap structure," *IEEE Microwave and Guided Wave Letters*, Vol. 8, 13–14, Jan. 1998.
9. Lim, J. S., S. W. Lee, C. S. Kim, J. S. Park, D. Ahn, and S. W. Nam, "A 4:1 unequal Wilkinson power divider," *IEEE Microwave and Wireless Components Letters*, Vol. 11, No. 3, 124–126, Mar. 2001.
10. Joung, M.-S., J.-S. Park, and H.-S. Kim, "A novel modeling method for defected ground structure using adaptive frequency sampling and its application to microwave oscillator design," *IEEE Trans. on Microwave Theory Tech.*, Vol. 41, No. 5, 1656–1659, May 2005.
11. Horii, Y. and M. Tsutsumi, "Harmonic control by photonic band gap on microstrip patch antenna," *IEEE Microwave and Guided Wave Letters*, Vol. 9, 13–14, Jan. 1999.
12. Karmakar, N. C., S. M. Roy, and I. Balbin, "Quasi-static modeling of defected ground structure," *IEEE Trans. Microwave Theory Tech.*, Vol. 54, No. 5, 2160–22168, 2006.
13. Li, G.-H., X.-H. Jiang, and X.-M. Zhong, "A novel defected ground structure and its application to a low pass filter," *Microwave and Optical Technology Letters*, Vol. 48, No. 9, 453–456, Sep. 2006.
14. Bandler, J. W. and M. A. Ismail, "Neuromodeling of microwave circuits exploiting space-mapping technology," *IEEE Trans. Microwave Theory Tech.*, Vol. 47, No. 12, 2417–24273, 1999.
15. Milovanović, B., V. Stanković, and Z. Stanković, "Neuromodeling for microwave design," *Conference Proceedings of NEUREL 2000*, 135–140, 2000.
16. Christodoulou, C. and M. Georgopoulos, *Applications of Neural Networks in Electromagnetics*, Artech House Publishers, Jan. 2001.
17. Vahedi, N., H. R. Dalili Oskouei, and K. Forooraghi, "Width band coupler modeling using neural network," *IEEE Conference*, Malaysia, 2005.
18. Oppenheim, A. V. and A. S. Willsky, *Signals and Systems*, Prentice Hall, New Jersey, 1997.

A Novel Multilayer Dual-mode Substrate Integrated Circular Cavity (SICC) Filter with Two Arc-shaped Coupling Slots

Zhigang Zhang, Yong Fan, Yujian Cheng, and Yonghong Zhang

Extreme High Frequency Key Laboratory, School of Electronic Engineering
University of Electronic Science and Technology of China, Chengdu, China

Abstract— A novel millimeter-wave multilayer dual-mode filter is developed based on the substrate integrated waveguide circular cavity (SICC). The dual-mode SICC filter with two arc-shaped coupling slots, which are etched in the conductor layer between SICC resonators, has been designed for Ka-band application. The multilayer dual mode filter has been firstly realized only by adjusting two arc-shaped coupling slots located in metal layers. The position and size of the two coupling apertures can determine the coupling amount between two degenerate modes. Meanwhile, it is possible to control the return loss, bandwidth and rejection level by adjusting the size and relative position of the two arc-shaped slots. Additionally, this novel filter is very compact, and the simulated results prove it has the advantages of return loss, very low insertion loss, and high selectivity.

1. INTRODUCTION

As well known, wireless communication systems are developing gradually towards millimeter wave band. Compact devices with low profile and high performance are required in many millimeter wave systems. As a matter of fact, substrate integrated waveguide (SIW) are gradually applied at high frequency band. It not only has low profile characteristic, but is easy to be integrated with planar circuitry. Substrate integrated waveguide (SIW) dual mode filter has asymmetry characteristic. It can realize very sharp transition by using less number of cavities. Recently, SIW filters with circular cavities are reported in [1–3].

More recently, special attention has been paid to multilayer cross-coupled substrate integrated waveguide (SIW) filters using low-temperature co-fired ceramic (LTCC) technology [4, 5]. At the same time, dual-mode filters and cross-coupled filters or a combination of the two has become increasingly important because of size reduction, high quality factor, and high frequency selectivity. Accordingly, multilayer filter with dual mode character is very attractive candidate to satisfy the requirements in miniaturized circuit [6, 7].

In this paper, multilayer filter with dual mode character has been firstly realized by the coupling aperture located in input/output port and two arc-shaped coupling slots etched between layers. The position and size of coupling aperture can determine the coupling amount between two degenerate modes. Meanwhile, it is then possible to control the bandwidth and the rejection level by adjusting the size and relative position of the two arc-shaped slots. This novel filter is not only very compact, but has the advantages of return loss, very low insertion loss, and high selectivity.

2. FILTER ANALYSIS AND DESIGN

2.1. Dual Mode SICC Principle

For a SICC cavity there are two degeneration modes: horizontal mode and vertical mode. Moreover, these two degeneration modes can exist in the circular-shaped dielectric loaded cavity for the same resonant frequency. This mode degeneration can be used to realize a dual-mode filter. It is well known that the resonant frequency (unloaded) of mode for circular cavity with solid wall can be calculated by [9]:

$$f_{mnp} = \begin{cases} \frac{c}{2\pi\sqrt{\mu_r\varepsilon_r}} \sqrt{\left(\frac{\mu'_{mn}}{R}\right)^2 + \left(\frac{p\pi}{\Delta h}\right)^2} & \text{TE}_{mnp} \\ \frac{c}{2\pi\sqrt{\mu_r\varepsilon_r}} \sqrt{\left(\frac{\mu_{mn}}{R}\right)^2 + \left(\frac{p\pi}{\Delta h}\right)^2} & \text{TM}_{mnp} \end{cases} \quad (1)$$

where μ_r and ε_r are relative permeability and permittivity of the filling material, μ_{mn} and μ'_{mn} is the n th roots of m th Bessel function of the first kind and its derivative, R is the radius of circular cavity with solid wall, and c is the speed of light in free space. For $m>0$, each m represents a pair of degenerate TM and TE modes ($\cos m\varphi$ or $\sin m\varphi$ variation). In circular cavity with dual mode, TM_{110} , the lowest higher order mode, has been selected as the working mode. Each different

directions represents a different modes ($\cos m\varphi$ or $\sin m\varphi$ variation). This degenerated mode can be used to realize a dual-mode filter. μ_{mn} is 3.832 for the TM₁₁₀ mode. So the corresponding resonant frequency of TM₁₁₀ is derived from formula (1).

$$f_{110} = \frac{c}{2\pi\sqrt{\mu_r\varepsilon_r}} \cdot \frac{3.832}{R} = \frac{0.61c}{R\sqrt{\mu_r\varepsilon_r}} \quad (2)$$

The radius of the SICC can be obtained according to the formula (2).

$$R = \frac{0.61c}{f_{110}\sqrt{\mu_r\varepsilon_r}} \quad (3)$$

And then the solid wall is replaced by metallic vias under guidelines of [6–8]. Consequently, using (3), the initial dimensions of the cavity are determined for a desired resonant frequency for the TM₁₁₀ mode and optimized with a full-wave electromagnetic simulator.

2.2. Multilayer Dual-mode SICC Filter

As shown in Figs. 1(a) and (b), there are two substrate layers. First and second layer is used for input/output port. Two dual mode cavity resonators are connected through two arc-shaped coupling slots etched in metal layer 2. By adjusting the position d_{slot} and size W_S , θ of the arc-shaped slots, the coupling between first and second resonators can be controlled. Dual mode character can be easily achieved by changing the angle α between the coupling slot and input/output port. In addition, it is possible to control the bandwidth and the rejection level by adjusting the size of the two arc-shaped slots.

Figure 2 shows electrical field distribution of TM₁₁₀ mode in a SICC cavity. There can be two orthogonal degeneration modes, which can be used to realize a dual-mode filter. The coupling apertures and two arc-shaped slots are used to disturb two degenerate modes

2.3. Design Considerations

Two poles and two transmission zeros can be found in the response of a dual-mode filter with single circular cavity [1]. Two poles below the zero Z_1 are denoted as P_1 and P_2 , respectively, which can be used to control the bandwidth of the passband. The first zero near the passband is denoted as

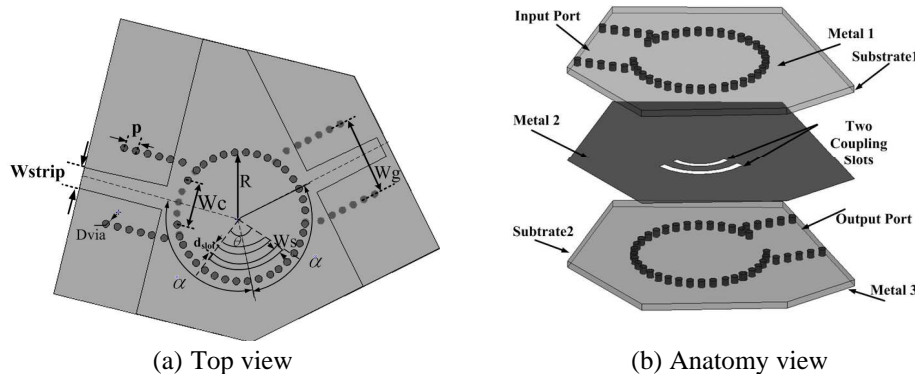


Figure 1: Proposed multilayer dual-mode SICC filter with two arc-shaped coupling slots.

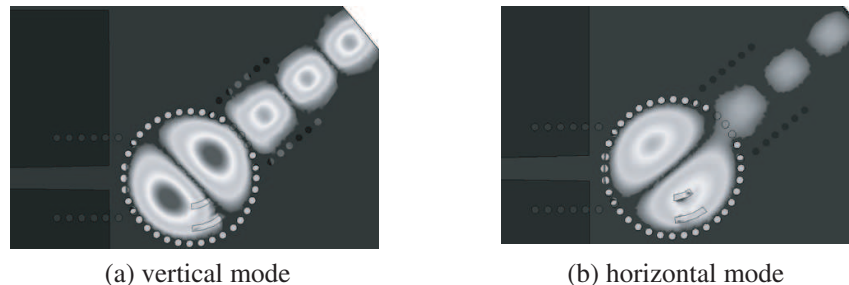


Figure 2: The E -field distribution of the TM₁₁₀ degenerated modes. (Setting output port along horizontal direction).

Z_1 , which is approximately equal to the eigenfrequency of the cavity TM_{110} mode. Being so close to the passband, zero Z_1 is very helpful to realize a steeper upper side response. The first pole P_1 is near the zero Z_1 . The space between the zero Z_1 and pole P_1 decides the rolloff slope in the transition band. As shown in Fig. 1, the waveguide located in input/output port can be used to suppress some undesirable response spur and improve the lower stop band characteristic.

From the above discussion, the conclusion can be reached that only a few parameters must be concerned, such as the angle α between coupling slots, the width of coupling slots W_C , W_S , θ , and d_{slot} , the radius of the circular cavity R . According to Fig. 1, for a given angle α , proper parameter W_C/R is limited in a relatively narrow interval. Beyond the limit, either the dual-mode character disappears or the reflection loss worsens. Generally, smaller α and W_S or smaller W_C/R corresponds to narrower bandwidth and narrower space. In addition, the proper parameter W_C and W_S assure more poles not to overlap and achieve better response character in passband.

2.4. Coupling Aperture

The coupling aperture size determines the amount of coupling for each mode. Fig. 3 illustrates the coupling for the TM_{110} mode when we vary the coupling aperture size W_S and d_{slot} . As we can see, the coupling increases when the aperture size is increased. It is then possible to control the bandwidth and the rejection level. When the aperture size is changed, the position of P_1 , P_2 and Z_1 is also modified in frequency because the amount of reactance introduced by the aperture has been changed. As shown in Fig. 3, the distance between the zero Z_1 and pole P_1 decreases evidently with the width of coupling slots W_s or d_{slot} decreased. Meanwhile, small change in the frequency of pole P_1 , P_2 . And the more rolloff slope and narrower bandwidth have been obtained in the transition band

Figure 4 shows the relation between zero Z_2 and α . Additionally, the other zero Z_2 is independent of the eigenmodes. The distance between Z_2 and the centre frequency f_0 enlarge as the angle α increased. It can be seen that the zero Z_2 is determined just by selecting the angle α between coupling slots. To suppress the undesirable spur, the angle α should be adjusted carefully to assure the second Z_2 just over the spur. Generally, smaller α or θ corresponds to narrower bandwidth and more rolloff slope in transition band

3. SIMULATION RESULTS

To verify the theoretical conclusions above, we designed multilayer dual-mode SICC filter with two arc-shaped coupling slots fabricated with standard PCB process. The proposed filter is designed with the frequency range 22–34 GHz and a center frequency of 27.3 GHz.

After optimization with Ansoft HFSS, the geometry parameters of the proposed filter working in the frequency range 22–34 GHz are listed in Table 1. The substrate used for the dual-mode filter is Rogers 5880 with relative permittivity of 2.2 and height of 0.508 mm.

As shown in Fig. 5, the proposed filter has a center frequency of 27.3 GHz with a bandwidth of 0.85 GHz, and it has a finite transmission zeros at 29.5 GHz. The return loss of the proposed filter is better than 21 dB over pass band and the insertion loss is 1.7 dB. Obviously, steeper rolloff slope and improved response in the transition band lead to better selectivity in the whole operating band.

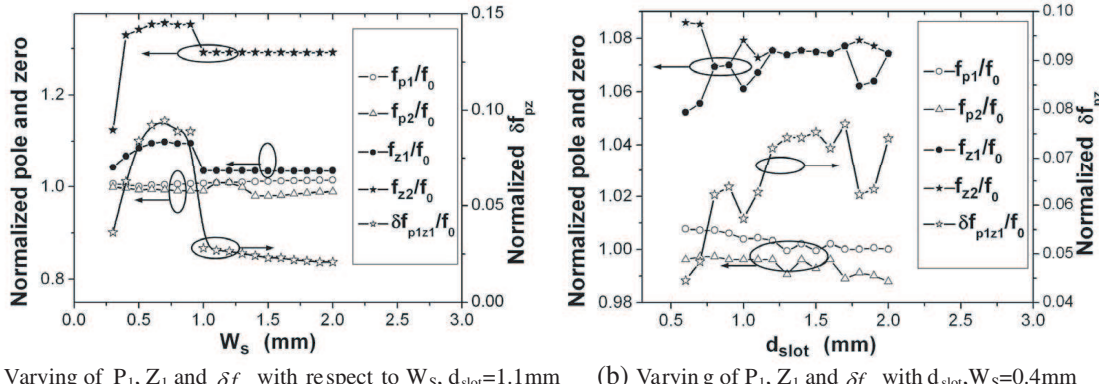


Figure 3: Varying of poles, zero and the distance between pole and zero, where, $f_0 = 27.3 \text{ GHz}$, $\delta f_{p1z1} = f_{z1} - f_{p1}$.

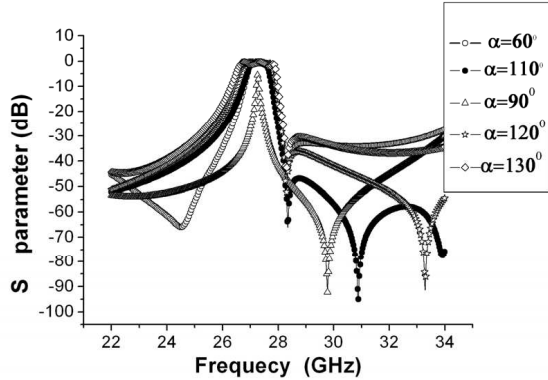
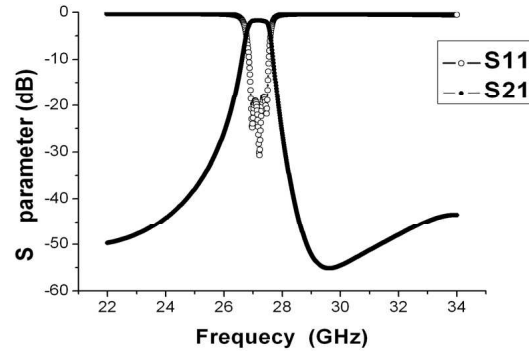
Figure 4: Relation between zero Z_2 and α .

Figure 5: Simulated results of the dual-mode SICC filter with two arc-shaped coupling slots.

Table 1: Parameters of the filter with double layers.

Dvia(mm)	0.5	Wstrip(mm)	1.5
ε_{rp} (mm)	0.85	Wg (mm)	5.5
	2.2	Wc (mm)	3.3
Ws(mm)	0.4	h(mm)	0.508
α (deg)	110	R(mm)	4.55
θ (deg)	36	d_{slot} (mm)	1.1

4. CONCLUSION

A novel multilayer dual-mode SICC filter with two arc-shaped coupling slots has been designed. Two transmission zeros can be created in this filter, which improve the selectivity of the filter to some extent. The simulated results prove it has the advantages of return loss, very low insertion loss and high frequency selectivity. The novel structure with good performance is very compact and easily achieved by normal multilayer PCB and LTCC technologies. Multilayer dual mode SICC filter has been firstly realized only by adjusting the coupling aperture located in input/output port and between layers. It is then possible to control the bandwidth and the rejection level by adjusting the position and size of the two arc-shaped slots. This new structure is well suited for microwave and millimeter wave applications.

ACKNOWLEDGMENT

This work is supported in part by the National Natural Science Foundation of China (NSFC) under grant 61001028 and in part by Research Fund for the Doctoral Program of Higher Education of China (RFDP) under grant 20100185110014.

REFERENCES

1. Tang, H. J., W. Hong, J.-X. Chen, G. Q. Luo, and K. Wu, "Development of millimeter-wave planar dippers based on complementary characters of dual-mode substrate integrated waveguide filters with circular and elliptic cavities," *IEEE Trans. Microw. Theory Tech.*, Vol. 55, No. 4, 776–781, Apr. 2007.
2. Li, R. Q., X. H. Tang, and F. Xiao, "Substrate integrated waveguide dual-mode filter using slot lines perturbation," *Electron. Lett.*, Vol. 46, No. 12, Jun. 10, 2010.
3. Potelon, B., J. C. Bohorquez, J. F. Favenne, C. Quendo, and E. Rius, "Design of Ku-band filter based on substrate-integrated circular cavities (SICCs)," *IEEE MTT-S International Microwave Symposium Digest*, 1237–1240, Jun. 2006.
4. Wei, Q.-F., Z.-F. Li, L.-S. Wu, W.-Y. Yin, J.-F. Mao, and L. Li, "Compact cross-coupled circular cavity filters using multilayer substrate integrated waveguide," *Electron. Lett.*, Vol. 45, No. 6, Mar. 12, 2009.

5. Ahn, K. and I. Yom, "A Ka-band multilayer LTCC 4-pole bandpass filter using dual-mode cavity resonators," *IEEE MTT-S International Microwave Symposium Digest*, 1235–1238, Jun. 2008.
6. Shen, W., X. W. Sun, W. Y. Yin, J. F. Mao, and Q. F. Wei, "A novel single-cavity dual mode substrate integrated waveguide filter with nonresonating node," *IEEE Microw. Wirel. Compon. Lett.*, Vol. 19, No. 6, 368–370, Jun. 2009.
7. Deslandes, D. and K. Wu, "Substrate integrated waveguide dual-mode filters for broadband wireless systems," *Proceedings RAWCON'03*, 385–388, Aug. 2003.
8. Wu, L.-S., X.-L. Zhou, Q.-F. Wei, and W.-Y. Yin, "An extended doublet substrate integrated waveguide (SIW) bandpass filter with a complementary split ring resonator (CSRR)," *IEEE Microw. Wirel. Compon. Lett.*, Vol. 19, No. 12, 777–779, Dec. 12, 2009.
9. Pozar, D. M., *Microwave Engineering*, 2nd Edition, Wiley, New York, 1998.

Design of an LNA with Ultra Low Noise and Model Noise Temperature at 2.45 GHz

S. A. Burney and C. Qunsheng

College of Electronic Information Engineering

Nanjing University of Aeronautics and Astronautics, Nanjing 210016, China

Abstract— This paper presents the design of a low-noise amplifier (LNA) that exhibits ultra low noise figure (NF) and noise temperature. Emphasis was given to achieve the minimum noise figure as offered by the device. The selected device uses E-PHEMT technology and has 0.25 micron gates allowing ultra low noise figure; furthermore requiring minimum feedback for stability. The present design of the LNA features simple structure, minimum NF and excellent overall performance. Furthermore, the present LNA has improved S_{11} value near -10 dB and output VSWR of 1.073, and obtained an excellent noise figure of 0.202 and model noise temperature of 13.8 K. This design has potential to serve in civil marine radar applications.

1. INTRODUCTION

Low-noise Amplifier (LNA) is a key component used in the receiving end of almost every communication system. The required input signal of these communication systems is usually very weak and needs to be amplified. The primary purpose of LNA is to amplify the input signal, but adding as little additional noise as possible. The core of any LNA design is the selection of the right transistor [1]. Among various LNA designs, the pseudomorphic high-electron mobility transistor (PHEMT) device provides high trans-conductance gain and high efficiency characteristics simultaneously [2]. The enhancement mode technology provides superior performance while allowing a DC grounded source amplifier with a single polarity power supply to be easily designed and built. As opposed to the depletion-mode PHEMT, where the gate must be made negative with respect to the source for proper operation, an enhancement-mode PHEMT requires that the gate be made more positive than the source. Biasing an enhancement-mode PHEMT is as simple as biasing a bipolar transistor [3].

Gawande et al. [1] designed an LNA with the lowest noise (achieved a simulated NF of 0.3) which used a device fbx45x by EUDYNA Technologies. Our work employed another device VMMK-1218, by Avago Technologies, that has a noise figure of approximately 0.2 at 2.45 GHz.

This paper focuses on the design of an LNA that achieves low noise figure and modal noise temperature. The next sections discuss the main design equations and the design methodology. The analytical treatment of complete design procedure has been expressed precisely. Various design options have been discussed depending upon the design cases and criteria. The present design has also been verified as shown in RF simulation results.

2. DESIGN METHODOLOGY

2.1. Transistor Selection

This is the most fundamental step in LNA design. Although many transistors could have been suitable for this application but the chosen transistor for our design is an ultra low-noise amplifier fabricated using Enhancement Mode PHEMT (EPHEMET) technology, the Avago Technologies VMMK-1218. Assessing several parameters, it was found that this device exhibits comparatively reasonable tradeoffs. The device VMMK-1218 characterizes high dynamic range, high gain and low noise figure that generates off of a single position DC power supply. The use of 0.25 micron gates allow ultra low noise figure. This device is intended for any 500 MHz to 18 GHz application including 802.11abgn WLAN, WiMax, BWA 802.16 & 802.20 and military applications [4].

The Avago enhancement mode PHEMT devices do not require a negative gate bias voltage as they are “normally off”. They can help simplify the design and reduce the cost of receivers and transmitters in many applications from 500 MHz to 18 GHz [4].

2.2. Design Equations

Consider the amplifier block shown in Fig. 1, it highlights the reflection coefficients used to design a microwave amplifier. In Fig. 1, Γ_s , Γ_{opt} , Γ_{in} , Γ_{out} , Γ_a and Γ_b are the reflection coefficients of the source impedance, the optimum noise impedance, at the input of transistor, output of transistor,

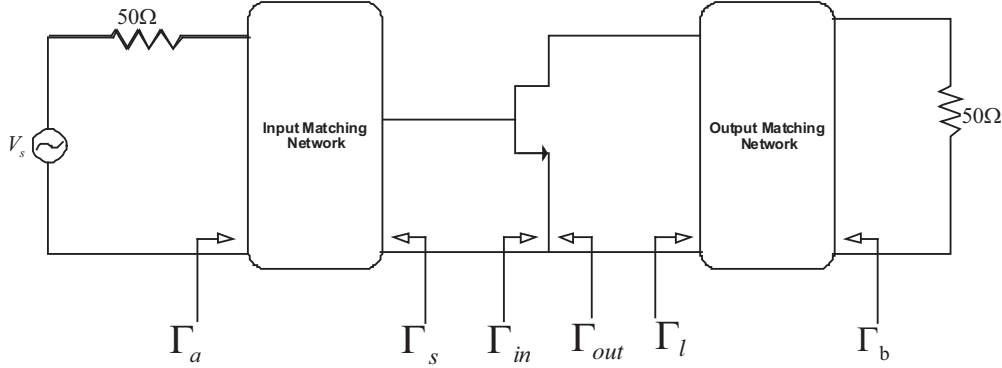


Figure 1: Microwave transistor amplifier.

input of matching network and output of matching network, respectively. It is by manipulating these values that the goals are achieved. In this design we start with the noise figure and the input VSWR. There exists a tradeoff between these two parameters. In LNA design noise has more importance as it plays a critical role in determining the overall system NF. In a receiver an LNA is the first element in the chain. The NF of the first element in the chain adds directly to the system NF. The design equations used are presented as follows [5].

$$\Gamma_s = \Gamma_{out} \quad \text{As } \Gamma_{out} \text{ depends on } \Gamma_s, \quad (1)$$

$$\Gamma_{out} = S_{22} + \frac{S_{12}S_{21}\Gamma_s}{1 - S_{11} \times \Gamma_s} \quad (2)$$

Assuming output VSWR = 1, then

$$\Gamma_l = \Gamma_{out}^* \quad (3)$$

Else choose a suitable point on another VSWR circle. As Γ_{in} depends on Γ_l ,

$$\Gamma_{in} = S_{11} + \frac{S_{12}S_{21}\Gamma_l}{1 - S_{22} \times \Gamma_l} \quad (4)$$

$$|\Gamma_a| = \left| \frac{\Gamma_{in} - \Gamma_s^*}{1 - \Gamma_{in}\Gamma_s} \right| \quad (5)$$

$$\text{VSWR}_{in} = \frac{1 + |\Gamma_a|}{1 - |\Gamma_a|} \quad (6)$$

$$\text{VSWR}_{out} = \frac{1 + |\Gamma_b|}{1 - |\Gamma_b|} \quad (7)$$

$$C_{v_o} = \frac{|\Gamma_{out}| (1 - |\Gamma_b|^2)}{1 - |\Gamma_b\Gamma_{out}|} \quad (8)$$

$$r_{v_o} = \frac{|\Gamma_b| (1 - |\Gamma_{out}|^2)}{1 - |\Gamma_b\Gamma_{out}|^2} \quad (9)$$

$$F = \text{NF}_{\min} + \frac{4r_n |\Gamma_s - \Gamma_{OPT}|^2}{(1 - |\Gamma_s|^2) |1 + \Gamma_{OPT}|^2} \quad (10)$$

where C_{v_o} and r_{v_o} represents the centre and radius of the Γ_b or the output VSWR circle respectively, r_n is the normalized noise resistance. To express the noise temperature of a two port network the following equations were used [1]. The noise temperature was calculated by [1, 6],

$$T_e = T_{\min} + \frac{4R_n T_o |\Gamma_s - \Gamma_{OPT}|^2}{Z_o (1 - |\Gamma_s|^2) |1 + \Gamma_{OPT}|^2} \quad (11)$$

$$\text{NF}_{\min} = 1 + \frac{T_{\min}}{290} \quad (12)$$

where T_e is the effective input noise temperature. T_{\min} is the minimum noise temperature that results if optimum impedance is presented to the transistor. R_n is the noise resistance, T_o is 290 K, and Z_o is the reference impedance (typically 50Ω).

2.3. Stability and Matching Analysis Based on Design Equations

The object is to design an ultra low noise amplifier so it is best to consider the optimum point for matching on the Smith chart. For proper matching circuit it is necessary to choose points for Γ_s and Γ_l that lie in the stable region of the Smith chart. The basic chip package layout is designed and simulated. This offers a noticeable advantage, the microstrip attached to the source acts as inductance, thus giving a better view of the stability circles. Small changes in inductance added to the source of an LNA can have large impacts on gain, NF and stability. As inductance increases, stability increases at the expense of gain. However, continued increases in inductance can soon lead to degraded gain and NF [7]. Γ_{opt} had a reasonable stability margin thus it was selected as Γ_s for our design. The gain at that point was found to be less than the ‘maximum stable gain’. We can thus use Equation (1) for our analysis and proceed. Using Equation (2) we obtained the value of Γ_{out} .

Next the output stability circles were drawn together with the constant Γ_b circles or can also be referred to as output VSWR circles. Here we assumed the value of output VSWR to be 1 and drew the circles using Equations (7) to (9). Equations (8) and (9) provide the centre and the radius of the circles to be drawn. To obtain the value of Γ_l output VSWR of 1 was assumed, the resulting point is in the stable region, it had a considerable stability margin. Taking this value of Γ_l , the input VSWR can be calculated using Equations (4) to (6). The resulting input VSWR was found slightly higher. The value of output VSWR was increased to get a suitable input VSWR. To decide these values both the above mentioned equations together and computer aided design softwares, the solutions can be achieved quickly and accurately. This gives us an idea of the final results (such as resulting VSWR, gain and NF) before the actual layout is designed.

2.4. Matching

Using these values of Γ_s and Γ_l , the input and output matching networks were designed. The procedure requires the use of Smith chart, since the admittance of the shunt stub adds to the load admittance, it is convenient to use the Y Smith chart [5].

The results were then optimized for further tuning. A harmonic balance (HB) simulation was used for the non-linear analysis. HB was used for the simulations of 1 dB compression point (P1 dB) and output third order intercept point (OIP3) [8]. The input signal driving the circuit in HB simulation was kept in the linear range. The results show the OIP3 to be 22.08 dBm, and the output 1 dB compression point at 8.28 dBm.

3. RESULTS

This section presents the co-simulations results of low noise amplifier. The substrate has a relative permeability (ϵ_r) of 2.55. The simulations were done using RF simulations. The RF mode uses a quasi-static formulation. In the quasi-static formulation, the Green functions are low-frequency

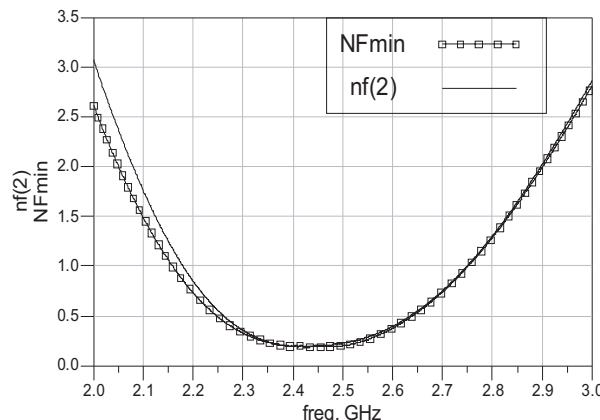


Figure 2: Simulated noise figure of the low-noise amplifier over 2–3 GHz frequency range.

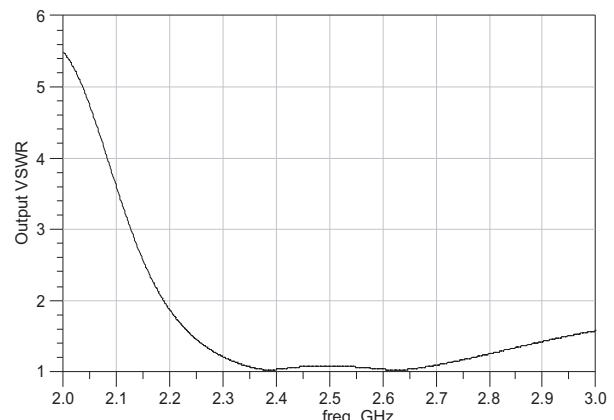
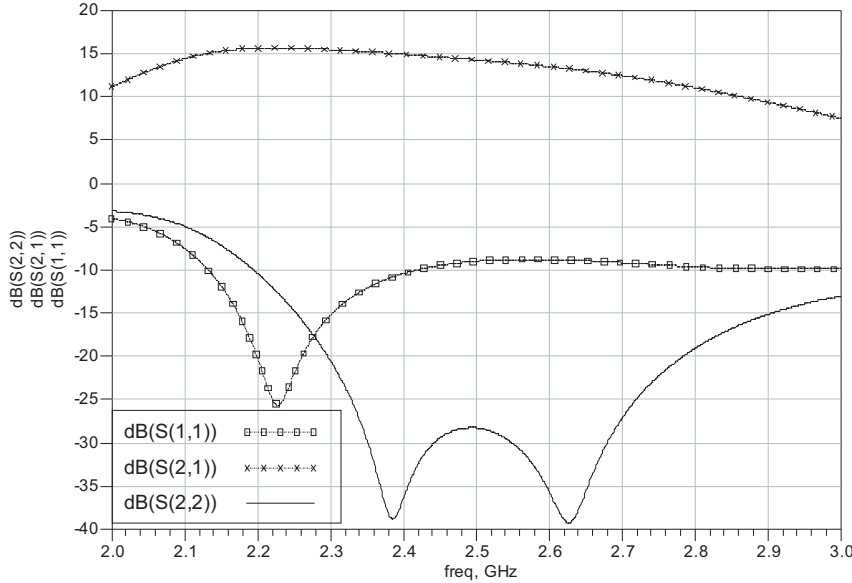


Figure 3: Simulated output VSWR of the low noise amplifier over 2–3 GHz frequency range.

Table 1: Summarized important results.

Results at 2.45 GHz	
Noise figure	0.202 dB
Modal Noise Temperature	13.8 K
Output VSWR	1.073
$S_{(1,1)}$	-9.4 dB
$S_{(2,2)}$	-29.4 dB
$S_{(2,1)}$	14.6 dB

Figure 4: Simulated S -parameters of the low noise amplifier over 2–3 GHz frequency range.

approximations to the full-wave and more general Green functions. Because of the approximations made in the RF mode, the simulations are more efficient [9].

The results shown in the Figures 2 to 4 specify that the LNA is optimized for ultra low noise at 2.45 GHz. The results also exhibit very good output VSWR, S -parameters and high OIP3. This shows that the LNA is operable from 2.2 to 2.7 GHz for low noise and high performance, with the lowest noise achieved at 2.45 GHz.

4. CONCLUSIONS

In this paper, an LNA with a model noise temperature of 13.8 K at 2.45 GHz, has been designed using E-PHEMT VMMK-1218 by Avago technologies. The LNA design has shown very good overall performance apart from the ultra low noise result. The frequency range from 2–4 GHz represents the S -band (wavelength 8–15 cm); this wavelength is not easily attenuated [10], thus in adverse weather conditions the S -band is preferred for marine radar applications. Nevertheless X-Band (because of its higher frequency) provides a higher resolution and a sharper image making it useful in normal conditions. Based on this experience and results it is intended to design a wideband LNA for civil marine radar applications.

ACKNOWLEDGMENT

We would like to thank Prof. Zhou Yong Gang for his technical support and guidance; and Mr. Ali Ahmed for his facilitation in the design process; especially in crucial bottle necks.

REFERENCES

1. Gawande, R. and R. Bradley, “Errata for low-noise amplifier at 2.45 GHz,” *IEEE Microwave Magazine*, Vol. 11, No. 2, 122–126, April 2010.

2. Baca, A. G., R. F. Kopf, and S. N. G. Chu, *G. O. Compound Semiconductor Power Transistors II and State-of-the-Art Program on Compound Semiconductors XXXII*, The Electrochemical Society Inc., 2000.
3. Avago Technologies, 2.0 GHz High-linearity Second-stage LNA/Driver using Avago Technologies' ATF-53189, Application Note 5244, Available: <http://www.avagotech.com/docs/5989-3846EN>, 2010.
4. Avago Technologies (Data Sheet), VMMK-1218 0.5 to 18 GHz Low Noise E-PHEMT in a Wafer Scale Package, 2009.
5. Gonzalez, G., *Microwave Transistor Amplifiers: Analysis and Design*, 2nd Edition, Prentice-Hall, Inc., 1996.
6. Johnston, E., Noise Temperature, Figure and Factor Calculations, Application note 5, Available: http://www.nitehawk.com/rasmit/ras_appl5.pdf, 2001.
7. Baker, T., Successful LNA design involves performance trade-offs, Available: <http://rfdesign.com/mag/611RFD33.pdf>, 2006.
8. Avago Technologies, Low Noise 2300 MHz Amplifier, Application Note 5294, Available: www.avagotech.com, 2010.
9. Agilent Technologies, RF Design Environment Documentation, RFDE Momentum [Online], Available: <http://cp.literature.agilent.com/litweb/pdf/rfde2004a/rfdemom/rfdemomA6.html>.
10. Hosseiniapanah, M. and Q. Wu, "Exposure reduction of S-band radar's staff by designing a frequency selective surface," *International Conference on Microwave and Millimeter Wave Technology 2008, ICMMT 2008*, 48–50, April 21–24, 2008.

The Study of Statistical Properties for Rainfall and Rain-induced Attenuation in Xi'an, China

Houbao Shi, Shuhong Gong, and Kexiang Liu

School of Science, Xidian University, Xi'an, Shaanxi 710071, China

Abstract— The year probability statistical properties of rain are analyzed based on the measurement data of 1 minute cumulative rainfall in Xi'an, China, in this paper. And the results are compared with ITU-R model, Moupfouma model. The dynamic characters of rain-induced attenuation are investigated using those measured data. The results given in this paper are significant for studying channel dynamic fade properties and Fade Mitigation Techniques (FMT).

1. INTRODUCTION

The satellite communication working at Ka bands or even higher frequencies is highly valued to expand communication capacity both for the military and civilian needs. Rain-induced attenuation has a great influence on the frequencies over 10 GHz, which is more serious on higher frequencies, Ku, Ka, Q and V, for example [1–3]. Many research institutions or scholars have been working on that and have given several models, such as ITU-R modelMoupfouma model and so on. These traditional models analyze year probability statistical properties, which is helpful for the technique of fixed power margin. However, power margin technique does not agree with cost-effectiveness ratio, because rainfall, especially rainstorm, is relatively rare event in time and space. Some scholars and research institutions recommend adopting adaptive power control technology to mitigate rain-induced attenuation. And, the real-time dynamic characteristics of rain-induced attenuation are needed for APC to follow the real-time change of rain-induced attenuation [1–6]. In this paper, the statistical properties of the rainfall and long-term rain attenuation characteristics in Xi'an are analyzed and compared with ITU-R and Moupfouma model based on the 1 minute cumulative rainfall measurement data. The results given in this paper are significant to investigate the dynamic property of rain-induced attenuation and adaptive anti-fading technology at millimeter-wave bands.

2. THE STUDY OF LONG-TERM STATISTICAL PROPERTIES

2.1. Long-term Statistical Characteristics of Rainfall

Rain intensity duration is the duration of rainfall intensity exceeds a certain threshold. Fig. 1 is an example to show how to calculate duration. As shown in Fig. 1, set a threshold y , some intersects will be found, select one of them (x_1, x_2), the previous value of x_1 less than y , the latter value of x_1 is greater than y , and the previous value of is greater than y , the latter value of is less than y , $\Delta t_i = x_2 - x_1$, is the duration of this section. The total duration of a certain rain event is the cumulative of all these sections. And, the duration of a year is the cumulative of all sections in a year. Different threshold will have different duration. The year probability statistical properties of rain are analyzed based on the measurement data of 1 minute cumulative rainfall in Xi'an, in this paper. And the results are compared with ITU-R model and Moupfouma model. The results are shown in Fig. 2.

2.2. The Long-term Statistical Properties of Rain Induced Specific Attenuation

The model of calculating specific attenuation is written as Equation (1), which is provided by Olsen etc. [2].

$$\gamma = a_r R^{b_r} \quad (\text{dB/km}) \quad (1)$$

a_r, b_r in Equation (1) are given as

$$\begin{aligned} a_r &= \frac{1}{2} [a_h + a_v + (a_h - a_v) \cos^2 \theta \cos 2\tau] \\ b_r &= \frac{1}{2a_r} [a_h b_h + a_v b_v + (a_h b_h - a_v b_v) \cos^2 \theta \cos 2\tau] \end{aligned} \quad (2)$$

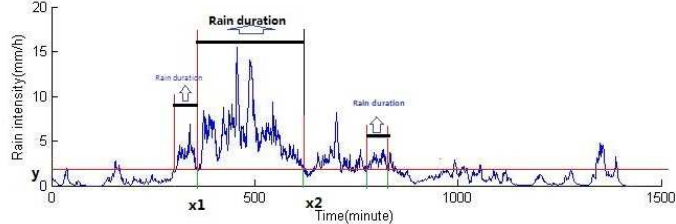


Figure 1: The sketch of defining rain intensity duration.

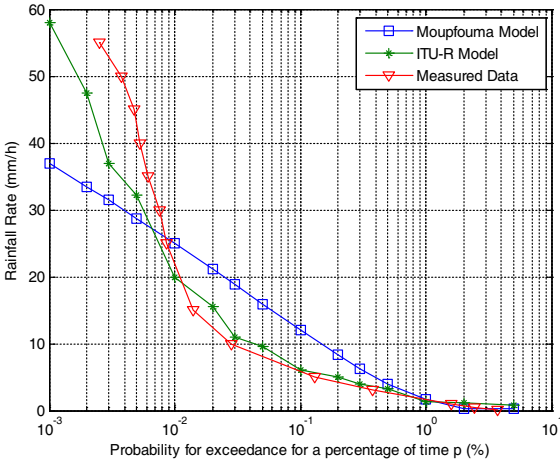


Figure 2: The cumulative distribution of rain rate.

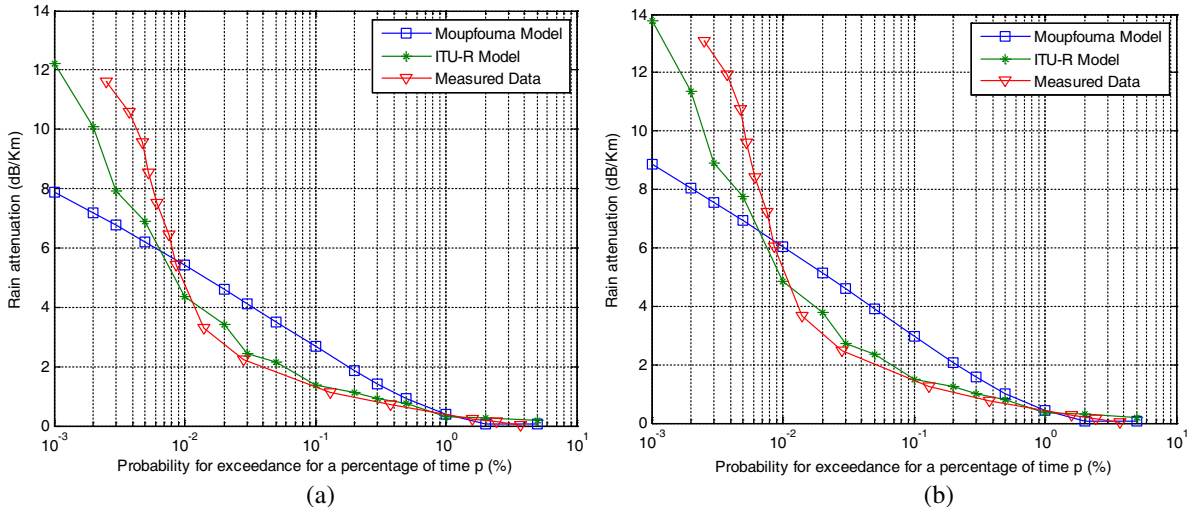


Figure 3: The cumulative distribution for specific attenuation. (a) Vertical polarization. (b) Horizontal polarization.

where a_h , a_v and b_h , b_v are the coefficients for different polarization, subscript h for horizontal polarization and v for vertical polarization, θ is link elevation and τ is polarization angle. a_h , a_v and b_h , b_v depend on frequency, environment temperature, rain drop distribution and so on, and mainly depend on frequency and rain drop distribution. The long-term statistical properties in X'an, China can be calculated using Equation (1) based on the measured data shown in Fig. 2, Fig. 3 gives an example with the conditions of $f = 35$ GHz, $\theta = 35^\circ$, $\tau = 90^\circ$ (vertical polarization) or $\tau = 0^\circ$ (horizontal polarization).

3. THE DYNAMIC CHARACTERS OF RAIN INDUCED SPECIFIC ATTENUATION

Rain induced specific attenuation slope can be defined as [6–9]

$$\varsigma(t) = \frac{A(t + \Delta t) - A(t)}{\Delta t} \quad (\text{dB/km/s}) \quad (3)$$

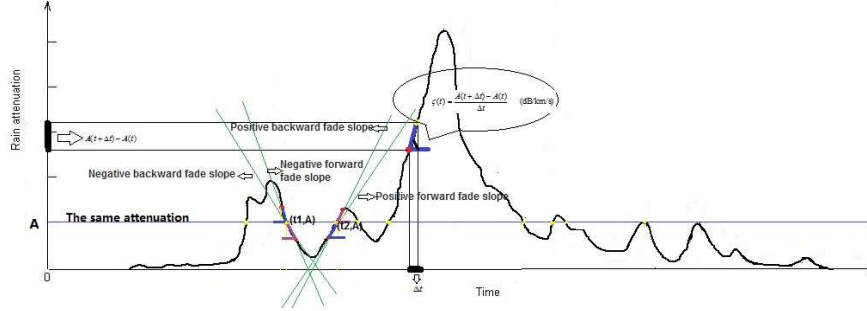


Figure 4: The sketch of calculating specific attenuation slope.

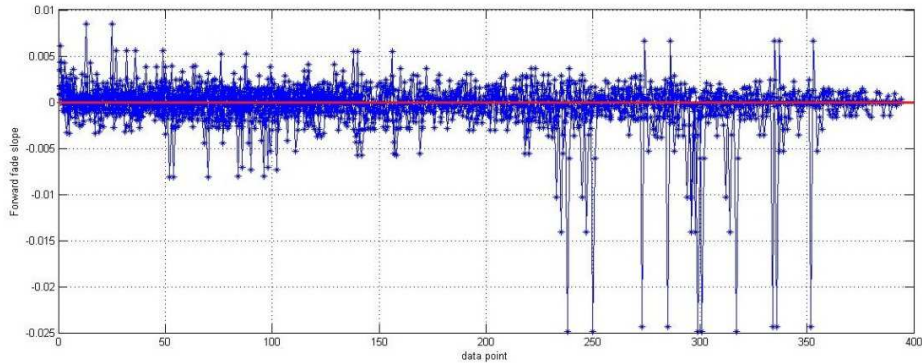
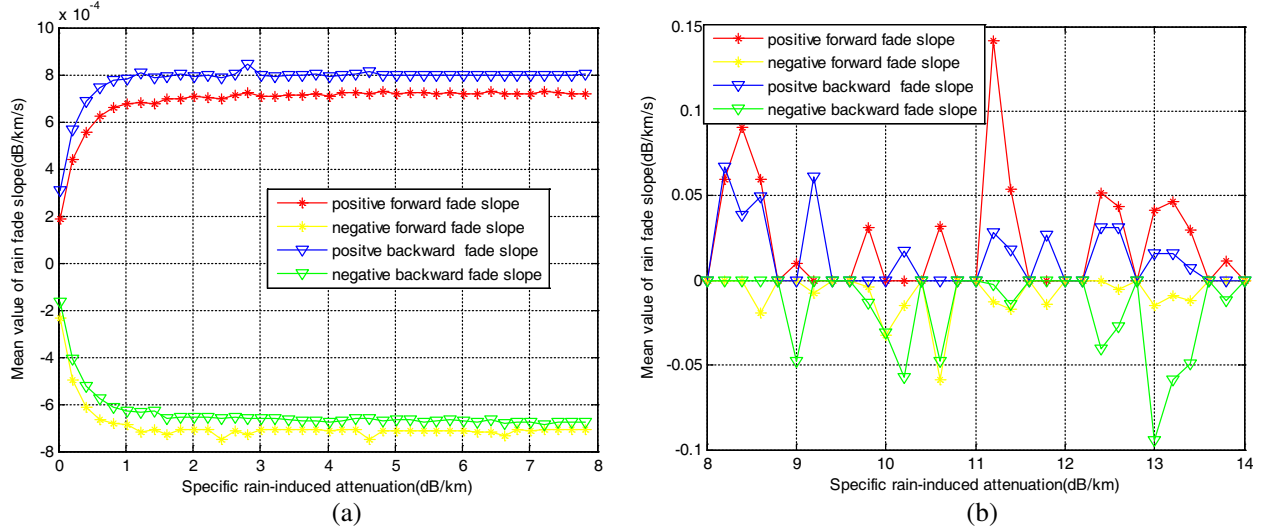
Figure 5: An example of analyzing the mean value of $\xi_f(t)$.

Figure 6: The mean value of rain fade slope at different rain attenuation (vertical polarization).

where $A(t + \Delta t)$ is the value at $t + \Delta t$, ($\Delta t = 1(\text{min}) = 60(\text{s})$ in this paper), $A(t)$ is the value at t . Fig. 4 is an example to show how to calculate rain induced specific attenuation slope.

Set a rain induced attenuation A each A has two fade slopes, forward fade slope and backward fade slope which both have positive and negative values. Forward fade slope ($\xi_f(t)$) is calculated as Equation (4), where $A(t)$ is the sample value, $A(t - \Delta t)$ is the previous value, Backward fade slope ($\xi_b(t)$) is calculated as Equation (5), where $A(t)$ is the sample value, $A(t + \Delta t)$ is the latter value.

$$\xi_f(t) = \frac{A(t) - A(t - \Delta t)}{\Delta t} \quad (\text{dB/km/s}) \quad (4)$$

$$\xi_b(t) = \frac{A(t + \Delta t) - A(t)}{\Delta t} \quad (\text{dB/km/s}) \quad (5)$$

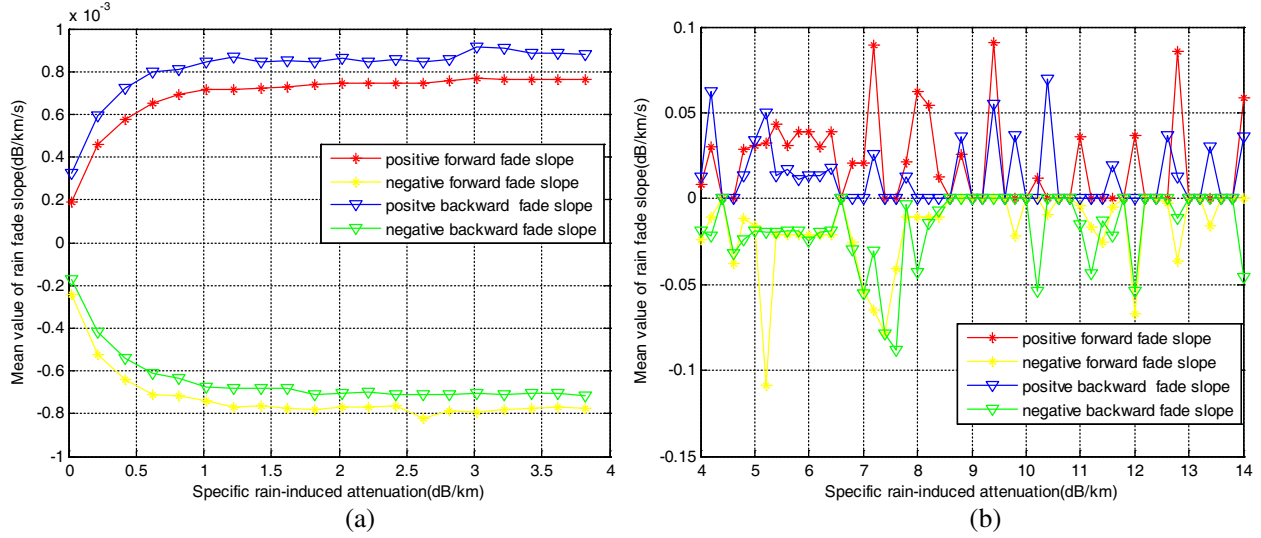


Figure 7: The mean value of rain fade slope at different rain attenuation (horizontal polarization).

As shown in Fig. 4, both sample point (t_1, A) and sample point (t_2, A) have two fade slopes $\varsigma_f(t_1)$, $\varsigma_b(t_1)$, $\varsigma_f(t_2)$, $\varsigma_b(t_2)$ ('f' for forward, 'b' for backward). If the value of $\varsigma_f(t)$ is known according to Equation (6), the previous value of $A(t - \Delta t)$ will be obtained; Also if the value of $\varsigma_b(t)$ is known the latter value of $A(t + \Delta t)$ will be got from Equation (7)

$$\varsigma_f(t) = \frac{A(t) - A(t - \Delta t)}{\Delta t} (\text{dB/km/s}) \Rightarrow A(t - \Delta t) = A(t) - \varsigma_f(t) * \Delta t \quad (6)$$

$$\varsigma_b(t) = \frac{A(t + \Delta t) - A(t)}{\Delta t} (\text{dB/km/s}) \Rightarrow A(t + \Delta t) = A(t) + \varsigma_b(t) * \Delta t \quad (7)$$

According to Equation (6) and Equation (7), if Δt , and the statistical value of $\varsigma_f(t)$, $\varsigma_b(t)$ are known, the transformed matrix can be obtained, which is important for forecasting dynamic process. Fig. 5 is an example for analyzing the mean value $\varsigma_f(t)$ of a certain value 'A'.

Operate averaging to the positive and negative flop of $\varsigma_f(t)$ separately, the distribution of the mean value at different specific rain induced attenuation can be calculated. The results are shown in Fig. 6, Fig. 7 with the condition of $f = 35 \text{ GHz}$, $\theta = 35^\circ$, $\tau = 90^\circ$ or $\tau = 0^\circ$.

4. CONCLUSIONS

From Fig. 2, Fig. 3, it can be concluded that: the measured date curve is deferent from the ITU-R model and Moupouma model, especially being deferent from Moupouma model. The practical statistic results relatively agree well with ITU-R model, however, the difference becomes greater when the rainfall intensity is large, and the maximum difference is up to 20 mm/h so it is necessary to carry out measurement in different areas.

As shown in Fig. 6, Fig. 7, when the specific rain-induced attenuation value is small, the curve changes smoothly and stably, however it becomes volatile, when the specific rain induced attenuation value is large. In other words, electromagnetic waves are influenced greatly when through the heavy rain zone. Notice that: the zero value in Fig. 6(b) and Fig. 7(b) do not indicate the mean value of rain induced attenuation are zero, which only because there are no samples at those attenuation values.

The results given in this paper are significant for investigating the rain-induced attenuation dynamic properties, certainly, these results should be confirmed by more measured data, because rain-induced attenuation is a random event.

ACKNOWLEDGMENT

This work has been supported by "The National Natural Science Foundation of China (61001065)" and "the Fundamental Research Funds for the Central Universities". And, thank all teachers and students, who do many contributions for measuring.

REFERENCES

1. Xiong, H., *Radio Wave Propagation*, Electronic Industy Press, Beijing, China, 2000.
2. Gong, S., "Study on some problems for radio wave propagating and scattering through troposphere," D. Chinese Thesis, Xi'dian University, Xi'an, China, Aug. 2008
3. Nelson, B. and W. L. Stutzman, "Fade slope on 10 to 30 GHz earth\space communication links\Measurements and modeling," *IEEE Proc. Microwave Antennas Propagat.*, Vol. 143, No. 4, 353–357, 1996.
4. Van de Kamp, M. M. J. L., "Rain fade slope predicted from rain rate data," *IEEE Transactions on Antennas and Propagation*, Vol. 51, No. 8, 1750–1759, Aug. 2003.
5. Sweeney, D. G. and C. W. Bostian, "The dynamics of rain-induced fades," *IEEE Transactions on Antennas and Propagation*, Vol. 40, No. 3, 275–278, 1992.
6. Van de Kamp, M. M. J. L., "Derivation of the dynamic parameters of rain attenuation from rain rate data," *Radio Wave Propagation Modeling and Measurements for SatCom and SatNav Systems Work-shop*, Netherlands, 2005.
7. Van de Kamp, M. M. J. L., and G. Brussaard, "Statistical analysis of rain fade slope," *AP2000 Millennium Conf. Antennas and Propagation*, Davos, Switzerland, Apr. 9–14, 2000.
8. Timothy, K. J., J. T. Ong, and E. B. L. Choo, "Descriptive fade slope statistics on INTELSAT Ku-band communication link," *Electron. Lett.*, 2000.
9. Van de Kamp, M. M. J. L., "Statistical analysis of rain fade slope," *IEEE Transactions on Antennas and Propagation*, Vol. 51, No. 8, 1750, 2003.

Inversion of Refractive Index in Marine Atmospheric Duct by Genetic Algorithm

X. L. Zhao, Y. P. Wang, and L. H. Bao
Tianshui Normal University, China

Abstract— Marine evaporation duct greatly strengthens or degrades the capability of the naval Radar, Communication, and Electronic Support Measures (ESM) system. Based on modified refractivity, the parabolic equation by Fourier split-step method (FSS) were introduced to analyze the anomalous propagation of electromagnetic wave in marine evaporation duct. By Genetic Algorithm (GA) and FSS, Refractivity from Clutter (RFC) is used to predict and forecast the refractive index profile of evaporation duct.

1. INTRODUCTION

Marine evaporation duct is a nearly permanent propagation mechanism due to the abrupt changes in the vertical temperature and humidity profiles just above the large ocean surface. Its existence greatly strengthens or degrades the capability of the naval Radar, Communication, and Electronic Support Measures (ESM) system. In October 1997, a exploring atmospheric duct experiment made by China Research Institute of Radio Propagation (CRIRP) had been performed On East sea and South sea of China at longitude 115°–120° during one month. The measured data show that: the occurrence probability of evaporation duct at experimental sea area is generally about 80 percent(e.g., [1]). For analyzing the anomalous propagation of electromagnetic wave in marine evaporation duct, the characteristic parameter of the atmospheric duct modified refractivity from clutter (RFC) by Genetic Algorithm are introduced.

2. FORMATION OF ATMOSPHERIC DUCT

Actually, the tropospheric atmosphere is non-uniform medium and its composition, pressure, temperature and humidity obviously vary with the height. The horizontal variety is usually negligible with comparison to the vertical. The refractive index of the lower atmosphere ranges from 1.00025 to 1.0004 and approximately equal to 1. The refractivity can be defined as the following:

$$N = 77.6 \frac{P}{T} + 3.73 \times 10^5 \times \frac{e}{T^2} = (n - 1) \cdot 10^6 \quad (1)$$

where, n is the refractive index, P is atmosphere pressure, e is vapor pressure, T is temperature. If the Earth's surface is assumed to a plane, the propagation path of radio waves can be equivalent to some bending rays. The modified refractivity is introduced as:

$$M = N + \frac{z}{a_e} \cdot 10^6 = N + 0.157z \quad (2)$$

where, a_e is the radius of the earth and equal to 6370 km, z is the height above the surface. Due to the non-uniform atmosphere, the propagation path of EM waves is not a straight line, but bends towards the Earth. If the curvature of radio rays is greater than the curvature of the Earth's surface, an inequality is satisfied by:

$$\frac{dM}{dz} < 0 \quad (3)$$

where the minimum value of the modified refractivity corresponds with the height of the atmosphere duct. Equation (3) implies that the phenomenon of the atmosphere duct will appear within a certain height near the surface. The duct height can be predicted by different kinds of atmosphere layer or sounding data (e.g., [2, 3]).

3. MODIFIED REFRACTIVITY PROFILE

Based on the boundary layer theory of atmospheric science and the median-scale mode of numerical simulation, the modified refractivity near the sea surface is given by:

$$M(z) = M(z_0) + 0.125z - 0.125z_0 - 0.125 \frac{d}{\Phi(\frac{d}{L})} \int_{z_0}^z \frac{\Phi(\frac{z'}{L})}{z'} dz' \quad (4)$$

where, z is the vertical height above the sea, z_0 is the roughness height and equal to 0.00015 m, d is the height of evaporation duct, L is Monin-Obukhov length, $M(z_0)$ is 339 M-unit at z_0 , Φ is a function of stability parameter z/L and is respectively equal to, less than and greater than 1 at neutral, unstable and stable layer. Using the relationship recommended by Jeske (e.g., [2]), the modified refractivity profile of the stable, unstable and neutral stratification is plotted by Figure 1. The reference model recommended by ITU-R P.853-3 (e.g., [4]) divides standard atmosphere into seven continuous layers according to temperature with height. The modified refractivity of standard atmosphere below the height of 11km near the surface is plotted by Figure 2 on the basis of Equation (1) and Equation (2).

A comparison between Figure 1 and Figure 2 shows that the modified refractivity of evaporation duct is obviously different from that of standard atmosphere. The M of standard atmosphere is nearly linear, and the M of evaporation duct rapidly decreases at tens of meters near the surface. For different atmosphere conditions, the strength ΔM of the evaporation duct is the greatest at unstable layer and the least at neutral layer.

4. FOURIER SPLIT-STEP METHOD

For the approximately horizontal radio propagation with small elevated angle in evaporation duct environment, the parabolic equation derived from Helmholtz equations is a proper choice. The parabolic equation can be used to solve satisfactorily the propagation problem in non-uniform atmosphere and has favorable stability (e.g., [6]). The expression of the parabolic equation is given by:

$$\partial_z^2 u + 2ik\partial_x u + k^2 \left(n^2 - 1 + \frac{2z}{a_e} \right) u = 0 \quad (5)$$

Equation (5) neglects the backscattering and is applicable to analyze the long-distance propagation for horizontal direction. By Fourier split-step method, the solution of the Equation (5) can be expressed as:

$$u(x + \Delta x, z) = \exp [i\Delta x m(x, z) k/2] \cdot F^{-1} \{ \exp (-i\Delta x p^2/2k) F[u(x, z)] \} \quad (6)$$

When Electromagnetic waves propagate in the atmosphere, the attenuation due to the spherical wave diffusion with propagation distance is defined as free space transmission loss, and the attenuation by the absorption, scattering, diffraction and reflection of the radio wave is known as medium transmission loss. According to EM wave theory, the basic transmission loss is given by:

$$L_b = 20 \log \left(\frac{4\pi r}{\lambda} \right) - A \text{ (dB)} \quad (7)$$

where, A is attenuation factor, r is a distance between the transmitter and the receiver, λ is wavelength. The attenuation factor A is transmission loss relative to free space and it is a effective

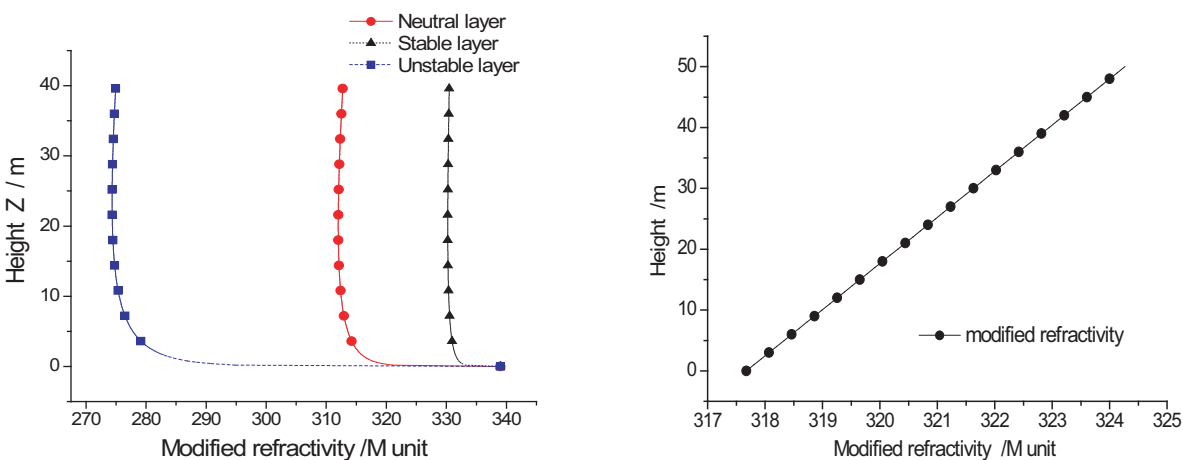


Figure 1: Modified refractivity of evaporation duct.

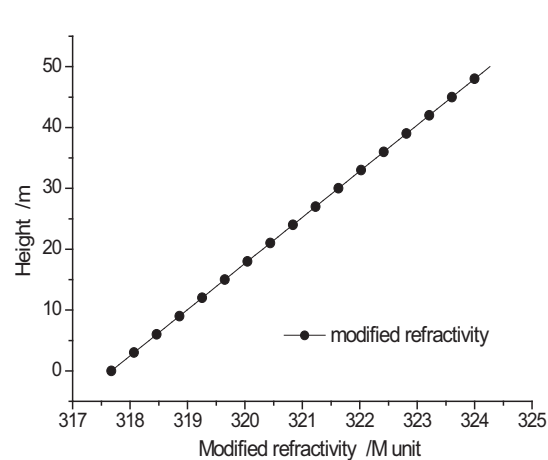


Figure 2: Modified refractivity of standard atmosphere.

parameter to calculate the echo power. Based on the parabolic Equation (5), the attenuation factor in evaporation duct is determined as in [7]:

$$A = \sqrt{x} |u(x, z)| \quad (8)$$

When the radio frequency is 10GHz, the antenna height is 5 m, the duct height is 20 m, and the elevation angle is 0.35° , the basic transmission loss can be calculated by Equation (6)–Equation (8) and the pseudo-color map of the transmission loss is used to simulate the anomalous propagation in evaporation duct. Figure 3 and Figure 4 is respectively the pseudo-color map at standard atmosphere and at neutral layer of evaporation duct with the duct height 20 m. we can conclude from Figure 6 and Figure 3 that the propagating rays and the reflected ray in standard atmosphere also seem some straight lines and there are obviously no bending rays by refraction; some rays are trapped in the evaporation duct and reflected more times than in standard atmosphere, and some rays propagate through the top of the duct layer and result in the leakage of electromagnetic energy.

5. REFRACTIVITY FROM CLUTTER (RFC)

The Refractivity of atmospheric duct estimated by the observed radar clutter is described by Krolik (see Ref. [8]). They convert the inversion of the refractive index into the maximum likelihood estimation of global parameters by the Bayesian theorem. If the modeled clutter power is $P_c(r, \mathbf{M})$ by the parabolic equation, the observed clutter power is:

$$P_{obs}(r, \mathbf{M}^{true}) = -2L(r, \mathbf{M}^{true}) + 10 \log(r) + \sigma^0(r) + C \quad (9)$$

where, \mathbf{M}^{true} is the unknown, true, range-and-height dependent refractive environment, L is the propagation loss (dB), $\sigma^0(r)$ is the true, unknown, range-dependent radar cross section of the sea surface at range r , and C takes into account radar parameters. If neither C nor $\sigma^0(r)$ are known a priori, the un-normalized power modeled clutter power $P'(r, \mathbf{m})$ can be expressed as:

$$P'(r, \mathbf{m}) = -2L(r, \mathbf{m}) + 10 \log(r) \quad (10)$$

where, the vector of the values of $P'(r, \mathbf{m})$ corresponding to the discrete ranges of interest is $\mathbf{P}'(r, \mathbf{m})$. The model parameter vector \mathbf{m} maps uniquely into \mathbf{M} , so the modeled clutter power value of \mathbf{P} can be referred to as either $\mathbf{P}_c(\mathbf{m})$ or $\mathbf{P}_c(\mathbf{M})$.

By the difference (dB) between the observed $\mathbf{P}_{obs}(\mathbf{M})$ and modeled $\mathbf{P}_c(\mathbf{M})$ clutter, a simple least squares objective function is:

$$\Phi(\mathbf{M}) = \sum_{i=1}^n [P_c(r_i, \mathbf{M}) - P_{obs}(r_i, \mathbf{M}_{obs})]^2 \quad (11)$$

The objective function equation is sensitive to the range-dependent variation in the clutter level, but not its absolute level. Each realization of \mathbf{M} is adjusted so that the objective function only depends on the variation in clutter return but not on the absolute level of the clutter return.

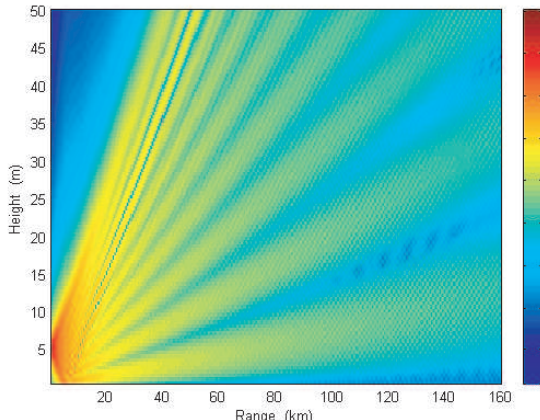


Figure 3: The space distribution of transmission loss in standard atmosphere.

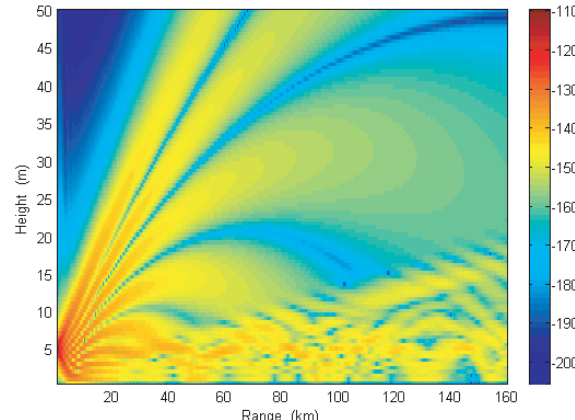


Figure 4: The space distribution of transmission loss in evaporation duct.

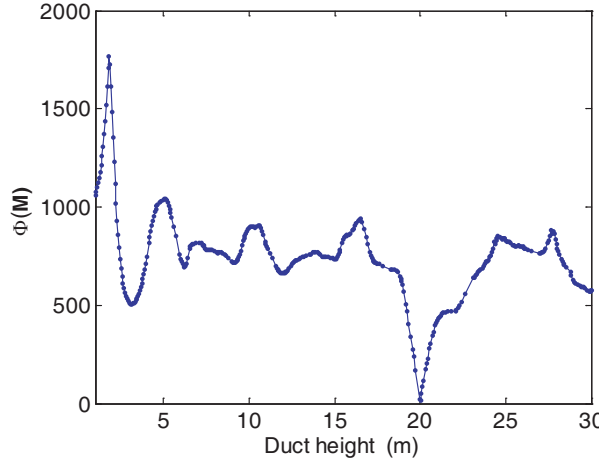


Figure 5: Objective function $\Phi(M)$ and duct height.

For neutral layer of evaporation duct with the duct height 20 m, Figure 5 shows that the objective function $\Phi(M)$ varies with the duct height. Searching the minimum of $\Phi(M)$ can determine the duct height of evaporation duct. By Equation (4), the refractivity profile can be determined for further evaluation of anomalous propagation in atmospheric duct. Genetic Algorithms (GA) are adaptive heuristic search algorithm premised on the evolutionary ideas of natural selection and genetic. For generation 100, population 40, cross probability 0.4 and mutation probability 0.2, twice duct height is 20.216 and 19.971 respectively. The inversion result is near to the true height 20. Consequently RFC technique by GA is an efficient method to estimate atmospheric refractive index profile.

6. CONCLUSIONS

For neutral layer of evaporation duct with the duct height by Genetic Algorithm (GA) and Fourier split-step method (FSS), Refractivity from Clutter (RFC) is used to predict and forecast the refractive index profile of evaporation duct. In contrast with traditional meteorological measure, refractive index profile from radar sea clutter does not need to add additional measuring equipment, and real time, military secracies is better. Therefore, the RFC technique is an efficient method to estimate atmospheric refractive index profile.

ACKNOWLEDGMENT

The authors acknowledge the financial support of NSFC (National Natural Science Foundation of China) grant No. 61002008, Foundation of Gansu Educational Committee grant No. 1008B-11 and ‘QingLan’ Talent Engineering Funds by Tianshui Normal University.

REFERENCES

1. Liu, C. G., J. Y. Huang, and C. Y. Jiang, “The occurrence of tropospheric ducts over the south-eastern coast of China,” *Chinese Journal of Radio Science*, Vol. 17, 509–513, 2002.
2. Dai, F. S., “The refractivity models in the marine atmospheric surface layer and their applications in the evaporation duct analysis,” *Chinese Journal of Radio Science*, Vol. 13, 280–286, Sep. 1998.
3. Yao, Z. Y., “The analysis on characteristics of atmospheric duct and its effects on the propagation of electromagnetic wave,” *Acta Meteorologica Sinica*, Vol. 58, 605–616, Oct. 2000.
4. Radio-wave Propagation, *ITU-R Recommendations*, Volume 2000, P Series-Part 1, 2.
5. Orfanidis, S. J., *Electromagnetic Waves and Antennas*, [Online]. Available: www.ece.rutgers.edu/~orfanidi/ewa, 169–193, 2004.
6. Dockery, G. D., “Modeling electromagnetic wave propagation in the troposphere using the parabolic equation,” *IEEE Trans. on Antenna and Propagation*, Vol. 36, 1464–1470, 1988.
7. Craig, K. H., et al., “Parabolic equation modeling of the effects of multipath and ducting on radar systems,” *IEE Proceedings-F*, Vol. 138, 153–162, 1991.
8. Gerstoft, P., “Inversion for refractivity parameters from radar sea clutter,” *Radio Science*, Vol. 38, No. 3, 8053, 2003, doi:10.1029/2002RS002640.

Subsurface Imaging with NIR Light Using Polarization Gating

M. Šormaz¹ and P. Jenny²

¹Laboratory for Media Technology

Swiss Federal Laboratories for Materials Science and Technology (EMPA)

Überlandstrasse 129, 8600 Dübendorf, Switzerland

²Institute of Fluid Dynamics, Swiss Federal Institute of Technology Zürich (ETH)

Sonneggstrasse 3, 8092 Zürich, Switzerland

Abstract— In this paper, a numerical study with the near infrared (NIR) laser light and polarization gating is used to show possible contrast improvement of the spherical inclusion hidden in the turbid medium. Inclusion has the same refractive index and scattering properties as surrounding medium but slightly higher absorption. Approach is based on time-resolved reflectance measurements and selection of photons with arc-like trajectories using polarization gating technique. Numerical studies performed for two turbid media, typically used to mimic biological tissues, reveal that coaxial setup of laser and detector is not suitable for detection of photons with arc-like trajectories. As well, the contrast improvement in ballistic-photon imaging strongly depends on the single-scattering phase function.

1. INTRODUCTION

Polarization gating was already considered in [1–4]. In [1] linearly polarized light was used to improve contrast in subsurface imaging. Image acquired with cross-polarized light was subtracted from the one acquired with co-polarized light. Photons with perpendicular polarization states were penetrated deeper into the tissue. Subsurface imaging using spectral and polarization discrimination of backscattered light was showed in [2]. In [3, 4], both circularly and linearly polarized light were considered to detect a mirror embedded in scattering medium composed of either small or large scattering particles. Circularly polarized light is preferred, if a scattering medium is composed of large scattering particles ($g = 0.911$ was used). Note that mirror is an ideal target since it flips helicity of the reflected light. This results in a nice signature compared to light backscattered from the background medium. In [5], reflecting, scattering and absorbing targets were probed using linearly and circularly polarized light in order to examine their optical properties.

In [6], was shown that polarization memory of circularly polarized light pulses results from the successive near-forward scattering events enhanced by a large anisotropy factor. These near-forward scattering events maintain the same circular polarization. Analytic solution of the time-dependent vector radiative transfer equation was used in [7] to compute backscattering of circularly polarized light. Time-independent Fokker-Planck approximation of the radiative transfer equation was used in [8] to compute light backscattered from forward scattering media. It was shown that the backscattered ring for circularly polarized incident light is mostly composed of light with the same helicity as the incident beam. Furthermore, in [9] it was shown that the observed ring structure of backscattered light is time dependent.

In this paper, we want to distinguish between diffuse and photons having arc-like trajectories by employing polarization gating. The setup looks like the one used in [10] where detection of ballistic-photons was performed using polarization gating. In all numerical experiments the light was detected in the time domain. For the studies considered in this paper we use circularly polarized laser light since the single-scattering phase functions are highly anisotropic ($g > 0.7$) which is typical for biological tissues. Note that photons with arc-like trajectories experience only forward or near forward scattering and thus their helicity is preserved.

In Section 2, the governing equation and some basic theory are shown, while in Section 3 simulation setup and used phantoms are described. The results are given in Section 4 and conclusions in Section 5.

2. THEORETICAL BACKGROUND

In the transport theory for polarized light, one has to consider a vector Boltzmann equation, which reads

$$\frac{d\mathbf{I}(\mathbf{x}, \mathbf{s}, \lambda, t)}{ds} = -\gamma_t \mathbf{I}(\mathbf{x}, \mathbf{s}, \lambda, t) + \frac{\gamma_s}{4\pi} \int_{4\pi} \mathbf{P}(\mathbf{s}, \mathbf{s}') \mathbf{I}(\mathbf{x}, \mathbf{s}', \lambda, t) d\omega', \quad (1)$$

where $\mathbf{I}(\mathbf{x}, \mathbf{s}, \lambda, t)$ is the Stokes vector defined as

$$\begin{aligned} I &= E_l E_l^* + E_r E_r^* = a_l^2 + a_r^2, \\ Q &= E_l E_l^* - E_r E_r^* = a_l^2 - a_r^2, \\ U &= E_l^* E_r + E_l E_r^* = 2a_l a_r \cos \delta \\ \text{and } V &= -i(E_l^* E_r - E_l E_r^*) = 2a_l a_r \sin \delta. \end{aligned} \quad (2)$$

Position in physical space is denoted as \mathbf{x} , \mathbf{s} is the propagation direction, λ the wavelength and t the time. The vectors \mathbf{s} and \mathbf{s}' form a so-called scattering plane for which the phase matrix $\mathbf{P}(\mathbf{s}, \mathbf{s}')$ is defined. Note that $\mathbf{P}(\mathbf{s}, \mathbf{s}')$ describes the interaction between the electromagnetic wave and an isolated particle; a detailed description of the phase matrix can be found in [11, 12]. E_l and E_r are the complex parts of the phasors $\mathbf{E}_l = \mathbf{a}_l \exp(-i\omega t - i\delta_0)$ and $\mathbf{E}_r = \mathbf{a}_r \exp(-i\omega t - i\delta_0 - i\delta)$. Here, \mathbf{E}_l and \mathbf{E}_r are the parallel and perpendicular components of the electric field vector with respect to the scattering plane. The phase difference between \mathbf{E}_r and \mathbf{E}_l is denoted by δ , $a_l = |\mathbf{a}_l|$ and $a_r = |\mathbf{a}_r|$ are the amplitudes of \mathbf{E}_l and \mathbf{E}_r , $\omega = 2\pi c/\lambda$ is the frequency and δ_0 is the phase of \mathbf{E}_l at $t = 0$ (c is the speed of light).

3. SIMULATION SETUP AND MATERIALS

As shown in Fig. 1, the circular detector with radius $R = 2.5$ mm is coaxial with the laser beam. Outgoing photons with all deflection angles from the surface normal are considered and in all test cases the center of the considered spherical target was placed on the line along the laser beam.

Two different scattering media labeled as phantom 1 and phantom 2 are used. Both phantoms can be considered as semi-infinite and are composed of scattering particles with diameter $d_{sp} = 400$ nm (phantom 1) and $d_{sp} = 1000$ nm (phantom 2) embedded in silicon with $n_{si} = 1.404$. In both phantoms, scattering particles are polystyrene spheres with $n_{sp} = 1.59$. The illumination is a near-infrared laser light with $\lambda = 780$ nm perpendicularly incident on the scattering medium and propagating along the positive z -direction. The Stokes vector (see Eq. (2)) of incident light is $\mathbf{I} = [1 \ 0 \ 0 \ 1]^T$. The background medium has the same scattering coefficient as the target ($\gamma_s = 10 \text{ cm}^{-1}$), but different absorption coefficients, i.e., $\gamma_{a,bg} = 0.2 \text{ cm}^{-1}$ for the background medium and $\gamma_{a,target} = 0.5 \text{ cm}^{-1}$ for the target. Note that background medium and target have same refractive index and single-scattering phase function. Matched refractive indices of phantoms and surrounding medium were used and the Stokes vector of the reflected particles is defined in the system $-\mathbf{x}$, \mathbf{y} and $-\mathbf{z}$ (Stokes vector of incident light is defined in \mathbf{x} , \mathbf{y} and \mathbf{z}). Lorenz-Mie theory was employed to compute single-scattering phase functions, whose anisotropy factors are $g \approx 0.72$ and $g \approx 0.92$ for the phantoms 1 and 2, respectively. Table 1 presents all considered test cases.

4. RESULTS

In first four cases, phantom 1 is considered and the results are shown in Fig. 2. In subplot (a) the signal-to-noise ratio (SNR) (here defined as the ratio of detected computational particles which hit the target over all detected particles) as a function of time-of-flight is shown. For unpolarized and copolarized light (cases 1 and 3) SNR is quite similar, while for the case 4 is slightly larger from 50 to 120 ps. The reason is polarization gating which eliminates some of diffuse light. SNR

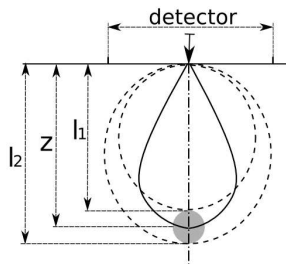


Figure 1: Simulation setup with semi-infinite background medium and spherical target with diameter $D = l_2 - l_1$ placed at depth z and the center on the line of the incident laser beam. Source and detector are coaxial. Ballistic photon trajectories are drawn with dash-dotted line (cases 2 and 6 in Table 1) and idealistic arc-like trajectories are drawn with dashed lines (cases 4 and 8).

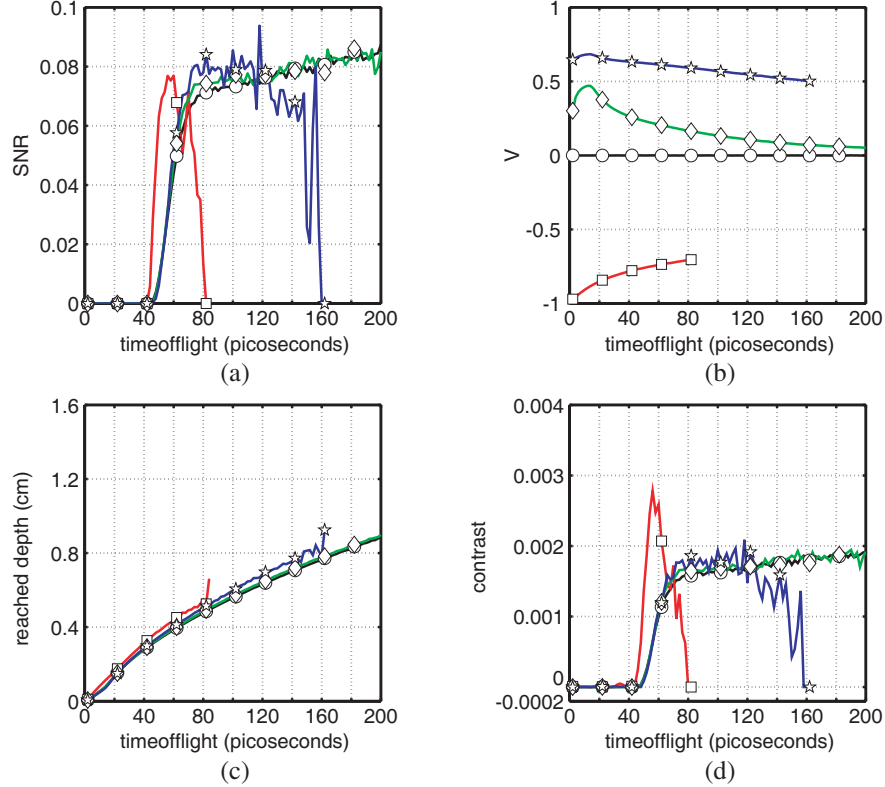


Figure 2: Results for the cases 1, 2, 3 and 4 (phantom 1). Lines marked with circles, squares, diamonds and pentagrams represent mean values for the cases 1, 2, 3 and 4, respectively. Subplots (a), (b), (c) and (d) show signal-to-noise ratio, V -component of the Stokes vector, reached depth and contrast as functions of time-of-flight, respectively.

Table 1: Overview of all considered cases. For cases 1 and 5 incident light is unpolarized $\mathbf{I} = [1 \ 0 \ 0 \ 0]^T$, while for all other cases is circularly polarized $\mathbf{I} = [1 \ 0 \ 0 \ 1]^T$. In all test cases, $\lambda = 780$ nm. Cases 2 and 6 represent ballistic-photon imaging [10].

case	D (mm)	z (mm)	phantom	polarization gating
1	1	5	1	NO
2	1	5	1	$V \in [-1, -0.7]$
3	1	5	1	$V \in [0.01, 1]$
4	1	5	1	$V \in [0.5, 1]$
5	1	5	2	NO
6	1	5	2	$V \in [-1, -0.7]$
7	1	5	2	$V \in [0.01, 1]$
8	1	5	2	$V \in [0.5, 1]$

for ballistic photons (case 2) reaches the same value at its peak as in other cases, but starts to grow before all others due to the shortest paths until the target is reached. Subplot (b) shows the V -component of the Stokes vector of detected particles. Of course, the V -component for the case 1, where unpolarized light was used, is zero. Reached depth as a function of time-of-flight is in subplot (c). As expected, the ballistic-photons (case 2) reach larger depths for the same times-of-flight compared to cases 1, 3 and 4. Finally, the contrast

$$\text{contrast} = \frac{I_0 - I}{I_0}, \quad (3)$$

where I and I_0 are the detected intensities with and without spherical target, respectively, is depicted in subplot (d). Note that in ballistic-photon imaging (cases 2 and 6) the distance l_1 in

Fig. 1 is approximately represented by the speed of light times half the time-of-flight for which contrast starts to rise, while l_2 is approximately equal to the speed of light times half the time-of-flight corresponding to the contrast peak. In this cases, is easy to estimate depth and size of the target from the contrast curve, while zero source-detector separation leads to the best possible localization in the xy -plane. As well, the best contrast is achieved in ballistic-photon imaging, while for other three cases is quite similar. Note that contrast curve for case 4 starts to rise around 50 ps which corresponds to reached depth of about 0.34 cm (assuming circular photon trajectories) instead of 0.45 cm. Obviously for the coaxial laser-detector setup the circular photon trajectories can not be assumed even when polarization gating is used. On the other hand, the contrast curve for the case 2 start to rise around 45 ps, which corresponds to reached depth of about 0.481 cm. Obviously, the detected photons in this case have slightly corrugated instead of straight trajectories.

Next, the same results obtained for phantom 2 are presented. In the subplot (a) SNR is shown and can be seen that it is approximately the same for all cases in the target region ($\approx 45\text{--}60$ ps). Again, in subplot (b) and (c) the V-component of the Stokes vector and the reached depth are shown, respectively. Finally, the contrast curves are depicted in subplot (d). The largest contrast is achieved for unpolarized light and ballistic-photon imaging (cases 5 and 6). As it was shown in [10], the difference between contrast curves obtained in ballistic-photon imaging and imaging with unpolarized light is negligible when media with highly anisotropic scattering phase functions are considered; i.e., all detected photons for coaxial laser-detector setup have weakly corrugated trajectories. Note that the contrast curves for cases 7 and 8 are lower at their peak compared to contrast curves obtained by imaging with unpolarized light and ballistic photons. The reason is in fact that the path length of ballistic photons through the spherical inclusion is ideally two times its diameter which is not the case for photons with preserved helicity; their realistic trajectories are represented with the solid line in Fig. 1 (their idealistic trajectories are drawn with dashed lines). Thus ballistic photons, which exist in unpolarized incident light as well, spend more time in higher absorbing spherical inclusion than the photons with preserved helicity, which results in

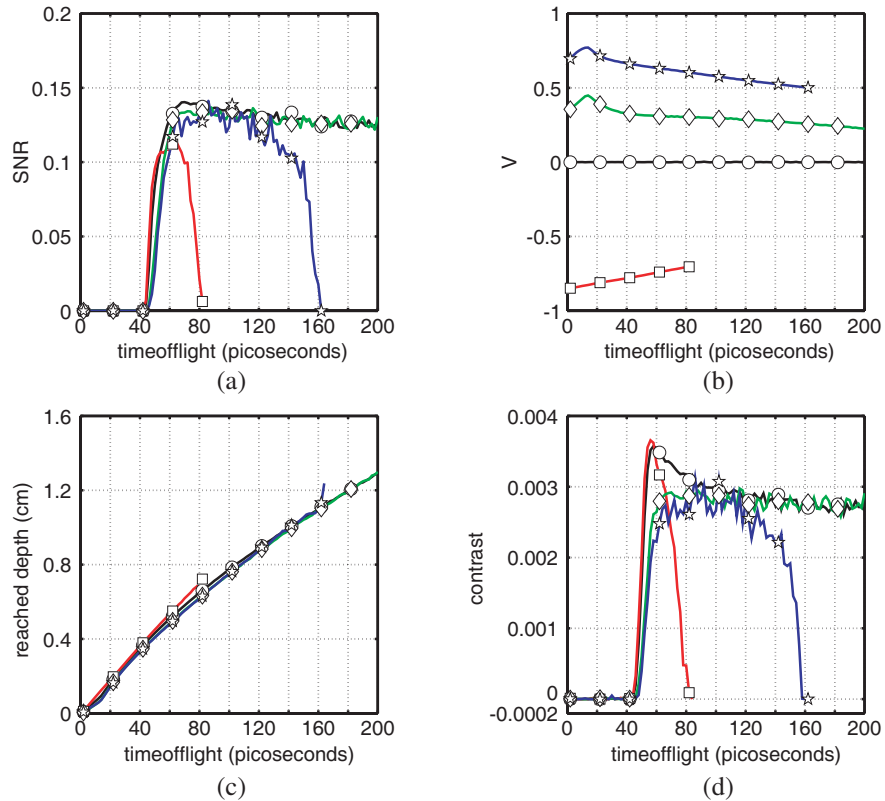


Figure 3: Results for the cases 5, 6, 7 and 8 (phantom 2). Lines marked with circles, squares, diamonds and pentagrams represent mean values for the cases 5, 6, 7 and 8, respectively. Subplots (a), (b), (c) and (d) show signal-to-noise ratio, V-component of the Stokes vector, reached depth and contrast as functions of time-of-flight, respectively.

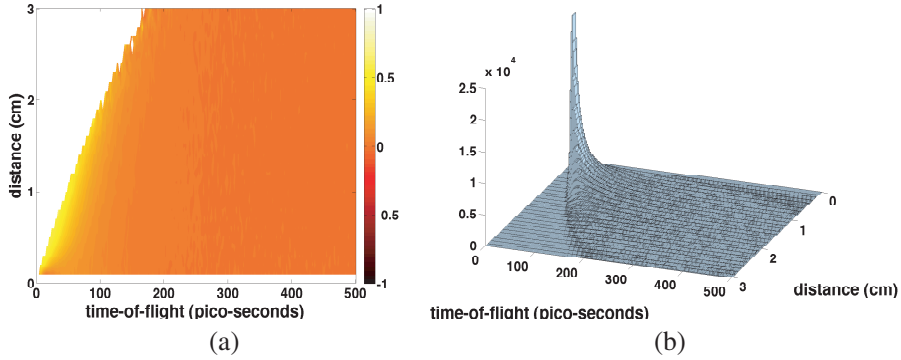


Figure 4: Results for the phantom 1. Subplots (a) and (b) show the polarization state of backscattered light and the photon number density, respectively, both conditioned on the time-of-flight and distance from the point of incidence. The number of simulated computational particles is 5×10^6 .

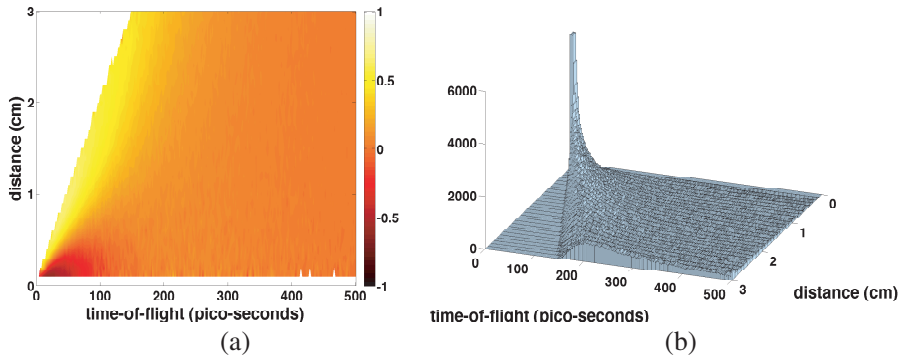


Figure 5: Results for the phantom 2. Subplots (a) and (b) show the polarization state of backscattered light and the photon number density, respectively, both conditioned on the time-of-flight and distance from the point of incidence. The number of simulated computational particles is 5×10^6 .

higher contrast.

Finally, the polarization and the photon number density for both phantoms conditioned on time-of-flight and distance from the point of incidence are shown in Figs. 4 and 5. Note that here all backscattered light is detected. Due to more anisotropic scattering phase function the number of detected computational particles for phantom 2, see subplot (b) of Fig. 5, is smaller compared to phantom 1. Obviously, the polarization of photons with preserved helicity is maintained over a larger optical path lengths compared to ballistic photons, which allows use of detectors with large collection areas and which are able to spatially resolve detected light [13].

5. CONCLUSION

In conclusion we report that no contrast improvement can be expected for coaxial laser-detector setup if polarization gating is employed to detect photons with preserved helicity. Such a setup is suitable only for detection of ballistic photons. Note as well that in cases 2, 4, 6 and 8 employed polarization gating can be done if one is able to select only that light with flipped or preserved helicity within a certain ellipticity range (which depends on the target depth). Nevertheless, it is shown that the polarization of backscattered light is preserved over large distances from the point of incidence making polarization gating a suitable technique for contrast improvement if a detector which is able to spatially resolve backscattered light is used for measurements in time domain. More studies are required to examine this statement and that work will be published elsewhere.

REFERENCES

1. Demos, S. G. and R. R. Alfano, "Optical polarization imaging," *App. Opt.*, Vol. 36, 150–155, 1997.
2. Demos, S. G., H. B. Radousky, and R. R. Alfano, "Deep subsurface imaging in tissues using spectral and polarization filtering," *Opt. Exp.*, Vol. 7, 23–28, 2000.

3. Ni, X. and R. R. Alfano, "Time-resolved backscattering of circularly and linearly polarized light in a turbid medium," *Opt. Lett.*, Vol. 29, 232773-3, 2004.
4. Kartazayeva, S. A., X. Ni, and R. R. Alfano, "Backscattering target detection in a turbid medium by use of circularly and linearly polarized light," *Opt. Lett.*, Vol. 30, 101168-3, 2005.
5. Nothdurft, R. and G. Yao, "Expression of target optical properties in subsurface polarization-gated imaging," *Opt. Exp.*, Vol. 13, 4185–4195, 2005.
6. Kim, A. D. and M. Moscoso, "Backscattering of circularly polarized pulses," *Opt. Lett.*, Vol. 27, 181589, 2002.
7. Cai, W., X. Ni, S. K. Gayen, and R. R. Alfano, "Analytical cumulant solution of the vector radiative transfer equation investigates backscattering of circularly polarized light from turbid media," *Phy Rew. E*, Vol. 74, 056605, 2006.
8. Kim, A. D. and M. Moscoso, "Backscattering of beams by forward-peaked scattering media," *Opt. Lett.*, Vol. 29, 010074, 2004.
9. Phillips, K. G., M. Xu, S. K. Gayen, and R. R. Alfano, "Time-resolved ring structure of circularly polarized beams backscattered from forward scattering media," *Opt. Exp.* Vol. 13, 7954–7969, 2005.
10. Šormaz, M. and P. Jenny, "Contrast improvement by selecting ballistic-photons using polarization gating," *Opt. Exp.*, Vol. 18, No. 23, 23746–23755, 2010.
11. Bohren, C. F. and D. R. Huffman, *Absorption and Scattering of Light by Small Particles*, Wiley, 1983.
12. Van de Hulst, H. C., *Light Scattering by Small Particles*, Wiley, 1957.
13. Niclass, C., C. Favi, T. Kluter, M. Gersbach, and E. Charbon, "A 128×128 single-photon image sensor with column-level 10-Bit time-to-digital converter array," *IEEE J. Solid-state Circ.*, Vol. 43, 2977–2989, 2008.

Pseudo Random Binary Sequence GPR Imaging via Compressive Sensing

Xin Xu^{1, 2}, Wei Wang^{1, 2}, Zhiwei Lin^{1, 2}, Peng Zhang^{1, 2}, and Xiaojuan Zhang²

¹Graduate School, Chinese Academy of Sciences, Beijing, China

²Institute of Electronics, Chinese Academy of Sciences, Beijing, China

Abstract— In this paper, the Pseudo Random Binary Sequence Ground Penetrating Radar (PRBS-GPR) is investigated under the Compressive Sensing (CS) framework. We show that the bernoulli signal transmitted by PRBS-GPR has an inherent connection with CS theory, and sampling rate can be reduced without loss of resolution. The Restricted Isometry Property (RIP) of subsampled toeplitz bernoulli matrix is obtained by theoretical analysis, then exact reconstruction is guaranteed by some well-known theorems. Our analysis is not restricted on the bernoulli case, so extensions can be made to a larger class of noise modulated radar systems.

1. INTRODUCTION

Pseudo random noise modulated radar offers some very attractive possibilities to the designer of Radar systems. The radiated power is evenly spread throughout the spectrum and the receiver is less susceptible to interference. Random noise (Gaussian) radar and Pseudo-Random Binary Sequence radar are the most widely used noise modulated radar systems [1]. Although resolution can benefit from large bandwidth, high sampling rate is still a burden to the system.

Compressive sensing states that if the target scene of interest is sparse, then one can just take a minor amount of samples and then reconstruct the scene without loss of resolution, provided that “appropriate” measurement is taken [2]. In the situation of Ground Penetrating Radar (GPR) imaging, target is sparse in most cases, which coincide with CS theory. The radar echo can be viewed as a convolution of transmitted signal and target scene, which can be further represented by a multiplication of a toeplitz matrix and a scene vector, in matrix-vector form. The toeplitz matrix is formulated by shifted versions of the transmitted signal, and its upper-right and lower-left corners are filled with zeros. Toeplitz random matrix for compressive sensing has received certain amounts of interests and a few results have been reported. In [3], the signs of nonzero entries of the sparse signal are restricted to be Bernoulli variables; in [4], the convolution is actually a circular one, while in radar applications linear convolution is preferred; in [5], all entries of the matrix are filled with nonzero values.

In [6], the toeplitz random matrix is treated as a special case of block diagonal matrix for channel sensing application. In channel sensing, the received signal is a linear convolution of known transmitted signal and unknown channel impulse response, and then a deconvolution is performed in order to get the channel impulse response. Subsampling is also introduced, and restricted isometry property of the corresponding subsampled toeplitz matrix is derived by using *Geršgorin's* theorem and Hoeffding's Inequality, which will be addressed later. However, a peculiar property of Gaussian distribution is used in the proof, so the result can not be extended to bernoulli random variable.

In this paper, our attention is focused on subsampled toeplitz matrix, which is generated by a bernoulli random vector. The RIP property is derived following the method introduced in [6]. Our paper can be organized as follow: First we give some introduction on compressive sensing theory; then theoretical analysis on RIP property of subsampled toeplitz bernoulli matrix is given, which is the main contribution of this paper; then we use one dimensional numerical simulation to verify our result; finally conclusions and future works is given.

2. FUNDAMENTALS OF COMPRESSIVE SENSING

In this section, fundamental theory of compressive sensing is introduced in brief, and some definitions, lemmas and theorems are also given for subsequent analysis.

The central problem of CS is to solve an noisy, underdetermined linear system

$$y = \Phi x + w, \quad y \in \mathbb{C}^M, \quad x, w \in \mathbb{C}^N, \quad \Phi \in \mathbb{C}^{M \times N}, \quad M < N \quad (1)$$

The uniqueness of the solution to this problem is guaranteed by imposing a sparsity constraint on x and a property, named Restricted isometry Property (RIP), on matrix Φ .

Definition 1. We say that a matrix Φ satisfies RIP of order K if there exists a $\delta_K \in (0, 1)$ such that

$$(1 - \delta_k)\|x\|_2^2 \leq \|\Phi x\|_2^2 \leq (1 + \delta_k)\|x\|_2^2 \quad (2)$$

for all $\|x\|_0 \leq K$.

Problem (1) is often transformed to a Basis Pursuit DeNoising (BPDN) problem as follow:

$$\min_x \|x\|_1 \quad \text{s.t. } \|y - \Phi x\|_2 \leq \epsilon \quad (3)$$

where ϵ is the variance of the noise vector w . The BPDN problem can be solved by interior point method [7], or other fast convex optimization methods [8]. The following theorem gives (3) a stability guarantee.

Theorem 2 ([9]). Let $y = \Phi x + w$ be defined as in (1). Assume that the columns of Φ have unit ℓ_2 -norms and further let Φ satisfies $2K$ order RIP property and $\delta_{2K} < 0.3$. Then solution x^* of (3) satisfies

$$\|x^* - x\|_2^2 \leq c_0 \left(c'_0 \epsilon + \frac{\|x - x_K\|_1}{\sqrt{K}} \right)^2 \quad (4)$$

where x_K is the vector formed by setting all but the K largest (in magnitude) entries of x to zeros, and c_0 and c'_0 are given by

$$\begin{cases} c_0 = 4 \left(\frac{1 + 3\delta_{2K}}{1 - 3\delta_{2K}} \right)^2 \\ c'_0 = 2(1 + \delta_{2K})^{-\frac{1}{2}}. \end{cases} \quad (5)$$

From the theorem above we know that matrix Φ plays a vital role in CS theory. However, there is no efficient algorithms available for checking the RIP property for any given matrix except for Gaussian, Bernoulli random matrix and partial Fourier matrix.

Next we give a lemma that will be useful in next section.

Lemma 3 (Hoeffding's Inequality). Let x_1, x_2, \dots, x_N be (real-valued) independent bounded random variables satisfying $\tau_i \leq x_i \leq v_i, i = 1, \dots, N$, almost surely. Define $S_N = \sum_{i=1}^N x_i$, then for any $t > 0$

$$\Pr(|S_N - \mathbb{E}(S_N)| \geq t) \leq 2 \exp \left(-\frac{2t^2}{\sum_{i=1}^N (v_i - \tau_i)^2} \right) \quad (6)$$

3. RIP FOR SUBSAMPLED TOEPLITZ BERNOUILLI MATRIX

In this section, we derive the RIP property of subsampled toeplitz Bernoulli matrix. The full toeplitz matrix can be formulated as:

$$\hat{\Phi} = \begin{bmatrix} \phi_1 & 0 & \dots & 0 \\ \phi_2 & \phi_1 & \dots & 0 \\ \vdots & \vdots & \ddots & \vdots \\ \phi_{P'} & \phi_{P'-1} & \dots & 0 \\ 0 & \phi_{P'} & \dots & 0 \\ 0 & 0 & \dots & \phi_1 \\ \vdots & \vdots & \ddots & \vdots \\ 0 & 0 & \dots & \phi_{P'} \end{bmatrix}. \quad (7)$$

where $\phi = \{\phi_1, \phi_2, \dots, \phi_{P'}\}^T$ is the signal transmitted by PRBS radar, and $\phi_i, i = 1, 2, \dots, P'$ are bernoulli random variables taking values $\pm c$ with probability $1/2$ for some quantity $c > 0$. The received signal can be written as:

$$\hat{y} = \hat{\Phi}x, \quad x \in \mathbb{C}^N, \quad \hat{\Phi} \in \mathbb{C}^{(P'+N-1) \times N}, \quad y \in \mathbb{C}^{P'+N-1} \quad (8)$$

Actually we are more interested in a subsampled version of \hat{y} . By subsampling, we offer two alternatives. The downsampling can be simply extracting one entry for every T entries, which yields

a length M vector y , here we assume $M = \lfloor \frac{P'+N-1}{T} \rfloor$; or we choose M entries out of $(P' + N - 1)$ entires of \hat{y} uniformly at random. Thus the subsampled version of received signal can be written as:

$$y = \Phi x, \quad y \in \mathbb{C}^M, \quad \Phi \in \mathbb{C}^{M \times N}, \quad N \in \mathbb{C}^N \quad (9)$$

where Φ is the corresponding subsampled version of $\hat{\Phi}$.

According to definition 1, a $M \times N$ matrix Φ satisfies RIP of order K when the following inequality holds for some constant $\delta_K \in (0, 1)$

$$\max_{\|x\|_0 \leq K, x \neq 0} \frac{|\|\Phi x\|_2^2 - \|x\|_2^2|}{\|x\|_2^2} \leq \delta_K \iff \max_{\Omega \subset [1 \dots N], |\Omega| \leq K} \|\Phi_{\Omega}^H \Phi_{\Omega} - I_{|\Omega|}\|_2 \leq \delta_K \quad (10)$$

The above inequality shows that to establish RIP for a given sensing matrix Φ , one needs to bound the spectral norms of all square submatrices of $(\Phi^H \Phi - I_N)$ having no more than K rows/columns. Trivially from the definition of the spectral norm, however, we have that

$$\|\Phi_{\Omega'}^H \Phi_{\Omega'} - I_{|\Omega'|}\|_2 \leq \|\Phi_{\Omega}^H \Phi_{\Omega} - I_{|\Omega|}\|_2 \quad (11)$$

for any $\Omega' \subset \Omega$. Therefore, we only need to bound the spectral norms of all $K \times K$ submatrices of $(\Phi^H \Phi - I_N)$. To move on, we need the following lemma derived from *Geršgorin's theorem*.

Lemma 4 ([9]). *Let Φ be an $M \times N$ matrix having unit ℓ_2 -norm columns. Then*

$$\|\Phi^H \Phi - I_N\|_{\Omega, K} \leq (K-1) \|\Phi^H \Phi - I_N\|_{\max} \quad (12)$$

where $\|M\|_{\Omega, K} = \|M_{\Omega \times \Omega}\|_2$ for any $|\Omega| = K$ and $\|M\|_{\max}$ is the largest entries of M in amplitude.

Let $a_i, i = 1, \dots, N$ be columns of Φ , and noting that $(\Phi^H \Phi - I_N)$ is a matrix whose diagonal entries are all zeros due to unit-norm columns of Φ , so we have

$$\|\Phi^H \Phi - I_N\|_{\max} = \max_{i \neq j} |\langle a_j, a_i \rangle| = \max_{i < j} |\langle a_j, a_i \rangle| \quad (13)$$

the last equation holds because of symmetry. Assuming $1 \leq i < j \leq N$, we can write the inner product $\langle a_j, a_i \rangle$ as

$$\langle a_j, a_i \rangle = \sum_{q=1}^Q \alpha_q \alpha_{q+\Delta} \quad (14)$$

where $\Delta = j - i$ and $Q = \lfloor P - \frac{\Delta}{T} \rfloor$, where P is the largest number of nonzero values of Φ 's columns. Note that we can not directly apply Hoeffding's Inequality to $\langle a_j, a_i \rangle$ because of the dependency between the items in the summation. However, we can split the summation to two independently parts, each with about $\frac{Q}{2}$ items. The split is apparent thanks to downsampling. So we can rewrite (14) as

$$\langle a_j, a_i \rangle = S_1 + S_2 \quad (15)$$

where S_1 and S_2 is dependent, and both of them are a summation of $\frac{Q}{2}$ bernoulli variables, taking values $\pm \frac{1}{P}$ with probability $\frac{1}{2}$. Here we assume that P is the largest number of nonzero values of Φ 's columns. Now we can bound $|\langle a_j, a_i \rangle|$ by applying lemma 3 as follows

$$\begin{aligned} Pr \left(|\langle a_j, a_i \rangle| > \frac{\delta_K}{K} \right) &\leq Pr \left(\left\{ |S_1| > \frac{\delta_K}{2K} \right\} \cup \left\{ |S_2| > \frac{\delta_K}{2K} \right\} \right) \\ &\leq 2 \max \{ Pr \left(|S_1| > \frac{\delta_K}{2K} \right), Pr \left(|S_2| > \frac{\delta_K}{2K} \right) \} \\ &\leq 4 \exp \left(-\frac{P\delta_K^2}{4K^2} \right) \end{aligned} \quad (16)$$

Recall (13), we get

$$\begin{aligned} Pr \left(\|\Phi^H \Phi - I_N\|_{\max} > \frac{\delta_K}{K} \right) &= Pr \left(\max_{i < j} |\langle a_j, a_i \rangle| > \frac{\delta_K}{k} \right) \\ &\leq 2N(N-1) \exp \left(-\frac{P\delta_K^2}{4K^2} \right) \end{aligned} \quad (17)$$

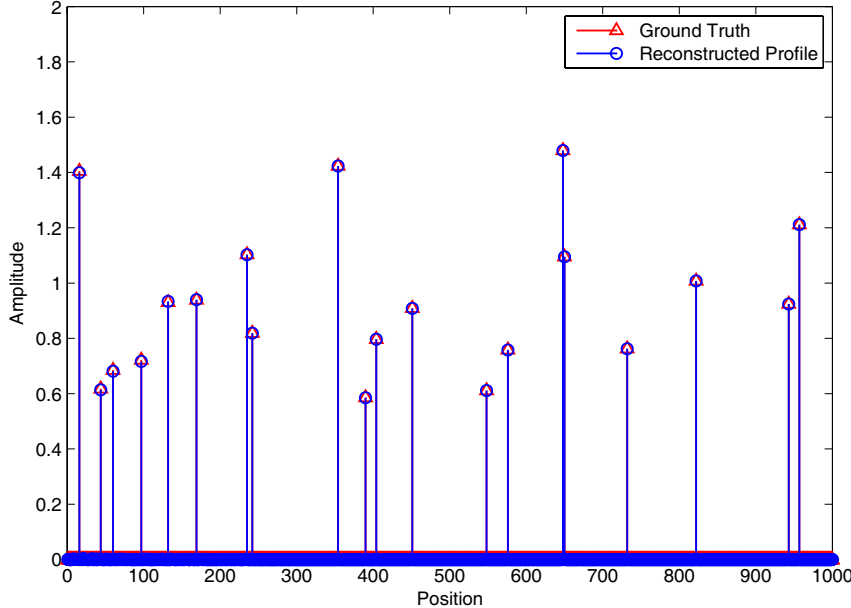


Figure 1: 1D PRBS radar simulation result.

The last inequality in (17) follows from taking union bound over a total of $p(p - 1)/2$ events. Let $c_1 < \delta_K^2/4$, $P \geq (12/(\delta_K^2 - 4c_1))K^2 \log N$, and combined with (12) we have

$$\Pr(\|\Phi^H \Phi - I_N\|_{\Omega, K} \leq \delta_K) > 1 - \exp(-c_1 P/K^2) \quad (18)$$

which means that matrix Φ satisfies RIP of order K with probability exceeding $1 - \exp(-c_1 P/K^2)$.

Note that P , the largest number of nonzero values of Φ 's columns, must be larger than a certain number, while in classical CS theory the restriction is put on M , the number of rows. This condition implies that the downsampling ratio T should not be too large.

4. NUMERICAL SIMULATION

Now we give one dimensional simulation result. We set the length of the scene vector to be 1000, and 20 out of them are nonzero. The amplitude of the nonzero values are chosen uniformly at random between 0.5 and 1.5, and phase between 0 and 2π . The length of bernoulli random vector is 127, and the full received signal length is 1126. Figure 1 shows the result when downsampling rate is 5. We use Fast Iterative Shrinkage-Thresholding Algorithm (FISTA) [10] for reconstruction, and the energy error is below 5×10^{-4} .

5. CONCLUSION

In this paper, we combine compressive sensing with pseudo random binary sequence radar imaging. The subsampled toeplitz bernoulli matrix is investigated using the method introduced in [6], and the result shows that the subsampled toeplitz bernoulli matrix has good RIP property. It implies that we can simply reduce the sampling rate at radar receiver end without loss of resolution by implementing CS reconstruction methods. The 1D simulation result conforms well with theoretical analysis. Experimental data from PRBS-GPR will be used to verify our theory in the future.

REFERENCES

1. Daniels, D. J., *Ground Penetrating Radar*, 2004.
2. Candès, E. J., “Compressive sampling,” *Proceedings of the International Congress of Mathematicians*, Vol. 3, 1433–1452, Citeseer, 2006.
3. Rauhut, H., “Circulant and Toeplitz matrices in compressed sensing,” Arxiv preprint arXiv:0902.4394, 2009.
4. Romberg, J., “Compressive sensing by random convolution,” *SIAM Journal on Imaging Sciences*, Vol. 2, No. 4, 1098–1128, 2009.
5. Yin, W., S. Morgan, J. Yang, and Y. Zhang, “Practical compressive sensing with Toeplitz and circulant matrices,” *Proc. SPIE*, Vol. 7744, 2010.

6. Park, J. Y., H. L. Yap, C. J. Rozell, and M. B. Wakin, “Concentration of measure for block diagonal matrices with applications to compressive sensing,” 2010.
7. Boyd, S. P. and L. Vandenberghe, *Convex Optimization*, Cambridge Univ. Pr., 2004.
8. Yang, A. Y., A. Ganesh, Z. Zhou, S. S. Sastry, and Y. Ma, “A review of fast l_1 -minimization algorithms for robust face recognition,” Arxiv preprint arXiv:1007.3753, 2010.
9. Bajwa, W. U. Z., “New information processing theory and methods for exploiting sparsity in wireless systems,” Ph.D. Thesis, University of Wisconsin, 2009.
10. Beck, A. and M. Teboulle, “A fast iterative shrinkage-thresholding algorithm for linear inverse problems,” *SIAM Journal on Imaging Sciences*, Vol. 2, No. 1, 183–202, 2009.

An Analytic Solution to the Scattering Fields of Shaped Beam by a Moving Conducting Infinite Cylinder with Dielectric Coating

Mingjun Wang^{1, 2}, Huayong Zhang³, Yingle Li¹, Jiadong Xu², and Ningjing Xiang¹

¹Institute of E.M. Wave Propagation & Scattering, Xianyang Normal College, Box 103, 712000, China

²School of Electronic Information, Northwestern Polytechnical University, Xi'an, Shaanxi 710072, China

³School of Electronic Science and Technology, Anhui University, Hefei, Anhui 230039, China

Abstract— In this paper, the coordinate transformations and the relation of wave vector and Electromagnetic fields and based on the generalized Lorenz-Mie theory (GLMT) that provides the general framework and expansion of the incident shaped beam in terms of cylindrical vector wave functions, an analytic solution to the electromagnetic scattering by coated moving infinite cylinders with high speed is constructed, for arbitrary incidence of a shaped beam. As an example, for a tightly focused Gaussian beam propagating perpendicular to the cylinder axis, the scattering characteristics that obviously demonstrate the three-dimensional nature are described in detail.

1. INTRODUCTION

Electrical engineers are often confronted with the need to evaluate fields in and around moving bodies. A fundamental understanding of the electrodynamics of moving bodies deeply preoccupied — and puzzled — the physicists of the second half of the nineteenth century [1–6]. Due to the theories have many problems, so many researchers have studied exact solutions of electromagnetic wave scattering by some static objects exhibiting regular shapes such as spheres, spheroids and infinite cylinders [7–10]. In recent years, with the development of the technology on space, people are urgent to study on the light scattering of the particles such as cosmic dust, interstellar atomies and particles, which have a high speed. Some basic theories of Wave four-vectors for the electromagnetic waves in relatively moving dielectric media are discussed in the Ref. [11]. The scattered field and differential scattered section (DSS) of spherical particle moving with a high speed were investigated numerically in Ref. [12]. According to our before research works Ref. [14], the Lorentz transformations will be combine with shape beam scattering to Scattering Fields of shaped beam by a high-speed moving conducting infinite cylinder with dielectric coating.

2. SCATTERING FIELDS OF SHAPED BEAM BY A CONDUCTING INFINITE CYLINDER WITH DIELECTRIC COATING IN STATIC CARTESIAN COORDINATE SYSTEM

As shown in Fig. 1, an incident shaped beam propagates in free space and from the negative z' to the positive z' axis of the static Cartesian coordinate system $O'x'y'z'$, with the middle of its waist located at origin O' . The system $Ox''y''z''$ that is parallel to $O'x'y'z'$ is introduced, and $Oxyz$ is obtained by rotating $Ox''y''z''$ through Euler angles α, β, γ . A conducting infinite cylinder with a dielectric coating is natural to the system $Oxyz$. In this paper, we assume that the time-dependent part of the electromagnetic fields is $\exp(-i\omega t)$, and consider the restricted case that O is on the $O'z'$ axis, i.e., at $(0, 0, z_0)$ in $O'x'y'z'$. Fig. 1. In the static condition the Cartesian coordinate system $Ox''y''z''$ is parallel to the shaped beam coordinate system $O'x'y'z'$, and the Cartesian coordinates of O in $O'x'y'z'$ are $(0, 0, z_0)$. $Oxyz$ is obtained by a rigid-body rotation of $O'x'y'z'$ through Euler angles α, β, γ , and a conducting infinite cylinder with dielectric coating is natural to $Oxyz$.

We have obtained an expansion in Ref. [14] of the electromagnetic fields of an incident shaped beam in terms of the cylindrical vector wave functions $\mathbf{m}_{m\lambda}^{(1)} \exp(ihz)$ and $\mathbf{n}_{m\lambda}^{(1)} \exp(ihz)$ with respect to the system $Oxyz$ in the following form

$$\mathbf{E}^i = E_0 \sum_{m=-\infty}^{\infty} \int_0^{\pi} \left[I_{m,TE}(\zeta) \mathbf{m}_{m\lambda}^{(1)} + I_{m,TM}(\zeta) \mathbf{n}_{m\lambda}^{(1)} \right] \exp(ihz) \sin \zeta d\zeta \quad (1)$$

$$\mathbf{H}^i = -iE_0 \frac{k}{\omega\mu} \sum_{m=-\infty}^{\infty} \int_0^{\pi} \left[I_{m,TE}(\zeta) \mathbf{n}_{m\lambda}^{(1)} + I_{m,TM}(\zeta) \mathbf{m}_{m\lambda}^{(1)} \right] \exp(ihz) \sin \zeta d\zeta \quad (2)$$

where $\lambda = k \sin \zeta$, $h = k \cos \zeta$, and $I_{n,TE}^m$, $I_{n,TM}^m$ are the beam shape coefficients.

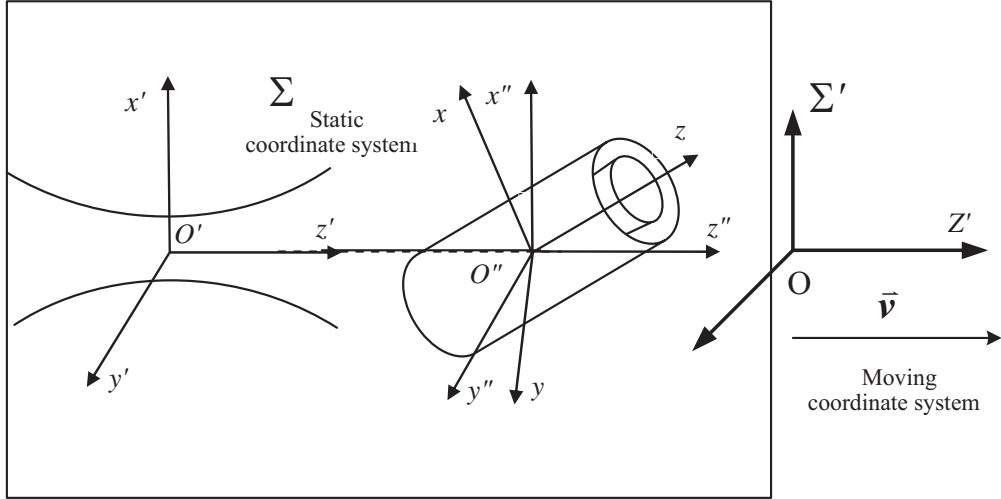


Figure 1: The relations between moving coordinate system Σ' where observer lies in the and the static coordinate system Σ where the cylinder with dielectric coating lies in.

We take the case of a TE mode as an example, and, without any loss of generality, assume Euler angles $\alpha = \gamma = 0$ (case of on-axis beams with diagonal incidence). The scattered fields for a TM mode can be obtained in a similar way.

Following Eqs. (1), (2), we can correspondingly have an appropriate expansion of the scattered and internal fields within the dielectric coating as

$$\mathbf{E}^s = E_0 \sum_{m=-\infty}^{\infty} \int_0^{\pi} [\alpha_m(\zeta) \mathbf{m}_{m\lambda}^{(3)} + \beta_m(\zeta) \mathbf{n}_{m\lambda}^{(3)}] e^{ihz} \sin \zeta d\zeta \quad (3)$$

$$\mathbf{H}^s = -iE_0 \frac{k}{\omega\mu} \sum_{m=-\infty}^{\infty} \int_0^{\pi} [\alpha_m(\zeta) \mathbf{n}_{m\lambda}^{(3)} + \beta_m(\zeta) \mathbf{m}_{m\lambda}^{(3)}] e^{ihz} \sin \zeta d\zeta \quad (4)$$

$$\mathbf{E}^w = E_0 \sum_{m=-\infty}^{\infty} \int_0^{\pi} [\chi_m(\zeta) \mathbf{m}_{m\lambda'}^{(1)} + \chi'_m(\zeta) \mathbf{m}_{m\lambda'}^{(3)} + \tau_m(\zeta) \mathbf{n}_{m\lambda'}^{(1)} + \tau'_m(\zeta) \mathbf{n}_{m\lambda'}^{(3)}] e^{ihz} \sin \zeta d\zeta \quad (5)$$

$$\mathbf{H}^w = -iE_0 \frac{k'}{\omega\mu} \sum_{m=-\infty}^{\infty} \int_0^{\pi} [\chi_m(\zeta) \mathbf{n}_{m\lambda'}^{(1)} + \chi'_m(\zeta) \mathbf{n}_{m\lambda'}^{(3)} + \tau_m(\zeta) \mathbf{m}_{m\lambda'}^{(1)} + \tau'_m(\zeta) \mathbf{m}_{m\lambda'}^{(3)}] e^{ihz} \sin \zeta d\zeta \quad (6)$$

where the parameter $k' = k\tilde{n}$, \tilde{n} is the refractive index of the material of the dielectric coating relative to that of free space, and $\lambda'k\sqrt{\tilde{n}^2 - \cos^2 \zeta}$.

The unknown coefficients $\alpha_m(\zeta)$, $\beta_m(\zeta)$, $\chi_m(\zeta)$, $\chi'_m(\zeta)$, $\tau_m(\zeta)$ and $\tau'_m(\zeta)$ in Eqs. (3)–(6) can be determined by applying the boundary conditions at $r = r_2$ and $r = r_1$ are

$$\left. \begin{aligned} E_\phi^i + E_\phi^s &= E_\phi^w, E_z^i + E_z^s &= E_z^w \\ H_\phi^i + H_\phi^s &= H_\phi^w, H_z^i + H_z^s &= H_z^w \end{aligned} \right\} \text{at } r = r_2, \quad \left. \begin{aligned} E_\phi^w &= 0 \\ E_z^w &= 0 \end{aligned} \right\} \text{at } r = r_1 \quad (7)$$

The unknown expansion coefficients of the scattered and internal electromagnetic fields can be determined in Ref. [14]. As far as the scattered fields are concerned, it is sufficient to solve for the expansion coefficients $\alpha_m(\zeta)$ and $\beta_m(\zeta)$, and, by substituting them into Eqs. (3), (4), the solution of the scattering of a shaped beam by an arbitrarily oriented conducting infinite cylinder with dielectric coating can be obtained.

Usually, one is interested in the behavior of the scattered wave at relatively large distances from the scatterer (far field), which can be deduced by taking the asymptotic forms of \mathbf{E}^s , as $kr \sin \zeta \rightarrow \infty$. In $\mathbf{m}_{m\lambda}^{(3)} \exp(ihz)$ and $\mathbf{n}_{m\lambda}^{(3)} \exp(ihz)$, as $kr \sin \zeta \rightarrow \infty$, there can be neglected terms of order higher than $1/\sqrt{r}$, then, from Eqs. (3), (4) the asymptotic forms of the scattered electric

field \mathbf{E}^s are expressed as

$$\mathbf{E}^s = E_0 \exp(-i\pi/4) \sum_{m=-\infty}^{\infty} (-i)^m \exp(im\phi) [a_m \hat{e}_\phi + b_m \hat{e}_r + c_m \hat{e}_z] \quad (8)$$

$$a_m = -(-i)^m \sqrt{\frac{2}{\pi kr}} \int_0^\pi \alpha'_m(\zeta) \frac{1}{\sqrt{\sin \zeta}} \exp[ik(r \sin \zeta + z \cos \zeta)] d\zeta \quad (9)$$

$$b_m = -(-i)^{m+1} \sqrt{\frac{2}{\pi kr}} \int_0^\pi \beta'_m(\zeta) \frac{\cos \zeta}{\sqrt{\sin \zeta}} \exp[ik(r \sin \zeta + z \cos \zeta)] d\zeta \quad (10)$$

where, to follow Eqs. (3),(4), we have introduced the following relations

$$\alpha_m(\zeta) = (-1)^{m-1} \frac{i^{m+1}}{k \sin^2 \zeta} \alpha'_m(\zeta) \quad \beta_m(\zeta) = (-1)^{m-1} \frac{i^{m+1}}{k \sin^2 \zeta} \beta'_m(\zeta)$$

According to Maxwell Equations, we can obtain the H^s fields.

$$\begin{aligned} B_r &= \frac{i}{\omega} E_0 \exp(-i\pi/4) \sum_{m=-\infty}^{\infty} (-i)^m \exp(im\phi) [imc_m - b'_m] \\ B_\phi &= -\frac{i}{\omega} E_0 \exp(-i\pi/4) \sum_{m=-\infty}^{\infty} (-i)^m \exp(im\phi) [c'_m - a'_m] \\ B_z &= -\frac{i}{\omega} E_0 \exp(-i\pi/4) \sum_{m=-\infty}^{\infty} (-i)^m \exp(im\phi) [b''_m - ima_m] \end{aligned} \quad (11)$$

where

$$\begin{aligned} a'_m &= -(-i)^m \sqrt{\frac{2}{\pi kr}} \int_0^\pi \alpha'_m(\zeta) \frac{ik \cos \zeta}{\sqrt{\sin \zeta}} \exp[ik(r \sin \zeta + z \cos \zeta)] d\zeta \\ b'_m &= -(-i)^{m+1} \sqrt{\frac{2}{\pi kr}} \int_0^\pi \beta'_m(\zeta) \frac{ik \cos^2 \zeta}{\sqrt{\sin \zeta}} \exp[ik(r \sin \zeta + z \cos \zeta)] d\zeta \\ b''_m &= -(-i)^{m+1} \sqrt{\frac{2}{\pi kr}} \int_0^\pi \beta'_m(\zeta) ik \sqrt{\sin \zeta} \exp[ik(r \sin \zeta + z \cos \zeta)] d\zeta \\ c'_m &= (-i)^{m+1} \sqrt{\frac{2}{\pi kr}} \int_0^\pi \beta'_m(\zeta) ik \sin \zeta \sqrt{\sin \zeta} \exp[ik(r \sin \zeta + z \cos \zeta)] d\zeta \end{aligned}$$

3. LORENTZ TRANSFORMATIONS AND THE RELATION OF WAVE VECTOR

In order to study the scattered field and differential scattered section of the conducting infinite cylinder with dielectric coating and moving with a high speed, we need to establish a theoretical basis of the coordinates and vectors transformations, which can be used to derive the relation between electromagnetic fields in the moving coordinate system and those in the static Σ' one (in Fig1). The coordinate system Σ' moves along the z axis of another one Σ , and \vec{v} is a constant vector by neglecting its fluctuation ($\vec{v}'_f = 0$). The relations of the four-dimensional wave vectors are obtained as:

$$k'_x = k_x, \quad k'_y = k_y, \quad k'_z = \gamma \left(k_z - \frac{v}{c^2} \omega \right), \quad \omega' = \gamma (\omega - v k_z) \quad (12)$$

The electromagnetic fields make up two-step tensors in the four-dimensional space. Then the scattering field in the system Σ and it in the system Σ' are related by

$$\begin{aligned} E'_x &= \gamma (E_x - v B_y), \quad E'_y = \gamma (E_y + v B_x), \quad E'_z = E_z, \\ B'_x &= \gamma \left(B_x + \frac{v}{c^2} E_y \right), \quad B'_y = \gamma \left(B_y - \frac{v}{c^2} E_x \right), \quad B'_z = B_z \end{aligned} \quad (13)$$

4. THE ANALYTICAL SCATTERING FIELDS SOLUTIONS OF SHAPED BEAM BY A HIGH-SPEED MOVING CONDUCTING INFINITE CYLINDER

For the relatively large distances, E and H fields will be given from the (3)–(4), (8) and (13) equations, the scattering fields of the moving conducting infinite cylinder with dielectric coating can be given as follow

$$E'_x^s = \gamma \left\{ E_0 \exp(-i\pi/4) \sum_{m=-\infty}^{\infty} (-i)^m \exp(im\phi) \left\{ \begin{aligned} & \cos \phi [a_m^2 + b_m^2]^{1/2} \\ & -v \sin \phi [(imc_m - b'_m)^2 + (c'_m - a'_m)^2]^{1/2} \end{aligned} \right\} \right\} \quad (14)$$

$$E'_y = \gamma \left\{ E_0 \exp(-i\pi/4) \sum_{m=-\infty}^{\infty} (-i)^m \exp(im\phi) \left\{ \begin{aligned} & \sin \phi [a_m^2 + b_m^2]^{1/2} \\ & -v \cos \phi [(imc_m - b'_m)^2 + (c'_m - a'_m)^2]^{1/2} \end{aligned} \right\} \right\} \quad (15)$$

$$E'_z^s = E_0 \exp(-i\pi/4) \sum_{m=-\infty}^{\infty} (-i)^m c_m \exp(im\phi) \quad (16)$$

To follow Eqs. (3),(4), we have introduced the following relations

$$\alpha_m(\zeta) = (-1)^{m-1} \frac{i^{m+1}}{k \sin^2 \zeta} \alpha'_m(\zeta), \quad \beta_m(\zeta) = (-1)^{m-1} \frac{i^{m+1}}{k \sin^2 \zeta} \beta'_m(\zeta) \quad (17)$$

In the same way, we can get the H' fields from the (8), (11) and (13) Equations.

5. CONCLUSION

Based on before our works, combined the coordinate transformations and the relation of wave vector and Electromagnetic fields and based on the generalized Lorenz-Mie theory (GLMT) we utilize the general framework and expansion of the incident shaped beam in terms of cylindrical vector wave functions in static coordinate system, in the same time, an analytic solution to the electromagnetic scattering by coated moving infinite cylinders with high speed is constructed. As an example, for a tightly focused Gaussian beam propagating perpendicular to the cylinder axis, the scattering characteristics that obviously demonstrate the three-dimensional nature are described in detail.

ACKNOWLEDGMENT

This works is partly supported by the National Natural Science Foundation of China (Grant No. 60801047, 60971079), China Postdoctoral Science Foundation funded project (Grant No. 20090461308), the Natural Science Foundation of Shaanxi Province (2010JQ8016)and the Natural Science Foundation of Shaanxi Province education office, China (Grant No. 2010Jk897).

REFERENCES

1. Kong, J. A., *Electromagnetic Wave Theory*, Wiley-Interscience, New York, 1986.
2. Jackson, J. D., *Classical Electrodynamics*, 3rd Edition, John Wiley & Sons, New York, 1998.
3. Jean, G. V., *Electromagnetic Fields*, 2nd Edition, John Wiley & Sons, New Jersey, 2007.
4. Wang, Y. P., *Fundamentals of Electrodynamics Field and Wave*, Xidian University Press, Xi'an, 2007.
5. Dudley, D. G., *Electromagnetic Fields*, John Wiley & Sons, New Jersey, 2007.
6. Van Bladel, J., *Relativity and Engineering*, Springer-Verlag, Berlin, 1984.
7. Bohren, C. F. and D. R. Huffman, *Absorption and Scattering of Light by Small Particles*, John Wiley & Sons, Inc., New York, 1983.
8. Wu, Z. S., L. X. Guo, K. F. Ren, G. Gouesbet, et al., "Improved algorithm for electromagnetic scattering of plane waves and shaped beams by multilayered spheres," *Appl. Opt.*, Vol. 36, 5188–5198, 1997.

9. Gouesbet, G., B. Maheu, and G. Gréhan, “Light scattering from a sphere arbitrarily located in a Gaussian beam, using a Bromwich formulation,” *J. Opt. Soc. Am. A*, Vol. 5, 1427–1443, 1988.
10. Zhang, H. Y. and Y. P. Han, “Scattering of shaped beam by an infinite cylinder of arbitrary orientation,” *Journal of the Optical Society of America B*, Vol. 25, 131–135, 2008.
11. Huang, Y. X., “Wave four-vectors for the electromagnetic waves in relatively moving dielectric media,” *J. Mod. Opt.*, Vol. 44, No. 3, 623–631, 1997.
12. Wang, M., Z. Wu, and Y. Li, “Influence of high-speed dielectric spherical particles movement on its scattering characteristics,” *Chinese Optics Letters*, Vol. 5, No. 4, 245–248, 2007.
13. Wang, M., H. Zhang, Y. Han, and Y. Li, “Scattering of shaped beam by a conducting infinite cylinder with dielectric coating,” *Applied Physics B-Lasers and Optics*, Vol. 96, No. 1, 105–109, 2009.
14. Zhang, H. Y., Y. P. Han, and G. X. Han, “Expansion of the electromagnetic fields of a shaped beam in terms of cylindrical vector wave functions,” *Journal of the Optical Society of America B*, Vol. 24, 1383–1391, 2007.
15. Gouesbet, G., G. Gréhan, and B. Maheu, “Computations of the g_n coefficients in the generalized Lorenz-Mie theory using three different methods,” *Applied Optics*, Vol. 27, 4874–4883, 1988.
16. Doicu, A. and T. Wriedt, “Computation of the beam-shape coefficients in the generalized Lorenz-Mie theory by using the translational addition theorem for spherical vector wave functions,” *Applied Optics*, Vol. 36, 2971–2978, 1997.

Error of Moisture Retrieving from the SMOS Radiobrightness with the Use of the Temperature Dependable Soil Dielectric Model

V. L. Mironov¹, L. G. Kosolapova¹, and F. Demontoux²

¹Kirensky Institute of Physics, SB, RAS, Russia

²IMS Laboratory, Bordeaux 1 University, France

Abstract— The error induced by the temperature dependable dielectric model used to retrieve the soil moisture from the SMOS radiobrightnesses is statistically evaluated, based on the measured dielectric data. The dielectrical model is tested in conjunction with the dielectric data base covering all soil types and moisture variations in the temperature range from 10 to 40°C.

1. INTRODUCTION

In connection with the European Space Agency's (ESA) Soil Moisture and Ocean Salinity (SMOS) mission [1], the evaluation of the error of soil moisture retrieved by the 1.4 GHz radiometer has emerged as an especially important issue. To retrieve the moisture from the radiobrightness measured, a specific dielectric model must be applied, which links the radiobrightness to the wave frequency, moisture, temperature, and soil type. We have previously shown [2], that the error of moisture retrieved from the SMOS observation depends to a large extend on the specific dielectric model of moist soil used to resolve the respective inverse problem. This research concerned only the dielectric models that are valid in the narrow range of temperatures from 20 to 22°C. At the same time the real temperature of thawed topsoil may fluctuate in a much wider range. Recently, a temperature and mineralogy dependable soil dielectric model (TMD SDM) was developed [3] to take into account the fluctuations of temperature in the range from 10 to 40°C. Based on this model, we have analyzed the error of moisture retrieved from the SMOS observation, covering the larger range of soil temperatures.

1.1. Confidence Intervals Confining Soil Moisture Retrieved

In this paper a statistical analysis similar to that of [2] to estimate the moisture error induced by imperfection of the model proposed in [3] was carried out. The 95% confidence intervals were obtained, in which a true moisture is confined, relative to the value retrieved with the use of the temperature dependable dielectric model [3]. In this case a data set for complex dielectric constant measured in the range of temperatures 10 to 40°C was formed on the basis of those published in [4, 5]. With this database available, the emission coefficients were calculated, using both the predicted and measured values of complex dielectric constant.

The radiobrightness, T_b , is proportional to the emission coefficient, χ , that is, $T_b(\theta) = \chi(\theta)T$, where θ and T are the viewing angle and thermodynamic temperature, respectively. According to [6], the emission coefficient can be modeled using the very simple approach:

$$\chi(\theta) = 1 - r(\theta), \quad (1)$$

with $r(\theta)$ being the reflectivity of the soil surface. The latter is determined through the Fresnel reflection coefficient $R(\theta)$ and roughness parameter H_r as follows:

$$r_q(\theta) = |R_q(\theta)|^2 \exp(-H_r). \quad (2)$$

Here the subscript q stands to denote either horizontal $q = h$ or vertical polarization of the emitted wave.

The reflection coefficients for vertical, R_v , and horizontal, R_h , polarizations are equal to

$$R_v = \frac{\varepsilon \cos \theta - \sqrt{\varepsilon - \sin^2 \theta}}{\varepsilon \cos \theta + \sqrt{\varepsilon - \sin^2 \theta}}, \quad R_h = \frac{\cos \theta - \sqrt{\varepsilon - \sin^2 \theta}}{\cos \theta + \sqrt{\varepsilon - \sin^2 \theta}}, \quad (3)$$

where $\varepsilon = \varepsilon' + i\varepsilon''$ is the complex dielectric constant (CDC) of moist soil, ε' and ε'' are the dielectric constant and loss factor, respectively. Let us carry out analysis when the viewing angle is equal to zero. In this case, the Fresnel coefficient does not depend on the polarization:

$$R_h = R_v = \frac{\sqrt{\varepsilon} - 1}{\sqrt{\varepsilon} + 1}. \quad (4)$$

The relationship between the complex index of refraction, $\sqrt{\epsilon}$, and the values of index of refraction, n , and normalized attenuation coefficient, κ , is determined by the following formula:

$$\sqrt{\epsilon} = n + i\kappa. \quad (5)$$

Further we will analyze the error of moisture retrieved which is induced only by imperfection of the dielectric model, assuming for simplicity no roughness present on the soil surface ($H_r = 0$). As a result, according to formulas (1), (2), and (4), the emission coefficient can be expressed through the index of refraction and normalized attenuation coefficient in the form:

$$\chi = \frac{4n}{(n+1)^2 + \kappa^2}. \quad (6)$$

With the use of formula (5), two values of emission coefficient, that is, χ_{meas} and χ_{pred} were calculated using for the refractive index and normalized attenuation coefficient the data measured in [4, 5], on the one hand, and the ones calculated with the use of the temperature and mineralogy dependable soil dielectric model (TMD SDM) given in [3], on the other hand. The deviation of calculated emission coefficients from those measured were employed as a basis to estimate the error in the emission coefficient model caused due to imperfection of the moist soil dielectric model. This analysis was performed for the ensemble of soils with clay content varying from 0 to 76%, and in the range of temperatures from 10 to 40°C.

A relative deviation (δ) of the emission coefficient calculated with the TMD SDM, χ_{pred} , from the one calculated using the measured dielectric data, χ_{meas} , is defined as

$$\delta = \frac{\chi_{\text{meas}} - \chi_{\text{pred}}}{\chi_{\text{pred}}}. \quad (7)$$

Further analysis was made with the use of software OriginPro 7.5. The mean of error ($\bar{\delta}$) was obtained by δ by adjacent smoothing over 30 points. The dispersion of error, d , was found as $d = (\delta - \bar{\delta})^2$. The mean of dispersion (\bar{d}) was obtained by adjacent smoothing over 30 points. The standard deviation, σ was calculated as $\sqrt{\bar{d}}$. The down and upper confidence intervals for emission coefficient were defined as $\chi_{\text{pred}}(1 + \bar{\delta} - 2\sigma)$ and $\chi_{\text{pred}}(1 + \bar{\delta} + 2\sigma)$, respectively. In Fig. 1 the emission coefficients calculated with the measured CDCs are given as a function of that calculated with the TDM SDM alongside with the confidence intervals and 1 : 1 line (Fig. 1).

The moisture retrieving error was estimated as a relative deviation of the predicted soil moisture from the upper and lower boundaries of the 95% confidence intervals. Using the result shown in Fig. 1 and the gage curve corresponding to the TDM SDM for every type of soil at a fixed temperature (see Fig. 2), we estimated the error of the moisture retrieved in terms of 95% confidence interval moisture, between which a true moisture is confined. As an example, the results of that estimation are shown in Figs. 3(a), (b) concerning the two types of soils analyzed in [4].

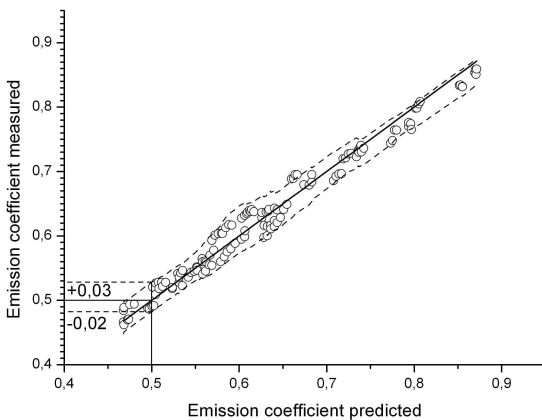


Figure 1: The confidence intervals for the emission coefficient measured as a function of the emission coefficient predicted. The solid line is the bisector, the dash lines are the upper and lower confidence intervals. The circles are the emission coefficient measured.

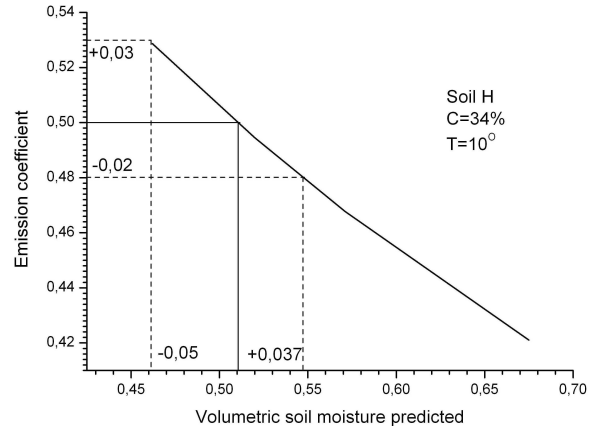


Figure 2: A gage curve linking the emission coefficient to the soil moisture. The temperature dependable soil dielectric model for the soil with 34% clay contents was used to compute this example of a gage curve.

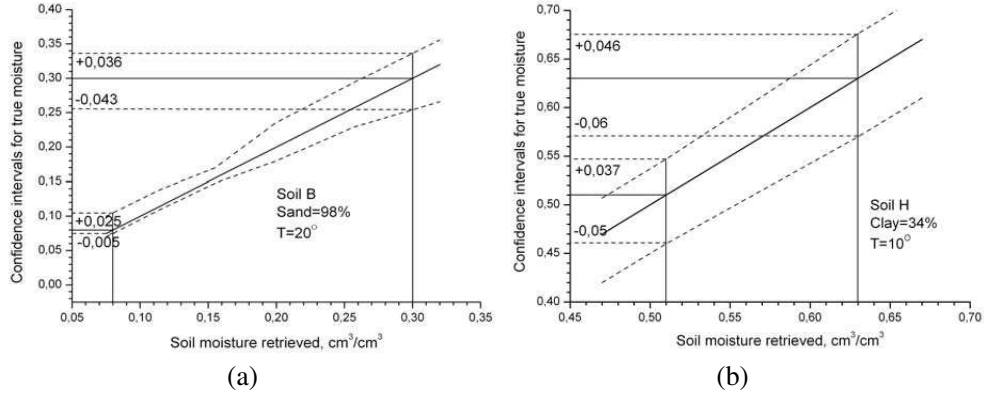


Figure 3: 95% confidence intervals (upper, +, and lower, −) for a true moisture as a function of moisture retrieved from radiobrightness observations corresponding to the SMOS mission: (a) for the sand at 20° and (b) for the soil with 34% clay content at 10°C.

2. CONCLUSIONS

The error thus obtained was shown to reach the value of $\pm 0.06 \text{ cm}^3/\text{cm}^3$ while the soil moisture precision target for the SMOS mission is equal to $\pm 0.04 \text{ cm}^3/\text{cm}^3$. Thus, the need to improve the dielectric model of moist soil, taking into account the temperature dependence, is still an actual problem for running the SMOS project. Further, we plan to develop a specific dielectric model of moist soil at 1.4 GHz which is applicable to meet the SMOS project requirements in terms of moisture retrieving error.

ACKNOWLEDGMENT

This research was supported by the Siberian Branch of the Russian Academy of Sciences under Project II.10.1.6 and by the Russian Foundation for Basic Research and Centre National de la Recherche Scientifique (France) under Grant 09-05-91061.

REFERENCES

1. Kerr, Y. H., P. Waldteufel, J.-P. Wigneron, J.-M. Martinuzzi, J. Font, and M. Berger, "Soil moisture retrieval from space: The soil moisture and ocean salinity (SMOS) mission," *IEEE IEEE Trans. Geosci. Remote Sensing*, Vol. 39, No. 8, 1729–1735, Aug. 2001.
2. Mironov, V. L., Y. Kerr, J.-P. Wigneron, L. G. Kosolapova, F. Demontoux, and C. Duffour, "Statistical error for the moisture retrieved with the SMOS radiobrightness data, as induced by imperfection of a dielectric model used," *IEEE Proceedings IGARSS*, 4430–4432, 2010.
3. Mironov, V. L. and S. V. Fomin, "Temperature and mineralogy dependable model for microwave dielectric spectra of moist soils," *PIERS Proceedings*, 938–942, Moscow, Russia, Aug. 18–21, 2009.
4. Curtis, J. O., C. A. Weiss, Jr., and J. B. Everett, "Effect of soil composition on dielectric properties," *Technical Report EL-95-34*, Dec. 1995.
5. Demontoux, F., B. Le Crom, G. Ruffi, J. P. Wigneron, J. P. Grant, and V. L. Mironov, "Electromagnetic characterization of soil-litter media — Application to the simulation of the microwave emissivity of the ground surface in forests," *European Physical Journal — Applied Physics*, Vol. 44, No. 3, 303–315, 2008.
6. Wigneron, J. P., et al., "Evaluating an improved parameterization of the soil emission in L-MEB," *IEEE Trans. Geosci. Remote Sensing*, Vol. 49, No. 4, 1177–1187, Apr. 2011.

Topographic Normalization of Landsat TM Images in Rugged Terrain Based on the High-resolution DEM Derived from ASTER

Yanli Zhang^{1, 2} and Xin Li¹

¹Cold and Arid Regions Environmental and Engineering Research Institute
Chinese Academy of Sciences, Lanzhou 730000, China

²College of Geography and Environment Science
Northwest Normal University, Lanzhou 730070, China

Abstract— A method for topographic correction for TM remote sensing image is presented in rugged terrain, with the help of high-resolution stereo image pairs provided by modern satellite sensors. Topographic effects and atmospheric factors interacted, and severely distorted the true information of surface nature characters. Some popular terrain correction models nowadays, such as the cosine model, Minnaert model, C model, SCS model and so on, are not a quantitative method. The mountain radiant transfer model with more strict physical meaning must be selected to remove terrain effects in mountainous quantitative remote application. However, because of its stringent requirements for digital elevation model DEM in the high precision and high resolution, it limited its development and wider application. Based on ASTER remote sensing stereo image pairs constituted by nadir images and backsight images, relatively high accuracy 15 m DEM data was obtained in the study area. Finally putting micro topographic factors and the main atmospheric parameters into Richter mountains radiation model, TM remote sensing image terrain correction was rapidly completed. The results show that this method has a remarkable ability to remove topographic and atmospheric effects, and also provides reliable basis data for surface parameters retrieval of quantitative remote sensing in the rugged terrain.

1. INTRODUCTION

In the rugged mountainous terrain, topographic effects distort severely the spectrum features of land surface. Slopes facing toward the sun receive more radiation and appear brighter than slopes facing away from the sun. Not only is illumination modified by topography, but the proportion of light reflected toward the satellite also varies with the geometry of sun, target and viewer [1, 8–10]. There are many of topographic effects that can cause topographic variation in the mountain area, including terrain shadow, slope effect, aspect effect, surrounding-reflected irradiance, and displacement of image points for high resolution image. Therefore, the process of topographic normalization may be critical in areas of rugged terrain, and is a preliminary step for the quantitative evaluation of the multispectral satellite imagery.

Till now, a variety of topographic correction models have been proposed. Methods for correcting the topographic effect may be grouped into two categories: 1) Empirical correction methods models which mainly correct the solar direct radiance affected by topography, such as solar direct radiance affected by topography, such as ratio model, cosine model, Minnaert model, sun-canopy-sensor (SCS) model, and C models. 2) Radiative transfer models for mountainous area, which employ a radiative transfer code to obtain a deterministic description of the correction of topographic effects. The advantage of the second method is that scene-dependent empirical parameters are avoided [8]. Introducing some terrain factors slope and azimuth, illumination angle, horizon, and view factors for radiation from sky and terrain with the help of the digital elevation model (DEM), investigators have done a lot of work [2–5, 7, 9].

In the quantitative application the second approach are the preferred to removing terrain effects. However, topographic correction are neglected in most practical TM image applications because the mountain radiative transfer models are complex and DEM data of the high precision and high resolution is difficult to obtain.

In this paper, a method for topographic correction of TM image in rugged terrain is presented. High accuracy DEM data was obtained based on ASTER remote sensing stereo image pairs constituted by nadir images and backsight images. Richter mountains radiation model ATCOR3 [9] is applied for its simplicity and maneuverability to accomplish three radiometric calibration steps.

2. DATA AND METHODS

2.1. Study Area

The selected study area is located in Dayekou watershed (DYK) in the upper stream of the Heihe river basin, Qilian mountains, China. It is hilly terrain, which has slope ranging from 0° to 88° with an average of 35° . There are four main land cover types in this area: forest, grass, water and bare surface. The Picea crassifolia is mainly located in the north-dominated-facing slope surface. The grass is in the flat and south-slope surface. The altitude ranges from 2360 to 3840 m above sea level. The mean annual air temperature is 0.7 Degrees Celsius and the mean annual precipitation is about 435.5 mm. Good measuring facilities such as permanent sampling plots for forest monitoring were available in this watershed [6], and two auto-meteorology observation were installed here.

2.2. Data

The data set for this study consists of ASTER images for extract DEM and a Landsat TM image acquired on 11 August 2009 with solar zenith of 31.82° and solar azimuth of 131.26° . Landsat TM image was obtained from the United States Geological Survey (USGS) Earth Resources Observation System (EROS) Data Center. And the ASTER image was provided by Environmental and Ecological Science Data Center for West China. These data is geocoded on a Universal Transverse Mercator (UTM) projection.

2.3. Extracting DEM Based on the ASTER Stereo Image Pairs

ASTER (Advanced Spaceborne Thermal Emission and Reflection Radiometer) is an imaging instrument flying on Terra, a satellite launched in December 1999 as part of NASA's Earth Observing System (EOS). Its visible near-infrared (VNIR) subsystem consists of two independent telescopes, a backward and a nadir looking one, with 15m ground resolution. For DEM extraction only the VNIR nadir and backward images (3N and 3B) are used.

The DEM extraction process requires a stereo pair of images containing rational polynomial coefficients (RPC) positioning from aerial photography or pushbroom sensors. RPCs are used to generate tie points and to calculate the stereo image pair relationship. There are three steps in creating a DEM that are crucial to generating acceptable results: epipolar image creation, image matching, and DEM geocoding. Before proceeding determine their accuracy and examine the likely error rankings of all the tie points. Ideally, the y parallax value should be as close to zero as possible. After creating the left and right epipolar images, the true stereo 3D epipoar image can be obtained, and you can view the result in 3D macyscope glasses. At last, setting the projection system, defining the pixel size, DEM will be created.

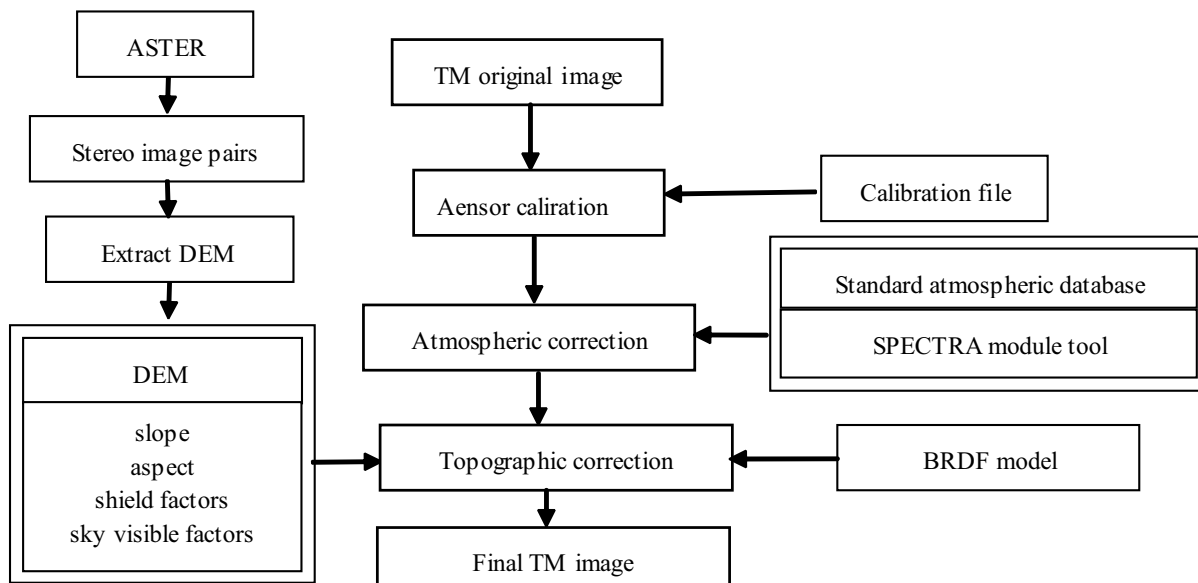


Figure 1: Block diagram of main processing steps of the topographic correction.

2.4. Topographic Correction Models

In rugged areas, the satellite obtained radiance was distorted by both of atmospheric and terrain effects. Atcor3 is an outstanding model to remove simultaneously two effects for high spatial resolution satellite sensors with a small swath angle such as LANDSAT TM. The atmospheric correction functions are supported by MODTRAN 4, and topographic algorithm is developed by [8].

The detailed description of the total irradiance on the slope land surface on each image pixel can be found in [9]. Most radiation calculations are made with the aid of DEM [2], which account some terrain parameters such as slope, illumination angle. The DEM was first created at 15 m resolution, and then was resampled to a 30 m grid to match the TM image using cubic convolution.

Figure 1 shows a block diagram of the main processing steps performed in this paper.

3. CASE STUDY

3.1. Generate DEM from ASTER

150 tie points (TPs) were collected between the stereo-pair. Through deleting all gross error points, about 120 tie points were left, and the total RMS of the TPs was 1.02 pixels. Then some important terrain factors were calculated such as slope, aspect, skyview and shadow according to DEM (Fig. 2).

3.2. Atmospheric and Topographic Correction

Before running the terrain correct program, atmospheric influence and haze must be removed. Fig. 3 shows the results, and it shows that no cloud pixel was detected, 10 percent of image land pixels are clear and 90.0 percent of image land pixels are hazy land.

Here, it is believed that the steep surface shows distinctly anisotropic reflectance properties where slope is greater than 60°. We could get BRDF spatial distribution and topographic correction result (Fig. 3). The correct report indicated that about 40 percent image area was affected by BRDF.

4. PRIMARY RESULTS

We see from Fig. 3 that the topographic variability has been removed and given a more ‘flat’ impression than the non-corrected image. To evaluate the correction, we randomly collected the reflectance of a *Picea crassifolia* sample from corrected and uncorrected images from shady slope (Fig. 4), and collected the reflectance of a grass sample from corrected and uncorrected images sun-facing (Fig. 5). These results suggest that in the uncorrected image the apparent reflectance of forest on the shady slope is very low.

However, this operation did not completely remove illumination and shadowing effects. For example, northerly slopes were still relatively darker than southerly slopes, even a very strange

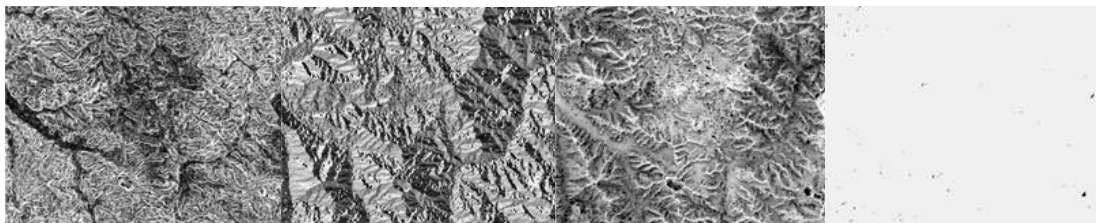


Figure 2: Derived terrain files slope, aspect, skyview and shadow (from left to right).



Figure 3: Original TM image, atmospheric correction image, BRDF correct factor and topographic correction image (from left to right).

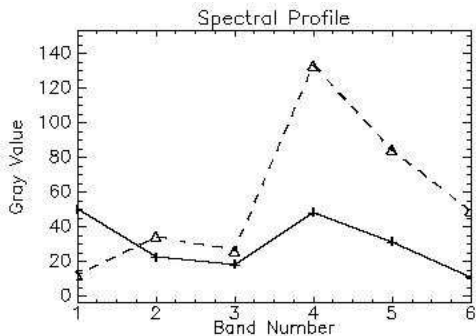


Figure 4: *Picea crassifolia* spectrum located in the north-facing slopes of 56° : dashed curve, atmospheric and topographic correction, solid curve, original image.

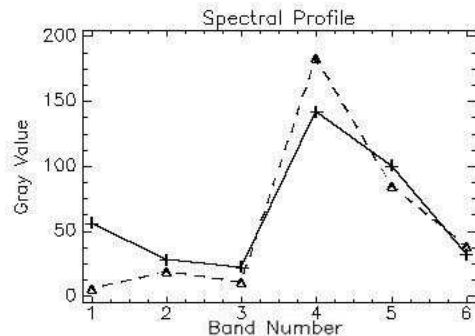


Figure 5: Grass spectrum located in the south-facing slopes of 10° : dashed curve, atmospheric and topographic correction, solid curve, original image.

phenomenon is occurred that the reflectance of *Picea crassifolia* shaded less than the south-slope grass.

5. SUMMARY AND CONCLUSIONS

The reason for the non-perfect correction lies probably in some reasons. First, the DEM generated from the satellite images may have small errors because of lacking ground control points. Second, some of the areas lie in so deep a shadow and thus have very dark pixel values, which lead to no reliable estimations can be obtained. Third, the experiential BRDF model selected may be too simple, and it can not represent anisotropic reflectance properties in study areas. Last but not least, in this study the multiple scattering phenomena were not taken into account within the pixel because of the complex terrain.

ACKNOWLEDGMENT

This work is supported by the National Science Fund for Distinguished Young Scientists — “Development of a Catchment-Scale Land Data Assimilation System” (grant number: 40925004) and the project “Land Surface Modelling and Data Assimilation Research” (grant number: 2009AA122104) from the National High Technology Research and Development Program (863) of China. The ASTER data used in the paper are provided by Prof. Shunlin Liang.

REFERENCES

- Colby, J. D., “Topographic normalization in rugged terrain,” *Photogrammetric Engineering and Remote Sensing*, Vol. 57, No. 5, 531–537, 1991.
- Dozier, J. and J. Frew, “Rapid calculation of terrain parameters for radiation modeling from digital elevation data,” *IEEE Transactions on Geoscience and Remote Sensing*, Vol. 28, No. 5, 963–969, 1990.
- Hay, J. E. and D. C. McKay, “Estimating solar irradiance on inclined surfaces: A review and assessment of methodologies,” *International Journal of Solar Energy*, Vol. 3, 203–240, 1985.
- Li, X., G. D. Cheng, X. Z. Chen, and L. Lu, “Modification of solar radiation model over rugged terrain,” *Chinese Science Bulletin*, Vol. 44, No. 15, 1345–1350, 1999.
- Li, X., T. Koike, and G. D. Cheng, “Retrieval of snow reflectance from Landsat data in rugged terrain,” *Annals of Glaciology*, Vol. 34, 31–37, 2002.
- Li, X., X. W. Li, Z. Y. Li, M. G. Ma, J. Wang, Q. Xiao, Q. Liu, T. Che, E. X. Chen, G. J. Yan, Z. Y. Hu, L. X. Zhang, R. Z. Chu, P. X. Su, Q. H. Liu, S. M. Liu, J. D. Wang, Z. Niu, Y. Chen, R. Jin, W. Z. Wang, Y. H. Ran, X. Z. Xin, and H. Z. Ren, “Watershed allied telemetry experimental research,” *Journal of Geophysical Research*, 114 (D22103), 2009, doi:10.1029/2008JD011590.
- Proy, C., D. Tanre, and P. Y. Deschamps, “Evaluation of topographic effects in remotely sensed data,” *Remote Sensing of Environment*, Vol. 30, 21–32, 1989.
- Richter, R., “Correction of atmospheric and topographic effects for high spatial resolution satellite imagery,” *International Journal of Remote Sensing*, Vol. 18, No. 5, 1099–1111, 1997.

9. Richter, R., "Correction of satellite imagery over mountainous terrain," *Applied Optics*, Vol. 37, No. 18, 4004–4015, 1998.
10. Wen, J. G., Q. H. Liu, Q. Xiao, Q. Liu, and X. W. Li, "Modeling the land surface reflectance for optical remote sensing data in rugged terrain," *Science in China Series D-earth Sciences*, Vol. 51, No. 8, 1169–1178, 2008, 10.1007/s11430-008-0085-5.

Monitoring Aurora in Day Light Side of the Earth in Relation to Solar Plasma Flow

Shigeisa Nakamura
Kyoto University, Japan

Abstract— This is a note to aurora in day light side of the earth in relation to the solar plasma flow. The solar plasma flow in a super high speed forces to form a shock front just in front of the magnetopause between the sun and the earth. The intrusion of the electron into the aurora oval zone along the magnetic line releases its energy to form a visible aurora. It is up-dated what process is reasonable to see the coloring of the interested aurora. An additional notice is given to see a non-natural energy release for a dark red sky in the subtropical zone on the ocean. Spacecraft monitoring of the planets in the solar system is also introduced in short.

1. INTRODUCTION

This work concerns the aurora which can be seen in the polar area around the north pole of the earth. It is said that some note was left about a red aurora boreales in one of the old records, for example, Nihon-Shoki, edited in 720AD (as noticed Sadami Matsushita). Birkeland must be the first aurora scientist who published the Norwegian Aurora Polaris Expedition (1902–1903) in 1903 as a part of the International Polar Year (IPY-1, 1882–1883). After IPY-2 (1932–1933), Chapman [1] published “Geomagnetism” in which the contribution of the geomagnetic daily variation Sq in a solar quiet day. In Kyoto University, Motokazu Hirono had given his theoretical model of geomagnetism with the poloidal and toroidal modes in 1957 for the advanced course of geophysics. Takeshi Nagata promoted the IGY (1957–1958) in the Asian area. In the first Antarctic Research Project in Japan, the leader on-site at the base settled on Antarctic was Eizaburo Nishibori, and Tai’iti Kitamura was the first Japanese scientist of aurora Australius. There have been many researches on ionosphere and on aurora as well as on geophysics.

There are many problems on geomagnetism in relation to ionosphere and aurora.

In this work, the author concentrates his interest on the problems on monitoring aurora in day light side of the earth in relation to the solar plasma flow. This solar plasma flow was ever named as solar wind.

Specific feature of the aurora found in day light side of the earth is noticed in contrast to the aurora found in dark night side of the earth.

The author notes briefly about a non-natural dark red sky found not in or inside of the aurora oval but in the subtropical zone on the ocean. The author wishes to have a more advanced contribution for realizing the aurora in the next following age.

2. SOLAR PLASMA FLOW

The solar plasma now is propagates as a reflection of the solar activity. The author has his understanding that the solar activity is evaluated after monitoring the variations of the surface of the sun facing the earth. The details of the mechanism of the solar activity are not yet clear even in a scope of science though the eleven years solar cycle is strongly effective to the earth surface variations.

It has been aware the effect of the solar activity or of solar wind. Chapman [2] had given us the new term of “solar plasma” instead of the solar wind. The term “solar plasma” is expressing itself the scientific specific pattern of the solar wind in relation to geomagnetism and aurora.

3. AURORA IN DAY LIGHT SIDE

In this work, a note is introduced for problems on monitoring aurora in day light side of the earth in relation to the solar plasma flow. The solar plasma flow (the solar wind) distorts the geomagnetic field to form a magnetopause (cf. Figure 1).

By this time the aurora scientists have believed that the solar plasma flow (the energy of the electron — ca 50 eV or 50 electron Volt) at a super high speed so that a shock front is appeared just outside of the magnetosphere. It has been monitored the aurora in the day light side of the earth after the energy of the electron increased between the shock front and the magnetopause (ca 100 eV). This electron is the trigger of the red aurora (630.0 nm). On the basis of the surveys

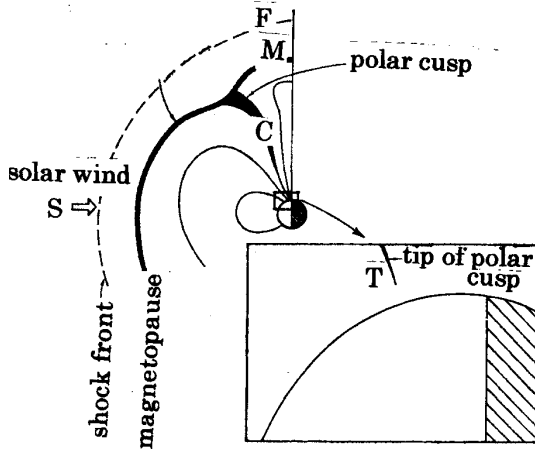


Figure 1: Structure between solar plasma flow and polar tip. (1) Solar plasma now for S . (2) Schock front for F . (3) Magnetopause for M . (4) Polar cusp for M . (5) Tip of polar cusp for T (inset).

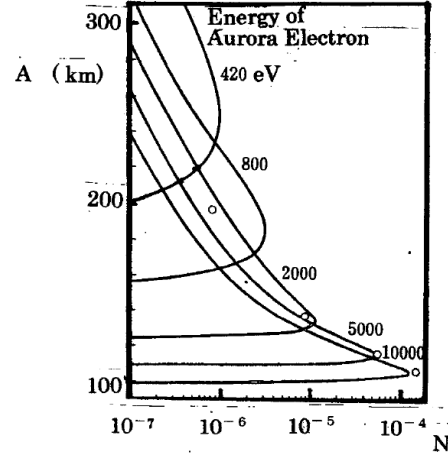


Figure 2: Count number of gas particles ionized by aurora electron. (1) N — for number of ionized gas particle (number per cubic cm-sec). (2) A — for altitude above the earth surface (km). (3) Parameter — for energy of aurora electron (electron Volt = eV).

it is clarifid that the polar cusp is a guide of the intruding electron of the solar plasma along the magnetic line into the upper atmosphere of the earth as shown in Figure 1. This red aurora is induced after energy release of the oxygen at the altitude of 200 km or more above the earth surface at intruding electron (ca 500 km/sec). Now, it should be noticed that the energy release of the electron to activate the oxygen atom is an order of several KeV in the visible aurora curtain (557.7 nm) found in the dark night side of the earth.

4. ALTITUDE OF AURORA

It is said that the altitude of the aurora boreares is depending on the incident electron out of the solar plasma into the polar oval zone as a aurora electron. An empirical result has been introduced as shown in Figure 2 in order to see what is the critical altitude of the aurora electron intrusion in a diagram of the critical altitude H above the earth surface and the counted number N (per cubic-cm second) of the ionized gas particles by the energy of the aurora electron ($1/\text{cm}^2$).

The author has to consider here what process is possible to release the aurora energy for the bright light line in the visible band at applying technique of spectroscopy.

The aurora electron at the critical altitude surely must have exhausted so that no energy can be effective to ionize or activate the gas particles in the atmosphere for making a bright light line of spectroscopy in the visible band.

The aurora scientists seems to consider that the aurora electron affects directly to transfer energy to the atoms and the molecules of oxygen and nitrogen in order make the visible bright light. The author has unfortunately no data for describe the details of the process. The aurora electron should be exhausted at the critical altitude just neighbor the earth surface.

5. AURORA IN VISIBLE BAND

Adding to the above, the bright line band noted the above section seems not to be consistent to what had been observed and recorded in any color print on the hard copy.

As far as the author concern, it should be considered that the aurora electron transferred to the hydrogen molecules for ionization and activation first. When the ionized and activated hydrogen release its energy, the visible light must be seen as the specific bright light line in the spectroscopic analysis. This bright light line has to have the specific one for the related hydrogen. As for the hydrogen, four visible bright light lines are known.

Introducing the bright light line of spectrum for the ionized hydrogen, it is understood to be a more consistent relation between the aurora observed optically and the bright light line of spectrum of the interested hydrogen.

For a convenience, the four bright light lines for the hydrogen is introduced as follow.

Balmer Series	Wave Length (nm)	Color	Band Zoning
	-	Infra-Red Band	(770 nm <)
Hydrogen — $\alpha(1)$	656.285	Red-Band Zone	(770-640 nm)
— $\alpha(2)$	656.273	Red-Band Zone	(770-640 nm)
	-	Orange-Band Zone	(640-590 nm)
	-	Yellow-Band Zone	(590-550 nm)
	-	Green-Band Zone	(550-490 nm)
— $\beta(3)$	486.133	Blue-Band Zone	(490-430 nm)
— $\gamma(4)$	434.047	Blue-Band Zone	(490-430 nm)
	-	Violet-Band Zone	(430-380 nm)
	-	Infra-Violet Band	(380 nm >)

In the case of solar quiet day, the red aurora in the day-light side appears by chance. No detail is known even at present.

In the case of the solar burst, the strong disturbances are found in the aurora pattern, in the ionosphere behaviour, and in the geomagnetic filed, which is called as “storm” [3].

6. MAN-MADE AURORA

The author here introduces one case of the non-natural energy release producing a similar pattern to the red aurora found in or inside of the aurora oval in the subtropical zone of the ocean.

After what is reported by Charles Day [4], his head-line of the report is like that “A high-altitude nuclear explosion would swell the radiation belt and imperil the global positioning system and other satellites. VLF transmission could forestall the damage”.

A happening was as follows. Day introduced that was on July 9, 1962. No solar storm has jolted the earth’s inner radiation belt more than the nuclear test. On that day, the US exploded a 1.4 megaton nuclear warhead 400 km above Johnston Atoll, a remote group of the Pacific Islands. In Hawaii, 1400 km away, it was lit up the sky, knocked out street lights, triggered burglar alarms, and fused power lines (cf. Figure 3). Beta particles from the blast flooded the thin upper reaches of the atmosphere. Trapped by earth’s magnetic field, the high-energy particles swelled the inner radiation belt. Seven satellites were damaged or put out of action. The radiation took more than a decade to dissipate. Alarmed by the unintended consequences, the nuclear powers banned testing in and above the earth’s atmosphere in 1965. Some related notice could be obtained in Geophysical Research Letters (Vol. 35, L09101, 2008) written by J.-A. Sauvauaud, R. Maggiolo, C. Jacquay, M. Parrot, J.-J. Berthelier, R. J. Gamble, and C. J. Roger.

Even this case of the man-made auroras, the process is same in the scope of science.

7. SPACECRAFT MONITORING OF PLANETS IN THE SOLAR SYSTEM

Several extensive works have been presented on the bases of the successful spacecraft monitoring of the planets in the solar system.

For example, Hasegawa et al. [5] noted about transport of solar wind into the earth magnetosphere through rolled-up Kelvin-Helmholtz vortices. Nevertheless, it is necessary to remind that Helmholtz instability was first noted for a two fluid mass of dynamically same property as Lamb [6] introduced in his publication. Any dynamical processes around the Earth’s magnetosphere must be equivalent to consider an interface between the magnetospheres of the earth and sun. In a scope of classical hydrodynamics, the Kelvin-Helmholtz vortices or waves must be accepted when the gas particle density in a unit volume on the solar side of the interface is surely same to that on the earth side of the interface, nevertheless, it seems to be not clear that such the condition was well satisfied around the interface in the work undertaken by Hasegawa et al. [5].

Boardsen et al. [7] has followed what was written by Hasegawa et al. [5] after observations of Mercury’s magnetosphere during MESSENGER’s third flyby. Their illustrations are easy to see what processes were found during the spacecraft monitoring of Mercury. What is noted in the work by Boardsen et al. [7] could be well accepted if what was surely complete in the work by Hasegawa et al. [5], because it looks that Boardsen et al. [7] are simply a group of the dynamics follower.

It should be clearly described for the hydrodynamic scientists as well for the scientists in the field of MagnetoHydroDynamics (MHD, in short). As for the ocean water motion around an ocean front,

several factors can be seen, for example, impact, shearing, turbulence, periodical wave motions, and irregular waves which could be transformed into a spectral pattern. As for winds or air flows in the atmospheric layer, front is formed as an interface to show a contact of the warm and cold air masses. In the ocean or in the atmosphere, observed process of the front is a three-dimensional process. Similarly, the process around the earth's magnetosphere must be three dimensional so that we have to understand that the presented report must be the tiny part of the main field.

The earth's magnetosphere bounded by the solar wind effect in a simple understanding though the main field of the earth's magnetic field must be taken as in the zeroth order. Any time variations must be in the first order or second order, for example. Some other undulations must be in the higher order. The author feels it necessary to have a more advanced observation using by a specific space crafts for the planet magnetic process in the solar system.

Finally, the author notes here his appreciation for the thoughtful assistance personally at completing this work in brief.

REFERENCES

1. Chapman, S. and J. Bartels, *Geomagnetism*, 1049, Clarendon Press, Oxford, 1940.
2. Chapman, S., *Solar Plasma, Geomagnetism and Aurora*, 133, Gordon-Breach, New York, 1964.
3. Attren, H., *Cosmic Electrodynamics*, 237, Clarendon Press, Oxford, 1950.
4. Day, C., "Very low-frequency radio waves drain earth's inner radiation belt of satellite-killing electrons," *Physics Today*, Vol. 61, No. 8, 18–21, 2008.
5. Hasegawa, H., M. Fujimoto, T.-D. Phan, H. Reme, A. Balog, M. W. Dunlop, C. Hashimoto, and R. TanDorko, "Transport of solar wind into earth's magnetosphere through rolled-up kelvin-helmholtz vortices," *Nature*, Vol. 430, 755–758, 2004, doi: 10.1038/nature02799.
6. Lamb, H., *Hydrodynamics*, 6th Edition (1st Edition, 1879), 738, Cambridge at the University Press, 1957.
7. Boardsen et al., "Observations of kelvin-helmholtz waves along the dusk-side boundary of mercury's magnetosphere during Messenger's third flyby," *Geophysical Research Letters*, Vol. 37, L12101 (5 pages), 2010, doi: 10.1029/2010GL043606.

Satellite Monitoring of Subglacial Volcano in Atlantic

Shigehisa Nakamura
Kyoto University, Japan

Abstract— This is a note to the subglacial volcano in the Atlantic. An eruption of a subglacial volcano in Iceland had transferred to the European Union in 2010. This volcano is one of the volcanoes in the Atlantic. The data of EUMETSAT and NASA are used for this work. There are volcanoes in the Atlantic. Some of them are in Azores Islands, in Canary Islands and Cape Verde Islands. Iceland is located in the zone of the mid-Atlantic ocean ridge, and one of the subglacial volcanoes had an event of the ash scattering to hit the land area of the European Union. The volcanic ash pattern is well governed by the winds around the volcano. This event has had a strong impact to the global net-work of the air-line transportation. Now, the author introduces his note about the volcanic islands in the Atlantic, including in Azores Islands, in Canary Islands, and in Cape Verde Islands.

1. INTRODUCTION

The author introduces his note on the subglacial volcano in Iceland. Volcanoes are seen in the Atlantic, for example, in Azores Islands, in Canary Islands and Cape Verde Islands. Some of them are active and the others are now inactive. In order to show some specific patterns of the active volcanoes, it is more convenient to show what patterns can be seen in one of the typical volcanoes. In this case, the author's interest is concentrated to the volcano Eyjafjallajokull in Iceland. This volcano erupted in April 2010 to spread the ash, which is called as phreia in the field of volcanology. This ash had drifted in the surface layer of the atmosphere, and was governed strongly by the winds just around the volcano. This eruption resulted to hit and disturb the normal operation of the air-line transportations into and out of European Union. The other volcanoes in Atlantic are in Azores Islands, in Canary Islands, and Cape Verde Islands.

2. SUBGLACIAL VOLCANO

In the volcanoes in the Atlantic, there are only located several subglacial volcanoes in Iceland. This Iceland is in the mid-Atlantic ocean ridge where the magma produces a new crust for the earth. Then, it may be possible to see the face of the magma by every one's eye-watch on the site of any volcano in Iceland.

On April 14, 2010, one of the volcanoes, named as Eyjafjaoekull, erupted and issued phreia which was called as ash in public. The ash cloud was transferred by the winds to the land area of European Union. So that, the function of air-line transportations was strongly affected by this ash cloud.

It was noticed first, the volcano erupted in Iceland on April 14, 2010. The volcanic ash track can be seen as shown in Figure 1. This illustrating set was issued by the meteorological office, the United Kingdom. This set tells us that the ash cloud is spreading after the effect of the northwest winds from the south of Iceland to the land area of European Union through the North Sea. On the day of April 16, 2010, the ash cloud had get to the coasts of German and of the Netherlands. This motion of the ash cloud was monitored by the satellite EUMETSAT, and issued by the meteorological office, the United Kingdom, and the satellite data of NASA.

After the issue by the NASA (National Agency of Space Aviation), as seen in Figure 2, the ash cloud had a track to cross over the sky of German to Poland. In this illustration, the ash cloud is displayed reddish patch in the natural white clouds.

On May 4, 2010, the author obtained an eye-watch weather chart in a part of Europe. An aircraft helped to have the information for the chart. A bold pattern on the weather chart is shown as in Figure 3.

Judging from these data and information, the winds around the interested volcano surely be governed the volcanic ash spread.

In the age of the sail navigation, no problem must be seen on the land in Europe and in the west coasts of Africa.

At present, the air-line net work has been developed for our needs. The volcanic ash cloud had given a chance to notice what should be considered for any volcanic event.

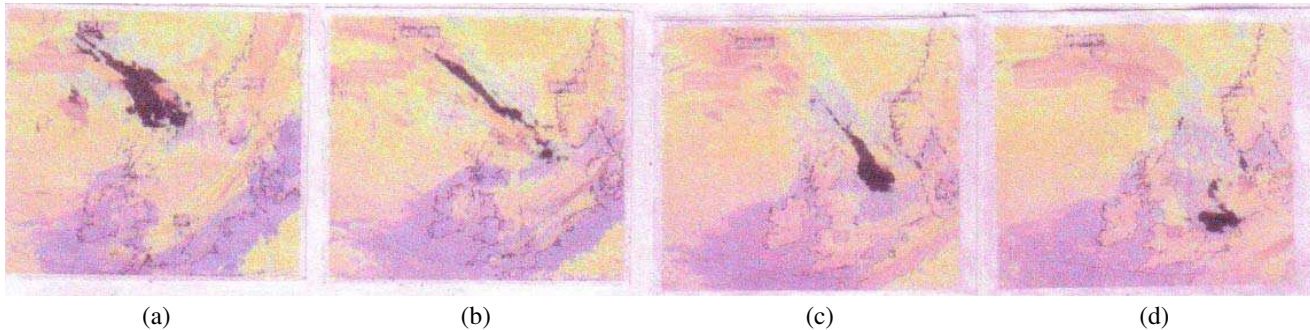


Figure 1: Ash track of volcano in Iceland (as shown by a black patch), (a) at 0930-GMT on April 15, 2010, (b) at 1530-GMT on April 15, 2010, (c) at 2130-GMT on April 15, 2010, (d) at 0330-GMT on April 16, 2010. [Monitored by EUMETSAT] courtesy of Meteorological Office, UK.

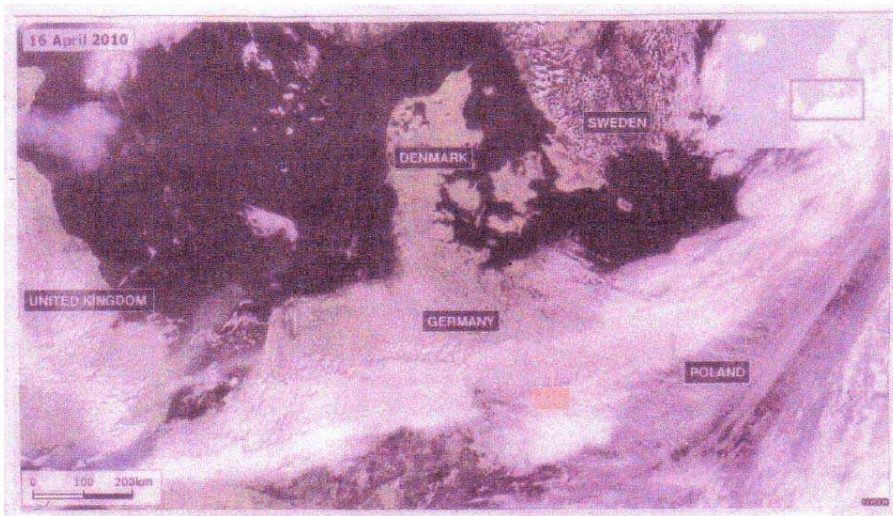


Figure 2: Iceland volcanic ash-cloud pattern in Germany. [transferred after the eruption on April 14, 2010], courtesy of NASA.

The author had some information that the survey team had been formed for their purpose. The leader was Dr. Kristin Vogfjord, and the head-quarter was located in the Meteorological Office of Iceland (Reykjavik). The team was formed by the geological experts in Iceland.

The author has to note here that the group in the meteorological office in Reykjavik are concentrating there interest to the volcanic activities of the volcanoes “Oraefajokull” and “Katla”, both of them are at the location of just neighbor of the volcano noted in this work.

The team reported that the magma could watched thou no lava flow was found on April 19, 2010. The repeated minor eruptions were explosive. The magma surface was under the glacier of 200 m thick, though the successive big volcanic ash (phreatic) eruption could be make a jet flow of the ash up to the height of about 10 km above the glacier surface. They found the continued frequent volcanic tremor.

Professor Pall Einarsson (Geo-Sciences, University of Island) had given his comment about the subglacial volcanoes. It must be more hazardous if the volcano “Katla” which is covered by the glacier of about 400 m thick. Though, we have no threat of such the eruption of this volcano.

3. GASES BURSTING OUT OF VOLCANO

Generally, a volcanic eruption uses to issue some accompanied materials containing an out-burst of gases. There might be various kinds of the gases, though it should be noticed that the gases of sulphur dioxide and sulphur hydride are surely be the most important chemical factors for consideration as well as to the physical and meteorological factors.

The sulphur acid is produced at the gas of sulphur dioxide at meeting to water vapor in the atmosphere. Molecule of sulphur dioxide is heavier in weight relative to the molecule of oxygen or

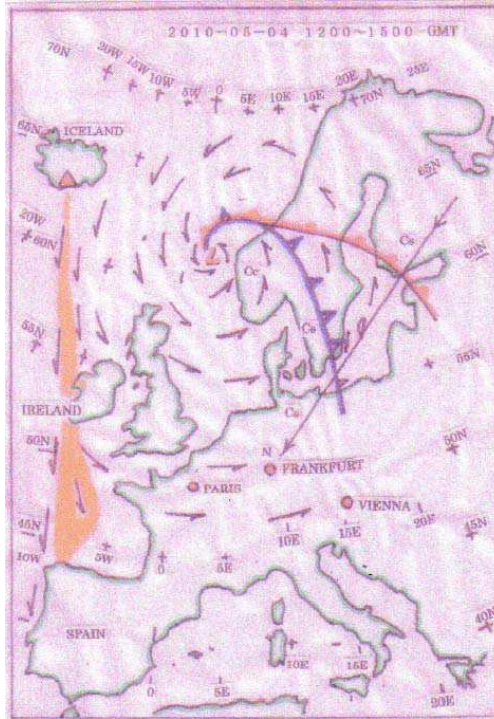


Figure 3: Local weather chart of Europe. (1200~1500-GMT on May 4, 2010) [the pattern is drawn by the author after his eye-watch monitoring].

of nitrogen, so that the gas contents must be compiled fast on the ground surface as the final stage. The acidic materials might be a cause of unexpected effect of the volcanic eruption to the air-line transportation net works. To the details, we should consider what effect might be more negative for our life.

4. HISTORICAL DATA

Around the volcano Eyjafjajoekull (location — 63.63N, 019.62W, and altitude — 1666 m above msl.), several seismometer and GPS monitoring system have been settled. The positioning had shown a swell of about 8 cm for these several months. The eruption was seen just after ceasing the motion to reverse in the ground motion. The tremor is the most important to have an eruption signal in advance. It must be effective to find remotely when the instruments (for example, seismometers) in the volcanic area of about 20 km radius. The ash, so-called as “phreia” size is very fine so that it can be intrude easily into the casing of the seismometers. The victims of the instruments tell us a warning signal for eruption. In addition, various areal information have been compiled by the optical photopgraphs and the other functions on-land.

The volcano in the author's interest now has a record that an eruption was on December 19, 1821 and duration time to cease was about two years (the date of eruption stop is on January 1, 1823). This record says that the volcanic explosivity index (degree of VEI) was degree “3” (moderate).

To the details, it should be referred the publication of “Volcanoes of the World” written by Simkin et al. (1981), though it must be now updated by Smithsonian Institute. The web-site must be more effective to see a detail of the information.

5. VOLCANOES IN ATLANTIC

The volcano introduced as above is one of the subglacial volcanoes, though the subglacial volcanoes must be found only in Island even in the Atlantic Ocean.

Simkin's volcanic chronology tells us that there are many volcanoes in the Atlantic. For example, Azores Islands, Canary Islands, and Cape Verde Islands, there are many cases of the past volcanic eruptions since 1332. It is not assured that which one can be doubtful or not. It is necessary at present to refer to the scientific data.

6. CONCLUSIONS

The author introduced a note to subglacial volcano. For his convenience, one of the specific examples was noticed, that was, the case of the volcano Eyjafjajokull in the southern part of Iceland. This volcano was just erupted in April 2010 to give a severe effect of volcanic ash. Historical data is limited so that it must be hard to see a long term trend in a time scale. Chemical factors should be considered as much as physical factors or meteorological factors, though the winds around the interested volcano are the most significant factor.

There are many volcanoes in the Atlantic, for example, in Azores Islands, Canary Islands, and Cape Verde Islands. Submarine volcanoes should be also considered.

Satellite Monitoring of Aurora Oval on the Earth in Relation to Solar Winds

Shigehisa Nakamura
Kyoto University, Japan

Abstract— This work concerns to a problem on satellite monitoring of the aurora oval on the earth in relation to solar winds. First, a brief review is introduced for helping of our understanding of what relation is between the earth and the solar winds. A history of dawn in geomagnetism is also noted briefly. The advance of research works help to get a mosaic illustration of the aurora which is monitored by an aurora scanner mounted on a polar orbital satellite. Spacecraft monitoring has given the aurora oval of the planet Saturn as reported by NASA.

1. INTRODUCTION

This work concerns on satellite monitoring of the aurora oval on the earth in relation to solar winds. First of all, a brief review is given for help of our understanding of what is seen in the solar-earth system. The earth is approximately taken as a dipole-magnet in order to realize the earth's main field. The variation of magnetic field on the earth is consisted mainly by the effect of ionized particles flowing in the atmosphere with some minor effects by the ocean tides and the solid earth crusts. Nevertheless, the mechanism of the aurora has to be realized after consideration of the solar winds which distort to form a shade of the magnetopause in the solar-earth planetary system. The shade front to the sun was found at a distant of about eight times of the earth's radius in the early age (cf. monitoring by Exploler-12). A brief note is introduced about the history of dawn in geomagnetism is also noted. The advance of the research works by the scientists helped to obtain the first mosaic illustration of the aurora oval boreares after the satellite monitoring by the aurora scanner mounted by a satellite on a polar orbital satellite.

2. DAWN OF GEOMAGNETISM

A primitive model of the earth had been taken as a planet of a simple dipole magnetic model. In these years, it has been understood that the magnetic field of the earth is not so simple referring to the data compiled by the various instruments and to the theoretical models developed for the model of the earth's magnetic field [1]. Main field is taken a magnet which is essentially same to a small magnet for students in primary educational course.

Christian Birkeland in Norway visited Henri Poincare in Paris first for learning Maxwell's theory of electromagnetism. After that, Birkeland learned electromagnetic wave under H. Herz. In 1895, many works had been done by the scientists about properties of X-ray. Then, Birkeland started his research and survey on the aurora boreares. His first expedition was in 1897. He found that the aurora appears higher position than any cloud in the atmospheric layer in his second expedition (1899–1900). Birkeland introduced a model of solar-originated electrons incidence in order to illustrate the geomagnetic variations found by his expedition and by the project of the IPY (International Polar Year). Birkeland published his contributions in "Norwegian Polaris Expedition". This might be the theoretical contribution of aurora in our understanding of the modern works presented by the scientists even in the 2010 age.

3. MODERN RESEARCHES

As far as we concern, the magnetic field of the earth had been understood as a dipole model in the primitive pattern. Nevertheless, it has been developed an advanced research for a more reasonable electromagnetic hydrodynamics in order to have a proper modeling under our renewal of modern knowledge of the earth's internal structure. This is the key to introduce the updated dynamo-theory for the earth's main field describing by the poloidal and toroidal modes. Research should be extended for the nonlinear processes.

In addition, the solar winds as a uniform plasma flow may force to form a shell of the magnetopause and to distort the magnetic field of the planet earth (cf. Figure 1).

On the other hand, several observation projects were in schedule as the International Polar Year (in brief, IPY-1 and IPY-2) and as the International Geophysical Year (IGY).

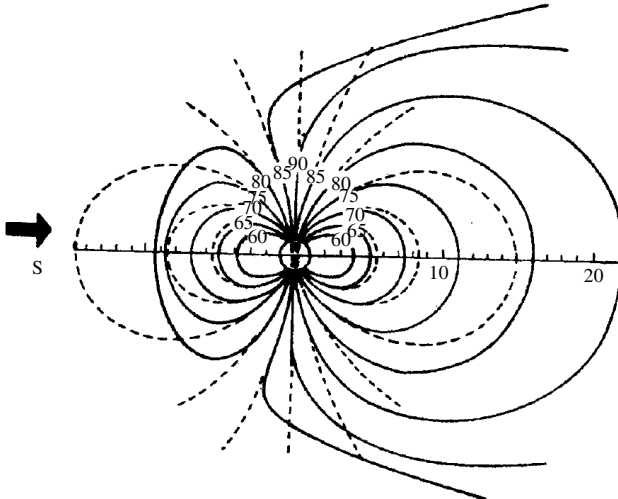


Figure 1: Magnetic field of dipole-Earth distorted by solar wind. (1) dot-line for dipole-Earth field, (2) full-line for distorted field, (3) arrow for solar-wind [modified from Akasohu, S.-I., 1975].

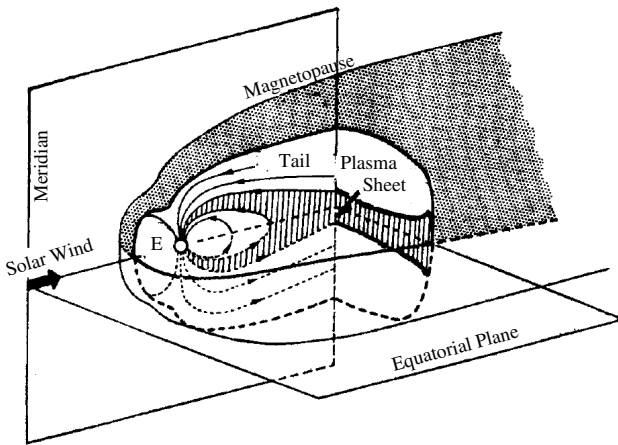


Figure 2: Solar-Earth system.

Electromagnetic understanding of the solar-earth system has been advanced to obtain a modeling image of a magneto-hydrodynamic dynamo. By this time, the scientists had the research projects of IPY as the IPY-1 (1882–1883) and the IPY-2 (1932–1933). Chapman and Bartels (1940) have introduced a model of a quiet day variation (S_q) in the geomagnetic variations. The model supports the harmonic analyses in Kyoto University for the IPY-1 data of the stations settled on the earth. Hirono had introduced his dynamo-theory in 1957 after Elsasser's hydromagnetic-dynamo theory [2]. The advanced project as IGY (1957–1958) was extended to start the Antarctic Research Program in a long term scale. Research on ionosphere had promoted during survey of the radio wave propagation to find E, F1 and F2-layers in a scale of the earth after 0. Heaviside's notice of a conductive layer which could form a wave guide of electromagnetic waves between the ocean surface and the interested conductive layer. As for the aurora, Birkeland published Norwegian Aurora Polaris Expedition (1913). Here, the author feels it necessary to note that Birkeland was acquainted to Akitu Tanakadate, Torahiko Terada, Hantaro Nagaoka in Japan. Significant contributions were by, for example, Alfvén in 1950 and Stenzel in 1955. A more advanced publication must be that written by Chapman in 1964 [3].

4. RADIATION IN UPPER ATMOSPHERE

Van Allen (Iowa State University) had some observations of the radiations in the upper atmosphere (1952–1953) by using several rockets. Then, he had found that some strong radiations were concentrated just in the aurora oval zone. After this finding, he had a chance to obtain some records by using his Geiger-counter for radiations. It was the first time of that the radiation belts were

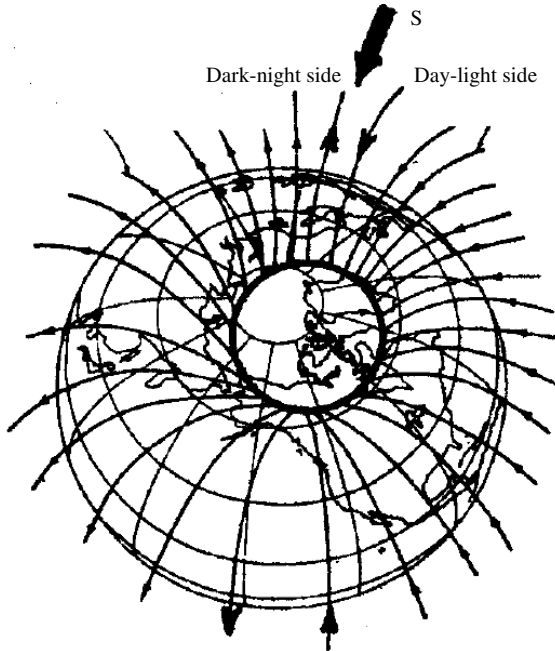


Figure 3: Electric-current around “Aurora Oval Boreares” [by the courtesy of Alasohu, S.-I.].

found by the sensors mounted on some artificial satellites. Some works are for the radiation belt enhancements appeared in the references (cf. [4] and [5]).

Later, it was clarified that the radiation belts (inside and outside) had no relation to the possible electron beam to induce the aurora. To the details, it should be referred to the other publications. Simply, the author notes that the belt denoted E in Figure 2. The magnetopause facing the sun (day light side) is in a shape of conical form and the magnetopause in the shadow zone (dark night side) is in a form of a tail.

The inside zone in the tail of the magnetopause is taken to be filled by plasma. A part of the plasma in the tail near the earth is in a form of plasma sheet on the equatorial plane. The extension of the plasma sheet separated in to two part (northern and southern) to contact on the earth surface. So that, it should be noticed that the solar winds in a form of an uniform plasma flow could hit the consisting atoms and molecules just outside of the plasma sheet to hit and activate the upper atmosphere which could be taken us as a kind of the visible aurora boreares. The aurora oval on the earth might be found in the fresh reports in these years, for example, Mandea and Papistoshvili [6].

5. SATELLITE MONITORING

Akasofu (1981) has given a digestive illustration for his review on the research of the aurora. Loomis had completed his map of the aurora oval boreares one hundred years before the IGY (1957–1958). Optical aspect of the aurora had clarified that the aurora was appeared when atoms and molecules in the atmosphere were exited stage under some specific condition. With the above noticed contributions, problem raised was to see the aurora oval by using an aurora scanner mounted on a artificial satellite in a polar orbital motion. One of the most typical cases was the aurora oval monitored by the satellite ICIS-2. The result of a monochromatic mosaic illustration of the aurora boreares was obtained by C. D. Anger. C. D. Anger at Calgary University in Canada had used his phototube applied system of an electric circuit for monitoring aurora oval in the northern hemisphere.

A geomagnetic flux field in the aurora oval zone is schematically introduced as shown in Figure 3. Since then, it is aimed to continue satellite monitoring of aurora boreares (which was presented at Kyoto in 1973). The polar orbital motion of the satellite had given aurora australis too (for example, National Polar Research Institute, Japan).

6. DISCUSSIONS AND CONCLUSIONS

This satellite monitoring of the aurora is surely be effective to see the more detailed structure of the aurora. As the results of the research on the aurora, it is confirmed that the ionized particles of the solar winds might surely be a trigger to induce an activated energy level of the gasses in the atmosphere (especially, the atoms and molecules of oxygen and nitrogen). This energy transfer makes it possible to form the visible aurora in the aurora oval zone in a high speed to ionize by transferring to the atoms and the molecules of oxygen and nitrogen. At this stage, the author has to notice that it is necessary to continue the successive satellite monitoring of the aurora for our advanced research. By the year of 2010, the advanced spacecraft monitoring has introduced the aurora oval of the planet Saturn in the soar system. Successive advanced contributions are expected in the next age.

REFERENCES

1. Chapman, S. and J. Bartels, *Geomagnetism*, 1049, Oxford University Press, London, 1940.
2. Elsasser, W. M., "Hydromagnetic dynamo theory," *Reviews of Modern Physics*, Vol. 28, 135–163, 1956.
3. Chapman, S., "Solar plasma, geomagnetism, and aurora," 141, Gordon and Breach, N.Y., 1964.
4. Summers, D., R. M. Thorne, and F. Xiao, "Relativistic theory of wave-particle resonant diffusion with application to electron acceleration in the magnetosphere," *Journal of Geophysical Research*, Vol. 103, No. 20, 487, 1998.
5. Liemohn, M. W. and A. A. Chan, "Unraveling the cause of radiation belt enhancements," *Eos, Transactions, American Geophysical Union*, Vol. 88, No. 42, 426–427, 2007.
6. Mandea, M. and V. Papistoshvili, "World wide geomagnetic data collection and management," *Eos, Transactions, American Geophysical Union*, Vol. 90, No. 45, 409–410, 2009.

RCS Reduction Assisted by Surface Plasmon Polaritons

Jiafu Wang^{1, 2}, Shaobo Qu^{1, 3}, Duolin Zhang¹, Zhuo Xu³, Hua Ma^{1, 3},
Song Xia³, Xinhua Wang¹, Hang Zhou¹, Lei Lu¹, and Fei Yu¹

¹College of Science, Air Force Engineering University, Xi'an, Shanxi 710051, China

²The Second Aviation College of Air Force, Huxian, Shanxi 710306, China

³Electronic Materials Research Laboratory, Xi'an Jiaotong University, Xi'an, Shanxi 710049, China

Abstract— We demonstrated that the RCS of a metallic cylinder can be drastically reduced based on surface plasmon polaritons. By enclosing the metallic cylinder with a plasmonic cover, surface plasmon polaritons can be excited on surface of the metallic cylinder. Due to the highly surface-confined property of surface plasmon polaritons, the otherwisely backscattered EM energy is transferred to other directions, even to the other side of the metallic cylinder, achieving enhanced transparency.

1. INTRODUCTION

A surface plasmon is the free electron density oscillation near the metal/dielectric interface. The propagation of the free electron density creates a coupled physical state between the electron and photon, resulting in a bound surface plasmon polariton (SPP) [1, 2]. For realistic metals, their effective plasma frequencies lie in the visible and near-infrared regimes. The SPP modes experience significantly high attenuation as they propagate, due to intrinsic electron oscillation damping loss in metals. At lower microwave frequencies, the properties of confined SPPs can be mimicked by geometrical induced SPPs, also known as spoof SPPs or designer SPPs [3, 4]. Due to the highly-confined fields near the interface, SPPs have great application potentials in optics, photonics and biosensing. In particular, by the assistance of SPPs, transparency of an otherwise opaque object can be achieved [5, 6]. In this paper, we investigated enhanced transparency of a metallic object at microwave frequencies by exciting SPP modes. Transmission spectra, field distributions and power flows were obtained by numerical simulations, which give an intuitive illustration of the enhanced transparency. By means of a plasmonic cover, SPP modes can be excited efficiently around the metallic object, leading to enhanced transmission. Finally, an experiment was carried out, which further verified the enhanced transparency.

2. THEROY AND DESIGN

Due to the highly surface-confined fields and along-surface propagation of surface plasmon waves (SPW), electromagnetic energy can be transferred around the metallic object and then reradiated into free space in the back side, as shown in Fig. 1. To efficiently couple incident EM waves to SPP modes, a plasmonic cover has to be introduced. The plasmonic cover serves both as a coupler and a decoupler. On the front side, it couples incident waves as SPPs; while on the back side, it couples SPPs as EM waves. A well-known structure that couples and decouples SPPs is the grating structure [7]. Under such a consideration, a cylindrical grating-like structure, which serves as the plasmonic cover, was designed, as shown in Figs. 2(a) and (b). Geometrical parameters of the plasmonic cover unit cell are: $h = 10$ mm, $h_1 = 8$ mm, $t = 1.574$ mm. The dielectric layer between the outer and inner metallic stripes is the Rogers 5880 dielectric material, with a thickness of 0.787 mm. The inner radius of the plasmonic cover is $r = 30$ mm. That is, it is expected to enhance the transparency of a metallic cylinder with a radius no greater than 30 mm.

3. NUMERICAL SIMULATIONS AND RESULTS

The transmission properties were simulated using the time domain solver of commercial software CST Microwave Studio. Figs. 3(a) and (b) give the simulated transmission and reflection spectra for a copper cylinder with and without the plasmonic cover, respectively, under the same simulation setup. By comparing Figs. 3(a) and (b), it is quite evident that the transmission is obviously enhanced in the frequency band 9.0–12.0 GHz. This indicates an enhanced transparency in this regime.

To determine whether it is the SPP mode excitation that enhances the transparency, snapshots of electric field distributions at 10.0 GHz were given for the two cases with and without plasmonic

cover. By comparing the two cases, it is apparent that SPPs are excited on the plasmonic cover, which carry and then release EM energy to the back side of the copper cylinder, as clearly shown in Figs. 4(a) and (b). Thus, in the near-field of the back side, a quite strong EM field is present for the case with plasmonic cover, while very weak for the case without plasmonic cover.

Figures 5(a) and (b) show, respectively, the simulated power flows at 10.0 GHz for the case with and without plasmonic cover. For the case with the plasmonic cover, forward power flow can be clearly seen at the back side of the copper cylinder. While for the case without plasmonic cover, backward power flow is induced. Due to the blockage of the copper cylinder, little EM energy can arrive near the back side, leading to an “empty” region. According to the Huygens-Fresnel

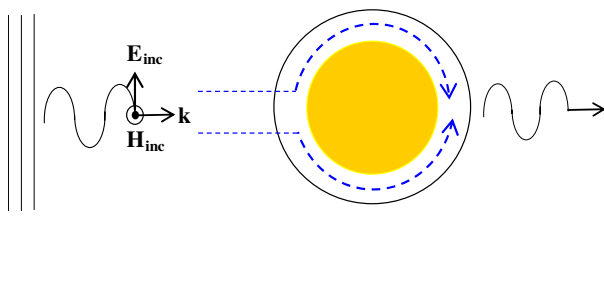


Figure 1: Schematic illustration of the mechanism of the plasmon-enhanced transparency. The dashed lines denote the paths EM waves pass through the plasmonic cover and the solid circular line indicates the plasmonic cover.

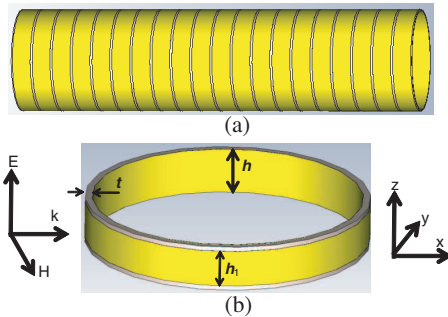


Figure 2: (a) The designed plasmonic cover and (b) its unit cell.

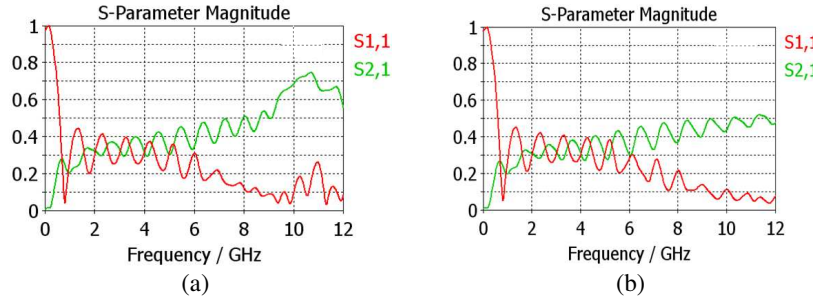


Figure 3: Transmission and reflection spectra for a copper cylinder with (a) and without (b) the plasmonic cover. S_{21} and S_{11} indicate the magnitudes of transmission and reflection, respectively.

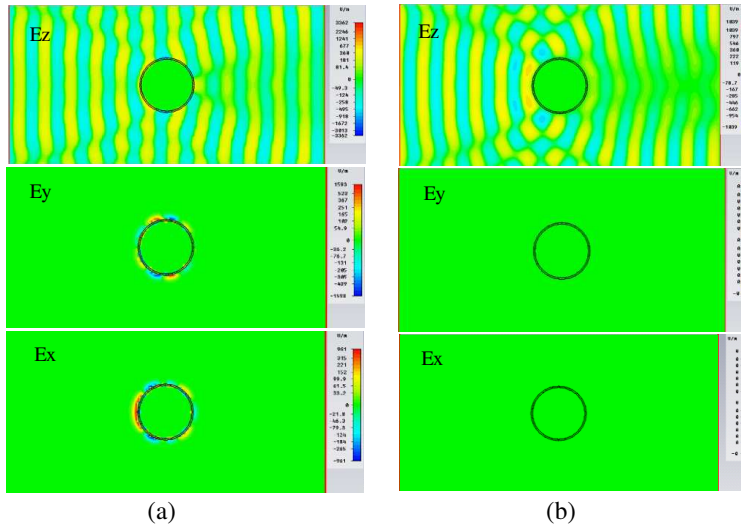


Figure 4: Snapshots of electric field distributions for the case with (a) and without (b) the plasmonic cover.

principle, EM waves in other regions will radiate EM energies into this “empty” region, resulting in a backward power flow. In contrast, for the case with plasmonic cover, the near back side is quite “full” because of the SPP-transferred EM energies, and correspondingly a forward power flow is present.

4. EXPERIMENT

A sample was fabricated and measured to verify our design. Fig. 6 gives the fabricated sample as well as the measurement system. The measurement system mocks a free space measurement environment. The field-sensing antenna is formed from a coaxial fixture inserted into a hole drilled through the upper plate, so the measurement system can only measure the field distribution on the upper plane of the cloaking system.

Figure 7 which shows the measured snapshots of electric field distributions at 11.0 GHz on the upper plane. For the case with plasmonic cover, the transmission is enhanced and the reflection is suppressed. While for the case without the plasmonic cover, there is a nearly “empty” region arising from the blockage of the metallic cylinder and the reflection is quite strong. The measured results clearly verify the enhanced transparency resulting from SPP mode excitation.

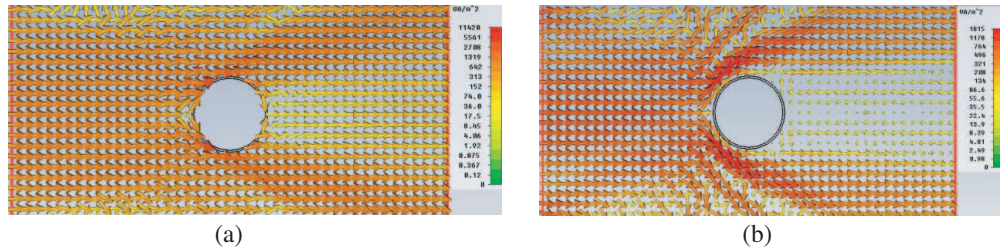


Figure 5: Simulated power flows for the case with (a) and without (b) the plasmonic cover at 10.0 GHz.

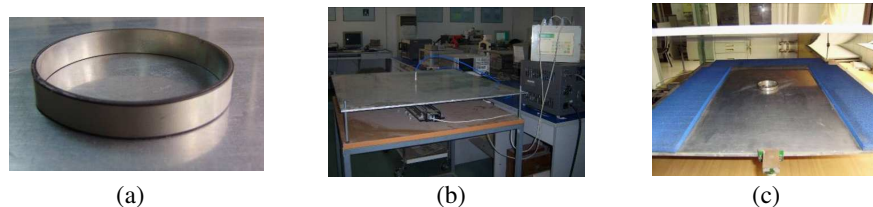


Figure 6: The test sample and measurement system. (a) Test sample. (b) Measurement system. (c) Sample placed in the measurement system.

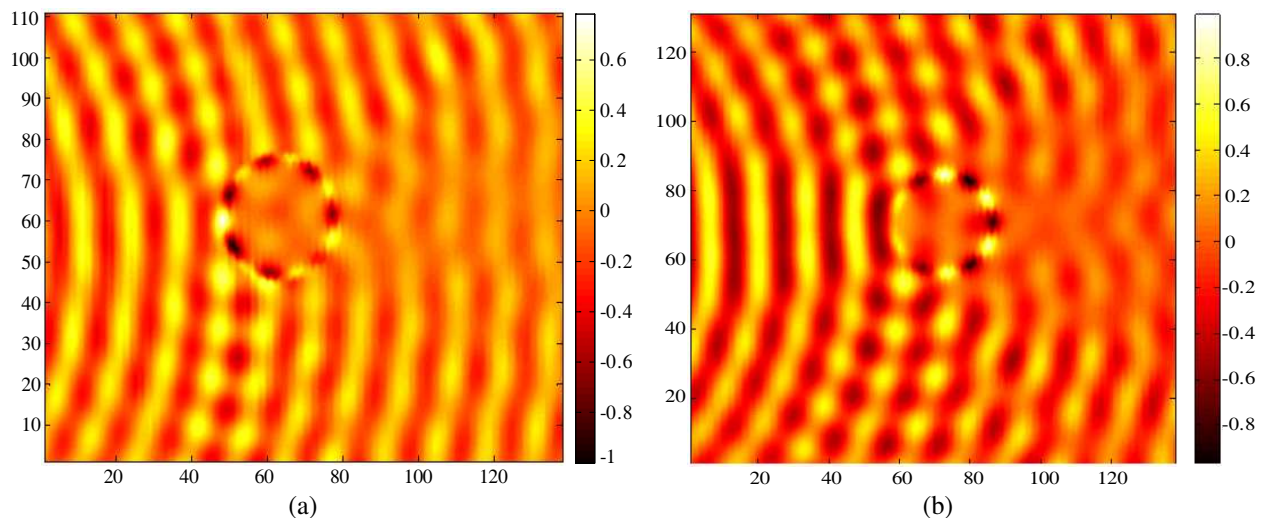


Figure 7: Measured electric field distributions with (a) and without (b) plasmonic cover at 11.0 GHz.

5. CONCLUSIONS

By numerical simulation and experiments, we investigated plasmon-enhanced transparency at microwave frequencies by introducing a plasmonic cover for metallic objects. Clear enhanced transparency was demonstrated and verified. To achieve plasmon-enhanced transparency, the key is to design the corresponding plasmonic cover. Such plasmonic covers can find potential applications in many fields such as RCS reduction.

ACKNOWLEDGMENT

This work is supported in part by the National Natural Science Foundation of China under Grants No. 50632030, 10804130, 60871027 and 61071058, and in part by the 973 Project of Science and Technology Ministry of China under Grant No. 2009CB613306.

REFERENCES

1. Maier, S. A., *Plasmonics: Fundamentals and Applications*, Springer, New York, 2007.
2. Maier, S. A., "Plasmonics: Metal nanostructures for subwavelength photonic devices," *IEEE J. Sel. Top. Quantum Electron.*, Vol. 12, No. 6, 1214–1220, 2006.
3. Pendry, J. B., L. Martín-Moreno, and F. J. García-Vidal, "Mimicking surface plasmons with structured surfaces," *Science*, Vol. 305, No. 5685, 847–848, 2004.
4. García-Vidal, F. J., L. Martín-Moreno, and J. B. Pendry, "Surfaces with holes in them: New plasmonic metamaterials," *J. Opt. A: Pure Appl. Opt.*, Vol. 7, No. 2, 97–101, 2005.
5. Alù, A. and N. Engheta, "Achieving transparency with plasmonic and metamaterial coatings," *Phys. Rev. E*, Vol. 72, 016623, 2005.
6. Rohde, C., K. Hasegawa, and M. Deutsch, "Plasmon assisted transparency in metal-dielectric microspheres," *Opt. Lett.*, Vol. 32, 415–417, 2007.
7. Hibbins, A. P., J. R. Sambles, and C. R. Lawrence, "Grating-coupled surface plasmons at microwave frequencies," *J. Appl. Phys.*, Vol. 86, No. 4, 1791, 1999.

Polarization Changes of Stochastic Spatially and Spectrally Partially Coherent Electromagnetic Pulsed Beams in Turbulent Atmosphere

Zhiguo Zhao¹, Jianguo Lu², Fengguo Fan³, Haixia Wang¹, and Yongtao Zhang¹

¹Department of Physics, Luoyang Normal College, Luoyang 471022, China

²Department of Primary Education, Jiaozuo Teachers College, Jiaozuo 454150, China

³Network Center, Shangqiu Teachers College, Shangqiu 476000, China

Abstract— Using the coherence theory of non-stationary fields and the method of two-time Fourier transform, the analytical expression for the spectral degree of polarization of stochastic spatially and spectrally partially coherent electromagnetic pulsed beams in turbulent atmosphere is derived, and used to study the polarization changes of stochastic electromagnetic pulsed beams propagating through turbulent atmosphere. The influence of pulse frequency and refraction index structure constant on the spectral degree of polarization is emphasized. It is shown that, in comparison with free-space case, the turbulent atmosphere plays an important role on the distribution of the spectral degree of polarization of stochastic electromagnetic pulsed beams propagating in turbulent atmosphere. The results obtained might find potential application for sensing, imaging and communication through the atmosphere.

1. INTRODUCTION

In the recent decades, there has been substantial interest in studying the polarization properties of stochastic electromagnetic beams on propagation [1–9]. However, most of studies have been restricted to the stationary beams. On the other hand, statistical optical pulses represent a wide class of partially coherent fields that find numerous applications as optical imaging and fiber optics etc. [10]. Recently, a scalar model of spectrally partially coherent pulses was introduced by Pääkkönen et al. [11]. The propagation properties of spatially and spectrally partially coherent scalar pulses were studied by Turunen et al. [12–15]. Ding et al. extended the scalar model of spectrally partially coherent pulses to a vectorial one, and investigated the characterization of stochastic spatially and spectrally partially coherent electromagnetic pulsed beams [16], and whose changes in the spectral degree of polarization in dispersive media were studied in detail [17]. The aim of this paper is to study the polarization changes of stochastic spatially and spectrally partially coherent electromagnetic pulsed beams in turbulent atmosphere. The influence of turbulent atmosphere and pulse frequency ω/ω_0 on the spectral degree of polarization are emphasized. In Section 2, the analytical expression for the spectral degree of polarization of stochastic spatially and spectrally partially coherent electromagnetic pulsed beams in turbulent atmosphere is derived, and used to study the polarization changes of stochastic electromagnetic pulsed beams propagating through turbulent atmosphere. In Section 3, illustrative numerical examples are presented to illustrate the dependence of spectral degree of polarization on pulse frequency and refraction index structure constant. Section 4 concludes the main results obtained in this paper.

2. THEORETICAL FORMULATION

In the space-time domain the electric mutual coherence matrix of a stochastic spatially and temporally partially coherent electromagnetic pulsed beams at the source plane $z = 0$ is given by

$$\overset{\leftrightarrow}{\Gamma}^0(\rho_1, \rho_2, t_1, t_2) = [\Gamma_{ij}^0(\rho_1, \rho_2, t_1, t_2)] = [\langle E_i^*(\rho_1, t_1) E_j(\rho_2, t_2) \rangle], \\ (i = x, y; j = x, y \text{ unless otherwise stated}), \quad (1)$$

where E_i and E_j are the polarization components of the electric field $E(\rho, t)$ at the plane $z=0$, $\rho_{i(j)}=(x_{i(j)}, y_{i(j)})$ is the position vector, $t_{1(2)}$ is the time. The asterisk denotes the complex conjugate and the angular brackets denote the ensemble average.

To simplify the analysis it is assumed that the electric vector components in the x and y directions are uncorrelated at the plane $z = 0$ [1, 18, 19], i.e.,

$$\begin{aligned}\Gamma_{ii}^0(\rho_1, \rho_2, t_1, t_2) &= A_i \exp\left[-\frac{t_1^2 + t_2^2}{2T_0^2}\right] \exp\left[-\frac{\rho_1^2 + \rho_2^2}{4\sigma^2}\right], \\ &\quad \times \exp\left[-\frac{(\rho_1 - \rho_2)^2}{2\delta_{ii}^2}\right] \exp\left[-\frac{(t_1 - t_2)^2}{2T_c^2}\right] \exp[i\omega_0(t_1 - t_2)] \\ \Gamma_{xy}^0(\rho_1, \rho_2, t_1, t_2) &= \Gamma_{yx}^0(\rho_1, \rho_2, t_1, t_2) = 0,\end{aligned}\quad (2)$$

where the coefficients A_i and the variables σ , δ_{ii} are independent of position but may depend on the frequency. δ_{ii} is related to the spatial correlation length. T_0 is the pulse duration. T_c describes the temporal coherence length of the pulse. ω_0 is carrier frequency of the pulse.

By using the Fourier-transform

$$\overleftrightarrow{\mathbf{W}}^0(\rho_1, \rho_2, \omega_1, \omega_2) = \frac{1}{(2\pi)^2} \int_{-\infty}^{+\infty} \int_{-\infty}^{+\infty} \overleftrightarrow{\mathbf{\Gamma}}^0(\rho_1, \rho_2, t_1, t_2) \exp[-i(\omega_1 t_1 - \omega_2 t_2)] dt_1 dt_2, \quad (3)$$

we can derive the cross-spectral density matrix at the plane $z = 0$

$$\overleftrightarrow{\mathbf{W}}^0(\rho_1, \rho_2, \omega_1, \omega_2) = [W_{ij}^0(\rho_1, \rho_2, \omega_1, \omega_2)], \quad (4)$$

where

$$\begin{aligned}W_{ii}^0(\rho_1, \rho_2, \omega_1, \omega_2) &= \frac{T_0 A_i}{2\pi\Omega_0} \exp\left(-\frac{\rho_1^2 + \rho_2^2}{4\sigma^2}\right) \exp\left[-\frac{(\rho_1 - \rho_2)^2}{2\delta_{ij}^2}\right] \\ &\quad \times \exp\left[-\frac{(\omega_1 - \omega_0)^2 + (\omega_2 - \omega_0)^2}{2\Omega_0^2}\right] \exp\left[-\frac{(\omega_1 - \omega_2)^2}{2\Omega_c^2}\right],\end{aligned}\quad (6a)$$

$$W_{xy}^0(\rho_1, \rho_2, \omega_1, \omega_2) = W_{yx}^0(\rho_1, \rho_2, \omega_1, \omega_2) = 0, \quad (6b)$$

$$\Omega_0 = \sqrt{\frac{1}{T_0^2} + \frac{2}{T_c^2}}, \quad (\text{spectral width}) \quad (7)$$

$$\Omega_c = \frac{T_c}{T_0} \Omega_0. \quad (\text{spectral coherence width}) \quad (8)$$

Eqs. (7) and (8) give the relation of the pulse duration T_0 , temporal coherence length T_c , spectral width Ω_0 , and spectral coherence width Ω_c . The spectral coherence width Ω_c is a measure of the correlation between different frequency components of the pulse [11].

Therefore, the spectral degree of polarization of stochastic electromagnetic pulsed beams at the plane $z = 0$ are expressed as [20]

$$P^0(\rho, \omega) = \sqrt{1 - \frac{4 \text{Det}[\overleftrightarrow{\mathbf{W}}^0(\rho, \rho, \omega, \omega)]}{\left\{ \text{Tr}[\overleftrightarrow{\mathbf{W}}^0(\rho, \rho, \omega, \omega)] \right\}^2}} = \left| \frac{A_x - A_y}{A_x + A_y} \right|, \quad (9)$$

The cross-spectral density matrix of stochastic electromagnetic pulsed beams at the plane $z \neq 0$ in turbulent atmosphere is expressed as [19]

$$\begin{aligned}\overleftrightarrow{\mathbf{W}}(\mathbf{r}_1, \mathbf{r}_2, z, \omega_1, \omega_2) &= \frac{\omega_1 \omega_2}{4\pi^2 c^2 z^2} \exp[i(\omega_2 - \omega_1)z/c] \iint \overleftrightarrow{\mathbf{W}}^0(\rho_1, \rho_2, \omega_1, \omega_2) \\ &\quad \times \exp\left\{ \frac{i}{2cz} [\omega_2(\mathbf{r}_2 - \rho_2)^2 - \omega_1(\mathbf{r}_1 - \rho_1)^2] \right\} \\ &\quad \times \langle \exp[\psi(\mathbf{r}_1, \rho_1, \omega_1) + \psi * (\mathbf{r}_2, \rho_2, \omega_2)] \rangle_m d^2\rho_1 d^2\rho_2,\end{aligned}\quad (10)$$

where $\psi(\mathbf{r}, \rho, \omega)$ is the random part of the complex phase of a spherical wave due to the turbulence.

In the condition of $\mathbf{r}_1 = \mathbf{r}_2 = \mathbf{r}$ and $\omega_1 = \omega_2 = \omega$, the ensemble average $\langle \cdot \rangle_m$ in Eq. (10) can be written as [21]

$$\langle \exp [\psi(\mathbf{r}_1, \rho_1, \omega_1) + \psi * (\mathbf{r}_2, \rho_2, \omega_2)] \rangle_m = \exp \left[-\frac{(\rho_1 - \rho_2)^2}{\rho_0^2} \right], \quad (11)$$

where $\rho_0 = (0.545C_n^2 k^2 z)^{-3/5}$ is the spatial coherence radius of a spherical wave propagating in turbulent atmosphere. C_n^2 is the refraction index structure constant which describes how strong the turbulence is. We have employed a quadratic approximation for the Rytov's phase structure function in order to obtain simple and viewable analytical result [21].

On substituting Eqs. (5) and (6) into Eq. (10) and letting $\mathbf{r}_1 = \mathbf{r}_2 = \mathbf{r}$ and $\omega_1 = \omega_2 = \omega$, and after straightforward integral calculations, the spectral degree of polarization of stochastic electromagnetic pulsed beams at the plane $z > 0$ in turbulent atmosphere are given by

$$P(\mathbf{r}, z, \omega) = \sqrt{1 - \frac{4 \text{Det} [\overleftrightarrow{W}(\mathbf{r}, \mathbf{r}, z, \omega, \omega)]}{\left\{ \text{Tr} [\overleftrightarrow{W}(\mathbf{r}, \mathbf{r}, z, \omega, \omega)] \right\}^2}} = \left| \frac{\frac{A_x}{Q_{xx}} \exp \left[-\frac{\mathbf{r}^2}{2\sigma^2 Q_{xx}} \right] - \frac{A_y}{Q_{yy}} \exp \left[-\frac{\mathbf{r}^2}{2\sigma^2 Q_{yy}} \right]}{\frac{A_x}{Q_{xx}} \exp \left[-\frac{\mathbf{r}^2}{2\sigma^2 Q_{xx}} \right] + \frac{A_y}{Q_{yy}} \exp \left[-\frac{\mathbf{r}^2}{2\sigma^2 Q_{yy}} \right]} \right|, \quad (12)$$

where

$$Q_{ii} = 1 + \frac{c^2 z^2}{2\sigma^2 \omega^2} \left(\frac{1}{2\sigma^2} + \frac{2}{\delta_{ii}^2} \right) + 2 (0.545C_n^2)^{\frac{6}{5}} \frac{\omega^{\frac{2}{5}} c^{-\frac{2}{5}} z^{\frac{16}{5}}}{\sigma^2}. \quad (13)$$

Eqs. (9), (12)–(13) are the main analytical results obtained in this paper, and describe the changes in the spectral degree of polarization of stochastic electromagnetic pulsed beams from the $z = 0$ plane to the z plane in turbulent atmosphere, which depend on the pulse frequency ω , refraction index structure constant C_n^2 , spatial correlation length δ_{ii} , coefficients A_x , A_y and propagation distance z .

3. NUMERICAL CALCULATION RESULTS AND ANALYSES

To illustrate the dependence of spectral degree of polarization on pulse frequency ω and refraction index structure constant C_n^2 , some numerical calculation results are presented.

The on-axis spectral degree of polarization P of stochastic spatially and spectrally partially coherent electromagnetic pulsed beams as a function of the propagation distance z for different pulse frequency ω/ω_0 in free space ($C_n^2=0$) and in turbulent atmosphere ($C_n^2 = 1 \times 10^{-13} \text{ m}^{-2/3}$) is given in Figs. 1(a) and (b), respectively. The calculation parameters are $\delta_{xx} = 0.5 \text{ mm}$, $\delta_{yy}=2\delta_{xx}$,

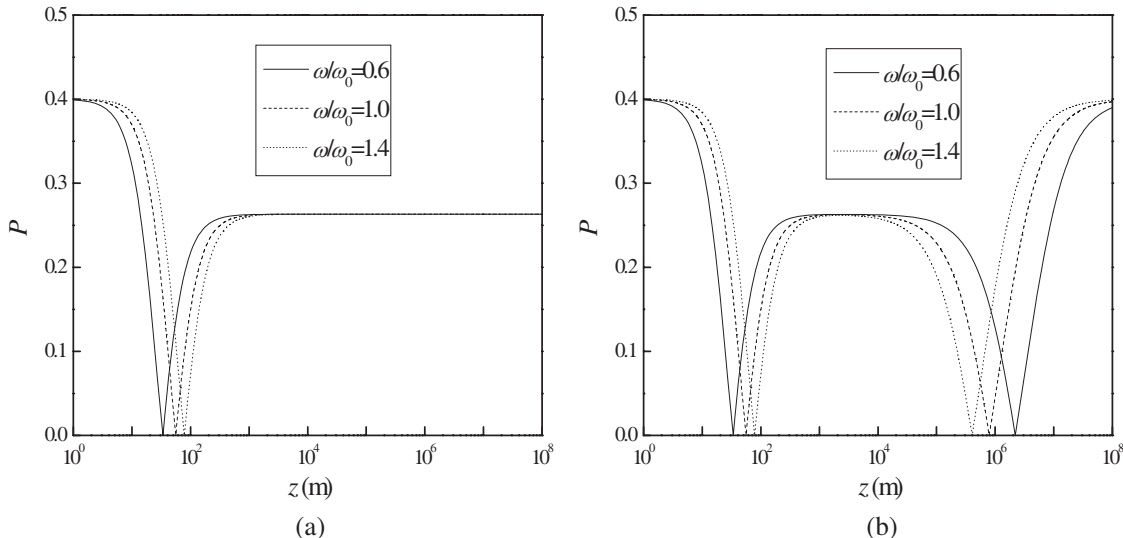


Figure 1: On-axis spectral degree of polarization P of stochastic spatially and spectrally partially coherent electromagnetic pulsed beams as a function of the propagation distance z for different pulse frequency ω/ω_0 in free space (a) and in turbulent atmosphere (b).

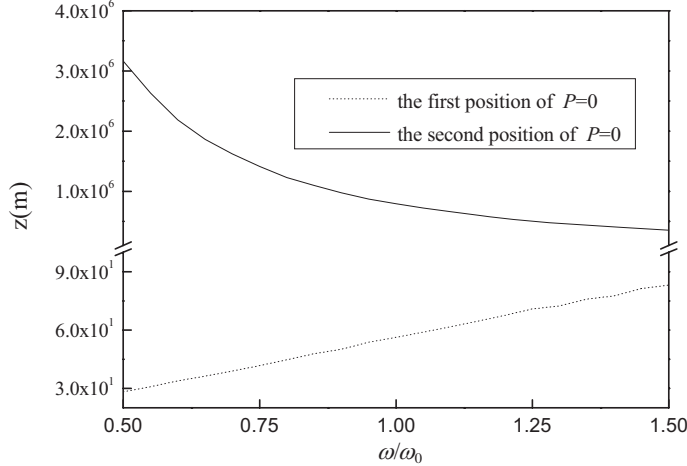


Figure 2: Position z of the on-axis spectral degree of polarization $P = 0$ as a function of pulse frequency ω/ω_0 .

$A_y=1$, $\sigma=50$ mm, $P^0=0.4$, $T_0=50$ fs and $T_c=5$ fs, $\omega_0=2.36$ rad/fs. It is seen that the pulse frequency ω/ω_0 and the refraction index structure constant C_n^2 influence the distribution of on-axis spectral degree of polarization P of stochastic spatially and spectrally partially coherent electromagnetic pulsed beams, and the position z of the on-axis spectral degree of polarization $P = 0$ changes for different values of ω/ω_0 . In comparison with free-space case, the second position z of $P = 0$ affected by ω/ω_0 appears in turbulent atmosphere ($C_n^2=1\times10^{-13}$ m $^{-2/3}$). The changes of the position z of the on-axis spectral degree of polarization $P = 0$ as a function of pulse frequency ω/ω_0 are shown in Fig. 2 where $C_n^2=1\times10^{-13}$ m $^{-2/3}$. The other calculation parameters are the same as those in Fig. 1(b). It is shown that, with increasing pulse frequency ω/ω_0 , the first position z of $P = 0$ increases, whereas the second position z of $P=0$ decreases.

4. CONCLUSION

In this paper, the analytical expression for the spectral degree of polarization of stochastic spatially and spectrally partially coherent electromagnetic pulsed beams in turbulent atmosphere is derived, and used to study the polarization changes of stochastic spatially and spectrally partially coherent pulsed beams propagating through turbulent atmosphere. It has been shown that the pulse frequency ω/ω_0 and the refraction index structure constant C_n^2 influence the distribution of on-axis spectral degree of polarization P of stochastic spatially and spectrally partially coherent electromagnetic pulsed beams. The results obtained might find potential application for sensing, imaging and communication through the atmosphere.

REFERENCES

1. James, D. F. V., “Change of polarization of light beams on propagation in free space,” *J. Opt. Soc. Am. A*, Vol. 11, No. 5, 1641–1643, 1994.
2. Agrawal, G. P. and E. Wolf, “Propagation-induced polarization changes in partially coherent optical beams,” *J. Opt. Soc. Am. A*, Vol. 17, No. 11, 2019–2023, 2000.
3. Shirai, T. and E. Wolf, “Coherence and polarization of electromagnetic beams modulated by random phase screens and their changes on propagation in free space,” *J. Opt. Soc. Am. A*, Vol. 21, No. 10, 1907–1916, 2004.
4. Korotkova, O. and E. Wolf, “Changes in the state of polarization of a random electromagnetic beam on propagation,” *Opt. Commun.*, Vol. 246, No. 1–3, 35–43, 2005.
5. Roychowdhury, H., G. P. Agrawal, and E. Wolf, “Changes in the spectrum, in the spectral degree of polarization, and in the spectral degree of coherence of a partially coherent beam propagating through a gradient-index fiber,” *J. Opt. Soc. Am. A*, Vol. 23, No. 4, 940–948, 2006.
6. Chen, Z. Y. and J. X. Pu, “Degree of polarization in Young’s double-slit interference experiment formed by stochastic electromagnetic beams,” *J. Opt. Soc. Am. A*, Vol. 24, No. 7, 2043–2048, 2007.

7. Wolf, E., "Polarization invariance in beam propagation," *Opt. Lett.*, Vol. 32, No. 23, 3400–3401, 2007.
8. Korotkova, O., T. D. Visser, and E. Wolf, "Polarization properties of stochastic electromagnetic beams," *Opt. Commun.*, Vol. 281, No. 4, 515–520, 2008.
9. Du, X. Y. and D. M. Zhao, "Changes in the polarization and coherence of a random electromagnetic beam propagating through a misaligned optical system," *J. Opt. Soc. Am. A*, Vol. 25, No. 3, 773–779, 2008.
10. Agrawal, G. P., *Nonlinear Fiber Optics*, Academic Press, 2007.
11. Pääkkönen, J. Turunen, P. Vahimaa, A. T. Friberg, and F. Wyrowski, "Partially coherent Gaussian pulses," *Opt. Commun.*, Vol. 204, No. 1-6, 53–58, 2002.
12. Lajunen, H., J. Turunen, P. Vahimaa, J. Tervo, and F. Wyrowski, "Spectrally partially coherent pulse trains in dispersive media," *Opt. Commun.*, Vol. 255, No. 1–3, 12–22, 2005.
13. Lajunen, H., P. Vahimaa, and J. Tervo, "Theory of spatially and spectrally partially coherent pulses," *J. Opt. Soc. Am. A*, Vol. 22, No. 8, 1536–1545, 2005.
14. Saastamoinen, K., J. Turunen, P. Vahimaa, and A. T. Friberg, "Spectrally partially coherent propagation-invariant fields," *Phys. Rev. A*, Vol. 80, No. 5, 053804, 2009.
15. Surakka, M., A. T. Friberg, J. Turunen, and P. Vahimaa, "Distinguishing between deterministic and stochastic pulse broadening," *Opt. Lett.*, Vol. 35, No. 2, 157–159, 2010.
16. Ding, C. L., L. Z. Pan, and B. D. Lv, "Characterization of stochastic spatially and spectrally partially coherent electromagnetic pulsed beams," *New J. Phys.*, Vol. 11, No. 8, 083001, 2009.
17. Ding, C. L., L. Z. Pan, and B. D. Lv, "Changes in the spectral degree of polarization of stochastic spatially and spectrally partially coherent electromagnetic pulses in dispersive media," *J. Opt. Soc. Am. B*, Vol. 26, No. 9, 1728–1735, 2009.
18. Huang, W. H., S. A. Ponomarenko, M. Cada, and G. P. Agrawal, "Polarization changes of partially coherent pulses propagating in optical fibers," *J. Opt. Soc. Am. A*, Vol. 24, No. 10, 3063–3068, 2007.
19. Mandel, L. and E. Wolf, *Optical Coherence and Quantum Optics*, Cambridge University, Cambridge, 1995.
20. Wolf, E., "Unified theory of coherence and polarization of random electromagnetic beams," *Phys. Lett. A*, Vol. 312, No. 5–6, 263–267, 2003.
21. Yura, H. T., "Mutual coherence function of a finite cross section optical beam propagating in a turbulent medium," *Appl. Opt.*, Vol. 11, No. 6, 1399–1406, 1972.

The Frequency Dependence Problem of Conducting Cylinder Buried in a Half-space

Wei Chien¹ Hsien-Wei Tseng², Kai-Xiang Huang¹, and Chi-Hsien Sun³

¹Electronic Engineering Department, De Lin Institute of Technology, Taiwan, R.O.C.

²Computer and Communication Engineering, De Lin Institute of Technology, Taiwan, R.O.C.

³Electrical Engineering Department, Tamkang University, Taiwan, R.O.C.

Abstract— Frequency dependence problem of conducting cylinder buried in a half-space is investigated. A conducting cylinder of unknown shape is buried in one half-space and scatters the incident wave from another half-space. By using measured scattered field, the image problem is reformulated into an optimization problem and solved by the genetic algorithm. Frequency dependence on image reconstruction is investigated and numerical results show that the reconstruction is quite good in the resonant frequency range. On the contrary, if the frequency is too high or too low, the reconstruction becomes bad. It is worth noting that the present work provides not only comparative information but quantitative information.

1. INTRODUCTION

The electromagnetic inverse scattering problem of conductors has been a subject of considerable importance in remote sensing and noninvasive measurement. In the past 20 years, many rigorous methods have been developed to solve the exact equations [1–9]. However, inverse problems of this type are difficult to solve because they are ill-posed and nonlinear [10]. As a result, many inverse problems are reformulated into optimization ones and then numerically solved by different iterative methods such as the Newton-Kantorovitch method [2, 3], the multifrequency method [4–7], multiscale approach [8] and the Jump-Diffusion algorithm [9]. Most of these approaches employ the gradient-based searching scheme to find the extreme of the cost function, which are highly dependent on the initial guess and usually get trapped in the local extreme. The genetic algorithm [10] is an evolutionary algorithm that uses the stochastic mechanism to search through the parameter space. As compared to the gradient-based searching techniques, the genetic algorithm is less prone to converge to a local extreme. This renders it an ideal candidate for global optimization. A few papers had applied the genetic algorithm to reconstruct the shape of a conductor [11–15].

In this paper, frequency dependence on image reconstruct for a buried conducting cylinder is presented. The SSGA is used to reconstruct the shape of a buried scatterer. In Section 2, the theoretical formulation is briefly presented. Numerical results for different frequencies of incident waves are given in Section 3. Finally, conclusions are drawn in Section 4.

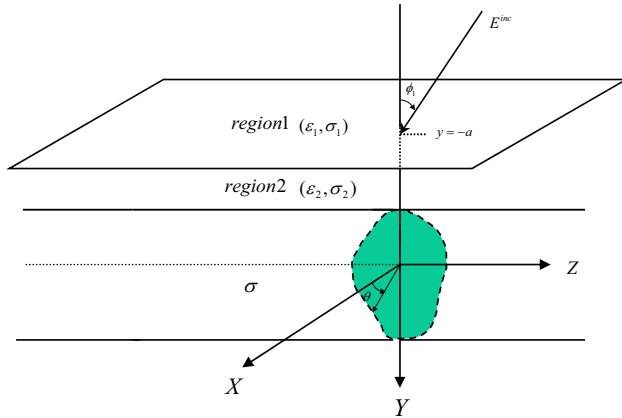


Figure 1.

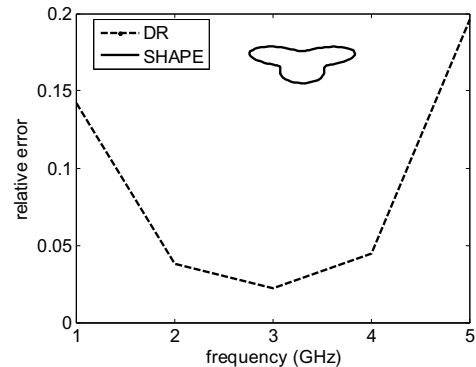


Figure 2.

2. THEORETICAL FORMULATION

Let's consider a conducting cylinder buried in a lossy homogeneous half-space, as shown in Fig. 1. The media in regions 1 and 2 are characterized by the permittivity and conductivity (ε_1, σ_1) and (ε_2, σ_2), respectively, while the permeability μ_0 is used for each region, i.e., only non-magnetic media are concerned here. The cross section of the cylinder is described by polar coordinates in the xy plane through the shape function $\rho = F(\theta)$. The cylinder is illuminated by a plane wave with time dependence $\exp(j\omega t)$, of which the electric field is assumed parallel to the z -axis (i.e., transverse magnetic or TM polarization). Let E^{inc} denote the incident E field from region 1 to region 2 with incident angle ϕ_1 . By using the induced current concept, the scattered field can be expressed as the integral of the two-dimensional Green's function multiplies by the induced surface current density, which is proportional to the normal derivative of the electric field on the conductor surface [3, 12]. As a result, for the direct problem, given the shape of the object, we can use the boundary condition to solve the surface current density, then calculate the scattered field by using the two dimensional half-space Green's function. For numerical calculation of the direct problem, the contour of the object is first divided into sufficient small segments so that the induced surface current density can be considered constant over each segment. Then the moment method is used to solve the equations with a pulse basis function for expanding and Dirac delta function for testing.

Let us consider the following inverse problem: given the scattered field, determine the shape $F(\theta)$. Here the shape $F(\theta)$ is assumed to be star-like. In other words, $F(\theta)$ can be expanded as:

$$F(\theta) = \sum_{n=0}^{N/2} B_n \cos(n\theta) + \sum_{n=1}^{N/2} C_n \sin(n\theta) \quad (1)$$

where B_n and C_n are real coefficient to be determined, and N is the number of unknowns for shape function of the object. In the inversion procedure, the SSGA is used to minimize the root mean square error of the measured scattered field and the calculated scattered field, through three genetic operators: reproduction, crossover and mutation. When the root mean square error changes by less than 1% in two successive generations, the SSGA is terminated and a solution is then obtained. Note that the regularization term can be added to avoid ill-conditioned problems. Please refer to the reference [11] for detail.

3. NUMERICAL RESULTS

Let us consider a conducting cylinder buried in a lossless half-space as Fig. 1. The permittivity in region 1 and region 2 is characterized by ε_0 and $2.56\varepsilon_0$ respectively. A TM polarization plane wave of unit amplitude is incident from region 1. The frequency of the incident wave is chosen to be 1 GHz, 2 GHz, 3 GHz, 4 GHz and 5 GHz. The object is buried at a depth 0.1 m and the scattered field is measured on a probing line along the interface between region 1 and region 2. Our purpose is to reconstruct the shape of the object by using the scattered field at different incident angles. To reconstruct the shape of the object, the object is illuminated by incident waves from three different directions and 20 measurement points at equal spacing are used along the interface for each incident angle. There are 60 measurement points in each simulation. The measurement is taken from $x = 0$ to 0.2 m for incident angle $-\pi/3$, from $x = -0.1$ to 0.1 m for incident angle 0, and from $x = -0.2$ to 0 m for incident angle $\pi/3$. To save computing time, the number of unknowns is set to be 9. The population size is chosen as 100. The binary string length of the unknown coefficient, B_n and C_n , is set to be 16 bits. The binary string length of conductivity is also set to be 16 bits. In other words, the bit number of a chromosome is 144. The search range for the unknown coefficient of the shape function is chosen to be from 0 to 0.1. The extreme value of the coefficient of the shape function can be determined by the prior knowledge of the objects. The crossover probability and mutation probability are set to be 0.8 and 0.1 respectively. In our example, the shape function is chosen to be $F(\theta) = (0.027 + 0.01 \sin 3\theta) \text{ m}$. The reconstructed relative root mean square errors for the shape versus different frequencies are plotted in Fig. 2. It is found that the reconstruction for 1GHz and 5 GHz are poor, which the reconstruction for 2 GHz, 3 GHz and 4 GHz are fair. Roughly speaking, the reconstruction for 3 GHz is fairly satisfactory. Physically this can be explained by the fact that the information available from the shadow region decreases if the wave number increases. On the other hand, the scattering pattern becomes isotropic at very low frequencies and thus insensitive to the variation of shape resulting in large errors.

4. CONCLUSIONS

We have presented the effect of the incident frequency on the shape reconstruction for a buried conducting cylinder. It is found that the information available from the shadow region decreases if the wave number increases. On the other hand, the scattering pattern becomes isotropic at low frequencies and thus insensitive to the variation of shape resulting in larger errors. In other words, the reconstruction is good in the resonant frequency. It is worth noting that in these cases the present work provided not only comparative information but also quantitative information.

REFERENCES

1. Bucci, O. M. and G. Franceschetti, "On the degrees of freedom of scattered fields," *IEEE Transactions on Antennas and Propagation*, Vol. 37, 918–926, Jul. 1989.
2. Roger, A., "Newton-Kantorovich algorithm applied to an electromagnetic inverse problem," *IEEE Transactions on Antennas and Propagation*, Vol. 29, 232–238, Mar. 1981.
3. Chiu, C. C. and Y. W. Kiang, "Microwave imaging of multiple conducting cylinders," *IEEE Transactions on Antennas and Propagation*, Vol. 40, 933–941, Aug. 1992.
4. Chiu, C. C. and Y. W. Kiang, "Inverse scattering of a buried conducting cylinder," *Inverse Problem*, Vol. 7, 187–202, Apr. 1991.
5. Dennison, M. L. and A. J. Devaney, "Inverse scattering in inhomogeneous background media: II. Multi-frequency case and SVD formulation," *Inverse Problems*, Vol. 20, No. 4, 1307–1324, Aug. 2004.
6. Belkebir, K., R. Kleinmann, and C. Pichot, "Microwave imaging-location and shape reconstruction from multifrequency data," *IEEE Transactions on Microwave Theory and Techniques*, Vol. 45, 469–475, Apr. 1997.
7. Bucci, O. M., L. Crocco, T. Isernia, and V. Pascazio, "Inverse scattering problems with multifrequency data: Reconstruction capabilities and solution strategies," *IEEE Transactions on Geoscience and Remote Sensing*, Vol. 38, 1749–1756, Jul. 2000.
8. Baussard, A., "Inversion of multi-frequency experimental data using an adaptive multiscale approach," *Inverse Problems*, Vol. 21, S15–S31, Dec. 2005.
9. Nikolic, M. M., M. Ortner, A. Nehorai, and A. R. Djordjevic, "An approach to estimating building layouts using radar and jump-diffusion algorithm," *IEEE Transactions on Antennas and Propagation*, Vol. 57, No. 3, 768–776, Mar. 2009.
10. Goldberg, D. E., *Genetic Algorithm in Search, Optimization and Machine Learning*, Addison-Wesley, 1989.
11. Chiu, C. C. and P. T. Liu, "Image reconstruction of a perfectly conducting cylinder by the genetic algorithm," *IEE Proc. Microw. Antennas Propag.*, Vol. 143, 249–253, Jun. 1996.
12. Xiao, F. and H. Yabe, "Microwave imaging of perfectly conducting cylinders from real data by micro genetic algorithm couple with deterministic method," *IEICE Trans. Electron.*, Vol. E81-C, Dec. 1998.
13. Meng, Z. Q., T. Takenaka, and T. Tanaka, "Image reconstruction of two-dimensional impenetrable objects using genetic algorithm," *Journal of Electromagnetic Waves and Applications*, Vol. 13, No. 1, 95–118, 1999.
14. Qian, Z., Z. Ding, and W. Hong, "Application of genetic algorithm and boundary element method to electromagnetic imaging of two-dimensional conducting targets," *5th International Symposium on ISAPE*, 211–214, 2000.
15. Li, C. L., S. H. Chen, C. M. Yang, and C. C. Chiu, "Image reconstruction for a partially immersed perfectly conducting cylinder using the steady state algorithm," *Radio Science*, Vol. 39, RS2016, Apr. 2004.

Far-field Diffraction Patterns Evolution of a Gaussian Laser Beam due to Thermo-optical Effect in Metal Nanocolloids

Yuri E. Geints¹, Nicolay S. Panamarev², and Aleksey A. Zemlyanov²

¹Zuev Institute of Atmospheric Optics SB RAS, 1 Zuev square, Tomsk 634021, Russia

²Siberian Physical and Technical Institute, 1 Novosobornaya square, Tomsk 634050, Russia

Abstract— We report on the results of our systematic experimental investigations of the diffraction pattern (DP) formed due to CW low-power laser beam propagation through a cell with metal nanocolloids (NC). We have used different types of metal NC and for the first time have studied thoroughly the temporal dynamics and structural characteristics of far-field DP. The experimental data has shown that in the observation plane the dynamic diffraction structure was formed. It consists of several coaxial light and dark rings, whose diameters and number increased with time and varied depending on the type and concentration of the colloidal solution. The stable diffraction pattern with the fixed number of fringes is formed at the screen for periods of several seconds from the beginning of the exposure to laser radiation. The number of formed rings is inversely proportional to the optical thickness of the colloid and to the laser power also.

The experimental results have been interpreted theoretically from the viewpoint of thermal self-action of laser radiation in the absorbing medium. Colloidal silver nanoparticles serve as centers which efficiently absorb laser radiation and transfer the heat to the host liquid due to the thermal conductivity, thus giving rise to the temperature gradient across the laser beam. Since the thermo-optical nonlinearity of the liquid leads to the decrease in the refractive index of the medium at the places, where the medium temperature is higher, the nonlinear negative phase shift appears in the zone of the beam action. This phase shift acts on the radiation as a defocusing aberration lens and leads to the formation of fringes observed in the far-field diffraction zone.

Based on the analytical solution to the heat transfer equation of a homogeneous medium with a thermal source caused by the linear absorption of laser radiation, we have calculated the spatiotemporal profiles of temperature increments of silver nanocolloids. To determine the structure of the far field, we used the Fresnel-Kirchhoff integral in Fraunhofer approximation. This allowed us to derive formulae, which related the number of bright rings in the observation plane and the angular size of the entire diffraction pattern to thermophysical characteristics of the liquid solvent, volume fraction of the metal sol, and parameters of the laser beam.

Metal nanocolloids (NCs) constitute suspended in liquid metal nanometer-sized particles and attract an increasing interest due to their unique physical-chemical and optical properties distinguishing from that of both bulk metal and pure liquid [1, 2]. NCs are characterized by the pronounced optical nonlinearity which manifests itself at rather low laser intensity ($\sim 1 \text{ W/cm}^2$) [2] and leads to the NC refractive index dependence on laser power. This, in turn, is responsible for the spatial self-modulation of optical wave upon its propagation through the colloidal medium. Various nonlinear optical effects such as self-focusing, soliton formation, self-channeling of the laser beam, supercontinuum generation, as well as thermal lensing and defocusing are observed in NCs. The latter physical phenomenon, the thermal lensing effect, is of particular interest due to the prospects of optical limiters (OL) designing.

The physical principle of OL operation is based on the effect of a self-induced negative thermal lens formed in an absorbing colloidal medium due to its heating by radiation. Colloidal particles possess the optical absorption several orders of magnitude higher than the host liquid and serve as localized heat sources distributed over the entire NC volume thus decreasing significantly the energy threshold needed for light thermal defocusing. The thermal lens is formed in a colloidal medium during the finite time interval and leads to the so-called self-diffraction (the thermal blooming) of radiation and to the formation of interference fringes in the far-field. The spatial structure of these diffraction patterns (DPs) and its dependence on the laser power and on the conditions of laser beam focusing also were the subject of numerous papers [3, 4]. Surprisingly, the transient stages of laser-induced thermal lens formation in metal colloids, the time interval needed for the build-up of stationary far-field intensity distribution remained underexplored yet, and this was the motivation for our work.

In this report, we present the results of our systematic experimental investigations of the diffraction pattern (DP) formed due to CW low-power laser beam propagation through a cell with metal nanocolloids (NC).

The experimental set-up is presented in Figure 1. Diffraction patterns from colloids were studied according to the following scheme. The radiation from a cw solid-state laser (LCS-DTL-317, wavelength $\lambda = 532\text{ nm}$, power 20 mW, beam diameter 1 mm, angular divergence 0.6 mrad) was launched onto the cell with NC solution. The projection on the white screen of the beam passed through NC was taken by Nikon D3000 photo camera and the temporal dynamics was recorded by the video camera. The distance (D) from the cell to the screen was 8 m.

We used commercially fabricated nanopowders consisting of nearly spherical particles having different sizes from tens to hundreds nanometers (in diameter) and different degree of aggregation. Nano-sized stuffs (collargol, Al, Cu, Ni, Zn, TiO_2) were suspended in ethanol, acetone, glycerin, and distilled water. The thicknesses of used optical cells (excluding walls) with NC were 100 μm , 630 μm , 2 mm, 3.2 mm, and 10 mm. The every cell was tested on all colloid samples. We have used only fresh solutes ($< 10\text{ min}$) because sol particles tend to aggregate and sediment with time.

The experimental data has shown that in the observation plane the dynamic diffraction structure was formed. It consists of several coaxial light and dark rings, whose diameters and number increased with time and varied depending on the type and concentration of the colloidal solution. The stable diffraction pattern with the fixed number of fringes is formed at the screen for periods of several seconds from the beginning of the exposure to laser radiation (see Figure 2). We have revealed that the observed DPs depend significantly on the laser beam power, on the concentration and size of nanoparticles, and on the cell thickness also. At the same time, no significant dependence of far-field structure on the nanoparticle material and type of liquid solvent (except for water) was found. When the water solution of any type of metal nanoparticles (for al width of the used optical cells) were irradiated by laser no diffraction fringes were observed.

The DP build-up time, e.g., the time elapsed from the onset of cell illumination by laser radiation to the moment where the stable DP is observed on the screen, in this situation has the values of about 1.5–2 s and was approximately the same for all investigated colloidal composition. The diameter of the most outer light ring d_0 as a function of the laser power P_0 is shown in Figure 3.

The experimental results we will interpret theoretically from the viewpoint of thermal self-action of laser radiation in the absorbing medium. We will use the free-space Fresnel-Kirchhoff diffraction integral, which at the Fraunhofer approximation allows one to calculate the transverse spatial distribution of the optical field intensity I in the far-field diffraction zone. Under the conditions of

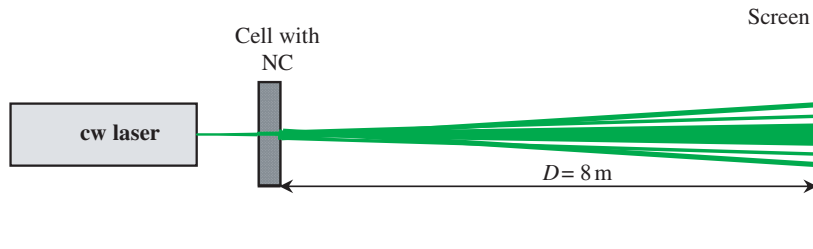


Figure 1: The experimental set-up.

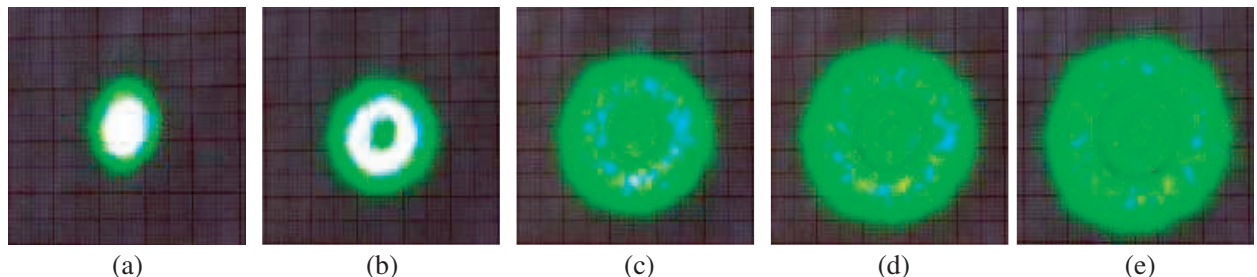


Figure 2: DP evolution of a laser beam passed through a cell (thickness 2 mm) with the glycerin solution of collargol (silver concentration 0.001%): (a) 0.01 s, (b) 0.15 s, (c) 0.5 s, (d) 1.1 s, (e) 3.5 s after beam passage.

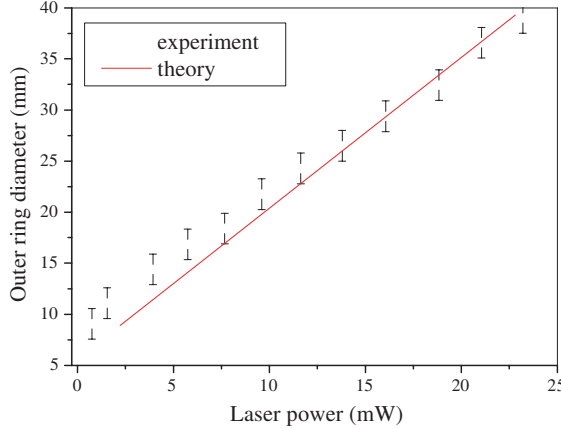


Figure 3: Diameter of the outer bright ring as a function of laser power in collargol-alcohol solution.

the cylindrical symmetry of the problem and an *optically thin* medium, we have

$$I(\beta, t) = \frac{\pi c}{2(\lambda D)^2} \exp(-\tau) \left| \int_0^\infty E_0(r) \cdot \exp(-i\Delta\varphi(r, t)) J_0(kr\beta) r dr \right|^2, \quad (1)$$

where $E_0(r)$ is the beam amplitude profile at the optical cell entrance plane; $\beta = r'/D$ is the far-field diffraction angle, r' , r are the radial coordinates in the observation plane (screen) and in the cell plane, respectively; D is the distance to the screen; $k = 2\pi/\lambda$ is the wave number; c is the speed of light in vacuum; t is time; $J_0(x)$ is the zero-order cylindrical Bessel function; $\Delta\varphi$ is the nonlinear phase-shift acquired by the beam in NC; τ is the optical thickness of the medium in cell. The complex field amplitude E_L can be found, neglecting the diffraction inside the cell.

During the thermal self-action of a light beam, the refractive index of the NC solution changes due to the temperature variation $\Delta T(r, t)$: $n_c(r, t) = n_c^0(r) + \frac{dn}{dT}\Delta T(r, t)$, where dn/dT is the thermo-optical coefficient of the medium. For most liquids $dn/dT < 0$, and therefore their heating by laser radiation leads to the local decrease in the refractive index, and hence, the defocusing of laser beam is realized. Thus, for instance, pure water has $dn/dT \approx -10^{-4} \text{ K}^{-1}$, whereas for ethanol this parameter is four times higher, $dn/dT \approx -4 \cdot 10^{-4} \text{ K}^{-1}$.

The spatiotemporal dynamics of the temperature field of a thin colloid layer exposed to a laser beam with the intensity I will be considered according to the two-dimensional heat transfer equation of an infinite single-phase medium. In the absence of convection and anisotropy of thermophysical properties of the medium, this equation in the Cartesian coordinate system has the following form:

$$\frac{\partial T(\mathbf{r}, t)}{\partial t} = \chi_T \Delta_{\perp} T(\mathbf{r}, t) + \frac{\alpha}{\rho C_p} I(\mathbf{r}, t), \quad (2)$$

where $\mathbf{r} = (x, y)$, α , ρ , C_p , χ_T are volume absorption coefficient, density, specific heat capacity at constant pressure and thermal diffusivity of colloidal medium, respectively. The solution to this equation is given in terms of the exponential integral $Ei(x)$ as follows:

$$T(r, t) = \frac{P_0 \alpha}{4\pi\Lambda} \left[Ei\left(-\frac{r^2}{R_0^2}\right) - Ei\left(-\frac{r^2}{R_0^2(1+t/\chi_T)}\right) \right]. \quad (3)$$

Here Λ is the thermal conductivity of a colloid, $P_0 = \pi R_0^2 I_0$ represents the power of laser radiation at the entrance plane of the colloidal cell.

Using Equations (1)–(3), we have calculated the temporal evolution of the far-field intensity of a laser beam passed through the silver colloids. The results of these calculations are shown in Figures 4(a) to 4(d) for the transverse intensity profile formed at a distance $D = 8 \text{ m}$ from the optical cell. Intensity value in every figure is normalized to its maximum.

It can be seen that similarly to our experimental results the numerical simulation gives the increase in the number and size of interference fringes with time. The stable DP on the screen

consisting of three pronounced light rings and the dark central zone is formed for the time interval of about 3–4 s and then remains nearly unchanged till the end of observation (~ 2 min). The diameter of the outer light ring in this case is ~ 3.5 cm, and that of the inner one is 1 cm. This result correlates well with the experimentally observed intensity patterns.

At the center of DP we first see the intensity maximum, which corresponds to a bright spot in two-dimensional profiles (Figures 4(a), 4(b)). Then the axial maximum decreases (Figure 4(c)) and finally the central dark spot is appeared (Figure 4(d)). The central dark spot is characteristic just for the case of the thermal self-action of initially divergent (or collimated) laser beam, and it plays a key role in OL functioning.

The number of bright rings observed in the screen characterizes the maximal phase shift $\Delta\varphi_{\max}$ acquired by the radiation in the nonlinear medium. According to the data of Ref. [3] under the conditions of thermal defocusing of the beam, every new bright ring in the DP intensity profile appears as the optical wave phase increases by a value being a multiple of 2π , which corresponds to the constructive interference of radiation fluxes coming from spatial zones of the beam with a phase shift of one optical cycle. Thus, the approximate number of bright rings N_R is determined as: $N_R = \lfloor |\Delta\varphi_{\max}| \rfloor / 2\pi$, where the angle brackets $\lfloor \cdot \rfloor$ denote the integer part of a value. Peak phase shift for the calculations shown in Figure 4 equals $\Delta\varphi_{\max}/2\pi \approx -4.2$, thus indicating the formation of four bright rings clearly visible in Figure 2(d).

Using the solution for the temperature of the colloid (Equation (3)), we can deduce that the

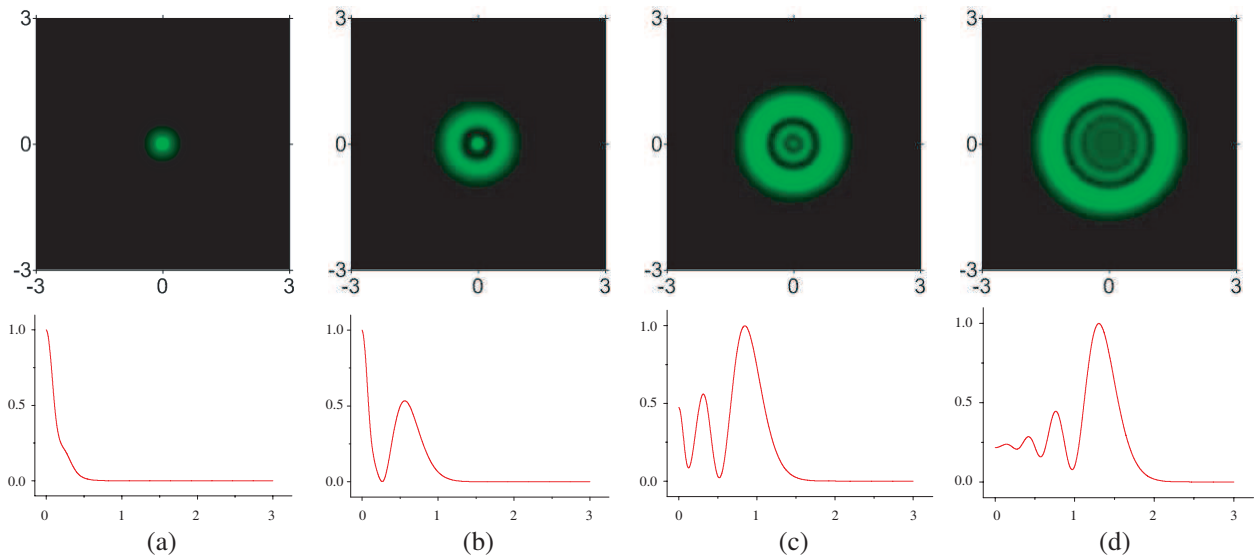


Figure 4: Calculated two-dimensional and corresponding radial transverse distributions of the normalized laser intensity in the far-field diffraction zone (on the screen) of the silver NC cell (alcohol solution, $L = 0.63$ mm, $\delta = 10^{-4}$), at different time instants: (a) 0.25, (b) 0.75, (c) 2.0, and (d) 4 s. The scales for x and y axes are in cm.

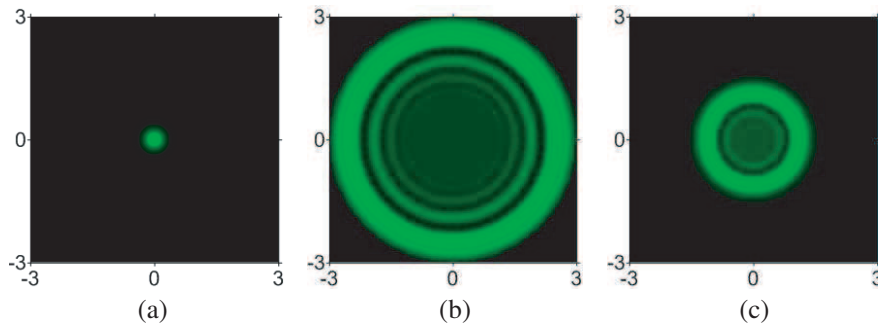


Figure 5: Calculated transverse intensity distribution of a laser beam passed through the layer ($\delta = 10^{-4}$, $L = 650$ nm) of colloidal silver in (a) water, (b) alcohol, and (c) glycerin. The scales for both x and y axes are in cm.

maximal number of observed bright rings in the stable DP is expressed as

$$N_R \approx \left\lfloor \frac{P_0 \tau_{eff}}{4\pi\lambda\Lambda} \left| \frac{dn}{dT} \right| \right\rfloor, \quad (4)$$

and is inversely proportional to the beam power absorbed by the medium (here, $\tau_{eff} = \alpha_{eff}L = 1 - \exp(-\tau)$).

Figure 5 demonstrates the influence of the solvent type on the far-field DP. The calculations were performed for fixed laser power $P_0 = 20$ mW and for the colloidal solution of collargol in three different liquids (water, alcohol, and glycerin) possessing similar refractive indices at the wavelength of 532 nm, but different physical properties.

It can be seen from the figures that, among three considered colloids, the alcohol solution produces the largest number of bright rings (five) and correspondingly the widest diffraction pattern. The aqueous solution with analogous silver particles concentration gives rise to a single bright central spot, while the glycerin colloid leads to three rings formation on the screen.

This fact becomes clear if we recall the Equation (4) which gives the estimation of the rings number N_R . Actually, this equation includes the combination of physical properties of the liquid basis $\mathbf{M} = (\Lambda^{-1} |dn/dT|)$, which the number of rings is proportional to. The corresponding calculations using tabulated data give the following values of M -parameter (in mm/W): $\mathbf{M} = 0.15$ (H_2O), 2.2 (C_2H_5OH), and 0.8 ($C_3H_8O_3$). Thus, ethanol having among all studied solvents the lowest thermal conductivity and simultaneously the highest thermo-optical coefficient favors the deeper spatial phase modulation ($\Delta\varphi_{max}$) of the optical wave propagating through the colloidal cell. In accordance with the M -parameter values, water possesses less thermo-optical activity than ethanol does and therefore, no fringes at $P_0 = 20$ mW were observed from aqueous colloids during the experiments. On the contrary, the DP build-up time t_{DP} which can be defined as $t_{DP} = 5t_\chi$, for all considered liquids has close values, $t_{DP} \approx 2 \div 3$ s. So, that is why we have not observed any substantial dependence of the DP transition time on the NC type.

REFERENCES

1. Kalele, S., S. Gosavi, J. Urban, and S. K. Kulkarni, *Current Science*, Vol. 91, 1038, 2006.
2. Ganeev, R. A., A. I. Ryasnyansky, S. R. Kamalov, M. K. Kodirov, and T. Usmanov, *J. Phys. D: Appl. Phys.*, Vol. 34, 1602, 2001.
3. Deng, L., K. He, T. Zhou, and C. Li, *J. Optics A: Pure Appl. Opt.*, Vol. 7, 409, 2005.
4. Mao, Z., L. Qiao, F. He, Y. Liao, C. Wang, and Y. Cheng, *Chin. Opt. Lett.*, Vol. 7, 949, 2009.

An Improvement of QR-M MLD for MIMO Wireless Communications

Tatsuki Fukuda, Tadaharu Takahashi, and Hua-An Zhao

Department of Computer Science and Electrical Engineering, Kumamoto University, Japan

Abstract— Recently, we can see a lot of wireless systems in many kind of products such as computers, broadcast, and mobile phones. It means that we need higher-speed wireless systems. There are many technique for higher wireless communications, especially a lot of researches for the signal detection technique. In this paper, we propose a new detection method based on the QRM MLD, which is based on the algorithm of QR-M MLD with a tree structure. The nodes on first level represent the symbol candidate of the symbol transmitted by N_T -th antenna. The nodes on d -th level represent the candidates of the symbol transmitted from $(N_T - d + 1)$ -th antenna. Each nodes have the M child nodes which represent the M constellation points, respectively. MLD method check the all of the nodes from first level to N_T -th level, so it takes a lot of times. QRM MLD method select M nodes for each level by selecting the nodes which have lower metrics. Our method selects kM nodes by selecting k nodes for each signal point, which have smaller metrics in the set of $N(S)$ in the level. Here we refer to nodes corresponding to the constellation point S as $N(S)$. By this method, we have no chance to delete the correct symbol candidate for all level, and we think the bit error ratio (BER) performance should get better than the other method.

1. INTRODUCTION

Recently, the Multiple-Input Multiple-Output (MIMO) systems employing multiple N_T transmit antennas and N_R receive antennas are watched with keen interest as important techniques for the forefront wireless communication systems. The performances of MIMO systems are often evaluated in terms of the bit error ratio (BER) performance, so the detection method is important for improving MIMO systems. Maximum Likelihood Detection (MLD) was proposed in [1] and its BER performance is the best in detection algorithms, but its computational complexity is an exponential order. To improve the computational complexity of MLD, the QRM-MLD was proposed in [2] and has good BER performance. However, the computational complexity of QRM-MLD needs more improvement, so the QRM-MLD with adaptive control of surviving symbol replica candidates (called AC-QRM-MLD hereafter) was proposed in [3]. The AC-QRM-MLD uses the threshold to determine the surviving symbol candidates in order to improve the computational time. However, the probability to delete the correct candidate with this threshold in earlier detection stage is so high that the BER performance becomes debasement at high SNR. Also QRM-MLD can delete the correct candidate in earlier stage because the method select M nodes whose error is smaller than the rest. In this paper, we propose a new method based on the QRM-MLD method. Our method doesn't delete the correct candidate in all detection stage, so the effect of error propagation becomes low. It follows the BER performance should be better than QRM-MLD and AC-QRM-MLD method.

2. PRELIMINARIES

The MIMO system we assumed is shown in Fig. 1. The system has N_T transmit antennas and N_R receive antennas.

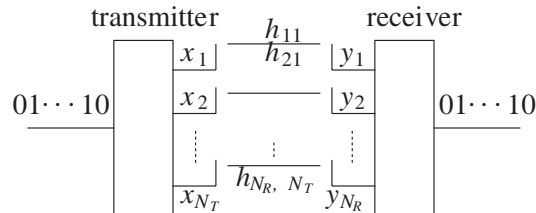


Figure 1: The concept of the MIMO systems.

The relationship between the transmitted signal vector \mathbf{X} and the received signal vector \mathbf{Y} in a general MIMO system can be expressed compactly in matrix form as follows:

$$\mathbf{Y} = \mathbf{H}\mathbf{X} + \mathbf{N} \quad (1)$$

where \mathbf{H} denotes the channel matrix and \mathbf{N} denotes the noise vector. Many detection methods were proposed, so we show you some of them.

2.1. MLD

Maximum Likelihood Detection (MLD) is the best detection method in view of the BER performance, but it takes exponential time.

For all combination of the transmitted symbols candidates, the method calculates the metric based on the following equation.

$$\text{metric} = |\mathbf{Y} - \mathbf{HC}|^2 \quad (2)$$

where $|\mathbf{D}|^2$ denotes the squared Euclidean distance of \mathbf{D} and \mathbf{C} denotes the symbol candidates $\mathbf{C} = [c_1 \ c_2 \ \dots \ c_{N_T}]$ whose c_k is the candidate of x_k . Metric become the smallest when \mathbf{C} is equal to \mathbf{X} , so MLD detects the symbols by selecting \mathbf{C} whose metric is minimum. The computational time of MLD is exponential order because the method calculates the metrics for all combination of c_k , so improved MLD methods reducing computational complexity were proposed.

2.2. QRM-MLD

MLD using QR decomposition and the M algorithm (QRM-MLD) can reduce computational complexity of MLD. In QRM-MLD, the signals are detected from x_{N_T} to x_1 , so the process of detecting x_{N_T} , x_{N_T-1} , ..., and x_1 are referred to as first stage, second stage, ..., N_T -th stage. QRM-MLD detects signals by the following process.

1. Perform QR decomposition for the estimated channel matrix \mathbf{H} and the matrix \mathbf{Q} and \mathbf{R} are obtained, then Eq. (1) can be rewritten as the following equation

$$\mathbf{Z} = \mathbf{RX} + \mathbf{N}' \quad (3)$$

where $\mathbf{Z} = \mathbf{Q}^H \mathbf{Y}$, $\mathbf{N}' = \mathbf{Q}^H \mathbf{N}$, and \mathbf{Q}^H denotes the hermitian matrix of \mathbf{Q} , respectively. As you can see, z_{N_T} has nothing to do with the signals from x_1 to x_{N_T-1} because \mathbf{R} is an upper triangular matrix, so the signals are detected from x_{N_T} .

2. • Detection of x_{N_T}
 - (a) Set a column vector of N_T elements \mathbf{C}_{init} as the zero vector. For all symbol candidates of x_{N_T} , replace the N_T -th element of \mathbf{C}_{init} with one of the symbol candidates and the replaced vector is referred to as \mathbf{C}_{N_T} . With \mathbf{C}_{N_T} made of one of the symbol candidates, calculate the branch metric $Met_B(N_T)$ based on the following equation.

$$Met_B(N_T) = |z_{N_T} - \mathbf{R}_{N_T} \mathbf{C}_{N_T}|^2 \quad (4)$$

where \mathbf{R}_{N_T} denotes the N_T -th row vector of \mathbf{R} .

- (b) Select one symbol candidate which has the smallest $Met_B(N_T)$ of all candidates (selected candidate is referred to as the surviving symbol candidate).

- Detection of $x_i (i = N_T - 1, N_T - 2, \dots, 1)$

- (a) For all surviving symbol candidates, replace the i -th element of \mathbf{C}_{i+1} with one of the symbol candidates of signal x_i and the replaced vector is referred to as \mathbf{C}_i . With \mathbf{C}_i made of one of the symbol candidates of x_i , calculate the branch metric $Met_B(i)$ based on the following equation.

$$Met_B(i) = |z_i - \mathbf{R}_i \mathbf{C}_i|^2 \quad (5)$$

After that, calculate the accumulated branch metric $Met_A(i)$ which is the sum of the branch metrics from $Met_B(N_T)$ to $Met_B(i)$.

- (b) Select M symbol candidates which have the smaller $Met_A(i)$ in all candidates.

The number of calculations of branch metrics is MS where M is the number of surviving symbol candidates at the detection process of each x_i and S denotes the number of candidates for each symbol. The computational complexity of QRM-MLD is lower than that of MLD and the BER performance of QRM-MLD is good.

2.3. AC-QRM-MLD

Hereafter, we refer to the QRM-MLD in Section 2.2 as the original QRM-MLD. QRM-MLD with adaptive control of surviving symbol replica candidates (AC-QRM-MLD) can reduce the computational complexity more than the original QRM-MLD.

The detection process of AC-QRM-MLD is like that of the original QRM-MLD. The difference between them is the process of selecting surviving symbol candidates.

The surviving symbol candidates of the AC-QRM-MLD are the candidates whose accumulated branch metrics are smaller than the threshold, while the surviving symbol candidates of the original QRM-MLD are selected M candidates whose accumulated branch metrics are smaller than the others.

The threshold at m -th stage proposed in [3] is expressed by

$$\Delta_m = E_{m,\min} + X\sigma^2 \quad (6)$$

where $E_{m,\min}$ denotes the minimum accumulated metric in the m -th symbol candidates, X denotes the predetermined fixed value, and σ^2 denotes the estimated interference plus noise power.

When SNR becomes high, the BER performance becomes bad because that the value $X\sigma^2$ becomes small and that the probability of deleting the correct symbol candidate in earlier stage becomes high.

3. PROPOSED METHOD

We propose the new detection method based on the QRM-MLD method. As I explained in Section 2.2, the method selects M candidates in each detection stage. However, when the detector selects only incorrect candidates by chance in earlier stage, the performance may become bad due to the error propagation. Our method prevent the detector from discarding the correct candidate in each stage.

Our method detects symbols as bellow.

1. Perform QR decomposition for the estimated channel matrix \mathbf{H} and the matrix \mathbf{Q} and \mathbf{R} are obtained, then Eq. (1) can be rewritten as the following equation

$$\mathbf{Z} = \mathbf{RX} + \mathbf{N}' \quad (7)$$

where $\mathbf{Z} = \mathbf{Q}^H \mathbf{Y}$, $\mathbf{N}' = \mathbf{Q}^H \mathbf{N}$, and \mathbf{Q}^H denotes the hermitian matrix of \mathbf{Q} , respectively. As you can see, z_{N_T} has nothing to do with the signals from x_1 to x_{N_T-1} because \mathbf{R} is an upper triangular matrix, so the signals are detected from x_{N_T} .

2. • Detection of x_{N_T}
 - (a) Set a column vector of N_T elements \mathbf{C}_{init} as the zero vector. For all symbol candidates of x_{N_T} , replace the N_T -th element of \mathbf{C}_{init} with one of the symbol candidates and the replaced vector is referred to as \mathbf{C}_{N_T} . With \mathbf{C}_{N_T} made of one of the symbol candidates, calculate the branch metric $Met_B(N_T)$ based on the following equation.

$$Met_B(N_T) = |z_{N_T} - \mathbf{R}_{N_T} \mathbf{C}_{N_T}|^2 \quad (8)$$

where \mathbf{R}_{N_T} denotes the N_T -th row vector of \mathbf{R} .

- (b) Select one symbol candidate which has the smallest $Met_B(N_T)$ of all candidates (selected candidate is referred to as the surviving symbol candidate).

- Detection of x_i ($i = N_T - 1, N_T - 2, \dots, 1$)
 - (a) For all surviving symbol candidates, replace the i -th element of \mathbf{C}_{i+1} with one of the symbol candidates of signal x_i and the replaced vector is referred to as \mathbf{C}_i . With \mathbf{C}_i made of one of the symbol candidates of x_i , calculate the branch metric $Met_B(i)$ based on the following equation.

$$Met_B(i) = |z_i - \mathbf{R}_i \mathbf{C}_i|^2 \quad (9)$$

After that, calculate the accumulated branch metric $Met_A(i)$ which is the sum of the branch metrics from $Met_B(N_T)$ to $Met_B(i)$.

- (b) For candidates corresponding to the same symbol, select k candidates which have the smaller $Met_A(i)$ in the group whose elements indicate the same symbol.
(There are kM surviving symbol candidates.)

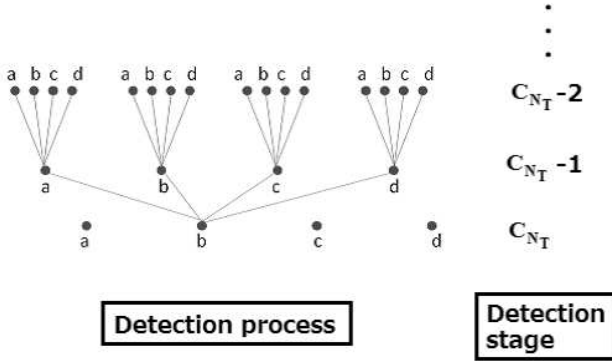


Figure 2: The process of detection with our method.

Figure 2 shows the concept of our method. Our method can be explained with a tree structure. In Fig. 2, the nodes are labeled by the alphabet of a, b, c, and d which correspond to the signal points of transmitted signal. In the first stage, it means the detection of x_{NT} , we select one candidate node labeled b, and proceed to the next stage which is the detection of x_{NT-1} . In second stage, there are four candidates, and there are one candidate for each signal point of a, b, c, and d, so that all of candidates are surviving symbol candidates. In third stage, there are 16 nodes, which are four nodes for each signal point. At first, we compare the metrics of the nodes which are labeled a, and select k candidates which have the lower metric. Next, we compare the nodes which are labeled b. Finally we can obtain $4k$ nodes. These candidates are the surviving symbol candidates of this stage. After that, we select the nodes in each stage by the same algorithm. In the last stage, we select one node which has a smallest accumulated branch metric and we track back from the node to the root node in order to get the detected symbols.

As you can see, at least one node is survived for each signal point. It means that the probability of discarding correct candidates in earlier stage should becomes low, and the effects of error propagation should becomes low.

4. CONCLUSION

In wireless communication systems, we demand the higher data rate with low power. The MIMO systems can transmit the signals with multiple antennas, so lots of data can transmit, but the receiver have to detect the signals. It follows that the detection method is very important in order to realize the higher data rate wireless systems.

MLD method is the best method in view of BER performance, but it need large amount of time. QRM-MLD method can detect with lower computational complexity than MLD. However, QRM-MLD method has the probability of discarding correct symbol candidate in earlier stage of detection, and it causes the error propagation.

Our method is based on the QRM-MLD method, so it needs less calculation time than MLD. QRM-MLD method select M candidates by selecting nodes which have the lower metric in each stage, while ours select k candidates for each symbol. With our method, we think that we can ease the probability of discarding correct candidate.

5. FUTURE WORK

In this paper, we propose the new detection method in order to prevent the detector from deleting the correct symbol candidate in earlier stage. We have to simulate MIMO systems with this method, and we have to prove that our method is superior to other detection method in view of BER performance.

REFERENCES

1. Zhu, X. and R. D. Murch, "Performance analysis of maximum likelihood detection in a MIMO antenna system," *IEEE Trans. Commun.*, Vol. 50, No. 2, 187–191, Feb. 2002.
2. Kim, K. J. and J. Yue, "Joint channel estimation and data detection algorithms for MIMO-OFDM systems," *Proc. 36th Asilomar Conf. Signals, Syst., Compute.*, 1857–1861, Nov. 2002.
3. Kawai, H., K. Higuchi, N. Maeda, and M. Sawahashi, "Adaptive control of surviving symbol replica candidates in QRM-MLD for OFDM MIMO multiplexing," *IEEE J. Sel. Areas Commun.*, Vol. 24, 1130–1140, 2006.

Experimental Validation that Optical Scintillation Obeys the Same Rules of Share Price Fluctuations

C. Yang^{1,2}, X. Li², W. Jiang², and C. Rao²

¹School of Science, Xi'an Shiyou University, Xi'an 710065, China

²Institute of Optics and Electronics, Chinese Academy of Sciences, Chengdu 610209, China

Abstract— It is traditionally treated that when optical wave propagates through a turbulent atmosphere, the optical signal fluctuates “randomly”. However, this paper validates that the optical signal fluctuations are not “random” by experiments. 3 optical propagation experiments are performed: ground-to-satellite-to-ground, horizontal propagation, and stellar observation. The experiments results show that: when it is observed in a small-scale period, the optical wave propagating through the atmosphere fluctuates “randomly”; but when it is observed in a large-scale period, the optical scintillation follows the same rules of share price fluctuations. Utilizing the techniques of share transaction to predict the optical scintillation has potential value for free-space optical communication system and laser transmitter system.

1. INTRODUCTION

Traditionally, optical wave propagating through a turbulent atmosphere experiences variation in its intensity [1]. It is called optical scintillation. Theoretically, optical scintillation is usually treated as “random” fluctuation, and is arrhythmic. Previously many experiments have confirmed this viewpoint. However all of the passed experiments analysis only focus on the quantity of the experimental data, and ignore to analyze the data from the viewpoint of a graph that the data appear as a whole. If we change to a new point of view, or say that if we observe the data from the viewpoint of a graph that the data take on, can we arrive at a new opinion about optical scintillation? Yes. This paper will answer this question.

Three optical propagation experiments are performed: ground-to-satellite-to-ground, horizontal propagation, and stellar observation. The experimental data show that the optical fluctuations obey some specific rhythm. It is noticed that the authors use a word “rhythm” instead of “law”. As we will point out as below that their rhythm has a great similarity with share prices fluctuations. The share prices fluctuations looks like the flood-tide and the ebb tide. Wave after wave and it is full of rhythm. The author will utilize the transaction techniques of shares market to analyze the experimental data.

2. THE TRANSACTION TECHNIQUES OF STOCKS MARKET

We start with a short introduction to the transaction techniques of stocks market [2]. Thus far the readers can have a clear understanding of how to use the techniques to analyze the experimental data. Share price usually moves in three kinds of trends: uptrend, downtrend and sideways trend [2], as shown in Fig. 1.

The trend is simply the direction of the market, which way it's moving. Generally the markets don't move in a straight line in any direction. In stead, they usually move in a series of zigzags. In these zigzags, there are a series of successive waves with fairly obvious peaks and troughs. It is the direction of those peaks and troughs that constitutes market trend.

Whether those peaks and troughs are moving up, down and sideways tell us the trend of the market. An uptrend is defined as a series of successively higher peaks and troughs; a downtrend is just the opposite, a series of declining peaks and troughs; horizontal peaks and troughs would define a sideways price trend.

The transaction techniques of stocks market can be concluded as follows: in an uptrend, hold on your shares; in a downtrend, hold on your money; in a sideways trend, just sell out your shares at the peaks and purchase them back at the troughs.

3. EXPERIMENTS

The three optical-link experiments include: 1, a laser propagates through an uplink, reflected back to the ground by a cube corner retro-reflector at the satellite, and then received by the ground telescope; 2, a laser propagates through a near-ground horizontal link; 3, stellar observation.

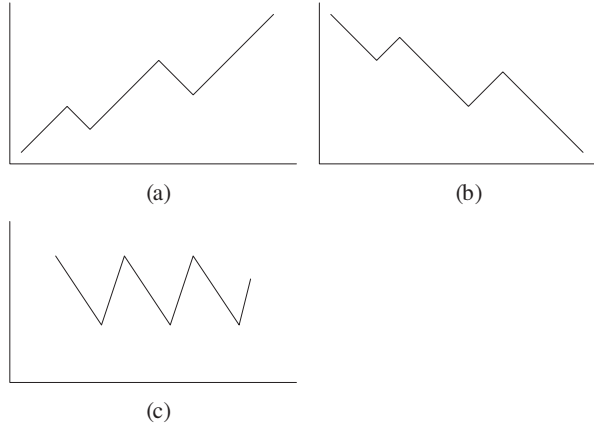


Figure 1: (a) Uptrend; (b) Downtrend; (c) Sideways trend.

The optical signals enter into the receiver aperture, and then focus on the image plane of the camera. This forms the speckle patterns of the signals. The sampling rate of the camera is 45 Hz.

Firstly, adds the intensity value of every pixel (the grey degree) in every frame image together, and the sum is the relative short-exposure intensity of this frame. In this paper, the sum's absolute value has no meanings. Repeat this work, and the total intensity of every frame image is obtained. Draw a picture, in which the vertical axis is about the intensity values, and the horizontal axis is about the time (the frame number). From which, the optical signal fluctuations can be shown clearly.

3.1. Ground-to-satellite-to-ground Propagation

In the first link, a laser is transmitted to a satellite. The distance between the ground telescope and the satellite is 550 km. A cube corner retro-reflector is installed at the satellite. And then, the laser is reflected back to the ground by the retro-reflector. In fact, this is a kind of link including an uplink and a downlink. We call it as the UD link. A group of data of the UD link is shown in Fig. 2.

In Fig. 2, the horizontal axis is the frame number, and the vertical axis is the total received intensity (in fact, it is the sum of the grey degree of the image). As to every frame image, a circle is used to label its intensity's value. Lines are used to connect the circles. It is shown in Fig. 2 that the optical signal runs in a sideways trend with horizontal peaks and troughs. The peaks and troughs limit the signal fluctuations range. Whenever the signals runs to the support or the resistance range, it means it is time to change direction.

3.2. Horizontal Link

In the second link, the optical signal propagates through a 2.4 km horizontal path. The atmospheric condition is weak turbulence. We call it as the H link. As shown in Fig. 3, it is the first group of data of the H link.

The authors are terribly astonished by the movement of the optical signal. This kind of movement is nearly the classic textbook behavior of stocks trading.

The 60-minute candlesticks pattern at the end of October of 2010 of one of the stocks of China (its code number is 000777) is shown in Fig. 4. It can be brought into comparison.

In Fig. 3, the optical signal builds in a bottom at the 17th frame, and then climbs up along a 45 degree uptrend channel. From the 33rd frame, the optical signal goes into a sideways trend fluctuation. In the standard textbook of stocks trading, this transverse fluctuation is called the air refueling. As shown in Fig. 3 by two bidirectional arrowheads, once it is sure to make a breakthrough upwards, the amount of increase after the breakthrough is nearly equal to that before the breakthrough. At the 39th frame, the optical signal selects the direction and moves upwards, and then at the 40th frame it steps back on the platform to ensure that the breakthrough is effective. Subsequently, the signal begins to accelerate upwards, and from the 44th frame it enters into a convergent triangle. The above actions are all classic behaviors of stocks.

The second group of data of the H link is shown in Fig. 5.

In Fig. 5, the optical signal is limited to move in a sideways trend with horizontal peaks and troughs. Sometimes the optical signal passes through the peaks and troughs, such as at the 14th

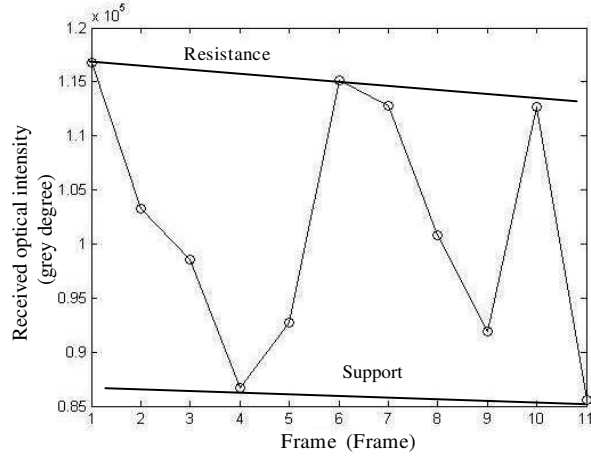


Figure 2: A group of data of the UD link.

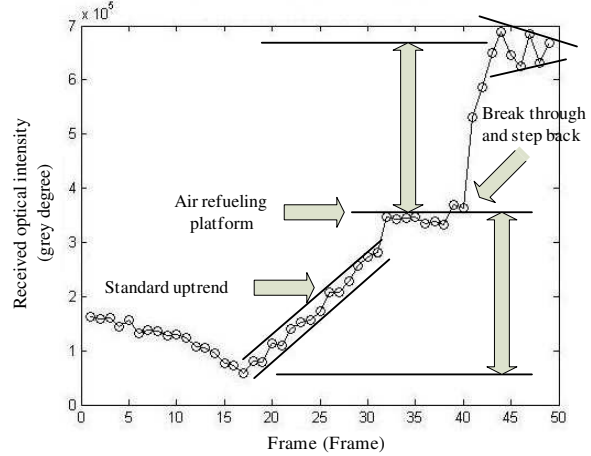


Figure 3: The first group of data of the H link.



Figure 4: The 60-minute candlesticks pattern of 000777.

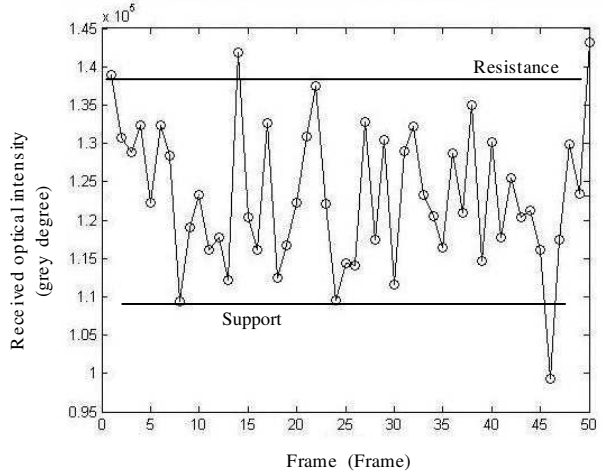


Figure 5: The second group of data of the H link.

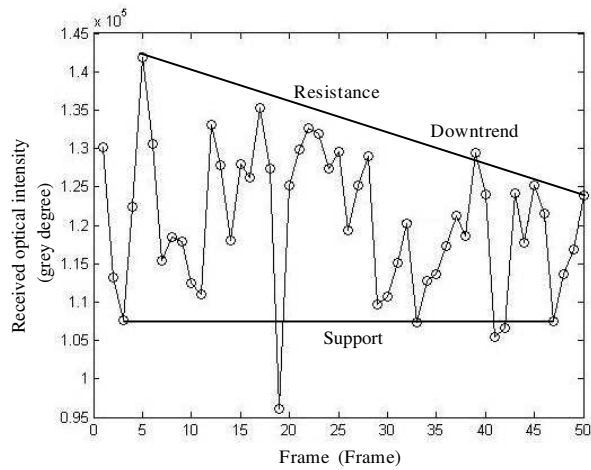


Figure 6: The third group of data of the H link.

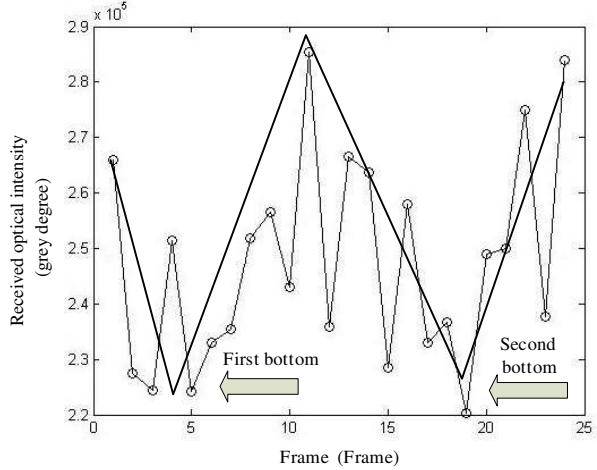


Figure 7: A group of data of the D link.

and the 46th frames. But they have been verified to be beguiling breakthroughs. These beguiling actions are also frequently used to manipulate the stocks market.

The third group of data of the H link is shown in Fig. 6.

The optical signal moves in a triangle downtrend pattern. Its oscillation amplitude becomes less

and less. It still has the same tradition of piercing the support to test the effectivity as it usually happens in the stocks market.

3.3. Stellar Observation

The third experiment is about the stellar observation. This is downlink propagation. We call it as the D link. A group of data of the D link is shown in Fig. 7.

In Fig. 7, this kind of pattern is usually called the double bottom or the W bottom. In the stocks market, it signifies that the stock price has touched the bottom area after a long time fall.

4. CONCLUSION

The authors find out that the optical scintillation obeys the same rules of the stock price fluctuations. If it is verified that it can be used to predict the scintillation in the future, it will have a great importance upon the signal's acquisition, tracking and pointing for the area of free-space optical communication.

If it is observed in a small-scale period, the optical scintillation is “random”. But the authors verify that if it is observed in a large-scale period, the optical signal fluctuations obey the same natural rules of the stocks market. Especially after the authors see Figs. 3, 5 and 6, they believe in this faith.

Why? It can be explained as follows: several factors contribute to the laser scintillation, including wind velocity, temperature, and atmospheric pressure. It is a basic phenomenon of the nature. Many factors contribute to the stocks prices, including money's flow direction, sudden news, international important affairs, and bargainers' psychology. It still is a natural phenomenon. Both must have obeyed some unknown natural laws.

REFERENCES

1. Andrews, L. C., R. L. Phillips, C. Y. Hopen, and M. A. Al-Habash, “Theory of optical scintillation,” *J. Opt. Soc. Am. A*, Vol. 16, No. 6, 1417–1429, 1999.
2. Murphy, J. J., *Technical Analysis of the Financial Markets*, New York Institute of Finance, New York, 1999.

The Analysis of Paired Unequally Spaced Reapeated Alternate Unequally Spaced Allocation Channels for FDM Lightwave System

Ashira Jumpates, Vissavavit Rachnarong, and Suthichai Noppanakeepong

Faculty of Engineering, Department of Telecommunication Engineering

King Mongkut's Institute of Technology Ladkrabang, Ladkrabang, Bangkok 10520, Thailand

Abstract— This paper proposes the new technique to improve the conventional techniques in the channel allocations, in order to reduce transmission loss, in case of there are a large number of channel and each of channel is nearby. We have found this case in Dense Wavelength Division Multiplexing (DWDM) that is the cause of transmission loss called Four-Wave Mixing due to the fiber nonlinear. The channel allocations that used to resolve this problem are Equally Spaced (ES), Unequally Spaced (US), Repeated Alternate US (RAUS). This paper present the new technique to arrange the channel allocation in called paired URAUS to avoid the four-wave mixing. From the simulation results, the new proposed technique has lower the effect of Four-Wave Mixing than the conventional techniques and decrease bit error probabilities and bandwidth, containing higher channels, in DWDM transmission systems.

1. INTRODUCTION

In this paper, we focus on the fact that characteristics of FWM are closely related to space channel allocations. From the viewpoint of channel allocations, Repeated Alternate US (RAUS) have been presented in [1]. Allocations were proposed and examined to overcome the problem in Equally Spaced (ES) [2] and RAUS allocations have been theoretically analysis to show lower FWM noise than that ES allocations. ES has a lot of FWM frequencies with $f_{\text{FWM}} = f_i$, where f_{FWM} is a frequency of an FWM light and f_i is a frequency of signal light with a channel index i . As a result, the signal-to-noise (S/N) ratios for ES are heavily degraded by FWM. On the other hand, in Unequally Spaced (US) [3, 4]. It is shown that if the frequency separation of any two channels of a DWDM system is a difference from that of any other pair of channels. However, the total bandwidth, which is occupied by all signal lights, expands drastically with an increase in the number of channels N_C . Thus, it is difficult to have a lot of channels in US and it can be said that there is no optimum US from the viewpoint of the total bandwidth. Especially in lightwave transmission system using optical fiber amplifiers, it is important to achieve total bandwidth as narrow as possible because the light frequency range to amplify signal light powers is limited. To overcome the problem previously described about RAUS and paired URAUS were demonstrated theoretically and experimentally. It was found that those RAUS and paired URUS have lower FWM efficiencies with $f_{\text{FWM}} = f_i$. In this paper, paired URAUS to arrange the channel allocation to avoid the effect of FWM. We consider the frequency spacing more than 50 GHz due to the limit of device optical multiplexer and demultiplexer [5]. For example, a Dispersion Shift Fiber (DSF) is supposed to have length L of 80 km, fiber loss coefficients α of 0.2 dB/km, derivative dispersion coefficient $dD/d\lambda$ of 0.06 ps/km/nm², efficiency η of 80% [6, 7]. And the generated wavelength of EDFA between 1529.55–1560.61 nm (C-band) of ITU-T G.694.1 standard for DWDM signals.

2. FUNDAMENTAL OF ANALYSIS

2.1. Four-wave Mixing

A light frequency f_{FWM} of FWM frequency, which is generated by third-order non-linear effected to three signal light frequencies f_i , f_j and f_k as follow $f_{\text{FWM}} = f_{ijk} = f_i + f_j - f_k$ ($i, j \neq k$). Because our primary concern in this paper is FWM, self-phase modulations, cross-phase modulations, and waveform degradation due to bandwidth limit are not concerned. In the DWDM system, the spacing between wavelengths may be uniformly distributed ranging from a few gigahertz to 100 GHz [8]. Which $P_{\text{FWM}}(f_m) = \sum_{fk=f_i+f_j-fm} \sum_{fj} \sum_{fi} P_{\text{FWM}}(f_{ijk})$.

The output power P_{FWM} of the FWM product is given by [9, 10].

$$P_{\text{FWM}}(f_{ijk}) = \frac{1024\pi^6}{n^4\lambda^2c^2} \left(\frac{d_{ijk}\chi^{(3)}L_{\text{eff}}}{A_{\text{eff}}} \right)^2 P_i P_j P_k e^{-\alpha L} \eta_{ijk} \quad (1)$$

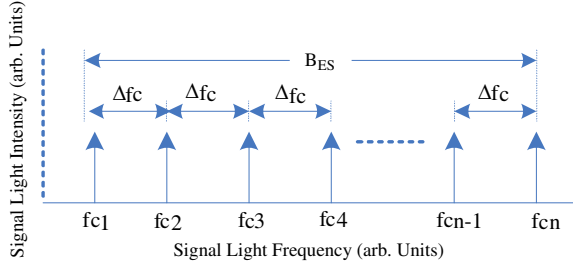


Figure 1: Channel allocation of ES.

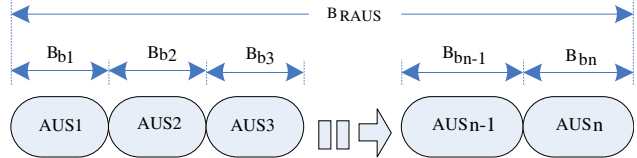


Figure 2: Channel allocation of RAUS.

where P_i , P_j and P_k represents the input power of the frequencies f_i , f_j and f_k , respectively P_{FWM} is the power of the lightwave from FWM at the frequency f_{FWM} , n is the fiber refractive index, λ is the wavelength, c is a velocity of light in a vacuum, A_{eff} is the effective core area of fiber, α is the fiber coefficients, L is fiber length, $d_{ijk} = 6$ for $i \neq j$, and $\chi^{(3)}$ is the third-order nonlinear susceptibility. The FWM efficiency η_{ijk} is given by [9, 10].

$$\eta_{\text{FWM}} = \frac{\alpha^2}{\alpha^2 + (\Delta\beta)^2} \left\{ 1 + \frac{4e^{-\alpha L} \sin^2(\Delta\beta L/2)}{(1 - e^{-\alpha L})^2} \right\} \quad (2)$$

where $\Delta\beta$ represents the phase mismatch and may be expressed in terms of signal frequency differences [9, 10]

$$\Delta\beta = \frac{2\pi\lambda^2}{c} |f_i - f_k| |f_j - f_k| \left[D + \frac{\lambda^2}{2c} \frac{dD}{d\lambda} (|f_i - f_o| + |f_j - f_o|) \right] \quad (3)$$

where f_i , f_j and f_k are light frequencies of signals, D is the fiber chromatic dispersion and $dD/d\lambda$ is a derivative dispersion coefficient of a optical fiber. If Gaussian approximation is used to describe the noise caused by FWM interference, the error probability of FWM P_e for an intensity-modulated On-Off Keying (OOK) signal is written as [9, 10].

$$P_e = \frac{1}{2\pi} \int_Q^\alpha \exp\left(-\frac{t^2}{2}\right) dt \quad (4)$$

FWM light is detected at the receiver together with the signal light, and induces the interference noise. The FWM noise power N_{FWM} is written as [9, 10]. Which $N_{\text{FWM}} = 2b^2 P_s (P_{\text{FWM}}/8)$, therefore in a DWDM system the nonlinear interaction among these frequency channels may generate interference frequency to a signal channel, and cause degradation of signal and increase bit error probability. In other words, actual noise due to FWM is expected to be lower than the calculated results in this paper.

Where P_s is the signal light power at the receiver. In case of the input light power to the fiber P_0 , the fiber length is L and fiber loss coefficients is α , $P_s = P_{\text{in}} e^{-\alpha L}$. The SNR can be expressed as [9, 10].

$$Q = \frac{bP_s}{\sqrt{N_{th} + N_{sh} + N_{\text{FWM}} + \sqrt{N_{th}}}} \quad (5)$$

Since the thermal noise N_{th} and shot noise N_{sh} are very small, N_{FWM} is the dominant factor of the denominator; $b = \eta e/\eta f$, Where h is Planck's constant, η is the quantum efficiency of the detector, and e is the elementary electric charge. It is also assumed that the APD has a quantum efficiency η of 80%.

2.2. ES and RAUS Channel Allocations

ES has signal lights with equally frequency separations between adjacent signals, as show Fig. 1. Using a channel spacing Δfc and number of channels N_C , a total bandwidth for ES B_{ES} is given by $B_{\text{ES}} = (N_C - 1)\Delta fc$.

Because Δfc is constant for each channel, a lot of FWM frequencies with $f_{\text{FWM}} = f_i$ are generated. From the frequencies of FWM lights generated within a total bandwidth always agree

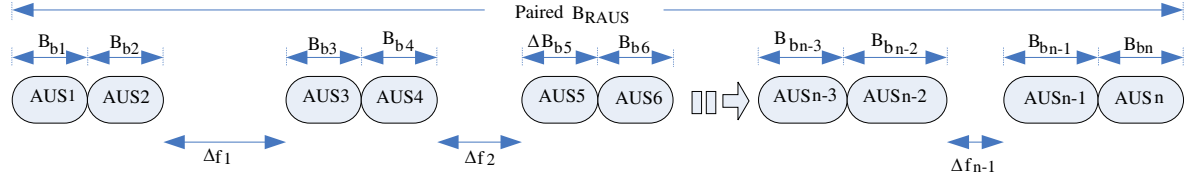


Figure 3: Channel allocation of paired URAUS.

Table 1: Example of ES Channel Allocation of ITU-T G.694.1.

Channel	1	2	3	4	5	6	7	8	38	39	40
fc (GHz)	100	100	100	100	100	100	100	100	100	100	100
fi (THz)	192.10	192.20	192.30	192.40	192.50	192.60	192.70	192.80	195.80	195.90	196.0

Table 2: Example of RAUS Channel Allocation of ITU-T G.694.1.

Channel	1	2	3	4	5	6	7	8	9	10	11	12	13	14	15	16	17	18	19	20
Δfc (GHz)	75	50	150	125	100	125	150	50	75	100	50	150	125	100	75	125	100	75	50	150
fi (THz)	192.10	192.17	192.22	192.37	192.50	192.60	192.72	192.87	192.92	193.00	193.10	193.15	193.30	193.42	193.52	193.60	193.72	193.82	193.90	193.95
Channel	21	22	23	24	25	26	27	28	29	30	31	32	33	34	35	36	37	38	39	40
Δfc (GHz)	100	75	50	150	125	75	100	125	150	50	75	50	150	125	100	75	50	125	100	100
fi (THz)	194.10	194.20	194.27	194.32	194.47	194.65	194.67	194.77	194.90	195.05	195.10	195.17	195.22	195.37	195.50	195.60	195.67	195.72	195.85	195.95

with those of signals. Table 1 shows an example of ES channel allocation with the number of channels $N_C = 40$ and the frequency spacing Δf_c of 100 GHz. US has signal lights who is frequency separation are different every two and dose not have FWM lights with $f_{FWM} = f_i$. This reason is as follows a frequency f_{ijk} of FWM frequency is related to frequencies f_i , f_j and f_k as $f_{ijk} - f_i = f_j - f_k$.

The RAUS is formed by repeating AUS_n as a base unit, is show in Fig. 2 a total bandwidth for RAUS B_{RAUS} is expressed as $B_{RAUS} = n(B_{b1} + B_{b2} + B_{b3} + \dots + B_{bn}) + B_{res}$, Here, n is the number of the base units, B_b is the bandwidth of the base unit, and B_{res} is the increases almost linearly with the number of channels N_C because RAUS repeated the base unit periodically. The term of B_{paired_URAUS} is in proportion to $(n_b - 1)$ where n_b is number of channels for the base unit and the second term is narrower than the bandwidth of the base unit B_b . If $n_c \gg n_b$, the first term is dominate in B_{RAUS} leading to $B_{RAUS} \approx nB_b$. The paired URAUS frequency allocation are new proposed, as shown in Fig. 3. Here, B_b are the same as those in RAUS [5]. The paired URAUS has difference spacings $\Delta fd = \Delta f_1, \Delta f_2, \Delta f_3, \dots$ between the adjacent paired base units. A total

bandwidth for paired URAUS is expressed as $B_{paired_URAUS} = n(B_{b1} + B_{b2} + \dots + B_{bn}) + \sum_{d=1}^{n-1} \Delta fd + B_{res}$.

Here, n is the number of paired base units, B_{b1} is the bandwidth of the AUS_1 , B_{b2} is the bandwidth of the AUS_2 , Δfd is the spacing between the d th paired base the $(d+1)$ th paired base unit, and B_{res} s the bandwidth of addition channels.

The Table 3 show paired URAUS, which corresponds to Fig. 3, and the paired based units are denoted as (AUS_1, AUS_2, \dots) in the follows. The first B_{b1} is composed of channels 1–6 next B_{b2} is composed of channel 6–11; between the channels 11 and 12 are additional channels (Δf_1), the second B_{b3} is composed of channels 12–17 and next B_{b4} is composed of channels 17–22; between the channels 22 and 23 are additional channels (Δf_2).

3. CALCULATED RESULTS AND DISCUSSION

We consider the generated wavelength of Erbium Dope Fiber Amplifier (EDFA) between 1529.55–1560.61 nm (C-Band) of ITU-T G.694.1 standard and compare the FWM characteristics of paired URAUS with ES, US and RAUS from viewpoint of FWM efficiency, and bit error probability are also briefly reviewed. For example, a Dispersion Shift Fiber (DSF) is supposed to have length L of 80 km, decay rate α of 0.2 dB/km, the derivative dispersion coefficient is $dD/d\lambda$ of 0.06 ps/km/nm², effective core area A_{eff} of 50 μm², and the Avalanche Photo Diode(APD) has a quantum efficiency η of 80%.

Table 3: Example of paired URAUS channel allocation of ITU-T G.694.1.

Channel	1	2	3	4	5	6	7	8	9	10	11	12	13	14	15	16	17	18	19	20
Δf_c (GHz)	75	50	150	125	100	125	150	50	75	100	62.5	50	150	125	100	75	125	100	75	50
f_i (THz)	192.10	192.17	192.22	192.37	192.50	192.60	192.72	192.87	192.92	193.00	193.10	193.16	193.21	193.36	193.48	193.58	193.66	193.78	193.88	193.96
Channel	21	22	23	24	25	26	27	28	29	30	31	32	33	34	35	36	37	38	39	40
Δf_c (GHz)	150	56.25	100	75	50	150	125	75	100	125	150	50	50	75	50	150	125	100	50	50
f_i (THz)	194.01	194.16	194.21	194.31	194.39	194.44	194.59	194.71	194.79	194.89	195.02	195.16	195.21	195.26	195.34	195.39	195.54	195.66	195.76	195.81

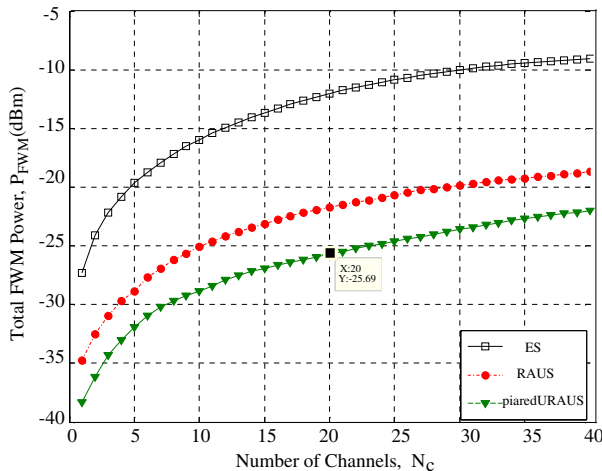


Figure 4: Compaired efficiency of FWM for channel allocations.

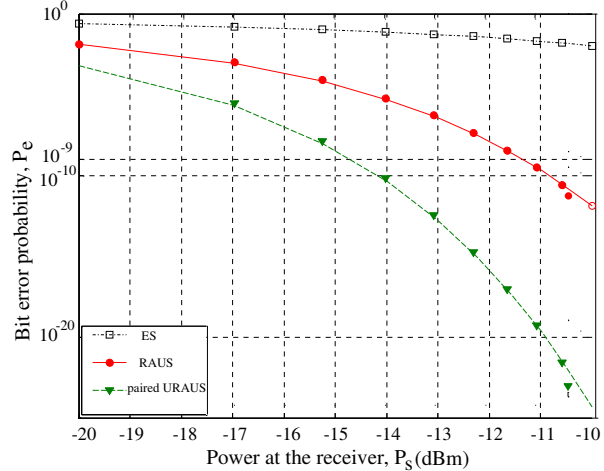


Figure 5: Compaired BER of FWM for channel allocations.

The Fig. 4 show a relation between an FWM efficiency with $f_{\text{FWM}} = f_c$ and a difference in light frequencies for ES, RAUS and paired URAUS. Here, f_{FWM} is a frequency of an FWM light and f_o is a zero-dispersion frequency, which is set at a mid-point of a total bandwidth of signal lights. It is a mid-point channel, which has the largest number of FWM frequency among all the constituent channels, for $\square = \text{ES}$, $\bullet = \text{RAUS}$ and $\blacktriangle = \text{paired URAUS}$ channel allocations respectively. An average of FWM efficiency with $f_{\text{FWM}} = f_c$ for ES, RAUS and paired URAUS is -12.03 , -21.72 and -25.69 dBm, respectively. These results are indicated that paired URAUS have lower FWM efficiencies than ES and RAUS channel allocations.

Finally, consider the error probability of FWM P_e for an intensity-modulated On-Off Keying (OOK) signal and input power per channel P_o . The horizontal line shows receiver at power per channel. The vertical line shows the bit error probability of FWM. Here, open squares, closed circles and closed triangles correspond to total power of FWM in RAUS, paired URAUS channel allocations, respectively. Receiver at power per channel P_o to achieve a BER of 10^{-9} for ES, RAUS, paired URAUS are -5 , -11.45 and -14.65 dBm, respectively. Therefor, the generated wavelength of EDFA between 1529.55–1560.61 nm, which the bit error probability of FWM P_e with $f_{\text{FWM}} = f_i$ for paired URAUS is lower bit error probabilities of FWM than ES and RAUS channel allocations.

4. CONCLUSIONS

In this paper, we proposed and analyzed the paired URAUS to arrange the channel allocation to avoid the effect of paired URAUS to arrange the channel allocation to avoid the effect of FWM by alternating groups (AUS) of the frequency spacing within base units, by the number of FWM frequencies which satisfy $f_i (i = 1, 2, 3, \dots, n)$ of paired URAUS is smaller than that of ES and RAUS. The causes of number of FWM frequencies at channel positions and FWM efficiencies reduced more than ES and RAUS allocations in DWDM system.

From the results in Figs. 4 and 5, it is concluded that paired URAUS are better than ES and RAUS channel allocations for DWDM system because of the low FWM efficiencies, and low bit error probabilities of FWM with $f_{\text{FWM}} = f_i$.

REFERENCES

1. Kojima, S. and T. Numai, "Theoretical analysis of modified repeated unequally spaced frequency allocation in FDM lightwave transmission systems," *J. Lightw. Technol.*, Vol. 24, 2786–2797, 2006.
2. Inoue, K., "Four-wave mixing in an optical fiber in the zero-dispersion wavelength region," *J. Lightw. Technol.*, Vol. 10, No. 11, 1553–1561, Nov. 1992.
3. Forghieri, F., R. Tkach, A. Chraplyvy, and D. Marcuse, "Reduction of four-wave mixing crosstalk in WDM system using unequally spaced channels," *IEEE Photon. Technol. Lett.*, Vol. 6, No.6, 754–756, Jun. 1994.
4. Forghieri, F., R. W. Tkach, and A. R. Chraplyvy, "WDM systems with unequally spaced channels," *IEEE Photon. Technol. Lett.*, Vol. 13, No. 5, 889–897, May 1995.
5. Agawal, G. P., *Fiber Optic Communication System*, 3rd Edition, John Wiley & Sons, 2002.
6. Kojima, S. and T. Numai, "Theoretical analysis of modified repeated unequally spaced frequency allocations in FDM lightwave transmission systems," *J. Lightw. Technol.*, Vol. 24, No. 7, 2786–2797, Jul. 2006.
7. Fujita, S., T. Suzuki, A. Matsuoka, S. Miyazaki, T. Torikai, T. Nakata, and M. Shikada, "High sensitivity 5Gb/s optical receiver module using Si IC and GaInAs APD," *Electron. Lett.*, Vol. 26, 175–176, 1990.
8. Kwong, W. C. and G. C. Yang, "An algebraic approach to the unequal-spaced channel-allocation problem in WDM lightwave system," *IEEE Trans. Commun.*, Vol. 45, No. 3, 352–359, Mar. 1997.
9. Zhang, L. and J. Tang, "Label-switching architecture for IP traffic over WDM network," *IEEE Proc.-Commun.*, Vol. 147, No. 5, 269–276, Oct. 2000,
10. Chin, T. S., F. M. Abbou, and E. H. Tat, "Impact of four wave mixing (FWM) in routing and wavelength assignment," *American Journal of Applied Sciences*, Vol. 5, No. 8, 1059–1063, 2008.

Generation of Diffraction-compensated Beams through a Phase Plate

Marc Brunel¹, Huanhuan Shen¹, Driss Mgharaz¹, Sébastien Coetmellec¹,
Qiulin Huang², and Kamel Ait Ameur³

¹UMR 6614 CORIA CNRS, Avenue de l'Université, BP 12, 76801 Saint-Etienne du Rouvray Cedex, France

²School of Electronic Engineering, Xidian University, Xi'an 710071, China

³CIMAP, ENSICAEN, CNRS, CEA/IRAMIS, Université de Caen, 14050 Caen Cedex, France

Abstract— We present an alternative method to generate non-diffracting beams. It consists in focusing a gaussian beam in the vicinity of a circular phase plate which transmission coefficient exceeds 90%. The latter is a binary diffractive optical element which introduces a phase shift ϕ in the central part of the incident beam. The dephasing area, which is circular, consists of a thin film of ITO (Indium Tin Oxide) disk of diameter D deposited on a silica substrate. Using our set-up, the diffracted beam can then be collimated to generate a diffraction-compensated beam.

1. INTRODUCTION

The generation of non-diffracting beams has been much investigated for the last two decades [1, 2]. Many applications exist from classical optics to nonlinear optics while different techniques exist to generate diffraction-free beams [2, 3]. Recently, we have reported a technique based on the diffraction of a gaussian beam by an opaque disk [4]. A compact configuration could be developed at the output of pigtailed laser diode [5]. The main disadvantage of this method concerns the relatively high losses induced by the opaque disk which stops the central part of the gaussian beam. Typically, the whole transmission through the opaque disk does not exceed 15 per cent [4]. This method would become particularly interesting if this difficulty could be solved. As the beam-shaping occurs by diffraction of a gaussian beam through a circular opaque disk (amplitude mask), we can wonder whether the use of a transparent diffractive optical element could lead to relatively similar results except losses. The latter is a binary diffractive optical element, referred to in this paper as a circular phase plate, which introduces a phase shift in the central part of the incident beam. Phase plates have important applications in laser physics. They allow indeed different beam shaping methods, while they do not introduce additional losses [6]. With such an element, the losses induced by the diffracting element would indeed become negligible. We present in this paper the results obtained with this new configuration. A gaussian beam is focused in the vicinity of this circular phase plate: the phase plate is actually set beyond the focus point of a gaussian beam. The diffracted beam is then collimated using a collimating lens. A beam is generated with a central spot which conserves its dimension over more than 1 meter. The results are well predicted theoretically.

2. EXPERIMENTAL RESULTS

The experimental set-up is presented in Figure 1. The laser beam is delivered by a CW He-Ne laser. The phase plate is an ITO disk of diameter D and of width e , that has been deposited on a silica substrate. The phase-shift introduced by the disk is still noted ϕ . The different parameters of the set-up are given by: $\lambda = 632.8 \text{ nm}$, $z_c = 7 \text{ cm}$, $z_l = 22 \text{ cm}$, $\phi = 0.84\pi$, $D = 280 \mu\text{m}$, $f_{\{L_2\}} = 25 \text{ cm}$. The role of the lens L_2 is to collimate the Bessel-like beam produced [4, 5, 7]. Figure 2 shows the pattern observed after the collimating lens L_2 , at different positions: 4 cm (case (a)), 48 cm (b), 72 cm (c), and 112 cm (d) after the lens L_2 . The different images are presented in pixel-unit (pixels of the CCD camera). The pixel dimension is $11 \mu\text{m} \times 11 \mu\text{m}$. We can observe a diffraction pattern composed of a central spot accompanied by concentric rings. The central spot conserves its dimension over more than one meter. Quantitatively, the dimension of the central spot radius (waist at $1/e^2$ of the maximal intensity) is $330 \mu\text{m}$, $360 \mu\text{m}$, $370 \mu\text{m}$, $360 \mu\text{m}$ in the different planes of observation (located at 4 cm, 48 cm, 72 cm and 112 cm respectively). For a gaussian laser beam of $330 \mu\text{m}$ at the wavelength of 632.8 nm , the Rayleigh length would be 54 centimeters. We can note that the beam generated here is diffraction-compensated over a propagation distance that seems smaller than what would be obtained in the case of diffraction by an opaque disk (see our previously published results in [4, 5]). Our primary simulations (whose principle is discussed in the next part) show that the ratio between this maximum propagation

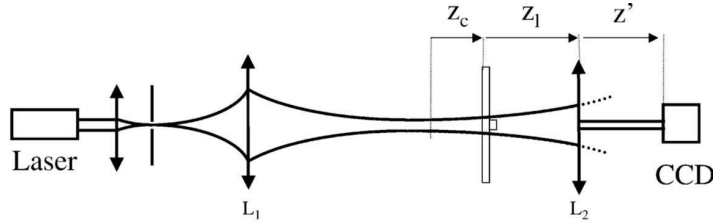
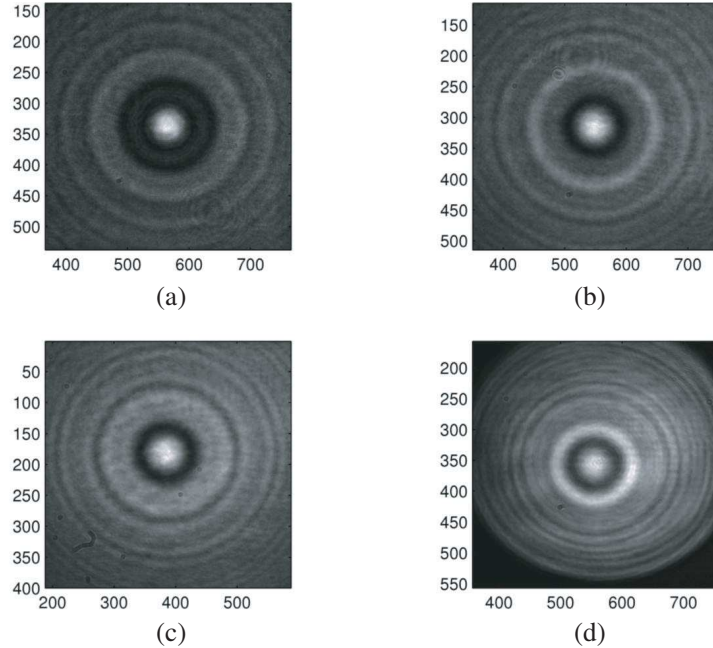


Figure 1: Experimental set-up.

Figure 2: Patterns recorded (a) 4 cm, (b) 48 cm, (c) 72 cm, and 112 cm (d) after the lens L_2 .

distance and the Rayleigh length depends strongly on the combination of the phase disk diameter, its longitudinal position, and the characteristics of the collimating lens. In addition, the phase shift that is introduced is another important parameter in our present case. In the next future, we will carry some systematic optimization to determine the best configuration while the present study establishes clearly the feasibility of the method. The most important property of our method concerns the losses introduced: the losses introduced by the phase plate are very low in the present case: only the residual losses induced by the reflection on the plate, i.e., approximately 8%. For comparison, the losses introduced by an opaque disk would approach 85%.

3. COMPARISON WITH SIMULATIONS

A theoretical investigation has then been realized. The incident beam is modeled by a Gaussian beam. The phase plate induces a phase-shift between the center and the wings of the transmitted beam. The theoretical expression of the electric field can be deduced from an analysis that is deduced from the one developed in the case of an opaque diffracting element [4] and that is detailed in reference [8] which considered the case of digital phase contrast experiments. The collimating lens L_2 is then modeled through a complex transmission function, while free space propagation is expressed by the propagation operator (Fresnel transform). The amplitude of the electric field that is diffracted at distance z' after the lens L_2 can finally be evaluated numerically.

Let us now model the behavior quantitatively, using this exact analysis. The exact parameters of the experiment have been used for our simulations. Figure 3 shows the patterns that are predicted in the plane of the lens L_2 (Figure 3(a)), 4 cm after the lens L_2 (Figure 3(b)) and 48 cm after the lens L_2 (Figure 3(c)). These two last patterns can be directly compared to the experimental patterns of Figures 2(a) and 2(b) respectively. For comparison, Figure 4 shows now the experimental (dotted)

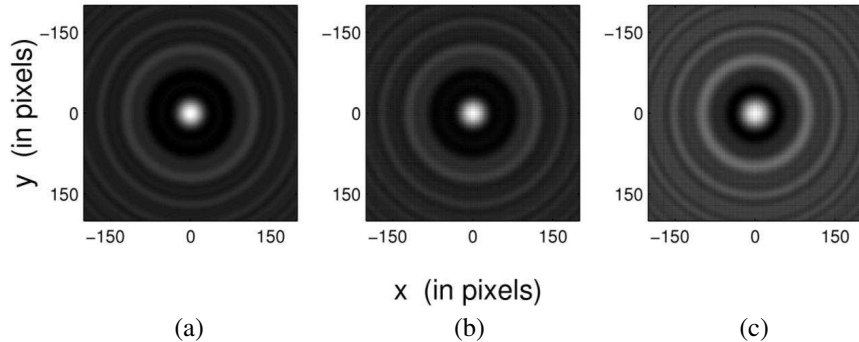


Figure 3: Patterns simulated in the plane of the lens L_2 (a), 4 cm after the lens L_2 (b) and 48 cm after the lens L_2 (c).

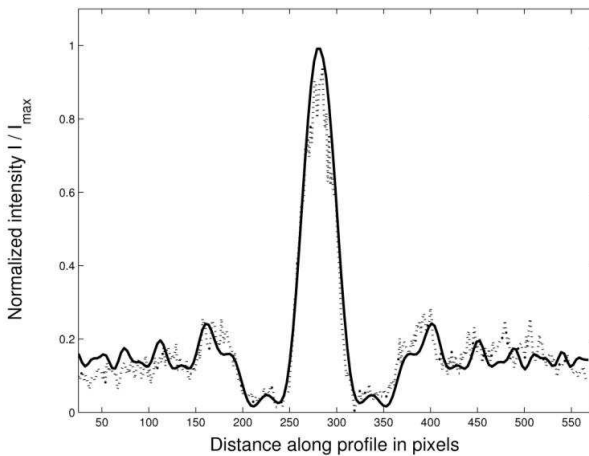


Figure 4: Experimental (dotted line) and theoretical (solid line) profiles of the beam observed 4 cm after the collimating lens.

line) and theoretical (solid line) intensity profiles extracted from the patterns observed or predicted 48 cm after the lens L_2 . Experimental results are well predicted by the simulations. The small differences are only due to some imprecision when evaluating the parameters z_l or z_c .

4. CONCLUSION

In conclusion, a new method has been proposed to realize diffraction-compensated beams. It consists in focusing a Gaussian beam in the vicinity of a circular phase plate. The diffracted beam can then be collimated to generate a beam that is diffraction-compensated over a distance which exceeds 1.1 meter. The phase plate introduces only low losses (only 8 percent). Our next developments will consider the numerical optimization of this configuration for the generation of diffraction-compensated beams over longer distances, without higher losses.

ACKNOWLEDGMENT

This work is supported by Carnot ESP and Pôle Universitaire Normand.

REFERENCES

1. Durnin, J., J. J. Miceli, Jr, and J. H. Eberly, "Diffraction free beams," *Phys. Rev. Lett.*, Vol. 58, 1499–1501, 1987.
2. McGloin, D. and K. Dholakia, "Bessel beams, diffraction in a new light," *Contemporary Physics*, Vol. 46, 15–28, 2005.

3. Wulle, T. and S. Herminghaus, “Nonlinear optics of Bessel beams,” *Phys. Rev. Lett.*, Vol. 70, 1401–1404, 1993.
4. Brunel, M. and S. Coëtmellec, “Generation of non diffracting beam through an opaque disk,” *J. Opt. Soc. Am. A*, Vol. 24, 3753–3761, 2007.
5. Brunel, M., D. Mgharaz, and S. Coëtmellec, “Generation of diffraction-compensated beams with a pigtailed laser diode,” *IEEE Photon. Technol. Lett.*, Vol. 20, 742–744, 2008.
6. Ait Ameur, K., F. Sanchez, and M. Brunel, “High transverse mode discrimination in apertured resonators using diffractive binary optics,” *Opt. Commun.*, Vol. 184, 73–78, 2000.
7. Khonina, S. N., V. V. Kotlyar, R. V. Skidanov, V. A. Soifer, et al., “Rotation of microparticles with Bessel beams generated by diffractive elements,” *Journal of Modern Optics*, Vol. 51, 2167–2184, 2004.
8. Brunel, M., S. Coëtmellec, D. Lebrun, and K. Ait Ameur, “Digital phase contrast with the fractional Fourier transform,” *Appl. Opt.*, Vol. 48, 579–583, 2009.

Generation of Perfect 3D Dark Spots Using Double-ring Cylindrical Vector Vortex Beams

Yaoju Zhang, Zhonghua Ma, and Youyi Zhuang

College of Physics and Electronic Information, Wenzhou University, Wenzhou, Zhejiang 325035, China

Abstract— A 3D dark spot is generated by using a double-ring-shaped cylindrical vector vortex beam which can be considered as a vector superposition of a double-ring-shaped radially-polarized light and a double-ring-ring-shaped azimuthally-polarized light. The volume of the 3D dark spot generated is very small and the light wall surrounding the dark spot is very uniform. This 3D dark spot is very perfect for particle trapping and for super-resolution fluorescence microscopy.

1. INTRODUCTION

Three-dimensional (3D) dark spots or bottle beams surrounded by light at all direction are applied in many areas in optics, such as dark-spot optical traps for atoms they will seek the dark or the low-field region so that the field distribution will not substantially be disturbed by the presence of atoms [1, 2] and for microparticles whose refractive index is smaller than the ambience [3, 4]. In super-resolution fluorescence microscopy, a 3D dark spot is used as the erase beam [5–8]. Several methods have been used to produce 3D bottle beams that have an intensity null surrounded by light in all directions. Some of these approaches require optical access from several sides or the use of custom optical polarization plates, holograms, or spatial light modulators. A simple method to create a 3D bottle beam is to use a one-order radially polarized beam ($R\text{-TEM}_{11}^*$) [9]. The $R\text{-TEM}_{11}^*$ beam can also be applied to increase the focal depth of a near-field optical storage system [10]. However, a serious drawback of the 3D dark spot generated by the $R\text{-TEM}_{11}^*$ beam is that the maximum light intensity surrounding the dark focal spot is much lower at the diagonal direction in light meridian plane than that along the optical axis (see Fig. 2(a)) and the uniformity of the light “wall” surrounding the 3D dark spot is about 0.35. Similar phenomena exists also in a interference generating an optical bottle beam trap by interfering two fundamental Gaussian beams with different waists [2] and in a circular two-zone π -phase plate method to create a 3D bottle beam where the maximum light intensity surrounding the dark focal spot is much lower in the transverse directions than along the optical axis [11]. If such beams are used as the erase beam in super-resolution fluorescence microscopy, the overall erase beam power cannot be increased to induce efficient fluorescence depletion in the diagonal direction or in the transverse direction, without causing photo-damage along the axial direction, limiting the super-resolution in the diagonal or transverse direction to a relatively small factor. In dark traps for atoms or biological particles, the depth of the trap is determined by the minimal intensity of the light wall, hence the high non-uniformity of the light wall reduces the trap depth for a given laser power. In this paper, we propose a method to generate a 3D dark spot using a double-ring-shaped cylindrical vector vortex beam. The volume of the generated 3D dark spot is very small and the uniformity of light wall surrounding the dark spot is quite high.

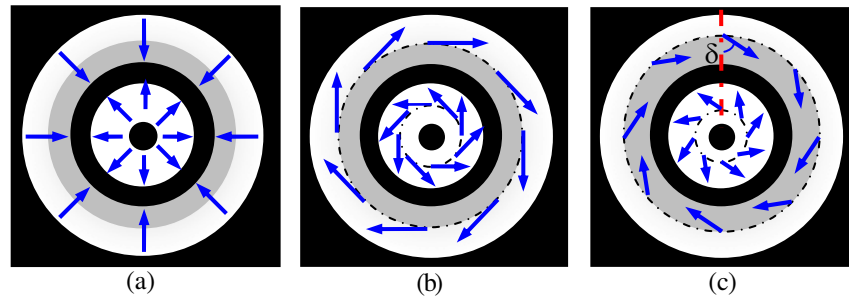


Figure 1: The instantaneous polarization states of the double-ring-shaped cylindrical vector beams. (a) Radially polarized beam, (b) azimuthally polarized beam, and (c) a general vortex vector beam with a vortex angle of δ .

2. GENERATION OF A PERFECT 3D DARK SPOT

Figure 1(c) shows the instantaneous polarization state of a double-ring-shaped cylindrical vector vortex beam. A general cylindrical vector vortex beam with vortex angle of δ can be considered as the coherent superposition of two radially (Fig. 2(a)) and azimuthally (Fig. 2(b)) polarized beams which can generate directly inside a laser cavity [12] or outside the laser cavity [13]. When a double-ring-shaped cylindrical vector vortex beams is incident on a high-numerical-aperture lens, electric fields in the focal region can be obtained, according to the vector diffraction theory [14], as

$$E_r(r, z) = \eta \cos \delta \int_0^\alpha \sqrt{\cos \theta} A(\theta) \sin 2\theta J_1(k_1 r \sin \theta) \exp(ik_1 z \cos \theta) d\theta, \quad (1)$$

$$E_\varphi(r, z) = 2\eta \sin \delta \int_0^\alpha \sqrt{\cos \theta} A(\theta) \sin \theta J_1(k_1 r \sin \theta) \exp(ik_1 z \cos \theta) d\theta, \quad (2)$$

$$E_z(r, z) = 2i\eta \cos \delta \int_0^\alpha \sqrt{\cos \theta} A(\theta) \sin^2 \theta J_0(k_1 r \sin \theta) \exp(ik_1 z \cos \theta) d\theta, \quad (3)$$

where η is a constant related to the power of the incident laser, $k_1 = kn = 2\pi n/\lambda$ is the wavenumber in the immersion liquid with the refractive index n . J_n is the n th-order Bessel function of the first kind. (r, φ, z) are the cylindrical coordinates centered at the geometric focus and the optical axis is along the z axis. $A(\theta)$ represents the amplitude and phase distribution at the exit pupil. For a double-ring-shaped beam, $A(\theta)$ can be expressed as [10]

$$A(\theta) = \frac{\beta \sin \theta}{\sin \alpha} \exp \left[- \left(\frac{\beta \sin \theta}{\sin \alpha} \right)^2 \right] L_1 \left[2 \left(\frac{\beta \sin \theta}{\sin \alpha} \right)^2 \right], \quad (4)$$

where L_1 is the generalized Laguerre polynomial with two rings and $\beta = R/w$ is called the truncation parameter where w is the waist of Gauss beam and R is the radius of the aperture inserted in the front of the objective. For the double-ring-shaped radially polarized beam, β should be larger than 1 because the outer ring of the beam will be completely blocked by the pupil if $\beta < 1$.

Figure 2 shows the intensity distributions in the immersion oil with $n = 1.515$ refractive index when $\beta = 1.3$ and NA = 1.48. If the vortex angle δ equals to 0.5π , the incident beam becomes an azimuthally polarized one. In this case, the intensity along the optical axis is null and a 2D hollow beam can be generated, as shown in Fig. 2(d), but a 3D dark spot can not be formed. When $\delta = 0$,

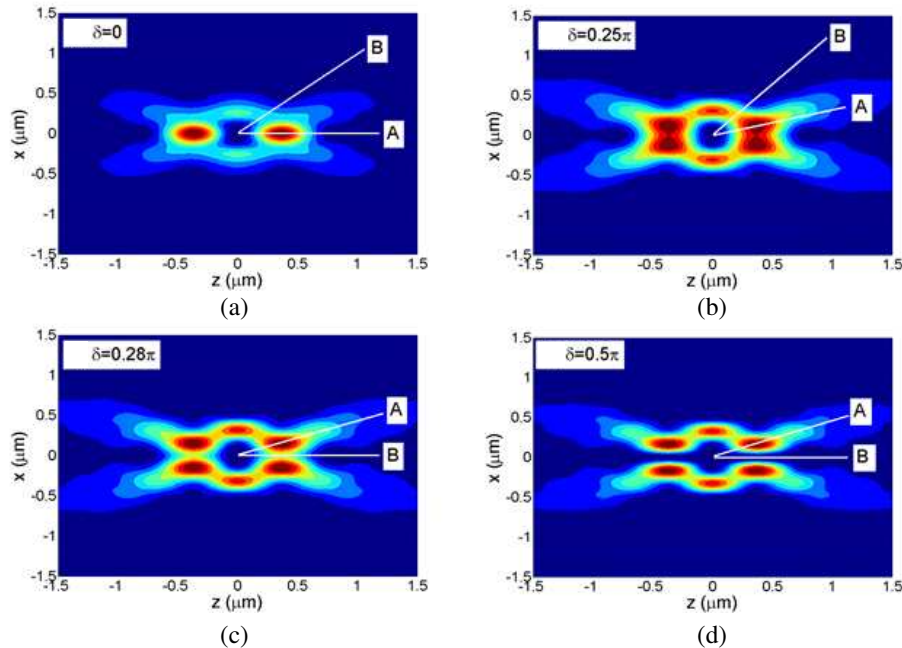


Figure 2: The focused patterns for double-ring-shaped cylindrical vector vortex beams with different vortex angles of δ .

the incident beam becomes a radially polarized one and a 3D dark spot can be generated (see Fig. 2(a)), as shown in Ref. [8]. However, the intensity at the diagonal direction is much smaller than that at the optical axis, that is to say, the uniformity of the light wall surrounding the 3D dark spot is low. If the uniformity (U) of light wall surrounding the 3D dark spot is defined as the ratio of the maximum intensity (I_B) of the lowest value in the light wall (at the B direction in Fig. 2) to the maximum intensity (I_A) of the highest value in the light wall (at the A direction), $U = 0.35$ for the double-ring-shaped radially polarized beam focusing in Fig. 1(a). When the vortex angle is close to 0.25π , however, the 3D dark spot is quite perfect, as shown in Figs. 2(b) and (c). From Fig. 2, it can be seen that the vortex angle δ determines the uniformity of a light wall. Our calculation results show that when $\delta=0.25\pi$, the light wall is most uniform with $U = 0.67$ (Fig. 2(b)) and the volume of the 3D dark spot is $0.311\lambda^3$ for the system parameters of $\beta = 1.3$ and NA = 1.48.

3. CONCLUSION

In conclusion, we have generated a 3D dark spot by using a double-ring-shaped cylindrical vector vortex beam with the vortex angle of 0.25π . The uniformity of the light wall of the generated 3D dark spot is quite high. This 3D dark spot is very perfect for particle trapping and for super-resolution fluorescence microscopy.

ACKNOWLEDGMENT

This work was supported by the National Natural Science Foundation of China under contract 61078023.

REFERENCES

1. Kaplan, A., N. Friedman, and N. Davidson, “Optimized single-beam dark optical trap,” *J. Opt. Soc. Am. B*, Vol. 19, No. 6, 1233–1238, 2002.
2. Isenhower, L., W. Williams, A. Dally, and M. Saffman, “Atom trapping in an interferometrically generated bottle beam trap,” *Opt. Lett.*, Vol. 34, No. 8, 1159–1161, 2009.
3. Gahagan, K. T. and G. A. Swartzlander, “Optical vortex trapping of particles,” *Opt. Lett.*, Vol. 21, No. 11, 827–829, 1996.
4. Zhang, Y., B. Ding, and T. Suyama, “Trapping two types of particles using a double-ring-shaped radially polarized beam,” *Phys. Rev. A*, Vol. 81, 023831, 2010.
5. Watanabe, T., Y. Iketaki, T. Omatsu, K. Yamamoto, M. Sakai, and M. Fujii, “Two-point-separation in super-resolution fluorescence microscope based on up-conversion fluorescence depletion technique,” *Opt. Express*, Vol. 11, No. 24, 3271–3276, 2003.
6. Hell, S. W., “Far-field optical nanoscopy,” *Science*, Vol. 316, 1153–1158, 2007.
7. Keller, J., A. Schönle, and S. W. Hell, “Efficient fluorescence inhibition patterns for RESOLFT microscopy,” *Opt. Express*, Vol. 15, No. 6, 3361–3371, 2007.
8. Harke, B., C. K. Ullal, J. Keller, and S. W. Hell, “Three-dimensional nanoscopy of colloidal crystals,” *Nano Letters*, Vol. 8, No. 5, 1309–1313, 2008.
9. Kozawa, Y. and S. Sato, “Focusing property of a double-ring-shaped radially polarized beam,” *Opt. Lett.*, Vol. 31, No. 6, 820–822, 2006.
10. Zhang, Y. and J. Bai, “Improving the recording ability of a near-field optical storage system by higher-order radially polarized beams,” *Opt. Express*, Vol. 17, No. 5, 3698–3706, 2009.
11. Bokor, N. and N. Davidson, “Tight parabolic dark spot with high numerical aperture focusing with a circular p phase plate,” *Opt. Commun.*, Vol. 270, No. 2, 145–150, 2007.
12. Moser, T., H. Glur, V. Romano, F. Pigeon, O. Parriaux, M. A. Ahmed, and T. Graf, “Polarization-selective grating mirrors used in the generation of radial polarization,” *Appl. Phys. B*, Vol. 80, No. 6, 707–713, 2005.
13. Yonezawa, K., Y. Kozawa, and S. Sato, “Generation of a radially polarized laser beam by use of the birefringence of a c-cut Nd:YVO₄ crystal,” *Opt. Lett.*, Vol. 31, No. 14, 2151–2153, 2006.
14. Youngworth, K. S. and T. G. Brown, “Focusing of high numerical aperture cylindrical-vector beams,” *Opt. Express*, Vol. 7 No. 2, 7787, 2000.